Etude des modifications du taux d'émission spontanée de sources internes utilisées comme sondes des variations de densités locales d'états photoniques dans des matériaux aussi divers que des milieux désordonnés polymères ou inorganiques, des cristaux photoniques et des nanostructures plasmoniques.

Renaud Vallée

▶ **To cite this version:**

Renaud Vallée. Etude des modifications du taux d'émission spontanée de sources internes utilisées comme sondes des variations de densités locales d'états photoniques dans des matériaux aussi divers que des milieux désordonnés polymères ou inorganiques, des cristaux photoniques et des nanostructures plasmoniques.. Optique [physics.optics]. Université Sciences et Technologies - Bordeaux I, 2012. tel-00700983

HAL Id: tel-00700983
https://theses.hal.science/tel-00700983

Submitted on 24 May 2012

HAL is a multi-disciplinary open access archive for the deposit and dissemination of scientific research documents, whether they are published or not. The documents may come from teaching and research institutions in France or abroad, or from public or private research centers.

L'archive ouverte pluridisciplinaire **HAL**, est destinée au dépôt et à la diffusion de documents scientifiques de niveau recherche, publiés ou non, émanant des établissements d'enseignement et de recherche français ou étrangers, des laboratoires publics ou privés.

Habilitation à Diriger des Recherches - Etude des modifications du taux d'émission spontanée de sources internes utilisées comme sondes des variations de densités locales d'états photoniques dans des matériaux aussi divers que des milieux désordonnés polymères ou inorganiques, des cristaux photoniques et des nanostructures plasmoniques.

R. A. L. Vallée*
Centre de Recherche Paul Pascal

Membres du jury:

Professeur Rémi Carminati, ESPCI, Paris: rapporteur
Professeur Brahim Lounis, LP2N, Bordeaux: rapporteur
Professeur Michel Orrit, MoNOS, Leiden: rapporteur
DR Bernard Pouligny, CRPP, Bordeaux: examinateur
Professeur Niek van Hulst, ICFO, Barcelone: examinateur

Date de soutenance: 02/05/2012

Le document ci-après regroupe:

1) un CV détaillé, présentant mes activités d'enseignement, de recherche et d'administration.
2) une copie de mon diplôme de thèse obtenue l'Université de Mons en Belgique en 2000.
3) des attestations d'encadrements d'étudiants en master et en thèse durant mes stages postdoctoraux effectués aux Pays-Bas et en Belgique.
4) une description concise de mes activités de recherche depuis la fin de ma thèse. Dans cette description, j'ai choisi de discuter 24 des 57 papiers mentionnés dans mon CV. 4 thèmes (grands axes de recherche) sont abordés:
i) Les changements des taux d'émission spontanée de sources internes dus aux variations locales de densité du milieu polymère environnant;
ii) Les changements des taux d'émission spontanée consécutives aux changements de conformation des molécules fluorescentes dus aux mouvements des chaînes environnantes;
iii) l'étude de l'inhibition/exaltation de l'émission de fluorescence dans les cristaux photoniques;
iv) l'émission dans les nanostructures plasmoniques.
Dans chacun des cas, quelques points pertinents ont été relevés et expliqués avec plus de détail notamment à l'aide d'une figure et la référence appropriée a été insérée.

5) une description concise des projets futurs envisagés qui se répartissent en trois thèmes:

i) développer des matériaux extrêment désordonnés afin d'étudier les phénomènes de localisation de la lumière et de lasers aléatoires, en collaboration avec Rénal Backov au CRPP et l'équipe de Rémi Carminati à l'ESPCI.
ii) développer des nanostructures plasmoniques combinant plasmons de surface localisés et propagatifs afin de générer des facteurs de Purcell élevés dans une gamme spectrale soit très large soit très fine, en collaboration avec Serge Ravaine au CRPP.
iii) développer des structures plasmoniques sensibles à l'effet Kerr optique afin de réaliser des bistables optiques.
6) une compilation des 24 papiers discutés dans la partie 4, que le lecteur intéressé pourra consulter à loisir.

* vallee@crpp-bordeaux.cnrs.fr;

Curriculum vitae Europass

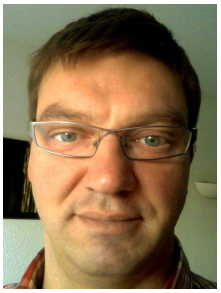

Information personnelle

Nom(s) / Prénom(s)	**Vallée Renaud**
Adresse	115, avenue du docteur Albert Schweitzer, 33600 Pessac (France)
Téléphone(s)	+33 556845612 Portable | +33 667496739
Télécopie(s)	+33 56845600
Courrier électronique	vallee@crpp-bordeaux.cnrs.fr
Nationalité	Belgian
Date de naissance	31/10/1969
Sexe	Masculin

Emploi recherché / Domaine de compétence

Researcher - Physicist

Expérience professionnelle

Dates	01/09/1998 - 31/12/2000
Fonction ou poste occupé	Ph. D. thesis
Principales activités et responsabilités	Assistant Professor at the University of Mons-Hainaut (Belgium) in the group of Prof. M. Dosière (Physical Chemistry of Polymers).
Nom et adresse de l'employeur	University of Mons-Hainaut 7000 Mons (Belgique)
Type ou secteur d'activité	Research
Dates	01/09/2000 - 31/08/2002
Fonction ou poste occupé	Postdoc
Principales activités et responsabilités	Postdoctoral researcher at the University of Enschedé (The Netherlands) in the groups of Profs. N. F. van Hulst (Applied Optics) and G. J. Vancso (Materials Science and Technology of Polymers).
Nom et adresse de l'employeur	University of Twente PO Box 217, 7500 Enschedé (The Netherlands)
Type ou secteur d'activité	Research
Dates	01/09/2002 - 30/09/2008
Fonction ou poste occupé	Postdoc
Principales activités et responsabilités	Postdoctoral researcher at the University of Leuven (Katholieke Universiteit Leuven) in the department of Chemistry (Prof. Van der Auweraer, Photochemistry and spectroscopy) and Institute of Nanoscale Physics and Chemistry (INPAC).
Nom et adresse de l'employeur	FWO - Fonds voor Wetenschappelijk Onderzoek Egmonstraat, 1000 Bruxelles (Belgique)
Type ou secteur d'activité	Research
Dates	01/10/2008 →
Fonction ou poste occupé	CNRS researcher
Principales activités et responsabilités	Researcher at The Centre de Recherche Paul Pascal
Nom et adresse de l'employeur	CNRS (Centre National de la Recherche Scientifique)

Pour plus d'information sur Europass: http://europass.cedefop.europa.eu
© Union européenne, 2002-2010 24082010

	Esplanade des Arts et Metiers, 33402 Talence (France)
Type ou secteur d'activité	Research
Dates	01/10/2009 →
Fonction ou poste occupé	
Principales activités et responsabilités	Member of the Cnano GSO (Nanoscience in the Great South West of France, Spain and Portugal) scientific commission.
Nom et adresse de l'employeur	
Type ou secteur d'activité	
Dates	01/03/2010 →
Principales activités et responsabilités	Member of the MCIA (Mesocenter for Intensive Calculation in Aquitaine) scientific commission.
Nom et adresse de l'employeur	
Dates	01/06/2010 →
Principales activités et responsabilités	Responsible of the scientific library at CRPP.
Nom et adresse de l'employeur	
Dates	18/11/2010 →
Principales activités et responsabilités	Member of the CRPP laboratory council.
Nom et adresse de l'employeur	

Education et formation

Dates	01/09/1987 - 30/06/1989
Intitulé du certificat ou diplôme délivré	Bachelor in Physics
Nom et type de l'établissement d'enseignement ou de formation	University of Mons- Hainaut (UMH) 7000 Mons (Belgium)
Dates	01/09/1989 - 30/06/1991
Intitulé du certificat ou diplôme délivré	Master in physics
Principales matières/compétences professionnelles couvertes	Theoretical Physics
Nom et type de l'établissement d'enseignement ou de formation	University of Mons-Hainaut (UMH) 7000 Mons (Belgium)

Aptitudes et compétences personnelles

Langue(s) maternelle(s) **French**

Autre(s) langue(s)

Auto-évaluation	Comprendre				Parler				Ecrire	
Niveau européen (*)	Ecouter		Lire		Prendre part à une conversation		S'exprimer oralement en continu			
English	C1	Utilisateur expérimenté	C1	Utilisateur expérimenté	C1	Utilisateur expérimenté	C1	Utilisateur expérimenté	C1	Utilisateur expérimenté
Dutch	B1	Utilisateur indépendant	B1	Utilisateur indépendant	B1	Utilisateur indépendant	B1	Utilisateur indépendant	B1	Utilisateur indépendant
German	A1	Utilisateur élémentaire	A1	Utilisateur élémentaire	A1	Utilisateur élémentaire	A1	Utilisateur élémentaire	A1	Utilisateur élémentaire

(*) *Cadre européen commun de référence (CECR)*

Pour plus d'information sur Europass: http://europass.cedefop.europa.eu
© Union européenne, 2002-2010 24082010

Aptitudes et compétences sociales	- Team spirit; - Good ability to adapt to multicultural environments, gained through my work experience abroad; - Good communication skills gained through my work experience abroad.
Aptitudes et compétences organisationnelles	- Leadership (currently responsible for 2 Ph. D students); - Sense of organisation; - Good experience in project management gained through regional, ANR, European contributions.
Aptitudes et compétences techniques	Experiment: X-ray diffraction, in geometry q/2q and Grazing Incidence X-ray Diffraction (GIXD, goniometer 4 circles) Fourier Transform Infrared Spectroscopy (FTIR) Differential Scanning Calorimetry (DSC), Dynamic Mechanical Analysis (DMA) Linear, nonlinear (pulsed LASER) Microscopy, Spectroscopy Confocal Microscopy Single Molecule Spectroscopy (scanning inverted optical confocal microscope) A tiny bit of Atomic Force Microscopy (AFM) and Near-field Scanning Optical Microscopy (NSOM) Simulation: Quantum Chemistry: semi-empirical AM1 (MOPAC and AMPAC packages) and ZINDO methods Atomistic and coarse-grained molecular dynamics simulation: expertise with the Materials Studio package (from Accelrys) and the OCTA suite, developed on the impulsion of Prof. M. Doi in Japan for the simulation of polymer and soft matter. Computation of band structures (dispersion relations) and electromagnetic modes of periodic dielectric structures (photonic crystals) via the MIT Photonic-Bands (MPB) package and time-domain simulations, reflection/transmission spectra via their complementary Meep package.
Aptitudes et compétences informatiques	Working knowledge of the Windows and Linux operating systems and their principal softwares Programming in Labview, Matlab, Python, C and Fortran Linux scripts (bash, ed, awk, tcl, …)
Autres aptitudes et compétences	Sports: biking, running, sailing, skiing, swimming, badmington, squash.
Permis de conduire	B
Information complémentaire	PUBLICATIONS DANS DES JOURNAUX INTERNATIONAUX AVEC COMITE DE LECTURE 1. P. Damman, R. Vallée, M. Dosière, J.-C. Wittmann, E. Toussaere, J. Zyss; Optical Material 9 (1998) 423. 2. R. Vallée, P. Damman, M. Dosière, E. Toussaere and J. Zyss; 'Nonlinear Optical Properties and Crystalline Orientation of 2-Methyl-4-nitroaniline Layers Grown on Nanostructured Poly(tetrafluoroethylene) Substrates'; J. Am. Chem.Soc. 122 (2000) 6701. 3. R. Vallée, P. Damman, M. Dosière, E. Toussaere and J. Zyss; 'Orientation and nonlinear optical properties of 4 – (N,N-dimethylamino) – 3 - acetamidonitrobenzene) crystals on nanostructured poly(tetrafluoroethylene) substrates'; J. Chem. Phys. 112 (2000) 10556. 4. R. Vallée, P. Damman, M. Dosière, E. Toussaere and J. Zyss; 'Orientation and non linear optical properties of DAN crystals on PTFE substrates'; Nonlinear Optics 25 (2000) 345. 5. R. Vallée, M. Wautelet, J. P. Dauchot and M. Hecq; 'Size and segregation effects on the phase diagrams of nanoparticles of binary systems'; Nanotechnology 12 (2001) 68. 6. M. García Parajó, J.-A. Veerman, Rudo Bouwhuis, R. Vallée, and N. F. van Hulst; 'Optical probing of single fluorescent molecules and proteins'; ChemPhysChem 2 (2001) 11.

Pour plus d'information sur Europass: http://europass.cedefop.europa.eu
© Union européenne, 2002-2010 24082010

7. P. Damman, R. Vallée, M. Dosière, E. Toussaere, J. Zyss; 'Oriented crystallization of NLO organic materials'; Synthetic Metals 124 (2001) 227.

8. R. Vallée, P. Damman, M. Dosière, G. Scalmani and J. L. Brédas; 'A Joint Experimental and Theoretical Study of the Infrared Spectra of 2-Methyl-4-nitroaniline Crystals Oriented on Nanostructured Poly(Tetrafluoroethylene) Substrates'; J. Phys. Chem. B 105 (2001) 6064.

9. R. Vallée, P. Damman, and M. Dosière, E. Toussaere, J. Zyss; 'Orientation and nonlinear optical properties of N-4-nitrophenyl-(L)-prolinol crystals on nanostructured poly(tetrafluoroethylene) substrates'; J. Chem. Phys. 115 (2001) 5589.

10. R. Vallée, N. Tomczak, H.Gersen, E.M.H.P. Vandijk, M.F. García-Parajó, G.J. Vancso and N. F. van Hulst, 'On the role of electromagnetic boundary conditions in single molecule fluorescence lifetime studies of dyes embedded in thin films'; Chem. Phys. Lett. 348 (2001) 161.

11. L. Beekmans, R. Vallée, G.J. Vancso; 'Nucleation and Growth of Poly(e-caprolactone) on Poly(tetrafluoroethylene) by in-Situ AFM'; Macromolecules 35 (2002) 9383.

12. Vallée, R.A.L.; Vancso, G.J.; van Hulst, N.F.; Calbert J.-P.; Cornil, J.; Brédas, J.L.; 'Molecular fluorescence lifetime fluctuations: on the possible role of conformational effects'; Chem. Phys. Lett. 372 (2003) 282.

13. Vallée, R. A. L.; Tomczak, N.; Kuipers, L.; Vancso, G.J.; van Hulst, N. F.; 'Single Molecule Lifetime Fluctuations Reveal Segmental Dynamics in Polymers'; Phys. Rev. Lett. 91 (2003) 038301.

14. Vallée, R.A.L.; Cotlet, M.; Hofkens, J.; De Schryver, F.C.; Müllen, K.; 'Spatially Heterogeneous Dynamics in Polymer Glasses at Room Temperature Probed by Single Molecule Lifetime Fluctuations'; Macromolecules 36 (2003) 7752.

15. Tomczak, N.; Vallée, R.A.L.; van Dijk, E.M.H.P.; Garcia-Parajo, M.; Kuipers, L.; van Hulst, N.F.; Vancso, G.J.; 'Probing polymer with single fluorescent molecules'; Eur Polym J 40 (2004) 1001.

16. Vallée, R.A.L.; Tomczak, N.; Kuipers, L.; Vancso, G.J.; van Hulst, N.F.; 'Effect of solvent on nanoscale polymer heterogeneity and mobility probed by single molecule lifetime fluctuations'; Chem. Phys. Lett. 384 (2004) 5.

17. Vallée, R.A.L.; Cotlet, M.; Van Der Auweraer, M.; Hofkens, J.; Müllen, K.; De Schryver, F.C.; 'Single-Molecule Conformations Probe Free Volume in Polymers'; J. Am. Chem. Soc. 126 (2004) 2296.

18. Tomczak, N.; Vallée, R.A.L.; van Dijk, E.M.H.P.; Kuipers, L.; Vancso, G.J.; van Hulst, N.F.; 'Segment Dynamics in Thin Polystyrene Films Probed by Single-Molecule Optics'; J. Am. Chem. Soc. 126 (2004) 4748.

19. Schroeyers, W.; Vallée, R.A.L.; Patra, D.; Hofkens, J.; Habuchi, S.; Vosch, T.; Cotlet, M.; Müllen, K.; Enderlein, J.; De Schyver, F.; 'Fluorescence Lifetimes and Emission Patterns Probe the 3D Orientation of the Emitting Chromophore in a Multichromophoric System'; J. Am. Chem. Soc., 126 (2004) 14310.

20. Vallée, R.A.L.; Van Der Auweraer, M.; De Schryver, F.C.; Beljonne, D.; Orrit, M.; 'A Microscopic Model for the Fluctuations of Local Field and Spontaneous Emission of Single Molecules in Disordered Media'; ChemPhysChem, 6 (2005) 81.

21. Vallée, R.A.L.; Tomczak, N.; Kuipers, L.; Vancso, G.J.; van Hulst, N.F.; 'Fluorescence lifetime fluctuations of single molecules probe local density fluctuations in disordered media: A bulk approach'; J. Chem. Phys., 122 (2005) 114704.

22. Vallée, R.A.L.; Marsal, P; Braeken, E.; Habuchi, S.; De Schryver, F.C.; Van Der Auweraer, M.; Beljonne, D.; Hofkens, J.; 'Single Molecule Spectroscopy as a Probe for Dye-Polymer Interactions'; J. Am. Chem. Soc. 127 (2005) 12011.

23. Baruah, M.; Qin, W.; Vallée, R.A.L; Beljonne, D.; Rohand, T.; Dehaen, W.; Boens, N.; 'A Highly Potassium-Selective Ratiometric Fluorescent Indicator Based on BODIPY® Azacrown Ether Excitable with Visible Light'; Org. Lett., 7 (2005) 4377.

24. K. Song, R. Vallée, M. Van der Auweraer, K. Clays; 'Fluorophores-modified silica sphere as emission probe in photonic crystals'; Chem. Phys. Lett. 421 (2006) 1.

25. K. Song, R. Vallée, M. Van der Auweraer, K. Clays; ' Spontaneous emission of nano-engineered fluorophores in photonic crystals', J. Nonlinear. Opt. Phys. 15 (2006) 1.

26. M. Baruah, W. Qin, C. Flors, J. Hofkens, R. A. L. Vallée, D. Beljonne, M. Van der Auweraer, W. M. De Borggraeve, and N. Boens; 'Solvent and pH Dependent Fluorescent Properties of a Dimethylaminostyryl Borondipyrromethene Dye in Solution'; J. Phys. Chem. A 110 (2006) 5998.

27. J. Baggerman, D. C. Jagesar, R. A. L. Vallée, J. Hofkens, F. C. De Schryver, F. Schelhase, F.

Pour plus d'information sur Europass: http://europass.cedefop.europa.eu
© Union européenne, 2002-2010 24082010

Vögtle, A. M. Brouwer; 'Fluorescent perylene diimide rotaxanes: Spectroscopic signatures of wheel-chromophore interactions'; Chem. - Eur. J. 13 (2007) 1291.

28. K. Baert; K. Song; R. Vallée; M. Van der Auweraer; K. Clays; 'Spectral narrowing of emission in self-assembled colloidal photonic superlattices'; J. Appl. Phys. 100 (2006) 123112.

29. R. A. L. Vallée; M. Van der Auweraer; W. Paul; K. Binder; 'Fluorescence lifetime of a single molecule as an observable of meta-basin dynamics in fluids near the glass transition'; Phys. Rev. Lett. 97 (2006) 217801.

30. R. A. L. Vallée; M. Baruah; J. Hofkens; N. Boens; M. Van der Auweraer; D. Beljonne; 'Fluorescence lifetime fluctuations of single molecules probe the local environment of oligomers around the glass transition temperature'; J. Chem. Phys. 126 (2007) 184902.

31. K. Baert; K. Wostyn; R. A. L. Vallée; K. Clays; 'Second-order nonlinear properties of chromophore-coated particles: symmetry considerations'; J. Nonlinear. Opt. Phys. 16 (2007) 27.

32. B. Kolaric, M. Sliwa, M. Brucale, R. A. L. Vallée, G. Zuccheri, B. Samori, J. Hofkens and F. C. De Schryver; 'Single molecule fluorescence spectroscopy of pH sensitive oligonucleotides switches'; Photoch. Photobio. Sci. 6 (2007) 61.

33. R. A. L. Vallée; M. Van der Auweraer; W. Paul; K. Binder; 'What can be learned from the rotational motion of single molecules in polymer melts'; Europhys. Lett. 79 (2007) 46001.

34. R. A. L. Vallée; K. Baert; B. Kolaric; M. Van der Auweraer; K. Clays; 'Nonexponential decay of spontaneous emission from an ensemble of molecules in photonic crystals'; Phys. Rev. B 76 (2007) 045113.

35. R. A. L. Vallée, W. Paul and K. Binder; 'Single molecule probing of the glass transition phenomenon: simulations of several types of probes', J. Chem. Phys. 127 (2007) 154903.

36. Anca Margineanu, Jun-ichi Hotta, Renaud A. L. Vallée, Mark Van der Auweraer, Marcel Ameloot, Alina Stefan, David Beljonne, Yves Engelborghs, Andreas Herrmann, Klaus Müllen, Frans C. De Schryver, Johan Hofkens; 'Visualization of membrane rafts using a perylene monoimide derivative and fluorescence lifetime imaging'; Biophysical Journal 93 (2007) 2877.

37. B. Kolaric; K. Baert; M. Van der Auweraer; R.A.L. Vallée; K. Clays; 'Controlling the fluorescence resonant energy transfer by photonic crystal bandgap engineering'; Chem. Mater. 19 (2007) 5547.

38. K. Baert, W. Libaers, B. Kolaric, R.A.L. Vallée, M. Van der Auweraer, D. Grandjean, M. Di Vece, P. Lievens, K. Clays; 'Development of magnetic materials for photonic applications'; J. Nonlinear. Opt. Phys. 3 (2007) 281.

39. R. A. L. Vallée, T. Rohand, N. Boens, W. Dehaen, G. Hinze and T. Basché; 'Analysis of the exponential character of single molecule rotational correlation functions for large and small fluorescence collection angles', J. Chem. Phys. 128 (2008) 154515.

40. B. Kolaric, R. A. L. Vallée; 'Polymer–dye interactions as a tool for studying phase transitions', Colloids Surf., A, 338 (2009) 61-67.

41. Wim Libaers, Branko Kolaric, Renaud A.L. Vallée, John E. Wong, Jelle Wouters, Ventsislav K. Valev, Thierry Verbiest, Koen Clays, 'Engineering colloidal photonic crystals with magnetic functionalities', Colloids Surf., A, 339 (2009) 13-19.

42. M. Di Vece, B. Kolaric, K. Baert, G. Schweitzer, M. Obradovic, R. A. L. Vallée, P. Lievens, K. Clays, 'Controlling the photoluminescence of CdSe/ZnS quantum dots with a magnetic field', Nanotechnology, 20 (2009) 135203.

43. Els Braeken, Philippe Marsal, Annelies Vandendriessche, Mario Smet, Wim Dehaen, Renaud Vallée, David Beljonne, Mark Van der Auweraer, 'Investigation of probe molecule - polymer interactions', Chem. Phys. Lett., 472 (2009) 48-54.

44. P. Massé, R. A. L. Vallée, J-F. Dechézelles, J. Rosselgong, E. Cloutet, H. Cramail, X.S. Zhao and S. Ravaine 'Effects of the Position of a Chemically or Size-Induced Planar Defect on the Optical Properties of Colloidal Crystals', J. Phys. Chem. C, 113 (2009) 14487-14492.

45. E. Braeken, G. De Cremer, P. Marsal, G. Pèpe, K. Müllen and R.A.L. Vallée 'Single Molecule Probing of the Local Segmental Relaxation Dynamics in Polymer above the Glass Transition Temperature', J. Am. Chem. Soc., 131 (2009) 12201-12210.

46. R.A.L. Vallée, W. Paul and K. Binder "Probe molecules in polymer melts near the glass transition: A molecular dynamics study of chain length effects", J. Chem. Phys., 132 (2010) 034901, 1-9

47. B. Kolaric, H. Vandeparre, S. Desprez, R.A.L. Vallée and Pascal Damman "In situ tuning the optical properties of a cavity by wrinkling", Appl. Phys. Lett., 96 (2010) 0431119, 1-3

48. B. Kolaric and R.A.L. Vallée "Dynamics and Stability of DNA Mechano-Nanostructures: Energy-

Pour plus d'information sur Europass: http://europass.cedefop.europa.eu
© Union européenne, 2002-2010 24082010

Transfer Investigations", J. Phys. Chem. C, 114, 3 (2010) 1430-1435

49. C. Marichy, J.F. Dechézelles, M.G. Willinger, N. Pinna, S. Ravaine and R. Vallée "Nonaqueous sol–gel chemistry applied to atomic layer deposition: tuning of photonic band gap properties of silica opals", Nanoscale, 2 (2010) 786-792

50. J-F. Dechézelles, T. Aubert, F. Grasset, S. Cordier, C. Barthou, C. Schwob, A. Maître, R.A.L. Vallée, H. Cramail and Serge Ravaine "Fine tuning of emission through the engineering of colloidal crystals", Phys. Chem. Chem. Phys., 12 (2010) 11993-11999

51. S. Mornet, L. Teule-Gay, D. Talaga, S. Ravain and R.A.L. Vallée "Optical cavity modes in semicurved Fabry–Pérot resonators", J. Appl. Phys., 108 (2010) 086109, 1-3

53. R.A.L. Vallée, W. Paul and K. Binder "Single Molecules Probing the Freezing of Polymer Melts: A Molecular Dynamics Study for Various Molecule-Chain Linkages", Macromolecules, 43, 24 (2010) 10714-10721

54. J-F. Dechézelles, G. Mialon, T. Gacoin, C. Barthou, C. Schwob, A. Maître, R.A.L. Vallée, H. Cramail and S. Ravaine "Inhibition and exaltation of emission in layer-controlled colloidal photonic architectures", Colloids Surf., A, 373 (2011) 1-5

55. G. Hinze, T. Basche and R.A.L. Vallée « Single molecule probing of dynamics in supercooled polymers », Phys. Chem. Chem. Phys., 13 (2011) 1813–1818

56. R. Morarescu, L. Englert, B. Kolaric, P. Damman, R.A.L. Vallée, T. Baumert, F. Hubenthal, and F. Trãger "Tuning nanopatterns on fused silica substrates: a theoretical and experimental approach", J. Mat. Chem. 21 (2011) 4076-4081

57. M. Ferrié, N. Pinna, S. Ravaine and R.A.L. Vallée "Wavelength - dependent emission enhancement through the design of active plasmonic nanoantennas", Optics Express, 19, 18 (2011) 17697-17712

PUBLICATIONS EN CONGRES (Proceedings)

1. Kai Song, Renaud Vallée, Koen Clays, André Persoons, “Different Bandgaps of Transmission and Emission Spectra in Artificial Opal”, presentation at the 8th international Conference on Organic Nonlinear Optics, ICONO’8, Tohoku, Japan, March 7-11, 2005 in Nonlinear Optics, Quantum Optics, Concepts in Modern Optics, Vol. 34, 1-4 (2005) 227-230

2. Koen Clays, Kasper Baert, Mark Van der Auweraer, Renaud Vallée, “Photonic superlattices for photonic crystal lasers”, Proc. of SPIE Vol. 6653 (2007) 665302

PRINCIPALES COMMUNICATIONS ORALES ET ECRITES PRESENTEES EN CONFERENCES NATIONALES OU INTERNATIONALES

1) AFFICHES

- Belgian Polymer Group meeting – Hengelhoef (B) – Mai 1999

- Fifth International Conference on Organic Nonlinear Optics – Davos (CH) – Mars 2000

- Second International Symposium on Physics, Chemistry and Biology with Single Molecules – Banz (D) – Mars 2001

- The Second International Conference on Scanning Probe Microscopy on Polymers – Weingarten (D) – Juillet 2001

- ISPAC15, International Symposium on Polymer Analysis and Characterization - Enschedé (NL) – Juin 2002

- Belgian Polymer Group meeting – Houffalize (B) – Mai 2004

- Second International Workshop on Dynamics in Viscous Liquids - Mainz (D) – Avril 2006

- Ninth International Conference on Photonic and lectromagnetic Crystal Structures (PECS IX) - Granada (Spain) - Septembre 2010

2) PRESENTATIONS ORALES

Pour plus d'information sur Europass: http://europass.cedefop.europa.eu
© Union européenne, 2002-2010 24082010

- Dutch Polymer Days – Lunteren (NL) – Février 2001

- Optical studies of Single Molecules and Molecular Assemblies in Chemical Physics and Biophysics – PHYS division symposium – ACS National meeting – San Diego (USA) – Avril 2001

- Joint meeting of the European Societies of Physical Chemistry, Interaction of Laser Radiation with Matter at Nanoscale Scales: from Single Molecule Spectroscopy to Materials Processing – Venice (I) – Octobre 2001

- Belgian Polymer Group meeting – Spa (B) – Mai 2003

- International Conference on Natural Polymers, BioPolymers, Biomaterials, their Composites, Blends, IPNs, and Gels: Macro to Nano Scales – Kottayam (Kérala, I) – Mars 2005

- Europen Polymer Federation Meeting – Moscou (R) Juin 2005

- The Fifth International Conference on Surface Plasmon Photonics (SPP5) - Busan (Korea) - Mai 2011

ACTIVITES D'ENSEIGNEMENT ET D'ENCADREMENT

Etant sorti agrégé de l'enseignement secondaire supérieur de l'Université de Mons-Hainaut en 1991, j'ai enseigné durant 7 ans avant de retourner effectuer une thèse de physique à la Faculté des Sciences de l'Université de Mons en 1998.

J'ai enseigné les mathématiques (20h/sem) aux étudiants de l'Athénée Royal Riva-Bella à BraineL'alleud (niveau équivalent à celui d'un lycée français) pendant deux ans (1991-1993).

Ensuite, j'ai enseigné les mathématiques, la physique et la chimie (19h/sem) à des élèves instituteurs et à des régents (niveau équivalent à celui d'un IUFM) à l'Institut d'Enseignement

Supérieur Pédagogique et Economique de la Communauté Française (Mons – Tournai) pendant trois ans (1993-1996).

Durant cette période, j'ai supervisé 4 étudiants dans leurs travaux de fin d'études.

Enfin, j'ai enseigné l'informatique et l'électronique (19h/sem) aux étudiants en graduat (niveau équivalent à celui d'un IUT) électronique à l'Institut de Promotion Sociale de Colfontaine pendant deux ans (1996-1998).

Durant cette période, j'ai supervisé 2 étudiants dans leurs travaux de fin d'études.

En 2011, j'ai enseigné un module de 5h en nanophotonique aux élèves ingénieurs de l'ENSCBP.

ACTIVITES DE RECHERCHE ET D'ENCADREMENT

De 2000 à 2002, j'ai été chercheur postdoctoral à l'Université de Twente (Pays-Bas) dans les groupes des Professeurs van Hulst (Techniques Optiques) et Vancso (Science des Matériaux et Technologie des Polymères), avec une subvention du fonds national de la recherche scientifique néerlandais (NWOCW). Ma recherche s'y est focalisée sur l'investigation locale (échelle nanoscopique) des propriétés des polymères à proximité de la température de transition vitreuse (Tg) en observant le comportement dynamique de molécules sondes, insérées dans le milieu, par microscopie de fluorescence “molécule unique”. J'y ai supervisé un étudiant (Nikodem Tomczak) en début de thèse durant les deux ans.

De 2002 à 2008, j'ai été chercheur postdoctoral à l'Université catholique de Leuven (KULeuven, Belgique) avec une subvention du fonds flamand de la recherche scientifique (FWO). J'y ai poursuivi l'investigation des propriétés de relaxation des polymères au voisinage de Tg à l'échelle nanoscopique par microscopie optique confocale de fluorescence “molécule unique”. J'y ai mis l'accent sur le vérification expérimentale des théories décrivant le phénomène de transition vitreuse actuellement disponibles et la découverte d'observables locales, non accessibles aux techniques dites d'ensemble et permettant de mieux comprendre les aspects microscopiques liés à la transition vitreuse. J'ai été co-directeur de thèse d'un étudiant sur cette thématique (Els Braeken).

D'autre part, en collaboration avec le groupe du Professeur Clays à Leuven, j'ai développé la recherche et le développement de nouveaux matériaux photoniques colloïdaux et leur investigation par des méthodes usuelles de transmission et/ou extinction optique ansi que par des techniques de fluorescence de molécules sondes préalablement insérées. J'y ai supervisé trois étudiants (Kasper Baert, Wim Libaers et Luis Gonzalez) en master et en thèse.

Afin de bien comprendre dans le détail les mécanismes responsables des effets observés dans les

Pour plus d'information sur Europass: http://europass.cedefop.europa.eu
© Union européenne, 2002-2010 24082010

deux types d'activités précités (phénomène de la transition vitreuse et développement de nouveaux matériaux photoniques) et de traiter ces activités efficacement, j'ai estimé à l'époque que des simulations réalistes des expériences réelles devaient coexister. Très intéressé par cette confrontation théorie (ou simulations numériques) - expériences, j'ai, au cours de mon dernier postdoctorat, effectué maints séjours dans d'autres groupes belges ou étrangers afin de me familiariser avec diverses techniques de calcul ou de simulation. Ainsi, j'ai appris à manipuler divers outils de la chimie quantique dans le service des matériaux nouveaux à l'Université de Mons avec le docteur Beljonne. J'ai appris à mettre au point et analyser le résultats de dynamique moléculaire dans le groupe de matière condensée du Professeur Binder, à l'Université de Mainz, où j'ai effectué un séjour d'études de 9 mois en 2006, subventionné par le FWO. Dans le but de parfaire mes connaissances en ingénieurie des colloïdes pour applications photoniques, j'ai effectué en 2007 un séjour d'études de 10 mois au Centre de Recherche Paul Pascal (CNRS) à Pessac, dans le groupe du Professeur Ravaine.

Finalement, j'ai passé le concours CR1 au CNRS en 1998 pour entrer au Centre De Recherche Paul Pascal où mes activités de recherche concernent la modélisation (codes numériques) et la caractérisation optique de matériaux synthétisés par une approche sol−gel pour des applications en photonique et en opto−électronique via des effets de localisation de la lumière, ingénierie de bande interdite photonique et plasmonique avec ou sans matériaux à gain.

J'ai encadré deux étudiants au niveau master 2 sur les thématiques milieux désordonnés inorganiques et lasers aléatoires (Laurent Maillaud, 2010) et plasmonique non linéaire : contrôler la lumière avec la lumière (Léo Pérès, 2011). Je co-encadre actuellement deux étudiants en thèse: Preeti Gaikwad (bourse ministérielle, 2009-2012) sur la thématique milieux désordonnés inorganiques et lasers aléatoires et Emeline Feltrin (bourse ministérielle, 2010-2013) sur la thématique surfaces polymères nanostructurées de rugosité et d'indice de réfraction périodique et modulable à des fins photoniques.

ACTIVITES ADMINISTRATIVES ET PROJETS DEPOSES DEPUIS MON ENTREE AU CNRS

- Membre du conseil scientifique Cnano GSO
- Membre du conseil scientifique du Mésocentre de Calcul Intensif Aquitain
- Membre de conseil de labo du CRPP
- Responsable scientifique de la bibliothèque du CRPP

- Projet Cnano GSO obtenu en 2008, en collaboration avec le groupe de Niek van Hulst à l'ICFO, Barcelone: Plasmonics with nano-shaped elements: towards optical nanoantennas and responsive materials
- Projet région obtenu en 2008, avec Philippe Barois du CRPP: Matériaux artificiels nanostructurés pour l'optique : matériaux photoniques et métamatériaux
- Projet ANR blanche en cours en collaboration avec l'équipe De Rémi Carminati à l'ESPCI, Paris: Interaction lumière-matière dans des matériaux désordonnés complexes

Pour plus d'information sur Europass: http://europass.cedefop.europa.eu
© Union européenne, 2002-2010 24082010

UNIVERSITÉ DE MONS-HAINAUT

FACULTÉ DES SCIENCES

Nous, président, secrétaire et membres du jury chargé par les autorités universitaires de l'Université de Mons-Hainaut de conférer le grade académique de docteur en sciences ;

Attendu que Monsieur ***Renaud VALLÉE***, né à Charleroi le 31 octobre 1969, est porteur d'un diplôme de licencié en sciences pour le groupe des sciences physiques délivré le 5 juillet 1991 par l'Université de Mons-Hainaut et entériné le 15 mars 1994 ;

Attendu qu'il a présenté et défendu publiquement une dissertation originale intitulée : "**Croissance et propriétés optiques non-linéaires quadratiques de cristaux organiques déposés sur substrat de poly(tétrafluoroéthylène)**" ainsi qu'une thèse annexe intitulée : "**La taille des systèmes binaires nanoparticulaires modifie considérablement leurs diagrammes de phase. La ségrégation y joue également un rôle non négligeable**", acceptées par le jury ;

Avons conféré et conférons à Monsieur ***Renaud VALLÉE*** le grade académique de **docteur en sciences**
avec la plus grande distinction

En foi de quoi nous lui avons délivré le présent diplôme, attestant en même temps que Monsieur ***Renaud VALLÉE*** a été réellement étudiant de l'Université de Mons-Hainaut et que les prescriptions du décret du 5 septembre 1994 relatif au régime des études universitaires et des grades académiques, quant aux conditions d'accès, aux programmes, à la durée des études et aux examens, ont été observées.

Mons, le 29 mars 2000.

Les Membres du Jury,

Le Titulaire,

Le Secrétaire,

Le Président,

Le Recteur,

MESA+ Research Institute

University of Twente
The Netherlands

Faculty of Science and Technology
Materials Science and Technology of Polymers
Prof. Dr. G. Julius Vancso

TO WHOM THIS MAY CONCERN

your reference		phone	053-4892967 / 2974 (secr.)
our reference	070101/TNW52/gr	fax	053-4893823
date	11 December 2007	e-mail	g.j.vancso@tnw.utwente.nl / mtp@tnw.utwente.nl (secr.)

subject Dr. Renaud Vallée, application for professorship

To Whom this may concern,

During his postdoctoral position at the University of Twente (The Netherlands) from 2000 to 2002, Dr. Renaud Vallée provided daily supervision to the PhD. student Nikodem Tomczak during the first two years of his research. This supervision included introducing Mr. Tomczak to the field of Single Molecule Spectroscopy and optics of polymers. In the framework of this research project, which consisted in the local (nm) scale investigation of the relaxation dynamics of chain segments around a probe molecule in a polymer matrix, Dr. Renaud Vallée has trained Nikodem Tomczak to the interpretation of fluorescence lifetime trajectories exhibited by the single probes in the complex matrix. The corresponding results were based on Dr. Vallée's personal contribution regarding free volume models. Dr. Vallée found a relationship between fluorescence lifetime distribution and distribution of free volume in polymers, which has been crucial for data interpretation. This research resulted in several highly cited papers in top journals. Contacts with Dr. Vallée were continued even following his departure to Belgium in 2002 which significantly contributed to the final results of this joint project.

As the Ph.D. program director and promotor of Nikodem Tomczak, it is a pleasure for me to acknowledge this scientific supervision by Dr. Vallée. Acknowledging his effective supervision, he was an expert member of the jury for the PhD Defense of Nikodem Tomczak which he passed on May 18, 2005.

With kind regards,

Prof. Dr. G.J. Vancso
Chair group Materials Science and Technology of Polymers

Department of Chemistry
Laboratory for Molecular Electronics and Photonics
Celestijnenlaan 200D
B-3001 Leuven

KATHOLIEKE
UNIVERSITEIT
LEUVEN

to whom it may concern

ONS KENMERK
UW KENMERK
LEUVEN, 22 November 2007

RE: qualification for professorship in France

I have learnt about the qualification for professorship in France that my colleague, dr. Renaud Vallée, is applying for. This letter is to state that dr. Renaud Vallée has gained expertise in supervising students during his postdoctoral research stay in my group in the Department of Chemistry of the Katholieke Universiteit Leuven, in Belgium.

Dr. Renaud Vallée has supervised the students Wim Libaers, Kasper Baert and Luis Gonzalez as master students. He is now continuing to supervise all three during their PhD research work. Dr. Renaud Vallée is formally one of the two members of these students' doctoral supervising committee. On a scientific level, dr. Renaud Vallée is providing suggestions and feedback, and also is adding to the interpretation of experimental data from time-resolved fluorescence data. More specifically, dr. Renaud Vallée has introduced Wim Libaers in Single Molecule Spectroscopy for his application in photonic crystals; he has helped Kasper Baert with the detailed analysis of non-exponential fluorescence decay in photonic crystals; and he has recently suggested new avenues for Luis Gonzalez for his analysis of the potential of spincoating to prepare photonic crystals.

It is a pleasure for me, as the promoter for these three students, to acknowledge this scientific supervision by dr. Renaud Vallée. As a postdoc, inherently on a temporary basis, dr. Renaud Vallée can not take up the formal role of a promoter, but I can state that his effective supervision is very much appreciated.

I hope this gives you a sufficient idea about my positive appreciation of dr. Renaud Vallée.

Prof. Dr. Koen CLAYS
Full Professor at the Department of Chemistry, Katholieke Universiteit Leuven, Leuven, Belgium
Adjunct Professor at the Department of Physics and Astronomy, Washington State University, Pullman, WA, USA
TEL.INT+ 32 16 32 75 08 FAX INT + 32 16 32 79 82
E-mail: koen.clays@fys.kuleuven.be

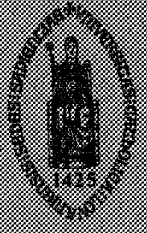

Katholieke Universiteit Leuven
Faculteit Wetenschappen
Departement Chemie
Afdeling Moleculaire en Nanomaterialen

Study of the heterogeneity and dynamics of polymers with single molecule spectroscopy

Els Braeken

Promotoren:
Prof. Dr. J. Hofkens
Prof. Dr. F.C. De Schryver
Dr. R.A.L. Vallée

Proefschrift voorgedragen tot het behalen van de graad van Doctor in de Wetenschappen

I. INTRODUCTION

Durant mes stages postdoctoraux, j'ai essentiellement investigué deux types de systèmes: les matrices polymères désordonnées à des températures proches de la transition vitreuse et les cristaux photoniques colloïdaux. Dans les deux cas, des molécules fluorescentes ont été insérées dans les systèmes afin de servir de sondes du comportement du milieu environnant. Dans les matrices polymères, ces sondes ont été insérées au niveau 'molécule unique' afin d'évaluer la dynamique locale et temporelle des chaines de polymères. La durée de vie radiative des molécules s'est avérée un paramètre de choix permettant de tracer la mobilité des espèces environnantes (segments de chaine ou trous) par suite de l'intéraction entre le moment dipolaire de transition des molécules et les dipoles induits environnants (fluctuations de la densité locale d'états photoniques, LDOS). Dans les cristaux photoniques, les études ont été effectuées au niveau de l'ensemble afin de tester la bonne ingénieurie des matériaux et donc observer l'effet d'une bande photonique interdite/permise (modification de la LDOS) sur l'inhibition/exaltation de fluorescence. Au niveau expérimental, ces études ont été réalisées par microscopie confocale de fluorescence résolues en temps, complémentées dans le cas des cristaux photoniques par des mesures de transmission/réflection UV-viBarcelonesible-IR (pour ne pas parler des caractérisations structurales, qui ne seront pas discutées dans cette synthèse). Afin de bien comprendre les résultats obtenus au niveau expérimental, ces études ont été complétées par des investigations théoriques et numériques de type simulations de Monte-Carlo, dynamique moléculaire, ou électromagnétiques (FDTD) des systèmes. Depuis mon entrée au CNRS (2008), j'ai poursuivi les études concernant l'effet des cristaux photoniques sur la dynamique d'émission spontanée des sondes actives insérées (sources internes) et ai étendu ces considérations aux nanostructures plasmoniques. La section II ci-dessous décrit les études réalisées au niveau de la molécule unique à des fins de compréhension des mécanismes responsables de la survenance de la transition vitreuse. Elle se scinde en deux sous-sections selon que la molécule d'intérêt, rigide, reporte la dynamique des chaines environnantes à travers les changements de densité locale qu'elle perçoit ou que la molécule d'intérêt, pouvant être sujette à des changements de conformation, reporte cette dynamique par les changements d'orientation ou de conformation que les chaines environnantes lui font subir. La section III reporte les études effectuées au niveau de l'ingénieurie des matériaux photoniques (sous-section 1) et plasmoniques (sous-section 2) afin d'exalter/inhiber le taux d'émission des émetteurs incorporés par modification de LDOS. Ces deux sections comportent chacune une troisième sous-section décrivant l'intérêt des études menées. Enfin, la section IV décrit les futures activités de recherche envisagées au CRPP et en collaboration avec des partenaires extérieurs.

II. MOLÉCULES UNIQUES DANS LES POLYMÈRES

La compréhension de la cause du ralentissement de la dynamique dans les liquides surfondus et de l'apparition résultante de la transition vitreuse vers un solide amorphe est un des défis principaux de la physique de la matière condensée. Les diverses théories qui ont été proposées pour expliquer le phénomène ont été globalement classifiées en deux catégories. L'une, thermodynamique, décrit la transition vitreuse comme une manifestation cinétiquement contrôlée d'une transition de phase de quasi-équilibre entre un état liquide surfondu méta-stable et un verre méta-stable également. Les théories de volume libre se rapportent à cette catégorie. Selon le point de vue non thermodynamique, bien représenté par la théorie des modes couplés, la vitrification survient du fait d'une transition purement dynamique d'un système à comportement ergodique vers un comportement non ergodique. Bien que récemment l'existence d'une dynamique spatialement hétérogène dans les liquides formant des verres ait été soulevée, aboutissant à une compréhension plus fine de l'origine du ralentissement, aucun accord n'a été atteint quant à savoir quel scénario décrit le mieux la transition vitreuse. Clairement, l'analyse d'observables sondant les corrélations dynamiques du liquide-verre et son comportement de relaxation sont cruciales pour une compréhension de ces systèmes. Dans ce contexte, le concept d' hypersurface d'énergie potentielle est devenu de plus en plus populaire, particulièrement pour l'analyse numérique de simulations. Considérant l'énergie potentielle comme une fonction des 3N coordonnées des N particules du système, on peut identifier des minimums locaux ou structures inhérentes . Aux températures suffisamment basses, e.g., au dessous de la température critique T_c de la théorie des modes couplés, le système séjourne longtemps dans un méta-bassin comprenant un groupe de tels minimums locaux voisins dans l'espace des phases, avant qu'une transition vers le prochain méta-bassin voisin puisse survenir. Il est tentant d'associer un tel saut de barrière dans l'espace des phases à un réarrangement d'une région coopérative comme postulé par Adam et Gibbs pour expliquer l'origine de la loi de Vogel-Fulcher décrivant l'augmentation rapide du temps de relaxation structural lorsque la température est abaissée. Cependant, la plupart des observables expérimentales ne sont pas sensibles aux transitions individuelles entre ces méta-bassins. Donc, pour de vrais systèmes, cette approche est de caractère purement hypothétique.

II.1. Changements des taux d'émission spontanée dus aux variations locales de densité

Parce qu'elle permet de s'affranchir des moyennes intrinsèques réalisées par les techniques dites 'd'ensemble', la spectroscopie de fluorescence type 'molécule unique' constitue un outil puissant pour évaluer la dynamique de matériaux complexes, hétérogènes.

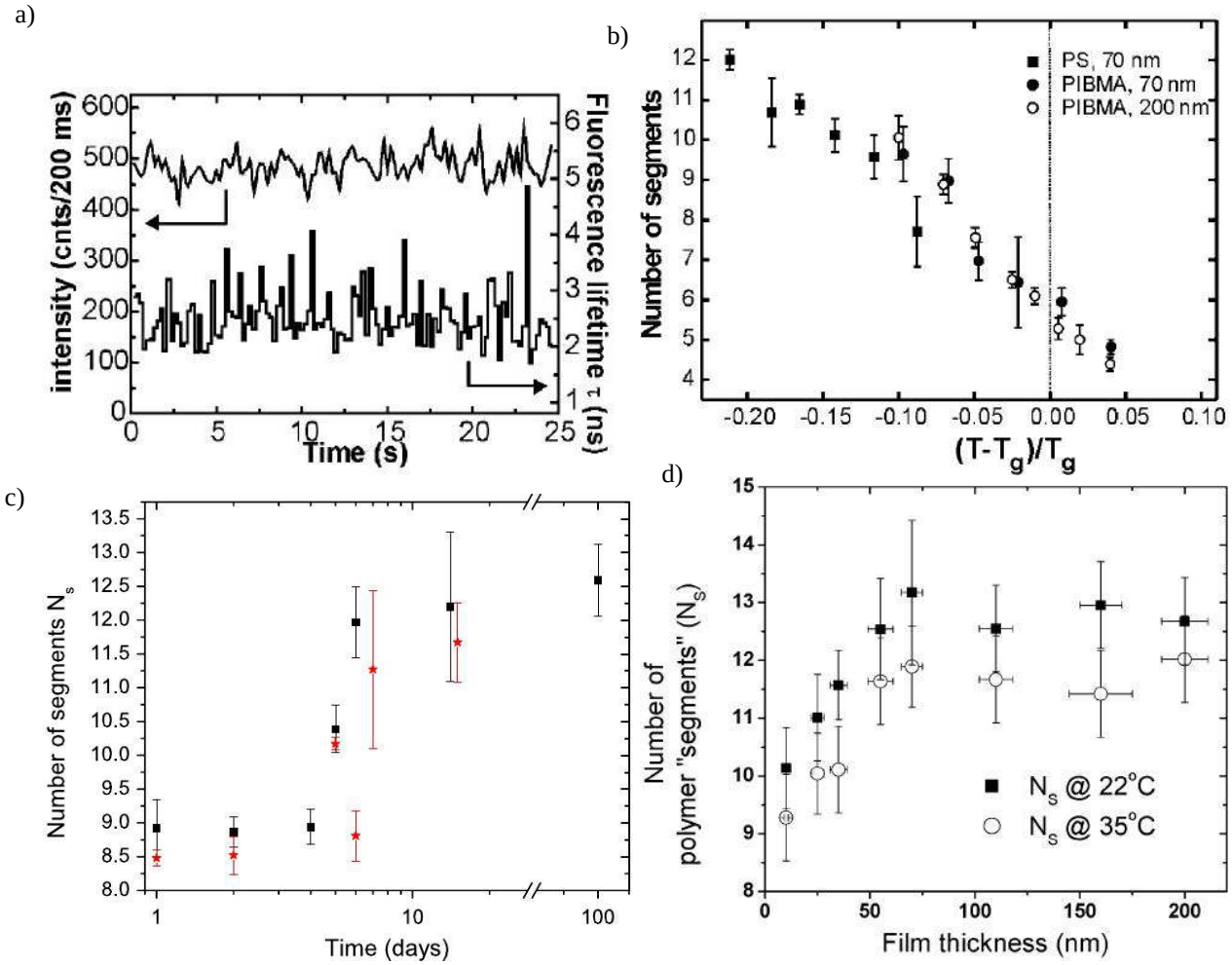

FIG. 1. a) Traces temporelles caractéristiques d'intensité de fluorescence et de durée de vie d'une molécule fluorescente de rendement quantique proche de 1 (DiD) dans une matrice de PS à température ambiante. La durée de vie fait de fréquentes excursions vers les grandes valeurs au cours du temps. Notons l'absence de corrélation entre ces excursions et le niveau d'intensité pratiquement constant délivré par cette molécule, écartant l'idée qu'un processus non-radiatif puisse être à l'origine du comportement observé. Sur base des distributions de durées de vie de telles molécules individuelles, il est possible [1] de déterminer un nombre de segments effectifs N_s des chaines, environnant la molécule, impliquées dans un réarrangement local. N_s est représenté en fonction de la température (b), du nombre de jours passés (c'est-à-dire en fonction de la teneur en solvant qui s'évapore au cours du temps) après dépôt à la tournette sur un substrat de verre (c) et en fonction de l'épaisseur du film déposé (d).

Dans une série de travaux (postdoctorat à l'Université d'Enschedé aux pays-Bas dans les groupes des professeurs van Hulst et Vancso), Nikodem Tomczak, l'étudiant en thèse dont j'ai supervisé les deux premières années et moi-même avons montré que la durée de vie de fluorescence de molécules uniques, ayant un rendement quantique proche de l'unité, était extrêmement sensible aux changements locaux de densité dans une matrice polymère. La trajectoire temporelle de la durée de vie de fluorescence de chaque molécule unique fluctue de manière très caractéristique dans un environnement polymère (Fig. 1a). Grâce aux théories de volume libre (en particulier la théorie de Simha-Somcynsky), nous avons pu relier ces variations de durée de vie de chaque molécule sonde au nombre de segments de chaines polymériques impliqués dans une cellule de réarrangement autour de cette dernière. Nous avons pu alors représenter la dépendance de ce nombre de segments en fonction de la température (Fig. 1b) [1], de la teneur en solvant (Fig. 1c) [2] et de l'épaisseur du film polymère investigué (Fig. 1d) [3]. Nous

avons trouvé un comportement générique pour divers polymères, que nous avons pu mettre en analogie avec la théorie d'Adam et Gibbs.

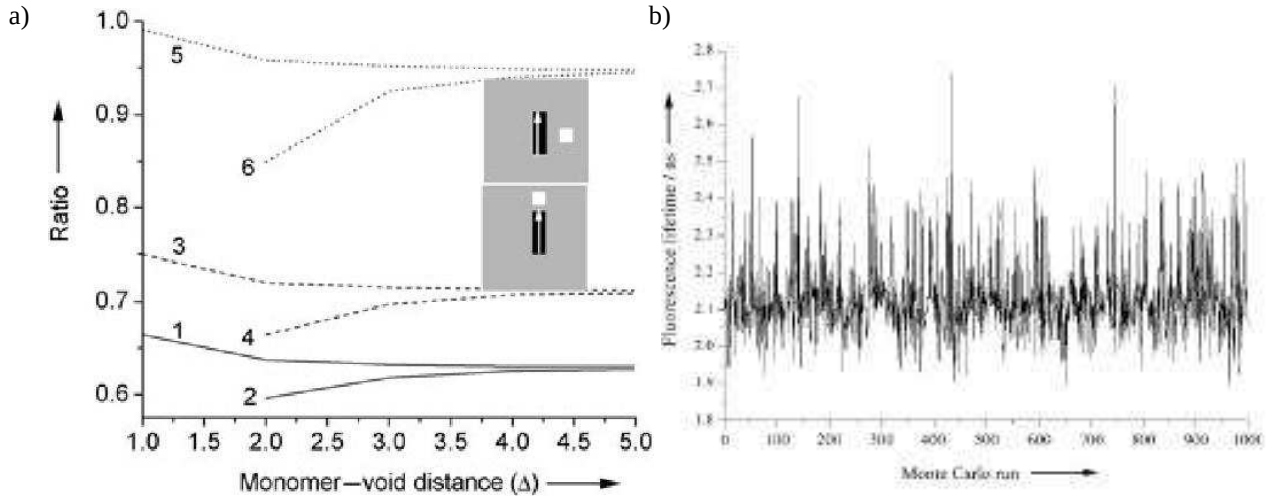

FIG. 2. a) Représentations schématiques (inserts) d'une matrice polymère environnant un émetteur fluorescent. Dus aux mouvements des chaines, des 'trous' peuvent localement être créés latéralement ou longitudinalement par rapport au moment dipolaire de transition des molécules [4]. La figure montre qu'en fonction de la position de création de ce trou par rapport à la molécule, le moment dipolaire de transition total du sytème avec trou peut être réduit / augmenté par rapport au moment dipolaire de transition total du sytème sans trou. La variation la plus grande peut être observée lorsqu'un trou est créé localement juste au dessus du dipole de transition de la molécule (courbe 6), créant ainsi une augmentation significative et momentanée de la durée de vie, comme observé en Fig. 1a. b) Runs successifs d'une simulation de Monte-Carlo d'un système tel que décrit en a) et comportant une fraction définie de trous dont les positions varient aléatoirement de run en run. Clairement, un comportement analogue à celui indiqué en Fig. 1a est observé.

Sur base d'un modèle microscopique des variations du champ local, généralisant le modèle de Lorentz, nous avons pu, **en collaboration avec le professeur Michel Orrit (Monos, Université de Leiden aux Pays-Bas) et lors de mon second postdoctorat à l'Université de Leuven en Belgique**, établir une corrélation entre les distributions de durée de vie de fluorescence mesurées pour les molécules uniques et les distributions locales simulées de polarisabilité dans la matrice, prenant en compte la proximité de monomères polarisables ou de trous environnants (Fig. 2) [4]. Par la suite, en mesurant à température ambiante la durée de vie radiative de sondes dans diverses matrices d'oligo(styrène) ayant des masses molaires différentes et donc des températures de transition vitreuse différentes, nous avons observé que la fraction moyenne de trous entourant les sondes est indépendante de la masse molaire de l'oligomère pour autant que ce dernier soit dans l'état vitreux, et qu'elle augmente significativement dans le régime surfondu [5]. Ces résultats nous ont permis de montrer que la théorie de Gibbs et Di Marzio était plus appropriée que le concept de volume libre associé aux bouts de chaines pour décrire le comportement de relaxation de très petites (oligo) chaines. Finalement, nous avons montré que, dans le régime surfondu, les trajectoires de durée de vie de fluorescence des sondes dans une matrice présentent un comportement de saut de plateau en plateau (Fig. 3a) [6]. Afin d'élucider ce comportement des durées de vie des molécules au-dessus de la température de transition vitreuse, **j'ai effectué un séjour de 9 mois dans le groupe du professeur Binder à l'Université de Mainz en Allemagne**. Les résultats de simulations numériques en dynamique moléculaire ont permis de démontrer que ces sauts de durée de vie de plateau en plateau correspondent à des transitions méta-bassins dans l'hypersurface d'énergie potentielle de l'oligomère (Fig. 3b) [6].

Toujours sur base de simulations numériques en dynamique moléculaire, nous avons montré que cette information très locale (occurrence de transitions entre méta-bassins de l'hypersurface d' énergie potentielle) peut aussi être extraite en suivant le mouvement de rotation (à 2 et à 3 dimensions) des molécules uniques insérées dans la matrice polymère à température très proche et supérieure à celle de la transition vitreuse (Fig. 3c) [7]. Les larges sauts angulaires observés causent par ailleurs l'apparition de relaxations temporelles exponentiellement étirées (Fig. 3d), reportées dans la littérature comme étant dues à l'hétérogénéité dynamique de la matrice polymère. Ces simulations ont également permis de déterminer les paramètres prédits par la théorie des modes couplés à partir de l'analyse des trajectoires des molécules uniques et de vérifier la validité du principe de superposition temps-température. De manière à déterminer dans quelle mesure ces conclusions dépendent du choix de la molécule sonde utilisée expérimentalement, nous avons investigué l'effet de la taille et / ou de la masse de ces sondes sur leur comportement de relaxation en matrice polymère [8]. En effet, dans le cas idéal, la sonde utilisée i) ne doit pas perturber et ii) doit rendre compte

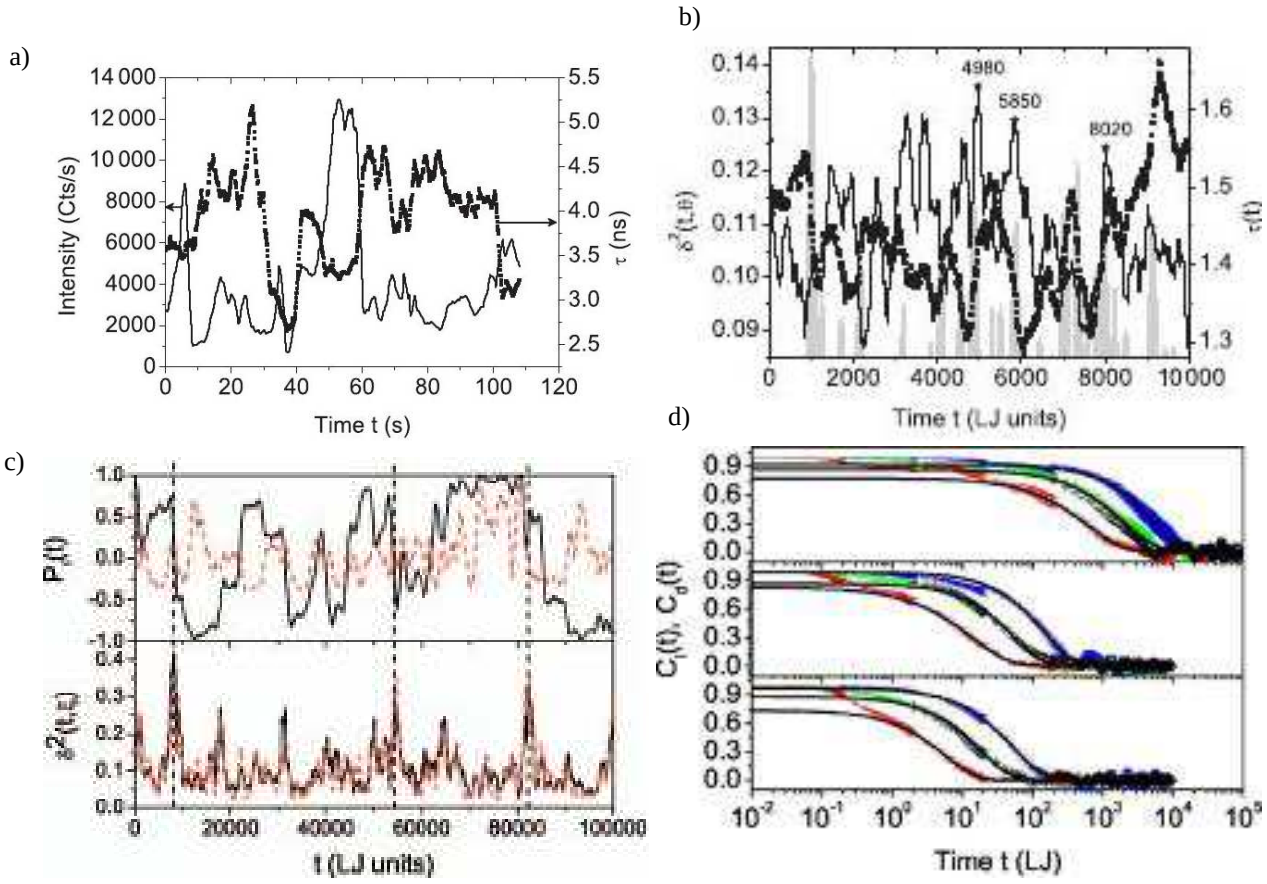

FIG. 3. a) Trajectoires expérimentales de durée de vie (symboles) et d'intensité (ligne) d'une molécule fluorescente de rendement quantique proche de 1 (Bodipy) dans une matrice d'oligostyrène au dessus de la température de transition vitreuse. b) trajectoires simulées de durée de vie (symboles) et du déplacement carré moyen $\delta^2(t,\theta)$ (ligne) entre les temps t et $t+\theta$ (paramètre qui signale l'occurence de sauts entre métabassins de l'hypersurface d'énergie potentielle) d'un fluorophore inséré dans la matrice oligomérique. Clairement, les extrema de δ^2 coïncident avec les sauts de durée de vie (les pics en gris représentent les dérivées absolues de la durée de vie). c) Trajectoires des polynômes de Legendre d'ordre 1 (line solide) et d'ordre 4 (ligne pointillée) décrivant la rotation tridimensionnelle des fluorophores dans la matrice d'oligostyrène. Remarquons l'observation de sauts angulaires simultanés de ces deux observables au cours du temps qui coïncident avec les maxima des déplacements carrés moyens, signalant, tout comme la durée de vie ci-avant, l'occurence de transitions métabassins dans l'hypersurface d'énergie potentielle de la matrice. d) Fonctions d'autocorrélation orientationnelles d'ordres 1, 2 et 4 en fonction de la température (augmentant du haut vers le bas) montrant une décroissance temporelle exponentiellement étirée.

le plus précisément possible du comportement du milieu environnant. Pour des observables telles que la durée de vie, le dichroïsme linéaire, et d'autres fonctions de corrélation orientationelles, il apparait de manière assez évidente que les temps de relaxation augmentent lorsque la masse et la taille de la sonde augmentent. Dans tous les cas de figure cependant, nous avons montré que les informations extraites de l'analyse des trajectoires individuelles sont très compatibles avec le comportement d'ensemble attendu tout en apportant beaucoup plus d'informations concernant les fluctuations de ces grandeurs. Toujours dans le soucis de pouvoir prédire ou orienter les études expérimentales en spectroscopie de molécule unique, nous avons également poursuivi des études en fonction de la longueur des chaines oligomériques [9] et de la position d'ancrage des molécules au sein de la matrice [10]. En sus de la simple dispersion des molécules dans la matrice polymère, nous avons investigué, dans ce dernier cas, l'effet de l'ancrage des molécules en bout de chaine ou en milieu de chaine sur les temps caractéristiques de relaxation de la matrice. De nouveau, de manière assez évidente, les résultats indiquent que, plus les chaines sont longues, plus les temps de relaxation sont longs. D'autre part, le résultats montrent également que le comportement à temps long (relaxation α) des observables de spectroscopie molécule unique ne permet pas de distinguer entre des molécules ancrées en bout de chaine ou en milieu de chaine. Au contraire, la différence entre les deux types d'ancrage ne se manifeste que dans le régime de cage (relaxation β dans la terminologie des modes couplés). De façon intéressante, toutes ces études ont permis de démontrer que des analyses de trajectoires individuelles peuvent par ailleurs permettre i) de déterminer la température critique T_c prédite par la théorie des modes couplés et la température de Vogel-Fulcher T_0 (transition

vitreuse calorimétrique) et ii) de mettre en évidence des déviations par rapport aux lois de Stokes-Einstein et de Stokes-Einstein-Debye concernant la translation et la rotation des molécules.

Pour conclure cette partie, mentionnons finalement que suite à ces investigations menées au niveau de la simulation numérique en dynamique moléculaire, **nous avons pu mettre au point, en collaboration avec le groupe du professeur Basché à l'Université de Mainz en Allemagne**, une série d'expériences de spectroscopie de molécules uniques permettant de mesurer simultanément la durée de vie et le dichroïsme linéaire de molécules insérées dans une matrice polymère, à différentes températures au dessus de la transition vitreuse [11]. Les fonctions de corrélations de la durée de vie décroissent temporellement plus vite que celles du dichroïsme linéaire, indiquant l'émergence de larges réorientations angulaires. De plus, les temps de relaxation croissent drastiquement lorsque la température est réduite.

II.2. Changements des taux d'émission spontanée dus aux changements de conformation des molécules

L'intéraction entre des molécules sondes spécialement synthétisées, présentant différents conformères possibles et les chaines de polymère environnantes peut également être étudiée afin d'en déduire certaines propriétés de la matrice. Ainsi, la dynamique conformationnelle d'une seule molécule dans une matrice polymère permet de visualiser localement le volume libre. Plus précisément, nous avons montré que la molécule de tétraphénoxy-pérylène-tétracarboxy-diimide (TPDI), connue pour présenter deux conformations distinctes selon que le coeur délocalisé est 'torsadé' ou plat, peut adopter chacune de ces conformations dans une matrice de Zéonex (poly-norbornène) et même passer localement et temporellement au cours de sa trajectoire d'une conformation à l'autre en fonction du volume libre dégagé dans son environnement immédiat [12].

Dans une série de travaux (postdoctorat à l'Université de Leuven en Belgique) combinant spectroscopie de molécule unique et chimie quantique, Els Braeken, l'étudiante dont j'ai co-supervisé la thèse et moi-même, en collaboration avec le groupe de David Beljonne à l'Université de Mons en Belgique, avons étudié l'intéraction entre la molécule de (1,1'- dioctadecyl -3,3,3',3'- tetraméthylindo-dicarbocyanine) (DiD) et la matrice de poly-styrène (PS) environnante en dessous de la température de transition vitreuse [13]. Deux types de conformères (conformères planaires et non-planaires) ont été attribués à la molécule, suite à l'analyse détaillée des trajectoires temporelles, présentant des caractéristiques bimodales des spectres d'émission et des durées de vie. Les conformères planaires ont de plus été classés trans ou cis selon la disposition de leurs chaines alkyles par rapport au segment polyène, modulant ainsi leur intéraction avec les chaines de polymère environnantes. Une molécule voisine de DiD mais de coeur conjugué plus compact (DiC) a également été synthétisée, selon deux espèces ayant différents types de chaines pendantes, notamment des chaines alkyles et des chaines oligostyrènes. Dans les deux cas, nous avons montré que ces molécules pouvaient également être stabilisées dans la matrice de PS sous forme de conformères planaires et non-planaires mais en différente proportion selon la nature des chaines pendantes [2]. Après recuit, cependant, les populations en chaque espèce deviennent similaires, le conformère le plus stable devenant le plus abondant. Cette observation indique clairement le passage d'un état de non-équilibre à celui d'équilibre, obtenu après recuit. Comme le type de conformère trouvé dans la matrice et son intéraction avec les chaines environnantes gouverne l'empaquettement local des chaines et donc le volume libre local, les perspectives de telles investigations pourraient conduire à une meilleure compréhension des effets plastifiants en fonction de la température et du veillissement. Finalement, nous avons étudié la dynamique temporelle de la molécule de terrylène diimide ayant quatre bras phénoxy (TDI) dans une matrice de PS à l'état surfondu. Par mesure simultanée des durées de vie de fluorescence et de dichroïsme linéaire, nous avons pu montrer que la molécule de TDI était une sonde polyvalente de la dynamique locale dans le polymère [15]. En effet, la molécule, suivie sur une trajectoire temporelle, a montré des changements conformationnels, indiqués par des fluctuations de durée de vie et / ou des sauts de réorientation à différentes échelles temporelles (Fig. 4). Grâce à la mécanique moléculaire et aux calculs quantiques, nous avons pu attribuer les changements conformationnels à des processus de repliement / dépliement d'un ou plusieurs bras par rapport aux coeurs conjugués. De plus, l'étendue spatiale des mouvements localement sondés nous a permis de tenter une attribution aux processus de relaxation α (mouvement de la chaine principale) et β (mouvement des goupes phényls) survenant dans la matrice de PS.

II.3. Intérêt de la démarche adoptée

A l'époque à laquelle j'ai démarré mon premier postdoctorat (septembre 2000), de nombreuses mesures d'ensemble avaient bien entendu été effectuées sur les polymères et les systèmes désordonnés en général afin de comprendre le cause du ralentissement de la dynamique menant à la transition vitreuse. Beaucoup de résultats et d'interpétations contradictoires ont émergé de cette multitude d'expériences et aucun consensus général n'avait été atteint permettant d'expliquer l'ensemble des résultats obtenus. Au niveau de la molécule unique, technique permettant de sonder très lo-

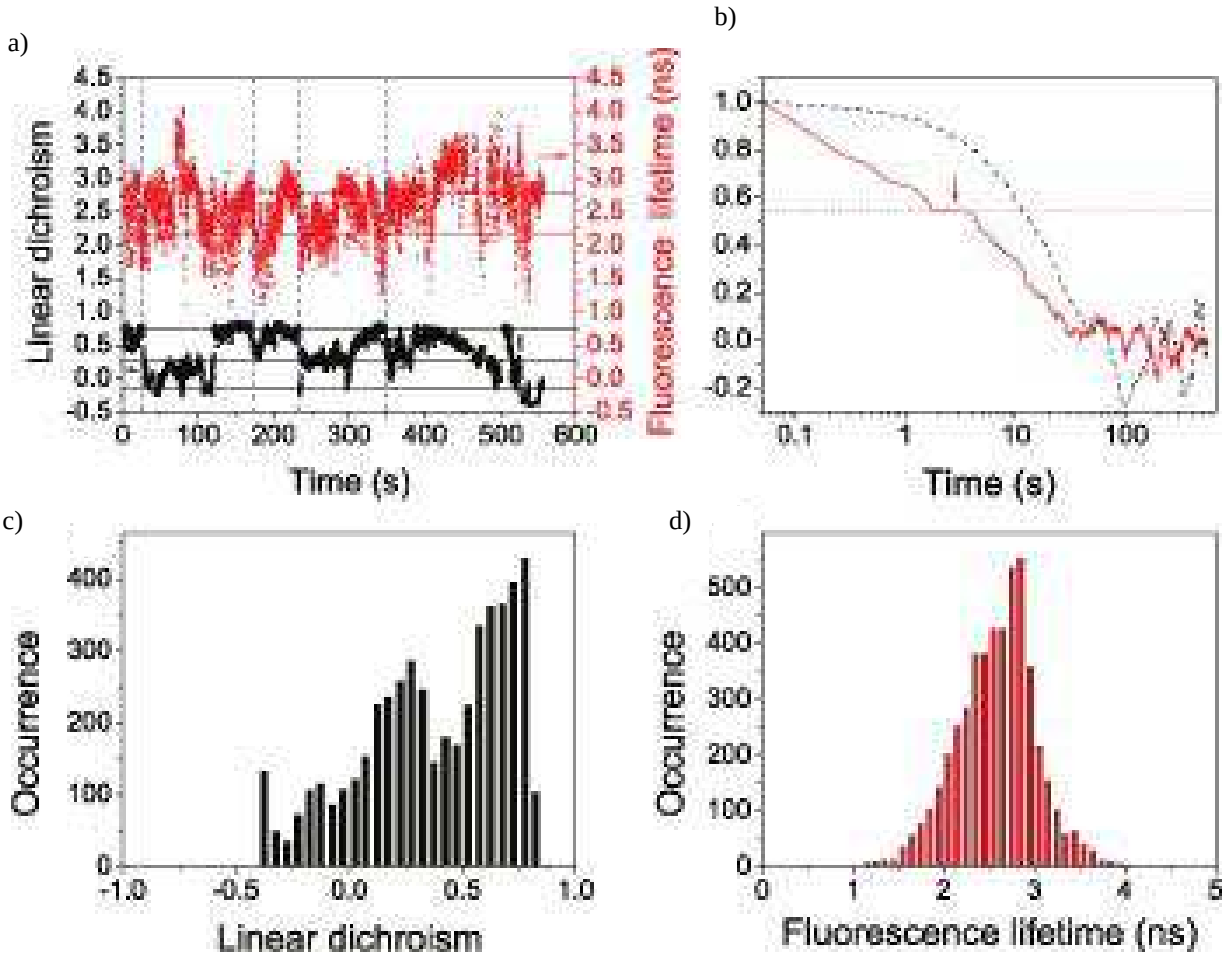

FIG. 4. a) Trajectoires expérimentales de dichroïsme linéaire (noir) et de durée de vie de fluorescence (rouge) d'une molécule de terrylène diimide ayant quatre bras phénoxy (TDI) qui se réoriente et subit des changements conformationnels dans une matrice de polystyrène au dessus de la température de transition vitreuse. Les lignes horizontales sont des guides pour situer les différents niveaux de dichroïsme (noir) et de durée de vie (rouge). Les lignes verticales montrent les instants auxquels des sauts corrélés de durée de vie et de dichroïsme linéaire interviennent, signalant essentiellement des réorientations de la molécule entière dans la matrice. Les fonctions d' autocorrélation correspondantes sont montrées en b) avec des temps de relaxation de 23 (dichroïsme linéaire) et 11s (durée de vie). Remarquons que la fonction d'autocorrélation temporelle de la durée de vie présente un plateau à mi-hauteur de la décroissance pour un temps typique d'1 s, plateau que l'on n'observe pas dans le cas du dichroïsme linéaire. Ce plateau indique en fait l'existence d'un phénomène de relaxation plus rapide que la réorientation complète de la molécule et que l'on a attribué au repliement d'au moins un bras de la molécule de TDI. Le faible changement d'orientation du moment dipolaire de transition de la molécule, lié au repliement de ce bras n'est pas perceptible par l'observable dichroïsme linéaire, moins sensible que l'observable durée de vie. En c) et d) sont représentées les distributions de dichroïsme linéaire et de durée de vie, respectivement. Elles indiquent trois orientations principales adoptées par la molécule au cours du temps, avec de larges fluctuations autour de chaque orientation et deux durées de vie de fluorescence principales, à 2.2 et 2.75 ns, liées à l'observation de 2 conformères différents de la molécule de TDI.

calement la dynamique des sytèmes désordonnés hétérogènes, deux types d'expérience avaient eu lieu. Le premier type d'expérience a été l'observation remarquable de sauts 'tunnels' de systèmes à deux niveaux dans des systèmes amorphes (ou semicristallins) plongés à température cryogénique, dont l'existence avait été postulée pour expliquer l'origine de la capacité calorifique, la conductivité thermique et l'atténuation d'ondes ultasonores anormalement élevées dans ces matériaux. Le second concerne les expériences effectuées dans l'état surfondu et sondant les temps caractéristiques de réorientation 2D ou 3D des molécules fluorescentes, menant à l'observation de l'existence d'une dynamique spatialement hétérogène pour expliquer l'origine de la non-exponentialité des fonctions de relaxation temporelles. A l'époque, il manquait donc une méthode permettant de mesurer localement la dynamique temporelle à n'importe quelle température. En particulier, il manquait une méthode permettant de sonder la dynamique à des températures proches mais en dessous de la température de transition vitreuse où des réorientations significatives d'une molécule entière sont très peu probables. L'enregistrement des trajectoires temporelles caractéristiques de durées de vie radiatives de molécules fluorescentes plongées dans ces systèmes désordonnés a fourni cette méthode. Comme expliqué

ci-dessus, l'analyse de ces trajectoires pour des centaines/milliers de molécules dispersées dans différents polymères pour différentes températures, épaisseurs de films, teneurs en solvant ont permis de déterminer pour chaque molécule dans chaque environnement un nombre de segments effectifs du polymère environnant se réarrangeant localement autour de la molécule afin de créer ces changements de durée de vie. Cette approche, qui a donné des résultats remarquables en termes des tendances observées, était macroscopique, puisque utilisant implicitement le concept d'indice de réfraction effectif dans la description, et donc inappropriée à un certain point. C'est pourquoi j'ai envisagé une description microscopique en termes de polarisabilté des espèces environnantes interagissant avec le moment dipolaire de transition de la molécule sonde. Basé sur cette description, les résultats obtenus expérimentalement à des températures en dessous et au dessus de la température de transition vitreuse ont pu être interprétés qualitativement et quantitativement. Des corrélations fortes ont pu être établies entre les trajectoires expérimentales et simulées et ont permis de commencer à comprendre sinon quantifier et confirmer certains points des théories microscopiques et d'autres phénoménologiques de la transition vitreuse. Les corrélations pouvant être établies entre trajectoires de durée de vie, trajectoires orientationelles et points forts de la théorie ont été simulées et analysées et certaines ont pu être vérifiées expérimentalement, à des températures supérieures à la transition vitreuse. C'est là une approche unique à mon sens dans le domaine de la molécule unique dans les systèmes désordonnés et elle a déjà montré son intérêt pour l'analyse de systèmes autres que ceux liés au phénomène de la transition vitreuse, notamment dans le domaine biologique.

L'observation de l'existence de différents conformères d'une molécule fluorescente donnée et des changements de conformation de ces molécules dans les polymères, basé sur l'observable durée de vie, est une nouvelle approche également, qui a été validée dans différents régimes de température. Elle est suffisante par elle-même pour déterminer certains paramètres comme le volume libre local (ou la distribution de volume libre dans l'échantillon) ou le degré d'empaquettement local dans un polymère à l'état vitreux et complète admirablement les mesures orientationelles afin de déterminer l'étendue spatiale des mouvements de chaine (processus α ou β) induisant les changements de conformation ou d'orientation de la molécule fluorescente.

Les deux thésards que j'ai eu l'occasion d'encadrer dans une partie de ces études ont fortunément tous deux trouvé un emploi, l'un dans un laboratoire de recherche à Singapour, l'autre dans l'enseignement de la physico-chimie en école supérieure en Belgique.

III. ENSEMBLES DE MOLÉCULES DANS LES CRISTAUX PHOTONIQUES ET NANOSTRUCTURES PLASMONIQUES

Le contrôle de la lumière émise spontanément par un matériau constitue le coeur de l'optique quantique. Il est essentiel pour diverses applications allant des lasers miniatures aux diodes électroluminescentes en passant par les sources de photon unique pour l'information quantique. Afin d'explorer de telles nouvelles applications de l'optique quantique, il est nécessaire de concevoir soigneusement un environnement diélectrique dédié, pour lequel le couplage avec les modes photoniques, qui contrôle l'émission spontanée, peut être manipulé.

Les cristaux photoniques fournissent un tel environnement. Ce sont des (nano) structures diélectriques ou métallo - diélectriques empilées périodiquement et conçues de manière à modifier la propagation des ondes électro-magnétiques de la même façon que le potentiel périodique dans un cristal semi-conducteur modifie le mouvement électronique par la création de bandes d'énergie électronique permises et interdites. L'absence de modes électro-magnétiques pouvant se propager dans les structures dans une gamme de longueur d'ondes bien définie est appelée une bande interdite photonique. La présence de cette bande interdite donne lieu à des phénomènes optiques très spécifiques, comme l'inhibition de l'émission spontanée, des miroirs autoréfléchissants omnidirectionnels, des filtres optiques et des guides d'onde sans pertes. Puisque le phénomène physique de base impliqué est la diffraction, la périodicité des structures photoniques doit être réalisée sur une échelle spatiale de l'ordre de la demi longueur d'onde de l'onde électro-magnétique utilisée, c'est-à-dire environ 300 nm pour des cristaux photoniques opérant dans la gamme visible du spectre lumineux. La forme la plus simple de cristal photonique est une structure périodique à une dimension (1D), par exemple multi-couches (miroir de Bragg); la propagation des ondes électro-magnétiques dans de tels milieux fut d'abord étudiée par Lord Rayleigh en 1887, qui a montré que toute structure à une dimension de cette forme présente une bande interdite. Ces systèmes ont été investigués plus en profondeur et des applications sont notamment apparues dans les revêtements réfléchissants (où la bande de réflexion correspond à la bande photonique interdite) et des structures à rétroaction distribuée (DFB distributed feedback diode lasers; où un défaut cristallographique est inséré dans la bande photonique interdite pour définir la longueur d'onde du laser). La possibilité de fabriquer des cristaux photoniques à deux (2D) et trois (3D) dimensions a été suggérée 100 ans après la découverte de Lord Rayleigh, par Eli Yablonovitch et Sajeev John et une réalisation pratique, permettant le contrôle du flux d'émission spontanée à l'aide ce ces cristaux tri-dimensionnels, a eu lieu très récemment.

Les nanostructures plasmoniques fournissent un autre terrain de jeu pour la manipulation des taux d'excitation et

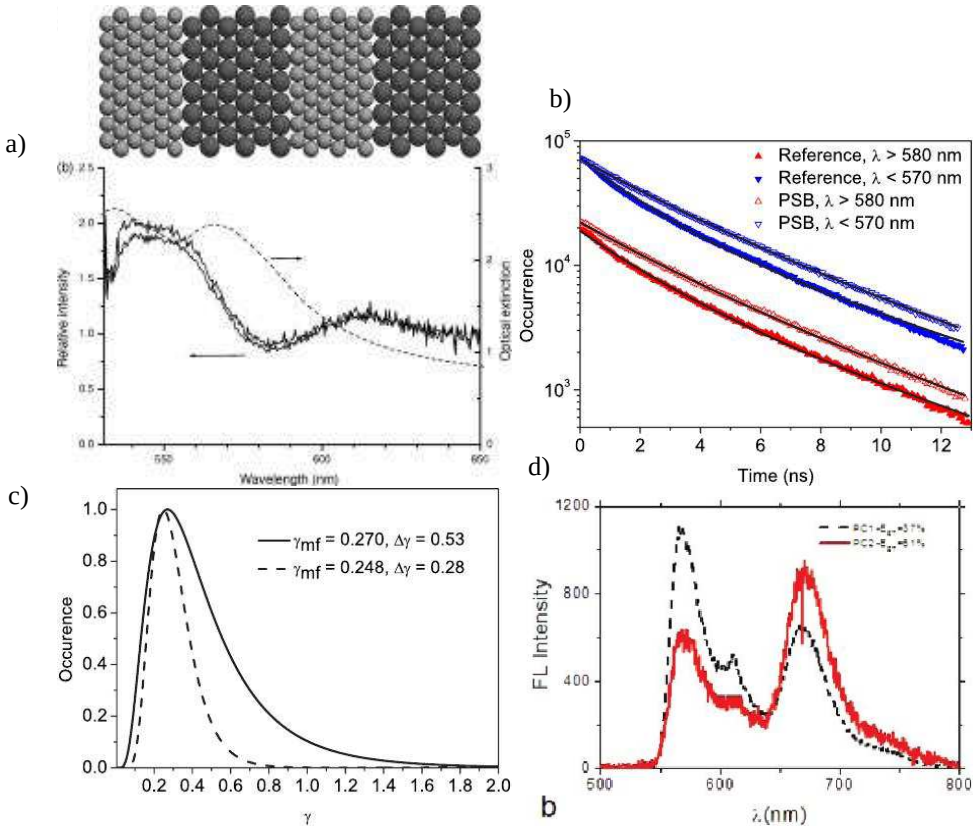

FIG. 5. a)Représentation schématique d'un super-réseau multicouches épais ABAB composé de billes de différentes tailles (A est composé de billes de 250 nm de diamètre et B de billes de 260 nm de diamètre). Chacun des sous-réseaux pris individuellement (soit A soit B) présente une BPI (à une longueur d'onde$\lambda = 532\,nm$ pour A et $\lambda = 577\,nm$ pour B). Leur juxtaposition en super-réseau génère l'apparition d'une bande photonique permise (BPP) dans la zone de recouvrement partiel des BPIs (il est connu que l'apparition d'une BPI correspond à une diminuation de la densité locale d'états d'états photoniques (LDOS) au centre de la bande et à une augmentation de cette LDOS en bords de bandes; l'idée de juxtaposer des réseaux ayant des BPIs spectralement proches étaient de profiter de ces augmentations de LDOS en bords de bandes de chacune de ces BPIs pour créer une BPP. Le spectre d'extinction normalisé (par rapport à celui d'un échantillon de référence ayant un BPI en dehors de la zone d'intérêt) montre bien l'apparition de cette BPP au sein de la BPI étendue du super-réseau. L'effet de cette BPP est également clairement visible sur le spectre d'émission normalisé des fluorophores insérés dans le cristal qui montre une exaltation de fluorescence à la longueur d'onde $\lambda = 550\,nm$ de la BPP, bien au centre des BPIs des sous-réseaux constituants. b) Profils de décroissance de fluorescence d'un ensemble d'émetteurs situés soit dans un échantillon de référence (ayant une BPI à 376 nm) soit dans l'échantillon actif (ayant une BPI à 566nm) enregistrés dans des gammes de longueurs d'onde se superposant à la BPI ($\lambda < 570\,nm$) ou supérieures ($\lambda > 580\,nm$). Les déclins temporels montrent une décroissance non exponentielle et les profils ont été ajustés au mieux par des distributions continues des taux d'émission spontanées montrées en c). Le taux d'émission spontanée est légèrement réduit en présence de la BPI (ce qui est attendu théoriquement) et présente une distribution plus fine que celle de l'échantillon de référence. Ce dernier fait peut s'intepréter par effet de la BPI qui interdit toute émission trop rapide d'un photon du fait de la diminution de la LDOS. d) Spectres d'émission d'un couple FRET Cy3-Cy5 dans un cristal photonique de référence (ligne rouge) et actif présentant une bande stoppante centrée sur $\lambda = 600\,nm$ (pointillé noir). Le transfert d'énergie résonante de Cy3 vers Cy5 est clairement favorisé dans l'échantillon actif: l'émission spontanée des molécules Cy3 est retardée du fait de la diminution de LDOS à cette fréquence et favorise donc les processus de transfert d'énergie vers Cy5 (la compétition entre le temps de fluorescence et de transfert d'énergie dans cette structure active favorise le FRET).

d'émission spontanée. Les particules métalliques ou métallo-diélectriques de diamètre $10 - 100\,nm$ et les nanostructures présentant un relief de surface de taille caractéristique similaire ($10 - 100\,nm$) sont connues pour modifier la distribution spatiale d'un champ électromagnétique incident. Une exaltation de champ local cause une augmentation de l'absorption des photons par des molécules ou nanocristaux adsorbés ou greffés à proximité de la surface. Cet effet est extrêmement prononcé dans des structures métallo-diélectriques du fait des résonances de plasmons de surface. L'exaltation de champ local joue un rôle non seulement dans le processus d'excitation mais il augmente également la densité locale d'états photoniques, favorisant ainsi les processus de photoluminescence et de diffusion. La différence majeure entre les procesus de photoluminescence et de diffusion (Raman en particulier) se situe au niveau des pro-

cessus de 'quenching' qui sont cruciaux pour l'observation d'émission spontanée et jouent un rôle moins important en diffusion. L'ingénieurie de nanostructures plasmoniques en vue d'exalter l'émission de fluorescence nécessite donc un contrôle plus important de paramètres tels que la position et l'orientation des molécules à proximité des surfaces métalliques, ...

III.1. Emission dans les cristaux photoniques

Durant mon postdoctorat à l'Université de Leuven en Belgique et en collaboration avec le groupe du professeur Clays, en particulier avec les étudiants Kasper Baert et Wim Libaers que j'ai co-supervisé durant leur master et thèse, nous avons pu manipuler l'émission spontanée de fluorophores insérés dans un super-réseau colloïdal [16]. Ce super-réseau photonique a été ingénieuré par auto-assemblage convectif de multicouches de billes de silice de deux tailles différentes. Cet assemblage particulier a permis de créer une bande photonique permise (BPP) afin d'exalter spécifiquement l'émission des fluorophores dans cette bande restreinte. Nous avons démontré expérimentalement l'émission spectrale restreinte des fluorophores insérés dans une telle structure, avec une largeur d'émission comparable à celle d'un seul mode électro-magnétique, première indication d'un phénomène d'émission laser (Fig.5a).

La mesure de la durée de vie des fluorophores incorporés dans ce type de matériaux a également été effectuée [17]. La durée de vie augmente considérablement (le taux d' émission est réduit), comme prédit par la théorie, lorsque le matériau étudié présente une bande stoppante. Le signal de fluorescence montre un profil fortement non exponentiel, du aux différences de positionnement et d'orientation des fluorophores par rapport aux billes de silice (Figs 5b et c). La réduction du nombre détats photoniques accessibles à l' émetteur en présence d'une bande stoppante entraîne une augmentation de la durée de vie de cet émetteur. De ce fait, nous avons démontré qu' on pouvait également contrôler le taux de transfert d'énergie du donneur (D) vers l'accepteur (A) dans un système FRET (Fluorescence Resonant Energy Transfer) usuel plongé dans un cristal colloïdal photonique proprement ingénieurié (Fig. 5d) [18].

Enfin, dans une approche combinant des propriétés de BPI et des fonctionnalités magnétiques à un matériau ingénieuré à différentes échelles de longueur, nous avons pu montrer une exaltation et une modulation de la rotation Faraday dans un cristal photonique, après infiltration de petites nanoparticules magnétiques d'oxyde de fer [19].

Arrivé au Centre de Recherche Paul Pascal comme chargé de recherche CNRS en 2008, **mes activités s'y sont tout de suite développées avec le professeur Serge Ravaine et son étudiant en thèse Jean-François Dechézelles avec lequel j'ai fortement intéragi durant ses deux dernières années de thèse**. Ainsi, nous avons étudié ensemble, dans un premier temps, les propriétés de transmission/réflexion UV-visible-IR d'opales présentant soit une bande photonique interdite soit une bande photonique permise (BPP) à l'intérieur de la BPI. Les matériaux à BPI furent ingénieurés en déposant couche par couche 10/20 monocouches à structure hexagonale de billes de silice de taille monodisperse par la technique de Langmuir-Blodgett. Cette même technique peut être utilisée pour déposer, à l'endroit voulu dans la multicouche, une monocouche de billes de taille différente soit plus petite / soit plus grande pour créer un défaut de type accepteur / donneur et donc une bande permise dans la BPI. Afin d'étudier les effets d'exaltation / inhibition dus à la modification de la LDOS dans ces cristaux photoniques, des émetteurs avaient été insérés dans les billes de silice préalablement à leur arrangement dans le cristal. Deux types d'émetteurs furent utilisés dans des expériences différentes. Dans le premier cas, nous avons utilisé de clusters de molybdène [20] à bande d'émission large, englobant la largeur spectrale de la BPI / BPP des cristaux considérés tandis que des nanoparticules de vanadate d'Europium ayant un spectre d'émission très fin [21] ont été utilisés dans le second cas. Dans les deux cas, la taille des billes synthétisées a été choisie de façon à ingénieurer des cristaux ayant une BPI / BPP coïncidant spectralement avec le maximum des spectres d'émission des deux espèces choisies, à incidence normale. **En collaboration avec le Groupe d'Agnès Maître à l'INSP à Paris**, nous avons alors effectué des expériences de réflexion et d'émission résolues en angle. Dans le premier cas, nous avons pu montrer un déplacement concomittant de la BPI / BPP (observé dans les spectres de réflexion UV-visibles) et de l'inhibition / exaltation de fluorescence (observé dans les spectres d'émission) en fonction de l'angle incidence (Fig. 6a) [20]. Le spectre large des clusters de molybdène nous a donc permis de tracer la variation de la LDOS lors du déplacement effectué dans l'espace réciproque en suivant la relation de dispersion des photons dans le cristal. Dans le second cas des spectres très fins de vanadate d'Europium, nous avons pu montrer un comportement on / off de l'exaltation / inhibition de fluorescence (Fig. 6b), une variation minime de l'angle d'incidence faisant entrer / sortir la BPP / BPI dans le spectre d'émission de l'espèce luminescente [21].

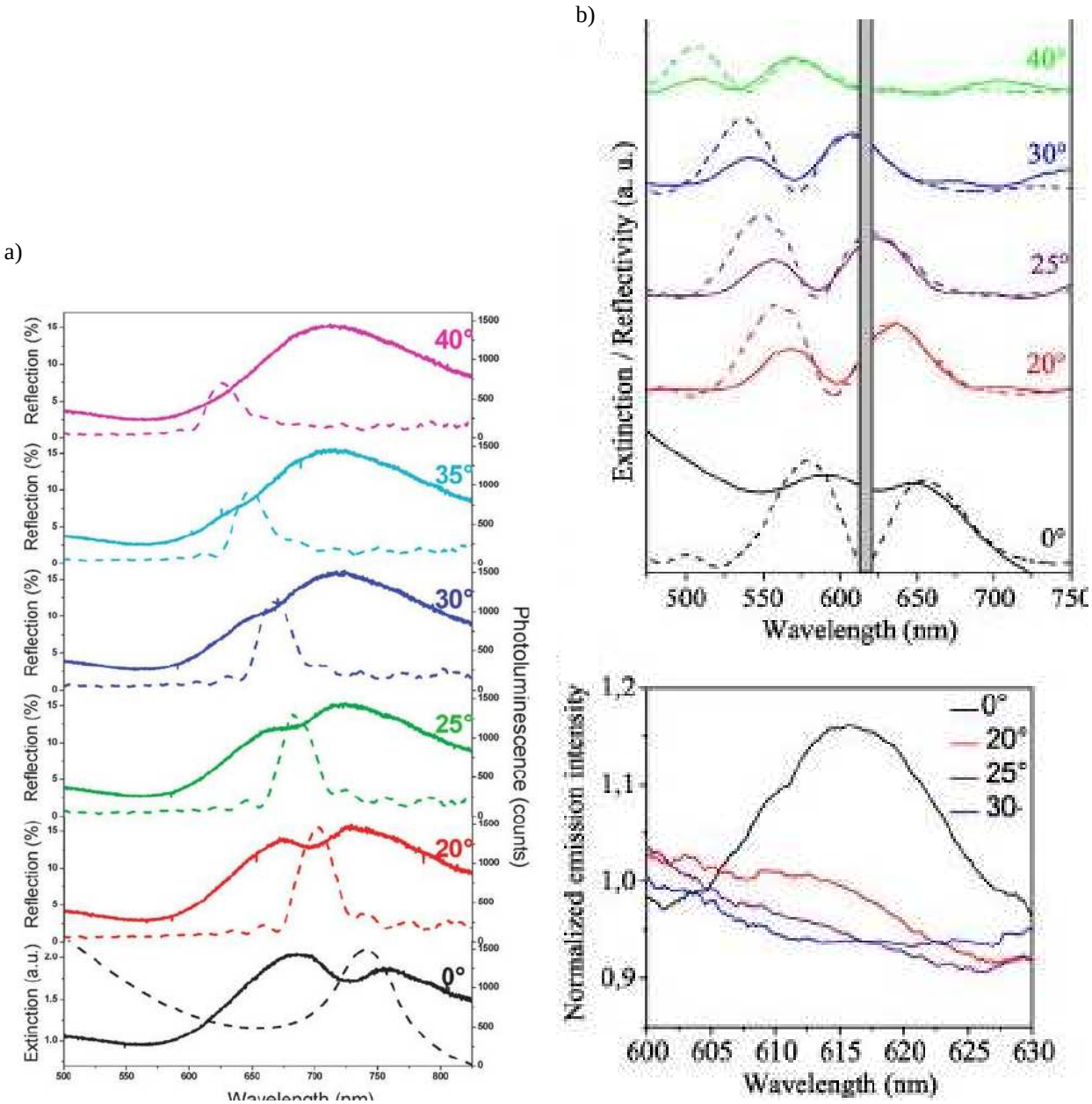

FIG. 6. a) Dépendance angulaire des spectres d'extinction (à$\alpha = 0^o$) et de réflexion (pour des angles splus grands) et spectres d'émission correspondants d'une structure à BPI contenant des clusters de $CS_2Mo_6BR_{14}@SiO_2$ comme émetteurs large bande. b)Dépendance angulaire des spectres d'extinction (à$\alpha = 0^o$) et de réflexion (pour des angles plus grands) d'une structure à BPP contenant des particules de $YVO_4 : EU@SiO_2$ comme émetteurs à bande étroite. Les spectres d'émission correspondants sont également montrés, normalisés par rapport au spectre enregitré à $\alpha = 40^o$ (angle pour lequel l'effet de la BPP ne se manifeste plus sur le spectre d'émission). Un comportement on/off de l'exaltation d'émission est clairement visible en fonction d'une modification de l'angle α.

III.2. Emission dans les nanostructures plasmoniques

Trois types d'activité ont été lancées en nanoplasmonique à mon arrivée au CRPP. Dans la première, **en collaboration avec Stéphane Mornet à l'ICMCB et David Talaga à l'ISM, à Bordeaux**, nous avons réalisé et étudié les propriétes optiques de résonateurs de type Fabry-Pérot semi-courbes. Ces résonateurs sont constitués d'une monocouche de billes de silice prise en sandwich entre deux surfaces métalliques d'or, l'une déposée à plat sur un substrat, l'autre déposée sur les billes et donc suivant la géométrie sphérique-périodique de la monocouche. Ces résonateurs, de taille submicrométriques, présentent des modes de cavité similaires à ceux décrits dans la littérature

pour des nanoparticules coeur de silice - écorce d'or. Ces modes se manifestent comme des minima dans les spectres d'émission relevés pour chacune des nanostructures, minima dont la position spectrale évolue avec la taille des billes [22]. Une comparaison simulations FDTD-expériences indique clairement que deux des trois minima observés proviennent d'un couplage entre les résonances quadrupolaire et dipolaire des plasmons de surfaces et les modes de cavité, couplage qui se révèle inexistant si les couches métalliques qui environnent la monocouche de billes étaient toutes deux plates.

Dans la seconde activité, **en collaboration avec le groupe de Pascal Damman à l'Université de Mons en Belgique et le groupe de Frank Träger à l'Université de Kassel en Allemagne**, nous avons développé une nouvelle approche pour créer et moduler la géométrie de nanocanaux sur des substrats de silice frittée par utilisation des effets de polarisation et d'intensité du champ proche localisé à proximité de nanoparticules métalliques triangulaires organisées en structure hexagonale. Ces structures hexagonales de triangles ont été créées par lithographie 'nanosphère'. Par la suite, ces structures ont été irradiées par de impulsions femtosecondes ($35\,fs$) avec une fluence plus ou moins grande. Cette irradiation conduit à l'excitation de plasmons de surface localisés au niveau des pointes de nanotriangles. En fonction de la fluence, le seuil d'ablation de la silice frittée peut être dépassé, conduisant à la génération de trous au bout des pointes des triangles ou de nanocanaux reliant les différents triangles. En tournant la polarisation de 90^o par rapport à l'orientation du réseau de nanoparticules, d'autres patrons d'ablation peuvent être obtenus. La comparaison simulations-expériences montre clairement que ces patrons d'ablation résultent de l'exaltation localisée du champ électromagnétique due aux résonances plasmons des nanotriangles [23].

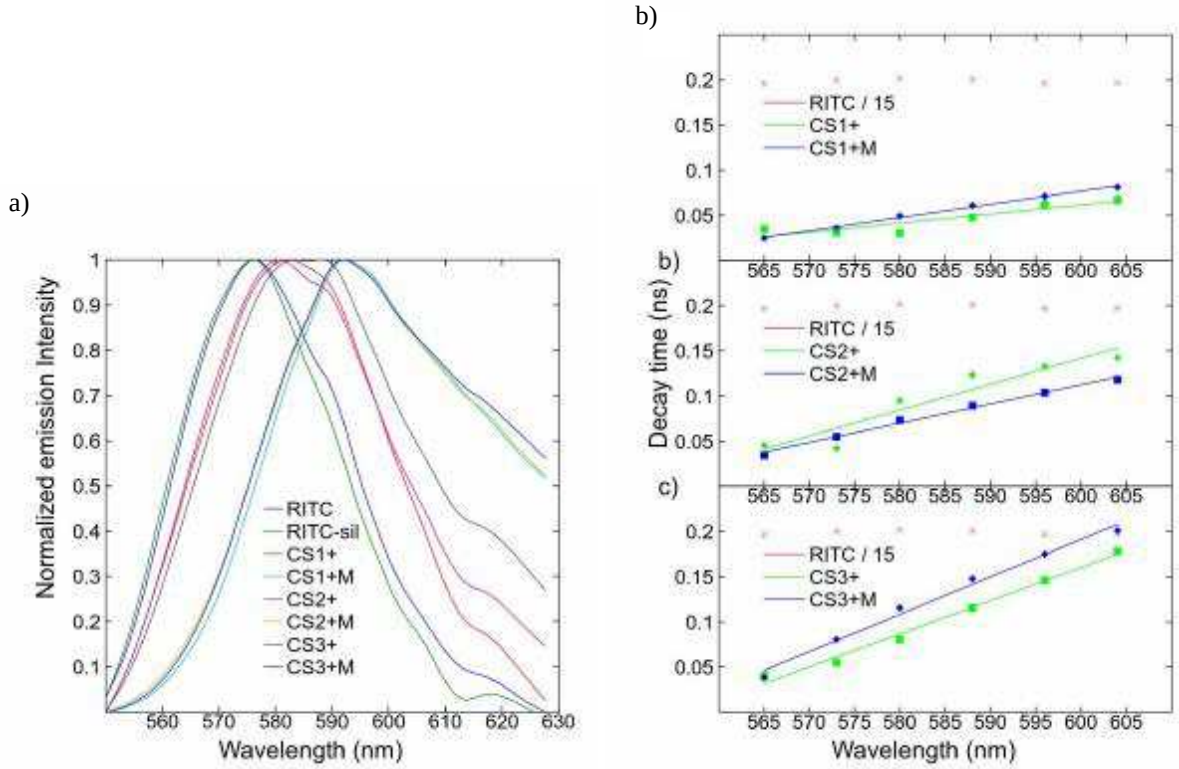

FIG. 7. a) Spectres d'émission de molécules de RITC, de molécules de RITC greffées sur un nanoparticule de silice de $100nm$ de diamètre et de molécules de RITC greffées sur une écorce de silice d'épaisseur 10 (CS1+), 20 (CS2+) et $30nm$ (CS3+) entourant le coeur d'or de diamètre $D = 60\,nm$ en solution éthanolique. Les spectres d'émission des multimères correspondants (CS1+M, CS2+M, CS3+M) sont également montrés. Notons l'aspect filtre passe-bas en émission bien marqué pour les multimères. b) Durées de vie moyenne, déterminés sur base d'un ajustement à l'aide d'une exponentielle étirée, en fonction de la longueur d'onde, des déclins de fluorescence correspondants aux différents groupements particulaires cités en a). Dans tous les cas où les molécules de RITC sont greffées sur une particle coeur d'or - écorce de silice, les durées de vie ont été drastiquement diminuées, ce d'autant plus que les molécule de RITC sont proches du coeur d'or (CS1+ et CS1+M). De plus, on oberve une croissance linéaire de la durée de vie en fonction de la longueur d'onde. Cette dernière résulte d'une compétition entre les processus non-radiatifs à la fréquence de résonance plasmon des particules et les processus radiatifs qui se développent à plus grande longueur d'onde.

Enfin, la troisième activité concerne **une partie du travail de thèse de Mélanie Ferrié, avec laquelle j'ai fortement intéragi** et consiste en la réalisation et l'étude des propriétés optiques de nanoparticules coeurs d' or -écorces de silice, englobant des émetteurs organiques (RITC ou Rhodamine B greffé avec un groupement IsoThioCyanate en l'occurence) situés à distance contrôlée du coeur d'or et de la surface extérieure. Trois types de nanoparticules, de tailles différentes, ont été synthétisées. Dans les trois cas, les coeurs d'or ont un diamètre de $60\,nm$. Ensuite, suivant les cas, une première écorce de silice a été greffée, dont la taille est de 10, 20 ou $30\,nm$. Les émetteurs sont alors greffés en surface avant d'être recouvert d'une seconde écorce de silice de $10\,nm$ d'épaisseur, afin de procurer le même environnement diélectrique de part et d'autre des émetteurs. Nous avons montré que les spectres d'émission de ces nanoparticules dispersées dans l'éthanol sont légèrement déplacés vers les grandes longueurs d'onde par rapport aux spectres d'émission des émetteurs seuls en solution (Fig. 7a) éthanolique. De plus, les durées de vie de fluorescence des émetteurs ont subi une réduction drastique dans toute la gamme spectrale enregistrée (Fig. 7b), réduction due d'une part aux processus non radiatifs à la résonance plasmon des nanoparticules et d'autre part aux processus radiatifs aux plus grandes longueurs d'onde [24]. L'assemblage de ces trois types de nanoparticules en multimères a également été réalisé, quoique sans contrôle du degré d'oligomérisation. Les spectres d'émission sont cette fois décalés plus fortement vers les grandes longueurs d'onde (Fig. 7a), les processus de transfert d'énergie non radiatives des émetteurs vers le métal réduisant fortement l'émission radiative à la résonance plasmon. Ce fait observé permet par ailleurs de considérer ces structures comme des filtres passe-bas pour l'émission de fluorescence. Les durées de vie mesurées des émetteurs dans ces multimères correspondent sensiblement à celles de nanoparticules monomériques (Fig. 7b) [24].

III.3. Intérêt de la démarche adoptée

Les cristaux photoniques sont souvent cités comme structures potentielles permettant de manipuler la lumière, spécialement jusqu'au niveau du contrôle, quantique, du taux d'émission spontanée avec des applications éventuelles en informatique quantique. Dès le début de cette activité, les voies top-down (de la physique) ont toujours dominé la fabrication des structures requises et la voie bottom-up (de la chimie) se posait en challenger. De bons résultats, rares malheureusement de par la difficulté de mise en oeuvre, ont été obtenus avec des opales inverses de titane, montrant une inhibition marquée (20%) de la durée de vie due à une diminution de la LDOS dans la BPI. C'est dans cette perspective de modulation de la LDOS que nous avons démarré nos activités de recherche dans les cristaux colloïdaux, les procédures de chimie sol-gel employées nous permettant d'ingénieurer aussi bien des structures à BPP (exaltation de fluorescence) et BPI (inhibition de fluorescence). Les résultats que nous avons obtenu sont significatifs et permettent de bien comprendre les phénomènes mis en jeu. En particulier, les expériences effectuées sur le couple FRET mettent bien en évidence la compétition entre processus radiatifs et non-radiatifs et la manière de favoriser l'un de ces composants par imposition d'une diminution de LDOS à l'autre. Remarquablement, le contrôle de cette compétition permet de générer une structure émettant une couleur différente. En combinant cette expérience avec l'expérience de dépendance angulaire (ou en envisageant une structure où le diamètre des billes serait modulable), il est à priori possible de modifier la couleur de manière plus uniforme (un trio FRET RGB serait même intéressant à envisager dans ce cas). Cependant les diminutions/augmentations de fluorescence observées sont trop faibles pour les applications telles que l'information quantique. Pour envisager ces dernières, il s'agit maintenant d'augmenter les contrastes d'indice et l'arrangement cristallin des structures, pierres d'achoppements sur lesquelles butent toutes les groupes travaillant en 3D actuellement.

D'autre part, les nanostructures plasmoniques s'avèrent extrêment intéressantes de par le contrôle et l'amplitude des exaltations de champ local qu'elle permettent d'engendrer, favorisant ainsi la création de patrons d'ablation et l'apparition de forts taux d'excitation et d'émission spontanée (et de diffusion) de molécules situées à proximité. Deux des trois perspectives / projets de travail pour le proche futur que je décris ci-après concernent ces systèmes.

IV. PERSPECTIVES - PROJETS FUTURS

J'envisage trois types d'activité à réaliser dans mon proche futur, en collaboration avec des collègues du CRPP et des partenaires extérieurs. Il s'agit: i) de développer des matériaux extrêmement désordonnés afin d'étudier les phénomènes de localisation de la lumière et de lasers aléatoires, en collaboration avec Rénal Backov au CRPP et l'équipe de Rémi Carminati à l'ESPCI. ii) de développer des nanostructures plasmoniques combinant plasmons de surface localisés et propagatifs afin de générer des facteurs de Purcell élevés dans une gamme spectrale soit très large soit très fine, en collaboration avec Serge Ravaine au CRPP. iii) de développer des structures plasmoniques sensibles à l'effet Kerr optique afin de réaliser des bistables optiques.

IV.1. Disordered materials for light localization and random lasing

Diffusive transport of light energy in 3D scattering samples can be understood using a particle point of view, corresponding to the image of light ray trajectories plotted between two scattering events. If the scattering mean free path becomes so small that even a single oscillation cannot be performed by a wave between successive scattering events, the diffusive picture breaks down. This limit is known as the Ioffe-Regel (localization) criterion $kl_t < 1$, where $k = 2\pi/\lambda$ is the wavenumber in the medium. In this regime, the wave spatially localizes in the disordered medium. This severe condition is hard to reach in the optical frequency range of electromagnetic waves, and the observation of 3D localization of light is still an open issue, in spite of the many efforts that have been made so far to create such conditions in artificial media.

While being first introduced for electron conductivity processes, Anderson localization [25] is possible for all types of waves provided the localization criterion is fulfilled in terms of sufficiently strong fluctuations of the physical parameters determining the speed of waves. For electromagnetic waves, refractive index fluctuations are the relevant parameters. S. John was the first to outline the possibility of Anderson localization of electromagnetic waves in 1984 [26]. This report was followed promptly by the elegant comment by P. W. Anderson [27] and since then localization of light has become a challenge for experimentalists. However, experimental observation of the Anderson localization of light is hard to perform and no straightforward observation of light localization has been reported up to now. The principal obstacle is the relatively low refractive index of materials in the optical range. Several experiments have been carried out towards the observation of Anderson localization of light [28–32]. Wiersma et al. [28] used GaAs powder ($n = 3.48$) with different average particle diameters. Upon reducing the average particle diameter, these authors found three distinctive regimes of light propagation. The first one was the known $T \simeq l_t/L$ behavior, inherent in diffusive light transport, where T is the total diffuse transmission, L the sample thickness and l_t is the transport mean free path. The second one, observed as the particle mean diameter was reduced down to $1\mu m$, was a quadratic dependence $T \propto L^2$, predicted by the scaling theory of localization at the localization transition [33]. Finally, for smaller particle diameter of about $0.3\mu m$, the exponential transmission law was observed: $T(L)exp^{(-L/l_{loc})}$, which is a distinctive manifestation of the light localization regime. The localization length l_{loc} was found to be $l_{loc} = 4.3\mu m$.

However, this exponential law formally coincides with the Beer-Lambert law inherent of inelastic (absorptive) losses, expressed in the form $T(L) = exp(-L/l_{abs})$. This fact generated a controversial issue concerning the real cause of the exponential behaviour: absorption or localization [29]. In experiments with Ge powders ($n = 4.1$) in the near infrared, a non-negligible absorption partially contributed to the observed exponential T(L) law [30]. It thus turned out that further signatures of light localization were to be searched for. Maret et al. [31, 32] considered possible alternative manifestations of the Anderson localization of light. They performed experiments with dense TiO_2 ground beads of a size close to the optical wavelength packed in dense layers of $1.2 - 2.5mm$ thickness. They observed and reported increasing deviations from the exponential time dependence predicted by the diffusive transport theory. For a sample with large kl_t value, the temporal profile of the output light pulse featured good agreement with the theory of diffusive transport and exhibited an exponential tail at longer times. For smaller kl_t values, a discrepancy with the diffusive transport theory manifested, which increased while kl_t was getting smaller and smaller. In these cases, the transmission tail was found to be reasonably well described by a modified diffusion equation taking into account a time-dependent diffusion coefficient $D(t)$. They found that D(t) beared witness to a decrease with time as 1/t, as expected from theory in the localization regime. The latter results clearly indicate that time-resolved measurements offer further insight towards the discrimination of light propagation regimes near the localization threshold.

A first objective of this project is the study of fundamental aspects of light transport in complex disordered materials (dielectric, metallic and hybrid). To reach this goal we will merge together knowledge in multiple scattering and transport of waves, nanophotonics and material design and fabrication. State-of-the-art bottom up approaches for the fabrication of materials will be used to design samples combining strong multiple scattering and local enhancement of optical intensities. Optical measurements, combining far field and near field as well as steady-state and time-resolved detection, will be used to characterize the photon transport parameters (e.g., mean free path, diffusion coefficient). An expected result with potential impact is the demonstration of the controlled fabrication of 3D samples in a wide range of scattering strengths in the optical regime (from $kl_t >> 1$ to $kl_t < 1$). The expertise of ESPCI in optical measurements (in particular in the near field) and the one of CRPP in physico-chemical approaches for material design and time-resolved optical detection should guarantee the successful achievement of this objective.

A second objective is to pave the way towards the design and realization of a new type of random lasers, based on both multiple scattering of light and local-field enhancement at the nanoscale by plasmon resonances. By adding gain to the multiple scattering samples fabricated and characterized in the project, we will check the existence of a random lasing threshold both theoretically and experimentally.

First, we plan to prepare multilayered reverse metal oxide opals (i.e. TiO_2, ZnO,) by using templates of various sizes. Multi-layered opals made of latex or silica spheres of various diameters (from 400 to 1200 nm) will be first prepared by controlled vertical deposition or by electrophoretic deposition. Then, a metal oxide precursor will be

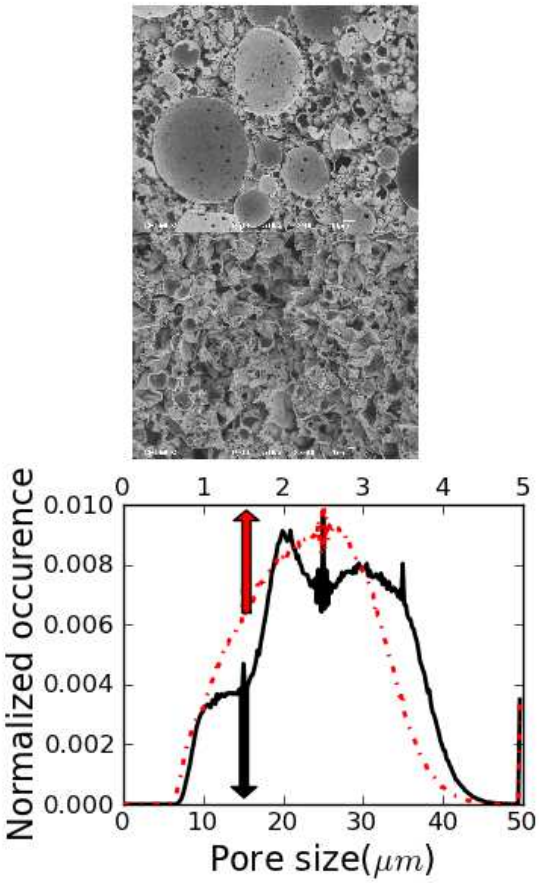

FIG. 8. SEM micrographs of the 30% (top) and 50% (middle) oil volumic fraction HIPE structures, together with their normalized distributions (dotted red lines: 50%; solid black lines: 30%) of pore diameters.

inserted and condensed in the voids to create the oxide walls, the latex or silica templates being removed upon annealing at high temperature or HF treatment, respectively. Inverse oxide opals were recently prepared according to this methodology. The controlled incorporation of colloidal spheres with different sizes or chemical natures in the templates will allow us to tune the degree of disorder of the resulting inverse opals. Furthermore, the assembly of metal@silica@polymer spherical particles with a core@double shell morphology followed by the specific dissolution of the outer polymer shell will permit the fabrication of porous materials containing a gold@silica NP in each pore.

The second step will be the development of 3D-networks bearing hierarchical meso- and macroporous textures. In this aim, metal oxide foams with controlled morphologies and textures (wall thickness, wall curvatures, wall textural topologies, wall degree of mesoporosity, cell diameter) will be prepared using an extension of previously reported procedures based on the use of HIPE (High Internal Polymeric Emulsion). This approach was previously established for silica-based materials and will be extended to metal oxide by playing with lyotropic mesophases and emulsions as dual templates. This emulsion route to prepare porous metal oxide will allow photons to penetrate the porous matrices through the internal surface specificity. The size monodispersity of the pores (i.e., control of the disordered state of the foams) and their density will be controlled through the adjustment of the oil volume fraction and the shearing rate. Free-standing slices of the porous materials with thickness ranging from $100\mu m$ to $10mm$ will be prepared by the doctor-blade technique.

Metal NPs will be inserted in the two types of porous structures following different routes: i) infiltration with a solution of a metal salt followed by chemical reduction; ii) incorporation of the metal salt in the sol of the metal oxide precursor before infiltration of the opals or emulsification followed by chemical reduction.

Preliminary experiments have been conducted and free-standing slices of silica based HIPEs prepared with various volumic fractions, namely 30% and 50%, have been obtained. Fig. 8 shows SEM micrographs of the HIPE structures, together with their normalized distributions of pore diameters. Clearly, by increasing the volumic fraction of oil (from top to middle), the pore size decreases and their size monodispersity is reduced from $10-40\mu m$ to $1-3.5\mu m$ (Fig. 8 bottom). This reduction in size of the pores is expected to decrease the transport mean free path of photons and the

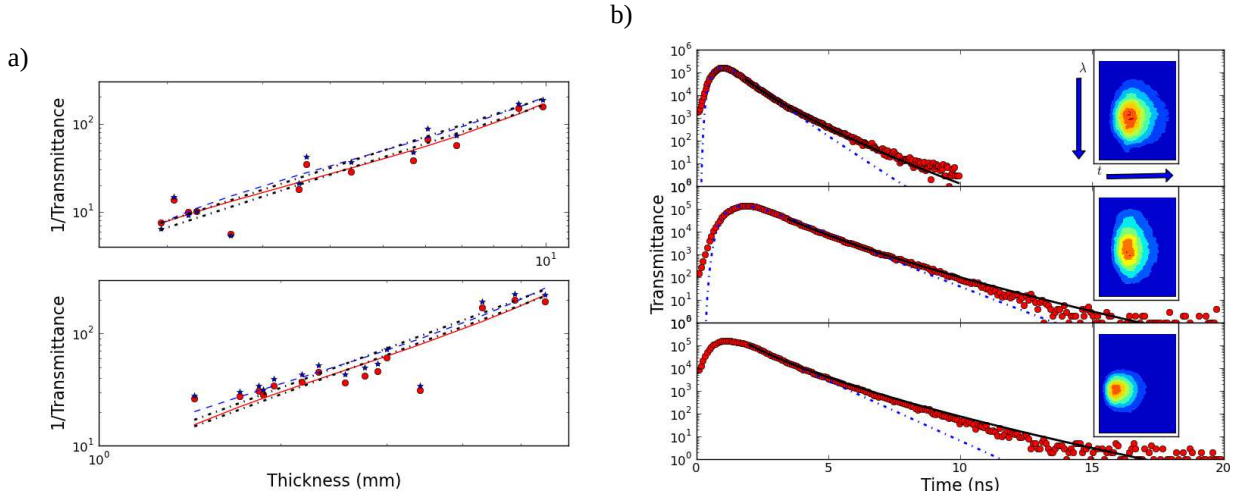

FIG. 9. a) Resistance versus thickness behavior for the 30% (top), 50% (down) volumic fraction HIPE at $\lambda = 500\,nm$ (blue stars) and $\lambda = 700\,nm$ (red circles) fitted by the stationary solution of the diffusion equation (blue dashed and red solid lines, respectively) as well as by the $1/T \propto L^2$ law (dashed-dotted lines). b) Time of flight experiments (red circles) performed on 30% (top, middle), and 50% (down) volumic fraction HIPE. The top and middle figures correpond to 30% samples of 9.8 mm and 12.1 mm thickness, repectively while the bottom one corresponds to a 50% sample with a 4.2 mm thickness. The fits corresponding to the full-dependent solution of the diffusion equation (blue dashed-dotted lines) and the ones corresponding to the asymptotic form of $T(t)$ near the localization transition (black solid lines) are also shown. Insets: part of the wavelength vs time intensity plots, obtained by use of a streak camera, from which the traces are built.

diffusion coefficient. White light transmission versus length T(L) (all angles integrated forward scattering experiment) have been performed on the two types of samples with thicknesses ranging from 2 to 10 mm. Fig. 9a exhibits the conductance versus thickness behavior for the two types of samples at 2 different wavelengths (blue stars: 500 nm and red circles: 700 nm). These results have been fitted by the stationary solution of the diffusion equation (blue dashed and red solid lines in Fig. 9a) leading to a transport mean free path $l_t = 25\,\mu m$, $l_t = 115\,\mu m$ for the 50%, 30% volumic fraction HIPE, respectively. The respective absorption mean free path are $l_a = 2.6\,mm$ and $l_a = 4.2\,mm$. As expected, the transport mean free path is shorter for the HIPE presenting the shorter pore sizes. Also, the latter being the more dense sample, it exhibits the shorter absorption mean free path. Although the stationary solution of the diffusion equation fits particularly well the experimental data, providing values for the transport mean free path such that $kl_t >> 1$, i.e. which are inherent to diffusive light transport, the log-log plot shown in Fig. 9a rather suggests a quadratic dependence $1/T \propto L^2$ (black dash-dot lines provide such fits in Fig. 9a), predicted by the scaling theory of localization at the localization transition [33].

Fig. 9b shows the time of flight experiments performed on three samples, namely two 30% oil volume fraction HIPEs with thicknesses of 9.8mm (top) and 12.1mm (middle) and one 50% oil volume fraction HIPEs with thickness of 4.2mm. Clearly, these samples exhibit a strongly multi-diffusive character, with photons being significantly delayed in the sample in all cases. As the thickness of the sample increases, so does the mean exit time of the photons, while not in a linear way (top and middle of Fig. 9b for small increases of the 30% sample thickness). Furthermore, there is a huge strengthening of the multi-diffusive process while densifying the sample. The 50% volumic fraction HIPE with a thickness $L = 4.2\,mm$ shows a time profile extremely comparable to the one exhibited by the 30% volumic fraction HIPE with a thickness $L = 12.1\,mm$. All traces have been fitted by the full dependent solution of the diffusion equation (blue dashed-dotted lines), which has an asymptotic exponential behavior. Clearly, at long times, the experimental traces deviate from the fits. To account for these deviations, we also fitted the experimental results with the asymptotic form of $T(t)$ near the localization transition, given by:

$$T(t \to \infty) \propto (1/t^{2/3}) exp(-3/2 D_0 (\pi/L)^2 \tau^{1/3} t^{2/3}, \quad (1)$$

featuring a time dependent diffusion constant $D(t) = D_0(\tau/t)^{1/3}$, where τ is the elastic scattering time.

These asymptotic forms (black solid lines) provide an excellent fit of the recorded data and thus give us more confidence that our samples are just not simple multi-diffusive ones, but samples where the induced disorder is such that they enter a regime of diffusion near the localization transition. The values of the diffusion coefficient extracted from the asymptotic forms are $D_0 \approx 750\,m^2/s$ and $D_0 \approx 6000\,m^2/s$ for the 50%, 30% oil volume fraction HIPEs, respectively.

Furthermore, these samples have all exhibited a random lasing behavior when impregnated with Rhodamine 6G laser dyes, with laser tresholds much lower than the one reached by the dyes in a solution.

The (many) next steps are to further densify the structures, to insert metal particles (grafted or not with laser dyes) in different ways in order to increase the localization behavior and use the plasmon resonances of the metallic nanoparticles to further reduce the laser treshold.

IV.2. Plasmonic materials combining localized and propagating surface plasmon resonances for an optimal enhancement of the Purcell factor

Surface plasmons polaritons (SPPs) are collective charge oscillations coupled to light that propagate along a metal-dielectric interface. They can be excited on a metal by grating coupling, the momentum mismatch between SPPs and free-space light being bridged by Bragg vectors inherent in the periodic nanostructures [34, 35]. Localized surface plasmon polaritons (LSPPs), on the other hand, are non propagating charge excitations in metal nanoparticles much smaller than the incident wavelength. The resonance wavelength of the LSPPs depends on the size, shape, and dielectric function of the nanoparticle as well as the dielectric environment [36]. The intense, localized electromagnetic fields associated to SPPs and LSPPs can be used to manipulate and enhance light-matter interactions at subwavelength scales [38, 66]. 2D plasmonic crystals [39] revealed as promising plasmonic components for thin-film photovoltaics [40], light emitting devices[41, 42] optical switches [43], label-free sensors [44–46] and negative index metamaterials [47].

The investigation of how LSPPs and SPPs interact proves to be highly interesting, as structures combining both phenomena could offer extreme light enhancement/manipulation properties. A dipole-surface interaction manifested by measuring the shift of the LSPP resonance when randomly arranged silver nanoparticles were placed near a silver film [48]. In such a structure, the SPP excited on the silver film was shown to further enhance the dipole - dipole interaction between individual nanoparticles [49]. Multiple resonance modes were reported in the extinction spectra of a hybrid structure combining a two-dimensional gold nanoparticle array and a thin gold film, resulting from the coupling between LSPPs and SSPs [50]. More recently, theoretical/experimental studies have predicted/demonstrated that strong coupling between LSPPs and SPPs occurs when their resonance frequencies are approximately equal [51, 52].

Besides the early elegant experiments of Drexhage [53], it has been shown recently [54–58] that the radiative lifetime of an exciton can be modified by the interaction with a plasmon (mainly LSPPs) through the Purcell effect [59]. There are two factors resulting in a increase of spontaneous emission rate. The first factor is proportional to the Q-factor $Q = \omega/\Delta\omega$ of the resonant mode in a cavity, with $\Delta\omega$ being the spectral width of the resonance at frequency ω. The second factor accounts for the actual volume V occupied by a given mode as compared to the λ^3 value of interest. Therefore for spontaneous emission rate in a cavity W_c versus rate in a vacuum W_v, Purcell [59] suggested the formula

$$\frac{W_c}{W_v} = \frac{3}{4\pi^2}\frac{\lambda^3}{V}Q \tag{2}$$

known as the Purcell factor.

The main objective of this project is to numerically investigate and experimentally demonstrate how LSPP - SPP interactions in plasmonic nanostructures can lead to an enhanced Purcell factor of embbeded emitters, either on a broadband range or on a very narrow range. The structures we propose to investigate are engineered in the following way: a gold core - silica shell (CS) nanoparticle (NP) hexagonal array will be sandwiched between two gold films, one film being deposited flat on the glass substrate, the other being deposited on top of the CS particules and thus following the periodical top hemi-sphericity of the CS particles. By embedding emitters at a controlled distance of the core metallic surface and by adjusting the sizes of the core diameters, of the shell ticknesses and the amounts of gold deposited underneath and above the CS particules, we expect different types of hybridization between SPP and LSPP resonances to occur, leading to various modes for which the interaction with the emitters has to be investigated.

In preliminary experiments, we have shown that such a structure, consisting in $60\,nm$ gold core - $40\,nm$ silica shell NPs, embedding emitters grafted at a distance of $30\,nm$ from the gold core, arranged in a hexagonal array sandwiched between two gold films of $30\,nm$ thicknesses, can strongly enhance (2 orders of magnitude), on a broadband range (the whole emission spectrum of the emitters), the spontaneous emission rate of quantum emitters grafted in the silica shell of the NP, through the Purcell effect.

Fig. 10a shows a very nice matching between the predicted (simulations, Fig. 10a, solid curves) and experimentally obtained (dashed curves) reflection spectra. The positions of the 2 dips exhibited in the simulated and experimental reflection spectra agree very well, with the second dip being broadened and weakened in the experimental case, resulting in a Q factor smaller than predicted. The two dips have been assigned to resonances resulting from hybridization

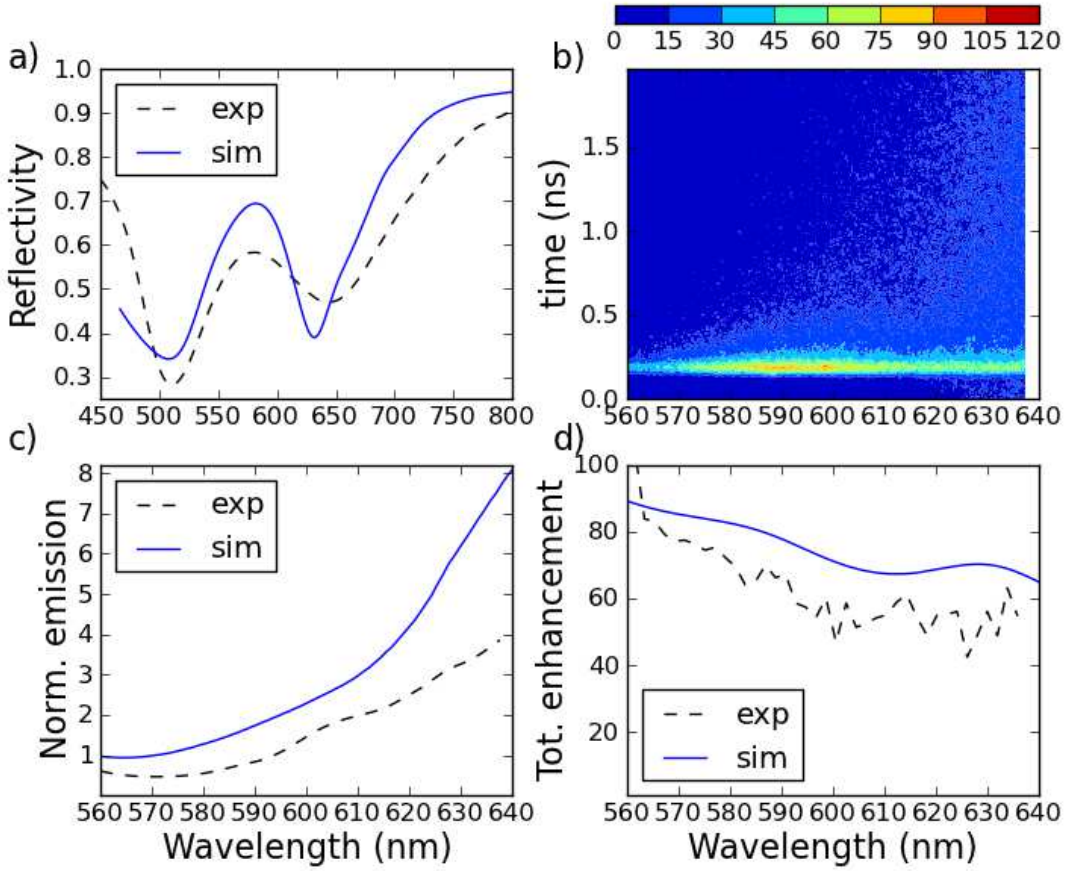

FIG. 10. Experimental (dashed lines) and numerical (solid lines) reflection spectra (a), normalized emission enhancements (c) and normalized spontaneous emission rates (d) for RITC emitters in the nanostructure. b) shows the time and spectrally resolved (experimental) spontaneous emission intensities of RITC molecules in the nanostructure.

of either the NP LSPPs (high-energy resonance) or the array plasmons (low-energy resonance) with the SPPs of the surrounding gold films. We have measured the Purcell factor enhancement of nanoemitters embedded in such a nanostructure by performing spectrally and temporally resolved measurements, simultaneously, owing to the use of a streak camera. Fig. 10b shows the intensity plots for RITC emitters in the nanostructure. Projecting the intensity on the x axis provides us with the emission spectra while, projecting the intensity on the y axis, one alternatively obtains the decay rates profiles. Fig. 10b clearly reveals that i) the emission spectrum is much more intense on the long wavelength side and ii) the decay profile is much shorter as compared to the same RITC emitters embedded in the same CS NPs in an ethanol solution [24]. To quantify these observations, we normalized the emission spectra of the RITC emitters in the sample by dividing them with the emission spectrum of RITC in ethanol. The result of this operation is shown in Figure 10c, which clearly exhibits an increase of the normalized emission intensity on the long wavelength range for the sample. We also proceeded the intensity plots to obtain the normalized spontaneous emission rates (formally defined as the reciprocals of the normalized decay times) (Fig. 10d). Remarkably, the normalized spontaneous emission rate is enhanced more than 50 times on a broadband (essentially flat above 600 nm) range extending from 560 to 640 nm. This is in contradistinction with the results obtained for RITC emitters embedded in the same CS NPs in an ethanol solution [24], where the emission rate enhancement is lower than 50 and decreases as $1/\lambda$ for an emission wavelength $\lambda > 570\,nm$, which points to the influence of the low-energy resonance on the Purcell factor enhancement. We compared the measurements of spontaneous decay rates and normalized emission spectra to simulated results. Figs; 10c and 10d show the simulated normalized emission intensity and (normalized) spontaneous emission rate. The matching of these results with the experimentally obtained ones is extremely good. Let us note here, as seen in Fig. 10d, that the (normalized) spontaneous rates of the RITC emitters do extend, both numerically and experimentally, at a very high level through the whole range of wavelengths, contrarily to the ones of RITC emitters embedded in CS NPs simply dispersed in ethanol solutions [24]. The last feature clearly shows the interest of manipulating the coupling of the plasmon modes to obtain large and controllable Purcell factor enhancements, here

obtained in a broadband range.

Future prospects involve the investigation of other sizes of the cores, shells of the NPs, thicknesses and nature of the surrounding metallic layers. Some theoretical work already achieved predicts the possibility of reaching much larger Purcell enhancement on a very narrow spectral range.

IV.3. Plasmonic nonlinear materials for optical bistability

All-optical signal processing in integrated photonic circuits and its applications in optical computing and communications require the ability to control light with light [60]. An amount of all-optical devices based on nonlinear optical effects have been proposed and investigated [61, 62]. However, there are two main drawbacks in most of these devices. Firstly, the minimum size is limited by enough light passlength. Secondly, high operational light intensity is necessary for sizeable nonlinear response [63]. In order to overcome these drawbacks, the nonlinear devices on the basis of photonic crystal defects have been proposed by using the field confinement and enhancement in the defect areas [64, 65]. Recently, surface plasmon polaritons (SPPs) were found to be capable of paving another way to realize strong nonlinear optical effects and minimize all-optical components, attributing to its significant enhancement of optical field intensity and the ability of light manipulation in a nanoscale domain [66–74]. Quite recently, several types of nonlinear optical devices based on SPPs have been studied [75–82].

Among the latter, achieving optical bistability in surface-plasmon polaritonic crystals [78] is the target we want to achieve, owing to the hexagonal arrays of curved gold/silver triangles we are able to engineer by nanosphere lithography. The basic physical principles allowing one to realize this function are now explained. For low intensity probe light, and neglecting the nonlinear response of the metal, we can consider the variations of the dielectric constant of the nonlinear material ϵ as solely induced by the pump light of frequency ω_c:

$$\epsilon(\vec{r},\omega) = \epsilon^{(0)} + 4 * \pi * \chi^{(3)} |E_L(\epsilon(\vec{r},\omega)), \omega_c, \vec{r})|^2 \tag{3}$$

where $\epsilon^{(0)}$ and $\chi^{(3)}$ are the linear dielectric constant and third-order nonlinear susceptibility of the used Kerr material, respectively. $E_L(\epsilon(\vec{r},\omega), \omega_c, \vec{r})$ is the local, position dependent $\vec{r}$ electric field of the pump light, which is determined by the SPP crystal parameters. Thus, the field distribution described by $E_L(\epsilon(\vec{r},\omega), \omega_c, \vec{r})$ depends on the induced permittivity changes in the nonlinear SPP crystal. As a consequence of this self-consistent process, the field distribution for a given pump intensity and wavelength corresponds to a unique spatial distribution of $\epsilon(\vec{r})$. The probe light then interacts with the SPP crystal whose eigenmodes, and, therefore, optical properties are determined by the distribution of the dielectric constant around the nanostructured system. If the pump intensity is changed, the changes in the induced permittivity of the Kerr material result in the modifications of the spatial distribution of $\epsilon(\vec{r})$ in addition to its magnitude and, therefore, a different optical response of the SPP crystal. This provides a mechanism for bistable behavior of the optical transmission with the intensity of the control light. The nonlinear transmission and its bistability are determined by both the value and spatial variations of $\epsilon(\vec{r})$, both being responsible for the SPP crystal eigenmodes. Thus, as in a typical configuration for optical bistability, the above described process requires a nonlinear transmission dependence on the pump light to achieve a transistor-type effect as well as a "built-in" feedback mechanism to enable bistability.

Preliminary experiments are shown in Fig. 11. The absorption spectra taken at two different locations in the bare (uncoated) structure consists of essentially one peak corresponding to the dipolar surface plasmon resonance localized at the tips of the triangles. As a consequence of the Kerr material coating, the localized plasmon modes are red-shifted due to the changed dielectric constant of the interface-adjacent medium. Taking advantage of the nonlinear response of the Kerr material, the control illumination could then be used to modify the density of states of the nonlinear SPP crystal and induce the intensity-dependent changes in its optical response at the probe light wavelength. However, the poor quality of the hexagonal array obtained and consequently the poor Q-factor exhibited by the absorption spectra did not allow us to go momentarily further.

Nevertheless, the results are encouraging and require much more effort to improve the quality of the array of triangles, by playing extensively with the deposition parameters and allowing us to obtain a nice monolayer prior to perform subsequent operations. Modifying either the size of the spheres arranged in the monolayer or the thickness of the metal deposition and after removal of the mask, we will be able to control the frequency of the surface plasmon resonances excited at the tips of the triangles and thus chose the working range of the optical bistable.

---

[1] Vallée, R. A. L.; Tomczak, N.; Kuipers, L.; Vancso, G.J.; van Hulst, N. F.; Single Molecule Lifetime Fluctuations Reveal Segmental Dynamics in Polymers'; Phys. Rev. Lett. 91 (2003) 038301.

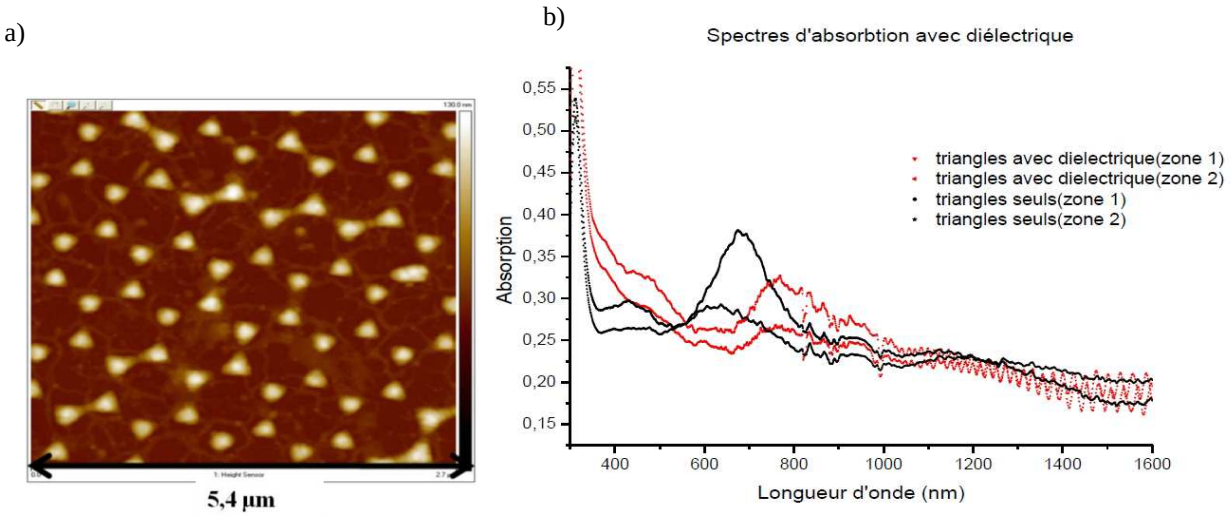

FIG. 11. a) AFM micrograph showing the arrangement of triangles obtained after silver deposition and removal of the mask constituted by a monolayer of polystyrene beads having a 1 μm diameter. b) Absorption spectra of the silver triangles 50 nm thick arranged in a hexagonal array covered (ref lines) and non covered (black lines) by the 6 nm thick dielectric coating of CdSe/ZnS quantum dots.

[2] Vallée, R.A.L.; Tomczak, N.; Kuipers, L.; Vancso, G.J.; van Hulst, N.F.; Effect of solvent on nanoscale polymer heterogeneity and mobility probed by single molecule lifetime fluctuations; Chem. Phys. Lett. 384 (2004) 5.

[3] Tomczak, N.; Vallée, R.A.L.; van Dijk, E.M.H.P.; Kuipers, L.; Vancso, G.J.; van Hulst, N.F.; Segment Dynamics in Thin Polystyrene Films Probed by Single-Molecule Optics; J. Am. Chem. Soc. 126 (2004) 4748.

[4] Vallée, R.A.L.; Van Der Auweraer, M.; De Schryver, F.C.; Beljonne, D.; Orrit, M.; A Microscopic Model for the Fluctuations of Local Field and Spontaneous Emission of Single Molecules in Disordered Media; ChemPhysChem, 6 (2005) 81.

[5] R. A. L. Vallée; M. Baruah; J. Hofkens; N. Boens; M. Van der Auweraer; D. Beljonne; Fluorescence lifetime fluctuations of single molecules probe the local environment of oligomers around the glass transition temperature'; J. Chem. Phys. 126 (2007) 184902.

[6] R. A. L. Vallée; M. Van der Auweraer; W. Paul; K. Binder; Fluorescence lifetime of a single molecule as an observable of meta-basin dynamics in fluids near the glass transition'; Phys. Rev. Lett. 97 (2006) 217801.

[7] R. A. L. Vallée; M. Van der Auweraer; W. Paul; K. Binder; What can be learned from the rotational motion of single molecules in polymer melts'; Europhys. Lett. 79 (2007) 46001.

[8] R. A. L. Vallée, W. Paul and K. Binder; Single molecule probing of the glass transition phenomenon: simulations of several types of probes, J. Chem. Phys. 127 (2007) 154903.

[9] R.A.L. Vallée, W. Paul and K. Binder Probe molecules in polymer melts near the glass transition: A molecular dynamics study of chain length effects, J. Chem. Phys., 132 (2010) 034901, 1-9

[10] R.A.L. Vallée, W. Paul and K. Binder Single Molecules Probing the Freezing of Polymer Melts: A Molecular Dynamics Study for Various Molecule-Chain Linkages, Macromolecules, 43, 24 (2010) 10714-10721

[11] G. Hinze, T. Basché and R.A.L. Vallée Single molecule probing of dynamics in supercooled polymers , Phys. Chem. Chem. Phys., 13 (2011) 18131818

[12] Vallée, R.A.L.; Cotlet, M.; Van Der Auweraer, M.; Hofkens, J.; Mllen, K.; De Schryver, F.C.; Single-Molecule Conformations Probe Free Volume in Polymers; J. Am. Chem. Soc. 126 (2004) 2296.

[13] Vallée, R.A.L.; Marsal, P; Braeken, E.; Habuchi, S.; De Schryver, F.C.; Van Der Auweraer, M.; Beljonne, D.; Hofkens, J.; Single Molecule Spectroscopy as a Probe for Dye-Polymer Interactions; J. Am. Chem. Soc. 127 (2005) 12011.

[14] Els Braeken, Philippe Marsal, Annelies Vandendriessche, Mario Smet, Wim Dehaen, Renaud Vallée, David Beljonne, Mark Van der Auweraer, Investigation of probe molecule - polymer interactions, Chem. Phys. Lett., 472 (2009) 48-54.

[15] E. Braeken, G. De Cremer, P. Marsal, G. Pèpe, K. Mllen and R.A.L. Vallée Single Molecule Probing of the Local Segmental Relaxation Dynamics in Polymer above the Glass Transition Temperature, J. Am. Chem. Soc., 131 (2009) 12201-12210.

[16] K. Baert; K. Song; R. Vallée; M. Van der Auweraer; K. Clays; Spectral narrowing of emission in self-assembled colloidal photonic superlattices'; J. Appl. Phys. 100 (2006) 123112.

[17] R. A. L. Vallée; K. Baert; B. Kolaric; M. Van der Auweraer; K. Clays; 'Nonexponential decay of spontaneous emission from an ensemble of molecules in photonic crystals'; Phys. Rev. B 76 (2007) 045113.

[18] B. Kolaric; K. Baert; M. Van der Auweraer; R.A.L. Vallée; K. Clays; 'Controlling the fluorescence resonant energy transfer by photonic crystal bandgap engineering'; Chem. Mater. 19 (2007) 5547.

[19] Wim Libaers, Branko Kolaric, Renaud A.L. Vallée, John E. Wong, Jelle Wouters, Ventsislav K. Valev, Thierry Verbiest, Koen Clays, 'Engineering colloidal photonic crystals with magnetic functionalities', Colloids Surf., A, 339 (2009) 13-19.

[20] J-F. Dechézelles, T. Aubert, F. Grasset, S. Cordier, C. Barthou, C. Schwob, A. Maître, R.A.L. Vallée, H. Cramail and Serge Ravaine "Fine tuning of emission through the engineering of colloidal crystals", Phys. Chem. Chem. Phys., 12 (2010) 11993-11999

[21] J-F. Dechézelles, G. Mialon, T. Gacoin, C. Barthou, C. Schwob, A. Maître, R.A.L. Vallée, H. Cramail and S. Ravaine "Inhibition and exaltation of emission in layer-controlled colloidal photonic architectures", Colloids Surf., A, 373 (2011) 1-5

[22] S. Mornet, L. Teule-Gay, D. Talaga, S. Ravaine and R.A.L. Vallée "Optical cavity modes in semicurved FabryPérot resonators", J. Appl. Phys., 108 (2010) 086109, 1-3

[23] R. Morarescu, L. Englert, B. Kolaric, P. Damman, R.A.L. Vallée, T. Baumert, F. Hubenthal, and F. Träger "Tuning nanopatterns on fused silica substrates: a theoretical and experimental approach", J. Mat. Chem. 21 (2011) 4076-4081

[24] M. Ferrié, N. Pinna, S. Ravaine and R.A.L. Vallée "Wavelength - dependent emission enhancement through the design of active plasmonic nanoantennas", Optics Express, 19, 18 (2011) 17697-17712

[25] P. W. Anderson, Absence of diffusion in certain random lattices, Phys. Rev. 109 , 14921505 (1958).

[26] S. John, Electromagnetic absorption in a disordered medium near a photon mobility edge, Phys. Rev. Lett. 53, 21692172 (1984).

[27] P. W. Anderson, The question of classical localization: a theory of white paint?, Philos. Mag. B 52, 505510 (1985).

[28] D. S. Wiersma, P. Bartolini, A. Lagendijk and R. Righini, Localization of light in a disordered medium, Nature 390, 671675 (1997).

[29] F. Scheffold, R. Lenke, R. Tweer and G. Maret, Localization or classical diffusion of light?, Nature 398, 206207 (1999); see also D. S. Wiersma, P. Bartolini, A. Lagendijk and R. Righini, Nature 398, 207 (1999).

[30] J. Gomez Rivas, R. Sprik and A. Lagendijk, Optical transmission through very strong scattering media, Ann. Phys. (Leipzig) 8, Spec. Issue, I-77 I-80 (1999).

[31] M. Störzer, P. Gross, C. M. Aegerter and G. Maret, Observation of the critical regime near Anderson localization of light, Phys. Rev. Lett. 96, 063904 (2006).

[32] C. M. Aegerter, M. Störzer, S. Fiebig, W. Buhrer and G. Maret, Observation of Anderson localization of light in three dimensions, J. Opt. Soc. Am. A 24, 2327 (2007).

[33] E. Abrahams, P. W. Anderson, D. C. Licciardello and T. V Ramakrishnan, Scaling theory of localization: absence of quantum diffusion in two dimensions, Phys. Rev. Lett. 42, 673676 (1979).

[34] Zayats, A. V.; Smolyaninov, I. I.; Maradudin, A. A. Nanooptics of Surface Plasmon Polaritons. Phys.Rep., *Rev. Sect. Phys. Lett.* **2005**, 408, 131-314.

[35] Raether, H. *Surface Plasmons*; Springer: Berlin, 1988.

[36] Kelly, K. L.; Coronado, E., Zhao, L.L.; and Schatz, G. G.. The Optical Properties of Metal Nanoparticles: The Influence of Size, Shape, and Dielectric Environment. *J. Phys. Chem. B* **2003**, 107, 668-677.

[37] Barnes, W. L.; Dereux, A.; Ebbesen, T. W. Surface Plasmon Subwavelength Optics. *Nature* **2003**, 424, 824-830.

[38] Halas, N. J.; Lal, S.; Chang, W.-S.; Link, S.; and Nordlander, P. Plasmons in strongly coupled metallic nanostructures *Chem. Rev.* **2011**, 111, 3913-3961.

[39] Baudrion, A.-L.; Weeber, J.-C.; Dereux, A.; Lecamp, G.; Lalanne, P.; Bozhevolnyi, S. I. Influence of the Filling Factor on the Spectral Properties of Plasmonic Crystals. *Phys. Rev. B* **2006**, 74, 125406.

[40] Ferry, V. E.; Sweatlock, L. A.; Pacifici, D.; Atwater, H. A. Plasmonic Nanostructure Design for Efficient Light Coupling into Solar Cells. *Nano Lett.* **2008**, 8, 4391-4397.

[41] Wedge, S.; Barnes, W. L. Surface Plasmon-Polariton Mediated Light Emission through Thin Metal Films. *Opt Express* **2004**, 12, 3673-3685.

[42] Vuckovic, J.; Loncar, M.; Scherer, A. Surface Plasmon Enhanced Light-Emitting Diode. *IEEE J. Quantum Electron.* **2000**, 36, 1131-1144.

[43] Dintinger, J.; Klein, S.; Ebbesen, T. W. Molecule-Surface Plasmon Interactions in Hole Arrays: Enhanced Absorption, Refractive Index Changes, and All-Optical Switching. *Adv. Mater.* **2006**, 18, 1267-1270.

[44] Gordon, R.; Sinton, D.; Kavanagh, K. L.; Brolo, A. G. A New Generation of Sensors Based on Extraordinary Optical Transmission. *Acc. Chem. Res.* **2008**, 41, 1049-1057.

[45] Gao, H. W.; Henzie, J.; Lee, M. H.; Odom, T. W. Screening Plasmonic Materials Using Pyramidal Gratings. *Proc. Natl. Acad. Sci. U.S.A.* **2008**, 105, 20146-20151.

[46] Stewart, M. E.; Mack, N. H.; Malyarchuk, V.; Soares, J. A. N. T.; Lee, T.-W.; Gray, S. K.; Nuzzo, R. G.; Rogers, J. A. Quantitative Multispectral Biosensing and 1D Imaging Using Quasi-3D Plasmonic Crystals. *Proc. Natl. Acad. Sci. U.S.A.* **2006**, 103, 17143-17148.

[47] Zhang, S.; Fan, W. J.; Panoiu, N. C.; Malloy, K. J.; Osgood, R. M.; Brueck, S. R. J. Experimental Demonstration of near-Infrared Negative-Index Metamaterials. *Phys. Rev. Lett.* **2005**, 95, 137404.

[48] Holland, W. R.; and Hall, D. G. Frequency shifts of an electric-dipole resonance near a conducting surface. *Phys. Rev. Lett.* **1984**, 52, 1041-1044.

[49] Stuart, H. R.; and Hall, D. G. Enhanced dipole-dipole interaction between elementary radiators near a surface. *Phys. Rev. Lett.* **1998**, 80, 5663-5666.

[50] Cesario, J.; Quidant, R., Badenes, G.; and Enoch, S. Electromagnetic coupling between a metal nanoparticle grating and a metallic surface. *Opt. Lett.* **2005** 30, 3404-3406.

[51] Papanikolaou, N. Optical properties of metallic nanoparticle arrays on a thin substrate film *Phys. Rev. B* **2007** 75, 235426.

[52] Chu, Y.; and Crozier, K. B. Experimental study of the interaction between localized and propagating surface plasmons. *Opt. Lett.* **2009**, 34, 244-246.

[53] Drexhage, K. H. *Progress in Optics*, edited by E. Wolf; North-Holland: Amsterdam, 1974.
[54] Biteen, J. S.; Lewis, N. S.; Atwater, H. A.; Mertens, H.; and Polman, A. Spectral tuning of plasmon-enhanced silicon quantum dot luminescence. *Appl. Phys. Lett.* **2006**, 88, 131109.
[55] Liaw, J.-W.; Chen, J.-H.; Chen, C.-S.; Kuo, M.-K. Purcell effect of nanoshell dimer on single molecules fluorescence. *Opt. Express* **2009**, 17, 13532-13540.
[56] Ausman, L. K.; Schatz, G. C. On the importance of incorporating dipole reradiation in the modeling of surface enhanced Raman scattering from spheres. *J. Chem. Phys.* **2009**, 131, 084708.
[57] Vandenbem, C.; Brayer, D.; Froufe, Pérez, L. S.; Carminati, R. Controlling the quantum yield of a dipole emitter with coupled plasmonic modes. *Phys. Rev. B* **2010**, 81, 085444.
[58] Ferrié, M.; Pinna, N.; Ravaine, S.; Vallée, R. A. L. Wavelength-dependent emission enhancement through the design of active plasmonic nanoantennas. *Opt. Express*, **2011**, 19, 17697-17712.
[59] Purcell, E. M. Spontaneous emission probabilities at radio frequencies. *Phys. Rev.* **1946**, 69, 681.
[60] H. M. Gibbs, Optical Bistability: Controlling Light with Light (Academic, New York, 1985).
[61] R. A. Innes, and J. R. Sambles, Optical non-linearity in liquid crystals using surface plasmon-polaritons, J. Phys. Condens. Matter 1(35), 62316260 (1989).
[62] W. Dickson, G. A. Wurtz, P. R. Evans, R. J. Pollard, and A. V. Zayats, Electronically controlled surface plasmon dispersion and optical transmission through metallic hole arrays using liquid crystal, Nano Lett. 8(1), 281286 (2008).
[63] G. A. Wurtz, and A. V. Zayats, Nonlinear surface plasmon polaritonic crystals, Laser Photon. Rev. 2(3), 125135 (2008).
[64] M. F. Yanik, S. Fan, M. Soljaci, and J. D. Joannopoulos, All-optical transistor action with bistable switching in a photonic crystal cross-waveguide geometry, Opt. Lett. 28(24), 25062508 (2003).
[65] X. Hu, P. Jiang, C. Ding, H. Yang, and Q. Gong, Picosecond and low-power all-optical switching based on an organic photonic-bandgap microcavity, Nat. Photonics 2(3), 185189 (2008).
[66] W. L. Barnes, A. Dereux, and T. W. Ebbesen, Surface plasmon subwavelength optics, Nature 424(6950), 824830 (2003).
[67] S. Enoch, R. Quidant, and G. Badenes, Optical sensing based on plasmon coupling in nanoparticle arrays, Opt. Express 12(15), 34223427 (2004).
[68] M. S. Kumar, X. Piao, S. Koo, S. Yu, and N. Park, Out of plane mode conversion and manipulation of Surface Plasmon Polariton waves, Opt. Express 18(9), 88008805 (2010).
[69] S. Randhawa, M. U. Gonzlez, J. Renger, S. Enoch, and R. Quidant, Design and properties of dielectric surface plasmon Bragg mirrors, Opt. Express 18(14), 1449614510 (2010).
[70] M. K. Kim, S. H. Lee, M. Choi, B. H. Ahn, N. Park, Y. H. Lee, and B. Min, Low-loss surface-plasmonic nanobeam cavities, Opt. Express 18(11), 1108911096 (2010).
[71] A. V. Krasavin, and A. V. Zayats, Silicon-based plasmonic waveguides, Opt. Express 18(11), 1179111799 (2010).
[72] V. P. Drachev, U. K. Chettiar, A. V. Kildishev, H. K. Yuan, W. Cai, and V. M. Shalaev, The Ag dielectric function in plasmonic metamaterials, Opt. Express 16(2), 11861195 (2008).
[73] A. V. Krasavin, and A. V. Zayats, All-optical active components for dielectric-loaded plasmonic waveguides, Opt. Commun. 283(8), 15811584 (2010).
[74] U. K. Chettiar, P. Nyga, M. D. Thoreson, A. V. Kildishev, V. P. Drachev, and V. M. Shalaev, FDTD modeling of realistic semicontinuous metal films, Appl. Phys. B 100(1), 159168 (2010).
[75] C. J. Min, P. Wang, C. C. Chen, Y. Deng, Y. H. Lu, H. Ming, T. Y. Ning, Y. L. Zhou, and G. Z. Yang, All-optical switching in subwavelength metallic grating structure containing nonlinear optical materials, Opt. Lett. 33(8), 869871 (2008).
[76] J. Porto, L. Martn-Moreno, and F. Garca-Vidal, Optical bistability in subwavelength slit apertures containing nonlinear media, Phys. Rev. B 70(8), 081402 (2004).
[77] I. I. Smolyaninov, Quantum fluctuations of the refractive index near the interface between a metal and a nonlinear dielectric, Phys. Rev. Lett. 94(5), 057403 (2005).
[78] A. Wurtz, R. Pollard, and A. V. Zayats, Optical bistability in nonlinear surface-plasmon polaritonic crystals, Phys. Rev. Lett. 97(5), 057402 (2006).
[79] Z. Yu, G. Veronis, S. Fan, and M. Brongersma, Gain-induced switching in metal-dielectric-metal plasmonic waveguides, Appl. Phys. Lett. 92(4), 041117 (2008).
[80] C. Min, and G. Veronis, Absorption switches in metal-dielectric-metal plasmonic waveguides, Opt. Express 17(13), 1075710766 (2009).
[81] Y. Shen, and G. P. Wang, Optical bistability in metal gap waveguide nanocavities, Opt. Express 16(12), 84218426 (2008).
[82] Z. J. Zhong, Y. Xu, S. Lan, Q. F. Dai, and L. J. Wu, Sharp and asymmetric transmission response in metal-dielectric-metal plasmonic waveguides containing Kerr nonlinear media, Opt. Express 18(1), 7986 (2010).

Single Molecule Lifetime Fluctuations Reveal Segmental Dynamics in Polymers

R. A. L. Vallée,[1,2] N. Tomczak,[2] L. Kuipers,[1] G. J. Vancso,[2] and N. F. van Hulst[1,*]

[1]*Applied Optics Group, MESA+ Research Institute, University of Twente, P.O. Box 217, 7500 AE Enschede, The Netherlands*

[2]*Materials Science and Technology of Polymers, MESA+ Research Institute, University of Twente, P.O. Box 217, 7500 AE Enschede, The Netherlands*

(Received 6 March 2003; published 17 July 2003)

We present a single molecule fluorescence study that allows one to probe the nanoscale segmental dynamics in amorphous polymer matrices. By recording single molecular lifetime trajectories of embedded fluorophores, peculiar excursions towards longer lifetimes are observed. The asymmetric response is shown to reflect variations in the photonic mode density as a result of the local density fluctuations of the surrounding polymer. We determine the number of polymer segments involved in a local segmental rearrangement volume around the probe. A common decrease of the number of segments with temperature is found for both investigated polymers, poly(styrene) and poly(isobutylmethacrylate). Our novel approach will prove powerful for the understanding of the nanoscale rearrangements in functional polymers.

DOI: 10.1103/PhysRevLett.91.038301 PACS numbers: 82.37.–j, 05.40.–a, 33.50.–j, 82.35.Np

Glasses are disordered materials usually obtained by cooling a viscous liquid or a polymer melt fast enough to avoid crystallization. Their static and dynamic properties deviate largely from the simple Debye behavior. The deviations are best interpreted in terms of dynamic heterogeneities of structure on the segmental (nanometer) scale [1]. Direct evidence for microscopic regions of different relaxation time has been obtained by multidimensional nuclear magnetic resonance [2], photobleaching [3], excess light scattering near the glass transition temperature (T_g) [4], dielectric hole burning [5], and, recently, single molecule spectroscopy [6]. However, the key question concerning the temperature dependence of the characteristic dimensions of the inhomogeneities in glass forming liquids and amorphous solids is still unanswered.

Single molecule detection has proven to be a unique method to investigate the behavior of complex condensed systems [7,8]. In contrast to ensemble methods, the single molecule approach provides information on time trajectories, distributions, and correlations of observables that would otherwise be hidden. Individual members of a heterogeneous population are examined, identified, and sorted to quantitatively compare their subpopulations. In the extreme case of cryogenic temperatures, it has been shown [9] that most of the spectral trails of single molecules obtained at around 1 K are consistent with the standard two-level system model of glasses [10]. At room temperature, the broad spectra and complexity of the system complicate the single molecule spectral analysis.

We present in this Letter a first study in the complementary time domain. The excited state lifetime of the individual dye molecules is monitored in time. In a static environment, the lifetime has a discrete value. Because of the heterogeneity of the nanoenvironment, the lifetime is different but constant for every molecule [11,12]. However, in a fluctuating environment, the lifetime will vary and develop a certain distribution. We show that lifetime fluctuations are due to variations of the radiative density of states (RDOS) and consequently reflect the local density fluctuations in the surroundings of the single molecule probe. We establish in a direct way the number of segments involved in the rearrangement volume surrounding the fluorophore, by connecting our observations to the Simha-Somcynsky (SS) equation of state [13]. Interestingly, a common decrease of the number of segments with temperature for different polymers is found, in agreement with the predictions of the thermodynamic Adam-Gibbs theory [14].

Dye-doped polymer films (70 and 200 nm) were prepared by spin coating a solution of 1,1'-dioctadecyl-3, 3, 3', 3' - tetramethylindodicarbocyanine (DiD, 5×10^{-10} M, Molecular Probes) and polystyrene [PS, 89 300 g/mol, polydispersity index (PI) of 1.06, Polymer Standard Service], or poly(isobutylmethacrylate) (PIBMA, 67 200 g/mol, PI = 2.8, custom made radical polymerization) in toluene onto a glass substrate. Further annealing was performed in order to relax the stresses induced by the deposition procedure. The choice of the dye was dictated by the following considerations: it possesses a high fluorescence quantum yield (close to unity), an absorption cross section of 7.5×10^{-16} cm^2, and is highly photostable when embedded in a polymer matrix [11]. PS ($T_g = 100\,^\circ$C) and PIBMA ($T_g = 56\,^\circ$C) were chosen due to to their different glass transition temperatures T_g. This allows us to probe polymer properties as a function of their relative distance to T_g, while working at the same laboratory temperatures for both polymers. Molecules in the sample were excited by 57 ps pulses at a wavelength of 635 nm and repetition rate of 80 MHz, generated by a ps pulsed diode laser (PicoQuant, PDL 800-B, 100 μW), at the focus of a confocal inverted microscope (Zeiss). Fluorescence intensity and lifetime of individual molecules were monitored in time, in

 © 2003 The American Physical Society

consecutive experiments, using a time-correlated single-photon counting card (Becker & Hickl, SPC 500) [15]. Integrating over 200 ms time intervals, a lifetime accuracy of typically 0.1–0.3 ns was obtained.

Figure 1 shows fluorescence lifetime trajectories of two individual molecules emitting at approximately the same intensity level. Both trajectories fluctuate in time, but in a different way: while the first molecule (a) has a lifetime restricted to small and rather symmetrical variations around the mean value, the second molecule dwells occasionally longer in the excited state, as is clear from the excursions to longer lifetimes in the transient (b). The corresponding single molecule fluorescence lifetime distributions built up from the transients further underline the difference in behavior between the two molecules. The characteristic shape varies from nearly symmetric (c) to asymmetric (d). Why does the fluorescence lifetime change? Three factors may potentially affect the fluorescence lifetime of dyes embedded in a dielectric medium: quenching effects, changes in the conformation of the fluorophore, and variations in the dielectric properties surrounding the probe molecule.

First, quenching effects may be discarded since the aperture of nonradiative decay channels in the matrix would simultaneously induce a lowering of the measured intensity and lifetime. This is not the case since intensity and lifetime are not correlated in the plots of Fig. 1. Furthermore, the quantum efficiency of the chosen fluorophore (close to unity) excludes the possibility that the large lifetime fluctuations result from fluctuations in the number of decay channels. Moreover, the excursions in the fluorescence lifetime trajectory [Fig. 1(b)] are always towards higher values, which rules out any nonradiative process as the cause of the fluctuations.

Second, the electronic properties of the conjugated DiD molecule are dominated by the presence of delocalized π electrons. The lowest optical excitation corresponds to a $\pi \rightarrow \pi*$ transition and vice versa for the emission. The molecule may thus be described as a simple two-level system. In the electric dipole approximation and in vacuum, the spontaneous emission rate Γ_0 of the molecule is given by the relation [16]

$$\Gamma_0 = \frac{\omega_0^3 d^2}{3\pi\epsilon_0 \hbar c^3}. \quad (1)$$

The radiative lifetime τ_0 is the inverse of Γ_0, where ω_0, d, and ϵ_0 designate the transition frequency, the transition dipole moment of the excited state of the fluorophore for the $\pi \rightarrow \pi*$ transition, and the dielectric constant of the vacuum, respectively. This equation reveals that a change in the transition frequency or the transition dipole moment of the dye due to the influence of the nanoenvironment can be responsible for the observed fluctuations of the lifetime. However, by quantum chemistry calculations, we showed [17] that low-cost energy motions of the DiD molecule compatible with thermal agitation at room temperature result in a fluctuation of at most 10% in the fluorescence lifetime when compared to the rest structure. Therefore conformational changes do not explain the large fluctuations observed.

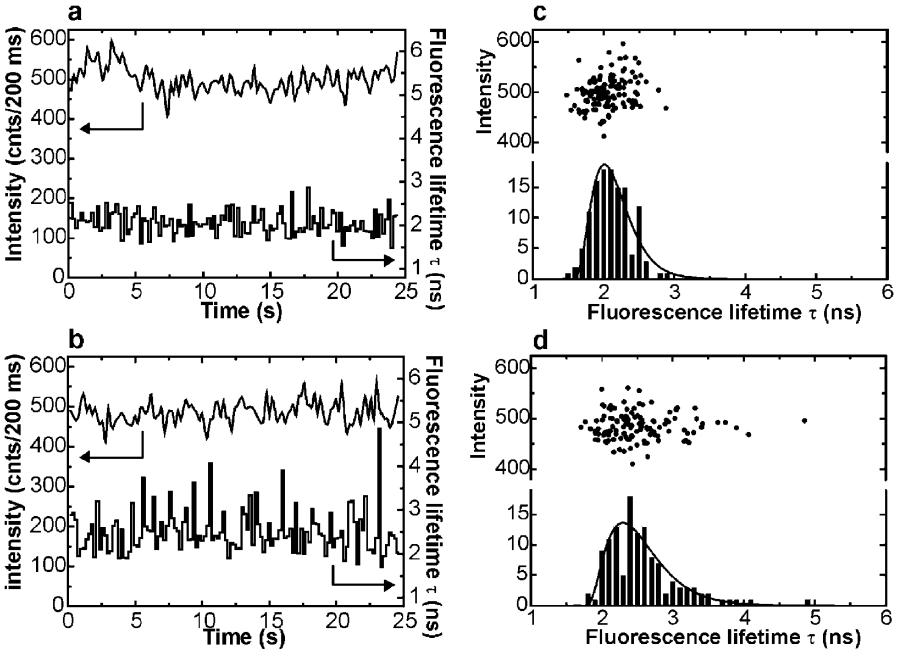

FIG. 1. (a),(b) Transients of fluorescence intensity and fluorescence lifetime for two different individual DiD molecules embedded in a 200 nm thick film of PIBMA at room temperature. Clearly, the second molecule exhibits excursions towards longer lifetime values. (c),(d) For the two transients corresponding fluorescence lifetime distributions (bottom) and correlation between intensity and lifetime (top) are shown. The shape of the distribution is more asymmetric for the second molecule. While the intensity remains within a 10% fluctuating range, the lifetime shows changes up to 100%.

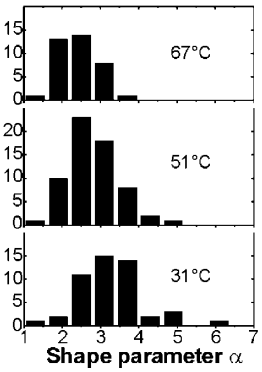

FIG. 2. Distributions of shape parameter for DiD molecules embedded in a 200 nm thick film of PIBMA for three temperatures. With increasing temperature, the distributions shift towards lower shape values.

As a result, we attribute the radiative lifetime fluctuations observed to the local density fluctuations of the surrounding polymer matrix. We quantified this effect for 778 individual probe molecules embedded in different polymer matrices, at various temperatures. For each single molecule trajectory lasting at least 15 s, we were able to build up a reliable distribution of fluorescence lifetimes. Interestingly, the experimental lifetime distribution is best fitted with a gamma distribution $g(x)$. This distribution $g(x) = \beta(\beta x)^{\alpha-1}e^{-\beta x}/\Gamma(\alpha)$ is generally accepted for a lower bounded continuous variable fully characterized by its first two moments x_{av} and $\langle \delta x^2 \rangle_{\mathrm{av}}$ or, equivalently, by its shape (α) and scale (β) parameters, where $x_{\mathrm{av}} = \frac{\alpha}{\beta}$, $\langle \delta x^2 \rangle_{\mathrm{av}} = \frac{\alpha}{\beta^2}$, and $\Gamma(\alpha)$ stands for the gamma function. From the fitted gamma distributions, we extract the value of the characteristic shape parameter α. At each given temperature, collecting the shape parameters of 30 to 60 of these molecules, we constructed the distribution of the shape parameter. Figure 2 shows the shape distributions for three different temperatures for DiD embedded in a 200 nm thick film of PIBMA. Surprisingly, upon increasing temperature, the average shape value as well as the width of the shape parameter distribution decrease. This temperature dependence further corroborates the conclusion that the density fluctuation in the polymer is the main factor in the observed lifetime fluctuations.

How can density changes within the polymer affect the fluorescence lifetime of an embedded fluorophore? The probe molecule is placed in a nonoccupied space (cavity) of a polymeric matrix. The energy it radiates thus depends on the dielectric properties of the local surroundings. The spontaneous emission rate $\Gamma(\epsilon)$ of the dye inside a homogeneous medium with dielectric constant ϵ is predicted to follow the $\sqrt{\epsilon}$ dependence of the RDOS [18]: $\Gamma(\epsilon) = \sqrt{\epsilon}\Gamma_0$. However, this result was obtained by quantizing the macroscopic electromagnetic field, while the dipole couples to the local field at the position of the molecule. Strictly the dipole-dipole interaction considering the surrounding polymeric voids should be calculated [19]; in practice, for complex systems, the concept of local field is introduced. The microscopic local field differs from the macroscopic field by a local field correction factor L_f given by

$$L_f = \frac{3\epsilon}{2\epsilon + 1 - \frac{2\alpha}{3\Omega}(\epsilon - 1)}, \tag{2}$$

where here α is the polarizability of the dye in a cavity of volume Ω [20]. For substitutional or interstitial impurities such as dyes in an otherwise homogeneous medium, Eq. (2) reduces to the empty-cavity (Lorentz) local field factor $L_f = \frac{3\epsilon}{2\epsilon+1}$. For dye molecules with a substantial polarizability the local field fluctuations might exceed the Lorentz factor. By including the local field factor the spontaneous emission rate is given by $\Gamma(\epsilon) = L_f^2\sqrt{\epsilon}\Gamma_0$.

Up to now, the polymer matrix has been considered as a homogeneous medium with a dielectric constant ϵ. However, polymer chain segments move in time in the polymer matrix at room temperature. For the probe molecule, the segmental rearrangements imply either creation or annihilation of voids in its nanoenvironment, and thus a change of its surrounding local dielectric constant. Consequently, the system has to be considered as an effective medium [21], consisting of polymer segments and voids competing to occupy space. A local effective dielectric constant ϵ modulated by the fraction h of holes present in the medium is given by

$$\epsilon = h\epsilon_{\mathrm{vac}} + (1 - h)\epsilon_{\mathrm{pol}}, \tag{3}$$

where $\epsilon_{\mathrm{vac}} = 1$ and $\epsilon_{\mathrm{pol}} = 2.5$ designate the vacuum and polymer (PS) dielectric constant, respectively.

Following usual statistical theory, the change of variables τ into h is accompanied by a corresponding change of the probability density $f(\tau)$ into $g(h) = f(\tau)|\frac{d\tau}{dh}|$. For the effective medium considered here, this dependence is smoothly linear: converting a gamma distribution of holes, characterized by its first two moments $h_{\mathrm{av}} = 10\%$ and $\langle \delta x^2 \rangle_{\mathrm{av}} = 0.4\%$ to the corresponding distribution of lifetimes, leads to a nonlinear deviation of only 5% in the corresponding value of the shape parameter.

To relate our claim to a classical polymer theory, it is interesting to note that the SS model [13] considers the polymer as a lattice of sites that can accommodate the chain segments of macromolecules. To account for molecular disorder, a temperature and volume dependent fraction h of holes is introduced. Knowing the configurational properties of the system, an equation of state has been established [22], which permits the determination of the fractional mean free volume h_{av} present in the system. However, due to thermal fluctuations, the free volume varies both in time and at every position. The mean-squared deviation from the mean free volume can be calculated once the number of polymer segments (N_s) involved in a segmental rearrangement cell is known. From the first two moments and by attributing a value to N_s, a gamma distribution of free volume is built [23,24]. Given a gamma distribution of free volume, the

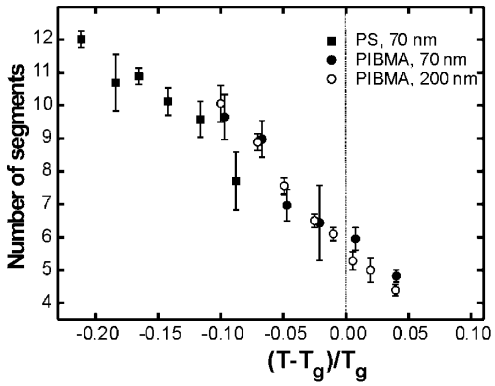

FIG. 3. Master plot of the number of segments N_s involved in a segmental rearrangement cell as a function of the reduced temperature $(T\text{-}T_g)/T_g$ for PS (squares, $T_g = 100\,^{\circ}\mathrm{C}$) and for PIBMA (circles, $T_g = 56\,^{\circ}\mathrm{C}$). In the case of PIBMA, data for both a 70 nm thick film (closed circles) and a 200 nm thick film (open circles) are shown. At the glass transition temperature, typically six segments play a role in the segmental rearrangement.

number of segments (N_s) becomes a linear function of the shape parameter α multiplied by a temperature and volume dependent factor, $N_s = \alpha f(h, \tilde{V}, \tilde{T})$. The shape distributions, as shown in Fig. 2, can therefore be converted into corresponding distributions of the number of segments N_s involved in a local segmental rearrangement cell.

Figure 3 shows the peak positions of the N_s distributions as a function of temperature for PIBMA, 70 and 200 nm thick films, and PS, 70 nm thick film. The striking feature of this master plot is the appearance of a general behavior, with the reduced temperature $(T - T_g)/T_g$ as a common parameter. The observation of the decrease of the number of segments when increasing temperature is in agreement with the configurational entropy model of Adam and Gibbs (AG), which predicts that the length scale of the cooperatively rearranging regions (CRR) decreases with increasing temperature. Furthermore, the changes in width and position of the distributions with temperature, shown in Fig. 2, clearly reveal the existence of microheterogeneous domains of different sizes and relaxation times, which is not considered in the AG theory, where the CRRs are assumed to be equivalent. Admitting a distribution of sizes of the independently relaxing CRRs, the theory thus does not give any guidance as to what the distribution should be. Single molecule spectroscopy and Fig. 2 provide such distributions and even show a reduction in the width of the distributions with increasing temperature, related to the appearance of a more homogeneous dynamics as the temperature is increased.

Having opened a route towards direct microscopic insight in the segmental dynamics of polymers, it will be interesting to explore the significance of the N_s value around T_g and the behavior towards higher temperatures. We believe that our novel approach has large potential for the understanding of the nanoscale dynamics of functional polymers and biopolymers.

The authors are grateful to Jeroen Korterik and Frans Segerink for technical support, Erik van Dijk for TCSPC interfacing and helpful discussion of the results, and María García-Parajó for introducing the first author to the single molecule field. This research is supported by the Council for Chemical Sciences of the Netherlands Organisation for Scientific Research (NWO-CW).

*Electronic address: n.f.vanhulst@tn.utwente.nl

[1] C. A. Angell, K. L. Ngai, G. B. McKenna, P. F. McMillan, and S. W. Martin, J. Appl. Phys. **88**, 3113 (2000).
[2] U. Tracht, M. Wilhem, A. Heuer, H. Feng, K. Schmidt-Rohr, and H. W. Spiess, Phys. Rev. Lett. **81**, 2727 (1998).
[3] M. D. Ediger, Annu. Rev. Phys. Chem. **51**, 99 (2000).
[4] C. T. Moynihan and J. Schroeder, J. Non-Cryst. Solids **160**, 52 (1993).
[5] B. Schiener, A. Loidl, R. Bohmer, and R. V. Chamberlin, Science **274**, 752 (1996).
[6] L. A. Deschesnes and D. A. Vanden Bout, Science **292**, 255 (2001).
[7] X. S. Xie and J. K. Trautman, Annu. Rev. Phys. Chem. **49**, 441 (1998).
[8] W. E. Moerner and M. Orrit, Science **283**, 1670 (1999).
[9] A.-M. Boiron, Ph. Tamarat, B. Lounis, and M. Orrit, Chem. Phys. **247**, 119 (1999).
[10] E. Geva and J. L. Skinner, J. Chem. Phys. **109**, 4920 (1998).
[11] J. J. Macklin, J. K. Trautman, T. D. Harris, and L. E. Brus, Science **272**, 255 (1996).
[12] J. A. Veerman, M. F. Garcia Parajo, L. Kuipers, and N. F. van Hulst, Phys. Rev. Lett. **83**, 2155 (1999).
[13] R. Simha and T. Somcynski, Macromolecules **2**, 342 (1969).
[14] G. Adam and J. H. Gibbs, J. Chem. Phys. **43**, 139 (1965).
[15] R. A. L. Vallée, N. Tomczak, H. Gersen, E. M. P. H. van Dijk, M. F. Garcia-Parajo, G. J. Vancso, and N. F. van Hulst, Chem. Phys. Lett. **348**, 161 (2001).
[16] R. J. Glauber and M. Lewenstein, Phys. Rev. A **43**, 467 (1991).
[17] R. A. L. Vallée, G. J. Vancso, N. F. van Hulst, J.-P. Calbert, J. Cornil, and J. L. Brédas, Chem. Phys. Lett. **372**, 282 (2003).
[18] G. Nienhuis and C. Th. J. Alkemade, Physica (Amsterdam) **81C**, 181 (1976).
[19] E. A. Donley, H. Bach, U. P. Wild, and T. Plakhotnik, J. Phys. Chem. A **103**, 2282 (1999).
[20] F. J. P. Schuurmans, P. de Vries, and A. Lagendijk, Phys. Lett. A **264**, 472 (2000).
[21] D. E. Aspnes, Am. J. Phys. **50**, 704 (1982).
[22] R. Simha, Macromolecules **10**, 1025 (1977).
[23] R. E. Robertson, R. Simha, and J. G. Curro, Macromolecules **17**, 911 (1984).
[24] R. E. Robertson, *Computational Modeling of Polymers, Free-Volume Theory and Its Application to Polymer Relaxation in the Glassy State,* edited by J. Bicerano (Marcel Dekker, Inc., New York, 1992).

Available online at www.sciencedirect.com
SCIENCE DIRECT®
Chemical Physics Letters 384 (2004) 5–8
CHEMICAL PHYSICS LETTERS
www.elsevier.com/locate/cplett

Effect of solvent on nanoscale polymer heterogeneity and mobility probed by single molecule lifetime fluctuations

R.A.L. Vallée [a,b,*], N. Tomczak [a,b], L. Kuipers [a], G.J. Vancso [b], N.F. van Hulst [a]

[a] Applied Optics Group, MESA+ Research Institute, University of Twente, P.O. Box 217, 7500 AE Enschede, The Netherlands
[b] Materials Science and Technology of Polymers, MESA+ Research Institute, University of Twente, P.O. Box 217, 7500 AE Enschede, The Netherlands

Received 7 November 2003; in final form 7 November 2003

Abstract

In this Letter, we address nanoscale heterogeneity in polymer mobility. Single molecule fluorescence lifetime fluctuations are exploited as a probe for local segmental dynamics in polymer films. Wide distributions in polymer mobility are observed, which depend on film fabrication, treatment and amount of solvent contained. Upon solvent evaporation mobile regions disappear, while more immobile regions settle, effectively increasing the glass transition temperature. Besides insight in polymer nanoscale dynamics and heterogeneity, our results bear specific relevance to photodynamic studies on single chromophores, where routinely polymer matrices are used for immobilization.
© 2003 Elsevier B.V. All rights reserved.

1. Introduction

In the last decade the study of single fluorophores immobilized in polymeric thin films has received increasing research attention. Initially the polymeric matrix helped increase photostability and quantum efficiency of the fluorophores for single molecule studies [1–4]. More and more the situation has reversed and the polymer has become the object of study by single molecule methods [5–7]. Polymer mobility both in the supercooled liquid regime [5] and in the glassy state are addressed [7–9]. Recently we have shown that lifetime fluctuations of single molecules embedded in a polymer matrix reflect the local polymer mobility [7]. Free volume theories [10–13], generally applied to describe molecular properties and physical behavior of polymers, can now be confronted with nanoscopic experiments. Using the Simha–Somcynsky free-volume theory [12,13], we can relate the lifetime fluctuations directly to the number of segments involved in a rearrangement of the polymer chains constituting the immediate surrounding of the molecule. In our previous study [7], the films were annealed after spin coating of the dye-doped polymer solution on a glass substrate, in order to remove the residual solvent and erase the history of the films. In this Letter we analyze the nanoscale heterogeneity of polymer mobility as a function of time for freshly prepared films, particularly the effect of solvent evaporation. Our observations are particularly relevant for the single molecule community where photodynamic on single chromophores is studied and routinely polymer matrices are used for immobilization.

2. Methodology

The Simha–Somcynsky (S–S) theory [12] considers the polymer as a lattice of sites that can accommodate the chain segments of macromolecules. To account for molecular disorder, a temperature and volume dependent fraction h of holes is introduced. Knowing the configurational properties of the system, an equation of state has been established [13], which permits the determination of the fractional mean free-volume h_{av}

* Corresponding author. Present address: Department of Chemistry, Catholic University of Leuven, Celestijnenlaan 200 F, B-3001 Leuven, Belgium. Fax: +3216327990.
E-mail address: renaud.vallee@chem.kuleuven.ac.be (R.A.L. Vallée).

0009-2614/$ - see front matter © 2003 Elsevier B.V. All rights reserved.
doi:10.1016/j.cplett.2003.11.086

present in the system. However, due to thermal fluctuations, the free-volume varies both in time and at every position. As a consequence, the probe molecule sees its immediate surrounding fluctuating, mediated by a change of its local dielectric constant ϵ [15]: $\epsilon = h\epsilon_{\text{vac}} + (1-h)\epsilon_{\text{pol}}$, where $\epsilon_{\text{vac}} = 1$ and $\epsilon_{\text{pol}} = 2.5$ designate the vacuum and polymer (polystyrene) dielectric constant, respectively. The fluctuations of the dielectric constant modulate the spontaneous emission rate $\Gamma(\epsilon)$ of the probe molecule, in accordance with [16]: $\Gamma(\epsilon) = \frac{9\epsilon^{5/2}}{(2\epsilon+1)^2}\Gamma_0$, where Γ_0 is the spontaneous emission rate of the molecule in vacuum. The radiative lifetime τ is the inverse of $\Gamma(\epsilon)$. A distribution of fluorescence lifetimes of the probe molecule is thus obtained as a result of the motion of the chain segments around the probe. Given the number (N_s) of these polymer segments, a mean-squared deviation from the mean free volume can be calculated and a gamma distribution of free volume is built [17,18]. This distribution of free volume is connected to the fluorescence lifetime distribution of the probe molecule, which is experimentally shown to be also best fitted by a gamma distribution [7]. Specifically, the shape parameters α of both distributions are shown to match within 5% accuracy. As a result, the shape parameter (α) of the lifetime-fitted gamma distributions gives directly the number N_s of chain segments involved in a rearrangement volume around the probe.

3. Experimental

Thin films (70 nm) of PS ($T_g = 373$ K, 89300 g/mol, polydispersity index (PI) of 1.06, Polymer Standard Service) with embedded 1,1′-dioctadecyl-3,3,3′,3′-tetramethylindodicarbocyanine (DiD, Molecular Probes) fluorescent probe molecules were prepared by either spin coating or casting the dye-doped polymer (5×10^{-10} M) in a toluene solution on a glass substrate at 295 K. For the duration of the experiment, the fresh samples were held isothermally in air and investigated using a confocal scanning fluorescence microscope. For the sake of comparison, an annealed film was also prepared, in vacuum, following a two stage procedure: 12 h at 323 K followed by 3 h at 378 K, in vacuum. The dye molecules were excited by 230 fs pulses at a wavelength of 647 nm, generated by a frequency doubled optical parametric oscillator pumped by a Ti:Sa laser (Spectra Physics). The fluorescence signal was collected in two orthogonal polarization channels in order to probe possible reorientation of the dye in the matrix. Fluorescence lifetime transients of single embedded molecules were acquired using time correlated single photon counting [14].

4. Results and discussion

Trajectories of both intensity and fluorescence lifetime trajectories of an individual DiD molecule in PS are shown in Fig. 1a. The intensity is constant within 15% during the investigated time window (60 s). While the fluorescence lifetime mostly stays around a value of 3 ns, it makes frequent excursions to longer lifetimes up to 7 ns. Fig. 1b shows the distribution of lifetimes and the correlation plot between intensity and lifetime. The correlation plot indicates that the lifetime is not correlated to the intensity, excluding the possibility that the lifetime fluctuations result from fluctuations in the available number of decay channels. The lifetime distribution is clearly asymmetric, with a tail towards longer lifetimes, which in fact rules out any non-radia-

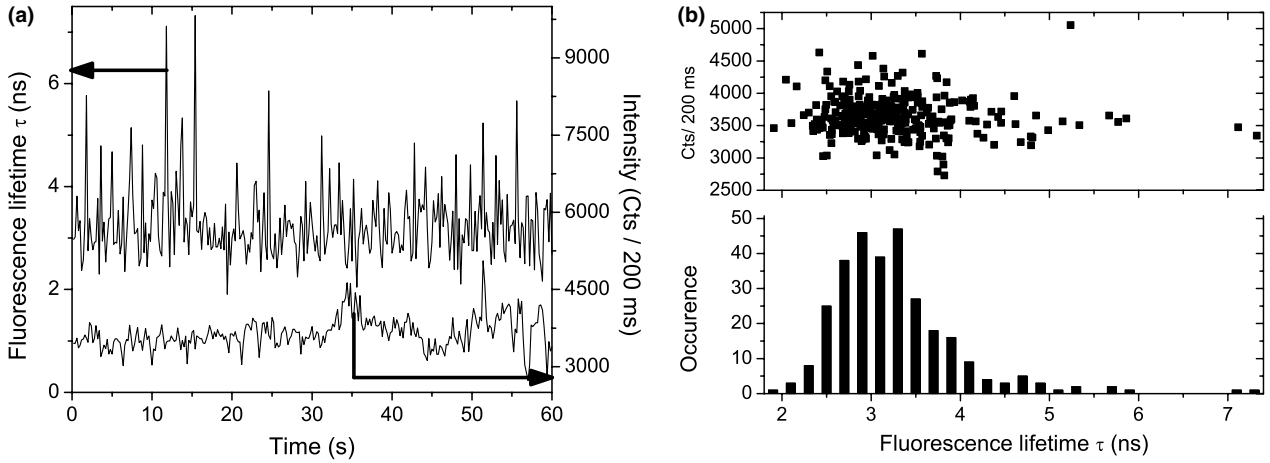

Fig. 1. (a) Transients of fluorescence intensity and lifetime for an individual DiD molecule embedded in a 70 nm thick film of PS obtained by spin coating of a dye-doped polymer solution on the glass substrate at room temperature. The molecule exhibits excursions towards longer lifetime values. (b) Corresponding fluorescence lifetime distribution and correlation plot between intensity and lifetime. While the intensity is constant within 15% the lifetime varies 100% from 3 up to 6–7 ns.

tive process as the cause of the fluctuations. Fluctuations of the fluorescence lifetime due to modifications of either the transition frequency or the transition dipole moment of a fluorophore [19], are prevented since the molecular conformation of the chosen carbocyanine dye is similar in both ground and excited state [20]. These observations are the prerequisites to attribute the lifetime fluctuations to polymeric density fluctuations [7].

On a daily basis, we collected 20–50 molecule lifetime transients in a time interval of 1 h. We fitted the lifetime distribution of each individual molecule with a gamma distribution to obtain the shape parameter, and consequently the number N_s of polymer segments rearranging around the probe molecule. From the obtained 20–50 values of N_s, we then constructed the distributions of N_s for each day. Fig. 2 shows the peak positions of the N_s distributions in time, for both spin coated (squares) and casted films (stars) of the dye-doped polymer solution on a glass substrate. Interestingly, both curves display an S-shape. Starting with 8–9 polymer segments involved in a rearrangement around the probe molecule for a freshly prepared sample, the curves stay flat as time evolves until four days are elapsed. At this point, the N_s values increase rapidly, to reach a plateau at $N_s = 12$ after a week.

Note that the number of segments $N_s = 12$ obtained two weeks after the spin coating or casting has been performed coincides with the N_s of a similar film when annealed. The fact that films obtained both by casting and spin coating give rise to the same behavior excludes the possibility that the S-shape is due to some relaxation process of the stresses induced by a spin coating procedure. The S-shape is thus attributed to the withdrawal of the solvent (toluene) trapped in the PS films during the coating. The effect of a given amount of solvent present in a polymer film is known to reduce the glass transition temperature T_g of the film [21–23]. We determined the temperature dependence of N_s as $dN_s/dT = -1$ segment per 9 K [7], so that a difference of three segments between the low- and high-N_s plateau corresponds to a difference of 27 K in T_g. The annealed film, free of solvent, has a glass transition temperature $T_{ga} = 373$ K. Consequently, the low-N_s plateau corresponds to a system PS with trapped solvent with a glass transition temperature $T_{gs} = 346$ K. The plasticizing effect of solvent is often described by: $k\omega_s = T_{ga} - T_{gs}$, where ω_s is the solvent weight fraction and k a constant, which for the PS/toluene system is equal to 500 K [24]. For a 27 K temperature difference between T_{gs} and T_{ga}, a solvent weight fraction $\omega_s = 5.5\%$ is trapped in the polymer film. This is the case for the film prepared by spin coating. Concerning the casted film, the values of N_s are slightly lower (Fig. 2) and the corresponding solvent weight fraction $\omega_s = 7\%$ is slightly higher than for the spin coated film, as expected.

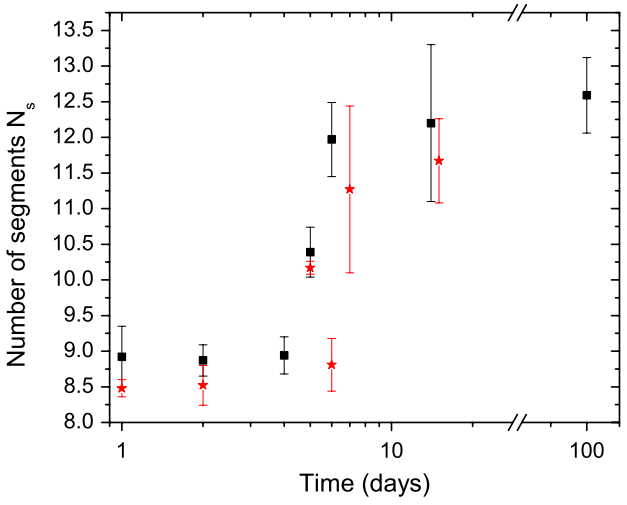

Fig. 2. Temporal evolution of the number of polymer segments N_s rearranging around DiD molecules embedded in a 70 nm thick polystyrene matrix. The values given correspond to the peaks of the distributions (Fig. 3), obtained on a daily basis after the spin coating (squares) or casting (stars) procedure has been initiated at room temperature 22 °C. The value pointed after break on the x scale corresponds to the peak value of the distribution of the number of segments obtained after annealing of the spin coated film.

The existence of a low-N_s plateau is probably due to the formation of a dense viscoelastic region at the exposed surface, at the early stages of the solvent desorption (during the spin coating or casting process) [25]. The formation of such a skin is undesirable in coating processes due to non uniformities in the polymer coating and a decrease in the drying rates [26]. The intrinsic dynamics of the system polymer chains-solvent and the presence of a drying front across the film thickness slowly react against the formation of the skin and drive the evaporation of the solvent.

So far we have discussed the development of the average properties of the polymer films in time. The exclusive advantage of our single molecule approach lies in the distribution. Each molecule reports on its nanoenvironment and by monitoring many molecules we find the nanoscale heterogeneity. Fig. 3 shows the N_s distributions for 4, 5 and 6 days after spin coating. Clearly a very broad distribution is observed, indicating the heterogeneity of the film ranging from mobile (low N_s) to immobile (high N_s) regions. The definition of T_g for the film only works on a macroscopic level as, on the nanoscale, domains with different N_s, i.e., different mobility and local 'effective T_g', occur. A detailed look at the distributions reveals how the average N_s increases day by day. The dominant changes occur at the low N_s side of the distribution where mobile regions vanish. This observation supports nicely the suggestion by Robertson [27] that regions of higher mobility should relax more rapidly than region with low mobility. On the contrary a certain fraction of low mobility regions is present from the beginning and becomes dominant as time elapses. In this context it is interesting to note that,

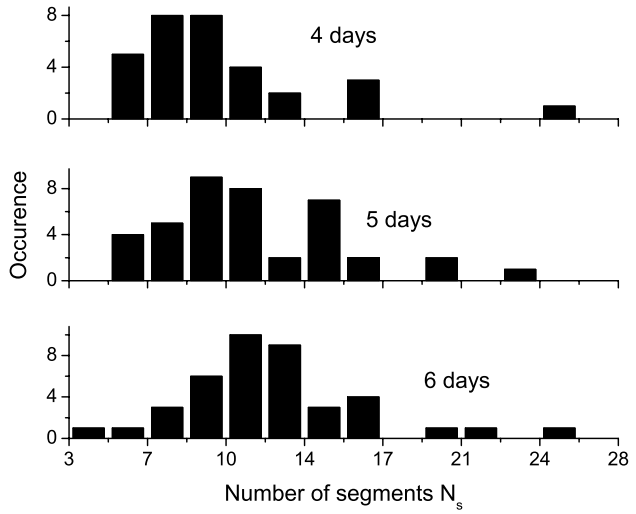

Fig. 3. Distributions of the number of segments N_s involved in a rearrangement of the polymer chains in the immediate surrounding of DiD molecules embedded in a 70 nm thick film of PS for 4, 5 and 6 days after the spin coating procedure.

at any stage throughout the solvent evaporation process, the N_s distribution is wider than the actual shift occurring: the heterogeneity is larger than the effect we observe. Even for an annealed film with $T_{ga} = 373$ K nanoregions exist with a local effective T_g much lower and also higher than the bulk value.

The analysis described in this Letter is crucial for the single molecule community. Indeed, in this community, one usually uses a polymer matrix to immobilize fluorescence molecules. The matrix is most often prepared by spin coating a dye-doped polymer solution on a glass substrate. In this case, it is important to realize that the T_g of the material is not that expected, but is mostly reduced, due to the presence of solvents, thus increasing the mobility of the matrix. Furthermore, the molecules (and especially their fluorescence lifetime) under study are sensitive to the subsequent evaporation process, as shown in the current investigation.

Acknowledgements

The authors are grateful to Jeroen Korterik and Frans Segerink for technical support, and Erik van Dijk for TCSPC interfacing. This research is supported by the Council for Chemical Sciences of the Netherlands Organisation for Scientific Research (NWO-CW).

References

[1] J.J. Macklin, J.K. Trautman, T.D. Harris, L.E. Brus, Science 272 (1996) 255.
[2] X.S. Xie, J.K. Trautman, Annu. Rev. Phys. Chem. 49 (1998) 441.
[3] D.A. Vanden Bout, W.-T. Yip, D.H. Hu, T.M. Swager, P.F. Barbara, Science 277 (1997) 1074.
[4] J.A. Veerman, M.F. Garcia Parajo, L. Kuipers, N.F. van Hulst, Phys. Rev. Lett. 83 (1999) 2155.
[5] L.A. Deschesnes, D.A. Vanden Bout, Science 292 (2001) 255.
[6] N.B. Bowden, K.A. Willets, W.E. Moerner, R.M. Waymouth, Macromolecules 35 (2002) 8122.
[7] R.A.L. Vallée, N. Tomczak, L. Kuipers, G.J. Vancso, N.F. van Hulst, Phys. Rev. Lett. 91 (2003) 038301.
[8] A.P. Bartko, R.M. Dickson, J. Phys. Chem. B 103 (1999) 3053.
[9] R.A.L. Vallée, M. Cotlet, J. Hofkens, F.C. De Schryver, K. Müllen, Macromolecules 36 (2003) 7752.
[10] M.H. Cohen, D. Turnbull, J. Chem. Phys. 31 (1959) 1164.
[11] D. Turnbull, M.H. Cohen, J. Chem. Phys. 52 (1970) 3038.
[12] R. Simha, T. Somcynski, Macromolecules 2 (1969) 342.
[13] R. Simha, Macromolecules 10 (1977) 1025.
[14] R. Vallée et al., Chem. Phys. Lett. 348 (2001) 161.
[15] D.E. Aspnes, Am. J. Phys. 50 (1982) 704.
[16] R.J. Glauber, M. Lewenstein, Phys. Rev. A 43 (1991) 467.
[17] R.E. Robertson, R. Simha, J.G. Curro, Macromolecules 17 (1984) 911.
[18] R.E. Robertson, Computational modeling of polymers, in: J. Bicerano (Ed.), Free Volume Theory and its Application to Polymer Relaxation in the Glassy State, Marcel Dekker, Inc, 1992.
[19] E.A. Donley, H. Bach, U.P. Wild, T. Plakhotnik, J. Phys. Chem. A 103 (1999) 2282.
[20] R.A.L. Vallée, G.J. Vancso, N.F. van Hulst, J.-P. Calbert, J. Cornil, J.L. Brédas, Chem. Phys. Lett. 372 (2003) 282.
[21] A. Laschitsch, C. Bouchard, J. Habicht, M. Schimmel, J. Rhe, D. Johannsmann, Macromolecules 32 (1999) 1244.
[22] A.-C. Saby-Dubreuil, B. Guerrier, C. Allain, D. Johannsmann, Polymer 42 (2001) 1383.
[23] T.S. Chow, Macromolecules 13 (1980) 362.
[24] T.P. Gall, E.J. Kramer, Polymer 32 (1991) 265.
[25] J. Gu, M.D. Bullwinkel, G.A. Campbell, Polym. Eng. Sci. 36 (1996) 1019.
[26] R.A. Cairncross, L.F. Francis, L.E. Scriven, AIChE J. 42 (1996) 2415.
[27] R.E. Robertson, J. Polym. Sci., Polym. Symp. 63 (1978) 173.

J|A|C|S
COMMUNICATIONS

Published on Web 00/00/0000

Segment Dynamics in Thin Polystyrene Films Probed by Single-Molecule Optics

Nikodem Tomczak,[†,‡] Renaud A. L. Vallée,[†,‡] Erik M. H. P. van Dijk,[‡] Laurens Kuipers,[‡] Niek F. van Hulst,[‡] and G. Julius Vancso*[,†]

Department of Materials Science and Technology of Polymers and Applied Optics Group, University of Twente, MESA+ Institute for Nanotechnology, Faculty of Science and Technology, P.O. Box 217, 7500 AE Enschede, The Netherlands

Received October 27, 2003; E-mail: g.j.vancso@ct.utwente.nl

Polymers have recently been demonstrated to exhibit different chain dynamic behavior, as compared to the bulk, when confined into the geometry of ultrathin films.[1,2] Investigations of the glass transition temperature (T_g) of thin, supported, polystyrene films by ellipsometry,[3] Brillouin light scattering,[4] dielectric spectroscopy,[5] or positron annihilation lifetime spectroscopy (PALS),[6] among others, showed large T_g depressions. This behavior is thought to be due to the existence of a surface layer where the polymer chain dynamics is enhanced over that in the bulk. This layer becomes dominant for very thin films, thereby shifting T_g of the films toward lower temperatures. The existence of such a surface layer is also supported by measurements of T_g for free-standing polymer films[7] and by a direct examination of the polymer surface by PALS.[8] However, all experimental techniques mentioned provide ensemble-averaged information. Furthermore, the depth at which deviation between the surface and the bulk dynamics becomes significant could not be addressed in detail due to the lack of depth resolution of these techniques on the nanometer scale.

Single molecule fluorescence detection (SMD) intrinsically avoids ensemble averaging. In combination with high spatial and temporal resolution, SMD is an ideal tool for investigating structure and dynamics of the probe environment on the nanoscale. Through the use of different approaches, SMD has already been employed with success to study macromolecular systems[9,10] and inorganic/organic composite films.[11] In a recent study[12] we have introduced a new single-molecule approach based on fluorescent lifetime fluctuations to give direct insight into local, nanoscale dynamics of the polymer matrix surrounding a chromophoric probe on the segmental level.

In this communication we report, for the first time, on the use of single-molecule fluorescence lifetime to investigate thin film effects in a glassy polymer system at temperatures far below bulk T_g. We find that the dynamics of the surroundings of the probe becomes enhanced when the constituent macromolecules are confined into a thin film. The characteristic film thickness at which this behavior becomes noticeable is several times larger than the radius of gyration (R_g) of the polymer chain used. Our result points toward the existence of interfacial regions with enhanced dynamics and represents the first step toward depth-resolved studies of polymer films on the nanoscale using SMD.

Thin-film samples were prepared by spin coating DiD (1,1′-dioctadecyl-3,3,3′,3′-tetramethylindodicarbocyanine, Molecular Probes D-307)/polystyrene (PS, M_n = 89300 g/mol, M_w/M_n = 1.06, Polymer Standard Service) solutions onto cleaned glass cover slides. The films were subsequently annealed, first for 12 h at 60 °C and later for 3 h at 105 °C in order to remove the residual solvent and relax all stresses induced by the spin coating procedure. The concentration of the dye was 10^{-9} M in the resulting PS films, and the thickness was varied between 10 and 200 nm. A NanoScope III Atomic Force Microscope (Digital Instruments, Santa Barbara) was used to estimate the planarity and the roughness of the samples (<2 nm) before and after the measurements, respectively. No dewetting of the thin films was observed at any stage. To detect the individual molecules within the polymeric matrix, we used a scanning fluorescence confocal microscope (custom built) equipped with suitable dichroic, excitation, and emission filters. A picosecond pulsed laser (PicoQuant, 800-B) was employed to excite the molecules at the wavelength of 635 nm. Fluorescence photons were collected by two avalanche photodetectors (SPCM-AQ-14, EG&G Electro Optics) placed after a polarization beam splitter. An SPC 500 time-correlated single-photon counting card (Becker & Hickl) was used for time-resolved lifetime measurements.[12] For higher temperature measurements, a custom-built hot stage was placed below the sample and the temperature was monitored with an accuracy of ±2 °C. For each film thickness, 400 probe molecules were analyzed for two different temperatures, 22 and 35 °C, respectively.

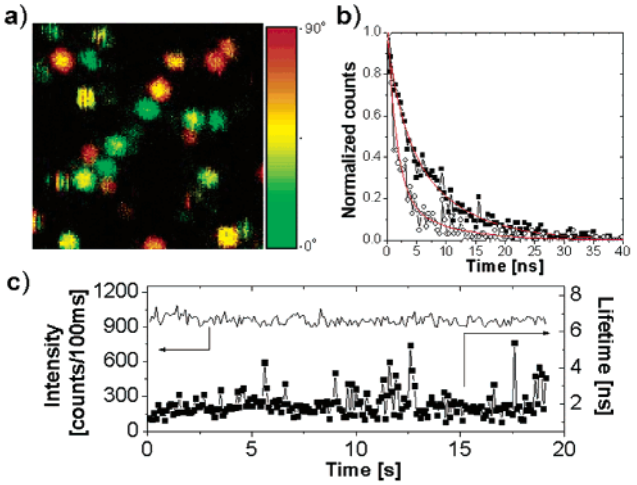

Figure 1. (a) 5 × 5 μm^2 fluorescence intensity scan of single DiD molecules in a 110 nm thick PS film at 22 °C. The color scale indicates the polarization of the fluorescence, which is a measure for the in-plane orientation of the molecules. Constant color confirms that the molecules are not rotating in the matrix. (b) Fluorescence decays of one DiD molecule from which a short (2.5 ns, ○) and long (6 ns, ■) fluorescence lifetime was extracted. The red lines correspond to single-exponential fits to the data. (c) Fluorescence intensity and lifetime traces for a single DiD in PS. Excursions to longer lifetimes (up to 5 ns) are clearly visible.

Figure 1a depicts a 5 × 5 μm^2 fluorescence intensity scan. Characteristic on−off behavior and single-step photobleaching observed confirm that the spots on the image correspond to single emitters. For each single molecule, we collected intensity and

[†] Department of Materials Science and Technology of Polymers.
[‡] Applied Optics Group.

10.1021/ja039249h CCC: $27.50 © xxxx American Chemical Society

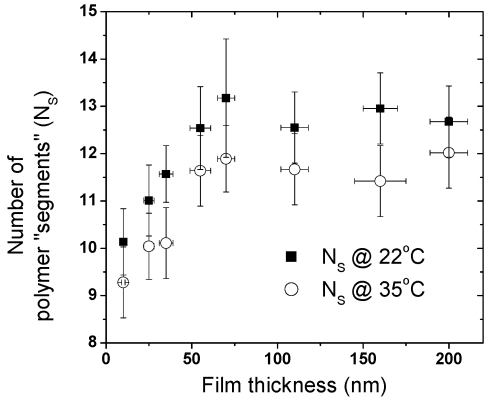

Figure 2. Mean value of the effective number of polymer "segments" in the rearrangement volume around the single-molecule probes as a function of PS film thickness for two different temperatures.

fluorescence lifetime traces with 100 ms time intervals, during 20−60 s total observation time. The accuracy of lifetime determination is on the order of 300 ps. Examples of decay curves (two snapshots at different times for the same molecule) are presented in Figure 1b. In Figure 1c, fluorescence intensity and lifetime traces are shown. Changes in the lifetime as a function of time for the same molecule are clearly visible. From the lifetime trajectory of each molecule we built lifetime distributions, which were fitted with a distribution function.[13] From the fitting parameters we determine the effective number of polymer "segments" (N_S) taking part in the rearrangement volume around the single probe using the method described in detail in ref 12. N_S determined by this procedure provides direct information concerning local, segmental scale polymer dynamics and its spatial distribution. The value of N_S is very sensitive for small density fluctuations around the probe within the probed time interval. Higher values of N_S can be visualized as a larger collection of polymer segments, which must move cooperatively during segmental relaxation around the probe, therefore indicating slower system dynamics.

In Figure 2, we present the mean of N_S values for single molecules as a function of PS film thickness for two different temperatures. The effect of temperature on N_S is consistent with our earlier results showing a decrease of N_S with increasing temperature.[12] The behavior of N_S as a function of film thickness can be divided into two regions. One region can be assigned to film thickness above a certain threshold value h_0, where N_S remains essentially constant. Below h_0, N_S becomes a function of thickness and decreases with decreasing film thickness. The transition (h_0) between the two regions is estimated from the graph to be around 50−60 nm.

Two main effects are known to be responsible for the observed decrease of N_S with decreasing film thickness: chain confinement (when the characteristic length scale of the polymer chain is comparable to the dimensions of the system) and the presence of interfaces with modified dynamics. However, for the molar mass of the polymer used here, the average radius of gyration (R_g) of the macromolecules is 9−10 nm assuming a chain conformation as in the θ state, i.e., 6 times smaller than the value of h_0. Thus, chain confinement is not expected to play a major role in our case. For a similar system consisting of air/polystyrene/glass, it was reported that the polymer/glass interface does not perturb the film dynamics.[14] Therefore, we attribute the decrease of N_S for small film thickness to modified polymer dynamics induced by the presence of a free polymer surface.[15] We also conclude that in such thin films, the dynamics of the polymer is modified far below the bulk glass transition temperature ($T_{g,b}$ = 100 °C as measured by DSC) even though a large fraction of the macromolecules cannot "sense" the possible effect of the interfaces nor are they forced to adopt a different conformation due to the confinement represented by the thin film. Apparently due to the connectivity and interpenetration of polymer chains, surface-induced enhancement of polymer dynamics propagate into the sample. The temperature dependence of N_S for PS films yields $dN_S/dT = -0.11$ [segments/deg][12] thus the dynamics in the thinnest film is equivalent to the dynamics in thicker films (thickness > h_0) if it was observed at temperatures elevated by as much as 30 °C.

From the mean lifetime of a collection of single molecules as a function of film thickness (not presented here), we rule out any dye segregation to one of the interfaces or at a certain depth within the samples. Also, from the stability of the fluorescence polarization state and from the mean fluorescence lifetime for each molecule during the observation time, we excluded the possibility that the decrease of N_S is caused by an increased rotational or translational activity of the probe in thinner films at the experimental temperatures (65 and 80 °C below $T_{g,b}$, respectively) that could cause lifetime fluctuations[16] and thus influence N_S.

In conclusion, we used a single-molecule lifetime technique to study the influence of the film thickness on local polymer dynamics on the nanometer length scale at temperatures far below the glass transition temperature. We find modified segment scale dynamics when the polymer is confined into films with thicknesses below 50−60 nm corresponding to 6 times the radius of gyration. In the future, we intend to extend our investigations to a controlled, depth-resolved dynamics study in thin polymer films from the surface to the bulk using NSOM-based approaches.

Acknowledgment. The Council for Chemical Sciences of the Netherlands Organization for Scientific Research (NWO-CW) is gratefully acknowledged for financial support. E.v.D. is financed by FOM, Dutch Foundation for Fundamental Research of Matter.

Supporting Information Available: Representative histograms of the width parameter and the corresponding N_S distributions (PDF). This material is available free of charge via the Internet at http://pubs.acs.org.

References

(1) Jones, R. A. L. *Curr. Opin. Colloid. Interface. Sci.* **1999**, *4*, 153−158.
(2) Forrest, J. A.; Dalnoki-Veress, K. *Adv. Colloid Interface Sci.* **2001**, *94*, 167−196.
(3) Keddie, J. L.; Jones, R. A. L.; Cory, R. A. *Europhys. Lett.* **1994**, *27*, 59−64.
(4) Forrest, J. A.; Dalnoki-Veress, K.; Dutcher, J. R. *Phys. Rev. E* **1997**, *56*, 5705−5716.
(5) Fukao, K.; Miyamoto, Y. *Phys. Rev. E* **2001**, *64*, Art. No. 011803.
(6) DeMaggio, G. B.; Frieze, W. E.; Gidley, D. W.; Zhu, M.; Hristov, H. A.; Yee, A. F. *Phys. Rev. Lett.* **1997**, *78*, 1524−1527.
(7) Forrest, J. A.; Dalnoki-Veress, K.; Stevens, J. R.; Dutcher, J. R. *Phys. Rev. Lett.* **1996**, *77*, 2002−2005.
(8) Cao, H.; Zhang, R.; Yuang, J. P.; Huang, C. M.; Jean, Y. C.; Suzuki, R.; Ohdaira, T.; Nielsen, B. *J. Phys.: Condens. Matter* **1998**, *10*, 10429−10442.
(9) Dickson, R. M.; Norris, D. J.; Tzeng, Y. L.; Moerner, W. E. *Science* **1996**, *274*, 966−969.
(10) Deschenes, L. A.; Vanden Bout, D. A. *Science* **2001**, *292*, 255−258.
(11) Bardo, A. M.; Collinson, M. M.; Higgins, D. A. *Chem. Mater.* **2001**, *13*, 2713−2721.
(12) Vallée, R. A. L.; Tomczak, N.; Kuipers, L.; Vancso, G. J.; van Hulst, N. F. *Phys. Rev. Lett.* **2003**, *91*, Art. No. 038301.
(13) Experimental data are best fitted with a gamma distribution function in the form of: $\gamma(\tau) = \beta\tau^{(\alpha-1)}e^{-\beta\tau}$.
(14) Keddie, J. L.; Jones, R. A. L.; Cory, R. A. *Faraday Discuss.* **1995**, *98*, 219−230.
(15) Mansfield, K. F.; Theodorou, D. N. *Macromolecules* **1991**, *24*, 6283−6294.
(16) Vallée, R. A. L.; Tomczak, N.; Gersen, H.; van Dijk, E. M. H. P.; García Parajó, M. F.; Vancso, G. J.; van Hulst, N. F. *Chem. Phys. Lett.* **2001**, *348*, 161−167.

JA039249H

A Microscopic Model for the Fluctuations of Local Field and Spontaneous Emission of Single Molecules in Disordered Media

Renaud A. L. Vallée,*[a] Mark Van Der Auweraer,[a] Frans C. De Schryver,[a] David Beljonne,[b] and Michel Orrit[c]

We develop a microscopic model to describe the observed temporal fluctuations of the fluorescence lifetime of single molecules embedded in a polymer at room temperature. The model represents the fluorescent probe and the macromolecular matrix on the sites of a cubic lattice and introduces voids in the matrix to account for its mobility. We generalize Lorentz's approach to dielectrics by considering three domains of electrostatic interaction of the probe molecule with its nanoenvironment: 1) the probe molecule with its elongated shape and its specific polarizability, 2) the first few solvent shells with their discrete structure and their inhomogeneity, 3) the remainder of the solvent at larger distances, treated as a continuous dielectric. The model is validated by comparing its outcome for homogeneous systems with those of existing theories. When realistic inhomogeneities are introduced, the model correctly explains the observed fluctuations of the lifetimes of single molecules. Such a comparison is only possible with single-molecule observations, which provide a new access to local field effects.

1. Introduction

While the interaction of electromagnetic fields with single molecules is well understood in vacuum,[1] the situation is much more complex in condensed phases: the presence of polarizable media considerably alters the quantum fluctuation properties of the fields.[2] Most approaches consider the electromagnetic field as a macroscopic field modified by the local field factor, which takes into account the effect of the nanosurrounding of the probe molecule. On the one hand, the validity of the old but still frequently used Lorentz field factor continues to be investigated.[3] On the other hand, Glauber et al.[2] derived an expression (empty cavity factor) for the spontaneous emission of an excited probe located within a uniform medium of dielectric constant ε. This expression was also derived and checked experimentally by Yablonovitch et al.[4] Recently, it was shown that the empty cavity factor applies for a substitutional probe while the Lorentz cavity factor applies for an interstitial probe (the probe is inserted without displacement of the matrix molecules).[5] However, these approaches consider a uniform surrounding, such that the influence of the discrete structure of nearby molecules on the probe molecule averages out. The local, inhomogeneous nature of the medium is neglected. The local dielectric properties play an important role in the structure and functionality of proteins.[6,7,8] A more microscopic picture of the local effects has to be considered. Due to its intrinsic ability to sense the nanosurrounding of a probe molecule,[9] single-molecule spectroscopy constitutes the ideal tool to perform this task. A first step forward has been accomplished in this respect by Donley et al., who reported on the observation of radiative lifetime distributions of single terrylene molecules embedded in polyethylene at a temperature of 30 mK.[10]

In a recent publication,[11] Vallée et al. reported on the temporal fluorescence lifetime fluctuations of DiD (1,1-dioctadecyl-3,3,3′,3′-tetramethylindodicarbocyanine) single molecules (Scheme 1) embedded in diverse polymer matrices frozen in the glassy state. The lifetime fluctuations were attributed to a fluctuating density of the polymer segments surrounding the nanoprobe. A polymer matrix is a highly disordered and inhomogeneous system that, according to hole theories,[12,13] may be seen as an ensemble of polymer segments and holes allowed to move on a lattice. In the frame of an effective medium theory, the fluctuating hole configuration was described by a fluctuating dielectric constant around each single

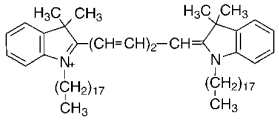

Scheme 1. *Chemical structure of a DiD molecule.*

[a] *Dr. R. A. L. Vallée, Prof. Dr. M. Van Der Auweraer, Prof. Dr. F. C. De Schryver*
Laboratory for Spectroscopy and Photochemistry
Catholic University of Leuven, Celestijnenlaan 200 F
3001 Leuven (Belgium)
Fax: (+32) 16-32-7990
E-mail: renaud.vallee@chem.kuleuven.ac.be

[b] *Dr. D. Beljonne*
Laboratory for Chemistry of Novel Materials
University of Mons, Place du Parc 20, 7000 Mons (Belgium)

[c] *Prof. Dr. M. Orrit*
Huygens Laboratory, P.O. Box 9504
2300 RA Leiden (The Netherlands)

 DOI: 10.1002/cphc.200400439 © 2005 Wiley-VCH Verlag GmbH & Co. KGaA, Weinheim

molecule.[14] The asymmetric fluorescence lifetime distribution for each individual molecule was related in this way to a corresponding distribution of holes surrounding the probe molecule. Consequently, a characteristic number of segments involved in a rearrangement cell around each individual molecule was determined. Interestingly, the shape of the fluorescence lifetime distributions, and consequently the number of segments involved in a rearrangement volume around the probe molecule, was found to decrease with increasing temperature.

Powerful though this model proved to be in interpreting the data, it presents several interrelated drawbacks. Firstly, the microscopic structure of the probe molecule is completely neglected: by using a spherical empty cavity factor[15] in the calculation of the fluorescence lifetime, the probe molecule has been considered as being of spherical shape and nonpolarizable.[11] In most treatments of local fields in dielectrics, a Lorentz factor is used. This assumes that a spherical molecule is placed in a isotropic, homogeneous medium.[3] In addition, the polarizability of the probe is taken equal to that of the matrix. In this work, we wish to go beyond these assumptions. We will consider 1) the elongated shape of the DiD molecule (Scheme 1),[16] 2) the actual polarizability of its conjugated system, which is much larger than that of the surrounding monomer units, 3) the microscopic structure of the first solvent shells around the probe, possibly including inhomogeneities.

This paper further explores the previous approach and provides a full microscopic interpretation of the lifetime fluctuations. The optical and structural properties of the individual molecule and of the surrounding monomer units are determined by quantum-chemical calculations. As the interaction between them is limited to a few nanometers, that is, is much smaller than the radiative emission wavelength $\lambda = 660$ nm, only nonretarded electrostatic interactions will be taken into account in the description.

2. Local Field in the Continuum Approach

Figure 1 a shows the fluorescence-lifetime time trace of a DiD single molecule embedded in a poly(styrene) (PS, $M_w =$ 133 000, polydispersity index $= 1.06$) matrix. While the lifetime has an average value of $\tau = 2.1$ ns, it deviates frequently and asymetrically towards higher values during the experiment. The fluorescence lifetime fluctuations of the individual molecule can be as large as 30 % with respect to the average value, as best represented by the corresponding distribution shown in Figure 1 b.

The spontaneous emission rate Γ_{r0} of a single fluorescent molecule in vacuum is given by the Einstein A_{eg} coefficient for emission in Equation (1):

$$\Gamma_{r0} = A_{eg} = \frac{1}{\tau_0} = \frac{4}{3}\frac{|\vec{\mu}_{eg}|^2}{4\pi\varepsilon_0\hbar}\left(\frac{\omega_{eg}}{c}\right)^3 \quad (1)$$

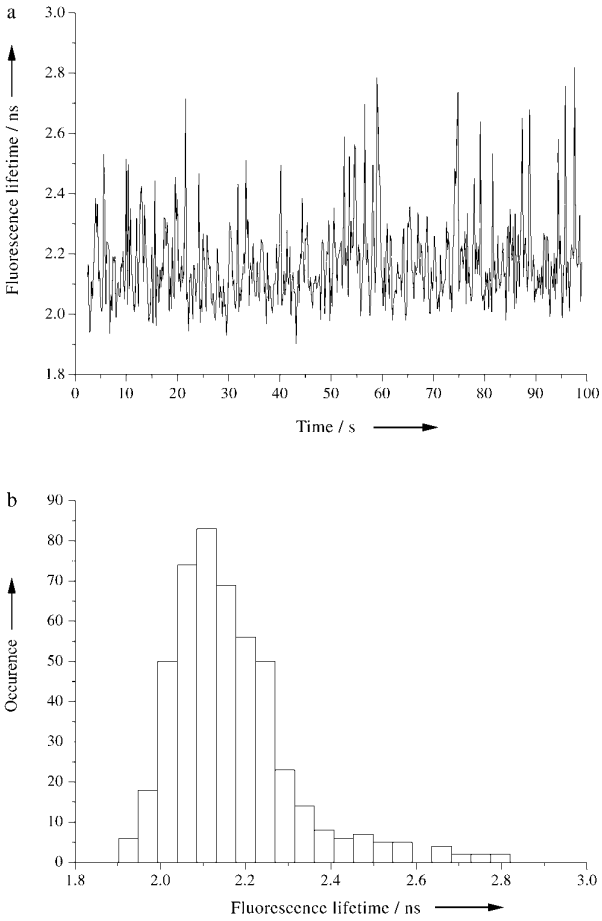

Figure 1. *Fluorescence lifetime time trajectory (a) and distribution (b) of a single DiD molecule embedded in a PS film.*

where $\vec{\mu}_{eg}$ and ω_{eg} are the transition dipole moment and transition frequency of the molecule, respectively; ε_0 is the dielectric permittivity of vacuum, $\hbar$ is the reduced Planck constant and c is the speed of light in vacuum. τ_0 is the inherent radiative lifetime of the molecule. This observable is an intrinsic property of the probe molecule. While this is indeed true in vacuum, the lifetime of the probe molecule strongly depends on its direct environment, and in particular on the dielectric properties of the medium in which it is embedded. In a transparent condensed medium of relative dielectric permittivity (high-frequency part), the energy of the emitted photon is renormalized through the substitutions $\varepsilon_0 \rightarrow \varepsilon_r\varepsilon_0$ and $c \rightarrow c/n$, such that the spontaneous emission rate can be written as Equation (2):

$$\Gamma_r = n\Gamma_{r0} \quad (2)$$

where $n = \sqrt{\varepsilon_r}$ is the refractive index of the considered medium ($n = 1.58$ in the case of PS). Nienhuis et al.[17] firstly derived this formula by quantizing the macroscopic Maxwell equations.

 © 2005 Wiley-VCH Verlag GmbH & Co. KGaA, Weinheim

It is worthwhile to mention here that the actual fluorescence lifetime of a single molecule embedded in a real medium results from both radiative (rate Γ_r) and nonradiative (rate Γ_{nr}) processes [Eq. (3)]:

$$\tau_f = \frac{1}{\Gamma_r + \Gamma_{nr}} \quad (3)$$

so that the opening of decay channels other than radiative can modify the lifetime. The quantum yield $\eta = \frac{\Gamma_r}{\Gamma_r + \Gamma_{nr}}$ of the DiD molecule has been shown to be very close to unity, which makes extra—nonradiative—decay channels irrelevant for the system under consideration.[11] In the remaining of this paper, we will only consider variations of the radiative rate.

The complex nature of the interaction of the probe molecule-surrounding dielectric, involving discrete and continuous parts, will be described by considering three separate domains (Figure 2): 1) the molecule with its elongated shape and specif-

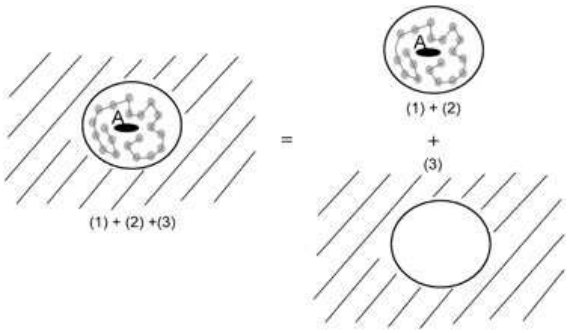

Figure 2. Description of the system under investigation: the probe molecule A (1) and its first few solvent shells (2) are considered with their discrete structure and embedded in the remainder of the matrix treated as a continuum (3).

ic polarizability, 2) the first few solvent shells with their discrete structure and their possible inhomogeneity, 3) the remainder of the solvent at long distances, treated as a continuum.

The molecule and the first solvent shells will be treated exactly by means of simulations given in Section 3. In this section, we replace them by one dipole at the center of a dielectric sphere with the same polarizability as the surroundings. We then reinsert this sphere into the dielectric, à la Lorentz, applying the relevant local field factor.

2.1 Lorentz Cavity Factor

We first consider a homogeneous, isotropic medium of identical molecules. Because of the relatively close proximity of the atoms or molecules in condensed phases, the local field $\vec{E}_l$ felt by the probe molecule can be very different from the applied electric field $\vec{E}_{ap}$. Figure 3 shows a two-dimensional representation of the Lorentz virtual spherical cavity model: a molecule A of the medium is surrounded by an imaginary sphere (represented by the circle) of such extent that beyond it the dielectric can be treated as a continuum.

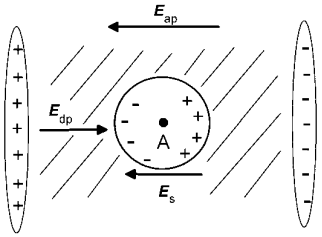

Figure 3. Two-dimensional representation of the Lorentz model.

When a field $\vec{E}_{ap}$ is applied to the sample (represented by the rectangle), charges accumulate on its surface in response to $\vec{E}_{ap}$. A depolarizing field $\vec{E}_{dp}$ is established, that opposes to $\vec{E}_{ap}$, thus lowering the net electrostatic field in the sample. The resultant macroscopic field $\vec{E}_m$ is then simply the sum $\vec{E}_{ap} + \vec{E}_{dp}$. Taking into account the discontinuous atomic or molecular nature of the dielectric within the sphere centered on the probe molecule A (but treating the region outside the sphere as a continuum), $\vec{E}_l$ can be written as Equation (4):

$$\vec{E}_l = \vec{E}_m + \vec{E}_s + \vec{E}_d \quad (4)$$

where $\vec{E}_s = \frac{\varepsilon - 1}{3}\vec{E}_m$ is the contribution of the charges at the surface of the sphere. $\vec{E}_d$ is due to the dipoles within the sphere, near to A, and must be calculated for each particular site and for each dielectric material as it depends strongly on the geometrical arrangement and polarizability of the contributing particles. When the molecules surrounding A are neutral, nonpolar molecules, or when they are arranged either in complete disorder or in a cubic lattice, the assumption (proved by Lorentz in the case of a cubic arrangement of identical molecules) is often made that the additional effects of these molecules on the probe molecule mutually cancel, such that $\vec{E}_d = \vec{0}$. The Lorentz local field factor L_L, which relates the microscopic local electric field to the macroscopic electric field $E_l = L_L \vec{E}_m$, is thus simply given by Equation (5):[18]

$$L_L = \frac{\varepsilon + 2}{3} \quad (5)$$

2.2 Effect of the Molecular Polarizability—Reaction Field

We now consider a probe molecule with a spherical shape but a specific polarizability. In a medium of polarizability α and dielectric constant ε relative to vacuum, a small volume is now replaced by the molecule A of interest: we model it by a point dipole $\vec{\mu}$ with polarizability χ, placed at the center of a spherical cavity. The field of the dipole in such a cavity polarizes the surrounding molecules, and the resulting inhomogeneous polarization of this nanoenvironment gives rise to the reaction field $\vec{E}_r$ acting at the position of the dipole. For symmetry reasons, the reaction field $\vec{E}_r$ has the same direction as the original dipole moment $\vec{\mu}$ and is proportional to $\vec{\mu}$ as long as no saturation effects occur: $\vec{E}_r = f\vec{\mu}$.[18] As the molecule is placed in a spherical cavity of radius R, a simple consideration of the

 © 2005 Wiley-VCH Verlag GmbH & Co. KGaA, Weinheim

continuity of the fields inside and outside the cavity leads to Equation (6) for the cavity field $\vec{E}_c$ (local field in the center):

$$\vec{E}_c = \frac{3\varepsilon}{2\varepsilon+1}\vec{E}_m \tag{6}$$

The local field felt by the molecule $\vec{E}_l = \vec{E}_c + \vec{E}_r$ is the sum of the cavity field and the reaction field, such that [Eq. (7)]:

$$\vec{E}_l = \vec{E}_c \frac{1}{1-f\chi} \tag{7}$$

where f writes as given in Equation (8):

$$f = 2\frac{\varepsilon-1}{2\varepsilon+1}\frac{1}{4\pi\varepsilon_0 R^3} \tag{8}$$

By combining Equations (6–8), the local field factor L that relates the local field effectively felt by the molecule to the macroscopic electric field becomes [Eq. (9)]:

$$L = \frac{3\varepsilon}{2\varepsilon+1-2(\varepsilon-1)\frac{\chi}{4\pi\varepsilon_0 R^3}} \tag{9}$$

In the special case where the molecule at the center has the polarizability α of the medium, we must recover Lorentz's theory of dielectrics. Inserting in Equation (9) the well-known Clausius–Mossotti relation in the slightly modified form [Eq. (10)]:

$$V = \frac{\alpha}{\varepsilon_0}\frac{\varepsilon+2}{3(\varepsilon-1)} \tag{10}$$

where $V = 4/3\,\pi R^3$ is the volume occupied by a single spherical molecule, one indeed finds back the Lorentz local field factor given by Equation (5). In the general case, $\chi = \alpha + \delta$, where δ is the polarizability difference of the molecule with respect to the medium. The local field factor [Eq. (11)]:

$$L = L_L \frac{1}{1-\frac{2}{9\varepsilon}(\varepsilon-1)^2\frac{\delta}{\alpha}} \tag{11}$$

is enhanced relative to the Lorentz cavity factor if the molecule is more polarizable than the medium. In particular, for $\delta > \frac{9\varepsilon\alpha}{2(\varepsilon-1)^2}$, the theory fails. This regime, known as the Clausius–Mossotti catastrophe, might describe a ferroelectric transition, which corresponds to a spontaneous polarization of the system. The local electric field felt by the probe molecule is enhanced, relative to the macroscopic field, by the local field factor L. The vacuum fluctuations of the electric field, which are responsible for spontaneous emission, are enhanced by the same factor. The spontaneous emission rate Γ_r is thus enhanced by a factor L^2 with respect to the one given in Equation (2): $\Gamma_r = nL^2\Gamma_{r0}$.

In order to apply these considerations in the case of a DiD molecule embedded in a PS matrix, we have calculated the polarizabilities and volumes of the DiD molecule and those of a styrene unit. Firstly, an optimization of the respective geometries has been performed in the ground state by using the semiempirical Hartree–Fock Austin Model 1 (AM1) technique and in the excited state by coupling the AM1 method to a full configuration interaction scheme (CI) within a limited active space, as implemented in the Ampac package.[19] Secondly, the optical absorption spectra of the optimized geometries have been computed by means of the semi-empirical Hartree–Fock intermediate neglect of differential overlap (INDO) method, as parameterized by Zerner et al.,[20] combined to a single configuration interaction (SCI) technique; the CI space is built here by promoting one electron from one of the highest sixty occupied levels to one of the lowest sixty unoccupied ones. Finally, the polarizabilities were determined by a sum over states (SOS) method over all states involved in the CI space just mentioned. Figure 4 shows the optimized geometry of the DiD

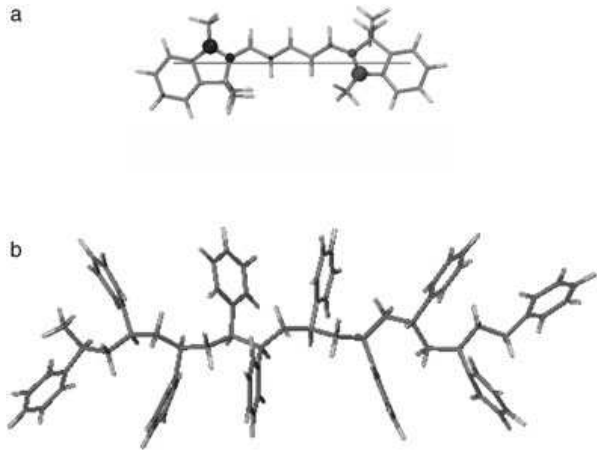

Figure 4. *Schematic structures of the DiD molecule (a) and of a section of the poly(styrene) chain (b). The atomic transition densities and the transition dipole moment associated to the HOMO–LUMO transition are also shown.*

molecule (only the most abundant conformer is shown) and of a section of a PS chain. The atomic transition densities, as well as the transition dipole moment ($|\vec{\mu}| = 4.97\times10^{-29}$ C m) associated to the transition between the ground state and the lowest excited state of the molecule are also shown.

The polarizabilities of the DiD molecule $\chi_0 = 6.1\times10^{-39}$ C^2 m^2 J^{-1} ($\chi_0 = 55\times10^{-30}\,4\pi\varepsilon_0$ m^3) and of the styrene unit $\alpha = 1.0\times10^{-39}$ C^2 m^2 J^{-1} ($\alpha = 9\times10^{-30}\,4\pi\varepsilon_0$ m^3) have thus been determined, as well as their volumes $V = 399\times10^{-30}$ m^3 and $V = 119\times10^{-30}$ m^3, respectively. Note that these effective polarizabilities have been averaged over the three tensor axes. As a check, we also deduced the volume V of the styrene unit by use of the Clausius–Mossotti equation [Eq. (10)], knowing the dielectric permittivity of PS ($\varepsilon = 2.5$) and the polarizability α of the unit. The value obtained this way $V = 113\times10^{-30}$ m^3 is consistent with the volume calculated by quantum chemistry.

In order to determine quantitatively the influence of the polarizability and the spatial extent of the DiD molecule on the spontaneous emission rate of the probe $\Gamma_r = nL^2\Gamma_{r0} = nL_L^2\,\hat{L}^2\Gamma_{r0}$, the ratio $\hat{L}^2 = (\frac{L}{L_L})^2$ was calculated in different cases. This ratio given by Equation (11) in the case of a spherical, polarizable

 © 2005 Wiley-VCH Verlag GmbH & Co. KGaA, Weinheim

probe, expresses the departure from the ideal Lorentz behavior, for which $\hat{L}^2=1$. Table 1 (fourth column, first two lines) shows the calculated ratios $\hat{L}^2$ in the case where the probe molecule is represented by a point dipole, which occupies the same volume $V=113\times10^{-30}\,m^3$ as the molecules of the medium (styrene units). Only the polarizability of the molecule changes, and takes, respectively, the values 0 and α, as indicated in the second column of the table. These two cases correspond to the empty and Lorentz cavity factors, respectively. The third line of the table pertains to the case where the probe molecule, with its actual polarizability χ_0, is represented by a point dipole occupying its actual volume $V=399\times10^{-30}\,m^3$.

Table 1. *Ratio $\hat{L}^2$ for the considered three polarizabilities and two spatial extensions of the probe molecule. "Extended" means ellipsoidal cavity in the theory and extended dipole in the simulations.*

Dipole	Polarizability	Shape theory	$\hat{L}^2$ theory	Shape simulation	$\hat{L}^2$ simulation
point	0	spherical	0.694	1 cubic cell	0.814
point	α	spherical	1	1 cubic cell	1
point	χ	spherical	1.369	-	-
"extended"	0	ellipsoidal	0.509	3 aligned cubic cells	0.512
"extended"	3α	ellipsoidal	0.578	3 aligned cubic cells	0.579
"extended"	χ	ellipsoidal	0.667	3 aligned cubic cells	0.771

Table 1 shows clearly that the ratio $\hat{L}^2$ increases as the polarizability of the probe molecule is increased, ranging from a value lower than 1 in the case of the empty cavity model, to 1 in the case of the Lorentz cavity model, and higher than 1 in case the polarizability of the probe molecule is enhanced with respect to the surrounding medium molecules. If the actual polarizability χ_0 of a DiD molecule would have been confined to the small volume of a styrene unit, a Clausius–Mossotti catastrophe would have been generated.

2.3 Effect of the Elongated Shape

In the three cases just mentioned, the probe molecule has been sized to an idealized spherical volume. However, a DiD molecule has an elongated shape (Scheme 1) and occupies a volume $V=399\ 10^{-30}\,m^3$, which is a bit more than three times the volume of a styrene unit. We thus propose to replace a small volume of the medium by an extended dipole in an ellipsoidal cavity with principal semi-axes *aR, bR* and *cR* ($a=1$, $b=1$ and $c=3$) along the *x, y* and z axes of a Cartesian coordinate system, respectively. In this case the local field factor is given by Equation (12):[18]

$$L=\frac{\varepsilon}{\varepsilon+(1-\varepsilon)A_c-3A_c(1-A_c)(\varepsilon-1)\,\frac{\chi}{4\pi\varepsilon_0 abcR^3}} \qquad (12)$$

where [Eq. (13)]:

$$A_c=\frac{abc}{2}\int_0^\infty \frac{1}{(s+c^2)\sqrt{(s+a^2)(s+b^2)(s+c^2)}}ds \qquad (13)$$

In the case of a spherical cavity ($a=b=c=1$), $A_c=1/3$, Equation (12) converts back to Equation (9). The calculated values [Eq. (12)] of the ratios $\hat{L}^2$ are given in Table 1 (last three lines) for the three polarizabilities of the probe molecule previously considered: 0, α and χ_0. By using such an extended dipole to represent the single molecule, no catastrophe is generated, as the "real" polarizability of the molecule is confined in a "real" volume. Table 1 shows that a probe molecule represented by an extended dipole has a spontaneous emission rate, which is enhanced as its polarizability is increased. Interestingly, the calculated ratios in the case of the molecule represented by either a point dipole of polarizability $\chi=0$ or a dipole in a ellipsoidal cavity of polarizability $\chi=\chi_0$ are similar, which justifies the approach adopted earlier in the literature.[11]

So far, although the described models are very relevant to calculate the spontaneous emission rate and thus the fluorescence lifetime of a DiD molecule embedded in the PS matrix, none of them is able to explain the lifetime fluctuations observed experimentally. We now consider inhomogeneities of the solvent shells in a microscopic approach, using numerical simulations.

3. Microscopic Lattice Model

An amorphous polymer matrix is a frozen disordered medium that consists of polymer chains and holes. Even 80 K below the glass transition temperature ($T_g=373$ K for PS), the glassy state relaxes as a result of local configuration rearrangements of chain segments, which are described by the hole motion and bond rotation.[21]

3.1 Description of the Model

The probe molecule is represented by a charge distribution $\rho(\vec{r})$ oscillating (for the considered HOMO–LUMO transition) at the transition frequency ω_{eg}. The charge distribution $\rho(\vec{r})$ is related to the transition dipole moment $\vec{\mu}$ of the molecule by the relation $\vec{\mu}=\int\vec{r}\rho(\vec{r})d\vec{r}$. Figure 4a shows an illustration of the atomic transition densities associated with the transition between the ground state and the lowest excited state of the DiD dye (predominantly described as a HOMO to LUMO transition). The arrow describes the orientation of the transition dipole moment $\vec{\mu}$ of the molecule; $|\vec{\mu}|=4.97\times10^{-29}$ C m. The probe molecule is placed at the origin of a three-dimensional cubic lattice and is surrounded by *N* polarizable monomers (Figure 5). In order to mimic the motion of the styrene units around the fixed probe molecule, a given fraction of holes is introduced in the lattice. Figure 4b shows the styrene units of a portion of a poly(styrene) chain that constitutes the matrix. To determine the lattice constant, Δ, the van der Waals volume

 © 2005 Wiley-VCH Verlag GmbH & Co. KGaA, Weinheim

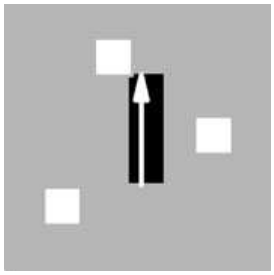

Figure 5. *Two-dimensional representation of a cubic lattice having the probe molecule at the center(black sites), surrounded by the styrene units (gray sites) and some holes (white sites).*

of a styryl unit $V=\Delta^3$ is simply attributed to the volume of a cell of the cubic lattice.

In the study, we represent the probe molecule as an extended dipole of length $l=8.9\times10^{-10}$ m (distance between N atoms) with point charge $q=\frac{|\vec{\mu}|}{l}$. This extended dipole, which closely mimics the transition density distribution in Figure 4, occupies three cells of the cubic lattice (Figure 5). The electric field created by this source dipole on the surrounding polarizable monomers situated at positions $\vec{r}_k$ is $\vec{E}(\vec{r}_k)=-\vec{\nabla}V(\vec{r}_k)$, with [Eq. (14)]:

$$V(\vec{r}_k)=\frac{q}{4\pi\varepsilon_0}\left(\frac{1}{|\vec{r}_k-\vec{r}_+|}-\frac{1}{|\vec{r}_k-\vec{r}_-|}\right) \tag{14}$$

where $\vec{r}_+=(0,0,\frac{l}{2})$ and $\vec{r}_-=(0,0,-\frac{l}{2})$ are the positions of the plus and minus charges of the source dipole, respectively. The case of a point source dipole will also be considered as a special case of the extended dipole with $l\to0$. In this case, the source dipole only occupies the cell at the origin of the cubic lattice. The dipoles $\vec{\mu}_k$ induced by the electric field on the surrounding monomers, considered as point dipoles, are obtained from the set of coupled Equations (15) and (16):

$$\vec{\mu}_k=\alpha_k\left[\vec{E}(\vec{r}_k)+\sum_{j=1}^{N}\hat{T}_{kj}\vec{\mu}_j)\right] \tag{15}$$

where $\hat{T}_{kj}$ is the dipole–dipole interaction tensor:

$$\hat{T}_{kj}=\frac{1}{r_{kj}^3}\left(\hat{I}-\frac{3\vec{r}_{kj}\vec{r}_{kj}}{\vec{r}_{kj}^2}\right) \tag{16}$$

where $\hat{I}$ is the identity tensor and $\vec{r}_{kj}=\vec{r}_k-\vec{r}_j$. The second term in the set of coupled equations [Eq. (15)] also includes the interactions between the monomers once they have been polarized (polarizabilities $\alpha_k=\alpha$) by the electric field $\vec{E}(\vec{r}_k)=-\vec{\nabla}V(\vec{r}_k)$ [Eq. (14)]. Interactions between polarized monomers and the polarizable probe molecule (polarizability $\alpha_k=\chi$), placed at the origin of the lattice and source of this electric field are also considered in this expression. The local electric field, felt by the probe molecule, is thus the sum of all electric fields experienced by the surrounding monomers and of the reaction field induced by all these polarized monomers that act back on the probe molecule.

We now have treated all interactions within the first solvent shells [see Figure 2, (1)+(2)]). This system has an effective transition dipole moment $\vec{\mu}_{tot}$, which is the sum of the molecular dipole moment (source dipole) $\vec{\mu}$ and of the induced dipoles $\vec{\mu}_k$ of the cubic array representing the solvent shells [Eq. (17)]:

$$\vec{\mu}_{tot}=\vec{\mu}+\sum_k\vec{\mu}_k \tag{17}$$

with $\vec{\mu}_k$ given by Equation (15).

We now embed our system into the continuous dielectric [see Figure 2, (3)] using Lorentz's procedure, which amounts to multiplying by the Lorentz local field factor. The spontaneous emission rate Γ_r of the probe molecule embedded in a heterogeneous disordered medium can thus be written as Equation (18):

$$\Gamma_r=nL_L^2|\frac{\vec{\mu}_{tot}}{\vec{\mu}}|^2\Gamma_{r0} \tag{18}$$

with Γ_{r0} given by Equation (1). The near-field effect of the disordered heterogeneous medium on the radiative lifetime can thus be evaluated completely on the base of electrostatic calculations of the ratio $r=|\frac{\vec{\mu}_{tot}}{\vec{\mu}}|^2$ between the total dipole in the cavity and the source dipole associated with the probe molecular charge distribution. It is worthwhile to note here the equivalence between the ratio $\hat{L}^2$, defined in Sections 2.2–2.3 and expressing the dependence of the polarizability and spatial extent of the probe molecule on its spontaneous emission rate (Table 1) and the ratio $r=|\frac{\vec{\mu}_{tot}}{\vec{\mu}}|^2$ just defined in Equation (18). Liver et al. first showed that a first-order quantum-mechanical perturbation theory of the solvent effect on molecular oscillator strengths is equivalent to the classical electrostatic approach.[22] The ratio $|\frac{\vec{\mu}_{tot}}{\vec{\mu}}|^2$ can be easily evaluated numerically for a disordered system. The results of this investigation are presented in the next subsection.

3.2 Numerical Evaluation of the Oscillator Strengths Ratio—Comparison with the Continuum Approach

As a first step, we consider the interaction of the probe molecule, represented as a point dipole located at the center of a cubic array in vacuum, and a monomer (styrene unit) placed either transversally or longitudinally with respect to the dipole axis of the single probe molecule. Figure 6 shows the computed ratio $r=|\frac{\vec{\mu}_{tot}}{\vec{\mu}}|^2$ as a function of the probe molecule—monomer distance, expressed in units of $\Delta=4.8\,10^{-10}$ m. If the monomer is placed at a large distance with respect to the probe molecule, the ratio is obviously equal to unity (very weak electrostatic interactions). As the distance separating the interacting species is reduced, the ratio is increased (de-

 © 2005 Wiley-VCH Verlag GmbH & Co. KGaA, Weinheim

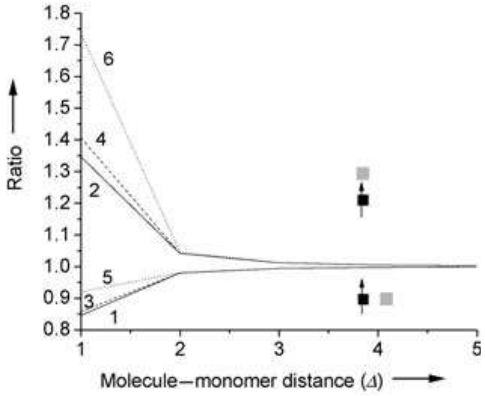

Figure 6. *Ratio* $r = |\frac{\mu_{tot}}{\mu}|^2$ *calculated in the case of a monomer placed transversally (curves 1, 3, 5) or longitudinally (curves 2, 4, 6) with respect to the axis of a point dipole located at the origin of the lattice. The molecule–monomer distance is expressed in units of cell interdistance* $\Delta = 4.8\,10^{-10}$ *m. Curves 1 and 2, 3 and 4, and 5 and 6, pertain to a point dipole with polarizability 0,* α*, and* χ*, respectively.*

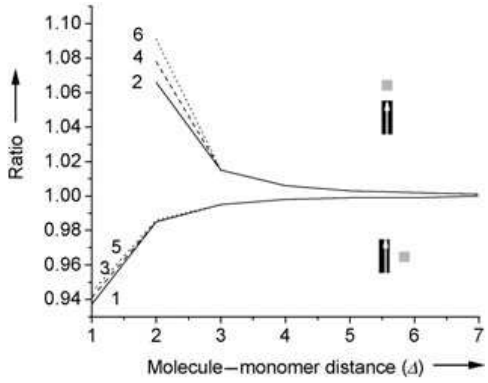

Figure 7. *Ratio* $r = |\frac{\mu_{tot}}{\mu}|^2$ *calculated in the case of a monomer placed transversally (curves 1, 3, 5) or longitudinally (curves 2, 4, 6) with respect to the axis of an extended dipole located at the origin of the lattice. The molecule–monomer distance is expressed in units of cell interdistance* $\Delta = 4.8\,10^{-10}$ *m. Curves 1 and 2, 3 and 4, and 5 and 6, pertain to a point dipole with polarizability 0, 3*α*, and* χ*, respectively.*

creased) in the case of a longitudinally (transversally) located monomer. The increased (decreased) value of the ratio obtained by placing the monomer longitudinally (transversally) with respect to the dipole axis simply results from the vector addition of the induced dipole moment $\vec{\mu}_k$ of the polarizable monomer to the source dipole moment to give the total dipole moment $\vec{\mu}_{tot} = \vec{\mu} + \vec{\mu}_k$.

Three cases are reported in Figure 6, corresponding to three different polarizabilities attributed to the probe molecule: zero for a nonpolarizable molecule (solid lines; ——), α for a probe molecule with the polarizability of a styrene unit (dashed lines; -----) and χ_0 for a molecule with the polarizability of DiD confined to a small volume (dotted lines; •••••). Figure 6 clearly shows that an increase in the polarizability of the probe molecule is accompanied by a corresponding increase in the ratio *r*. As the fluorescence lifetime of a single molecule is the reciprocal of the spontaneous emission rate, the effect of placing a monomer close to the molecule, along the dipole axis, is thus to reduce its lifetime by a factor *r*. This effect can be as drastic as a modification of 35 to 70% of the lifetime, depending on the polarizability of the probe molecule. It is also worth noting that the variation induced by placing a monomer longitudinally with respect to the dipole axis is significantly larger than the one induced by placing the monomer transversally.

In case the probe molecule, placed at the origin of the cubic lattice, is represented by the extended dipole, the effect of the molecule–monomer interaction on the ratio *r*, as a function of the separating distance, is very similar, but attenuated with respect to the case of the point dipole. Figure 7 shows that, in this case, the fluorescence lifetime variations can only reach 6 to 9% of the natural lifetime of the molecule, in the best case that of a longitudinally positioned monomer. The three polarizabilities attributed per cell occupied by the probe molecule are 0, α and $\frac{\chi_0}{3}$, respectively. The polarizability of the DiD molecule has been split equally into three parts, in the last case, assuming it fulfills the additivity property. In each of the three cases, the monomer, which occupies one cell of the lattice, interacts with the three cells occupied by the probe molecule. These three cells occupied by the probe molecule also interact with each other.

Figure 8 shows the computed ratio $r = |\frac{\vec{\mu}_{tot}}{\vec{\mu}}|^2$ as a function of the number of added polarization shells of monomers around the probe molecule on the cubic lattice. Both results for the point dipole and the extended dipole are shown in this Figure. The minimum radiative lifetime (maximum oscillator strength $|\vec{\mu}_{tot}|^2$) is observed with the completion of a full first solvation layer of styrene units around the probe molecule.[23] Adding a second or third layer lengthens the lifetime. The saturation of the probe molecule's lifetime with larger number of styrene units in its vicinity is associated with an approximate continuum dielectric behavior, where Equations (9) and (12) apply in the case of a point dipole and an extended dipole, re-

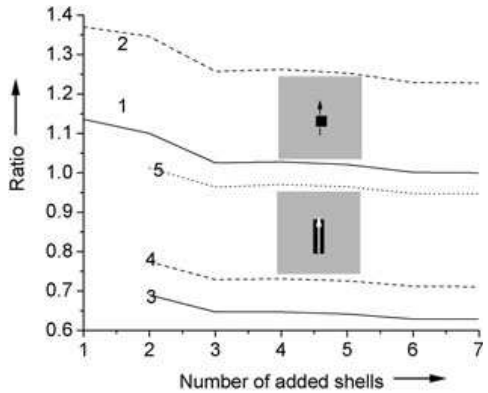

Figure 8. *Ratio* $r = |\frac{\mu_{tot}}{\mu}|^2$ *calculated in case the cubic lattice is filled with several shells of monomers around the probe molecule located at the origin of the lattice. Curves 1 and 2 pertain to the probe molecule represented as a point dipole with polarizability 0 and* α*, respectively. Curves 3, 4 and 5 pertain to the probe molecule represented as an extended dipole with polarizability 0, 3*α *and* χ*, respectively.*

spectively. It is remarkable that the approximate continuum behavior is reached only after a few (actually six) solvation shells have been added to the probe molecule. Very interestingly, Figure 6 and Figure 7 show that curves 2, 4 and 6 (curves 1, 3, 5) join already as an interdistance of 2Δ separates the molecule from the monomer placed longitudinally (transversally) with respect to the dipole axis of the molecule: the influence of the molecular polarizability vanishes rapidly with an increase of the molecule–monomer interdistance. In both cases, two terms can be considered to contribute to the effective dipole moment [Eq. 17)]: 1) The source dipole of the molecule polarizes the surrounding monomer (direct mechanism), a process that scales as the reciprocal of the third power of the distance separating the source dipole and the dipole induced on the monomer [Eq. (16)]; 2) Due to the reaction field of the monomer on the probe molecule, a consecutive forwards (molecule→monomer)–backwards (monomer→molecule) dipole–dipole interaction mechanism leads to a weak interaction (scaling as the reciprocal of the sixth power) for long interdistances between the two species. This forwards–backwards mechanism can thus not compete with the direct mechanism for long interdistances between the molecule and the considered monomer. On the contrary, Figure 8 shows well separated curves, as shells of monomers are added around the probe molecule. In this case, a number of terms, growing as the third power of the cluster radius (each term being proportional to the inverse of the sixth power of the interdistance between the molecule and the monomer of a given shell), sum to give a significant contribution of the forwards–backwards mechanism to the effective dipole moment $\vec{\mu}_{tot}$ [Eq. (17)].

Once the saturation value of the ratio r is reached, after having filled the lattice with successive polarization shells, an approximate continuum dielectric behavior is attained (Figure 2). The numerical calculation of the ratios $\hat{L}^2 = \frac{L^2}{L_L^2}$ may then be compared with the results of the continuum theories [Eqs. (9) and (12)]. At this point, note that curve 2 in Figure 8 reaches a ratio $r = 1.23$ instead of the ratio $r = 1$ which is expected in the case of the ideal Lorentz behavior. We attribute this discrepancy to several possible factors: 1) We use polarizabilities averaged on the three tensor axes. While being very satisfactory in the case of a styrene unit, this approximation is probably not fully appropriate in the case of the elongated DiD molecule; 2) The lattice constant Δ is defined in our microscopic model as $\Delta = V^{1/3}$ (cubic cells), while continuum theories consider spherical molecules, with $V = \frac{4}{3}\pi R^3$ such that $\Delta = 2R$. For obvious packing reasons, we preferred to choose cubic cells instead of spherical ones. Doing so, we have reduced the lattice constant and thus enhanced the dipole–dipole interactions between neighboring cells. This in turn increases the ratio r.

Prior to perform the comparison between our microscopic results and the continuum theories, we thus normalized the different curves shown in Figure 8 with respect to the ideal Lorentz behavior. Table 1 provides the comparisons for each of the considered cases, obtained after renormalization of the curves by a factor 1.23. The matching of the values obtained by theory and by numerical calculations is very good.

3.3 Numerical Evaluation of the Oscillator Strengths Ratio—Effects of the Holes

In order to simulate the mobility of the chain segments surrounding the probe molecule, holes are introduced in the lattice. Figure 9 shows the influence on the ratio $r = |\frac{\vec{\mu}_{tot}}{\vec{\mu}}|^2$ of a

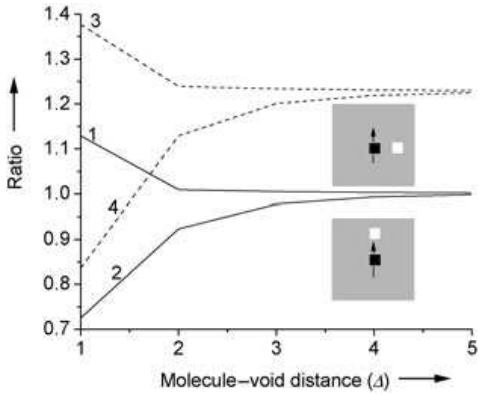

Figure 9. *The cubic lattice is filled with seven shells of polarizable monomers, surrounding the point dipole located at the origin. The ratio* $r = |\frac{\mu_{tot}}{\mu}|^2$ *is calculated in the case of a void placed transversally (curves 1, 3) or longitudinally (curves 2, 4) with respect to the axis of the point dipole. The molecule–void distance is expressed in units of cell interdistance* $\Delta = 4.8\,10^{-10}$ *m. Curves 1 and 2, 3 and 4, pertain to a point dipole with polarizability 0,* α*, respectively.*

void (site of polarizability zero) that approaches the point dipole transversally with respect to its axis, from the continuum to the position just on the right of the source dipole (curves 1 and 3). If this void is added far away from the dipole, its presence has no effect on the radiative lifetime of the probe molecule. The ratio is identical to the one in the absence of the void. On the contrary, as the void approaches the molecule, the ratio r is considerably enhanced. A simple explanation of this effect is the following: the dipole moments induced on the monomer placed transversally with respect to the dipole axis of the probe molecule are opposite to the inducing molecular dipole, and thus add destructively to it. Replacing a monomer by a void at those positions reduces this negative contribution and thus increases the total dipole moment.

Conversely, by putting such a void in a lattice site along the dipole axis of the probe molecule, and approaching it step by step till it reaches the top of the positive charge of the source dipole, the spontaneous emission rate is decreased (curves 2 and 4). These effects are further enhanced if the polarizability of the probe molecule is increased from zero (curves 1 and 2) to α (curves 3 and 4).

Similar effects are observed in case an extended dipole is placed at the origin of the cubic lattice. In this case however, the variations of the ratios are attenuated with respect to the previous case of the point dipole (Figure 10). The maximum lifetime increase, obtained by placing a void close to the molecule with polarizability χ_0 and along its dipole axis, is 11.5%

 © 2005 Wiley-VCH Verlag GmbH & Co. KGaA, Weinheim

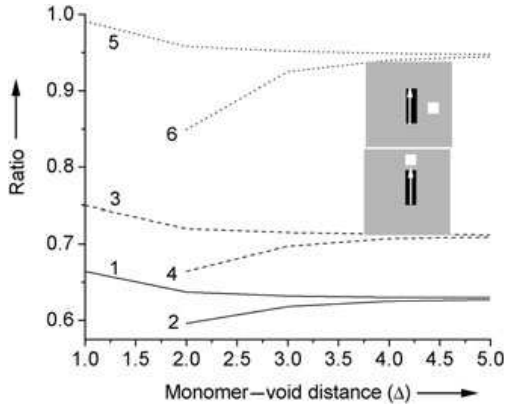

Figure 10. *The cubic lattice is filled with seven shells of polarizable monomers, surrounding the extended dipole located at the origin. The ratio is calculated in the case of a void placed transversally (curves 1, 3, 5) or longitudinally (curves 2, 4, 6) with respect to the axis of the extended dipole. The molecule–void distance is expressed in units of cell interdistance $\Delta = 4.8\,10^{-10}$ m. Curves 1 and 2, 3 and 4, and 5 and 6 pertain to an extended dipole with polarizability 0, 3 α, and χ, respectively.*

(curve 6). In case the void is placed close to the molecule on an axis perpendicular to the dipole axis, the maximum lifetime decrease is 4.4% of the natural lifetime of the probe molecule (curve 5).

It is interesting here to compare the results obtained in Figure 10 with those displayed in Figure 7. Figure 7 indeed shows that, not only by placing a monomer longitudinally (curves 2, 4, 6) but also (although less significantly) transversally (curves 1, 3, 5) with respect to the dipole axis of the molecule, the ratio r is increased as the polarizability of the molecule is increased from 0 to χ_0, at short molecule–monomer interdistances. The forwards–backwards mechanism always give a positive contribution to the sum in Equation (17). On the contrary, the direct polarization mechanism gives a positive (negative) contribution to the right hand side of Equation (17), in case the monomer is placed longitudinally (transversally) with respect to the dipole axis of the molecule. As a consequence, the two terms add constructively (destructively), increasing significantly (slightly) the ratio r, in case a monomer is placed longitudinally (transversally).

These effects are similarly responsible for the rather high increase of the lifetime (11.5%) once a void is placed close to the molecule with polarizability χ_0 and along its dipole axis (Figure 10) as compared to the transversal case (4.4%) and give a clear explanation to the observation of signicant positive excursions in the fluorescence-lifetime time trace of a single molecule embedded in a PS matrix (Figure 1) as due to the presence of hole(s) positioned close to the molecule and along its dipole axis.

3.4 Numerical Evaluation of the Fluorescence Lifetimes—Monte Carlo Simulations

As a last step, in order to build a distribution of the ratios r or, equivalently, a distribution of the fluorescence lifetimes of a DiD molecule embedded in a PS matrix, we have finally performed a Monte Carlo simulation of the actual configuration of the molecule with polarizability $\chi = 6.1\times10^{-39}\,C^2\,m^2\,J^{-1}$ and volume $V = 399\times10^{-30}\,m^3$ spread over three cubic cells of the lattice and surrounded by styrene units and holes. A Monte Carlo run is implemented in the following way: 1) We specify the fraction of holes (threshold value) that will be present in the system; 2) For each cell on the lattice, a uniformly distributed (between zero and one) random number is chosen; 3) If the random number falls below the threshold value, then the given cell is occupied by a hole, else the cell is occupied by a monomer. The complete Monte Carlo simulation involves 1000 runs for each given threshold value.

Figure 11a shows the result of such a Monte Carlo simulation in the case of a hole fraction $h = 6\%$. Remarkably the fluorescence lifetime shows peaks towards higher values, which results from configurations with holes localized longitudinally with respect to the source dipole axis. The histogram of the calculated fluorescence lifetimes is asymmetric and shows de-

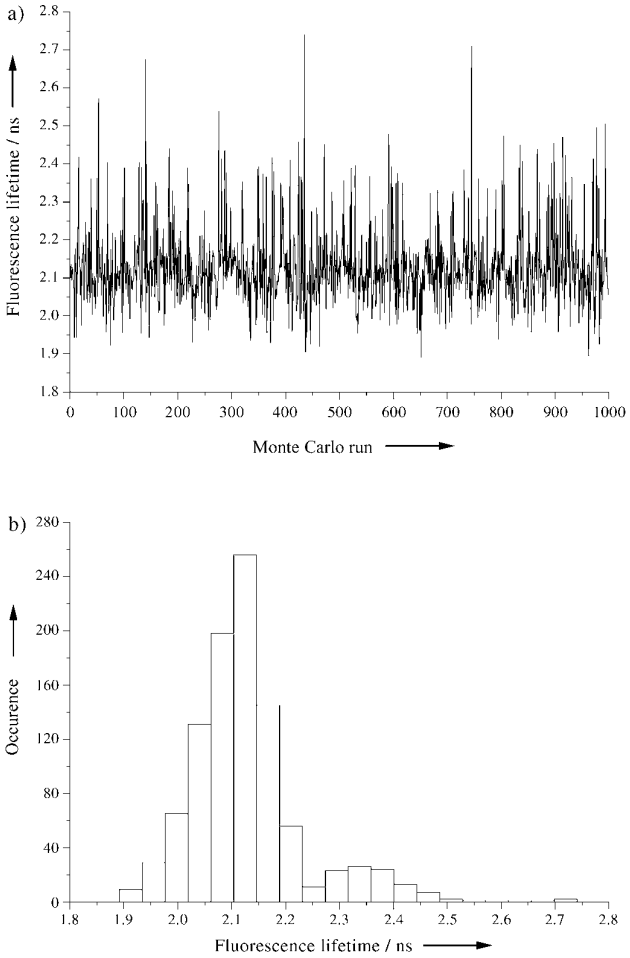

Figure 11. *Fluorescence lifetime calculations (a) and corresponding distribution for a Monte Carlo run of 1000 steps. The cubic lattice is here filled with six shells of polarizable monomers surrounding the extended dipole of polarizability χ, located at the origin. Holes are placed at random positions on the lattice with a fraction* h = *6%.*

 © 2005 Wiley-VCH Verlag GmbH & Co. KGaA, Weinheim

viations reaching 30% of the average lifetime, in a very similar way as the experimental results shown in Figure 1. The two maxima in the histogram (Figure 11b) for long lifetimes are due to the discreteness of the lattice and correspond to voids positioned against the molecule for the bunch observed around 2.7, one site away from it for the bunch at 2.35.

Figure 12 shows the same results in case a fraction $h=1\%$ (a), $h=10\%$ (b), $h=20\%$ (c) and $h=40\%$ (d) of holes is introduced in the system. Figure 12 clearly shows that, by increasing the fraction of holes present in the system, the fluorescence lifetime distribution gets broadened and asymmetric. For a hole fraction $h=1\%$, the lifetime distribution is very narrow and mainly symmetrical. If the local environment of the probe molecule is composed of a $h=10\%$ fraction of holes (which is a typical amount in a polymer matrix[24]), the distribution gets asymmetric towards higher lifetimes. This result is in very good agreement with the experimental results, reported by Vallee et al.,[11] that the asymmetry of the fluorescence lifetime distributions increases as the temperature of the PS matrix is raised: the fraction of holes present in a matrix is indeed an increasing function of the temperature.

As the hole fraction still increases above $h=10\%$, the lifetime distribution becomes mainly broadened, while keeping its asymmetry (Figures 12c and 12d).

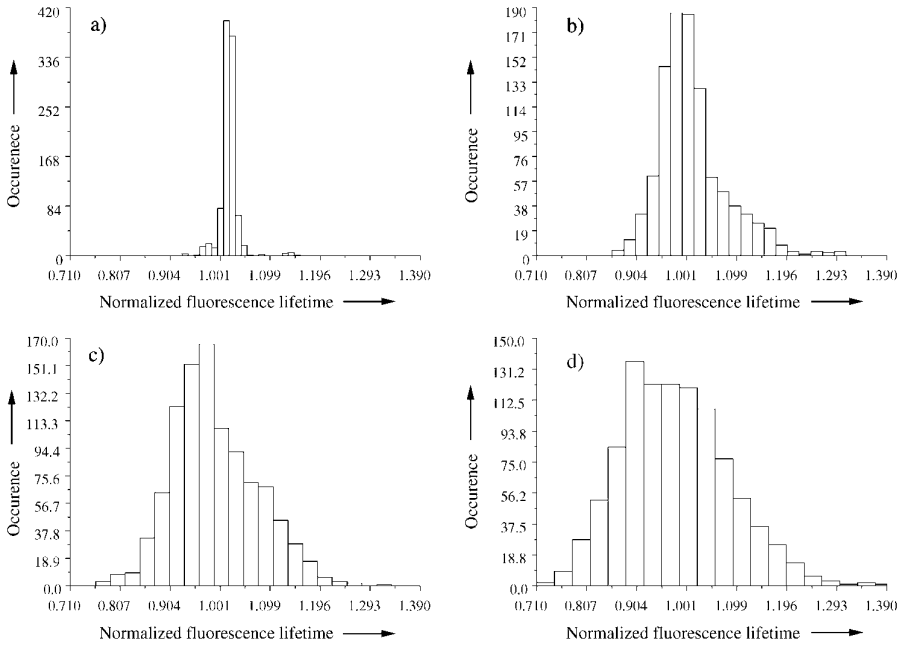

Figure 12. *Fluorescence lifetime distributions for Monte Carlo runs of 1000 steps. The cubic lattice is filled with six shells of polarizable monomers surrounding the extended dipole of polarizability χ, located at the origin. Holes are placed at a random positions on the lattice with a fraction* h = *1% (a),* h = *10% (b),* h = *20% (c),* h = *40% (d).*

4. Conclusions

A microscopic model has been developed to account for the observed temporal lifetime fluctuations of a single DiD molecule embedded in a poly(styrene) matrix at room temperature. The model is based on the description of the system as a cubic lattice with sites that can accommodate the repeating units of a macromolecule, the probe molecule, and some voids to account for the mobility of the matrix. The probe molecule has been represented as a point dipole or as an extended dipole with different values of the polarizability. Firstly, the model has been validated, by comparing its approximate continuum dielectric behavior to existing theories. Secondly, we have shown that the observed asymmetry of lifetime variations towards higher values very probably results from positional fluctuations of voids close to the extremities of the extended dipole representing the probe molecule. Thirdly, Monte Carlo simulations have been performed successively to describe such systems possessing a different but fixed fraction h of holes. The calculated radiative lifetime distributions have been shown to be more and more broadened and asymmetric as the fraction h of holes present in the system is increased. This behavior is in excellent agreement with the one experimentally observed by Vallée et al.[11] As such, the approach considered in this paper is a first attempt to describe the effect of the local, near field on the behavior of a probe molecule. This type of approach is only possible with the advent of single-molecule spectroscopy that allows to perform such detailed investigations.

Acknowledgements

R. A. L. Vallée thanks the FWO for a postdoctoral fellowship. D. Beljonne is a research associate of the FNRS. The authors are grateful to the University Research Fund, the Federal Science Policy through the IAP/V/03, and the FWO, for supporting this research project.

Keywords: dielectric properties · local field · luminescence · polymers · single-molecule studies

[1] D. P. Craig, T. Thirunamachandran, *Molecular Quantum Electrodynamics: An Introduction to Radiation–Molecule Interactions*, Academic Press, London **1984**.
[2] R. J. Glauber, M. Lewenstein, *Phys. Rev. A* **1991**, *43*, 467.
[3] A. Lagendijk, B. Nienhuis, B. A. van Tiggelen, P. de Vries, *Phys. Rev. lett.* **1997**, *79*, 657.
[4] E. Yablonovitch, T. J. Gmitter, R. Bhat, *Phys. Rev. Lett.* **1988**, *61*, 2546.

 © 2005 Wiley-VCH Verlag GmbH & Co. KGaA, Weinheim

[5] P. de Vries, A. Lagendijk, *Phys. Rev. Lett.* **1998**, *81*, 1381.
[6] M. F. Perutz, *Science* **1978**, *201*, 1187.
[7] A. Warshel, S. T. Russell, *Q. Rev. Biophys.* **1984**, *17*, 283.
[8] Xueyu Song, *J. Chem. Phys.* **2002**, *116*, 9359.
[9] W. E. Moerner, M. Orrit, *Science* **1999**, *283*, 1670.
[10] E. A. Donley, T. Plakhotnik, *J. Chem. Phys.* **2001**, *114*, 9993.
[11] R. A. L. Vallée, N. Tomczak, L. Kuipers, G. J. Vancso, N. F. van Hulst, *Phys. Rev. Lett.* **2003**, *91*, 038301.
[12] R. Simha, T. Somcynski, *Macromolecules* **1969**, *2*, 342.
[13] R. Simha, *Macromolecules* **1977**, *10*, 1025.
[14] D. E. Aspnes, *Am. J. Phys.* **1982**, *50*, 704.
[15] F. J. P. Schuurmans, P. de Vries, A. Lagendijk, *Phys. Lett. A* **2000**, *264*, 472.
[16] R. A. L. Vallée, G. J. Vancso, N. F. van Hulst, J.-P. Calbert, J. Cornil, J. L. Brédas, *Chem. Phys. Lett.* **2003**, *372*, 282.
[17] G. Nienhuis, C. Th. J. Alkemade, *Physica B+C* **1976**, *81*, 181.
[18] C. J. F. Böttcher, *Theory of electric polarization, Vol.* 1, *2nd ed.*, Elsevier, Amsterdam, **1973**.
[19] AMPAC Semichem, 7204 Mullen, Shawnee, KS 66216.
[20] M. C. Zerner, G. H. Loew, R. Kichner, U. T. Mueller-Westerhoff, *J. Am. Chem. Soc.* **2000**, *122*, 3015.
[21] T. S. Chow, *Mesoscopic Physics of Complex Materials*, Springer, New York, **2000**.
[22] N. Liver, A. Nitzan, A. Amirav, J. Jortner, *J. Chem. Phys.* **1988**, *88*, 3516.
[23] J. Gersten, A. Nitzan, *J. Chem. Phys.* **1991**, *95*, 686.
[24] R. E. Robertson, R. Simha, J. G. Curro, *Macromolecules* **1984**, *17*, 911.

Received: September 16, 2004

 © 2005 Wiley-VCH Verlag GmbH & Co. KGaA, Weinheim

Fluorescence lifetime fluctuations of single molecules probe the local environment of oligomers around the glass transition temperature

R. A. L. Vallée,[a] M. Baruah, J. Hofkens, F. C. De Schryver, N. Boens, and M. Van der Auweraer
Department of Chemistry and Institute of Nanoscale Physics and Chemistry (INPAC), Katholieke Universiteit Leuven, 3001 Heverlee, Belgium

D. Beljonne
Laboratory for Chemistry of Novel Materials, University of Mons-Hainaut, Place du Parc 20, 7000 Mons, Belgium

(Received 8 November 2006; accepted 20 March 2007; published online 10 May 2007)

Single molecule fluorescence experiments have been performed on a BODIPY-based dye embedded in oligo(styrene) matrices to probe the density fluctuations and the relaxation dynamics of chain segments surrounding the dye molecules. The time-dependent fluorescence lifetime of the BODIPY probe was recorded as an observable for the local density fluctuations. At room temperature, the mean fraction of holes surrounding the probes is shown to be unaffected by the molecular weight in the glassy state. In contrast, the free volume increases significantly in the supercooled regime. These observations are discussed in the framework of the entropic theories of the glass transition. © *2007 American Institute of Physics*. [DOI: 10.1063/1.2728902]

I. INTRODUCTION

Understanding the cause for the slowing down of the dynamics of supercooled liquids and the occurrence of the resulting glass transition to an amorphous solid is one of the main challenges of condensed matter physics.[1–6] The various theories that have been put forward to explain the phenomenon have been broadly classified into two categories. Thermodynamic ones describe the observed glass transition as a kinetically controlled manifestation of an underlying quasi-equilibrium phase transition between the supercooled metastable fluid and an ideal metastable glass phase.[3,6] Both entropy and free volume theories pertain to this category.[3] According to the nonthermodynamic (kinetic) viewpoint, best represented by the mode coupling theory,[2] vitrification occurs as a result of a purely dynamic transition from an ergodic to a nonergodic behavior.[2,3,6] Although recent experimental evidences of spatially heterogeneous dynamics in glass-forming liquids have led to a further understanding of the origin of the slowing-down mechanism,[7–9] no consensus has been reached as to which scenario better describes the glass transition.

Because it allows bypassing the ensemble averaging intrinsic to bulk studies, single molecule spectroscopy (SMS) constitutes a powerful tool to assess the dynamics of heterogeneous materials at the nanoscale level.[10–13] Using two-dimensional (2D) orientation techniques, the in-plane (of the sample) projection of the transition dipole moment of the single molecule (SM) [the so-called linear dichroism $d(t)$] has been followed in time, and its time correlation function $C_d(t)$ has been computed and fitted by a stretched exponential function $f(t)=e^{-(t/\tau)^{\beta}}$.[14–17] These investigations have allowed identifying static and dynamic heterogeneity in the samples,[8,9] i.e., SMs exhibit τ and β values varying according to (i) their actual position in the matrix and (ii) the time scale at which they are probed as a result of the presence of different nanoscale environments. More recently, the full three-dimensional (3D) orientation of the emission transition dipole moment of a SM has been recorded as a function of time.[18–22] In particular, the distribution of nanoscale barriers to rotational motion has been assessed by means of SM measurements[23] and related to the spatial heterogeneity and nanoscopic α-relaxation dynamics deep within the glassy state. Owing to the high barriers found in the deep glassy state, only few SMs were able to reorient, while somewhat lower barriers could be overcome when increasing the temperature. In another context, we have shown that the fluorescence lifetime of single molecules with quantum yield close to unity is highly sensitive to changes in local density occurring in a polymer matrix.[24–29] Using free volume theories, we have related the lifetime fluctuations to hole (free volume) distributions and have determined the number of polymer segments involved in a rearrangement cell around the probe molecule as a function of temperature,[24,27] solvent content,[25] and film thickness.[26] Based on a microscopic model for the fluctuations of the local field,[28] we have established a clear correlation between the fluorescence lifetime distributions measured for single molecules and the local fraction of surrounding holes.

In this paper, we extend our investigations to the behavior of a newly synthesized bifluoroborondipyrromethene (BODIPY) probe embedded in various molecular weight M_n oligo(styrene) (OS) matrices. Indeed, the glass transition temperature T_g depends on the degree of polymerization of the chain (N), according to the Fox-Flory empirical equation $T_g(\infty)-T_g(N)\propto 1/N$.[30] The free volume approach provides a

[a]Electronic mail: renaud.vallee@chem.kuleuven.be

 © 2007 American Institute of Physics

Downloaded 11 May 2007 to 134.93.131.89. Redistribution subject to AIP license or copyright, see http://jcp.aip.org/jcp/copyright.jsp

theoretical foundation to the Fox-Flory equation, which rests on the assumption that chain ends contribute an excess free volume. A decrease in N leads to an increase of chain end concentration and thus an increase in free volume. This increase in free volume should, in turn, lead to a decrease in T_g. Experimental investigations[31] have led to the conclusion that the Fox-Flory equation is not valid anymore at very low molecular weights. The Gibbs and Di Marzio entropy theory[32] was found to better describe $T_g(N)$, especially for short chains.[31] The lattice model of Gibbs and Di Marzio is a minimal model for polymers that accounts for chain stiffness and the variation of volume with temperature. It predicts the occurrence of an ideal thermodynamic second-order glass transition, with vanishing configurational entropy, occurring at a temperature T_2 which is about 50 K below T_g. According to this theory, and in contrast to the free volume concept, the number of holes present in the matrix below T_2 is constant.[32] Our SMS experimental approach based on fluorescence lifetime fluctuations[24–29] provides a direct access to the fraction of holes surrounding the probe molecule in the considered polymer matrix and thus appears as a particularly relevant technique able to discriminate between these two theories. At room temperature, we observe that the mean fraction of holes surrounding the probes is independent of the molecular weight of the polymer in the glassy state. In contrast, it increases significantly in the supercooled regime. These observations clearly support the interpretation formulated by Gibbs and Di Marzio.

The paper is organized in the following way: (i) We first show that we have really measured single molecules by checking the outcome of antibunching experiments (Sec. III A). (ii) We determine the typical time scale on which the lifetime fluctuations occur by use of a minimal binning approach in the analysis of the successive photon arrival time lags between excitation and emission (Sec. III B). (iii) We describe the observed fluorescence lifetime fluctuations on the time scale determined in (ii) and give evidence for the importance of the use of the proper time scale in order to observe the fluctuations (Sec. III C). (iv) We (re)describe the local field microscopic theory that allows us to determine the local fraction of holes surrounding the probe molecule on the basis of their lifetime fluctuations (Sec. III D) and provide the actual values determined by a comparison between theory and experiment (Sec. III E). (v) We provide clear evidence that the lifetime fluctuations cannot be due to reorientations of the SMs close to the polymer film-air interface, reinforcing our interpretation in terms of a fluctuating density of the local surrounding in the bulk (Sec. III F). We finish with our conclusions.

II. MATERIALS AND METHODS

The BODIPY probe [Fig. 1(a)] (4,4- difluoro-8-(4-methoxyphenyl)-3-[-2-(4-methoxyphenyl)ethenyl]- 1,5,7-trimethyl-3a,4a-diaza-4-bora-s-indacene) used in this study has been designed specifically to fulfill the following criteria: (i) it is highly photostable; (ii) it has a luminescence quantum yield close to 1 (0.99 in toluene) such that the observed fluorescence lifetime has a largely dominant radiative part;

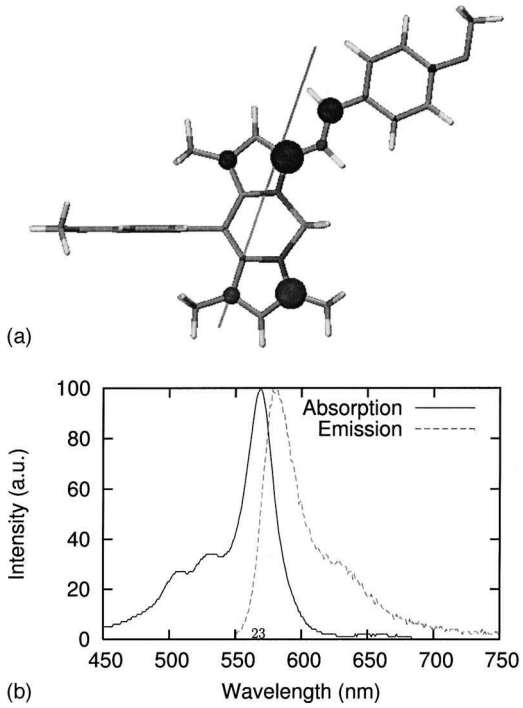

FIG. 1. 2D schematic structure of the BODIPY probe synthesized specifically for the present study. The arrow describes the orientation of the emission transition dipole moment of the molecule ($|\boldsymbol{\mu}|=11.4$ De); the atomic transition densities are also displayed (Ref. 25) (b) Steady state absorption and emission spectra of the probe molecule dissolved in toluene at $10^{-6}M$.

(iii) it emits in the red part of the visible spectrum [emission maximum at 584 nm, Fig. 1(b)], hence minimizing overlap with the autofluorescence of the matrix; and (iv) it is structurally rigid.

Samples were prepared by spin-coating a dilute solution of the probe ($10^{-10}M$) and oligo(styrene) (OS) in toluene onto a glass substrate. Annealing was performed in order to remove the solvent and relax the stresses induced by the deposition procedure. The films obtained this way had a thickness of $\approx$100 nm. Eight samples were prepared, each sample consisting of highly monodisperse OS chains (Polymer Source, polydispersity index ranging from 1.06 to 1.10, $M_n=1860$, 2000, 2500, 3700, 4700, and 7500 and Polymer Standard Service, $M_n=662,869$), in order to perform the experiments below and above T_g while keeping the temperature fixed at $T=292$ K. The glass transition temperatures (T_g) of the OS compounds were determined by the use of a differential scanning calorimeter (DSC) (822e, equipped with an intracooler, Mettler Toledo).

The single molecule experiments were performed with an inverted confocal scanning optical microscope (Olympus IX70). The excitation light, i.e., pulses of 1.2 ps at a repetition rate of 8 MHz (Spectra Physics, Tsunami, OPO, Pulse Picker and Doubler) and a wavelength $\lambda=568$ nm [Fig. 1(b)], was circularly polarized and the power set to 1.1 μW at the entrance port of the microscope. In order to eliminate any residual excitation signal in the fluorescence emission, a suitable combination of filters was used, consisting of a bandpass (BP568, Chroma) placed in the excitation path, a dichroic (Olympus 570), a notch (Kaiser Optics, 568) that matches the bandpass, and a long pass (LP580, Chroma) in

Downloaded 11 May 2007 to 134.93.131.89. Redistribution subject to AIP license or copyright, see http://jcp.aip.org/jcp/copyright.jsp

the emission path. The time lags between excitation and emission were measured by use of an avalanche photodiode (SPCM-AQ-14, EG & G Electro Optics) equipped with a time-correlated single photon counting (TCSPC) card (Becker & Hickl GmbH, SPC 630) used in the first in first out (FIFO) mode. A suitable window of 18.4 ns (time width of 72 ps per channel for the 256 channels available in the FIFO mode) was chosen to adequately build the decay profiles. In order to observe the dynamics (lifetime transients) of single molecules in a polymer matrix, short bin sizes have to be taken (100 ms, see below). The decay profiles built on such a time scale count 500–10 000 photons. The maximum likelihood estimation (MLE) method that is known to give stable results even at total counts less than 1000 (Ref. 33) was used to fit these profiles. In the antibunching experiment, the fluorescence signal from individual BODIPY molecules was split by a 50/50 nonpolarizing beam splitter and led towards two avalanche photodiodes, delayed by 1.47 μs, according to the classical Hanbury-Brown and Twiss coincidence experiment.[34] The delay time between consecutive photons was acquired using the TCSPC card mentioned above. Histograms of the interphoton times (coincidences) were built. Given the pulsed excitation, coincidences in the histogram accumulate at nT (n integer), where T is the time between two consecutive pulses (125 ns).

The quantum-chemical calculations were performed using the following methodology. Ground-state optimizations were performed at the semiempirical Hartree-Fock Austin Model 1 (AM1) level[35] and excited-state optimizations by coupling the AM1 Hamiltonian to a full configuration interaction (CI) scheme within a limited active space, as implemented in the AMPAC package.[36] The optical absorption and emission spectra were then computed by means of the semiempirical Hartree-Fock intermediate neglect of differential overlap (INDO) method, as parametrized by Zerner *et al.*,[37] combined to a single configuration interaction (SCI) technique; the CI active space is built here by promoting one electron from one of the highest 60 occupied to one of the lowest 60 unoccupied levels.

The Monte Carlo simulations, allowing us to calculate the radiative lifetime of a dye molecule embedded in a disordered medium, were performed using a homemade software.[28] In these simulations, the spectroscopic properties (transition dipole moment, transition energy, polarizability) of the BODIPY probe determined by quantum-chemical calculations were used. To model the effect of the environment on the probe molecule, the polarizability of a monomer of poly(styrene) was also determined.

III. RESULTS

A. Coincidence measurement

A sophisticated method that allows one to insure the probing of single molecules consists in performing an antibunching (or coincidence) measurement.[38–43] Photon antibunching is a clear signature of a nonclassical radiation field, which reflects the fact that a single quantum system cannot spontaneously emit two photons at the same time, without cycling back to its excited state. Photon antibunching has been measured for individual molecules by measuring the interphoton arrival times.

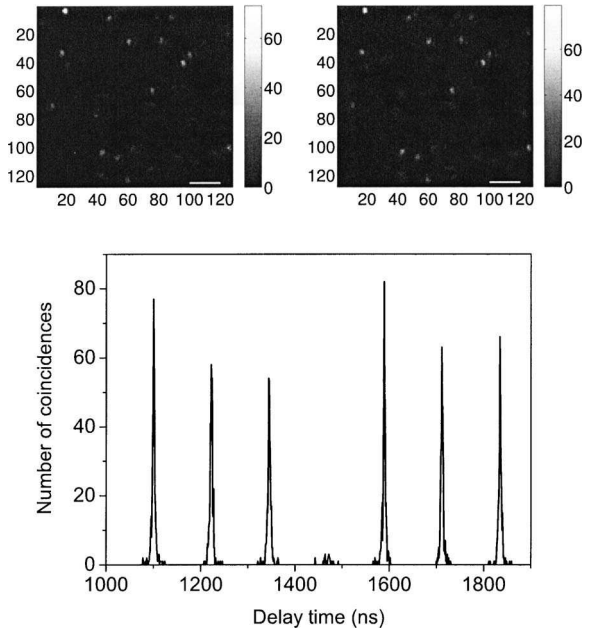

FIG. 2. (Top) 10×10 μm^2 (128×128 pixels) areas of the sample scanned at a rate of 500 Hz/pixel in order to localize the molecules. Two channels delayed by 1.47 μs were used in this case to perform an antibunching experiment. (Bottom) The coincidence measurement shows that two photons are not simultaneously emitted by the same spot (intensity close to zero at the time corresponding to the delay introduced between the two channels). The chosen molecule is the bright upper left one in the scan plots. The interdistance between the successive peaks in this graph corresponds to the inverse repetition rate of the laser, set to 8 MHz.

Figure 2 (top) shows two 10×10 μm^2 areas, scanned at a rate of 500 Hz/pixel and obtained by collecting the signals from two avalanche photodiodes delayed one with respect to the other by 1.47 μs, of an OS sample (M_n=7500) containing the probe molecules. The number of molecules observed in each frame is the one expected for the concentration of probe molecules incorporated in the OS matrix. Neither blinking nor photobleaching behavior is observed on these frames, which confirms the characteristic features of the probe molecule (very high quantum yield and high photostability). Remarkably, the probe molecule has an average fluorescence rate of 40 000 counts/s with peaks as high as 70 000 counts/s for the upper left very bright molecule, at the set excitation power, which makes this substance a very good choice for SMS measurements. A coincidence measurement performed on the bright upper left molecule is shown in Fig. 2 (down). Clearly, at the delay time corresponding to the delay introduced between the two channels, no coincident photons occur. Peaks of coincidence only appear at discrete steps nT (n integer), where T=125 ns is the time between repeated pulsed excitations. The full width at half maximum of these peaks gives an estimation of the fluorescence lifetime of the observed dye ($\approx$3.5 ns). These observations performed on a few dye molecules insure that we are indeed recording the fluorescence emission of single monochromophoric systems, which is essential in achieving our goal of probing the nanosurrounding of a single dye in a polymer matrix.

Downloaded 11 May 2007 to 134.93.131.89. Redistribution subject to AIP license or copyright, see http://jcp.aip.org/jcp/copyright.jsp

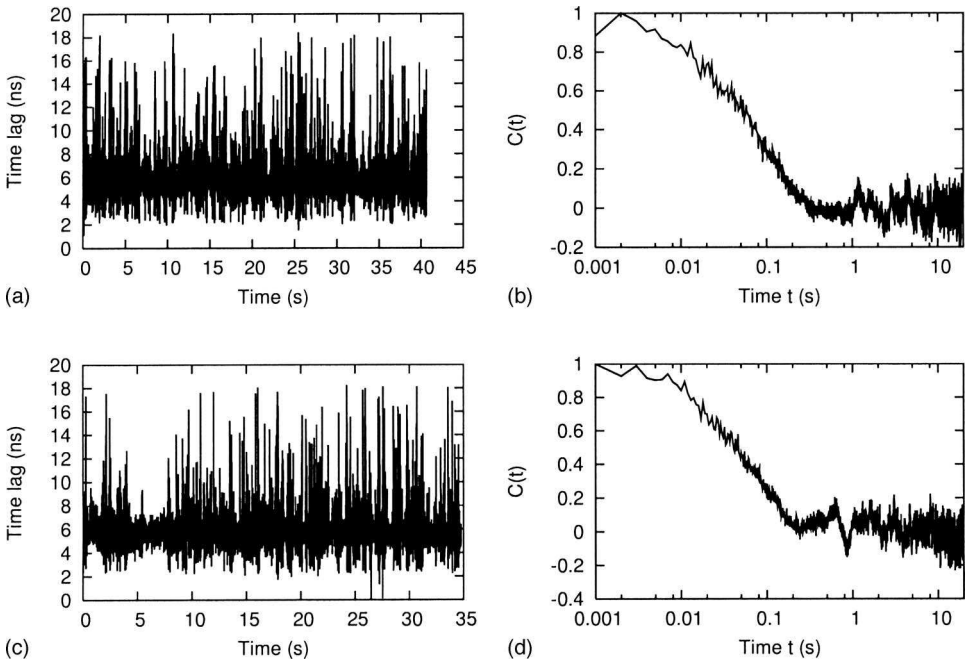

FIG. 3. Trajectories of decay times obtained via a minimal binning approach (see text for details), for the probe molecule (molecule 1) embedded in an OS matrix with M_n=662 during the first 40 s (a) and the following 35 s time range (c). [(b) and (d)] Corresponding autocorrelation functions.

B. Minimal binning approach

According to previously reported studies,[24–29] the fluorescence lifetime of a single molecule embedded in a polymer matrix exhibits (strong) fluctuations. In order to determine the time scale on which these fluctuations occur, we performed a minimal binning analysis[13,45] of the arrival time lags between excitation and spontaneously emitted photons in the case of a single dye molecule embedded in the OS matrix that is expected to show the highest mobility, i.e., the OS matrix with M_n=662, T_g=272 K. Following this methodology, the single molecule time trajectory is discretized with a time increment $\Delta_{\max}$ such that there is at least one photon in each chronological bin. The value of $\Delta_{\max}$ is simply dictated by the value of the maximum difference in the chronological time between consecutive detected photons in the selected part of the whole trace. In each chronological bin, the decay time τ_b is then defined as the arithmetic mean of the time lags $\tau(t)$ between excitation and fluorescence photons for the number of photons n_b detected in this bin: $\tau_b=\Sigma\tau(t)/n_b$.

Figure 3 shows two subtraces [(a) and (c)] of the decay time of the recorded transient of a dye (specific dye molecule followed in this study, referred to as molecule 1) embedded in a M_n=662 OS matrix, obtained with the minimal binning approach. For each of the traces, $\Delta_{\max}$ has been determined to be very close to 1 ms, so that, for the sake of simplicity, we just apply the minimal binning analysis with $\Delta_{\max}$ =1 ms. The corresponding autocorrelation functions of τ_b are shown in Figs. 3(b) and 3(d). In both cases, the autocorrelation functions decay with a relaxation time ζ of about 100 ms. Owing to the facts that the binning time $\Delta_{\max}$ =1 ms (i.e., much shorter than the determined correlation time) and the chosen subtraces last for about 40 s (i.e., much longer than the determined decay time), the decays and thus the values obtained for the mean relaxation time ζ $\approx$100 ms are statistically reliable.[44]

C. Observation of fluorescence lifetime fluctuations

The reference fluorescence lifetime of the molecules dissolved in a toluene solution is 3.44 ns as determined by TCSPC. Figure 4 shows the decay profiles obtained by accumulating all photons falling in a bin time of 100 ms, comparable to the relaxation time ζ. The three decay profiles correspond to three subtraces extracted from the trajectory of molecule 1, i.e., a molecule embedded in an OS matrix with M_n=662, during the first 20 s of its recording [Fig. 3(a)]. Very interestingly, on this binning time scale of 100 ms, the three decay profiles show large variations of the decay time. All three decays were best fitted by single exponential functions, with fluorescence lifetimes τ=3.21, 3.65, and 5.15 ns.

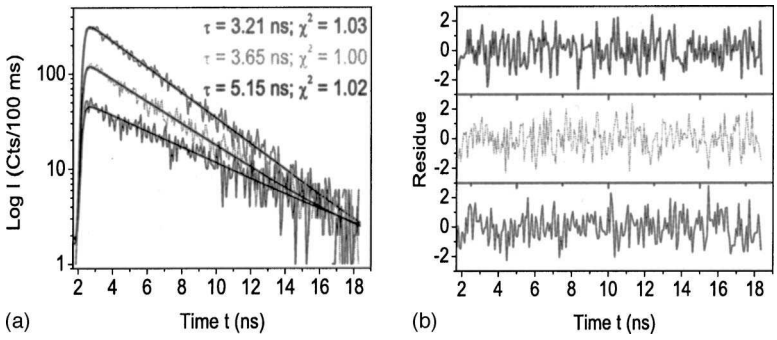

FIG. 4. Decay profiles (a) recorded (during 100 ms) at different times during the measurement of molecule 1. Also shown are the best fits obtained by MLE fitting of the profile together with the plot of the weighted residuals (b) and the values of the χ^2 criterion used in the MLE fit. All data were best fitted by single exponential functions. The estimated lifetimes are indicated.

Downloaded 11 May 2007 to 134.93.131.89. Redistribution subject to AIP license or copyright, see http://jcp.aip.org/jcp/copyright.jsp

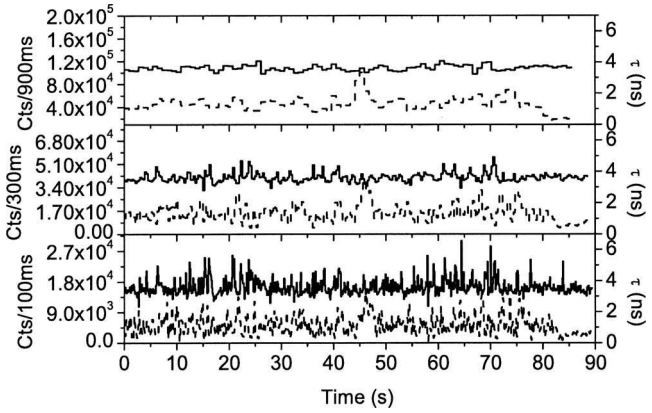

FIG. 5. Fluorescence intensity (dash) and lifetime (solid) trajectories of molecule 1, with all photons grouped in successive bins of 100, 300, 900 ms from bottom to top, respectively. The contribution of statistical noise in the determination of the lifetime is negligible for the number of counts considered in these traces [see also Fig. 8(a)] (Ref. 33).

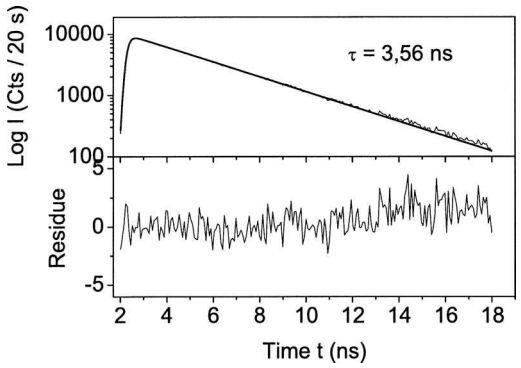

FIG. 6. Decay profile (top) recorded during the first 20 s of the measurement of molecule 1 in the OS matrix with M_w=662. Also shown are the best fit obtained by MLE fitting of the profile and the plot of the weighted residuals (bottom). The profile was fitted by a single exponential function with τ=3.56 ns (Ref. 48).

Performing a binning on the time scale ζ of the relaxation process taking place in the matrix, as observed in the minimal binning analysis, thus allows one to observe strong fluctuations of the fluorescence lifetime. As reported elsewhere,[24–29] these fluctuations of the probe fluorescence lifetime reflect local density fluctuations of the surrounding polymer matrix. The basic explanation for the observed behavior is the following: after pulsed photoexcitation, the probe relaxes to its ground state by spontaneous emission of a photon. The electric field associated with this photon (electric field generated by the transition dipole moment of the molecule) polarizes and thus induces dipole moments $\boldsymbol{\mu}_k$ on the surrounding OS monomer units. The observed emission consequently originates from an effective transition dipole moment $\boldsymbol{\mu}_{\text{tot}}$, which is the sum of the molecular emission transition dipole moment (source dipole) $\boldsymbol{\mu}$ and of the dipoles $\boldsymbol{\mu}_k$ induced in the medium surrounding the probe,

$$\boldsymbol{\mu}_{\text{tot}} = \boldsymbol{\mu} + \sum_k \boldsymbol{\mu}_k. \tag{1}$$

The measured radiative lifetime $\tau \infty |\boldsymbol{\mu}|^2/|\boldsymbol{\mu}_{\text{tot}}|^2$ of the probe (quantum yield very close to 1) thus crucially depends on the positions and polarizabilities of the dye and the surrounding OS monomers.

We want to point out that the time scale chosen to bin the photons is a very critical parameter. Figure 5 (bottom) shows the intensity and fluorescence lifetime trajectories of molecule 1 built by binning the photons on the 100 ms time scale. Strong fluctuations of the lifetime are observed as a result of the expected strong fluctuations of the positions of the styrene units surrounding the probe in the polymer melt. However, if the chosen binning time is too large, an intrinsic averaging effect takes place, which smooths out the whole trace. Figure 5 (from bottom to top) shows such traces, where the binning time has been set to 100, 300, and 900 ms.

These figures clearly evidence smearing out of the fluorescence lifetime fluctuations as the binning time scale is increased. The physical effect behind these observations is simply that the monomers surrounding the probe have had time to spatially rearrange their position many times so that, on these longer binning time scales, only an average polarization effect is observed. It is worth noticing that the decay times reported in Fig. 5 (top and middle) still are true fluorescence lifetimes, as in each case the decay profiles obtained were best fitted by monoexponential functions. As a further proof of this averaging effect, we built a decay profile by accumulating all the photons recorded during the first 20 s of the observation of molecule 1. This decay profile, shown in Fig. 6, is still fitted by a monoexponential function with a fluorescence lifetime τ=3.56 ns.[48]

In order to observe fluorescence lifetime fluctuations, special care has thus to be taken in the choice of the binning time of the photons, which must be lower or equal to the intrinsic time scale for the local motion of the monomers. Of course, this time scale depends on the mobility of the polymer matrix, and thus on the difference $T-T_g$ (T=292 K being the temperature at which the experiment is performed). By choosing a binning time of 100 ms, i.e., approximately equal to the relaxation time ζ determined in the most mobile matrix, we make sure to observe the lifetime fluctuations in all other matrices (being more supercooled or in the glassy state), which have a longer relaxation time scale.

D. Fluorescence lifetime fluctuations: Theory

The fluorescence lifetime fluctuations of the BODIPY probe reflect the local density fluctuations of the surrounding matrix. In particular, the time scale for these fluctuations reflect the time scale for the segmental rearrangements and thus the mobility of the investigated matrix. Based on a macroscopic approach,[24,27] we have indeed related the fluorescence lifetime fluctuations to an effective dielectric constant (defined as a spatially averaged quantity on a length scale comparable to the transition wavelength), varying from position to position in the matrix and depending on the local fraction of holes surrounding directly the SM in the matrix. This way, we could determine the number of polymer segments involved in a rearrangement cell around the probe molecule as a function of temperature,[24,27] solvent content,[25] and film thickness.[26] More recently, we have developed a microscopic model[28] generalizing the Lorentz approach to local field effects. Owing to this model,[28] we have estab-

Downloaded 11 May 2007 to 134.93.131.89. Redistribution subject to AIP license or copyright, see http://jcp.aip.org/jcp/copyright.jsp

lished a clear correlation between the fluorescence lifetime distributions measured for SMs and the local fraction of surrounding holes. We have further validated this model in investigating the specific interaction of SMs with the surrounding polymer chains.[29] For the sake of completeness, we outline briefly here below the main steps involved in the simulations of this microscopic model, which allows us to assess the simulated lifetime distributions of the system under investigation.

(i) We used the Hartree-Fock semiempirical AM1 technique to assess the geometric and electronic structures of the BODIPY molecule in both the S_0 singlet ground state and the S_1 lowest singlet excited state. Frequency calculations were performed to validate the existence of the recovered local minima. The excited-state properties of the molecule were determined by INDO/SCI calculations on the basis of the AM1 excited-state geometries. The transition dipole moment $|\boldsymbol{\mu}|=3.8\times10^{-29}$ *SI* and the polarizability $\chi=5.7\times10^{-39}$ *SI* were estimated for the probe molecule. Similar calculations performed for the styrene unit lead to a polarizabilty $\alpha=1.0\times10^{-39}$ *SI*.

(ii) The probe molecule is represented by an ensemble of atomic transition densities [Fig. 1(a)] and displays a polarizability χ. The probe is located at the origin of a 3D cubic lattice and surrounded by z polarizable monomers of polarizability α. To mimic the motion of the styrene units around the fixed probe molecule, a given fraction of holes (with zero polarizability) is introduced in the lattice. To determine the lattice constant Δ, the van der Waals volume of a styrene unit $V=1.19\times10^{-28}$ m^3 is simply attributed to the volume $V=\Delta^3$ of a cell in the cubic lattice. To calculate the effective transition dipole of the probe, we have solved the system of coupled linear equations

$$\boldsymbol{\mu}_k = \alpha_k \left[\mathbf{E}(\mathbf{r}_k) + \sum_{j=1}^{N} T_{kj}\boldsymbol{\mu}_j \right], \tag{2}$$

where $\mathbf{E}(\mathbf{r}_k)$ is the electric field generated by the source dipole $\boldsymbol{\mu}$ on cell k and $T_{kj}=(1/r_{kj}^3)(\delta_{kj}-3\mathbf{r}_{kj}\mathbf{r}_{kj}/r_{kj}^2)$ is the dipole-dipole interaction tensor between cells at positions $\mathbf{r}_k$ and $\mathbf{r}_j$ ($\mathbf{r}_{kj}=\mathbf{r}_k-\mathbf{r}_j$). From the total transition dipole moment thus obtained [Eq. (1)], the lifetime is estimated as (in adimensional units)[28]

$$\tau = \frac{|\boldsymbol{\mu}|^2}{|\boldsymbol{\mu}_{\mathrm{tot}}|^2}. \tag{3}$$

(iii) To build a statistical distribution of the fluorescence lifetimes of a BODIPY molecule embedded in an OS matrix, Monte Carlo realizations of the molecule surrounded by styrene units and holes have been achieved. A Monte Carlo run was implemented in the following way: (1) The fraction of holes (threshold value) was first fixed. (2) For each cell on the lattice, a uniformly distributed (between 0 and 1) random number was chosen. (3) If the random number falls below the threshold value, then the given cell is occupied by a hole, else it is occupied by a monomer. The Monte Carlo simulations were repeated typically 1000 times for each given threshold value.

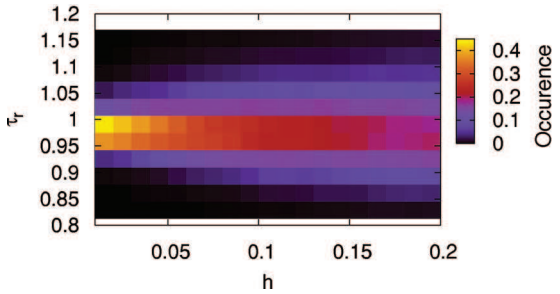

FIG. 7. (Color) Reduced fluorescence lifetime τ_r distributions of a probe as a function of the fraction of holes h introduced in the matrix, calculated by means of Monte Carlo simulations of the system (see text for details).

Figure 7 shows the results of these Monte Carlo simulations for a hole fraction ranging from $h=1\%$ to $h=20\%$ by step of 1%. The distribution of the normalized (with respect to the mean value) fluorescence lifetimes τ_r is very narrow and symmetric around 1 for $h=1\%$. It gets broader and more asymmetric (longer tail) as the fraction of holes is increased.[28,29]

E. Fluorescence lifetime fluctuations: Distributions of holes

On the experimental side, we have estimated the accuracy in the fluorescence lifetime determination by recording a trace of an ensemble of molecules dropped onto a glass substrate from a toluene solution at a probe molecule concentration of $10^{-6}M$, in the same emission conditions (i.e., same emission intensity in the confocal microscope) as the ones applied for the single molecule experiments performed in this study. We have performed the analysis of the recorded trace with the same binning time of the photons (100 ms) as the one chosen in the single molecule experiments in order to get a fair comparison. Figure 8(a) shows the intensity and fluorescence lifetime trajectories of this measurement. The figure clearly shows that for a fluorescence intensity slightly increasing from 10 000 to almost 15 000 counts/s (probably due to solvent evaporation), the value of the determined fluorescence lifetime $\tau=3.44$ ns barely changes. This type of experimental checking is important because it has been reported recently[46] that SPCM modules like the one we are using show a strong shift of the instrumental response function (IRF) with a variation of the count rate, which could make experiments with fluctuating signals difficult to be analyzed quantitatively. According to our results, as evidenced by Fig. 8 (top), this effect does not play a role, as we automatically correct for the shift between the IRF and the decay profile of the molecule in the fitting procedure. As a consequence, the distribution of measured lifetimes in this nonfluctuating environment (on this time scale) is very narrow and gives an estimate on the uncertainty in the lifetime determination (5% of the absolute value of the lifetime, i.e., 0.17 ns in our case). Furthermore, the comparison of this

Downloaded 11 May 2007 to 134.93.131.89. Redistribution subject to AIP license or copyright, see http://jcp.aip.org/jcp/copyright.jsp

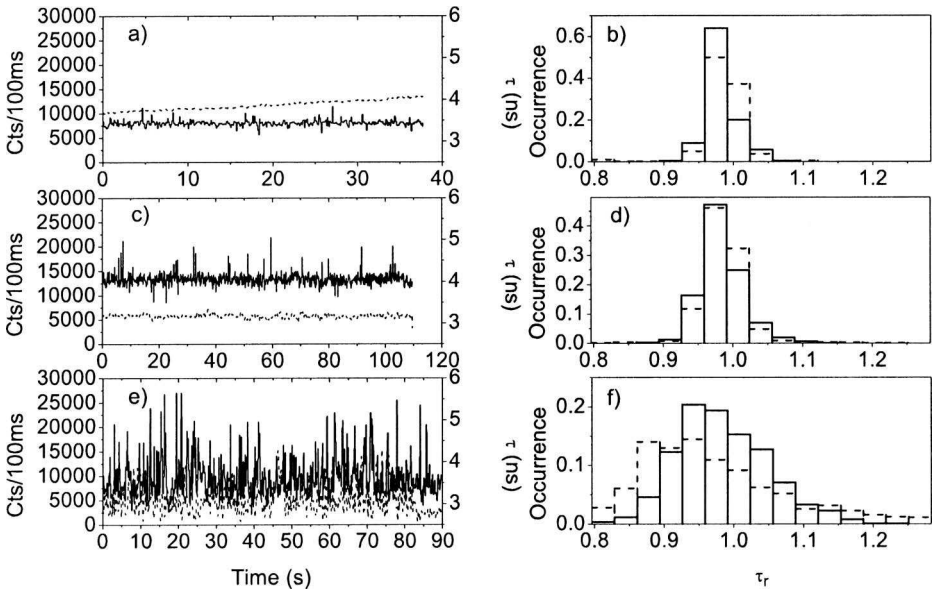

FIG. 8. (Left) (a) Fluorescence intensity (dash) and lifetime (solid) trajectories of dyes embedded in a toluene solution. (c) An OS matrix with M_n =4700 in the glassy state. (e) An OS matrix with M_n=662 and T_g=272 K in the supercooled regime. (Right) Corresponding experimental (dash) lifetime distributions matched with the calculated (solid) ones. The reduced fluorescence lifetime is obtained by dividing the fluorescence lifetime by its average along the trajectory. In the toluene solution (top), the fluctuations of the lifetime can be taken as a measure of the uncertainty in the determination of the lifetime. (b) The corresponding uncertainty in the determination of the fraction of holes is h=1%. (d) h=5%. (f) h=20%.

experimentally obtained distribution with our lifetime simulations also provide a measure for the uncertainty in the determination of the fraction of holes h: Δh=1%.

Figure 8 shows the fluorescence intensity and lifetime trajectories of individual probes embedded in an OS matrix with T_g=322 K [glassy, Fig. 8(c)] and T_g=272 K [supercooled, Fig. 8(e)]. Clearly, the lifetime trajectory displays much more pronounced fluctuations around the mean value in the supercooled regime than in the glassy state. A comparison of the amplitude and frequency of these fluctuations with the (very) small ones exhibited in Fig. 8(a) clearly indicates that the fluctuations only can be the result of different fluctuation dynamics in the different OS matrices. These fluctuations can be accounted for by Monte Carlo simulations of the local density fluctuations,[28] with the fraction of holes surrounding the probe in the matrix as sole parameter. In Figs. 8(d) and 8(f), measured and simulated normalized (with respect to the mean value) radiative lifetime $\tau_r=\tau/\langle\tau\rangle$ histograms are shown for the two OS matrices. In the glassy state, the fraction of holes surrounding the probe is h=5% [Fig. 8(d)], while in the supercooled regime h=20% [Fig. 8(f)].

For the eight polymer matrices of different molecular weights M_n (and hence different T_g values), we recorded the intensity and lifetime trajectories of 50 to 100 single molecules, built the normalized lifetime τ_r distributions, and determined the fraction of holes surrounding each molecule. Figure 9 shows the distributions of the fraction of holes (extracted from the best fits of the MC simulations to the experimental data) as a function of T_g of each investigated matrix. The fraction of holes surrounding the probes peaks in all cases at $h\approx 5\%$ in the glassy state, irrespective of the T_g of the OS sample. A similar h value was found for a different molecular probe (DiD) embedded in a PS matrix,[26] which suggests that this fraction of holes is a characteristic of the polymer in the glassy state. In the supercooled regime ($T > T_g$), the fraction of holes increases up to h=20%. It is worthwhile to note here that for the two matrices explored in the supercooled regime (M_n=662, T_g=272 K and M_n=869, T_g=282 K), 20% of the intensity and lifetime trajectories show a peculiar hopping behavior (not shown) between few levels and were ruled out of the present analysis. This behavior is described elsewhere.[47]

Our results do not agree with the excess free volume concept associated with chain ends: although a reduction of the glass transition temperature is observed by DSC as the degree of polymerization of the chains is decreased, we do not observe an increase of the fraction of holes h in the glassy state. According to the Gibbs and Di Marzio theory, as the temperature is decreased to T_2 at constant pressure, the number of allowed rearrangements for the chains is reduced because (i) the number of holes decreases and the configurational entropy due to permuting holes and chains decreases and (ii) the configurational entropy of the chain decreases because the chains favor low energy states at lower temperatures. At T_2 and lower temperatures, each chain is frustrated by its neighbors and does not reach its Boltzmann equilibrated distribution of shapes. Instead, the distribution encountered at T_2 persists as the temperature is lowered so that the fraction of holes h in the glassy state is constant, as observed. The SMS experimental evidence of a constant fraction of holes below T_2 is furthermore well supported by

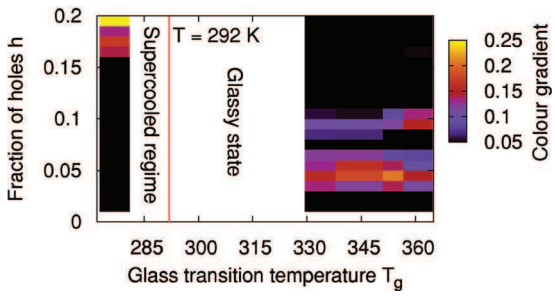

FIG. 9. (Color) Distributions of the fraction of holes surrounding the probe molecules as a function of the glass transition temperature for all samples investigated in this study. A constant fraction of holes h=5% is dominant in the glassy state while h is increased to 20% in the supercooled regime. The working room temperature T=292 K is indicated by the red line.

Downloaded 11 May 2007 to 134.93.131.89. Redistribution subject to AIP license or copyright, see http://jcp.aip.org/jcp/copyright.jsp

the parallelism between the volume versus temperature curves for a glass and for a crystal, as evidenced in bulk experiments.

F. Fluorescence lifetime as a function of orientation of the SM with respect to the air interface

In view of the results displayed in Fig. 5 (bottom) [or equivalently Fig. 8(e)] for the fluorescence lifetime of molecule 1 embedded in an OS matrix with M_n=662, i.e., in the supercooled regime for which the matrix allows the SM for having an enhanced mobility, one could argue that the magnitude of the lifetime fluctuations (ratio$\approx$1.6) might be due to reorientations of the SM close to the polymer-air interface. Indeed, the early experiments by Drexhage and Fleck[49] have shown that the spontaneous emission of chromophores close to an interface between two media is altered due to reflection and absorption at the interface. Chance *et al.*[50] and Lukosz and Kunz[51] have described this interaction, showing that the field of the dipole is perturbed by the presence of a second medium. In a simple approximation, a dye molecule can be considered as an oscillating dipole, when driven by the alternating electric field of the incoming light wave. The dipole generates a secondary wave. When surrounded by an isotropic medium, this secondary wave does not influence the oscillator. Close to an interface, the interference with the first and successive reflections of the emitted light wave occurs causing the total radiated power to be strongly dependent on the distance d separating the dipole from the interface, as well as on the orientation α of the dipole with respect to the normal at the interface. This approach, applied in the case of a SM close to an interface, has been well developed in the literature.[52,53]

In order to investigate the influence of the electromagnetic boundary (EB) conditions, due to the presence of the interface, on the fluorescence lifetime of the SM, we follow here a strategy we developed in Ref. 53: We model an oligo(styrene) film containing the SM as a three-layer system consisting of the OS layer sandwiched between air and the glass substrate. Knowing the dielectric constants of the three media, ϵ=1, 2.5, and 2.3, respectively, for air, OS, and glass, we determine numerically[53] the fluorescence lifetime of the molecule embedded in the polymer as a function of depth and orientation with respect to the air interface. Specifically, we consider the cases of the SM situated a distance d =1,2,3,... nm away from the air interface, and having an angle ranging from 0 to 90 in steps of 3.

Figure 10 (top) shows a plot of the fluorescence lifetime versus depth and orientation of a SM located in the 10 nm polymer top layer of a 70 nm thick matrix, where the EB effect is the strongest one, with d=0 at the air-polymer interface, and α=0 as the SM transition dipole is normal to the interface. Remarkably, this figure exhibits a fluorescence lifetime of 3.44 ns for a molecule located at a depth of 1 nm from the interface and having its transition dipole in the plane of the sample. The molecule reaches a lifetime at least four-times larger than this (in-plane) value as the molecule has its transition dipole normal to the plane of the sample. The figure further shows that this effect is reduced as the

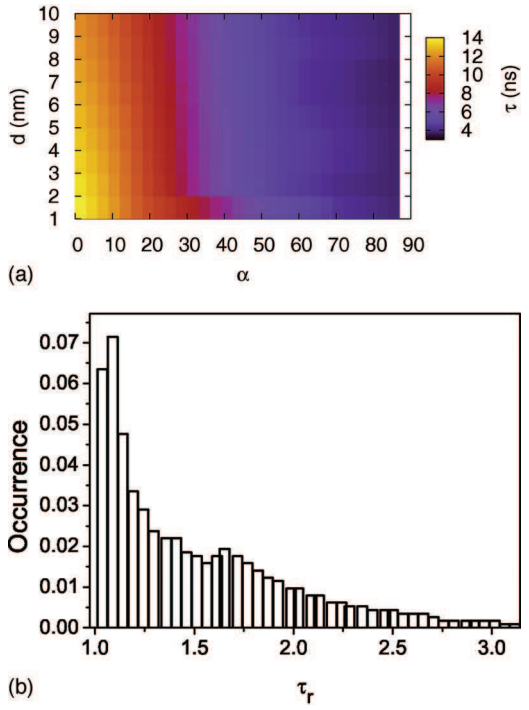

FIG. 10. (Color) (Top) Fluorescence lifetime as a function of orientation α and distance d of the SM with respect to the air interface. We consider here a 70 nm thick film and the SM is in the 10 nm top layer. (Bottom) Reduced fluorescence lifetime τ_r distribution of a SM rotationally and translationally diffusing freely in the 70 nm thick film.

distance between the SM and the interface is increased. So, with no doubt, large changes observed in the fluorescence lifetime of a SM could be attributed to this effect. However, two points have to be considered in order to go further with this possibility: (i) Molecules that are oriented out of plane with respect to the interface are hardly excited by the incoming light beam. Indeed, contrary to 3D techniques[18–22] that aim to enhance the z component of the incoming electric field, usual focusing techniques are used in this study, with a very weak z component of the excitation light. If very large lifetimes are going to be observed, the corresponding intensities of the SM at these times or positions must be very weak. Accordingly, only dipoles with an angle α>30 have a chance to be considered, giving a maximum observable lifetime of $\approx$9.5 ns. (ii) Molecules show such large variations in the fluorescence lifetime only if they are very close to the interface. Further away, the ratio between out-of-plane and in-plane transition dipoles is strongly reduced.

With these two points in mind, we can exclude the orientational dynamics of the SM close to the polymer-air interface as the cause of the observed lifetime fluctuations. Indeed, only a fraction (typically 10%) of the SMs observed in our study are located close to the air-polymer interface in the more than 100 nm thick polymer film. According to (ii), only this small fraction of the SMs might exhibit the observed lifetime fluctuations. Nevertheless, we observe many more lifetime fluctuating molecules in our study (most of them, in fact). Furthermore, such large lifetimes as 9.5 ns, expected [see (i)] for a SM oriented at α=30 have never been observed. As it is highly improbable that any molecule allowed to rotate close to the interface (previous point)

Downloaded 11 May 2007 to 134.93.131.89. Redistribution subject to AIP license or copyright, see http://jcp.aip.org/jcp/copyright.jsp

would not be able to reach this angle, we conjecture that the orientational effect is not the cause of the observed lifetime fluctuations.

In order to strengthen this point, we have simulated the case of a SM allowed to rotationally and translationally diffuse in a 70 nm thick matrix, forcing the angle $\alpha > 30$ (i). We have calculated the fluorescence lifetimes of this SM and built the corresponding distribution. Figure 10 (bottom) shows this fluorescence lifetime distribution. Very interestingly, and as noted previously, the fluorescence lifetimes can be very large, even larger to what we have ever observed. Furthermore, and more importantly, the shape of this distribution does not match the one shown in Fig. 8(f). Specifically, the distribution shown in Fig. 10 (bottom) lacks the lower part (the raising part) of the lifetime distribution shown in Fig. 8(f). The lowest lifetime of a SM close to the interface occurs as the transition dipole moment of this SM is in the plane of the matrix. It can only get larger as the dipole moment is going out of plane, hence the lack of the lower part in Fig. 10 (bottom). The lower part of the distribution shown in Fig. 8(f) results, in fact, from the presence of a void located close to the SM and transversally with respect to the transition dipole axis; the long tail (right part) of this distribution results from the presence of a void located close to the SM and longitudinally with respect to the transition dipole axis.[28] Note that the effect leading to the change in fluorescence lifetime is basically the same if one adopts either the point of view of the electromagnetic boundary conditions[53] or the point of view of a locally fluctuating environment: in both cases, the molecule sees a change in the polarizabilities (or in the high frequency dielectric constant) of its direct surrounding, a molecule oriented out of plane with respect to the air-polymer interface facing basically a big void. However, the in-depth comparison of these approaches allows us to distinguish which mechanism is responsible for the observed lifetime changes. The EB effect associated with the assumption of dynamically reorienting SMs close to the air-polymer interface does not allow one to observe the lower part of the lifetime distribution experimentally observed in Fig. 8(f). Furthermore, the especially long lifetimes expected for significantly out-of-plane oriented molecules have not been observed. On the contrary, the distributions obtained by simulations of a locally fluctuating environment around the SM match very well the experimentally obtained distributions.

IV. CONCLUSIONS

We have shown that the radiative lifetime of single molecules embedded in oligo(styrene) matrices shows large fluctuations induced by the local dielectric environment probed by the dye. This behavior can be reproduced quantitatively by a microscopic version of local field theory when accounting for the presence of holes surrounding the probe molecule. According to these results, two regimes can be clearly distinguished: (i) In the glassy state, the local fraction of holes has been found to be independent of the molecular weight of the polymer and amounts to 5% in the matrices studied here. (ii) The fraction of holes is much larger (close to 20%) once the system is brought in the supercooled regime. These results have been discussed in the framework of the free volume and Gibbs–Di Marzio entropy theories and tend to support the latter, especially in the case of short polymer chains. It is important to keep in mind, however, that the microscopic model used here involves lattice sites of the size of a monomer unit. Hence, fluctuations taking place over more confined spatial domains are not accounted for. While this will not affect the whole picture, such a refinement in the model might improve the agreement between simulated and measured results. Namely, one can notice that the simulated distribution in Fig. 8(f) does not perfectly match the experimental one, with the latter being more asymmetric (as observed in many cases for a molecule in the supercooled regime). This discrepancy is not observed for molecules in the glassy state [Fig. 8(c)]. A more detailed model taking into account a distribution of hole sizes might therefore allow for a more quantitative description of the lifetime fluctuations in the supercooled regime and is currently under scrutiny.

ACKNOWLEDGMENTS

Pascal Damman and Sylvain Desprez (University of Mons, Belgium) are kindly acknowledged for having performed the DSC measurements. The authors thank the Research Fund of the KU Leuven for financial support through GOA2001/2 and GOA2006/2, ZWAP 4/07, and the Belgium Science Policy through IAP 5/03. The Fonds voor Wetenschappelijk Onderzoek Vlaanderen is thanked for a postdoctoral fellowship for one of the authors (R.A.L.V.) and for Grant Nos. G.0320.00 and G.0421.03. Another author (D.B.) is a research associate of the Fonds National de la Recherche Scientifique.

[1] J. Jäckle, Rep. Prog. Phys. **49**, 171 (1986).
[2] W. Götze and L. Sjögren, Rep. Prog. Phys. **55**, 241 (1992).
[3] P. G. Debenedetti, *Metastable Liquids* (Princeton University Press, Princeton, 1997).
[4] E.-W. Donth, *The Glass Transition: Relaxation Dynamics in Liquids and Disordered Materials* (Springer, Berlin, 2001).
[5] *Proceedings of the Fourth International Discussion Meeting on Relaxations in Complex Systems*, edited by K. L. Ngai, special issues of J. Non-Cryst. Solids 307–310 (2002).
[6] K. Binder and W. Kob, *Glassy Materials and Disordered Solids: An Introduction to their Statistical Mechanics* (World Scientific, Singapore, 2005).
[7] H. Sillescu, J. Non-Cryst. Solids **243**, 81 (1999).
[8] M. D. Ediger, Annu. Rev. Phys. Chem. **51**, 99 (2000).
[9] R. Richert, J. Phys.: Condens. Matter **24**, R703 (2002).
[10] W. E. Moerner and M. Orrit, Science **283**, 1670 (1999).
[11] X. S. Xie and J. K. Trautman, Annu. Rev. Phys. Chem. **49**, 441 (1998).
[12] F. Kulzer and M. Orrit, Annu. Rev. Phys. Chem. **55**, 585 (2004).
[13] R. A. L. Vallée, M. Cotlet, J. Hofkens, F. C. De Schryver, and K. Müllen, Macromolecules **36**, 7752 (2003).
[14] L. A. Deschenes and D. A. Vanden Bout, J. Phys. Chem. B **106**, 11438 (2002).
[15] N. Tomczak, R. A. L. Vallée, E. M. H. P. van Dijk, M. García-Parajó, L. Kuipers, N. F. van Hulst, and G. J. Vancso, Eur. Polym. J. **40**, 1001 (2004).
[16] A. Schob, F. Cichos, J. Schuster, and C. von Borczyskowski, Eur. Polym. J. **40**, 1019 (2004).
[17] E. Mei, J. Tang, J. M. Vanderkooi, and R. M. Hochstrasser, J. Am. Chem. Soc. **125**, 2730 (2003).
[18] R. M. Dickson, D. J. Norris, and W. E. Moerner, Phys. Rev. Lett. **81**, 5322 (1998).
[19] B. Sick, B. Hecht, and L. Novotny, Phys. Rev. Lett. **85**, 4482 (2000).

Downloaded 11 May 2007 to 134.93.131.89. Redistribution subject to AIP license or copyright, see http://jcp.aip.org/jcp/copyright.jsp

[20] A. Lieb, J. M. Zavislan, and L. Novotny, J. Opt. Soc. Am. B **21**, 1210 (2004).
[21] M. Böhmer and J. Enderlein, J. Opt. Soc. Am. B **20**, 554 (2000).
[22] H. Uji-i, S. Melnikov, A. Deres, G. Bergamini, F. De Schryver, A. Herrmann, K. Müllen, J. Enderlein, and J. Hofkens, Polymer **47**, 2511 (2006).
[23] A. P. Bartko, K. Xu, and R. M. Dickson, Phys. Rev. Lett. **89**, 026101 (2002).
[24] R. A. L. Vallée, N. Tomczak, L. Kuipers, G. J. Vancso, and N. F. van Hulst, Phys. Rev. Lett. **91**, 038301 (2003).
[25] R. A. L. Vallée, N. Tomczak, L. Kuipers, G. J. Vancso, and N. F. van Hulst, Chem. Phys. Lett. **384**, 5 (2004).
[26] N. Tomczak, R. A. L. Vallée, E. M. H. P. van Dijk, L. Kuipers, N. F. van Hulst, and G. J. Vancso, J. Am. Chem. Soc. **126**, 4748 (2004).
[27] R. A. L. Vallée, N. Tomczak, G. J. Vancso, L. Kuipers, and N. F. van Hulst, J. Chem. Phys. **122**, 114704 (2005).
[28] R. A. L. Vallée, M. Van der Auweraer, F. C. De Schryver, D. Beljonne, and M. Orrit, ChemPhysChem **6**, 81 (2005).
[29] R. A. L. Vallée, P. Marsal, E. Braeken, S. Habuchi, F. C. De Schryver, M. Van der Auweraer, D. Beljonne, and J. Hofkens, J. Am. Chem. Soc. **127**, 12011 (2005).
[30] T. G. Fox and P. J. Flory, J. Am. Chem. Soc. **70**, 2384 (1948).
[31] G. Pezzin, F. Zilio-Grandi, and P. Sanmartin, Eur. Polym. J. **6**, 1053 (1970).
[32] J. H. Gibbs and E. A. Di Marzio, J. Chem. Phys. **28**, 373 (1958).
[33] M. Maus, M. Cotlet, J. Hofkens, T. Gensch, F. C. De Schryver, J. Schaffer, and C. A. M. Seidel, Anal. Chem. **73**, 2078 (2001).
[34] R. Hanbury-Brown and R. Q. Twiss, Nature (London) **177**, 27 (1956).
[35] M. J. S. Dewar, E. G. Zoebisch, E. F. Healy, and J. J. P. Stewart, J. Am. Chem. Soc. **107**, 3902 (1985).
[36] AMPAC, Semichem, 7204 Mullen, Shawnee, KS 66216.
[37] M. C. Zerner, G. H. Loew, R. Kichner, and U. T. Mueller-Westerhoff, J. Am. Chem. Soc. **122**, 3015 (2000).
[38] T. Basché, W. E. Moerner, M. Orrit, and H. Talon, Phys. Rev. Lett. **69**, 1516 (1992).
[39] L. Fleury, J.-M. Segura, G. Zumofen, B. Hecht, and U. P. Wild, Phys. Rev. Lett. **84**, 1148 (2000).
[40] B. Lounis and W. E. Moerner, Nature (London) **407**, 491 (2000).
[41] P. Tinnefeld, C. Muller, and M. Sauer, Chem. Phys. Lett. **345**, 252 (2001).
[42] P. Tinnefeld, K. D. Weston, T. Vosch, M. Cotlet, T. Weil, J. Hofkens, K. Müllen, F. C. De Schryver, and M. Sauer, J. Am. Chem. Soc. **124**, 14310 (2002).
[43] S. Masuo, T. Vosch, M. Cotlet *et al.*, J. Phys. Chem. B **108**, 16686 (2004).
[44] C.-Y. Lu and D. A. Vanden Bout, J. Chem. Phys. **125**, 124701 (2006).
[45] H. Yang and X. S. Xie, J. Chem. Phys. **117**, 10965 (2002).
[46] S. Felekyan, R. Kühnemuth, V. Kudryavtsev, C. Sandhagen, W. Becker, and C. A. M. Seidel, Rev. Sci. Instrum. **76**, 083104 (2005).
[47] R. A. L. Vallée, M. Van der Auweraer, W. Paul, and K. Binder, Phys. Rev. Lett. **97**, 217801 (2006).
[48] The reason why we observe an increase of the residuals at long time scale ($t > 12$ ns) is unclear. It is probably due to a small contribution of naturally occurring long lifetimes in the time trajectories [Fig. 5 (bottom)]. Nevertheless, we do not succeed to best fit the profile with a multiexponential function.
[49] K. H. Drexhage and M. Fleck, Ber. Bunsenges. Phys. Chem. **72**, 330 (1968).
[50] R. R. Chance, A. Prock, and R. Silbey, Adv. Chem. Phys. **37**, 1 (1978).
[51] W. Lukosz and R. E. Kunz, J. Opt. Soc. Am. **67**, 1607 (1977); T. Basché, Abstr. Pap. - Am. Chem. Soc. **S221**, U235 (2001).
[52] J. J. Macklin, J. K. Trautman, T. D. Harris, and L. E. Brus, Science **272**, 255 (1996).
[53] R. A. L. Vallée, N. Tomczak, H. Gersen, E. M. H. P. van Dijk, M. F. García-Parajó, G. J. Vancso, and N. F. van Hulst, Chem. Phys. Lett. **348**, 161 (2001).

Downloaded 11 May 2007 to 134.93.131.89. Redistribution subject to AIP license or copyright, see http://jcp.aip.org/jcp/copyright.jsp

Fluorescence Lifetime of a Single Molecule as an Observable of Meta-Basin Dynamics in Fluids Near the Glass Transition

R. A. L. Vallée* and M. Van der Auweraer

Department of Chemistry and Institute of Nanoscale Physics and Chemistry (INPAC), Katholieke Universiteit Leuven, Heverlee, Belgium

W. Paul and K. Binder

Department of Physics, Johannes-Gutenberg University, Mainz, Germany

(Received 28 July 2006; published 22 November 2006)

Using single molecule spectroscopy, we show that the fluorescence lifetime trajectories of single probe molecules embedded in a glass-forming polymer melt exhibit strong fluctuations of a hopping character. Using molecular dynamics simulations targeted to explain these experimental observations, we show that the lifetime fluctuations correlate strongly with the average square displacement function of the matrix particles. The latter observable is a direct probe of the meta-basin transitions in the potential energy landscape of glass-forming liquids. We thus show here that single molecule experiments can provide detailed microscopic information on system properties that hitherto have been accessible via computer simulations only.

DOI: 10.1103/PhysRevLett.97.217801 PACS numbers: 61.20.Ja, 61.20.Lc, 64.70.Pf, 87.64.Ni

Introduction and motivation.—Understanding the slow dynamics of undercooled liquids and the mechanisms by which these fluids freeze into a glassy state has been, and still is, an outstanding challenge [1–5]. In many systems [2,4,5], some aspects of the initial stages of slowing down can be accounted for by mode coupling theory [6]. This theory can be viewed as a momentum space description of the ''cage effect''. However, this ensemble averaged perspective is not able to describe observations of dynamic heterogeneity [7] in the liquid which experimentally become more important around the viscosimetric T_g. These heterogeneities have to be caused by different local environments, and the particles constituting these environments will rearrange in some cooperative fashion. So far only scarce experimental evidence [5,8] exists for this phenomenological idea of cooperatively rearranging regions [8,9] employed since a long time to rationalize the slow ''α-relaxation'' [1–5].

A more detailed view of these cooperative rearrangements has been provided by recent computer simulations [10,11] studying the dynamics in the rugged potential energy landscape (PEL) of glass-forming liquids. The minima of the PEL are arranged in meta-basins (MB) [10–12] separated by high energy barriers. Within one MB only barriers with heights of order k_BT occur. The basic process leading to structural relaxation is the motion of the system from one MB in the PEL to another. Computer simulations [11] have shown that this motion involves only a fraction of the particles in the liquid which cooperatively rearrange during this MB transition.

However, the typical time window for the simulations is of order 100 ns [4,5], whereas the experiments detect dynamic heterogeneity on a time scale of the order of 100 s close to T_g [5,8]. There exists also no known connection between these experimental results and the MB transitions analyzed in computer simulations. Thus it would be of great value to provide experimental observables that (i) can be linked to the MB dynamics; i.e., are able to observe a single cooperatively rearranging region of nanoscopic size, and (ii) can bridge the huge gap in relaxation times between the current experiments on heterogeneous dynamics and the computer simulations on much shorter time scales.

In the present Letter we propose that the analysis of fluctuations of the fluorescence lifetime of suitable probe molecules [13] can provide precisely this information. Our evidence contains the following steps: (i) We show that the time trajectories of the fluorescence lifetime and intensity of a single fluorescent molecule embedded in a matrix near the glass transition show large fluctuations of a ''hopping'' character (while such a hopping behavior was not observed in the glass [13]). (ii) To interpret these fluctuations, we carry out a molecular dynamics (MD) simulation of a coarse-grained model for a melt of short (nonentangled) polymer chains containing a dumbbell as a model for the probe molecule. We establish that insertion of this dumbbell does not create any significant disturbance of the dynamics of the matrix which, in previous work [4,14] has been shown to exhibit all the behavior of real glass-forming polymer melts. We also show that the dynamics of the probe molecule (monitored, e.g., by its self-intermediate scattering function [5]) faithfully mirrors the matrix dynamics. (iii) The crucial step then is to analyze from the simulation a quantity that corresponds to the experimentally measured fluorescence lifetime. We show that the corresponding ''signal'' trajectory from the simulation exhibits fluctuations fully analogous to the experiment. The average lifetime of these fluctuations (as

 © 2006 The American Physical Society

obtained from a stretched exponential fit to the autocorrelation curve) is practically identical to the α-relaxation time scale (as extracted from the scattering function). The analysis of correlations between these lifetime fluctuations and square displacement trajectories exhibits then all the signatures of transitions between MB, similar to recent simulation evidence for other models [11]. As a result, compelling evidence emerges that the fluorescence lifetime of a single molecule is a suitable probe for the dynamics of the cooperatively rearranging region in which this probe molecule is embedded.

Experiment.—In order to probe the local dynamics of a low molecular weight oligo(styrene) (OS) matrix above the glass transition temperature T_g, a newly synthesized fluorescent molecule [15] was used. Single molecule experiments were performed with a confocal scanning inverted microscope [13,16]. Samples of highly monodisperse OS chains (Polymer Standard Service, $M_n = 869$, $T_g = 281$ K, $PI = 1.1$) were prepared by spin coating a dilute solution of the probe (10^{-10} M) and OS in toluene onto a glass substrate. The probe [15] was specially designed to fulfill the following criteria: (i) it is highly photostable; (ii) it has a luminescence quantum yield close to 1 (0.99 in toluene) such that the observed fluorescence lifetime has a largely dominant radiative part; (iii) it emits in the red part of the visible spectrum (emission maximum at 584 nm), hence minimizing overlap with the autofluorescence of the matrix and; (iv) it is structurally rigid.

Figure 1 shows the intensity and fluorescence lifetime trajectories of an individual probe embedded in the OS matrix at room temperature 292 K. In contrast to observations in the glassy state [13], the lifetime trajectory exhibits a strong hopping character on the measurement time scale of several hundred seconds.

To understand this behavior, we note that, after pulsed photoexcitation, the probe relaxes to its ground state by emitting spontaneously a photon. The electric field associated with this photon (electric field generated by the transition dipole moment of the molecule) polarizes its environment and thus induces dipole moments $\vec{\mu}_k$ on the surrounding OS monomer units. The observed emission consequently originates from an effective transition dipole moment $\vec{\mu}_{\rm tot} = \vec{\mu} + \sum_k \vec{\mu}_k$, i.e., the sum of the source dipole $\vec{\mu}$ and of the induced dipoles $\vec{\mu}_k$ [13]. The measured radiative lifetime $\tau \propto |\vec{\mu}|^2/|\vec{\mu}_{\rm tot}|^2$ of the probe thus crucially depends on the positions and polarizabilities [17] of the monomers surrounding the probe.

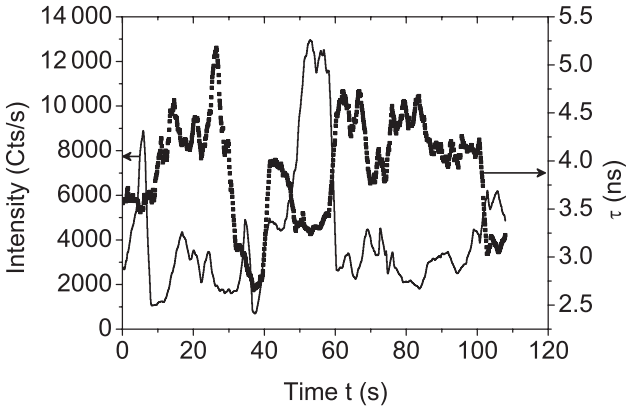

FIG. 1. Fluorescence lifetime (symbols) and intensity (line) trajectories of a single probe molecule embedded in the OS matrix.

Simulation model and technique.—In order to explain the physical origin of the hopping behavior observed in the single molecule fluorescence lifetime trajectories for which Fig. 1 is one out of many examples, we performed MD simulations of a system containing 120 bead-spring chains of 10 effective monomers. The interaction between two beads of type A (probe) or B (monomers) is given by the Lennard-Jones (LJ) potential $U_{\rm LJ}(r_{ij}) = 4\epsilon[(\frac{\sigma_{\alpha\beta}}{r_{ij}})^{12} - (\frac{\sigma_{\alpha\beta}}{r_{ij}})^{6}]$, where r_{ij} is the distance between beads i, j, and α, $\beta \in A, B$. The LJ diameters used are $\sigma_{AA} = 1.22$, $\sigma_{BB} = 1.0$ (unit of length) and $\sigma_{AB} = 1.11$, while $\epsilon = 1$ sets the scale of energy (and temperature T, since Boltzmann's constant $k_B = 1$). These potentials are truncated at $r_{\rm cut}^{\alpha\beta} = 2^{7/6}\sigma_{\alpha\beta}$ and shifted so that they are zero at $r_{ij} = r_{\rm cut}^{\alpha\beta}$. Between the beads along the chain, as well as between the beads of the dumbbell, a finitely extendable nonlinear elastic potential is used $U_F = -\frac{k}{2}R_0^2 \ln[1 - (\frac{r_{ij}}{R_0})^2]$, with parameters $k = 30$, $R_0 = 1.5$ [14]. This model system (without the probe) has been shown to reproduce many features of the relaxation of glass-forming polymers [4,14]. It is also very close to the experimental situation, as the molecular weight of the chosen OS corresponds to 9 monomers on average. The mass of the beads are chosen to be $m_B = 1$ in the chains and $m_A = 2.25$ in the dumbbell. The mass and the size of the beads in the dumbbell were chosen in order to fit the experimental conditions for which the van der Waals volume (mass) of the fluorophore is 3.6 (4.5) times bigger than a monomer of styrene. In the MD simulations, the equations of motion at constant particle number N, volume V, and energy E are integrated with the velocity Verlet algorithm [18,19] with a time step of 0.002, measuring time in units of $(m_B\sigma_{BB}^2/48\epsilon)^{1/2}$. All NVE simulations have been performed after equilibrating the system in the NPT ensemble, using a Nosé-Hoover thermostat [19], keeping the average pressure at $p = 1.0$ at all temperatures. These runs lasted up to 5×10^7 MD steps. Ten different configurations were simulated at each temperature, in order to ensure good statistics.

Dynamic structure factor.—A basic question about probe techniques is to ask how well does the behavior of the probe follow the behavior of the polymer matrix, and is the latter disturbed by the probe? We answer this question by comparing (Fig. 2) the self intermediate scattering function [5] $F_q(t) = \langle \frac{1}{M} \sum_{i=1}^{M} e^{i\vec{q}.[\vec{r}_i(t) - \vec{r}_i(0)]} \rangle$, $\vec{r}_i(t)$ being the position of the ith particle at time t. The sum is

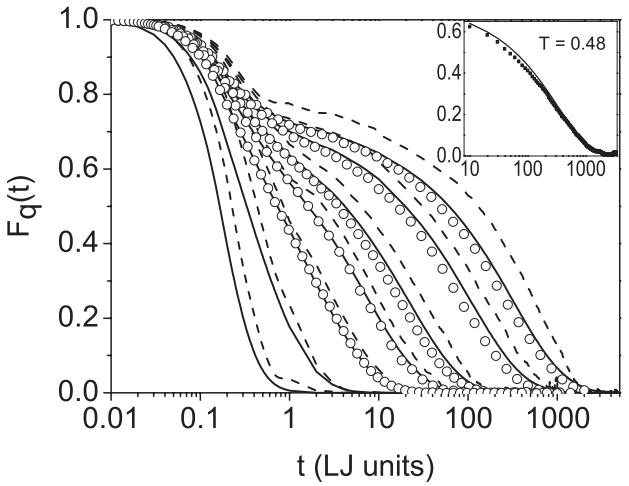

FIG. 2. Self-intermediate scattering functions $F_q(t)$ at the first maximum of the static structure factor. Straight (dashed) lines stand for $F_q(t)$ of the polymer (dumbbell) beads in the polymer-probe system. Symbols stand for $F_q(t)$ of the polymer beads in the polymer without probe system. From right to left, $T = 0.48$, 0.5, 0.55, 0.6, 0.7, 1.0, 2.0. The inset shows a comparison of $F_q(t)$ calculated for the first shell (symbols) of monomers surrounding the probe molecule and the full simulation box (line), excluding the probe in both cases.

extended either over the 2 particles of the dumbbell ($M = 2$), or over all the monomers of the chains ($M = 1200$). We furthermore compare our results to those of the analogous system [14] without a dumbbell. Figure 2 shows $F_q(t)$ at the peak position of the static structure factor (wave number $q = 6.9$ [14]) for the single molecule (dashed lines) and the polymer chains (solid lines).

Figure 2 shows that the relaxation of the fluorophore closely follows that of the surrounding polymer. Furthermore, the latter is not disturbed by the presence of the fluorophore, as the comparison with the analogous system without a probe molecule shows (symbols [14]). In all cases, $F_q(t)$ exhibits a two-step process as T is lowered, the so-called β- and α-processes [1–6]. In the ballistic regime ($t < 0.1$), the fluorophore relaxes more slowly than the polymer since it is more massive. Subsequently, as T is lowered, the fluorophore stays a bit longer in the plateau regime than the monomers do. Since the size of the dumbbell is larger than the distance between beads of the polymer, its escape from the cage [2,4,5] is more difficult and thus takes longer than that of the polymer beads. The inset of Fig. 2 shows that $F_q(t)$ barely changes if calculated ($T = 0.48$ in the α-relaxation zone) either for the monomers of the first shell surrounding the probe (symbols) or for all monomers of the simulation box (line), which shows that the probe molecule does not even significantly disturb the dynamics of its immediate neighbors.

Fluorescence lifetime, meta-basin transitions.—In order to model the fluorescence lifetime of the fluorophore embedded in the OS matrix, we proceed as follows. We solve the system of coupled linear equations $\vec{\mu}_k = \alpha_k[\vec{E}(\vec{r}_k) + \sum_{j=1}^{N} T_{kj}\vec{\mu}_j]$, where $\vec{E}(\vec{r}_k)$ is the electric field generated by the source dipole $\vec{\mu}$ on bead k and $T_{kj} = \frac{1}{r_{kj}^3}(\delta_{kj} - \frac{3\vec{r}_{kj}\vec{r}_{kj}}{r_{kj}^2})$ is the dipole-dipole interaction tensor between beads at positions $\vec{r}_k$, $\vec{r}_j$ ($\vec{r}_{kj} = \vec{r}_k - \vec{r}_j$). In practice, the total transition dipole is mainly determined by the induced polarization of the first two neighbor shells of the probe molecule. From the total transition dipole moment thus obtained, the lifetime is estimated as $\tau = \frac{|\vec{\mu}|^2}{|\vec{\mu}_{\mathrm{tot}}|^2}$ [13,20].

Figure 3 shows an example of a fluorescence lifetime trajectory thus obtained for a fluorophore embedded in the OS matrix at a temperature $T = 0.48$. Indeed, this trajectory exhibits a hopping behavior similar to the experiment (Fig. 1). Furthermore, the time scale on which this hopping mechanism occurs is typically several hundred LJ time units. This time scale corresponds closely to that found in [11] for the typical sojourn time within one MB of the PEL of a binary LJ mixture at similar conditions. The simulation was performed some 20% above the glass transition temperature of this model. Comparing Fig. 1 to Fig. 3, qualitatively the same fluctuations are observed, shifted to a larger time scale upon approaching T_g.

To identify MBs also in our system, we calculated the "distance matrix" (DM) [11]: $\Delta^2(t', t'') = \frac{1}{N}\sum_{i=1}^{N} |\vec{r}_i(t') - \vec{r}_i(t'')|^2$. This matrix gives the system average square displacement in the time interval starting at t' and ending at t''. Figure 4 shows the DM corresponding to the same OS matrix giving rise to the trajectory of Fig. 3. It can be seen that the system dynamics is very heterogeneous in time, staying relatively long close to one region (MB, dark squarelike region) in its configuration space prior to a jump to another region. Furthermore, the jumps in the lifetime trajectory correlate with these MB transitions

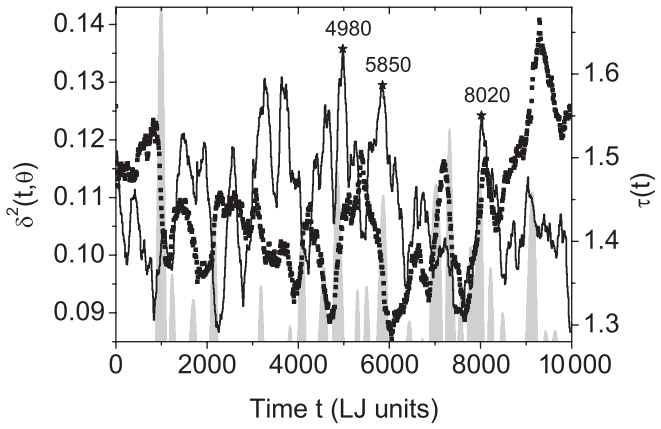

FIG. 3. Fluorescence lifetime τ (symbols, right ordinate) and average square displacement between t and $t + \theta$, $\delta^2(t, \theta)$ (line, left ordinate), trajectories calculated for a fluorophore embedded in the OS matrix at a temperature $T = 0.48$. The value of θ is 20. The gray shaded peaks represent the absolute derivatives of the fluorescence lifetime.

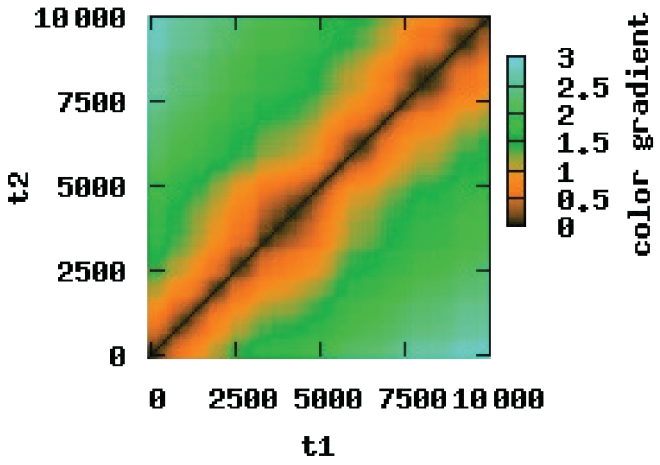

FIG. 4 (color). Distance matrix $\Delta^2(t', t'')$ of the system used already in Fig. 3 for $T = 0.48$. The color levels correspond to values of $\Delta^2(t', t'')$ that are given in the color gradient on the right of the figure.

observed at the crossings between successive dark square-like regions. To show this correlation quantitatively , we calculated the mean square displacement (MSD) of the particles within a time interval $\theta = 20$ (chosen to be 4% of the α relaxation time)[11]. This function, defined as $\delta^2(t, \theta) = \Delta^2(t, t + \theta)$ is shown in Fig. 3 as well. One can see that each jump of the fluorescence lifetime (best represented by a maximum of its absolute derivative, gray shaded peaks on Fig. 3) is accompanied by a maximum of the MSD function (some of the highest MSD peaks correlated with the absolute values of the lifetime derivative are also shown) and can thus signal a MB transition.

Conclusions.—Using MD simulations targeted to explain fluorescence lifetime measurements of probes embedded in glass-forming polymer melts, we have shown that the lifetime fluctuations correlate strongly with the meta-basin transitions in the potential energy landscape of the matrix particles. We thus show here that single molecule experiments can provide detailed microscopic information on system properties that hitherto have been accessible via computer simulations only. In this way, a new tool is provided for the experimental study of long-standing issues in the physics of the glass transition.

R. V. thanks the Fonds voor Wetenschappelijk Onderzoek Vlaanderen for a grant for a "study" stay abroad in the group of K. B. and for Grants No. G.0320.00 and No. G.0421.03, the K. U. Leuven Research Fund for GOA 2006/2 and IWT for ZWAP 04/007.

*Electronic address: renaud.vallee@chem.kuleuven.be

[1] P. G. Debenedetti, *Metastable Liquids* (Princeton University, Princeton, 1997).
[2] W Götze, J. Phys. Condens. Matter **11**, A1 (1999).
[3] *Proceedings of the Fourth International Discussion Meeting on Relaxations in Complex Systems*, edited by K. L. Ngai [J. Non-Cryst. Solids 307, 1 (2002)].
[4] K. Binder, J. Baschnagel, and W. Paul, Prog. Polym. Sci. **28**, 115 (2003).
[5] K. Binder and W. Kob, *Glassy Materials and Disordered solids* (World Scientific, Singapore, 2005).
[6] W. Götze and L. Sjögren, Rep. Prog. Phys. **55**, 241 (1992).
[7] C. Donati *et al.*, Phys. Rev. Lett. **80**, 2338 (1998); D. N. Revera and P. Harrowell, J. Chem. Phys. **111**, 5441 (1999); H. Sillescu, J. Non-Cryst. Solids **243**, 81 (1999); M. D. Ediger, Annu. Rev. Phys. Chem. **51**, 99 (2000); R. Richert, J. Phys. Condens. Matter **14**, R703 (2002); L. A. Deschenes and D. A. Vanden Bout, J. Phys. Chem. B **106**, 11 438 (2002); J. P. Garrahan and D. Chandler, Phys. Rev. Lett. **89**, 035704 (2002).
[8] E.-W. Donth, *The Glass Transition* (Springer, Berlin, 2001).
[9] G. Adam and J. H. Gibbs, J. Chem. Phys. **43**, 139 (1965).
[10] B. Doliwa and A. Heuer, Phys. Rev. E **67**, 031506 (2003); M. Vogel *et al.*, J. Chem. Phys. **120**, 4404 (2004).
[11] G. A. Appignanesi, J. A. Rodrigues Fris, R. A. Montani, and W. Kob, Phys. Rev. Lett. **96**, 057801 (2006).
[12] M. Goldstein, J. Chem. Phys. **51**, 3728 (1969); C. A. Angell, J. Non-Cryst. Solids **131**, 13 (1991); P. G. Debenedetti, F. H. Stillinger, T. M. Truskett, and C. P. Lewis, Adv. Chem. Eng. **28**, 21 (2001); C. Monthus and J. P. Bouchaud, J. Phys. A **29**, 3847 (1996); H. Teichler, Phys. Rev. E **71**, 031505 (2005); F. H. Stillinger and T. A. Weber, Phys. Rev. A **25**, 978 (1982).
[13] R. A. L. Vallée *et al.*, Phys. Rev. Lett. **91**, 038301 (2003); R. A. L. Vallée *et al.*, Chem. Phys. Chem. **6**, 81 (2005); R. A. L. Vallée *et al.*, J. Am. Chem. Soc. **127**, 12 011 (2005).
[14] C. Bennemann, W. Paul, K. Binder, and B. Dünweg, Phys. Rev. E **57**, 843 (1998).
[15] 4,4-difluoro-8-(4-methoxyphenyl)-3-[-2-(4-methoxyphenyl)ethenyl]-1,5,7-trimethyl-3a,4a-diaza-4-bora-s-indacene.
[16] The excitation light, at a wavelength $\lambda = 568$ nm, was circularly polarized and the power set to 1.1 μW. The fluorescence lifetimes were determined by fitting, using a maximum likelihood estimator, the decay profiles built on 100 ms time bins with single exponentials.
[17] The transition dipole moment $|\vec{\mu}| = 3.8 \times 10^{-29} SI$ and the polarizabilities $\alpha = 5.7 \times 10^{-39} SI$ and $\chi = 1.0 \times 10^{-39} SI$ for the probe and the styrene monomers, respectively, have been estimated by quantum chemistry calculations [13].
[18] Using OCTA (http://octa.jp).
[19] *Monte Carlo and Molecular Dynamics of Condensed Matter*, edited by K. Binder and G. Ciccotti (Societa Italiana di Fisica, Bologna, 1996).
[20] Being only interested in the lifetime fluctuations, the constant of proportionality is chosen as unity.

A Letters Journal Exploring the Frontiers of Physics

August 2007

EPL, **79** (2007) 46001
doi: 10.1209/0295-5075/79/46001

www.epljournal.org

What can be learned from the rotational motion of single molecules in a polymer melt near the glass transition?

R. A. L. Vallée[1], M. Van der Auweraer[1], W. Paul[2] and K. Binder[2]

[1] *Department of Chemistry, Katholieke Universiteit Leuven - 3001 Leuven, Belgium*
[2] *Institute of Physics, Johannes-Gutenberg University - 55099 Mainz, Germany*

received 17 April 2007; accepted in final form 25 June 2007
published online 19 July 2007

PACS 61.20.Ja – Computer simulation of liquid structure
PACS 61.20.Lc – Time-dependent properties; relaxation
PACS 64.70.Pf – Glass transitions

Abstract – We develop a framework for the interpretation of single-molecule (SM) spectroscopy experiments of probe dynamics in a complex glass-forming system. Specifically, from molecular dynamics simulations of a single probe molecule in a coarse-grained model of a polymer melt, we show the emergence of sudden large angular reorientations (SLARs) of the SM as the mode coupling critical temperature is closely approached. The large angular jumps are intimately related to meta-basin transitions in the potential energy landscape of the investigated system and cause the appearance of stretched exponential relaxations of various rotational observables, reported in the SM literature as dynamic heterogeneity. We show that one can determine parameters predicted by the mode coupling theory from SM trajectory analysis and check the validity of the time temperature superposition principle.

Copyright © EPLA, 2007

Introduction. – Understanding the physical mechanisms of the dramatic slowing-down observed in under-cooled fluids still is a challenge that only is partially resolved [1–3]. Techniques based on the determination of orientational time correlation functions (OTCFs) $C_l(t)$ of different order l [4–7], like dielectric spectroscopy (determination of $C_1(t)$) or light scattering and nuclear magnetic resonance (determination of $C_2(t)$), have been widely used to investigate the phenomenon. Also electron spin resonance techniques [8] have been used to characterize orientational relaxation of probes in a polymer matrix. However, since the different OTCFs are addressed by these techniques through different observables, the resulting relaxation times τ_l are poorly comparable. Detailed insight on relaxation processes on the nanoscale is available from the study of the behavior of single molecules (SM) [9–11]. With two-dimensional (2D) orientation techniques, the in-plane (of the sample) projection of the transition dipole moment of the SM, the so-called linear dichroism $d(t)$, has been followed in time and its time correlation function $C_d(t)$ computed and fitted by a stretched exponential function [12–15]

$$f(t) = e^{-(\frac{t}{\tau})^{\beta}}. \tag{1}$$

The results of these investigations have been the observation of dynamic heterogeneity [16,17] *i.e.* SMs exhibit i) varying τ and β from position to position in the matrix and ii) varying τ and β on long time scales while at the same position, as a result of probing different nanoscale environments [18,19]. However, the details of the local dynamic changes are not fully understood.

Nowadays, the full 3D orientation of the emission transition dipole moment of a SM can be recorded as a function of time [20–24], allowing for the calculation of the l-th ranks ($l \geqslant 1$) of the SM OTCFs $C_l(t)$ [25,26] and rotational mean square displacements. These advances in SM spectroscopy promise that local rotational dynamics will be observable in much greater detail in the near future. In this letter, we mimic a typical system investigated by SM spectroscopy and present a framework that will allow SM experimentalists to get a detailed microscopic information on the glass transition phenomenon. From molecular dynamics simulations of a single large probe molecule in a coarse-grained model of a polymer melt, we show that the SM dynamics, faithfully mirroring the one of its surrounding, undergoes a crossover from a rotational diffusion type of motion [27,28] with $2\tau_1/\tau_l = l(l+1)$ to a sudden large angular reorientation (SLAR)

type of motion with τ_l independent of l [29,30] as the temperature is lowered and gets very close to T_c, the mode coupling critical temperature [1]. Furthermore, this change of motion is shown to be related to the above-mentioned distributions of τ and β and to the occurrence of metabasin (MB) transitions in the potential energy landscape (PEL) of the considered system as the temperature is lowered [31,32]. Finally, we show that rotational and translational motions of the probe are strongly coupled and have relaxation times that follow the same mode-coupling temperature power law as the melt. Interestingly, while translational relaxation times follow the time-temperature superposition principle (TTSP), the latter is violated in case of rotational motions. We compare our results with other models of molecular glass formers [33–37] and the SM literature [12–15].

We perform molecular dynamics simulations of a coarse-grained model for a melt of 120 bead-spring chains of 10 effective monomers containing a dumbbell as a model for the SM. The dumbell is chosen as a dimer of the polymer model, *i.e.*, we are studying a probe which is larger than the surrounding monomers and larger than the typical intermolecular packing distance in the melt. The interaction between two beads of type A (SM) or B (monomers) is given by the Lennard-Jones potential

$$U_{LJ}(r_{ij}) = 4\epsilon\left[\left(\frac{\sigma_{\alpha\beta}}{r_{ij}}\right)^{12} - \left(\frac{\sigma_{\alpha\beta}}{r_{ij}}\right)^{6}\right], \qquad (2)$$

where r_{ij} is the distance between beads i, j and $\alpha, \beta \in A, B$. The LJ diameters used are $\sigma_{\alpha\beta} = 1$ (unit of length) while $\epsilon = 1$ sets the scale of energy. Since we are in a dense-packed situation of a polymer melt we expect variations in the strength of the unspecific Lennard-Jones interaction to be less important than the packing constraints, and we therefore fixed all ϵ to one. These potentials are truncated at $r_{cut}^{\alpha\beta} = 2^{7/6}\sigma_{\alpha\beta}$ and shifted so that they are zero at $r_{ij} = r_{cut}^{\alpha\beta}$. Between the beads along the chain and those of the dumbbell, a finitely extendable nonlinear elastic (FENE) potential is used

$$U_F = -\frac{k}{2}R_0^2 \ln\left[1 - \left(\frac{r_{ij}}{R_0}\right)^2\right], \qquad (3)$$

with parameters $k = 30$, $R_0 = 1.5$ [38–41]. In the MD simulations, the equations of motion at constant particle number N, volume V and energy E are integrated with the velocity Verlet algorithm [42] (see footnote [1]) with a time step of 0.002, measuring time in units of $(m_B\sigma_{BB}^2/48\epsilon)^{1/2}$. All *NVE* simulations have been performed after equilibrating the system in the *NpT* ($p = 1.0$) ensemble, using a Nosé-Hoover thermostat [42]. These runs lasted up to 5.10^7 MD steps. Ten different configurations were simulated at each temperature, in order to ensure good statistics. The model (without the probe) is known to exhibit

[1]Using OCTA (`http://octa.jp`).

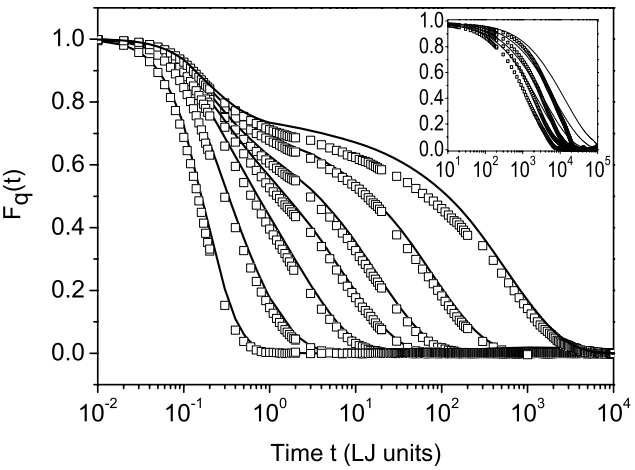

Fig. 1: Incoherent intermediate scattering functions $F_q(t)$ ($q = 6.9$) as a function of time for a dumbbell (symbols) and the surrounding matrix (solid lines) at $T = 0.47, 0.50, 0.55, 0.6, 0.7, 1.0, 2.0$ (from right to left). The insert shows the corresponding $F_q(t)$ ($q = 1.5$) at $T = 0.47, 0.48, 0.49, 0.50$.

all the behavior of real glass-forming polymers [38–41], allowing us to explore the rotational motion of a SM in a realistic model as opposed to those considered previously [18,19].

To check that the dynamics of the dumbbell faithfully mirrors the dynamics of the surrounding matrix, we analyze the self-intermediate scattering function [2]

$$F_q(t) = \left\langle \frac{1}{M}\sum_{i=1}^{M} e^{i\vec{q}\cdot[\vec{r}_i(t) - \vec{r}_i(0)]} \right\rangle, \qquad (4)$$

$\vec{r}_i(t)$ being the position of the ith particle at time t. The sum is extended either over the 2 particles of the dumbbell ($M = 2$), or over all the monomers of the chains ($M = 1200$). Figure 1 shows $F_q(t)$ at the peak position of the static structure factor (wave number $q = 6.9$ [38–41]) for the SM (symbols) and the polymer chains (solid lines).

The relaxation of the dumbbell closely precedes that of the surrounding polymer. In both cases $F_q(t)$ exhibits a two-step process as the temperature is lowered, the so-called β- and α-processes [1]. Due to its reduced connectivity, the relaxation of the dimer is slightly faster but still closely matches that of the surrounding matrix. Remarkable is the observation of a decoupling of the SM and melt dynamics in the intermediate (plateau-like) regime for $T = 0.47$ ($T_c = 0.45$ for the investigated system [38–41], so that $T_c/T = 0.96$). As our system mimics closely experimental ones, the behavior is likely to occur in real systems as well, although it might not be noticeable in a SM experiment due to the fast time scale involved. In the α-relaxation zone, the dynamics of the SM and the melt match again, which is important for the remainder of the paper, concerned primarily with the α-relaxation behavior. $F_q(t)$ describes both rotational and

translation dynamics, especially at $q = 6.9$ (*i.e.* distance between neighboring monomers) where both motions are very interrelated. The insert of fig. 1 shows $F_q(t)$ for $q = 1.5$ where the translational diffusion of the center of mass can be better investigated. As expected, the relaxation of the 10-mers is slower than the SM, in this case. Increasing the mass and the size of the dumbbell, we have checked that its relaxation behavior depends very slightly on these properties (in the case of a larger and more massive SM, $F_q(t)$ of the SM and the polymer chains match better for $q = 1.5$) but is always strongly dominated by the matrix in which it is embedded [32]. This agrees with the experimental findings on the orientational relaxation of large probe molecules in polymer matrices, where a decoupling of the probe reorientation from the structural relaxation of the polymer could only be observed for temperatures below T_c [8,43].

Orientational time correlation functions (OTCFs) are defined as

$$C_l(t) = \langle P_l(\cos(\theta(t)))\rangle, \tag{5}$$

where $\cos(\theta(t)) = \vec{u}(t)\cdot\vec{u}(0)$ and $\vec{u}(t)$ is the unit vector defining the orientation of a linear molecule at time t. $P_l(x)$ are the Legendre polynomials of order l. The linear dichroism d(t) is calculated from the simulations as [25,26]

$$d(t) = 7/8[(\vec{e}_1\cdot\vec{u})^2 - (\vec{e}_2\cdot\vec{u})^2], \tag{6}$$

where $\vec{e}_1$ and $\vec{e}_2$ are unit vectors along the two in-plane orthogonal polarization directions, in case a high numerical aperture objective is used [18,19]. The correlation function $C_d(t)$ of the linear dichroism, defined in this way, has been shown to match $C_2(t)$ in the isotropic case of the melt [25,26]. Figure 2 shows the $C_l(t), l = 1, 2, 4$ of a dumbbell in the polymer melt at temperatures $T = 0.47$, $T = 0.5$ and $T = 0.7$.

For $T = 0.7$, *i.e.* for a slightly under-cooled liquid (the melting point is $T_m = 0.75$ for this system [38–41]), the curves decay essentially but not exactly in a single exponential way, showing already a departure from the rotational diffusion model of Debye [27,28]. For $T = 0.5$ and $T = 0.47$, the curves exhibit a plateau with a height decreasing for increasing l, where the correlations are lost slowly (β process: angular trapping of the dumbbell in the cage of its neighbors), before the final relaxation occurs (α relaxation: escape from the cage). The emergence of the plateau is akin to what is observed for OTCFs in supercooled liquids of rigid A-B dumbbells at low temperatures [33–37]. The long-time decays are well described by stretched exponential functions (eq. (1)), with an exponent $(0 < \beta < 1)$ that decreases with increasing l in the cases of $C_2(t)$ and $C_4(t)$. At all temperatures, the $C_1(t)$ decay exponentially and the $C_d(t)$ and $C_2(t)$ curves superimpose nicely. As also reported in the SM literature [12–15], $C_d(t)$ (fig. 2) becomes extremely non-exponential as the temperature of the system is getting close to the glass-forming region. This observation has been conjectured [18,19] to be related to the dynamic heterogeneity [16,17] of the matrix, by which the SM would probe different local environments as time evolves. Furthermore, the statistical estimation of the errors performed by the Jackknife approach [44] in fig. 2 exemplifies that, from run to run of the simulations, the relaxations times obtained are different, especially for $T = 0.47$, in agreement with reported studies of SM experiments [12–15]. Finally, the facts that i) the ratios of the relaxation times of the various order l of the OCTFs $C_l(t)$ depart from those predicted by the Debye model [27,28] (with $\tau_1/\tau_4 = 10$) to get closer to each other (ideally $\tau_1 \approx \tau_4$), and ii) the stretched exponent β departs significantly from 1, as the temperature gets very close to T_c, indicate the emergence of sudden large angular reorientations [29,30]. The physical picture behind these observations is the trapping of the SM in a well of the effective potential created by the neighboring chains. As the temperature is decreased, the cage around the SM tightens and shallow minima appear in the effective potential created by the surrounding particles, separated by very low-energy barriers. The relaxation times increase as a simple consequence of the decrease of the available kinetic rotational energy (of order kT) with

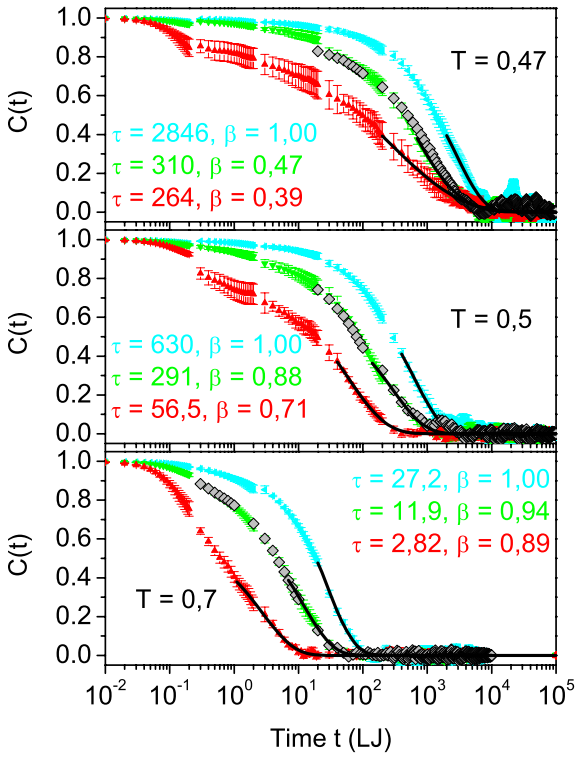

Fig. 2: Orientational time correlation functions $C_l(t)$ of order $l = 1$ (left triangles), 2 (down triangles) and 4 (up triangles) and $C_d(t)$ (diamonds) for the dumbbell in the considered system at temperatures $T = 0.47$, $T = 0.5$ and $T = 0.7$. The error bars are estimated by the Jackknife approach [44]. Black lines are the best stretched exponential fits performed in the α relaxation zone of the decays ($C_l(t) < 0.4$), with τ and β values indicated.

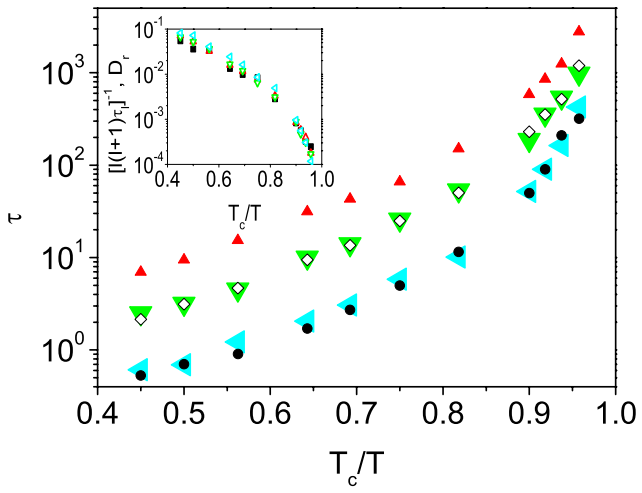

Fig. 3: Angell plot of the relaxation times of $C_1(t)$ (up triangles), $C_2(t)$ (down triangles), $C_4(t)$ (left triangles), $C_d(t)$ (open diamonds) and $F_q(t)$ (circles). Note that in the standard Angell plot, T is normalized by the glass transition temperature T_g, while we normalize T here by the critical temperature of mode-coupling theory. The inset shows the temperature dependence of $[l(l+1)\tau_l]^{-1}, l=1,2,4$ (same symbols as big figure) and of the rotational diffusion coefficient (filled squares).

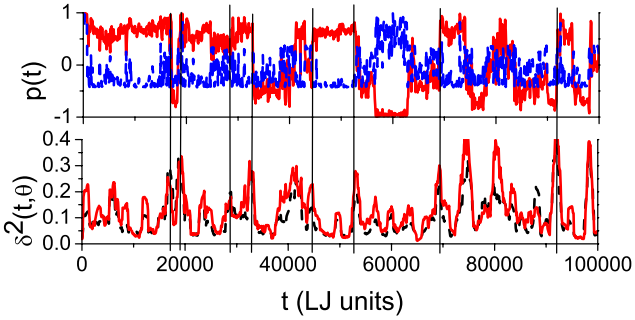

Fig. 4: Up: $P_1(t)$ (solid) and $P_4(t)$ (dashed) trajectories of a SM in the model system at $T_c/T=0.96$. Down: corresponding translational (dashed) and rotational (solid) average square displacements of the SM.

respect to the barrier heights. As the temperature gets close to T_c, the wells of the effective potential become deeper than kT so that, at short times (plateau regime), the SM is trapped in a well of the effective potential. The SM then performs a very restricted diffusion in angular space leading to a long time decay governed by a jump process to other wells. The plateau height decreases by increasing the rank l of the correlators due to their larger sensitivity to small-angle librations. The low l correlators are only sensitive to large angular displacements and are thus affected by an effective time-averaged rotational process, making their decays more exponential.

Figure 3 shows an Angell plot of the rotational relaxation times τ_l, $l=1,2,4$ and τ_d for temperatures ranging from $T=1.0$ to $T=0.47$. [38]).

The τ_l have been defined in an empirical way [38] as the values for which the $C_l(t)$ drop to 0.3. For sake of comparison, we have extracted the translational relaxation times from the intermediate scattering functions $F_q(t)$ (fig. 1) of the dumbbell. The corresponding relaxations times τ are collected in fig. 3. The same Arrhenius behavior is visible for all quantities in a region ranging from $T=1.0$ to $T=0.8$ ($T_c/T=0.45$ to 0.56). At lower temperatures, the apparent activation energy of the various relaxation times increases. This figure exhibits the gradual transition from a rotational-diffusion mechanism with $\tau_1/\tau_4 \propto 10$ at high temperatures to a rotational-jump mechanism (τ_l closer to each other) as the temperature is lowered, due to the physics of the caging process discussed above. For the Debye model one expects $[l(l+1)\tau_l]^{-1}=D_r$ for all l. The inset of fig. 3 shows that these quantities agree qualitatively over the whole temperature range we analyzed. Due to the statistical uncertainties involved in the analysis of single probe molecule trajectories, we can, however, not test this prediction on a quantitative level. Very interestingly, fig. 3 also shows that the relaxation times of $C_2(t)$ and $C_d(t)$, on the one hand, and $C_4(t)$ and $F_q(t)$, on the other hand, are identical over the entire temperature range, indicating that these observables are similarly influenced by the molecular motions of the matrix.

In order to further exhibit which mechanisms lead to the occurrence of the SLARs, we show in fig. 4 the $P_1(t)$ and $P_4(t)$ trajectories of a SM in the deeply super-cooled liquid, at $T=0.47$.

Very remarkably, the two trajectories clearly exhibit jumps in time, with angles changing abruptly and relatively frequently by about 60 deg (at $t=18000$ LJ units for example). This is a clear proof of the observation of SLARs [29,30], whose occurrence causes the relaxation of all OTCFs at the same time. In order to get further information about the nature of these jumps, we performed further calculations of the translational

$$\delta_t^2(t,\xi=100)=\frac{1}{2}\sum_{i=1}^{2}|\vec{r}_i(t)-\vec{r}_i(t+\xi)|^2 \qquad (7)$$

and rotational

$$\delta_r^2(t,\xi=100)=|\vec{\phi}(t)\vec{\phi}(t+\xi)|^2 \qquad (8)$$

average square displacements of the SM in time, *i.e.*, the Einstein formulation of translational and rotational dynamics [33–37]. In this case, the variable $\vec{\phi}(t)$, which is not bounded to the sphere (contrarily to $\theta(t)$) traversed by $\vec{u}(t)$ is defined as

$$\vec{\phi}(t)=\vec{\phi}(0)+\int_0^t \mathrm{d}t'\vec{\omega}(t') \qquad (9)$$

with $\vec{\omega}=\vec{u}(t)\times\dot{\vec{u}}(t)$. Peaks in $\delta_t^2(t,\xi)$ have been shown to correspond to zones of high mobility at a given time and to

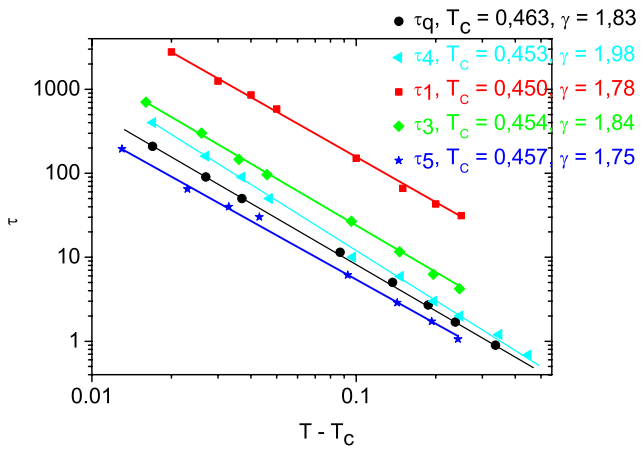

Fig. 5: Log-log plot of the relaxation times from $C_4(t)$ (triangles), $F_q(t)$ (circles), $C_1(t)$ (squares), $C_3(t)$ (diamonds) and $C_5(t)$ (stars) *vs.* $T - T_c$. The parameters T_c and γ obtained from the fits to a power law (see text) are indicated.

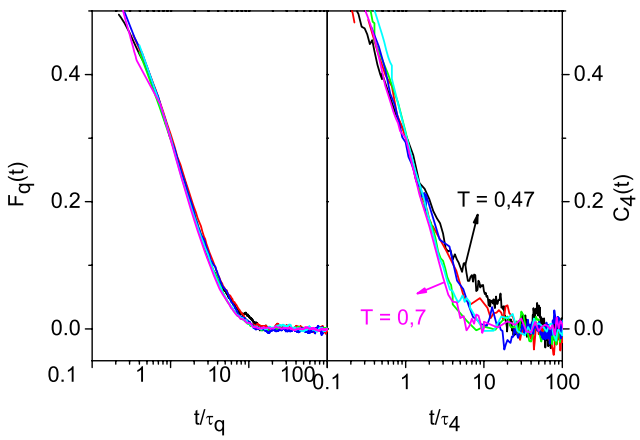

Fig. 6: Time dependence of $F_q(t)$ and $C_4(t)$ for $T = 0.47, 0.49, 0.5, 0.55, 0.6, 0.7$ *vs.* rescaled times t/τ_q and t/τ_4, respectively.

signal MB transitions in the PEL of the investigated glass former [31]. Figure 4 shows that these peaks of $\delta_t^2(t,\xi)$ correlate strongly with the ones of $\delta_r^2(t,\xi)$ and with the SLARs observed in the $P_1(t)$ and $P_4(t)$ trajectories.

The model system without the dumbbell [38–41] exhibits the main features of mode-coupling theory (MCT). To check further whether a SM might provide such information, we plotted the relaxation times of $C_4(t)$ and $F_q(t)$ *vs.* $T - T_c$ in fig. 5.

The τ_4 and $\tau_q(t)$ have been defined in an empirical way [38] as the values for which the $C_4(t)$ and $F_q(t)$ drop to 0.3, respectively. According to MCT, a scaling law

$$\tau_l \propto (T - T_c)^{-\gamma} \tag{10}$$

must hold with the same value of T_c for any relaxation time. Figure 5 shows this plot and the corresponding values of T_c and γ. All obtained values agree with each other and the reported values [38–41] of the model system: $T_c = 0.45 \pm 0.01$ and $\gamma = 1.95 \pm 0.15$ within uncertainties.

The time-temperature superposition principle (TTSP) is another key phenomenological feature of the glass transition. The TTSP holds as long as the underlying relaxation mechanism does not change with temperature. In the case of the exponentially decaying $C_1(t)$ (fig. 2), the TTSP principle obviously holds. Plotting the higher-order $C_l(t)$ *vs.* the rescaled time t/τ_l for all temperatures, we found a discrepancy in the slopes of the curves at $t/\tau_l = 1$ ($C_4(t)$ is shown in fig. 6) and the TTSP fails. Interestingly, and contrary to $C_4(t)$, the TTSP holds for $F_q(t)$ observed at $q = 6.9$ so that, although these correlators have similar relaxation times, their underlying relaxation mechanisms behave differently. This again reflects the transition from rotational diffusion to a SLAR type mechanism, which is observable in the higher-order rotational correlation functions but does not show up in $C_1(t)$ in the same temperature range.

In which way the glass transition of the matrix influences the rotational relaxation of a probe depends somewhat on the details of the model studied. For almost spherical dumbells reorienting in a melt of equal molecules [33,34], it was found that all orientational correlation functions including C_1 exhibited stretching close to T_c, and also a failure of TTSP was reported for all C_l. In these models the reorientational motion of the SM was only weakly coupled to the translational motion of the molecules leading to a breakup of the cage, and reorientation occured through 180° jumps affecting all C_l in the same way. In our case of roughly 60° jumps, C_1 decay involves an averaging over several transitions leading to an exponential decay in our complete temperature window and thus to a validity of TTSP of C_1. The stronger coupling to the matrix also leads to a smaller variation in the γ-exponent of the mode-coupling structural relaxation as compared to the small-dumbell models, where a decoupling of translational and rotational time scales was reported [33,34].

In conclusion, we have shown that for sufficiently large probe molecules the rotational dynamics of a SM is a faithful probe of the glass transition of the surrounding matrix, allowing for a quantitative determination of its mode-coupling critical temperature and exponent parameter. The orientational correlators $C_d(t)$ and $C_2(t)$ of the SM coincide for all temperatures, allowing one to study them both by in-plane and 3D-rotational SM techniques. At temperatures close to T_c, we have clearly evidenced a crossover from a rotational diffusion to a jump-like relaxation. These SLARs of the SM are intimately related to MB transitions in the PEL of the investigated system (fig. 4) and cause the appearance of the stretched exponential decays of the high l $C_l(t)$ correlators shown in fig. 2, clear signatures of the dynamic heterogeneity of the matrix. Furthermore they lead to the departure of the ratios τ_1/τ_l shown in fig. 3 from the ones predicted by the Debye theory. Finally, our findings are similar

(with understandable differences) to the behavior of molecules in glass-forming molecular fluids [33,34], although the surrounding of the probe consists here of rotationally constrained polymer chains. Thus, the violation of the TTSP for the rotational motion (fig. 5) must not be attributed too specifically to the effect of orientational correlations between distinct molecules [33].

* * *

RV thanks the Fonds voor Wetenschappelijk Onderzoek Vlaanderen for a postdoctoral fellowship and a grant for a "study" stay abroad in the group of KB Partial support from Sonderforschungsbereich 625/A3 of the German National Science Foundation and the EU network of excellence SOFTCOMP is also acknowledged.

REFERENCES

[1] Götze W., *J. Phys.: Condens. Matter*, **10** (1999) A1.
[2] Debenedetti P. G., *Metastable Liquids* (Princeton University Press, Princeton) 1997.
[3] Binder K. and Kob W., *Glassy Materials and Disordered solids* (World Scientific, Singapore) 2005.
[4] Dixon P. K., Wu L., Nagel S. R., Williams B. D. and Carini J. P., *Phys. Rev. B*, **42** (1990) 8179.
[5] Dixon P. K., *Phys. Rev. B*, **42** (1990) 8179.
[6] Li G., Du M., Sakai A. and Cummins H. Z., *Phys. Rev. A*, **46** (1992) 3343.
[7] Böhmer R., Diezemann G., Hinze G. and Rössler E., *Prog. Nucl. Magn. Reson. Spectrosc.*, **39** (2001) 191.
[8] Faetti M., Giordano M., Leporini D. and Pardi L., *Macromolecules*, **32** (1999) 1876.
[9] Moerner W. E. and Orrit M., *Science*, **283** (1999) 1670.
[10] Xie X. S. and Trautman J. K., *Annu. Rev. Phys. Chem.*, **49** (1998) 441.
[11] Kulzer F. and Orrit M., *Annu. Rev. Phys. Chem.*, **55** (2004) 585.
[12] Deschenes L. A. and Vanden Bout D. A., *J. Phys. Chem. B*, **106** (2002) 11438.
[13] Tomczak N., Vallée R. A. L., van Dijk E. M. H. P., García-Parajó M., Kuipers L., van Hulst N. F. and Vancso G. J., *Eur. Polym. J.*, **40** (2004) 1001.
[14] Schob A., Cichos F., Schuster J. and von Borczyskowski C., *Eur. Polym. J.*, **40** (2004) 1019.
[15] Mei E., Tang J., Vanderkooi J. M. and Hochstrasser R. M., *J. Am. Chem. Soc.*, **125** (2003) 2730.
[16] Ediger M. D., *Annu. Rev. Phys. Chem.*, **51** (2000) 99.
[17] Richert R., *J. Phys.: Condens. Matter,* (2002) R703.
[18] Hinze G., Diezemann G. and Basché Th. , *Phys. Rev. Lett.*, **93** (2004) 203001.
[19] Wei C.-Y. J., Kim Y. H., Darst R. K., Rossky P. J. and VandenBout D. A., *Phys. Rev. Lett.*, **95** (2005) 173001.
[20] Dickson R. M., Norris D. J. and Moerner, *Phys. Rev. Lett.*, **81** (1998) 5322.
[21] Sick B., Hecht B. and Novotny L., *Phys. Rev. Lett.*, **85** (2000) 4482.
[22] Lieb A., Zavislan J. M. and Novotny L., *J. Opt. Soc. Am. B*, **21** (2004) 1210.
[23] Böhmer M. and Enderlein J., *J. Opt. Soc. Am. B*, **20** (2000) 554.
[24] Uji-i H., Melnikov S., Deres A., Bergamini G., De Schryver F., Herrmann A., Müllen K., Enderlein J. and Hofkens J., *Polymer*, **47** (2006) 2511.
[25] Lu C.-Y. and Vanden Bout D., *J. Chem. Phys.*, **125** (2006) 124701.
[26] Gelin M. F. and Kosov D. S., *J. Chem. Phys.*, **125** (2006) 054708.
[27] Debye P., *Polar Molecules* (Dover, New York) 1929.
[28] Berne B. J. and Pecora R., *Dynamic Light Scattering* (Dover, New York) 1976.
[29] Beevers M. S., Crossley J., Garrington D. C. and Williums G., *J. Chem. Soc., Faraday Trans.*, **2** (1977) 458.
[30] Kivelson D. and Kivelson S. A., *J. Chem. Phys.*, **90** (1989) 4464.
[31] Appignanesi G. A., Rodrigues Fris J. A., Montani R. A. and Kob W., *Phys. Rev. Lett.*, **96** (2006) 057801.
[32] Vallée R. A. L., Van der Auweraer M., Paul W. and Binder K., *Phys. Rev. Lett.*, **97** (2006) 217801.
[33] Kämmerer S., Kob W. and Schilling R., *Phys. Rev. E*, **56** (1997) 5450.
[34] De Michele C. and Leporini D., *Phys. Rev. E*, **63** (2001) 036702.
[35] Kim J. and Keyes T., *J. Chem. Phys.*, **121** (2004) 4237.
[36] Mazza M. G., Giovambattista N., Starr F. C. and Stanley H. E., *Phys. Rev. Lett.*, **96** (2006) 057803.
[37] Lombardo T. G., Debenedetti P. G. and Stillinger F. H., *J. Chem. Phys.*, **125** (2006) 174507.
[38] Bennemann C., Paul W., Binder K. and Dünweg B., *Phys. Rev. E*, **57** (1998) 843.
[39] Buchholz J., Paul W., Varnik F. and Binder K., *J. Chem. Phys.*, **117** (2002) 7364.
[40] Binder K., Baschnagel J. and Paul W., *Prog. Polym. Sci.*, **28** (2003) 115.
[41] Baschnagel J. and Varnik F., *J. Phys.: Condens. Matter*, **17** (2005) R851.
[42] Binder K. and Ciccotti G. (Editors), *Monte Carlo and Molecular Dynamics of Condensed Matter* (Società Italiana di Fisica, Bologna) 1996.
[43] Dhinojwala A., Wong G. K. and Torkelson J. M., *J. Chem. Phys.*, **100** (1994) 6046.
[44] Berg B. A., *Markov Chain Monte Carlo Simulations and Their Statistical Analysis* (World Scientific, Singapore) 2004, p. 103.

Single molecule probing of the glass transition phenomenon: Simulations of several types of probes

R. A. L. Vallée[a)]
Department of Chemistry, Katholieke Universiteit Leuven, 3001 Leuven, Belgium

W. Paul and K. Binder
Department of Physics, Johannes-Gutenberg University, D-55099 Mainz, Germany

(Received 14 August 2007; accepted 12 September 2007; published online 16 October 2007)

Molecular dynamics simulations of a system of short bead-spring chains containing an additional dumbbell are presented and analyzed. This system represents a coarse-grained model for a melt of short, flexible polymers containing fluorescent probe molecules at very dilute concentration. It is shown that such a system is very well suited to study aspects of the glass transition of the undercooled polymer melt via single molecule spectroscopy, which are not easily accessed by other methods. Such aspects include data which can be extracted from a study of fluctuations along a trajectory of the single molecule, probing the rugged energy landscape of the glass-forming liquid and transitions from one metabasin of this energy landscape to the next one. Such an information can be inferred from "distance maps" constructed from trajectories characterizing the translational and orientational motion of the probe. At the same time, determining autocorrelation functions along such trajectories, it is shown for several types of probes (differing in their size and/or mass within reasonable limits) that this time-averaged information of the probe is fully compatible with ensemble averaged information on the relaxation of the glass-forming matrix, accessible from bulk measurements. The analyzed quantities include the fluorescence lifetime, linear dichroism, and also various orientational correlation functions of the probe, in order to provide guidance to experimental work. Similar to earlier findings from simulations of bulk molecular fluids, deviations from the Stokes-Einstein and Stokes-Einstein-Debye relations are observed. © *2007 American Institute of Physics*. [DOI: 10.1063/1.2794334]

I. INTRODUCTION

Understanding the cause for the slowing down of the dynamics in supercooled liquids and the occurrence of the resulting glass transition to an amorphous solid is one of the main challenges of condensed matter physics.[1–6] The various theories that have been put forward to explain the phenomenon have been broadly classified into two categories. Thermodynamic ones describe the observed glass transition as a kinetically controlled manifestation of an underlying quasiequilibrium phase transition between the supercooled metastable fluid and an ideal metastable glass phase.[3,6] Both entropy and free volume theories pertain to this category.[3] According to the nonthermodynamic (kinetic) viewpoint, best represented by mode coupling theory,[2] vitrification occurs as a result of a purely dynamic transition from an ergodic to a nonergodic behavior.[2,3,6] Although recent experimental evidences of spatially heterogeneous dynamics in glass-forming liquids have led to a further understanding of the origin of the slowing-down mechanism,[7–9] no consensus has been reached as to which scenario better describes the glass transition.

Clearly, the analysis of quantities probing dynamical correlations of the glass-forming fluid and its relaxation behavior is crucial for an understanding of these systems.[10–16] In this context, the concept of the potential energy landscape[10] has become increasingly popular, particularly for the analysis of computer simulations.[11–14,17,18] Considering the potential energy as a function of the $3N$ coordinates of the N particles, one can identify local minima (corresponding to the so-called "inherent structures[11]"). At sufficiently low temperatures, e.g., below the critical temperature of mode coupling theory,[2] the system stays for a long time in a "metabasin" comprising a group of such local minima neighboring in phase space,[12] before a transition from one metabasin to the next one can occur. It is tempting to associate such a "barrier hopping" transition in phase space with the rearrangement of a "cooperative region" postulated by Adam and Gibbs[19] to account for the Vogel-Fulcher law[20] describing the rapid increase of the structural relaxation time as the temperature is lowered. However, so far experimental probes have been missing that would be sensitive to individual transitions between such metabasins and hence for real systems, this approach still is of hypothetical character.

Because it allows bypassing the ensemble averaging intrinsic to bulk studies, single molecule spectroscopy (SMS) constitutes a powerful tool to assess the dynamics of heterogeneous materials at the nanoscale level.[21–24] Using two-dimensional (2D) orientation techniques, the in-plane (of the sample) projection of the transition dipole moment of the single molecule (SM) [the so called linear dichroism $d(t)$] has been followed in time and its time correlation function

[a)]Electronic mail: renaud.vallee@chem.kuleuven.be

 © 2007 American Institute of Physics

Downloaded 17 Oct 2007 to 147.210.82.22. Redistribution subject to AIP license or copyright, see http://jcp.aip.org/jcp/copyright.jsp

$C_d(t)$ has been computed and fitted by a stretched exponential function $f(t)=e^{-(t/\tau)^\beta}$.[25–28] These investigations have allowed identifying spatial and temporal heterogeneity in the samples,[8,9] i.e., SMs exhibit τ and β values varying according (i) to their actual position in the matrix and (ii) the time scale at which they are probed, as a result of the presence of different nanoscale environments. More recently, the full three-dimensional (3D) orientation of the emission transition dipole moment of a SM has been recorded as a function of time.[29–32] In particular, the distribution of nanoscale barriers to rotational motion has been assessed by means of SM measurements[33] and related to the spatial heterogeneity and nanoscopic α-relaxation dynamics deep within the glassy state. Owing to the high barriers found in the deep glassy state, only few SMs were able to reorient, while somewhat lower barriers need to be overcome at higher temperature. In a series of works, we have shown that the fluorescence lifetime of single molecules with quantum yield close to unity is highly sensitive to changes in local density occurring in a polymer matrix.[34–41] We have related the lifetime fluctuations to the number of polymer segments involved in a rearrangement cell around the probe molecule as a function of temperature,[34,37] solvent content,[35] and film thickness.[36] Based on a microscopic model for the fluctuations of the local field,[38] we have established a clear correlation between the fluorescence lifetime distributions measured for single molecules and the local polarizability, modeled as a fraction of surrounding holes.[39] By measuring the radiative lifetime of single probes in various molecular weight M_n oligostyrene (OS) matrices at room temperature, we have observed that the mean fraction of holes surrounding the probes is independent of the molecular weight of the polymer in the glassy state while it increases significantly in the supercooled regime.[41] Finally, we have shown that, in the supercooled regime, the fluorescence lifetime trajectories of single probes in an oligo(styrene) matrix exhibit a jump behavior from plateau to plateau and presented simulation results showing that these jumps are correlated with metabasin transitions of the potential energy landscape of the oligomer.[40]

In addition, we recently have pointed out[42] that closely related information can also be extracted from following the rotational motion of single molecules embedded in a polymer melt near the glass transition. However, the question needs to be addressed to what extent these findings depend on the choice of probe molecule, which we will capture by studying different sizes and masses of the probe.

Using molecular dynamic simulations we show that experimental single molecule fluorescence studies allow one to measure time trajectories of well defined observables (fluorescence lifetime, linear dichroism, and other 3D rotational and translational observables) and the corresponding correlation functions very locally, at any position of the polymer matrix occupied by the molecule. The link between dynamic heterogeneities and metabasin transitions in the potential energy landscape of the investigated system can thus be elucidated. Furthermore, an in-depth investigation of the relaxation times extracted from correlation functions of the temporal behavior of the single molecule can shed light on the meaning of the concept of "fragility[13]" and the validity of phenomenological (Vogel-Fulcher,[20] Adam-Gibbs,[19] and free volume[6]) or more microscopic[2] (mode coupling theory, MCT) theories. A link between these theories and the concepts of heterogeneity,[7–9] metabasin transitions,[12] sudden large angular reorientations[44,45] (SLARs), and fragility[43] might then be established. Last but not least, although the choice of the probe is very important on the level of the fluorescence experiment (photostability of the probe, high quantum yield, and rigidity to avoid isomerizations are required) to perform this task, we aim to show that this choice (within certain limits of sizes and masses) barely affects the results of the model system investigation.

The paper is organized in the following way: Sec. II introduces the coarse-grained model used for our molecular dynamics (MD) simulations and briefly recalls some methodological aspects of these simulations. Section III collects our main results, while Sec. IV concludes the paper with a summarizing discussion.

II. METHODS

We performed MD simulations of a system containing 120 bead-spring chains of ten effective monomers. A cubic simulation volume with periodic boundary conditions is used throughout. The interaction between two beads of type A (probe) or B (monomers) is given by the Lennard-Jones potential $U_{\mathrm{LJ}}(r_{ij})=4\epsilon[(\sigma_{\alpha\beta}/r_{ij})^{12}-(\sigma_{\alpha\beta}/r_{ij})^{6}]$, where r_{ij} is the distance between beads i,j and $\alpha,\beta\in A,B$. The LJ diameters used are $\sigma_{AA}=1$ or $\sigma_{AA}=1.22$, $\sigma_{BB}=1.0$ (unit of length), and $\sigma_{AB}=1$ or $\sigma_{AB}=1.11$, while $\epsilon=1$ sets the scale of energy (and temperature T, since Boltzmann's constant $k_B=1$). These potentials are truncated at $r_{\mathrm{cut}}^{\alpha\beta}=2^{7/6}\sigma_{\alpha\beta}$ and shifted so that they are zero at $r_{ij}=r_{\mathrm{cut}}^{\alpha\beta}$. Between the beads along the chain, as well as between the beads of the dumbbell, a finitely extendable nonlinear elastic potential is used $U_F=-(k/2)R_0^2\ln[1-(r_{ij}/R_0)^2]$, with parameters $k=30$ and $R_0=1.5$.[46] This model system (without the probe) has been shown to qualitatively reproduce many features of the relaxation of glass-forming polymers.[46–48] In the case of our fluorescence experiments on probe molecules in oligomers,[40] the system investigated here is also very close to the experimental situation, as the molecular weight of the chosen oligomer corresponds to nine monomers on average. Note that our aim is not a chemically realistic modeling of a particular material, but rather we wish to elucidate the generic behavior of polymer melt plus probe molecule systems. The mass of the beads are $m_B=1$ in the chains and $m_A=1$ or $m_A=2.25$ in the dumbbell. The case of the dumbbell with mass $m_A=2.25$ and size $\sigma_{AA}=1.22$ was chosen in order to fit the experimental conditions for which the Van der Waals volume (mass) of the fluorophore is 3.6 (4.5) times bigger than a monomer of styrene.[40,41] In the MD simulations, the equations of motion at constant particle number N, volume V, and energy E are integrated with the velocity Verlet algorithm[49,50] with a time step of 0.002, measuring time in units of $(m_B\sigma_{BB}^2/48\epsilon)^{1/2}$. All NVE simulations have been performed after equilibrating the system in the NpT ensemble, using a Nosé-Hoover thermostat,[50] keeping the average pressure at $p=1.0$ at all temperatures. These runs lasted up to 5×10^7 MD steps. Ten different configurations

Downloaded 17 Oct 2007 to 147.210.82.22. Redistribution subject to AIP license or copyright, see http://jcp.aip.org/jcp/copyright.jsp

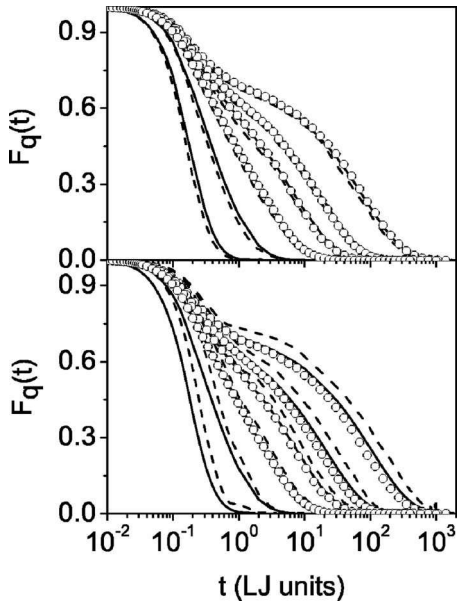

FIG. 1. Self-incoherent scattering functions of the dumbbell (dash), the polymer chains surrounding it (solid), and of the model system simulated in the absence of the probe (open circles). The probe is either a dimer of the surrounding mers ($M=1$, $\sigma=1$, top) or a larger probe ($M=2.25$, $\sigma=1.22$, bottom). $T=0.5$, 0.55, 0.55, 0.6, 0.7, 1.0, and 2.0 from right to left, respectively.

were simulated at each temperature ($T=0.47$, 0.48, 0.49, 0.5, 0.55, 0.6, 0.65, 0.7, 0.8, 0.9, and 1.0), in order to ensure good statistics. Note that the melting temperature of the crystalline phase of this model polymer has been estimated[51] to be $T_m=0.75$, while the critical temperature T_c of mode coupling theory (where in our model a smooth crossover to activated dynamics occurs) is about $T_c=0.45$. Thus, our data include equilibrated melts as well as the moderately supercooled regime.

III. RESULTS

A. Probe and matrix

When dealing with probe techniques, it is important to know how much the probe behavior follows and, thus, can report on the matrix behavior, and how much the latter can be disturbed by the presence of the probe. While this question is very difficult to answer in practice in a real experiment (because only the probe behavior is accessible), all needed details are available in the molecular dynamics simulations of the model system. As such, from the knowledge of the coordinates $\mathbf{r}_i(t)$ of all particles $i=1, M$ at any time t, any observable of interest can be followed in time. For example, by summing only over the two particles of the dumbbell ($M=2$), the intermediate scattering function

$$F_q(t)=\left\langle \frac{1}{M}\sum_{i=1}^{M} e^{i\mathbf{q}\cdot[\mathbf{r}_i(t)-\mathbf{r}_i(0)]} \right\rangle \quad (1)$$

of the probe itself can be calculated. Instead, by summing only over all monomers of the chains ($M=1200$), we get the incoherent scattering function of the surrounding matrix. Figure 1 shows $F_q(t)$ at the peak position of the static structure factor [wavenumber $q=6.9$ for the probe (dashed lines) and the matrix (solid lines) for temperatures ranging from $T=0.48$ to $T=1.0$ (from right to left)].

$F_q(t)$ exhibits a two-step relaxation process as T is lowered, the so-called β and α processes. A probe that has the size and mass of a dimer of the surrounding monomers (Fig. 1, top) relaxes slightly faster than the polymer chains. This is a consequence of the lower connectivity of the beads constituting the dumbbell with respect to that of the polymer chains. On the contrary, a probe that is more massive and slightly larger relaxes more slowly than the polymer in the ballistic regime ($t<0.1$, Fig. 1, bottom). Subsequently, and as T is lowered, the probe stays a bit longer in the plateau regime than the surrounding monomers do. Since the size of the dumbbell in this case (Fig. 1, bottom) is larger than the distance between beads of the polymer, its escape from the cage formed by the neighboring monomers is more difficult and thus takes longer than that of the polymer beads.

In both cases, however, the relaxation of the probe faithfully follows the one of the surrounding chains, making it a good reporter of the matrix. To test how much the probe disturbs the surrounding matrix, we also compared our results to those of the analogous system without dumbbell (open circles in Fig. 1).[46] Clearly, in the case where the probe is a dimer of the surrounding monomers (Fig. 1, top), the relaxations of the model system and of our system (not summing on the beads of the dumbbell) perfectly mirror each other. In the case of a more massive and larger probe, our system is only slightly perturbed by the presence of the probe: at low temperatures, our system relaxes slightly slower than the model system. Of course this conclusion depends on the choice of simulation volume (dilution of the probe), but with our choice of system size we can establish that there is some small effect of the dumbbell on the relaxation of the surrounding matrix, while the system is still large enough that this perturbation is not self-interacting through the periodic boundary conditions.

B. Probe: Single molecule lifetime trajectories

Experimentally, fluorescence lifetime time trajectories of single molecules exhibit fluctuations that reflect local density fluctuations of the surrounding polymer matrix.[40,41] The basic explanation for the observed behavior is the following: After photoexcitation, the probe relaxes to its ground state by spontaneous emission of a photon. In vacuum, the spontaneous emission rate Γ_{r0} of this single emitter is given by $\Gamma_{r0}=4/3(|\boldsymbol{\mu}_{eg}|^2/4\pi\epsilon_0\hbar)(\omega_{eg}/c)^3$, where $\boldsymbol{\mu}_{eg}$ and ω_{eg} are the transition dipole moment and the transition frequency of the emitter, ϵ_0 is the dielectric permittivity of vacuum, $\hbar$ is the reduced Planck constant, and c is the speed of light in vacuum. However, the spontaneous emission rate Γ_{r0} and its reciprocal, the spontaneous lifetime τ_0, are modified by the dielectric properties of the medium in which the emitter is embedded. In a transparent medium of refractive index n, the spontaneous emission writes, following simple renormalization of both the dielectric permittivity and the speed of light, $\Gamma_r=n\Gamma_{r0}$. Furthermore, taking into account the local field effects that relate the macroscopic electric field to the local microscopic electric field associated with the photon emitted

Downloaded 17 Oct 2007 to 147.210.82.22. Redistribution subject to AIP license or copyright, see http://jcp.aip.org/jcp/copyright.jsp

by the probe (electric field generated by the transition dipole moment of the emitter), Lorentz has shown that, in the case of a cubic arrangement of identical molecules, the spontaneous emission rate writes $\Gamma_r = nL_L^2\Gamma_{r0}$, where $L_L=(\epsilon+2)/3$ is the so-called Lorentz field factor.[54] However, for the complex system we are investigating in this paper, the Lorentz model does not strictly apply: Locally, within the Lorentz sphere, we have to account for the different microscopic "dielectric" and geometric properties of the single emitter with respect to its direct environment, which is a disordered system. In fact, the electric field associated to the photon spontaneously emitted by the probe polarizes its surrounding and thus induces dipole moments $\boldsymbol{\mu}_k$ on the surrounding monomer units. The observed emission consequently originates from an effective transition dipole moment $\boldsymbol{\mu}_{\text{tot}}$, which is the sum of the molecular emission transition dipole moment (source dipole) $\boldsymbol{\mu}$ and of the dipoles $\boldsymbol{\mu}_k$ induced in the medium surrounding the probe,

$$\boldsymbol{\mu}_{\text{tot}} = \boldsymbol{\mu} + \sum_k \boldsymbol{\mu}_k. \tag{2}$$

In the highly symmetric arrangement considered by Lorentz, $\Sigma_k \boldsymbol{\mu}_k = 0$, so that $\boldsymbol{\mu}_{\text{tot}} = \boldsymbol{\mu}$. However, in the case of a single emitter embedded in a disordered matrix, the spontaneous emission rate must be corrected by the factor $\hat{L}^2 = |\boldsymbol{\mu}_{\text{tot}}|^2/|\boldsymbol{\mu}|^2$, such that $\Gamma_r = nL_L^2\hat{L}^2\Gamma_{r0}$.[38] This last factor, correcting the Lorentz local field factor and taking into account the disordered nature of our system, is the crucial parameter to be determined in our simulations.

Accordingly, we express the radiative lifetime of a probe with quantum yield very close to 1 as $\tau = |\boldsymbol{\mu}|^2/|\boldsymbol{\mu}_{\text{tot}}|^2$. As just shown, it crucially depends on the positions and polarizabilities of the dye and the surrounding monomers (OS monomers in our experiments[40,41]).

Through our molecular dynamic simulations, combined with quantum chemistry calculations, we could calculate this observable as a function of time. Here are the main steps involved in the evaluation of this microscopic model, which allows us to assess the simulated lifetime trajectories of the system under investigation. (i) We used the Hartree-Fock semiempirical Austin Model 1 (AM1) technique[52] to assess the geometric and electronic structures of the BODIPY probe molecule[53] in both the S_0 singlet ground state and the S_1 lowest singlet excited state.[41] Frequency calculations were performed to validate the existence of the recovered local minima.[55] The excited-state properties of the molecule were determined by INDO/SCI calculations[56] on the basis of the AM1 excited-state geometries. The transition dipole moment $|\boldsymbol{\mu}| = 3.8\times10^{-29}$ C m and the polarizability $\chi = 5.7\times10^{-39}$ C^2 m^2 J^{-1} were estimated for the probe molecule. Similar calculations performed for the styrene unit lead to a polarizability $\alpha = 1.0\times10^{-39}$ C^2 m^2 J^{-1}. (ii) To calculate the effective transition dipole of the probe, we have solved the system of coupled linear equations,

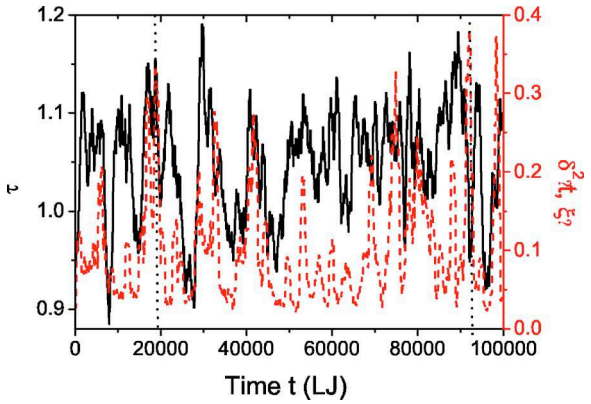

FIG. 2. (Color online) Reduced radiative lifetime $\tau(t)$ (full curves, left ordinate scale) and translational average square displacement $\delta^2(t,\xi)$ (broken curve, right ordinate scale), $\xi=100$ trajectories of a probe ($M=1$, $\sigma=1$) in a polymer matrix for $T=0.47$.

$$\boldsymbol{\mu}_k = \alpha_k \left[\mathbf{E}(\mathbf{r}_k) + \sum_{j=1}^{N} T_{kj}\boldsymbol{\mu}_j \right], \tag{3}$$

where $\mathbf{E}(\mathbf{r}_k)$ is the electric field generated by the source dipole $\boldsymbol{\mu}$ (dumbbell) on the kth monomer and $T_{kj} = (1/r_{kj}^3)(\delta_{kj} - 3\mathbf{r}_{kj}\mathbf{r}_{kj}/r_{kj}^2)$ is the dipole-dipole interaction tensor between monomers at positions $\mathbf{r}_k, \mathbf{r}_j$ ($\mathbf{r}_{kj} = \mathbf{r}_k - \mathbf{r}_j$). From the total transition dipole moment thus obtained (Eq. (2)), the lifetime is estimated as (in adimensional units)

$$\tau = \frac{|\boldsymbol{\mu}|^2}{|\boldsymbol{\mu}_{\text{tot}}|^2}. \tag{4}$$

(iii) The lifetime trajectory is then obtained by evaluating these relations for all configurations of the time trajectory generated in the simulation.

Figure 2 shows an example of a reduced radiative lifetime trajectory $\tau(t)$ (straight line) obtained in this way for a small probe $M=1$, $\sigma=1$ embedded in the supercooled matrix at a temperature $T=0.47$. This trajectory exhibits a hopping behavior similar to the experiment, with the lifetime fluctuating around a mean value at a given plateau, prior to a jump to another plateau value.[40] The time scale on which this hopping mechanism occurs is typically a few thousands LJ time units at this temperature. Recently, we have shown[40] that these jumps in lifetime for a larger and more massive probe $M=2.25$, $\sigma=1.22$ embedded in the oligomer matrix signal metabasin (MB) transitions in the potential energy landscape (PEL) of the medium. Here, we show that this finding is the same for the probe giving rise to Fig. 2.

To identify MBs in the system, we have calculated the "distance matrix" (DM),[18]

$$\Delta_t^2(t',t'') = \frac{1}{2}\sum_{i=1}^{2} |\mathbf{r}_i(t') - \mathbf{r}_i(t'')|^2, \tag{5}$$

which describes the average translational square displacement of the probe in the time interval starting at t' and ending at t''. Figure 3 (top) shows the DM corresponding to the small probe in the oligomer matrix at a temperature $T=0.47$, i.e., the system giving rise to the radiative lifetime trajectory of Fig. 2. The figure clearly reveals the dynamic

Downloaded 17 Oct 2007 to 147.210.82.22. Redistribution subject to AIP license or copyright, see http://jcp.aip.org/jcp/copyright.jsp

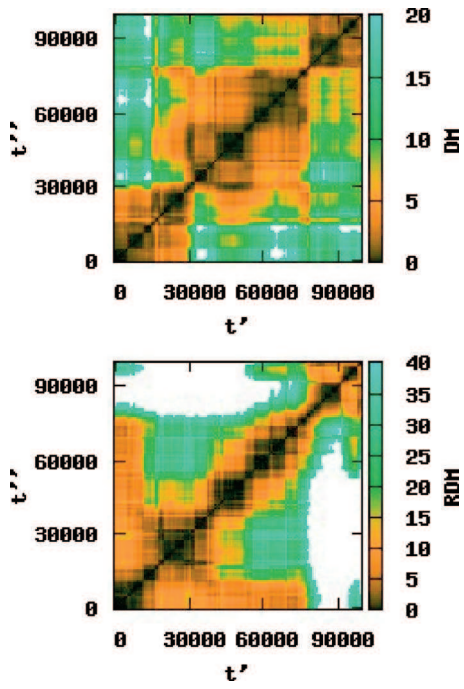

FIG. 3. (Color) Distance matrix for translational DM $[\Delta_t^2(t',t'')]$ (top) and rotational RDM $[\Delta_r^2(t',t'')]$ (bottom) diffusion of a single probe ($M=1$, $\sigma=1$, cf. Fig. 2) in the considered system at temperature $T=0.47$. The gray scale indicates the values of $\Delta^2(t',t'')$ (color online).

heterogeneity of the system, the probe staying relatively long in one dark squarelike region (where the DM is close to zero) prior to suddenly moving to another such region. These dark squarelike regions are the MBs of the PEL where the system remains within a certain region of its multi dimensional configuration space. The crossings (much brighter points where the DM gets positive) between the successive dark squarelike regions signal the MB transitions in the PEL. As Appignanesi *et al.* showed,[18] these crossings correspond to times of larger mobility of the particles constituting the system. In our case, these crossings correspond simply to times of higher translational mobility of the probe itself, of course, highly correlated to the one of the matrix (Fig. 1).

In order to establish the correlation between the translational mobility of the probe (driven by the motions of surrounding medium) and the radiative lifetime of the probe, we have calculated the translational average square displacement of the probe $\delta^2(t,\xi)=\Delta^2(t,t+\xi)$ within a time interval $\xi=100$. This function is shown in Fig. 2 (dashed curve) as well. Clearly, each maximum of this function, which signals a period of high mobility of the probe, coincides with a jump of the radiative lifetime. In other words, the jumps of the radiative lifetime trajectory of a probe in the system signal MB transitions in the PEL of the considered system as well as the maxima of the function $\delta^2(t,\xi)$ do.

C. Probe: Single molecule rotational trajectories

Besides measurements of the fluorescence lifetime and, thus, acquisition of the lifetime time trajectories, SMS also allows one to measure the rotational motion of the probes. In most SM studies, the in-plane projection of the SM emission intensity I along two mutually perpendicular (I_p and I_s) polarization directions in the plane of the sample is recorded in order to calculate the reduced linear dichroism trajectory,[25,26]

$$d(t)=\frac{I_p-I_s}{I_p+I_s}. \tag{6}$$

Recently, owing to the development of 3D-orientation techniques,[29–32] the 3D orientation of the emission dipole moment has been recorded as a function of time. This technique, in principle, allows for a calculation of all order l Legendre polynomials $P_l(\cos(\theta(t)))$, with

$$\cos(\theta(t))=\mathbf{u}(t)\cdot\mathbf{u}(0), \tag{7}$$

where $\mathbf{u}(t)$ is the unit vector defining the orientation of a linear molecule at time t.[57] Such a determination of the various $P_l(t)$ is interesting since it allows to characterize the type of motion performed by a probe in an oligomer matrix. In the framework of the Debye model for rotational diffusion,[58] the various orientational time correlation functions (OTCFs),

$$C_l(t)=\langle P_l(\cos(\theta(t)))\rangle \tag{8}$$

are predicted to decay exponentially and the relaxation times to scale as

$$\frac{\tau_l}{\tau_m}=\frac{m(m+1)}{l(l+1)}, \tag{9}$$

where τ_l being the orientational correlation time corresponding to $C_l(t)$. By enabling one to investigate high order $l>1$ OTCFs, the 3D technique reduces significantly the time scale on which the orientational relaxation of the probe molecule has to be followed ($\tau_1/\tau_4=10$) and, thus, insures that good statistics can be obtained for the $C_l(t)$, $l>1$ from a finite trajectory length.[57] This property largely compensates the drawback of the 3D orientation technique, namely, that many more photons (high excitation intensity) are needed as compared to the in-plane projection technique to insure good signal-to-noise ratio, taking into account that the duration of SM measurements is limited due to irreversible photobleaching. The previous argument is limited to the range of validity of the rotational-diffusion model. If this model does not apply, the 3D-imaging technique further allows one to distinguish between various models of rotational motion: Contrary to the rotational-diffusion model, the rotational-jump model predicts the various τ_l to be independent of l.[44,45] The emergence of hopping involving large angular jumps (SLARs) is often put forward to explain the breakdown of the Debye model, which requires small-angle rotational Brownian motion as the underlying motion mechanism:[45] A large jump may lead to the decay of all OTCFs $C_l(t)$ at the same time, so that the correlation times are equal and correspond to the waiting time for this large jump to occur.

Figure 4 shows the $P_1(t)$ and $P_4(t)$ trajectories of a large probe $M=1$, $\sigma=1.22$ at $T=0.47$, i.e., in the deeply supercooled liquid and at $T=0.7$, i.e., in the liquid near the melting temperature. Very remarkably, at $T=0.47$, the two trajectories clearly exhibit jumps in time, with angles changing abruptly and relatively frequently by about 60°. At the high temperature, the $P_1(t)$ and $P_4(t)$ trajectories evolve smoothly in time, the molecules rotating rather continuously, in a way

Downloaded 17 Oct 2007 to 147.210.82.22. Redistribution subject to AIP license or copyright, see http://jcp.aip.org/jcp/copyright.jsp

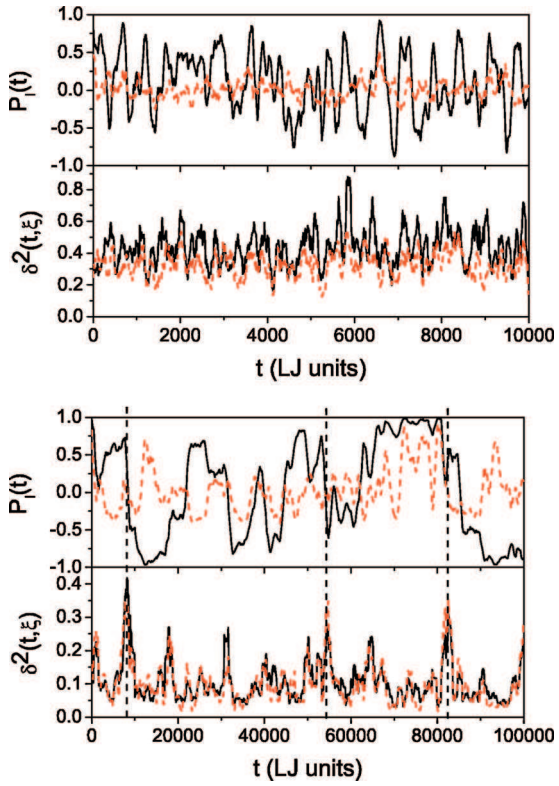

FIG. 4. (Color) Legendre polynomials $P_1(t)$ (solid) and $P_4(t)$ (dashed) trajectories of a probe ($M=1$, $\sigma=1.22$) in a polymer matrix for $T=0.7$ (top) and $T=0.47$ (bottom). Corresponding translational $\delta_t^2(t,\xi)$ (solid) and rotational $\delta_r^2(t,\xi)$ (dashed) average square displacement trajectories ($\xi=100$ in the case of the probe in the system at $T=0.47$ and $\xi=10$ for $T=0.7$).

compatible with the Debye[58] description. At $T=0.47$ on the contrary, the figure clearly shows the occurrence of SLARs manifesting themselves in the various order orientational autocorrelation functions. This is a clear signature of a non-Debye behavior, expected to occur at this temperature. Recently,[42] we have shown for small probes $M=1$, $\sigma=1$ embedded in the system, that these jumps also signal metabasin transitions in the potential energy landscape of the considered system. In order to show this as well for the larger probe considered here, we have calculated the rotational average square displacements of the probe in time, i.e.,

$$\delta_r^2(t,\xi=100)=|\boldsymbol{\phi}(t)\boldsymbol{\phi}(t+\xi)|^2. \tag{10}$$

In this Einstein formulation of rotational dynamics, the variable $\boldsymbol{\phi}(t)$, which is not bounded to the sphere [contrarily to $\theta(t)$] traversed by $\mathbf{u}(t)$, is defined as

$$\boldsymbol{\phi}(t)=\boldsymbol{\phi}(0)+\int_0^t dt'\,\boldsymbol{\omega}(t') \tag{11}$$

with $\boldsymbol{\omega}=\mathbf{u}(t)\times\dot{\mathbf{u}}(t)$.

We have shown here in Fig. 2 for a different probe geometry as reported on earlier[40] that peaks in the distance traversed within a time interval ξ at time t $[\delta_t^2(t,\xi)]$ correspond to zones of high mobility at that time and thus signal MB transitions in the PEL of the investigated glass former. Figure 4 shows that these maxima of the function $\delta_t^2(t,\xi)$ correlate strongly with the ones of $\delta_r^2(t,\xi)$ (lower part, bottom) and with the SLARs observed in the $P_1(t)$ and $P_4(t)$ trajectories (lower part, top). A probe molecule embedded in the system at $T=0.7$ clearly exhibits larger translational and rotational average square displacements (Fig. 4, upper part, bottom) on an even shorter time scale ($\xi=10$ in the case of the system at $T=0.7$), as expected for a system with larger mobility. As such, we have now identified three observables which are in principle experimentally accessible by the SMS techniques that allow identification of metabasin transitions and thus provide microscopic details of motions potentially responsible for the occurrence of the glass transition phenomenon in real systems.

In Fig. 3 (bottom), we have also illustrated the occurrence of such MB transitions in the PEL of the considered system, as probed by the rotational motion of a single molecule, by using the rotational displacement matrix (RDM), defined as the rotational displacement of the probe between times t' and t'',

$$\Delta_r^2(t',t'')=|\boldsymbol{\phi}(t')\boldsymbol{\phi}(t'')|^2. \tag{12}$$

While probing different observables, coupling differently to the variables of the multidimensional space, the plots in Fig. 3 clearly exhibit similarities with most MBs and MB transitions recognizable at the same positions (times) for the two graphs.

D. Probe: Correlations functions of the various trajectories

From the fluorescence (radiative) lifetime trajectories $\tau(t)$ (Fig. 2) and the various order l rotational trajectories $P_l(t)$ (Fig. 4), we construct the time (auto)correlation functions $C_f(t)=\langle\tau(t)\rangle$ and $C_l(t)=\langle P_l(\cos(\theta(t)))\rangle$ and extract the characteristic relaxation times τ_f and τ_l of these observables. Of interest in this respect is to determine also the autocorrelation function $C_d(t)$ of the linear dichroism trajectory $d(t)$, which can readily be obtained experimentally by using standard 2D techniques. $C_d(t)$ has been shown[59] to have, in the melt phase, a relaxation behavior identical to SM OTCF of the second rank $C_2(t)$, provided that one uses a high numerical aperture NA>1.2 in the microscope to focus the excitation beam in and collect the fluorescence signal out of the sample.[59–61] As such, the relaxation time τ_d of this function $C_d(t)$ is expected to be equal to τ_2 in the melt phase. Assuming the above mentioned conditions of the use of a high NA aperture in the fluorescence experiment and of a system in the isotropic melt phase, the linear dichroism trajectory can be extracted from the successive frames of the molecular dynamics simulations as[59]

$$d(t)=7/8[(\mathbf{e}_1\cdot\mathbf{u})^2-(\mathbf{e}_2\cdot\mathbf{u})^2], \tag{13}$$

where $\mathbf{e}_1$ and $\mathbf{e}_2$ are unit vectors along the two in-plane orthogonal polarization directions of the sample. Experimentally, the plane of the sample is perfectly well defined by the way it is posed on the microscope. Numerically, we define such a plane by choosing rather arbitrarily two directions in the simulation box.

Figures 5 and 6 exhibit the relaxation behavior $C_f(t)$ of the radiative lifetime observable. For both figures, the relaxation curves exhibit a two-step behavior in the supercooled

Downloaded 17 Oct 2007 to 147.210.82.22. Redistribution subject to AIP license or copyright, see http://jcp.aip.org/jcp/copyright.jsp

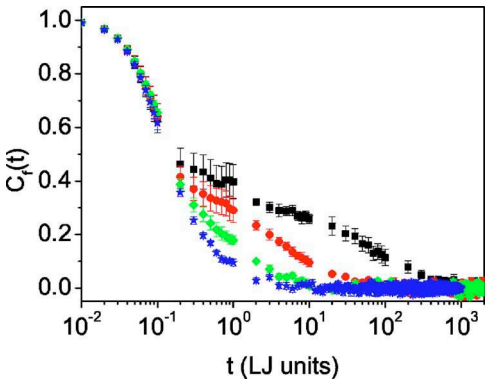

FIG. 5. (Color online) Fluorescence lifetime time correlation functions $C_f(t)$ for the dumbbell ($M=1$, $\sigma=1$) in the considered system at temperatures $T=0.48$ (squares), $T=0.55$ (circles), $T=0.7$ (diamonds) and $T=1.0$ (stars). The error bars are estimated by the Jackknife approach (Refs. 63 and 64).

regime [for a temperature $T<0.7$, the melting point in this system being $T_m=0.75$ (Ref. 51)] reminiscent of the one observed in the self-intermediate scattering functions $F_q(t)$ shown in Fig. 1. So, the radiative lifetime observable would, *a priori*, allow one to identify the β (caging) and α (escaping of the cage) regimes predicted by MCT.[2] A noticeable difference between the two sets of curves is that the plateau height is lower in the case of $C_f(t)$ than $F_q(t)$, $q=6.9$, suggesting that the former probes higher q modes than the latter. The theoretical description of the effects of local polarizability around the probe, briefly developed here above but fully explained in Ref. 8, indeed shows that the radiative lifetime is extremely sensitive to changes of polarizability and motion of monomers directly surrounding the probe, and much less sensitive to the modifications of more external shells. Experimentally, the observation of the β regime (subnanosecond time regime) by SMS is virtually hindered because of the binning time of minimum of 20–50 ms required to record a fluorescence decay profile with sufficient statistics in order to fit it adequately.[41] Only the α regime is thus possibly observable by SMS. In the remainder of this paper, we will focus the discussion on this regime only with the aim to provide guidance for the interpretation of SMS experiments.

Figure 5 shows the emergence of the plateau in the autocorrelation function of the fluorescence lifetime in the supercooled regime and the final relaxation (α relaxation) exhibited by a small probe $M=1$, $\sigma=1$ in the system. As the temperature of the system is decreased, the plateau regime extends longer and longer as does the following α relaxation. In this graph and the following ones, each correlation function is not computed only from one probe trajectory but results from an averaging process over ten different molecular dynamics runs of the identical system. We found that from run to run the results could be quite different (as in a single molecule experiment) since each individual probe in a simulation box performs a unique stochastic time trajectory. In order to take into account this disparity of the individual trajectories, we have performed an estimation of the variance by using the Jackknife approach. This statistical procedure, in its simplest form, allows one to make estimates of a parameter based on a set of N observations by deleting each observation in turn, to obtain, in addition to the usual estimate based on N observations, N estimates each based on $N-1$ observations. Combinations of these give estimates of both bias and variance in complicated situations. The method does not need to make any assumptions on the underlying distribution, resulting in greater reliability in practice. An elementary review can be found in Ref. 63 and the extension of such methods to time series analysis is reviewed by Thomson and Chave.[64] Figure 5 clearly exhibits that this variance is relatively small in the α relaxation regime, allowing us to presuppose that experimentally measured systems, if identical, might present well defined curves with a minimum variance as the number of measured probes is increased (usually a minimum of 100 molecules are measured in a given system in a SM fluorescence experiment[40]). If this is not the case, i.e., if the variance of such curves is relatively high even after recording 100 SM trajectories, the analysis performed here would allow one to make an estimation of the heterogeneity of the sample.

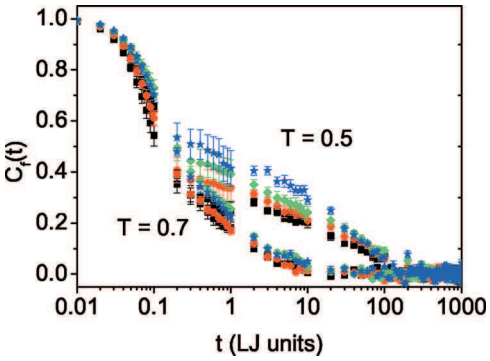

FIG. 6. (Color) Fluorescence lifetime time correlation functions $C_f(t)$ for the small ($M=1$, $\sigma=1$, squares; $M=2.25$, $\sigma=1$, circles) or large ($M=1$, $\sigma=1.22$, diamonds; $M=2.25$, $\sigma=1.22$, stars) dumbbell in the considered system for two temperatures: $T=0.5$ and $T=0.7$. The error bars are estimated by the Jackknife approach (Refs. 63 and 64).

By increasing the size and/or mass of the probe, we expect the probe molecule to become more inert and, as such, to observe a slower decay of the function $C_f(t)$, i.e., an increase of the correlation time τ_f. Figure 6 exhibits this behavior for two different temperatures $T=0.5$ and $T=0.7$ and four types of probes: small and light $M=1$, $\sigma=1$; small and heavy $M=2.25$, $\sigma=1$; large and light $M=1$, $\sigma=1.22$; and large and heavy $M=2.25$, $\sigma=1.22$. As can be seen in this figure, changing the mass of the probe does not affect much the time scale of the relaxation behavior, while changing the length of the probe clearly increases the relaxation time. This effect is more pronounced in the deeply supercooled regime $T=0.5$, where the caging process plays an important role on the final relaxation. Also, the height of the plateau of the curves at $T=0.5$ is higher for large probes than for small probes, indicating the reduced vibrational contribution to the relaxation of the surrounding matrix at the lower temperature.

With the SMS we can also use the OTCFs of the probe to obtain information concerning the relaxation behavior of the polymer matrix around the probe. Figure 7 shows the $C_l(t)$, $l=1$, 2, and 4 and $C_d(t)$ of a large and heavy dumbbell $M=2.25$, $\sigma=1.22$ in the polymer melt at temperatures $T=0.48$, $T=0.6$, and $T=0.7$. For $T=0.7$, i.e., for a slightly su-

Downloaded 17 Oct 2007 to 147.210.82.22. Redistribution subject to AIP license or copyright, see http://jcp.aip.org/jcp/copyright.jsp

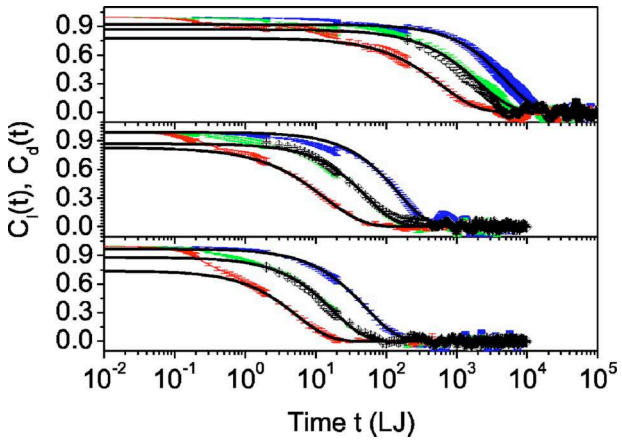

FIG. 7. (Color online) Orientational time correlation functions $C_l(t)$ of order $l=1$ (solid), 2 (dash), and 4 (dot) and $C_d(t)$ (open diamonds) for the dumbbell ($M=2.25$, $\sigma=1.22$) in the considered system at temperatures $T=0.48$ (top), $T=0.6$ (middle) and $T=0.7$ (bottom). The error bars are estimated by the Jackknife approach (Refs. 63 and 64). Black lines are the best stretched exponential fits performed in the α relaxation zone of the decays ($C_l(t)<0.6$), with τ and β values given in Table I.

percooled liquid, the curves decay essentially but not exactly in a single exponential way, showing already a departure from the rotational-diffusion model of Debye.[58] For $T=0.6$ and $T=0.48$, the curves for $C_2(t)$ and $C_4(t)$ exhibit a plateau with a height decreasing for increasing l, where the correlations are lost slowly (β process: angular trapping of the dumbbell in the cage of its neighbors), before the final relaxation occurs (α relaxation: escape from the cage). The emergence of the plateau is akin to what is observed for the self-incoherent scattering functions $F_q(t)$ (Fig. 2) and radiative lifetime autocorrelation functions $C_f(t)$ (Fig. 5). The long time decays are well described by stretched exponential functions (KWW) $f(t)=Ae^{-(t/\tau)^\beta}$ (see Table I), with an exponent $(0<\beta<1)$ that decreases with increasing l in the case of $C_2(t)$ and $C_4(t)$.

Let us note here that building a correlation function and fitting it by a stretched exponential function in the α relaxation regime are delicate matters. Performing these without caution may lead to significant errors in the determination of τ and β. Indeed, as already reported elsewhere,[57] correlation functions obtained from time trajectories of length less than 100 times the correlation time constant τ_l exhibit significant deviations from the "true" correlation function, leading to a "false" determination of τ and β values. Furthermore, if the range of values used to perform the fit spans less than a decade in time, significant errors also occur in the determination of the τ and β. In order to show the occurrence of such errors in a quantitative way, on the base of our simulation results, we have reported in Table I the amplitudes A, relaxation times τ, and stretching parameters β of the OTCFs $C_l(t)$ for $l=1$, 2, and 4 at various temperatures $T=0.47$, 0.48, 0.5, 0.6, and 0.7 for the large and heavy dumbbell $M=2.25$, $\sigma=1.22$ in the considered system. Also, the estimated errors $\Delta\tau$ and $\Delta\beta$ are indicated. In all cases, we have fitted the curves by using a Levenberg-Marquadt algorithm with a least squares minimization method. Let us recall that our curves (Fig. 7) have been averaged on ten simulation runs and that the error bars, determined by the Jackknife method, have been used in the fitting procedure, increasing the reliability of our results with respect to a single molecule experiment. For each temperature and order l of the correlation functions, we have considered three starting points in the fits: we have started the fits at $C_l=0.6$, (0.5), and [0.4], respectively, reducing the time range available for the fit progressively. The quality of each fit has been judged on the base of the usual χ^2 criterion. For each temperature and each order l of the correlation function, Table I clearly exhibits the increased error ($\Delta\tau$ and $\Delta\beta$) obtained in the determination of

TABLE I. Amplitudes, relaxation times τ, and stretching parameters β of the OTCFs $C_l(t)$ for $l=1$, 2, and 4 at various temperatures for the large and heavy dumbbell $M=2.25$, $\sigma=1.22$, determined by fitting the KWW function $Ae^{-(t/\tau)^\beta}$ to the curves in the α relaxation zone. Three values are indicated in most columns for each line, which concern fits starting at $C_l=0.6$, (0.5), and [0.4], respectively. In each case, the amplitude has only been given for the best fit (shown on Fig. 7). The errors determined by the fitting procedure, using a Levenberg-Marquadt algorithm with a least square minimization method, are also indicated for $\tau:\Delta\tau$ and $\beta:\Delta\beta$. The quality of the fits has been judged on the base on the usual χ^2 criterion.

			$f(t)=Ae^{-(t/\tau)^\beta}$				
T	l	A	τ	$\Delta\tau$	β	$\Delta\beta$	χ^2
0.47	1	1	6505 (6515) [6284]	682 (1542) [4156]	1 (1) [1]	0.1 (0.2) [0.46]	0.97 (0.95) [0.92]
	2	0.97	2639 (2607) [3636]	120 (262) [380]	0.81 (0.80) [1]	0.03 (0.05) [0.09]	0.998 (0.996) [0.994]
	4	0.8	1119 (1434) [1741]	50 (69) [72]	0.7 (0.82) [0.94]	0.02 (0.03) [0.03]	0.998 (0.998) [0.998]
0.48	1	0.92	4929 (4832) [4684]	216 (415) [789]	1 (1) [1]	0.04 (0.07) [0.12]	0.993 (0.987) [0.980]
	2	0.87	2004 (2468) [2481]	140 (261) [421]	0.88 (1) [1]	0.04 (0.08) [0.12]	0.989 (0.977) [0.965]
	4	0.78	602 (665) [444]	40 (58) [195]	0.84 (0.91) [0.72]	0.05 (0.07) [0.16]	0.996 (0.995) [0.990]
0.5	1	1	1453 (1449) [1426]	187 (456) [1240]	1 (1) [1]	0.14 (0.28) [0.65]	0.989 (0.977) [0.956]
	2	0.86	591 (600) [600]	15 (30) [55]	0.99 (1) [1]	0.03 (0.05) [0.07]	0.999 (0.998) [0.999]
	4	0.67	239 (222) [185]	6 (14) [40]	0.94 (0.86) [0.76]	0.04 (0.06) [0.1]	0.995 (0.995) [0.995]
0.6	1	0.99	145 (145) [143]	14 (33) [101]	1 (1) [1]	0.11 (0.21) [0.54]	0.993 (0.990) [0.977]
	2	0.87	52 (45) [46]	4 (7) [11]	1 (0.93) [0.95]	0.09 (0.11) [0.17]	0.995 (0.996) [0.994]
	4	0.83	13.4 (13.7) [17]	0.9 (1.9) [3]	0.8 (0.83) [0.95]	0.05 (0.08) [0.14]	0.997 (0.994) [0.990]
0.7	1	0.97	51 (49) [50]	2 (5) [10]	0.95 (0.93) [0.93]	0.04 (0.07) [0.12]	0.999 (0.998) [0.996]
	2	0.88	17.5 (19) [19]	0.6 (1) [3]	0.96 (1) [1]	0.03 (0.04) [0.09]	0.999 (0.999) [0.998]
	4	0.74	5.4 (5.9) [6]	0.3 (0.4) [0.7]	0.93 (1) [1]	0.05 (0.06) [0.1]	0.997 (0.997) [0.994]

Downloaded 17 Oct 2007 to 147.210.82.22. Redistribution subject to AIP license or copyright, see http://jcp.aip.org/jcp/copyright.jsp

the τ and β parameters as the time range used in the fits is decreased. Furthermore, the relaxation times τ and stretching parameters β determined from the successive fits (starting at $C_l=0.6$, (0.5) and [0.4]) of the same curves do not always match each other within the error bars. For example, at $T=0.47$ for $C_4(t)$, the $\tau=1119$ and $\beta=0.7$ values determined when starting the fits at $C_4(t)=0.6$ are far from the $\tau=1741$ and $\beta=0.94$ values determined when starting the fits at $C_4(t)=0.4$ while the error bars of these fits are below 100 ($\Delta\tau$) and 0.05 ($\Delta\beta$). Thus, extreme care has to be taken as one constructs the correlation functions and fits them with a KWW law. Similarly, extreme care has to be paid in order not to overinterpret the results of these fits. For the experimentalist, this means that he has to choose carefully the binning size of the trace and the corresponding length of this trace, as compared to the obtained relaxation time.

At all temperatures, Fig. 7 (and Table I) nicely shows that the $C_1(t)$ decay exponentially and the $C_d(t)$ and $C_2(t)$ curves superimpose nicely. As also reported in the SM literature,[25–28] the $C_d(t)$ curves (diamonds) become extremely nonexponential as the temperature of the system is getting close to the glass-forming region. This observation has been conjectured[60,61] to be related to the dynamic heterogeneity[8,9] of the matrix, by which the SM would probe different local environments as time evolves. Furthermore, the statistical estimation of the errors performed by the Jackknife approach[63,64] exemplifies the fact that, from run to run of the identical system in molecular dynamics simulations, the relaxation times obtained are different. This is especially true for $T=0.47$ (deeply supercooled liquid) and is in agreement with reported studies of SM experiments.[25–28] Finally, the facts that (i) the ratios of the various order l of the OCTFs $C_l(t)$ depart from the ratio $\tau_1/\tau_l=l(l+1)/2$ to get closer to each other (ideally $\tau_l\approx\tau_1$) and (ii) the stretching exponent β departs significantly from 1 confirm the departure from a Debye relaxation behavior[58] and the emergence of SLARs (Refs. 44 and 45) as the temperature gets closer to T_c, as previously shown by the orientational time trajectories in Fig. 4.

The physical picture behind these observations is the trapping of the SM in a well of the effective potential created by the neighboring chains. A decrease in temperature or, equivalently, an increase in density then leads to a tightening of the cage around the SM and the appearance of shallow minima in the effective potential created by the surrounding particles, separated by very low energy barriers. The relaxation times increase simply as a consequence of the decrease of the available kinetic rotational energy (of order kT) with respect to the barrier heights. As the temperature gets close to T_c, the wells of the effective potential become deeper than kT so that, at short times (plateau regime), the SM is trapped in a well of the effective potential. The SM then performs a very restricted diffusion in angular space leading to a long time decay governed by a jump process to other wells. The plateau height decreases by increasing the rank l of the correlators due to their larger sensitivity to small-angle librations. This relaxation process of librations in the potential wells and activated jumps to neighboring wells exhibits a large dispersion for two reasons: (i) Activated processes generally show a large dispersion of the mean first passage time across the barrier inherent to the statistics of activated events. (ii) These processes depend sensitively on the detailed form of the effective angular potential. This potential created by the cage of the surrounding polymer matrix varies spatially as well as temporally, with the temporal evolution occurring on the time scale of the structural relaxation of the matrix, thus giving rise to the spatial and temporal heterogeneity observed in SM experiments.

The way in which this heterogeneity shows up in the different orientational correlation functions depends on the matrix undergoing the glass transition as well as on the probe. For the regime of masses and sizes of the probe we analyzed here, we always find a strong coupling of the orientational and translational motions of the probe to the matrix relaxation. This is also manifest in the typical jump distance of the angular reorientation which we find to be about 60°. Orientational correlation functions which decorrelate by a jump of this size will be strongly affected by the heterogeneity in the matrix and consequently will show stretching behavior and strong deviation from the Debye prediction for the correlation times. In our case, we find this starting at $l=2$. The $l=1$ correlator is only sensitive to larger angular displacements and, thus, only decays by several of the angular jumps occurring, thus averaging over jumps as well as the time variation of the effective potential which leads to an exponential decay of this correlation function. For the time scale τ_1 in relation to the time scales of the higher order correlators, however, we already observe a deviation from the Debye prediction due to the crossover to the SLARs behavior. For dumbbells reorienting in a matrix of equal dumbbells,[65,66] i.e., a model for a glass-forming molecular liquid, a weak coupling of the orientational motion to the translational freezing of the matrix was observed when one chooses dumbbells with a small aspect ratio of 0.5. The low temperature reorientation of these dumbbells then occurred by 180° jumps. Consequently, all orientational correlation functions showed stretched exponential relaxation and a failure of time-temperature superposition, which for our model system only occurs for the higher order orientational correlation functions.

E. Probe: Relaxation times of the various observables—connections to the glass transition theories

Figure 8 shows an Angell[43] plot of the relaxation times τ_l, $l=1,2,4$, τ_d, τ_f, and τ_q of a small and light probe $M=1$, $\sigma=1$ embedded in the model system at temperatures ranging from $T=1.0$ to $T=0.47$. The τ_l, τ_d, and τ_q have been defined here in an empirical way[46] as the values for which the $C_l(t)$, $C_d(t)$, and $F_q(t)$ drop to 0.3. Because of the lower value (around 0.3) of the plateau present in the case of the radiative lifetime correlation functions (Figs. 5 and 6), τ_f has been defined also in an empirical way as the value for which $C_f(t)=0.1$ (i.e., at a value equal to roughly a third of the plateau value, in full consistency with the other cases). The same Arrhenius behavior is visible for all quantities in a region ranging from $T=1.0$ to $T=0.8$ ($T_c/T=0.45$ to 0.56). At lower temperatures, the apparent activation energy of the

Downloaded 17 Oct 2007 to 147.210.82.22. Redistribution subject to AIP license or copyright, see http://jcp.aip.org/jcp/copyright.jsp

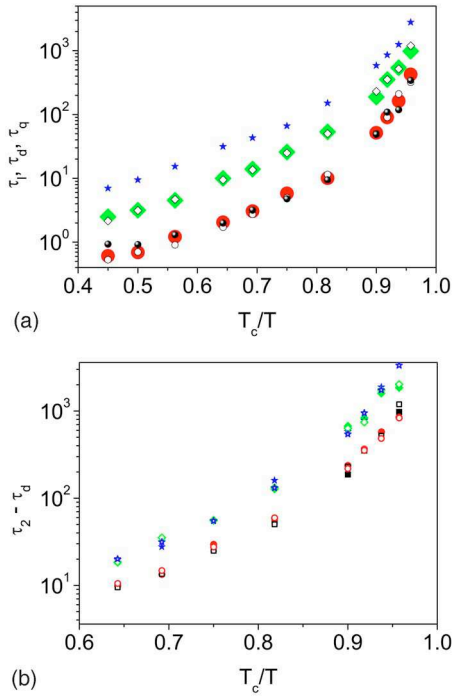

FIG. 8. (Color online) (a) Angell plot of the relaxation times of $C_1(t)$ (stars), $C_2(t)$ (large full diamonds), $C_4(t)$ (large filled circles), $C_d(t)$ (small open diamonds), $F_q(t)$ (small open circles), and $C_f(t)$ (small balls) for the dumbbell ($M=1$, $\sigma=1$) in the considered system. (b) Angell plot of the relaxation times of $C_2(t)$ (full symbols) and $C_d(t)$ (open symbols) for a small ($M=1$, $\sigma=1$, square; $M=2.25$, $\sigma=1$, circle) or large ($M=1$, $\sigma=1.22$, diamond; $M=2.25$, $\sigma=1.22$, star) dumbbell in the considered system. Note that, in the standard Angell plot, T is normalized by the glass transition temperature T_g, while we normalize T here by the critical temperature of mode coupling theory.

various relaxation times increases, and the curves show a super-Arrhenius behavior. This figure also exhibits the gradual transition from a rotational-diffusion mechanism with $\tau_1/\tau_4 \propto 10$ at high temperatures to a rotational-jump mechanism (τ_l closer to each other) as the temperature is lowered, due to the physics of the caging process discussed above.

Let us note here that, usually, Angell plots use a reduced temperature scale T/T_g, i.e., the temperature is reduced with respect to the so-called glass transition temperature T_g, defined (for small molecule glass formers) as the temperature for which the viscosity $\eta(T_g)=10^{13}$ P or, alternatively (for polymers, the viscosity would be strongly dependent on their molecular weight), as the temperature for which the relaxation time $\tau(T_g)=100$ s. On this kind of plot, one finds that certain liquids seem to show in the whole experimentally accessible temperature range an Arrhenius law, such as SiO_2, whereas other glass formers show a pronounced curvature.[6] According to Angell, these two limiting cases are called "strong" and "fragile" glass formers.[43] One popular possibility to characterize the so-called "fragility" of a glass former in a more quantitative way is to define it as

$$m = \left. \frac{d \log_{10} \eta}{dT_g/T} \right|_{T=T_g}, \tag{14}$$

i.e., m is just the slope of the curve $\eta(T_g/T)$ in the Angell-plot at $T=T_g$.

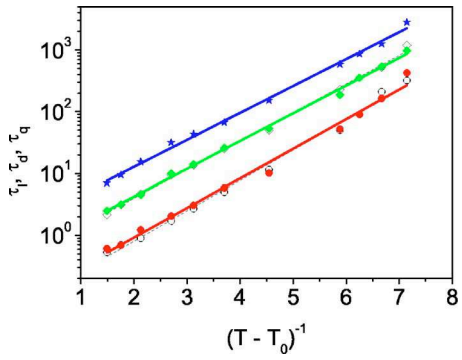

FIG. 9. (Color online) Vogel-Fulcher plots of the relaxation times τ_l [$l=1$ (stars), $l=2$ (full diamonds), $l=4$ (full circles)] τ_d (open diamonds) and τ_q (open circles) for the dumbbell ($M=1$, $\sigma=1$) in the considered system. The values of the Vogel temperature T_0 and of the "fragility parameter" B/T_0 are presented in Table II.

Figure 8 shows that our model system falls in the category of "fragile" glass-formers since the curves exhibit a pronounced curvature while entering the supercooled regime. However, a close inspection of Fig. 8(a) clearly reveals that the curves $C_1(t)$, $C_2(t)$, and $C_4(t)$ get closer as the temperature is decreased towards $T=0.47$. Accordingly, the slope m increases as the order l of the OTCF increases. To see whether this behavior continues to lower temperatures, we discuss a Vogel-Fulcher-type analysis of these data below.

Very interestingly, Fig. 8(a) also shows that the relaxation times of $C_2(t)$ and $C_d(t)$ on one hand and $C_4(t)$, $C_f(t)$ and $F_{q=6.9}(t)$ on the other hand are identical over the entire temperature range, indicating that these observables are similarly influenced by the molecular motions of the matrix. These conclusions do not change when moderate variations in the mass and/or size of the probe molecule are allowed for Fig. 8(b).

To determine the mechanisms that are responsible for the slowing down of the glass-forming system, it is highly desirable to understand the precise form for the increase of the relaxation time with decreasing T. One very popular function which seems to describe temperature dependence of relaxation times rather well is the so-called "Vogel-Fulcher (VF)" law,[20]

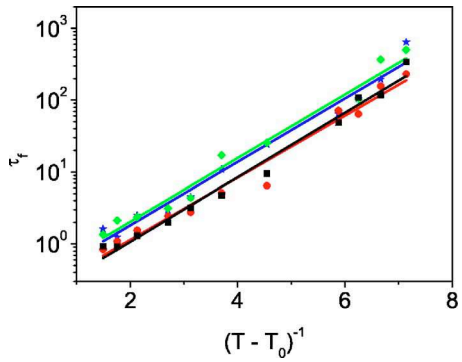

FIG. 10. (Color online) Vogel-Fulcher plots of the relaxation times τ_f for a small ($M=1$, $\sigma=1$, squares; $M=2.25$, $\sigma=1$, circles) or large ($M=1$, $\sigma=1.22$, diamonds; $M=2.25$, $\sigma=1.22$, stars) dumbbell in the considered system. The values of the Vogel temperature T_0 and of the "fragility parameter" B/T_0 are presented in Table III.

Downloaded 17 Oct 2007 to 147.210.82.22. Redistribution subject to AIP license or copyright, see http://jcp.aip.org/jcp/copyright.jsp

TABLE II. Parameters obtained by fitting the Vogel Fulcher law to the various relaxation times of the small and light dumbbell. Results of fits obtained by fixing the Vogel temperature to the known value for this polymer model (T_0=0.33) are given in column 3 (Data and fits are shown in Fig. 9). Results of the "best" fits obtained by varying both Vogel temperature and the B/T_0 parameter are given in columns 4 and 5.

$M=1$, $\sigma=1$				
Observable	T_0	B/T_0	T_0 (best fit)	B/T_0
τ_1	0.33	3.05	0.34	2.71
τ_2	0.33	3.14	0.34	2.79
τ_d	0.33	3.23	0.34	2.86
τ_4	0.33	3.34	0.38	1.74
τ_q	0.33	3.43	0.37	2.06

$$\eta(T) = \eta_0 \exp\left(\frac{B}{T - T_0}\right). \quad (15)$$

This functional form predicts a divergence of the viscosity at $T=T_0$, the so-called "Vogel temperature" and a super-Arrhenius increase of η close to T_0. The parameter B/T_0 determines whether $\eta(T)$ shows the Arrhenius dependence of strong glass formers, which corresponds to the case $T_0=0$ and, hence, a large B/T_0, or the strong curvature found in the fragile glass formers, which corresponds to a small B/T_0. It should be noted, however, that Eq. (15) merely is an empirical fitting formula, lacking a fundamental theoretical justification.[6] Moreover, when experimental data are fitted to Eq. (15), one often finds a systematic dependence of the parameters η_0, B, and T_0 obtained from the fit on the range of temperatures included in the fit and a failure of the VF law for temperatures close to T_g.[48,67] In our simulations, we have to apply the VF law to the increase in relaxation times which we can only follow over a limited range.

Figure 9 shows VF plots for the relaxation times of the various OTCFs $\tau_l(T)$ and for the $\tau_q(T)$ in the case of a small and light probe $M=1$, $\sigma=1$, and Fig. 10 shows these plots for the relaxation times of the fluorescence lifetime $\tau_f(T)$ for all kinds of probes investigated in this paper. Both figures clearly exhibit the suitability of the VF law to fit our data. For the figures, the Vogel temperature $T_0=0.33$ was used as obtained earlier for this model.[47,62] The normalized effective activation energies B/T_0 found this way are shown in Tables II and III. Also included in this table are "best fit" parameters

TABLE III. Parameters obtained by fitting the Vogal Fulcher law to the fluorescence lifetime relaxation time τ_f for the four types of dumbbell. Results of fits obtained by fixing the Vogel temperature to the known value for this polymer model (T_0=0.33) are given in column 3 (Data and fits are shown in Fig. 10). Results of the "best" fits obtained by varying both the Vogel temperature and the B/T_0 parameter are given in column 4 and 5.

τ_f for the four dumbbells				
Dumbbell	T_0	B/T_0	T_0 (best fit)	B/T_0 (best fit)
$M=1$, $\sigma=1$	0.33	3.13	0.39	1.40
$M=2.25$, $\sigma=1$	0.33	3.01	0.39	1.35
$M=1$, $\sigma=1.22$	0.33	3.09	0.37	1.86
$M=2.25$, $\sigma=1.22$	0.33	3.07	0.39	1.39

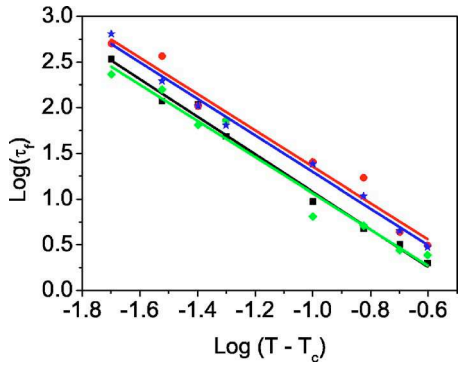

FIG. 11. (Color online) Log-log plot of the relaxation times $\tau_f(t)$ for the small ($M=1$, $\sigma=1$, squares; $M=2.25$, $\sigma=1$, diamonds) or large ($M=1$, $\sigma=1.22$, circles; $M=2.25$, $\sigma=1.22$, stars) dumbbell in the considered system. The parameters T_c and γ obtained from the fits to a power law (see text) are given in Table IV.

for Vogel temperature and normalized activation energy when both parameters are varied. In this case, both the Vogel temperature and the normalized effective activation energy display some large statistical scatter between different fits and deviate systematically from the result obtained by keeping the Vogel temperature at the known value. Only in the latter case do we obtain a (within uncertainties) unique value for the normalized effective activation energy, i.e., the fragility of the system. The main conclusion to be drawn from this comparison, however, is that one should use complementary experimental techniques for the analysis of the glass transition in a polymer melt. Ensemble average techniques such as dynamic mechanical or dielectric measurements are much better suited than SM techniques to determine properties such as the Vogel temperature. SM experiments should be checked whether they provide results for these properties consistent with the ensemble average techniques and can then be used to obtain information on heterogeneous dynamics not available for the ensemble average techniques. We will reach the same conclusion below, discussing an analysis of the relaxation times in terms of mode coupling predictions.

The description of the relaxation times in terms of the Vogel-Fulcher relation is not unique as can be seen also from the fact that a similarly good fit can be obtained in terms of a simple mode coupling power law, $\tau \propto (T/T_c - 1)^{-\gamma}$ (Fig. 11). Here, only the fluorescence lifetime is analyzed for the four different choices of probe size and/or mass that we investigated here. Both the estimated values for the critical temperature T_c and the exponent γ as well as the estimate for γ keeping the critical temperature to the known value for this polymer system are shown in Table IV. The best fit results for T_c and γ are compatible with the earlier results obtained for a pure melt without probe molecule[46,47,62] reiterating our conclusion[40] that studying the relaxation time of fluorescence lifetime fluctuations from SMS is a valid experimental probe of glass-forming liquids.

In the simulations, many more observables are accessible to strengthen this conclusion, however. As an example, Fig. 12 presents both translational (top) and rotational (bottom) mean square displacements on log-log plots versus time, for the four different choices of probe size and/or mass

Downloaded 17 Oct 2007 to 147.210.82.22. Redistribution subject to AIP license or copyright, see http://jcp.aip.org/jcp/copyright.jsp

TABLE IV. Parameters obtained by fitting the MCT law to the fluorescence lifetime relaxation time τ_f for the four types of dumbbell. Results of fits obtained by fixing the critical temperature to the known value for this polymer model (T_c=0.45) are given in column 3 (Data and fits are shown in Fig. 11). Results of the "best" fits obtained by varying both the critical temperature and the γ parameter are given in column 4 and 5.

τ_f for the four dumbbells				
Dumbbell	T_c	γ	T_c (best fit)	γ (best fit)
M=1, σ=1	0.45	2.05	0.452	1.99
M=2.25, σ=1	0.45	1.99	0.449	2.01
M=1, σ=1.22	0.45	1.98	0.447	2.08
M=2.25, σ=1.22	0.45	2.0	0.458	1.72

that are studied here. While at short times ($t<0.1$) both quantities exhibit a ballistic regime (increase proportional to t^2), for T=0.47 a pronounced plateau is observed before a smooth crossover towards Einstein relations (increase proportional to time t) occurs. For the high temperature (T=0.7), a plateau indicating confinement of the probe molecule (position and orientation) in a cage formed by its neighboring monomers is almost completely absent, as expected.

From the regime of times where the Einstein relation holds, estimates for the translational [$D_T \propto T/(\tau R)$, Stokes-Einstein (SE)] and rotational [$D_R \propto T/(\tau R^3)$, Stokes-Einstein-Debye (SED)] diffusion constants can be obtained.[16] Here, R denotes a measure of the size of the probe and τ a suitable relaxation time. Unfortunately, due to the lack of statistics (we have only one probe molecule in each simulation run and all together ten runs for each choice of probe) and the limited range of time available for these fits, the accuracy of

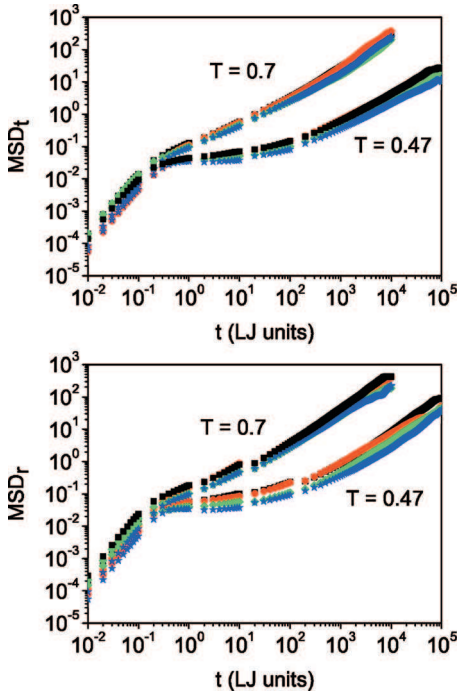

FIG. 12. (Color) Translational (top) and rotational (bottom) mean square displacement curves for the small (M=1, σ=1, squares; M=2.25, σ=1, circles) or large (M=1, σ=1.22, diamonds; M=2.25, σ=1.22, stars) dumbbell in the considered system for two temperatures: T=0.47 and T=0.7.

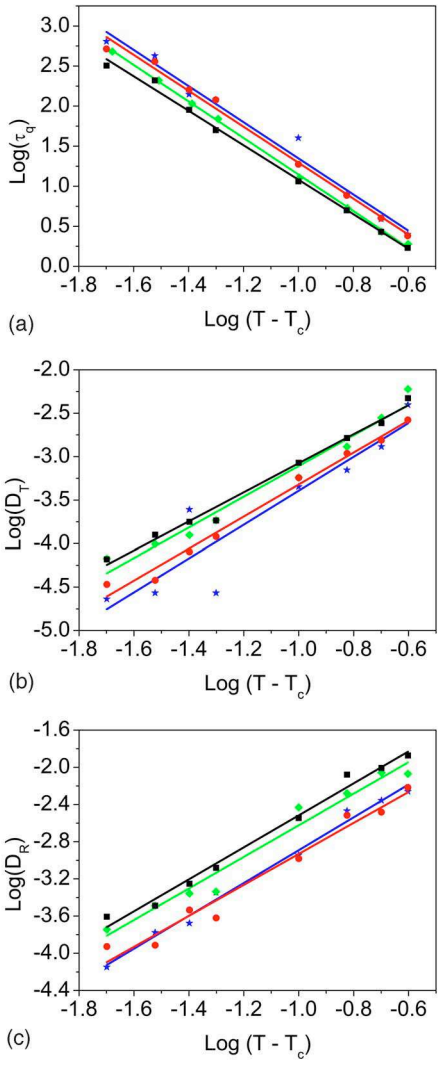

FIG. 13. Log-log plot of the relaxation times obtained from the incoherent scattering functions at q=6.9 (a) and translational (b) and rotational (c) mean square displacement curves for the small (M=1, σ=1, squares; M=2.25, σ=1, diamonds) or large (M=1, σ=1.22, circles; M=2.25, σ=1.22, stars) dumbbell in the considered system. The parameters T_c and γ obtained from the fits to a power law (see text) are given in Table V.

these estimates is limited. Figures 13(a)–13(c) shows that the data are compatible with a (apparent) vanishing of both D_T and D_R at the same critical temperature, T_c=0.45 as for the pure polymer melt, irrespective of the size and/or mass of the probe used. In Table V, we again give the results for the fit parameters performing a free fit versus fixing the mode coupling critical temperature. Holding T_c fixed strongly reduced the scatter in the results for the exponent γ. The fact that this exponent for both D_T and D_R seems to be distinctly smaller than the exponent γ extracted from the structural relaxation time τ_q is an indication that, in our system, neither the Stokes-Einstein nor the Stokes-Einstein-Debye relation will hold. Clear violations of these relations have been found in simulations of melts of glass-forming small molecules with rotational degrees of freedom, such as orthoterphenyl[15] and water.[16] If the SE and SED relations fail, the fractional functional forms

Downloaded 17 Oct 2007 to 147.210.82.22. Redistribution subject to AIP license or copyright, see http://jcp.aip.org/jcp/copyright.jsp

TABLE V. Parameters obtained by fitting the MCT law to the fluorescence lifetime relaxation time τ_q and the translational. D_T and rotational D_R diffusion constants for the four types of dumbbell. Results of fits obtained by fixing the critical temperature to the known value for this polymer model (T_c=0.45) are given in column 4 (Data and fits are shown in Fig. 13). Results of the "best" fits obtained by varying both the critical temperature and the γ parameter are given in column 4 and 5.

τ_q, D_T and D_R for the four dumbbells					
Observable	dumbbell	T_c	γ	T_c (best fit)	γ (best fit)
τ_q	M=1, σ=1	0.45	2.15	0.44	2.26
	M=2.25, σ=1	0.45	2.24	0.44	2.59
	M=1, σ=1.22	0.45	2.24	0.449	2.28
	M=2.25, σ=1.22	0.45	2.25	0.44	2.61
D_T	M=1, σ=1	0.45	1.67	0.44	1.94
	M=2.25, σ=1	0.45	1.76	0.44	2.13
	M=1, σ=1.22	0.45	1.84	0.44	2.05
	M=2.25, σ=1.22	0.45	1.95	0.44	2.26
D_R	M=1, σ=1	0.45	1.72	0.447	1.99
	M=2.25, σ=1	0.45	1.70	0.44	1.93
	M=1, σ=1.22	0.45	1.67	0.446	1.81
	M=2.25, σ=1.22	0.45	1.76	0.453	1.68

$$D_T \propto \left(\frac{\tau}{T}\right)^{-\xi_t}, \quad D_R \propto \left(\frac{\tau}{T}\right)^{-\xi_r} \tag{16}$$

are often used to replace them, with exponents $\xi_t < 1$ and $\xi_r < 1$. In order to check if our system obeys the SE or SED relations, we thus plotted the translational- and rotational-diffusion constants for the four different types of probes as a function of reduced relaxation times τ/T. Figure 14(a) shows these plots in case τ_q, the relaxation time associated with the self-intermediate scattering function of the probe $F_q(t)$, q =6.9 is chosen. Furthermore, in order to check the possibility for the SMS experimentalist to test these relations, we also plotted these fractional functional forms versus τ_f/T [Fig. 14(b)], with τ_f the relaxation time of the fluorescence lifetime observable. We have shown that $\tau_f \approx \tau_q$ in Fig. 8(a). The values obtained by fitting the data curves with the fractional forms [Eq. (16)] are given in Table VI. As is visible in this table and in Fig. 14, the values obtained for the various probes are compatible. We estimate $\xi_t \approx 0.76$ and $\xi_r \approx 0.72$ in the case of τ_q and $\xi_t \approx 0.82$ and $\xi_r \approx 0.78$ in the case of τ_f exhibiting a clear violation of the Stokes-Einstein as well as the Stokes-Einstein-Debye laws.

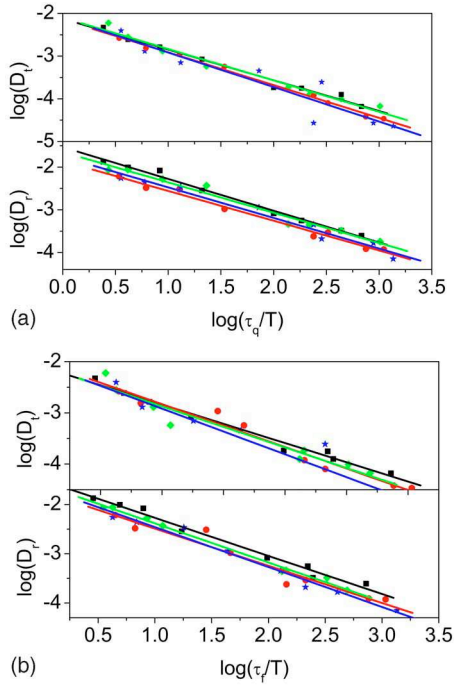

FIG. 14. Power law fits of translational (a) and rotational (b) diffusivities D_t and D_r as functions of τ_q/T (q=6.9, upper part) and τ_f/T (lower part); $D_t \approx (\tau_{q,f}/T)^{-\xi_t}$ and $D_r \approx (\tau_{q,f}/T)^{-\xi_r}$ for the small (M=1, σ=1, squares; M =2.25, σ=1, diamonds) or large (M=1, σ=1.22, circles; M=2.25, σ=1.22, stars) dumbbell in the considered system. Results for the exponents are collected in Table VI.

IV. DISCUSSION AND CONCLUDING REMARKS

In this paper, MD simulations targeted to guide experimental studies using single molecule spectroscopy (SMS) in glass-forming undercooled fluids were presented. The motivation for this study were recent experimental SMS studies analyzing the fluorescence lifetime of a rigid molecule (BODIPY) (Refs. 40, 41, and 43) in a melt of short polymers (oligostyrene). In these studies, it was found that the time dependence of both the fluorescence lifetime and intensity show large fluctuations of a hopping character, features that are never present in a polymer melt in thermal equilibrium

TABLE VI. Parameters obtained by fitting the fractional functional forms [Eq. (16)] to the relaxation times τ_q and τ_f for the four types of dumbbell (data and fits are shown in Fig. 14).

$D_T \propto (\tau/T)^{-\xi_t}$, $D_R \propto (\tau/T)^{-\xi_r}$				
Dumbbell	ξ_t (D_T vs τ_q)	ξ_r (D_R vs τ_q)	ξ_t (D_T vs τ_f)	ξ_r (D_R vs τ_f)
M=1, σ=1	0.72	0.75	0.75	0.77
M=2.25, σ=1	0.74	0.71	0.80	0.79
M=1, σ=1.22	0.77	0.70	0.84	0.76
M=2.25, σ=1.22	0.81	0.72	0.89	0.81

Downloaded 17 Oct 2007 to 147.210.82.22. Redistribution subject to AIP license or copyright, see http://jcp.aip.org/jcp/copyright.jsp

nor in a polymer in the frozen glassy state. The plausible conclusion of these experimental studies is that the hopping behavior should be linked to the anomalous features of relaxation phenomena expected to occur in deeply undercooled fluids (dynamical heterogeneity, rugged potential energy landscape, cooperatively rearranging regions, etc.). While the anomalous features of relaxation phenomena are involved, mostly in a qualitative way, in the interpretation of many experimental studies applying a large varieties of techniques, a precise quantitative characterization of the physical mechanisms responsible for the anomalous character of the relaxation is lacking in most cases. The main idea of the present work is that SMS offers a possibility to close this gap. Due to the facts that a single molecule probes and reports on local properties in space at a given instant in time and that the fluorescence signal emitted by this molecule can be followed for reasonably long times (limited by the photobleaching of the molecule), SMS yields a very suitable information concerning the mechanisms leading to hops between barriers in phase space (such as the concept of "metabasin dynamics," etc.), which is complementary to the information one can get from other experimental techniques.

However, by inserting a probe into a matrix, the latter can, in principle and also sometimes in practice, be perturbed, at least locally (sometimes also globally if we consider the plasticizing effect of small amounts of certain solvent molecules in polymer melts, e.g., carbon dioxide in polystyrene). Even if the disturbance is small, the probe molecule dynamics might be decoupled to a large extent from the dynamics of the matrix. In such cases, the information obtained by using SMS techniques might not give a faithful description of the matrix behavior.

In the present work, we have addressed such issues in terms of a generic coarse-grained model of a glass-forming polymer melt, namely, an off-lattice bead-spring model of perfectly flexible short polymer chains whose beads interact with Lennard-Jones forces. In the spirit of this coarse graining, the chemical structure of the real fluorescent probe is completely disregarded; the probe molecule in the simulation is a simple dumbbell, but both the size and the mass of this dumbbell are varied over some reasonable range.

While this lack of chemically realistic modeling clearly precludes a quantitative "fitting" of experimental data by the simulations, we note that the used coarse-grained model does account qualitatively for a vast variety of experimental observations on glass-forming polymer melts very well. In addition, we are not hampered by the uncertainties about force fields, which still constrain the possibilities of a quantitative match between experimental work and simulations significantly. Moreover, the simulations and the experiments explore essentially complementary regimes of relaxation times, with rather little mutual overlap, and corresponding to somewhat different ranges of temperatures: While MD work addresses relaxation times in the time window from the picosecond to the microsecond range (temperatures have to be chosen high enough so that this time window suffices to equilibrate the system), SMS can follow trajectories over many seconds. Using chemically realistic models would make the accessible time windows significantly shorter and, thus, even reduce the possibility to compare simulation results and experimental data in the temperature regime of interest. Thus, the purpose of the present work rather is to give some general insight into the questions under which conditions a probe molecule is a faithful "reporter" of the relaxation behavior of the matrix in which it is embedded, what can be learned from the fluctuations of the signal of the probe, and also whether the average correlation functions extracted from averages along the trajectory of the probe coincide with the ensemble averages one can get from matrix observables though other techniques.

To achieve these goals, we have chosen four distinct probes, differing by the masses of the beads in the dimer [$m_A=m_B$ (=1), the mass of an effective monomer of the polymer chains, or $m_A=2.25m_B$] and/or the size measured via the Lennard-Jones parameter $\sigma_{AA}=\sigma_{BB}$(=1) or $\sigma_{AA}=1.22$. These particular numbers are chosen such that the van der Waals volume and the mass for the choice $\sigma_{AA}=1.22$, $m_A=2.25$ are close to the corresponding values for the real fluorophore (in units of the corresponding values of the styrene monomer). Each "sample" system in our simulation contained only one probe and 120 chains with $N=10$ effective monomers, so that no effects due to direct interactions between probe molecules (or segregation of clusters of probe molecules) were at all possible. A drawback of our approach is the difficulty to obtain reasonably good statistics: We have taken ten independent samples in each case (for each considered temperature and choice of the probe) and, as it is obvious from our data, this effort is just enough to draw reasonably firm conclusions on most quantities of interest. Comparing our simulation results with those of models for molecular fluids, one should note that our work involves a factor of 40 more effort (four different probes, ten independent runs). Therefore, we did not make any effort to go beyond the time scale of 10^5 LJ time units; one needs to wait for new generations of substantially faster computers in order to do this. These constraints have restricted us to explore only the temperature region above the critical temperature of mode coupling theory of our model.

In this regime, however, the differences in average relaxation functions between the four types of probes are rather minor, irrespective of whether one considers the incoherent scattering function $F_q(t)$, orientational time correlation functions $C_l(t)$ and $C_d(t)$, or fluorescence lifetime time correlation functions $C_f(t)$, respectively. Comparing $F_q(t)$ with the corresponding correlator of both the surrounding matrix and the polymer melt without a probe molecule, we note very good agreement, minor deviations occur only mostly for the initial ballistic regime and onset of cage behavior. This proves, at least for a reasonable range of both probe sizes and probe masses, that at the considered mole fraction of less than 1 in a 1000 there is neither a significant plasticizing or antiplasticizing effect of the probe and, in addition, the dynamics of the probe follows closely the dynamics of the matrix. Of course, if m_A and/or the size of the probe would get too large or too small, a different behavior must be expected, and the dynamics of the probe molecule will decouple from

Downloaded 17 Oct 2007 to 147.210.82.22. Redistribution subject to AIP license or copyright, see http://jcp.aip.org/jcp/copyright.jsp

the matrix dynamics: It remains an interesting challenge for the future to clarify for which range of parameters this happens.

For our range of sizes and masses, where we have a strong coupling of the probe relaxation to the glass transition of the surrounding matrix, the temperature dependence of the various autocorrelation times of SM relaxations (fluorescence lifetime, incoherent scattering, and different order orientational correlation functions) allows to determine the glass transition temperature in the matrix. We have shown that the temperature dependence of the different relaxation times is in good agreement with both the Vogel temperature T_0 and the mode coupling temperature T_c obtained for this glass-forming polymer model before, but the inevitable scatter in the SM experiments make it preferable to obtain these observables from ensemble average techniques. However, a consistency check of SM experiment results for these properties with the results from ensemble average experimental techniques should be performed. We have furthermore shown a clear violation of the Stokes-Einstein as well as Stokes-Einstein-Debye laws for the translational- and rotational-diffusion coefficient of the probe molecules.

Of course, the main strength of SMS is not that one can obtain the same information that one can get also from the observation of ensemble averaged bulk properties by analyzing time averages along trajectories: the main interest is that fluctuations along the trajectories contain a wealth of information on the details of relaxation behavior in a dynamically heterogeneous environment that the probe explores in the course of its motion. We have exemplified this fact by presenting "distance matrix" maps for both the translational and rotational motion of the probe. The block structure along the diagonal of these distance matrices is generally taken as an evidence for the transitions from one metabasin of local minima in the potential energy landscape to the next one. Our MD simulations suggest that such an information, so far elusive to all experimentally available techniques, in fact is readily accessible via SMS! However, it is still a challenge to theory to clarify quantitative connections between such distance matrices and other relevant properties (e.g., size and nature of cooperatively rearranging regions, height of saddle points in the potential energy landscape, connectivity of paths over many saddle points, etc.). We do hope, however, that our work will stimulate both experimentalists to obtain corresponding data from SMS on real systems and theorists to seriously consider the related theoretical issues. In this way, we feel that a better understanding of the relaxation of glass-forming fluids will be achievable.

ACKNOWLEDGMENTS

One of the authors (R.V.) thanks the Fonds voor Wetenschappelijk Onderzoek Vlaanderen for a postdoctoral fellowship and a grant for a "study" stay abroad in the group of another author (K.B). Partial support from Sonderforschungsbereich 625/A3 of the German National Science Foundation and the EU network of excellence SOFTCOMP is also acknowledged.

[1] J. Jäckle, Rep. Prog. Phys. **49**, 171 (1986).
[2] W. Götze and L. Sjögren, Rep. Prog. Phys. **55**, 241 (1992).
[3] P. G. Debenedetti, *Metastable Liquids* (Princeton University Press, Princeton, 1997).
[4] E.-W. Donth, *The Glass Transition: Relaxation Dynamics in Liquids and Disordered Materials* (Springer, Berlin, 2001).
[5] *Proceedings of the Fourth International Discussion Meeting on Relaxations in Complex Systems*, edited by K. L. Ngai, special issue of J. Non-Cryst. Solids 307–310 (2002).
[6] K. Binder and W. Kob, *Glassy Materials and Disordered Solids: An Introduction to Their Statistical Mechanics* (World Scientific, Singapore, 2005).
[7] H. Sillescu, J. Non-Cryst. Solids **243**, 81 (1999).
[8] M. D. Ediger, Annu. Rev. Phys. Chem. **51**, 99 (2000).
[9] R. Richert, J. Phys.: Condens. Matter **14**, R703 (2002).
[10] M. Goldstein, J. Chem. Phys. **51**, 3728 (1969).
[11] F. H. Stillinger and T. A. Weber, Phys. Rev. A **28**, 2408 (1983).
[12] B. Doliwa and A. Heuer, Phys. Rev. E **67**, 235501 (2003); Phys. Rev. Lett. **91**, 295501 (2003).
[13] L. Angelani, G. Ruocco, M. Sampoli, and F. Sciortino, J. Chem. Phys. **119**, 2120 (2003).
[14] J. Kim and T. Keyes, J. Chem. Phys. **121**, 4237 (2004).
[15] T. G. Lombardo, P. G. Debenedetti, and F. H. Stillinger, J. Chem. Phys. **125**, 174507 (2006).
[16] M. G. Mazza, N. Giovambattista, F. C. Starr, and H. E. Stanley, Phys. Rev. Lett. **96**, 057803 (2006); M. G. Mazza, N. Giovambattista, H. E. Stanley, and F. W. Starr, Phys. Rev. E **76**, 031203 (2007).
[17] D. Coslovich and G. Pastore, Europhys. Lett. **75**, 784 (2006).
[18] G. A. Appignanesi, J. A. Rodrigues Fris, R. A. Montani, and W. Kob, Phys. Rev. Lett. **96**, 057801 (2006).
[19] G. Adam and J. H. Gibbs, J. Chem. Phys. **43**, 139 (1965).
[20] H. Vogel, Phys. Z. **22**, 645 (1921); G. S. Fulcher, J. Am. Ceram. Soc. **8**, 339 (1925).
[21] W. E. Moerner and M. Orrit, Science **283**, 1670 (1999).
[22] X. S. Xie and J. K. Trautman, Annu. Rev. Phys. Chem. **49**, 441 (1998).
[23] F. Kulzer and M. Orrit, Annu. Rev. Phys. Chem. **55**, 585 (2004).
[24] R. A. L. Vallée, M. Cotlet, J. Hofkens, and F. C. De Schryven, and K. Müllen, Macromolecules **36**, 7752 (2003).
[25] L. A. Deschenes and D. A. Vanden Bout, J. Phys. Chem. B **106**, 11438 (2002).
[26] N. Tomczak, R. A. L. Vallée, E. M. H. P. van Dijk, M. García-Parajó, L. Kuipers, N. F. van Hulst, and G. J. Vancso, Eur. Polym. J. **40**, 1001 (2004).
[27] A. Schob, F. Cichos, J. Schuster, and C. von Borczyskowski, Eur. Polym. J. **40**, 1019 (2004).
[28] E. Mei, J. Tang, J. M. Vanderkooi, and R. M. Hochstrasser, J. Am. Chem. Soc. **125**, 2730 (2003).
[29] R. M. Dickson, D. J. Norris, and W. E. Moerner, Phys. Rev. Lett. **81**, 5322 (1998).
[30] B. Sick, B. Hecht, and L. Novotny, Phys. Rev. Lett. **85**, 4482 (2000).
[31] A. Lieb, J. M. Zavislan, and L. Novotny, J. Opt. Soc. Am. B **21**, 1210 (2004).
[32] M. Böhmer and J. Enderlein, J. Opt. Soc. Am. B **20**, 554 (2000).
[33] A. P. Bartko, K. Xu, and R. M. Dickson, Phys. Rev. Lett. **89**, 026101 (2002).
[34] R. A. L. Vallée, N. Tomczak, L. Kuipers, G. J. Vancso, and N. F. van Hulst, Phys. Rev. Lett. **91**, 038301 (2003).
[35] R. A. L. Vallée, N. Tomczak, L. Kuipers, G. J. Vancso, and N. F. van Hulst, Chem. Phys. Lett. **384**, 5 (2004).
[36] N. Tomczak, R. A. L. Vallée, E. M. H. P. van Dijk, L. Kuipers, N. F. van Hulst, and G. J. Vancso, J. Am. Chem. Soc. **126**, 4748 (2004).
[37] R. A. L. Vallée, N. Tomczak, G. J. Vancso, L. Kuipers, and N. F. van Hulst, J. Chem. Phys. **122**, 114704 (2005).
[38] R. A. L. Vallée, M. Van der Auweraer, F. C. De Schryver, D. Beljonne, and M. Orrit, ChemPhysChem **6**, 81 (2005).
[39] R. A. L. Vallée, P. Marsal, E. Braeken, S. Habuchi, F. C. De Schryver, M. Van der Auweraer, D. Beljonne, and J. Hofkens, J. Am. Chem. Soc. **127**, 12011 (2005).
[40] R. A. L. Vallée, M. Van der Auweraer, W. Paul, and K. Binder, Phys. Rev. Lett. **97**, 217801 (2006).
[41] R. A. L. Vallée, M. Baruah, J. Hofkens, F. C. De Schryver, N. Boens, M. Van der Auweraer, and D. Beljonne, J. Chem. Phys. **126**, 184902 (2007).
[42] R. A. L. Vallée, M. Van der Auweraer, W. Paul, and K. Binder, Europhys. Lett. **79**, 46001 (2007).
[43] C. A. Angell, *Relaxation in Complex Systems*, edited by K. L. Ngai and

Downloaded 17 Oct 2007 to 147.210.82.22. Redistribution subject to AIP license or copyright, see http://jcp.aip.org/jcp/copyright.jsp

G. B. Wright (U.S. Department of Commerce, Springfield, 1985), p. 1.
[44] M. S. Beevers, J. Crossley, D. C. Garrington, and G. Williams, J. Chem. Soc., Faraday Trans. 2 **73**, 458 (1977).
[45] D. Kivelson and S. A. Kivelson, J. Chem. Phys. **90**, 4464 (1989).
[46] C. Bennemann, W. Paul, K. Binder, and B. Dünweg, Phys. Rev. E **57**, 843 (1998).
[47] K. Binder, J. Baschnagel, and W. Paul, Prog. Polym. Sci. **28**, 115 (2003).
[48] W. Paul, *Reviews in Computational Chemistry* (Wiley, New York, 2007), Vol. 25, p. 1.
[49] OCTA, http://octa.jp
[50] *Monte Carlo and Molecular Dynamics of Condensed Matter*, edited by K. Binder and G. Ciccotti (Societa Italiana di Fisica, Bologna, 1996).
[51] J. Buchholz, W. Paul, F. Varnik, and K. Binder, J. Chem. Phys. **117**, 7364 (2002).
[52] M. J. S. Dewar, E. G. Zoebisch, E. F. Healy, and J. J. P. Stewart, J. Am. Chem. Soc. **107**, 3902 (1985).
[53] 4,4-difluoro-8-(4-methoxyphenyl)-3-[-2-(4-methoxyphenyl)ethenyl]-1,5,7-trimethyl-3a,4a-diaza-4-bora-s-indacene.
[54] C. J. F. Böttcher, *Theory of Electric Polarization* (Elsevier, Amsterdam, 1973).
[55] AMPAC, Semichem, 7204 Mullen, Shawnee, KS 66216.
[56] M. C. Zerner, G. H. Loew, R. Kichner, and U. T. Mueller-Westerhoff, J. Am. Chem. Soc. **122**, 3015 (2000).
[57] C.-Y. Lu and D. Vanden Bout, J. Chem. Phys. **125**, 124701 (2006).
[58] P. Debye, *Polar Molecules* (Dover, New York, 1929); B. J. Berne and R. Pecora, *Dynamic Light Scattering* (Dover, New York, 1976).
[59] M. F. Gelin and D. S. Kosov, J. Chem. Phys. **125**, 054708 (2006).
[60] G. Hinze, G. Diezemann, and Th. Basche, Phys. Rev. Lett. **93**, 203001 (2004).
[61] C.-Y. J. Wei, Y. H. Kim, R. K. Darst, P. J. Rossky, and D. A. VandenBout, Phys. Rev. Lett. **95**, 173001 (2005).
[62] J. Baschnagel and F. Varnik, J. Phys.: Condens. Matter **17**, R851 (2005).
[63] B. Efron and G. Gong, Am. Stat. **37**, 36 (1983).
[64] D. J. Thomson and A. D. Chave, in *Advances in Spectrum Analysis and Array Processing*, edited by S. Haykin (Prentice Hall, Englewood Cliffs, New Jersey, 1991), Vol. 1, Chap. 2, p. 58113.
[65] S. Kämmerer, W. Kob, and R. Schilling, Phys. Rev. E **56**, 5450 (1997).
[66] C. De Michele and D. Leporini, Phys. Rev. E **63**, 036702 (2001).
[67] F. Stickel, E. W. Fischer, and R. Richert, J. Chem. Phys. **102**, 6251 (1995); **104**, 2043 (1996).

Downloaded 17 Oct 2007 to 147.210.82.22. Redistribution subject to AIP license or copyright, see http://jcp.aip.org/jcp/copyright.jsp

Probe molecules in polymer melts near the glass transition: A molecular dynamics study of chain length effects

R. A. L. Vallée,[1] W. Paul,[2,a)] and K. Binder[3]
[1]*Centre de Recherche Paul Pascal (CNRS), 115 Avenue du Docteur Albert Schweitzer, 33600 Pessac, France*
[2]*Institut für Physik, Martin-Luther-University, 06099 Halle, Germany*
[3]*Institut für Physik, Johannes-Gutenberg University, 55099 Mainz, Germany*

(Received 5 October 2009; accepted 11 December 2009; published online 15 January 2010)

Molecular dynamics simulations of a dense melt of short bead-spring polymer chains containing $N=5$, 10, or 25 effective monomers are presented and analyzed. Parts of our simulations include also a single dumbbell ($N=2$) of the same type, which is interpreted to represent a coarse-grained model for a fluorescent probe molecule as used in corresponding experiments. We obtain the mean-square displacements of monomers and chains center of mass, and intermediate incoherent scattering functions of both monomers in the chains and particles in the dumbbells as function of time for a broad regime of temperatures above the critical temperature T_c of mode-coupling theory. For both the chains and the dumbbell, also orientational autocorrelation functions are calculated and for the dumbbell time series for the time evolution of linear dichroism and its autocorrelation function are studied. From both sets of data we find that both the mode-coupling critical temperature T_c (representing the "cage effect") and the Vogel–Fulcher temperature T_0 (representing the caloric glass transition temperature) systematically increase with chain length. Furthermore, the dumbbell dynamics yields detailed information on the differences in the matrix dynamics that are caused by the chain length variation. Deviations from the Stokes–Einstein relation are discussed, and an outlook to related experiments is given. © *2010 American Institute of Physics*.
[doi:10.1063/1.3284780]

I. INTRODUCTION

Polymer melts are very well suited for experimental studies[1–4] of the slowing down of the dynamics when one approaches the glass transition: The free energy barriers against crystallization from the random coil state in supercooled melts are extremely high,[2,5] and hence very slow cooling protocols can be applied, without encountering the problem that formation of crystalline nuclei spoils the results. Moreover, a wealth of experimental techniques to explore the dynamics of the polymer coils is available,[1,2] including also the possibility of adding a small fraction of small molecule probes[6–21] that explore the heterogeneous environment[22–24] in such systems near the glass transition, without creating too much disturbance to these environments.[25–27] In this paper, we shall emphasize another important advantage of flexible macromolecules: One can vary the degree of polymerization (henceforth referred to as "chain length") without changing the intermolecular forces.[28] Thus characteristics such as the size of the polymer coils, the configurational entropy in the system, the diffusion constant of the coils, etc., are changed[2,28,29] but interactions among the monomeric groups (which act as the driving force for the densification of the melt when the temperature is lowered and hence are ultimately responsible for the glass-like freezing which results) stay unaffected. The presence of such an additional control parameter that can be changed without affecting the "chemistry" of the system is a valuable tool for testing the validity of theoretical concepts.[3,4] In fact, the early experimental finding[30] that the glass transition temperature $T_g(N)$ varies with chain length N as

$$T_g(N) = T_g(\infty)(1 - \text{const}/N) \tag{1}$$

has found considerable attention; in particular Eq. (1) was also obtained from, the "entropy theory" proposed by Gibbs and di Marzio[31] (suggesting that the glass transition of polymer melts results from the vanishing of their configurational entropy, a concept motivated[32] by Kauzmann's observation that for many glass forming fluids the extrapolation of their calorimetric entropy data falls below the crystal entropy at a nonzero temperature T_K, the "Kauzmann temperature"). We now know that the experimental validity of Eq. (1) is not a sufficient proof to claim the validity of the "entropy catastrophe" concept of Gibbs and di Marzio;[31] in fact, unjustifiable approximations in their treatment are well documented.[33,34] Moreover, there is no thermodynamic principle that forbids the entropy of a supercooled fluid to fall below the entropy of a crystal (in fact, this is known to happen for a very simple model system, the fluid of hard spheres).[35]

Nevertheless, it is of significant interest to explore in detail the effects of varying the chain length N on the slow dynamics near the glass transition, and thus gain better insight into its properties. In the present work, we contribute to this problem by presenting molecular dynamics (MD) results for a simple model system, a melt of simple bead-spring

a)Electronic mail: wolfgang.paul@physik.uni-halle.de.

 © 2010 American Institute of Physics

Author complimentary copy. Redistribution subject to AIP license or copyright, see http://jcp.aip.org/jcp/copyright.jsp

chains, varying N in the regime where the melts are not yet entangled, $5 \leq N \leq 25$. In previous work, this model has been extensively characterized, but for a single chain length ($N=10$) only.[36–44] Since in recent work[25–27] it was shown that useful complementary information can be extracted when one includes a dumbbell molecule [which can be regarded as a coarse-grained description of fluorescent probe molecules[25–27] which have yielded a wealth of information in single molecule spectroscopy (SMS) experiments[6–20]], we perform additional simulations where a dumbbell ($N=2$) is included in the simulations in the present case as well. As shown previously,[25–27] the study of the slow translational and rotational dynamics of this probe in the glass forming fluid environment yields information on the energy landscape of the system.[45–53] Since in the course of its motion the dumbbell probes regions of different local structures and mobilities, it is clear that analysis of this motion gives very direct information on the dynamic heterogeneity in the supercooled melt. Moreover, also the dynamics of transitions from one "metabasin"[48–51] in the energy landscape to the other[54] can be elucidated as we have shown.[25–27]

In Sec. II, we briefly recall the model and simulation method, while in Sec. III we present results on the intermediate incoherent dynamic structure factors and mean-square displacements. Also orientational correlation functions are explored, which would be experimentally accessible for fluorescent probe molecules. These results are analyzed within the framework of idealized mode-coupling theory[55] (MCT) to test to what extent the critical temperature T_c of MCT actually depends on chain length N. Since our data are restricted to the temperature range $T/T_c - 1 \geq 0.04$, the fact that the singularities predicted by the idealized MCT at T_c are actually rounded off does not affect our analysis. We obtain both the relaxation time τ_q for "α-relaxation"[1–5,56,57] and the self-diffusion constant D and also address the question whether the Stokes–Einstein relation $D\tau_q/T=\text{const}$ holds in this regime.

In Sec. IV we present a tentative brief discussion whether an alternative analysis of the same data in terms of fits to the Vogel–Fulcher relation[58] leads to a chain length dependence of the Vogel–Fulcher temperature T_0. Section V then presents some discussion of trajectories $d(t)$ that would correspond to the linear dichroism of a fluorescent probe molecule, and the resulting correlation function, while Sec. VI briefly summarizes our conclusions.

II. METHODS

We performed MD simulations of a system containing either 240, 120, or 48 bead-spring chains of 5, 10, or 25, respectively, effective monomers. A cubic simulation volume with periodic boundary conditions is used throughout. The interaction between two beads of type A (probe) or type B (monomers) is given by the Lennard-Jones (LJ) potential $U_{\mathrm{LJ}}(r_{ij})=4\epsilon[(\sigma_{\alpha\beta}/r_{ij})^{12}-(\sigma_{\alpha\beta}/r_{ij})^{6}]$, where r_{ij} is the distance between beads i,j and $\alpha,\beta \in A,B$. The LJ diameters used are $\sigma_{AA}=1.22$, $\sigma_{BB}=1.0$ (unit of length), and $\sigma_{AB}=1.11$, while $\epsilon=1$ sets the scale of energy (and temperature T since Boltzmann's constant $k_B=1$). These potentials are truncated at $r_{\mathrm{cut}}^{\alpha\beta}=2^{7/6}\sigma_{\alpha\beta}$ and shifted so that they are zero at $r_{ij}=r_{\mathrm{cut}}^{\alpha\beta}$. Between the beads along the chain, as well as between the beads of the dumbbell, a finitely extendable nonlinear elastic potential is used $U_F=-(k/2)R_0^2\ln[1-(r_{ij}/R_0)^2]$, with parameters $k=30$ and $R_0=1.5$.[36] This model system (without the probe) has been shown to qualitatively reproduce many features of the relaxation of glass forming polymers.[36–44] In the MD simulations, the equations of motion at constant particle number N, volume V, and energy E are integrated with the velocity Verlet algorithm[59,60] with a time step of 0.002, measuring time in units of $(m_B\sigma_{BB}^2/48\epsilon)^{1/2}$. All NVE simulations have been performed after equilibrating the system in the NpT ensemble, using a Nosé–Hoover thermostat,[60] keeping the average pressure at $p=1.0$ at all temperatures. These runs lasted up to 5×10^7 MD steps. Ten different configurations were simulated at each temperature ($T=0.47, 0.48, 0.49, 0.5, 0.55, 0.6, 0.65, 0.7, 1.0, 2.0$) in order to ensure good statistics. Note that the melting temperature of the crystalline phase of this model polymer has been estimated[42] to be $T_m=0.75$ while the critical temperature T_c of MCT (where in our model a smooth crossover to activated dynamics occurs) is at $T_c=0.45$ (Refs. 36–42) (both values were obtained for chains of length $N=10$). Thus our data include equilibrated melts as well as the moderately supercooled regime.

III. RESULTS FOR THE INTERMEDIATE STRUCTURE FACTOR AND MEAN SQUARE DISPLACEMENTS: MODE COUPLING ANALYSIS

A. Pure melts

Previous experience[31,36–40,42–44] has shown that a quantity that is particularly useful to analyze the slow dynamics of glass forming liquids in the context of theory and simulations is the incoherent intermediate scattering function $F_q(t)$,

$$F_q(t) = \frac{1}{M}\sum_{i=1}^{M} \langle \exp[i\vec{q}\cdot(\vec{r}_i(0)-\vec{r}_i(t))]\rangle. \tag{2}$$

In Eq. (2), the sum is extended over all M effective monomers in the system, and $\vec{r}_i(t)$ is the position of the ith monomer at time t, while $\vec{q}$ is the scattering wave vector. The angular brackets indicate a thermal as well as an orientational average. Being interested in the slow dynamics associated with the cage effect,[3,4,55] it is most useful to choose q such that it roughly corresponds to the position where the static structure factor $S(q)$ of the melt has its peak, which is (for the chosen conditions) $q=6.9$ [note that in the temperature regime of interest, $S(q)$ changes with temperature only very little[3,36]]. Of course, an analogous quantity can be immediately defined for the dumbbell if the simulated system contains one; the only problem then is that due to the small number $M=2$ (rather than $M=1200$), the poor statistics necessitates to carry out multiple runs (as mentioned in Sec. II, ten independent runs were hence performed).

As an example of our results for pure systems (without dumbbell) and their analysis, we present $F_q(t)$ for $N=5$ versus the scaled time, t/τ_q, where the α-relation time τ_q is defined by the condition

Author complimentary copy. Redistribution subject to AIP license or copyright, see http://jcp.aip.org/jcp/copyright.jsp

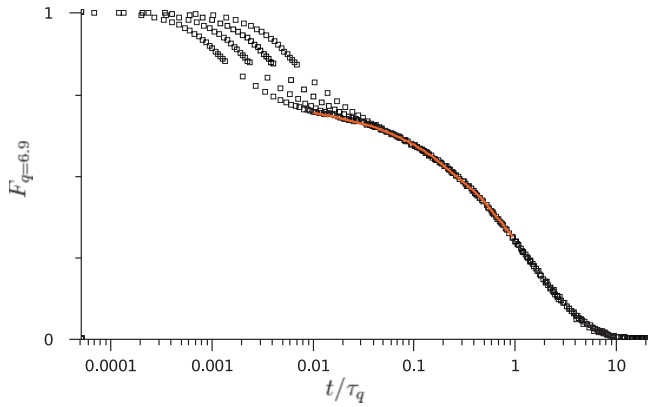

FIG. 1. Intermediate dynamic structure factor (black open squares) for the model system of chains with five monomers. Time is scaled by the α-relaxation time τ_q for the four lowest investigated temperatures $T=0.47$,0.48, 0.49, and 0.50 (from left to right), where the time-temperature superposition principle notably holds. Also shown (red curve) is the best fit $F_q(t)=f_q^c-h_q(t/\tau_\alpha)^b+h_qB_q(t/\tau_\alpha)^{2b}$ performed simultaneously to these four curves (see text).

$$F_{q=6.9}(t=\tau_q)=0.3. \tag{3}$$

Figure 1 shows that in this temperature range $0.47 \leqq T \leqq 0.50$ $F_q(t)$ has a two-step decay, and the second step [the decay of $F_q(t)$ from about $F_q(t)=0.5$ to zero] displays the expected[3,4,55,56] time-temperature superposition principle very well. We have also checked that a different convention, such as defining τ_q via $F_{q=6.9}(t=\tau_q)=0.1$, only would lead to a change in τ_q by a constant factor, but would not affect our results.

We will analyze the incoherent scattering function in Fig. 1 following a simplified procedure compared to the more elaborate analysis presented in Ref. 43. The first step of the decay seen in Fig. 1 ("critical decay"[3,4,55,56]) leads to a plateau (described by the "nonergodicity parameter" f_q^c), and will not be analyzed in detail here. However we are interested in the decay of the plateau, which according to MCT (Ref. 55) can be described in the β-relaxation regime by (f_q^c, h_q, B_q, and b are fitting parameters)

$$F_q(t)=f_q^c-h_q(t/\tau_\alpha)^b+h_qB_q(t/\tau_\alpha)^{2b}+-\cdots. \tag{4}$$

From a simultaneous fit of Eq. (4) to the four curves corresponding to the four lowest temperatures investigated here, notably $T=0.47$, $T=0.48$, $T=0.49$, and $T=0.5$, the MCT parameter $b\approx 0.57$ is extracted. MCT exponent relations then fix the exponent of the α-relaxation in the law

$$\tau_{q=6.9}(T) \propto (T/T_c(N)-1)^{-\gamma} \tag{5}$$

to $\gamma=2.5$. This law implies that a plot of $(\tau_{q=6.9})^{-1/\gamma}$ versus T should be linear and intersect zero at $T_c(N)$. Figure 2 shows that in the temperature regime $0.47 \leq T \leq 0.65$ used for these fits good straight lines are in fact obtained [with $T_c \simeq 0.42 \pm 0.02$ and $\gamma \approx 2.64$ for $N=5$ (which agrees reasonably with the expectation according to the MCT exponent relations), while within our accuracy the estimates for $T_c(N)$ for $N=10$ and $N=25$ coincide, $T_c(N \geq 10)=0.45 \pm 0.02$]. The error bars are conservative to account for the fact that our simplified analysis obtains $T_c(N)$ and $\gamma(N)$ from just one fit. A full MCT analysis with a simultaneous fit of several quantities in the α- and β-relaxation regimes is beyond the scope of this manuscript and will be presented in future work.

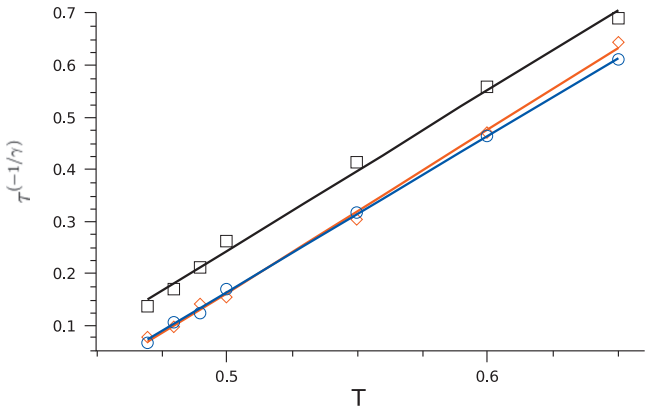

FIG. 2. Critical behavior of the α-relaxation time scale as a function of temperature, allowing for a determination of the critical temperature T_c. Black squares, red diamonds, and blue circles give the α-relaxation times as a function of temperature for chains with lengths of 5, 10, and 25, respectively. The solid curves of corresponding color provide the best fits (MCT power law divergence) to the data, allowing for the determination of $T_c=0.42$ in the case of chain lengths of five monomers and $T_c=0.45$ in the case of chain lengths of 10 and 25 monomers. The α-relaxation times have been determined empirically in this case by the requirement $F_q(\tau_q)=0.3$. The same analysis performed by defining empirically the α-relaxation times with the requirement $F_q(\tau_q)=0.1$ provides the same estimates for $T_c(N)$.

The cage effect which MCT captures originates in the dense packing of the molecules. As we are studying the glass transition along an isobar, the variation of $T_c(N)$ with chain length has to be at least partly due to the variation of density with chain length at fixed temperature along the isobar. In fact, in our earlier work[39] we found an increase in T_c at fixed chain length ($N=10$) with increasing pressure, i.e., increasing density at fixed temperature. In Fig. 3 we show the density variation with temperature in our three simulated melts. In the displayed temperature regime, the densities vary linearly with chain length according to $\rho_5(T)=1.153-0.268$ T, $\rho_{10}(T)=1.172-0.279$ T, and $\rho_{25}(T)=1.172-0.264$ T. This yields densities at T_c of $\rho_5(T_c)=1.040$, $\rho_{10}(T_c)=1.046$, and $\rho_{25}(T_c)=1.053$. Within our analysis we therefore find a slight increase in the critical density with chain length, presumably due to connectivity influences on the cage effect in a polymer melt.

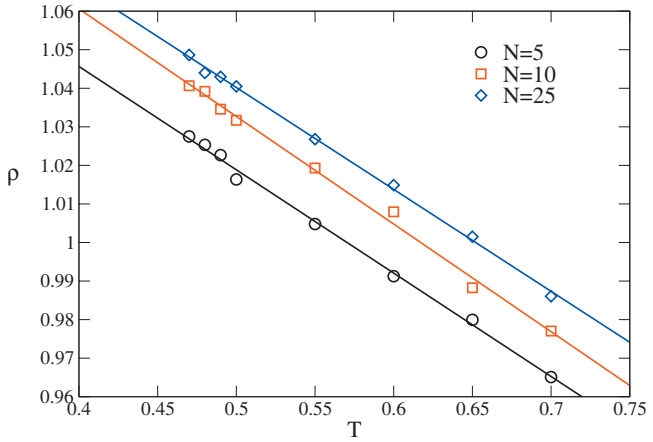

FIG. 3. Density variation along the $p=1$ isobar for the three chain lengths studied. In the displayed temperature regime, the density variation is linear as shown by the regression lines (see text).

Author complimentary copy. Redistribution subject to AIP license or copyright, see http://jcp.aip.org/jcp/copyright.jsp

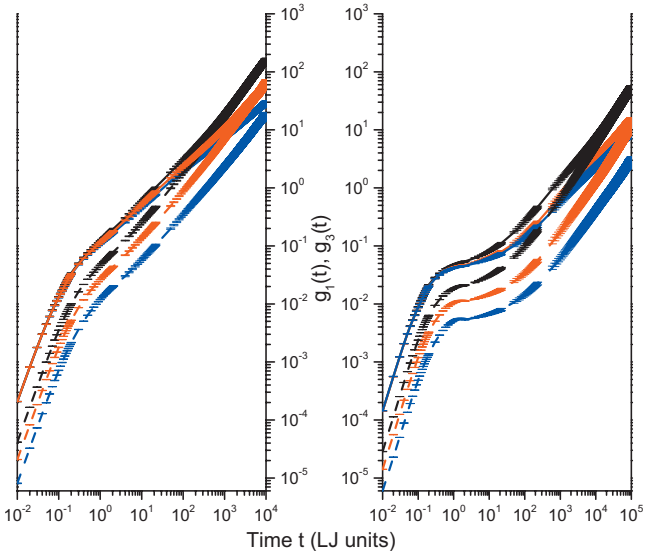

FIG. 4. Mean square displacements as a function of time for $T=0.7$ (left) and $T=0.48$ (right). g_1 (solid curves) and g_3 (dashed curves) describe the monomers and the center of mass of the chains, respectively. The black, red, and blue curves pertain to chains with lengths of 5, 10, and 25 monomers in the simulation boxes.

The second quantity that we analyze is mean-square displacements of individual effective monomers,

$$g_1(t) \equiv \frac{1}{M}\sum_{i=1}^{M} \langle [\vec{r}_i(t) - \vec{r}_i(0)]^2 \rangle \tag{6}$$

and of the center of mass of the chains ($n=M/N$)

$$g_3(t) = \frac{1}{n}\sum_{j=1}^{n} \langle [\vec{r}_{CM,j}(t) - \vec{r}_{CM,j}(0)]^2 \rangle, \tag{7}$$

where the sum in Eq. (6) runs over all monomers and the sum in Eq. (7) runs over all chains, $\vec{r}_{CM,j}(t)$ being the position of the center of mass of the jth chain. These quantities are shown in Fig. 4 for two representative temperatures and all three chain lengths investigated. For the high temperature ($T=0.7$) the center of mass motion after an initial "ballistic" regime[3] crosses over to a slightly subdiffusive regime $\simeq t^{0.8}$ (see Ref. 61) and then to standard diffusive motion, D_t being the translational diffusion coefficient,

$$g_3(t) = 6D_t t. \tag{8}$$

At the lower temperature ($T=0.48$), however, there is a clear plateau due to the cage effect. For $g_1(t)$ the displacements in the ballistic regime are larger than $g_3(t)$ by a factor of N, as it must be, and there occurs a regime of subdiffusive growth [ideally, there should be Rouse-like behavior $g_1(t) \propto t^{1/2}$] before $g_1(t)$ and $g_3(t)$ merge, and also $g_1(t)$ shows the expected diffusive behavior, $g_1(t)=6D_t t$. At the lower temperatures, where the cage effect comes into play, $g_1(t)$ displays a pronounced plateau after the ballistic regime, and the escape from the plateau also involves another power law [accounted for by MCT (Refs. 3 and 41)], but this shall not be further discussed here. From the Fickian diffusion regime reached for g_3 for times larger than the Rouse time, estimates for the translation diffusion constants D_t have been extracted. Again

TABLE I. Parameters obtained by fitting the MCT law to α relaxation times τ_q, τ_2, and τ_4 and to the translational diffusion coefficients D_t for the model systems with chains of either 5, 10, or 25 monomers. Results of fits obtained by fixing the critical temperature to the known value for each polymer model (Fig. 4).

	τ_x					
Bulk	T_c (5)	γ (5)	T_c (10)	γ (10)	T_c (25)	γ (25)
τ_q	0.42	2.64	0.45	2.19	0.45	2.44
τ_2	0.42	2.24	0.45	1.87	0.45	2.21
τ_4	0.42	2.64	0.45	2.22	0.45	2.55
D_t	0.42	2.24	0.45	1.77	0.45	1.93
Dumbbell	T_c (5)	γ (5)	T_c (10)	γ (10)	T_c (25)	γ (25)
τ_q	0.42	2.72	0.45	2.23	0.45	2.51
τ_2	0.42	2.41	0.45	2.08	0.45	2.18
τ_4	0.42	2.71	0.45	2.23	0.45	2.49
D_t	0.42	2.45	0.45	1.90	0.45	2.03

one expects from the idealized MCT (Ref. 55) a power law as in Eq. (5),

$$D_t \propto (T/T_c(N) - 1)^{\gamma}. \tag{9}$$

The various estimates both for $T_c(N)$ and for γ, including those extracted from the dumbbell (see Sec. III B) are collected in Table I. As already found in our earlier work for $N=10$,[36] the exponent estimate γ extracted from D_t is distinctly smaller than the estimate from $\tau_{q=6.9}$. MCT (Ref. 55) implies that asymptotically close to $T_c(N)$, the exponents γ appearing in Eqs. (5) and (9) should be the same. The discrepancy between both estimates may be due to the fact that our data are not close enough to $T_c(N)$; on the other hand, the singularities predicted by the idealized MCT anyway are rounded off, and hence the true asymptotic region of idealized MCT may not be observable in our system. In addition to this problem, Table I also implies that the exponent(s) γ may depend on chain length.

B. Melts containing a dumbbell

As mentioned above, it is straightforward to obtain $F_{q=6.9}(t)$ for the dumbbell as well. Figure 5 compares the resulting data with those of the chains at two temperatures. One can see that the function $F_{q=6.9}(t)$ is very similar to the corresponding function of the melt (the decorrelation of the dumbbell always is a bit slower due to the choice of the larger ranges of the potentials σ_{AA}, σ_{AB}, chosen for the two monomers in the dumbbell). In spite of the small difference between the time scale for α-relaxation of the dumbbell and the melts in which it moves, one can infer from dumbbell data alone how much additional slowing down occurs when N is increased. Thus we conclude from Fig. 5 that SMS studies of probe dynamics can yield valuable information on subtle differences between different matrices in which the probe is embedded, at least for temperatures above and close to T_c.

It is also very interesting to explore the rotational dynamics of the probe.[25–27] Defining $\vec{u}(t)$ as a unit vector along

Author complimentary copy. Redistribution subject to AIP license or copyright, see http://jcp.aip.org/jcp/copyright.jsp

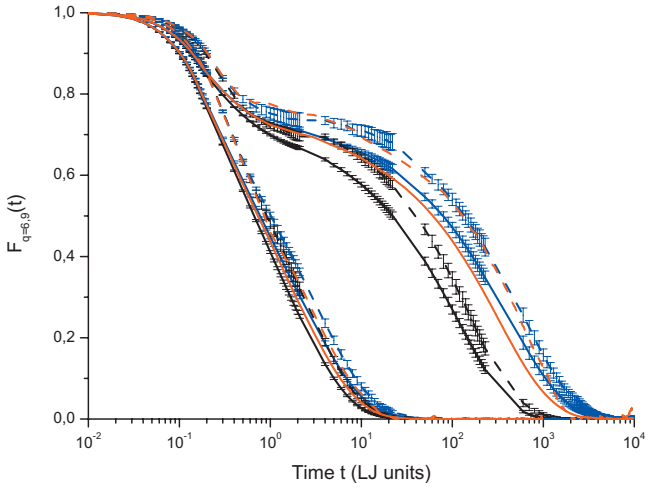

FIG. 5. Intermediate dynamic structure factor at the first maximum ($q=6.9$) of the static structure factor for the NVE simulations performed at temperatures $T=0.7$ (left) and $T=0.48$ (right) for various chain lengths. Black, red, and blue curves represent the results for chains of 5, 10, and 25 monomers in the simulation boxes, respectively. Dashed curves stand for the probe (dumbbell) dynamics while solid curves stand for the bulk dynamics. The error bars, estimated by the Jackknife approach on the base of the ten simulation runs for each temperature, are obviously larger for the dumbbell dynamics than for the bulk dynamics.

the axis connecting the positions of the two particles in the dumbbell at time t, it is useful to define orientational time correlation functions in terms of

$$\cos(\theta(t)) = \vec{u}(t) \cdot \vec{u}(0) \tag{10}$$

via the Legendre polynomials $P_\ell(\cos\theta)$ as

$$C_\ell(t) \equiv \langle P_\ell(\cos\theta(t)) \rangle \tag{11}$$

and corresponding relaxation times $\tau_\ell = \int_0^\infty C_\ell(t)dt$. As discussed previously,[26,27] the relaxation times τ_2 and τ_4 are of particular interest, and are included in Table I. Here we have included also data for the orientational correlations of bonds in the polymer chain, which can be defined analogously (averaging the data over all bonds in all polymers, irrespective of whether a monomer is at a chain end or not).

Figures 6 and 7 then present the various relaxation times τ_q, τ_2, and τ_4 on a log-log plot versus $T-T_c(N)$, both for the bulk (i.e., monomers of the melt) and the dumbbell. It is seen that the simple power law is only a rough description of the data, but the latter clearly suffers from some statistical errors, in particular, in the case of the dumbbells. The resulting exponents γ (which are estimated from the slopes of this plot) are collected in Table I. The exponents of τ_q and τ_4 always are very similar because they probe motions on the same scale, as already noted in Ref. 27. The exponent of τ_2 agrees with the exponent of D_t in the case of $N=5$, while in the case of $N=25$ the exponent of D_t is clearly smaller. If this result is not an artifact of insufficient statistics, the argument could be that the diffusion constant is related to a scale of the order of the coil size, which is clearly larger than the bond length for $N=25$, but not for $N=5$. However, we add the caveat that a log-log plot of the diffusion constant versus $T-T_c(N)$, Fig. 8, exhibits inevitably pronounced scatter for the dumbbell, and hence these data have to be considered with caution.

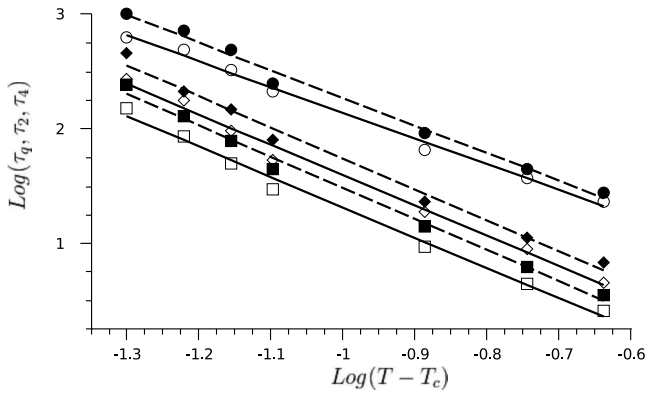

FIG. 6. Log-log plots of the relaxation times τ_q (squares), τ_2 (circles), and τ_4 (diamonds) for the bulk (open symbols) or the dumbbell (full symbols) in the model system with chains of five monomers. Relaxation times have been determined empirically by requiring a decay of the correlation function to a value of 0.3. The parameters T_c and γ obtained from the fits (solid curve: bulk and dashed curve: dumbbell) to a power law (see text) are given in Table I.

Surprisingly, a somewhat less noisy behavior is obtained if we plot D_t as a function of τ_q/T (Fig. 9): In all cases rather convincing evidence for power law behavior is observed,

$$D_t \propto (\tau_q/T)^{-\xi_t}, \tag{12}$$

the exponent ξ_t being given in Table II. We observe a small but significant deviation of ξ_t from unity, signifying that the breakdown of the Stokes–Einstein relation sets in for $T>T_c$ (but in the supercooled regime) already. For $N=10$, a related finding was already reported in Ref. 27.

IV. AN ATTEMPT TO ESTIMATE THE CHAIN-LENGTH DEPENDENCE OF THE VOGEL–FULCHER TEMPERATURE

As is well known,[3,4] the fit of the α-relaxation time by idealized MCT holds over a rather restricted temperature window only, and an equally good fit often is provided by the Vogel–Fulcher relation,[58] i.e.,

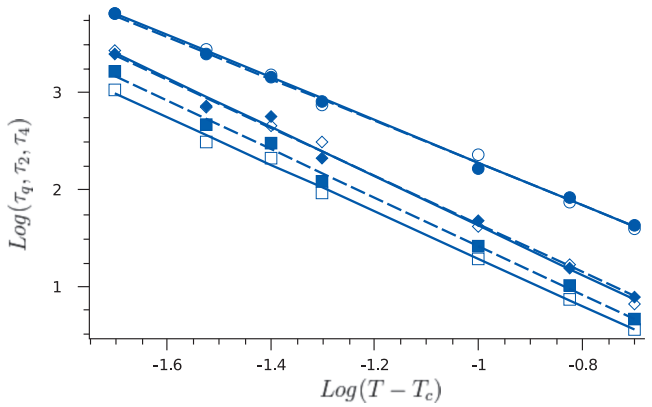

FIG. 7. Log-log plots of the relaxation times τ_q (squares), τ_2 (circles), and τ_4 (diamonds) for the bulk (open symbols) or the dumbbell (full symbols) in the model system with chains of 25 monomers. Relaxation times have been determined empirically by requiring a decay of the correlation function to a value of 0.3. The parameters T_c and γ obtained from the fits (solid curve: bulk and dashed curve: dumbbell) to a power law (see text) are given in Table I.

Author complimentary copy. Redistribution subject to AIP license or copyright, see http://jcp.aip.org/jcp/copyright.jsp

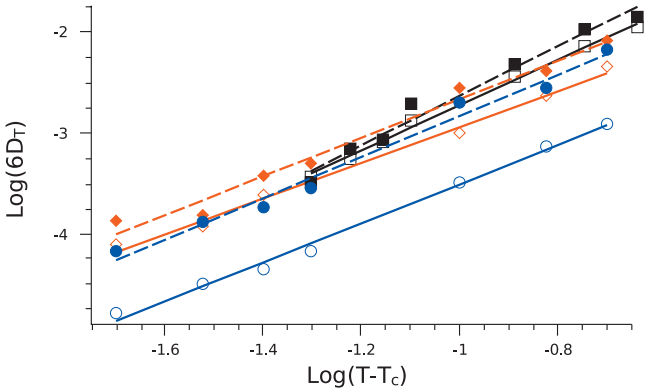

FIG. 8. Log-log plots of the translational diffusion coefficients for the bulk (open symbols) or the dumbbell (full symbols) in the model system with chains of 5 (black squares and curves), 10 (red diamonds and curves), and 25 (blue circles and curves) monomers. The parameters T_c and γ obtained from the fits (solid curve: bulk and dashed curve: dumbbell) to a power law (see text) are given in Table I.

$$\tau = \tau_0(N)\exp[B(N)/(T - T_0(N))], \tag{13}$$

where $\tau_0(N)$ is a prefactor of no interest here, $B(N)$ is some effective activation energy, and $T_0(N)$ is the Vogel–Fulcher temperature. Figures 10 and 11 demonstrate that all our data for $N=5$ and $N=25$ can be nicely fitted by Eq. (13); similar fits for $N=10$ can be found in Ref. 27.

The results of the present fits are collected in Table III, leading to $T_0(N=5) \approx 0.32 \pm 0.03$ while $T_0(N=10) \approx 0.33 \pm 0.04$ (Ref. 27) and $T_0(N=25) \approx 0.37 \pm 0.03$. Plotting these estimates versus $1/N$, as one would expect a straight line from Gibbs–DiMarzio-type arguments, one notes appreciable curvature; however, this is similar to the experimental observations.[30] The three chain length studied therefore do not allow an identification of the exact form of the N-dependence. Performing a tentative extrapolation to $N \to \infty$ employing the Gibbs–DiMarzio prediction would imply $T_0(N \to \infty) \approx 0.38 \pm 0.03$. These estimates suffer, of course, from the fact that they are extrapolated quite some distance below the smallest temperature accessible to us in the simulation. Furthermore, one has to bear in mind that typically the estimate for T_0 decreases when lower temperature data become available, until for temperatures close to the calorimetric glass transition temperature also the Vogel–Fulcher law breaks down.[62] For the results presented in Table III we first determined the best common estimate for $T_0(N)$ and then kept this estimate fixed in the determination of the other parameters. As one would have anticipated, the fits to τ_q and τ_4 lead to comparable values of the activation energy $B(N)$; these observables probe the same type of motion and have comparable relaxation times.[26,27] The second Legendre polynomial of the bond vector (or dumbbell) decays on longer time scales and is more susceptible to collective motion of the environment of the bond (or probe). This is reflected in the reduced value of the activation energy $B(N)$ in Table III as well as in the reduced value of the mode-coupling exponent γ in Table I, which in turn agrees with the exponent for the center of mass diffusion coefficient (zeroth Rouse mode). Relaxation processes on these scales are captured by the Rouse model and were shown to follow the same temperature dependence.[63,64]

TABLE II. Parameters obtained by fitting the fractional functional forms (SE relation modified by ξ_t) to the relaxation times τ_q for either the bulk or dumbbell dynamics in the model systems containing chains of either 5, 10, or 25 monomers.

$$D_T \propto \left(\frac{\tau}{T}\right)^{-\xi_t}$$

	ξ_t (5)	ξ_t (10)	ξ_t (25)
Bulk	0.88	0.85	0.82
Dumbbell	0.89	0.86	0.87

V. LINEAR DICHROISM TRAJECTORIES OF THE PROBE MOLECULES

In many SMS studies, emphasis is placed on the measurement of the linear dichroism trajectories, $d(t)$. In terms of the single molecule emission intensities I_p and I_s along two mutually perpendicular polarization directions, $d(t)$ is defined as

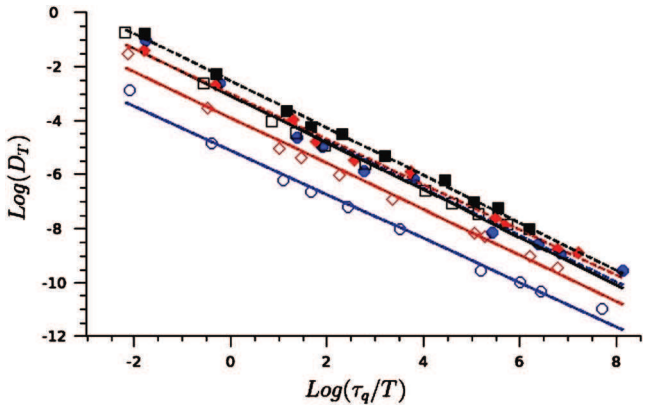

FIG. 9. Power law fits of translational diffusivities D_t as a function of τ_q/T ($q=6.9$): $D_t \approx (\tau_q/T)^{-\xi_t}$ for the bulk (open symbols, solid curves) or the dumbbell (full symbols, dashed curves) in the model system with chains of 5 (black squares and curves), 10 (red diamonds and curves), and 25 (blue circles and curves) monomers. Results for the exponent are given in Table II.

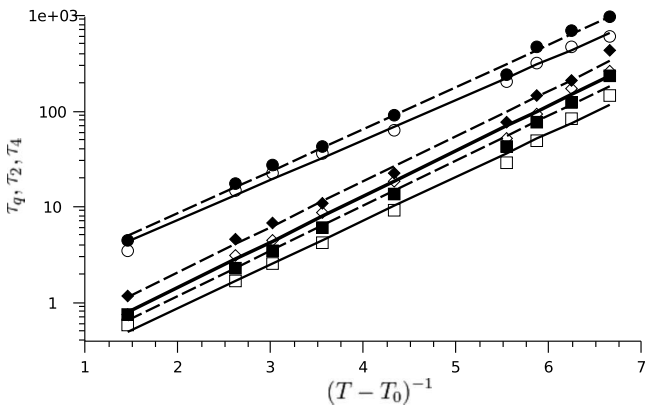

FIG. 10. Vogel–Fulcher plots of the relaxation times τ_q (squares), τ_2 (circles), and τ_4 (diamonds) for the bulk (open symbols, solid curves) or the dumbbell (full symbols, dashed curves) in the model system with chains of five monomers. The values of the Vogel temperature T_0 and of the fragility parameter B/T_0 are presented in Table III.

Author complimentary copy. Redistribution subject to AIP license or copyright, see http://jcp.aip.org/jcp/copyright.jsp

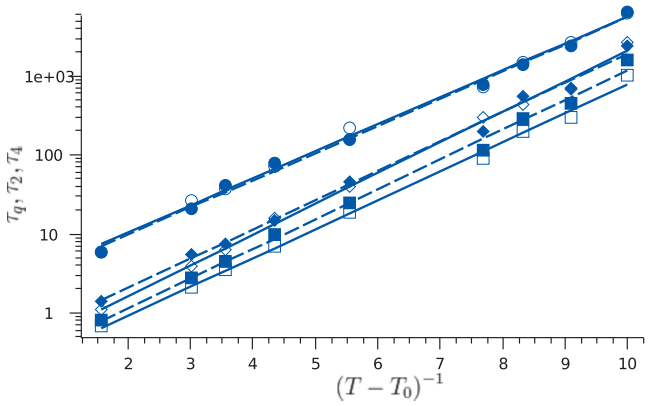

FIG. 11. Vogel–Fulcher plots of the relaxation times τ_q (squares), τ_2 (circles), and τ_4 (diamonds) for the bulk (open symbols, solid curves) or the dumbbell (full symbols, dashed curves) in the model system with chains of 25 monomers. The values of the Vogel temperature T_0 and of the fragility parameter B/T_0 are presented in Table III.

$$d(t) = (I_p - I_s)/(I_p + I_s). \tag{14}$$

In simulations, an equivalent quantity can be defined as[27,65]

$$d(t) = (7/8)[(\vec{e}_1 \cdot \vec{u})^2 - (\vec{e}_2 \cdot \vec{u})^2], \tag{15}$$

where $\vec{e}_1$ and $\vec{e}_2$ are orthogonal unit vectors defining an arbitrary plane intersecting the simulation box and $\vec{u}$ is a unit vector along the dumbbell axis, as before. Figure 12 shows typical raw data of the $d(t)$ trajectory of a dumbbell at $T=0.48$ and the corresponding autocorrelation function. The trajectory exhibits the typical jumps between distinct states, similar as discussed in our earlier work[25–27] for the trajectories of the fluorescence lifetime. The unconventional jumpwise relaxation again can be attributed to the transitions between metabasins in the energy landscape of our model system.[25–27]

TABLE III. Parameters obtained by fitting the Vogel–Fulcher law to α relaxation times τ_q, τ_2, and τ_4 for the model systems with chains of either 5, 10, or 25 monomers. Results of fits obtained by fixing the Vogel temperature to either $T_0=0.32$ (5 monomers), $T_0=0.33$ (10 monomers), or $T_0=0.37$ (25 monomers) are given.

	τ_x					
Bulk	T_0 (5)	B/T_0 (5)	T_0 (10)	B/T_0 (10)	T_0 (25)	B/T_0 (25)
τ_q	0.32	3.29	0.33	3.52	0.37	2.28
τ_2	0.32	3.03	0.33	3.18	0.37	2.13
τ_4	0.32	3.43	0.33	3.63	0.37	2.42
Dumbbell	T_0 (5)	B/T_0 (5)	T_0 (10)	B/T_0 (10)	T_0 (25)	B/T_0 (25)
τ_q	0.32	3.40	0.33	3.60	0.37	2.35
τ_2	0.32	3.18	0.33	3.45	0.37	2.14
τ_4	0.32	3.42	0.33	3.67	0.37	2.31

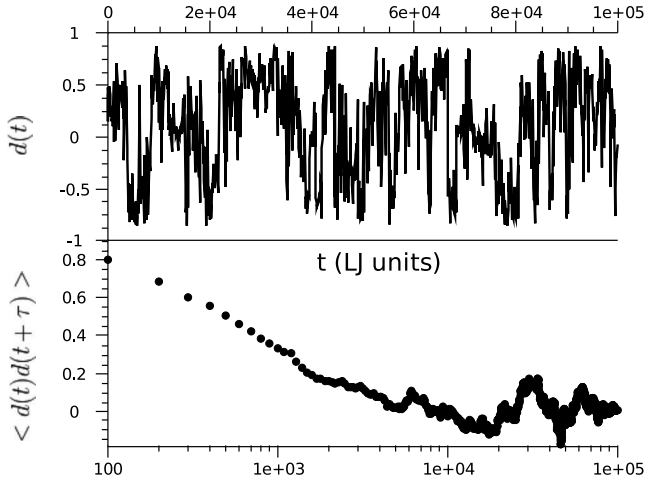

FIG. 12. Linear dichroism $d(t)$ trajectory (top) and corresponding autocorrelation function (bottom) of a dumbbell in a model system with polymer chains of five monomers at a temperature of $T=0.48$.

While the autocorrelation function

$$C_d(\tau) = \langle d(t)d(t+\tau)\rangle \tag{16}$$

shown in Fig. 12 (bottom) corresponds to the single trajectory shown in the top of this figure, one needs to average such data over (at least) ten independent trajectories to get relevant statistics from our simulations. In SMS, the trajectories have been shown to have a required length at least 100 times larger than the typical relaxation times obtained from their time correlation functions in order to ensure a properly built function and a relevant value for the extracted relaxation time.[66] Such averaged data are shown in Fig. 13, where for each temperature again a relaxation time τ_d is extracted requiring $C_d(\tau)=0.3$. The right part illustrates that the time-temperature superposition principle also holds for this quan-

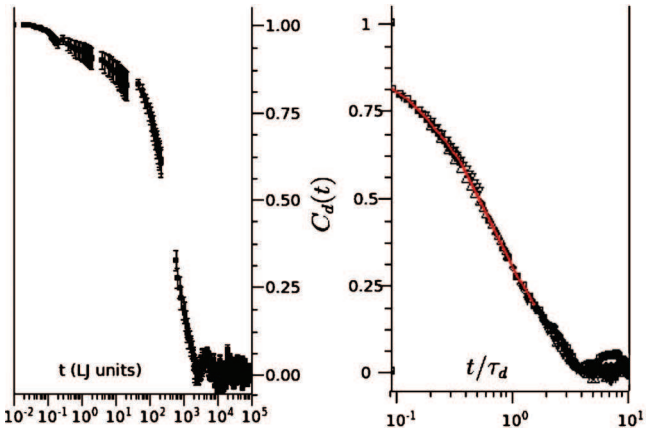

FIG. 13. Left: orientational time correlation function $C_d(\tau)$ (linear dichroism) for the dumbbell in the model system of chains with five monomers at a temperature $T=0.48$. The error bars are estimated by the Jackknife approach on the base of the ten simulation runs at this temperature. Right: time is scaled by the α-relaxation time τ_d of the linear dichroism for the four data sets (black symbols) pertaining to the lowest temperatures investigated in this study $0.47 \leqq T \leqq 0.5$, where the time-temperature superposition principle notably holds. Also shown (red curve) is the best fit $C_d(\tau) = f_d^c - h_d(\tau/\tau_\alpha)^b + h_d B_d(\tau/\tau_\alpha)^{2b}$ performed simultaneously on these four data sets, allowing for the determination of the MCT parameters: $b=0.57$ and $\gamma=2.5$, in agreement with Fig. 1.

Author complimentary copy. Redistribution subject to AIP license or copyright, see http://jcp.aip.org/jcp/copyright.jsp

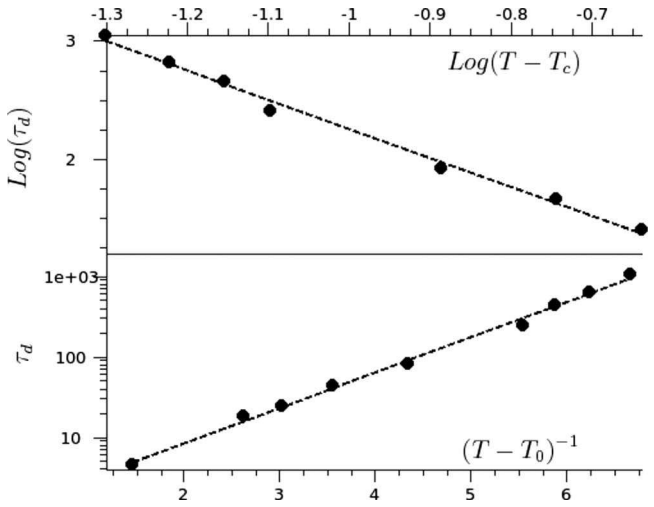

FIG. 14. Top: log-log plot of the relaxation times τ_d for the dumbbell in the model system with chains of five monomers. All relaxation times have been determined empirically by the requirement $C_d(\tau_d)=0.3$. The parameters T_c and γ obtained from the fits to a power law are reported in Table I. Bottom: Vogel–Fulcher plot of the relaxation times τ_d for the dumbbell in the model system with chains of five monomers. The values of the Vogel temperature T_0 and of the fragility parameter B/T_0 are reported in Table III.

tity, if $C_d(\tau)$ is plotted versus τ/τ_d at different temperatures (for $\tau/\tau_d \geq 0.1$ in the α relaxation regime) close to T_c. Those data can be fitted to the analog of Eq. (4), and if one imposes $b=0.57$ (which resulted from the fit of the data in Fig. 1), one finds an estimate for γ ($\gamma \approx 2.49$) which is reasonably consistent with the value previously found and agrees with the prediction from the MCT exponent relations.

The point which we wish to make in the context of these results is that the observation of the dynamics of the probe molecule suffices to obtain detailed information on the slow dynamics of the matrix. In fact, the relaxation time τ_d extracted in this way yields data for $T_c(N)$ and $T_0(N)$ nicely compatible with the analysis of the data that were presented in sections III and IV, as Fig. 14 demonstrates. In this way, our simulations establish the usefulness of the SMS approach to study the slow dynamics of supercooled liquids. Experimental results[19,20] indicate that the coupling of the probe to transitions in its local environment (which we could identify with metabasin transitions in the supercooled liquid) persists at temperatures close to T_g, where the average dynamics is orders of magnitude slower. We can therefore conjecture that the coupling of the probe dynamics to the matrix dynamics remains qualitatively similar upon lowering T, although we are not able to establish this on a microscopic scale by simulations.

VI. CONCLUSIONS

The present paper has addressed two important questions about the properties of glass forming polymer melts, applying MD simulation methods for the study of a simple coarse-grained bead-spring model of polymer chains.

(i) How do parameters that are useful for the empirical description of the slowing down as the glass transition is approached change when the chain length N is varied, keeping the conditions strictly unchanged in all other respects? Specifically, we addressed quantities such as the critical temperature $T_c(N)$ and exponent $\gamma(N)$ when a power law fit is made to describe the increase in various relaxation times on cooling, as well as the Vogel–Fulcher temperature $T_0(N)$. Since the bead-spring model includes only two basic properties of flexible macromolecules, namely, the connectivity of the chains and the generic feature of all intermolecular interactions, which show dispersion-type attraction at larger distances but excluded-volume type repulsion at short distances, but completely neglects effects of local chain stiffness due to bond bending, and torsional potentials, it is not completely obvious that this model captures correctly subtle features such as these chain length variations.

(ii) The second question that is asked concerns the accuracy of SMS techniques that have recently become rather popular as a local probe of glassy dynamics: Are such local probes sensitive enough that they faithfully "notice" subtle differences in the matrix due to the chain length dependence? The size of a linear dumbbell mimicking a fluorescent probe molecule is rather comparable to the gyration radius of a short oligomer with only $N=5$ (effective) monomers, but it is much smaller than the gyration radius in the case of a chain with $N=25$. This crossover in the size ratio could lead to additional effects, obscuring the pure properties of the matrix.

Although in our study only three short chain lengths ($N=5$, $N=10$, and $N=25$) were available, we nevertheless could obtain rather definitive answers to both questions: (i) the simple, fully flexible, bead-spring model does faithfully reproduce the chain length dependence familiar from the experimental studies (although, of course, the exact form of the N-dependence could not be established from simulations of only three chain lengths), underscoring one more time the high degree of universality of the description of the qualitative properties of glass forming polymers. (ii) These trends can also be extracted rather well from the various relaxation functions and associated relaxation times that one can define (and experimentally measure) for single molecule probes. Our results thus lend additional credence to the reliability of this technique.

We end this discussion with a caveat, however: One should not conclude that our findings imply that the glassy freeze-in of polymer melts is basically understood. In fact, the precise features how the (idealized) MCT breaks down very close to $T_c(N)$, and the precise nature of the slowing down at temperatures lower than $T_c(N)$ clearly have not been elucidated by our study due to excessive demands on computer resources; also the power law describing the breakdown of the Stokes–Einstein relation (cf. Fig. 9) is just an empirical finding, of which an explanation in terms of a microscopic theory is lacking. Moreover while our findings clearly are compatible with ideas such as transitions of the system between various metabasins in phase space, reflecting the dynamic heterogeneity of the glass forming melt, the need to quantify these concepts more precisely remains.

Author complimentary copy. Redistribution subject to AIP license or copyright, see http://jcp.aip.org/jcp/copyright.jsp

Nevertheless, we hope that our study will encourage more comprehensive experimental and theoretical work on these issues.

ACKNOWLEDGMENTS

Partial support from the Sonderforschungsbereich 625/A3 of the German National Science Foundation and the EU network of excellence SOFTCOMP is acknowledged.

[1] E.-W. Donth, *The Glass Transition. Relaxation Dynamics in Liquids and Disordered Materials* (Springer, Berlin, 2001).
[2] G. Strobl, *The Physics of Polymers* (Springer, Berlin, 1996).
[3] K. Binder, J. Baschnagel, and W. Paul, Prog. Polym. Sci. **28**, 115 (2003).
[4] K. Binder and W. Kob, *Glassy Materials and Disordered Solids: An Introduction to Their Statistical Mechanics* (World Scientific, Singapore, 2005).
[5] I. Gutzov and J. Schmelzer, *The Vitreous State. Thermodynamics, Structure, Rheology and Crystallization* (Springer, Berlin, 1995).
[6] W. E. Moerner and M. Orrit, Science **283**, 1670 (1999).
[7] X.-S. Xie and J. K. Trautmann, Annu. Rev. Phys. Chem. **49**, 441 (1998).
[8] F. Kulzer and M. Orrit, Annu. Rev. Phys. Chem. **55**, 585 (2004).
[9] R. A. L. Vallée, M. Coltet, J. Hofkens, F. C. De Schryver, and K. Müllen, Macromolecules **36**, 7752 (2003).
[10] L. A. Deschenes and D. A. Vanden Bout, J. Phys. Chem. B **106**, 11438 (2002).
[11] N. Tomczak, R. A. L. Vallée, E. M. H. P. van Dijk, M. Garcia-Paragio, L. Kuipers, N. F. van Hulst, and G. J. Vancso, Eur. Polym. J. **40**, 1001 (2004).
[12] A. Schob, F. Cichos, J. Schuster, and C. von Borczyskowski, Eur. Polym. J. **40**, 1019 (2004).
[13] E. Mei, J. Tang, J. M. Vanderkovi, and R. M. Hochstrasser, J. Am. Chem. Soc. **125**, 2730 (2003).
[14] R. M. Dickson, D. J. Norris, and W. E. Moerner, Phys. Rev. Lett. **81**, 5322 (1998).
[15] B. Sick, B. Hecht, and L. Novotny, Phys. Rev. Lett. **85**, 4482 (2000).
[16] A. Lieb, J. M. Zavislan, and L. Novotny, J. Opt. Soc. Am. B **21**, 1210 (2004).
[17] M. Böhmer and J. Enderlein, J. Opt. Soc. Am. B **20**, 554 (2003).
[18] A. P. Bartko, K. Xu, and R. M. Dickson, Phys. Rev. Lett. **89**, 026101 (2002).
[19] R. A. L. Vallée, N. Tomczak, L. Kuipers, G. J. Vancso, and N. F. van Hulst, Phys. Rev. Lett. **91**, 038301 (2003).
[20] R. A. L. Vallée, N. Tomczak, G. J. Vancso, L. Kuipers, and N. F. van Hulst, J. Chem. Phys. **122**, 114704 (2005).
[21] M. Faetti, M. Giordano, D. Leporini, and L. Pardi, Macromolecules **32**, 1876 (1999).
[22] H. Sillescu, J. Non-Cryst. Solids **243**, 81 (1999).
[23] M. D. Ediger, Annu. Rev. Phys. Chem. **51**, 99 (2000).
[24] R. Richert, J. Phys.: Condens. Matter **14**, R703 (2002).
[25] R. A. L. Vallée, M. Van der Auweraer, W. Paul, and K. Binder, Phys. Rev. Lett. **97**, 217801 (2006).
[26] R. A. L. Vallée, M. Van der Auweraer, W. Paul, and K. Binder, Europhys. Lett. **79**, 46001 (2007).
[27] R. A. L. Vallée, W. Paul, and K. Binder, J. Chem. Phys. **127**, 154903 (2007).
[28] P. G. de Gennes, *Scaling Concepts in Polymer Physics* (Cornell University Press, Ithaca, NY, 1979).
[29] P. J. Flory, *Principles of Polymer Chemistry* (Cornell University Press, Ithaca, NY, 1953).
[30] G. Pezzin, F. Zilio-Grande, and P. Sanmartin, Eur. Polym. J. **6**, 1053 (1970) (and references therein).
[31] J. H. Gibbs and E. A. di Marzio, J. Chem. Phys. **28**, 373 (1958).
[32] W. Kauzmann, Chem. Rev. (Washington, D.C.) **43**, 219 (1948).
[33] H.-P. Wittmann, J. Chem. Phys. **95**, 8449 (1991).
[34] M. Wolfgardt, J. Baschnagel, W. Paul, and K. Binder, Phys. Rev. E **54**, 1535 (1996).
[35] See the discussion on p. 324 of Ref. 4.
[36] C. Bennemann, W. Paul, K. Binder, and B. Dünweg, Phys. Rev. E **57**, 843 (1998).
[37] C. Bennemann, J. Baschnagel, W. Paul, and K. Binder, Comput. Theor. Polym. Sci. **9**, 217 (1999).
[38] C. Bennemann, J. Baschnagel, and W. Paul, Eur. Phys. J. B **10**, 323 (1999).
[39] C. Bennemann, W. Paul, J. Baschnagel, and K. Binder, J. Phys.: Condens. Matter **11**, 2179 (1999).
[40] J. Baschnagel, C. Bennemann, W. Paul, and K. Binder, J. Phys.: Condens. Matter **12**, 6365 (2000).
[41] M. Aichele and J. Baschnagel, Eur. Phys. J. E **5**, 229 (2001); **5**, 245 (2001).
[42] J. Buchholz, W. Paul, F. Varnik, and K. Binder, J. Chem. Phys. **117**, 7364 (2002).
[43] J. Baschnagel and F. Varnik, J. Phys.: Condens. Matter **17**, R851 (2005).
[44] W. Paul, *Reviews in Computational Chemistry* (Wiley, New York, 2007), Vol. 25, p. 1.
[45] M. Goldstein, J. Chem. Phys. **51**, 3728 (1969).
[46] F. H. Stillinger and T. H. Weber, Phys. Rev. A **28**, 2408 (1983).
[47] B. Doliwa and A. Heuer, Phys. Rev. Lett. **91**, 235501 (2003).
[48] B. Doliwa and A. Heuer, Phys. Rev. E **67**, 030501 (2003).
[49] M. Vogel, B. Doliwa, A. Heuer, and S. C. Glotzer, J. Chem. Phys. **120**, 4404 (2004).
[50] R. A. Denny, D. R. Reichman, and J.-P. Bouchaud, Phys. Rev. Lett. **90**, 025503 (2003).
[51] L. Angelani, G. Ruocco, M. Sampoli, and F. Sciortino, J. Chem. Phys. **119**, 2120 (2003).
[52] J. Kim and T. Keyes, J. Chem. Phys. **121**, 4237 (2004).
[53] D. Coslovich and G. Pastore, Europhys. Lett. **75**, 784 (2006).
[54] G. A. Appignanesi, J. A. Rodrigues Fris, R. A. Montani, and W. Kob, Phys. Rev. Lett. **96**, 057801 (2006).
[55] W. Götze and L. Sjögren, Rep. Prog. Phys. **55**, 241 (1992).
[56] J. Jäckle, Rep. Prog. Phys. **49**, 171 (1986).
[57] P. G. Debenedetti, *Metastable Liquids* (Princeton University Press, Princeton, 1977).
[58] H. Vogel, Phys. Z. **22**, 645 (1921); G. S. Fulcher, J. Am. Ceram. Soc. **8**, 339 (1925).
[59] The software package OCTA (http://octa.jp) was used.
[60] *Monte Carlo and Molecular Dynamics of Condensed Matter*, edited by K. Binder and G. Ciccotti (Societa Italiana di Fisica, Bologna, 1996).
[61] W. Paul, Chem. Phys. **284**, 59 (2002).
[62] F. Stickel, E. W. Fischer, and R. Richert, J. Chem. Phys. **104**, 2043 (1996).
[63] A. Barbieri, E. Campani, S. Capaccioli, and D. Leporini, J. Chem. Phys. **120**, 437 (2004).
[64] A. Ottochian, D. Molin, A. Barbieri, and D. Leporini, J. Chem. Phys. **131**, 174902 (2009).
[65] M. F. Gelin and D. S. Kosov, J. Chem. Phys. **125**, 054708 (2006).
[66] C.-Y. Lu and D. A. Vanden Bout, J. Chem. Phys. **125**, 124701 (2006).

Author complimentary copy. Redistribution subject to AIP license or copyright, see http://jcp.aip.org/jcp/copyright.jsp

DOI: 10.1021/ma101975j

Macromolecules
ARTICLE

Single Molecules Probing the Freezing of Polymer Melts: A Molecular Dynamics Study for Various Molecule-Chain Linkages

R. A. L. Vallée,*,† W. Paul,‡ and K. Binder§

†*Centre de Recherche Paul Pascal (CNRS), 115 avenue du docteur Albert Schweitzer, 33600 Pessac, France,* ‡*Institut für Physik, Martin-Luther University, 06099 Halle, Germany, and* §*Institut für Physik, Johannes-Gutenberg University, 55099 Mainz, Germany*

Received August 27, 2010; Revised Manuscript Received November 2, 2010

ABSTRACT: We present molecular dynamics simulations of coarse-grained model systems of a glass-forming polymer matrix containing fluorescent probe molecules. These probe molecules are either dispersed in the matrix or covalently attached to the center or the end of a dilute fraction of the polymer chains. We show that in all cases the translational and rotational relaxation of the probe molecules is a faithful sensor for the glass transition of the matrix as determined from a mode-coupling analysis or Vogel−Fulcher analysis of their α-relaxation behavior. Matrix and dumbbell related relaxation processes show a clear violation of the Stokes−Einstein−Debye laws. In accordance with recent experimental results, the long time behavior of single molecule spectroscopy observables like the linear dichroism is not susceptible to distinguish between center-attached and end-attached fluorophores. However we show that it is different from the behavior of dispersed fluorophores. We also show that the difference between the two attachment forms does show up in the caging regime of the relaxation functions and that this difference increases upon supercooling the melt toward its glass transition.

Introduction

Understanding the mechanisms responsible for the tremendous slowing down of the mobility when approaching the glass transition is one of the most important challenges in modern soft condensed matter physics, both for low-molecular-weight and polymeric materials.[1−5] Rotational motions of both backbone segments and side groups are the principal relaxation mechanisms in amorphous polymers. Such relaxation processes have been studied experimentally in the vicinity of the glass-transition temperature T_g by viscosity,[6] compliance,[6] quasi-elastic neutron scattering,[7] NMR,[8−10] photon correlation spectroscopy,[11,12] dielectric relaxation,[13−15] photobleaching,[16] and second harmonic generation techniques[17,18] to name and cite but a selection of the studies performed. It has been established that above the glass-transition temperature, the α-relaxation is the primary relaxation process for the collective motion of polymer segments.

Because it allows bypassing the ensemble averaging intrinsic to bulk studies, single molecule spectroscopy (SMS) constitutes a powerful tool to assess the dynamics of heterogeneous materials at the nanoscale level.[19−22]

On the one hand, by following the temporal evolution of the fluorescence lifetime of single molecules with quantum yield close to unity, this observable revealed highly sensitive to changes in local density occurring in a polymer matrix.[23−28] Using free volume theories, the lifetime fluctuations were related to hole (free-volume) distributions and allowed the determination of the number of polymer segments involved in a rearrangement cell around the probe molecule as a function of temperature,[23,26] solvent content,[24] and film thickness.[25] On the basis of a microscopic model for the fluctuations of the local field,[27] a clear correlation was established between the fluorescence lifetime distributions measured for single molecules and the local fraction of surrounding holes both in the glassy state and in the supercooled regime for various molecular weight oligo(styrene).[28] Furthermore, fluorescence lifetime trajectories of single probe molecules embedded in a glass-forming PS melt were shown to exhibit strong fluctuations of a hopping character. Using MD simulations targeted to explain these fluctuations,[29] the lifetime fluctuations were correlated with the meta-basin transitions in the potential energy landscape of the polymer matrix, thus providing a new tool for the experimental study of long-standing issues in the physics of the glass transition. Finally, the interaction between the probe molecule and the polymer matrix can also be investigated. The interaction between several conformers of a given fluorophore and poly(styrene) (PS) polymer chains was investigated.[30−32] The existence of different conformations, stabilized owing to favorable interactions with the surrounding polymer matrix, lead to specific spectroscopic responses, i.e., specific fluorescence lifetimes and emission spectra. The type of conformer found in the matrix and its interaction with the surrounding chains governed the local packing of the matrix and thus allowed one to probe the local free volume.

On the other hand, single-molecule rotational imaging also proved to be very powerful in probing the local dynamics of polymers. By using two-dimensional (2D) orientation techniques, the in-plane (of the sample) projection of the transition dipole moment of the single molecule (SM) (the so-called linear dichroism $d(t)$) has been followed in time and its time correlation function $C_d(t)$ has been computed and fitted by a stretched exponential function $f(t) = e^{-(t/\tau)^\beta}$.[33−36] These investigations have allowed to identify static and dynamic heterogeneity in the samples;[37,38] i.e., SMs exhibit τ and β values varying according to (i) their actual position in the matrix and (ii) the time scale at which they are probed, as a result of the presence of different nanoscale environments. Zondervan et al.[39] investigated the rotational motion of perylene diimide in glycerol. Observations of environmental exchanges were very

*To whom correspondence should be addressed. E-mail: vallee@crpp-bordeaux.cnrs.fr.

 Published on Web 12/06/2010 © 2010 American Chemical Society

scarce. They assumed that glycerol consists of heterogeneous liquid pockets separated by a network of solid walls. This was supported by rheology measurements at very weak stresses of glycerol and *o*-terphenyl.[40] With 3D orientation techniques, the emission transition dipole moment of a SM has been recorded as a function of time.[41−44] In particular, the distribution of nanoscale barriers to rotational motion has been assessed by means of SM measurements[45] and related to the spatial heterogeneity and nanoscopic α-relaxation dynamics deep within the glassy state. Owing to the high barriers found in the deep glassy state, only few SMs were able to reorient, while somewhat lower barriers could be overcome when increasing the temperature.

However, in all investigations described here above, the local dynamics of the polymers was ascertained through the behavior of single molecules inserted as dopants in the host polymer. Very scarce studies of the motion of the polymer chains themselves have been reported.[46,47] Bowden et al.[46] prepared several polymers with a perylene diimide dye at the end or in the middle of each polymer chain, and the orientation of the labeled segments of polybutadiene (PB) chains in a matrix of poly(methyl methacrylate) (PMMA) was detected using a fluorescence polarization modulation technique. However, the PMMA matrix used in those experiments was glassy and reorientation occurred for only 5% of the dye-labeled polymers. Since the dye was intimately attached to the polymer backbone, the orientation of the dye reflected the motion of the local portion of the polymer chain. The extent to which the dye orientation could be used to infer the overall motion of the entire polymer molecule still has to be elucidated.

It is clearly of interest to further study segmental polymer motion in less rigid environments, such as melts and rubbers. Gravanovich et al.[47] investigated the dynamics of various dye-labeled polymer chains in similar but unlabeled polymer chains in the melt. Their experiments notably allowed for the analysis of the importance of factors such as the position of the dye molecule in the chain, the chemical identity of the dopant and matrix polymers and the pumping intensity on the observed rotational dynamics of the dye. Using autocorrelation analysis of both the total emitted intensity and the orientation angle, a few conclusions were reported: (i) there was no distinguishable difference in the characteristic correlation times between center- and end-positioned dyes; (ii) molecules in the rubbery matrix displayed the longest correlation times while those in the low-viscosity host displayed the shortest times; (iii) the laser illumination intensity had little impact on the intensity autocorrelation decay times, but higher intensity did lead to shorter correlation times in the angle autocorrelation analysis. This seemed to indicate that high intensity provided more thermal energy for the molecules to reorient. The authors[47] further concluded that the dye molecule is quite large compared to the size of a monomer so that the innate motion of the chain might be altered. As such, while the observed motion of the dye molecules might not be representative of unhindered polymer motion, these dyes certainly behave as reporters of the local environment surrounding their position at either the chain end or the chain center. The similar behaviors exhibited for end- and center-labeled dyes on the rather long time scales addressed in the experiments might suggest that differences between the mobilities of chain ends and chain centers had been averaged out on the long time scale, but might still be observable at shorter times. The authors suggested further experiments to examine untethered fluorophores in these polymer melts to compare their behavior to those built into the polymer backbone. By following such parameters as the in-plane dipole moment and the overall brightness of the fluorophore over time and versus temperature can lend insight into dynamic processes that occur within the polymer host.

The aim of our current paper is precisely to shed some light on the dynamical behavior of fluorophores positioned in the center, at the end and simply mixed to polymer chains, to investigate the difference between these behaviors and the bulk relaxation of the polymer itself. For probe molecules dispersed into a glass-forming polymer matrix we have analyzed in detail their ability to faithfully monitor the glass transition of the host matrix. We have shown that the probes record a change in mechanism from rotational diffusion to large angular jumps[48] on approaching the mode-coupling critical temperature of the polymer melt, have analyzed how the coupling between probe and melt depends on the size and the mass of the probe[49] and have shown that the probes are sensitive to chain length effects in the glass transition of the matrix.[50] These studies have employed molecular dynamics simulations of a bead−spring dumbbell dissolved in a bead−spring polymer melt as a coarse-grained model system for probe molecules in a polymer matrix. We are employing the same model here but now attach the probe dumbbell into a polymer chain, either at the end or in the center of the chain.

In the next section, we will explain our simulation model and the way the simulations were performed, and the ensuing section will discuss our results for the translational and rotational dynamics of probes in a polymer matrix, comparing free probes to end-attached and center-attached probes. A final section will then present our conclusions.

Methods

We performed MD simulations of a system containing 48 bead−spring chains of 25 effective monomers. A dumbbell is also inserted in the system to act as a reporter of the behavior of the local environment, mimicking a single molecule as used in single molecule spectroscopy (SMS). The dumbbell has been either inserted as a free dopant (further named free) in the system or covalently linked in the middle (further named center) or at the end (further named end) of one chain of the simulation box, keeping the total number of beads to 25. While our aim is not a chemically realistic modeling of a particular material since we wish to elucidate the generic behavior of polymer melt plus probe molecule systems, the mass of the beads have been chosen to be $m_B = 1$ for the monomers of the chains and $m_A = 2.25$ for the monomers of the dumbbell in order to closely match the experimental conditions[47] for which the probe molecules are always heavier than a dimer in the chains. A cubic simulation volume with periodic boundary conditions is used throughout. The interaction between two beads of type A (probe) or B (monomers) is given by the Lennard-Jones potential

$$U_{LJ}(r_{ij}) = 4\varepsilon\left[\left(\frac{\sigma_{\alpha\beta}}{r_{ij}}\right)^{12} - \left(\frac{\sigma_{\alpha\beta}}{r_{ij}}\right)^{6}\right]$$

where r_{ij} is the distance between beads i, j and $\alpha,\beta \in$ A,B. The LJ diameters used are $\sigma_{AA} = 1.22$, $\sigma_{BB} = 1.0$ (unit of length) and $\sigma_{AB} = 1.11$, while $\varepsilon = 1$ sets the scale of energy (and temperature T, since Boltzmann's constant $k_B = 1$). These potentials are truncated at $r_{cut}^{\alpha\beta} = 2^{7/6}\,\sigma_{\alpha\beta}$ and shifted so that they are zero at $r_{ij} = r_{cut}^{\alpha\beta}$. Between the beads along the chain, as well as between the beads of the dumbbell, a finitely extendable nonlinear elastic (FENE) potential is used

$$U_F = -\frac{k}{2}R_0^2 \ln\left[1 - \left(\frac{r_{ij}}{R_0}\right)^2\right]$$

with parameters $k = 30$, $R_0 = 1.5$.[51] This model system (without the probe) has been shown to qualitatively reproduce many features of the relaxation of glass-forming polymers.[51−59] In the MD simulations, the equations of motion at constant particle number N, volume V, and energy E are integrated with the velocity Verlet algorithm[60,61] with a time step of 0.002, measuring time in units of $(m_B\sigma_{BB}^2/48\varepsilon)^{1/2}$. All NVE simulations have been performed after equilibrating the system in the NpT ensemble,

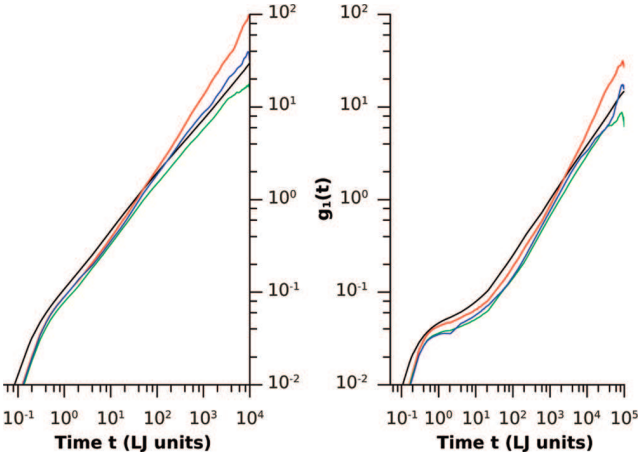

Figure 1. Mean square displacements as a function of time for $T = 0.7$ (left) and $T = 0.5$ (right). The black curves describe $g_1(t)$ for all the monomers of all the chains for the bulk model system. The red, green and blue curves pertain to similar information for the free dumbbell, the dumbbell covalently linked in the center or at the end of one chain, respectively.

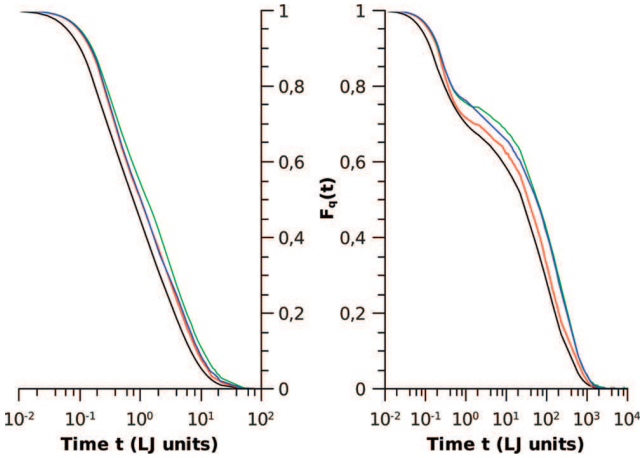

Figure 2. Intermediate dynamic structure factor $F_q(t)$ at the first maximum ($q = 6.9$) of the static structure factor for the NVE simulations performed at temperatures $T = 0.7$ (left) and $T = 0.5$ (right). The black curves describe $F_q(t)$ for the chains in the bulk model system. The red, green, blue curves pertain to similar information for the free dumbbell, the dumbbell covalently linked in the center or at the end of one chain, respectively.

using a Nosé−Hoover thermostat,[61] keeping the average pressure at $p = 1.0$ at all temperatures. These runs lasted up to 5×10^7 MD steps. Ten different configurations were simulated at each temperature ($T = 0.47, 0.48, 0.49, 0.5, 0.55, 0.6, 0.65, 0.7, 1.0, 2.0$), in order to ensure good statistics. Note that the melting temperature of the crystalline phase of this model polymer has been estimated[57] to be $T_m = 0.75$ while the critical temperature T_c of mode coupling theory (where in our model a smooth crossover to activated dynamics occurs) is about $T_c = 0.45$.[50] Thus, our data include equilibrated melts as well as the moderately supercooled regime.

Results

We begin by analyzing the translational motion of the probes and the monomers as observed in the simulation in the mean square displacement of the particles and in simulation and experiment in the incoherent scattering function. The mean square displacements of individual effective monomers is defined as

$$g_1(t) \equiv \frac{1}{M}\sum_{i=1}^{M}\langle[\vec{r}_i(t) - \vec{r}_i(0)]^2\rangle \tag{1}$$

when we average over all monomers within a polymer chain. The long time behavior of the mean square displacement defines the translational diffusion coefficient, D_t, by

$$g_1(t) = 6D_t t \tag{2}$$

We obtain the diffusion constant in this work by fitting this linear law to the late time behavior of the mean squared displacement. As we will see in Figure 1, this entails some systematic error because our results for the late time displacement of the dumbbells are susceptible to large statistical fluctuations. For the chain attached dumbbells there is furthermore an extended crossover regime from Rouse-mode dominated to free diffusion behavior and we can not claim in all cases that this crossover is completed within our simulation time window. The incoherent intermediate scattering function, $F_q(t)$, is defined as

$$F_q(t) = \frac{1}{M}\sum_{i=1}^{M}\langle\exp[i\vec{q}\cdot(\vec{r}_i(0) - \vec{r}_i(t))]\rangle \tag{3}$$

In eq 3, the sum is extended over all M effective monomers in the system, and $\vec{r}_i(t)$ is the position of the i'th monomer at time t, while $\vec{q}$ is the scattering wave vector. Being interested in the slow dynamics associated with the cage effect,[2] it is most useful to choose q such that it roughly corresponds to the position where the static structure factor $S(q)$ of the melt has its peak, which is (for the chosen conditions) $q = 6.9$ (note that in the temperature regime of interest, $S(q)$ changes with temperature only very little. Of course, analogous quantities to eq 1 and eq 3 can be immediately defined for the dumbbell if the simulated system contains one; the only problem then is that, due to the small number $M = 2$ (rather than $M = 1200$), the poor statistics necessitates to carry out multiple runs (as mentioned in the Methods, 10 independent runs were hence performed). In Figure 1 we show results for the mean square displacements for all monomers g_1, of all chains and for the dumbbells included in the melt for two temperatures. The higher temperature, $T = 0.7$ displayed on the left shows the typical melt behavior in the polymer displacements. After an initial inertia dominated period, lasting until $t \simeq 0.5$, one observes, in the monomer displacement, a crossover to a subdiffusive, Rouse mode dominated regime, and at long times another crossover to the free diffusion limit, from which we read of the translational diffusion coefficient at that temperature. At the lower temperature, $T = 0.5$, depicted on the right, a plateau regime is clearly visible in the monomer displacement extending about one decade in time. This regime of caged dynamics is indicative of the approach to the glass transition in the supercooled melt. When we analyze the motion of the dumbbell as an indicator for the matrix glass transition, we observe that it mirrors the matrix behavior irrespective of whether it is free (red curves), center-attached (green curves), or end-attached (blue curves). The free dumbbell is not following the late stages of the Rouse mode dominated dynamics and crosses over to free diffusion at an earlier time than the chains. Both chain-attached dumbbells of course have to participate in the Rouse mode dynamics of the chains. While at the higher temperature the end-attached dumbbell seems to be slightly faster than the center-attached one for displacements larger than one monomer diameter, there is no discernible difference between these displacements at the lower temperature. However, we have to keep in mind the limited statistical accuracy we can obtain with one dissolved dumbbell for the long-time behavior of correlation functions, even when we average over 10 independent runs.

When we now look at the incoherent intermediate scattering function shown in Figure 2, we can observe the same built-up of a two-step relaxation behavior upon approach of the glass transition

as discussed for the mean square displacements. At both temperatures, all dumbbell scattering functions relax more slowly than the monomer one. At the higher temperature there is an observable difference between the free dumbbell and the end-attached dumbbell on the one side and the center-attached dumbbell on the other side, which relaxes more slowly than the other two for times around the typical relaxation time (time to decay to $1/e$) which is about 5. We can see in Figure 1 that at these times the spheres have moved over roughly 20% of their diameter and for these time scales Figure 1 also displays a slightly slower motion of the center-attached dumbbell than of the end-attached one, although this feature, is hardly visible on the logarithmic scale of Figure 1.

Looking at the lower temperature, we see interesting differences developing in the mobilities of the dumbbells. In the inertia regime, all dumbbells move in the same way and similarly to the monomers of the chains. The inertial regimes end at around $t \simeq 0.5$. The extent of motion, however, is very different for the different situations. The scattering function of the monomers decays faster and to the largest extent through the inertial and vibrational motion. Next comes the free dumbbell which relaxes more slowly but to almost the same extent. The slower motion can be understood by a larger resistance that the dumbbell experiences compared to two bonded monomers due to the increased diameter of the spheres making up the dumbbell. The inertial relaxation of the dumbbell is damped on the same time scale as for the surrounding matrix, and the extent of its relaxation is limited by that of the matrix. The chain-attached dumbbells share the inertia time scale with the free dumbbell, but the extent of the inertial relaxation is much smaller, that is, they are experiencing about the same amount of spatial constraint, i.e., caging. The end-attached dumbbell, however, is able to break out of the cage earlier than the center-attached dumbbell, so its relaxation is faster in the β-regime and early α-regime in the nomenclature of mode-coupling theory. In the late alpha regime, i.e., for the final 50% of the relaxation the relaxation functions for both dumbbell types agree again, however. This indicates that this regime is determined by Rouse mode contributions affecting all parts of the chain in a similar way.

To investigate the behavior of the end-attached and center-attached dumbbells in this plateau regime in more detail, we plot in Figure 3 their mean square displacements as well as the corresponding incoherent scattering functions at two slightly lower temperatures, $T = 0.49$ and $T = 0.47$. At $T = 0.49$, we observe the behavior discussed above for $T = 0.5$: the end-attached dumbbell breaks out of the plateau regime earlier than the center-attached dumbbell. At $T = 0.47$, however, closer to the mode-coupling temperature, this behavior has changed and the behavior of both dumbbells is not longer distinguishable. This indicates that at the onset of the caging ($T = 0.5$ and $T = 0.49$) chain connectivity plays a stronger role than deeper in the caging regime ($T = 0.47$) where packing effects dominate.

We turn now to the rotational relaxation of the matrix and the probes which is accessible through SMS techniques. Defining $\vec{u}(t)$ as a unit vector along the axis connecting the positions of the two particles in the dumbbell at time t, one defines orientational time correlation functions in terms of

$$\cos(\theta(t)) = \vec{u}(t)\cdot\vec{u}(0) \tag{4}$$

via the Legendre polynomials $P_\ell(\cos\theta)$ as

$$C_\ell(t) \equiv P_\ell(\cos\theta(t)) \tag{5}$$

and corresponding relaxation times

$$\tau_\ell = \int_0^\infty C_\ell(t)\,\mathrm{d}t$$

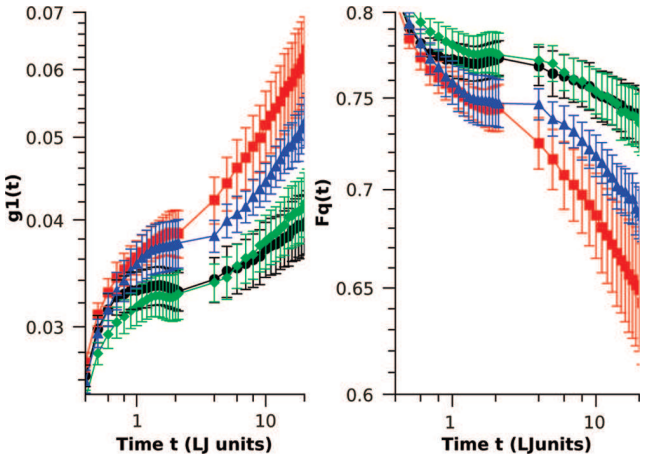

Figure 3. Mean squared displacement (left side) and incoherent scattering function (right side) of end-attached dumbells (red squares are for $T = 0.49$ and black circles are for $T = 0.47$) and center-attached dumbbells (blue triangles are for $T = 0.49$ and green diamonds are for $T = 0.47$). Error bars are from a Jacknife procedure of the simulation trajectory.

Here we have determined also analogous data for the orientational correlations of bonds in the polymer chain, which can be defined in the same way by averaging the data over either the last bonds or all bonds except the last ones in all polymer chains, to compare to the two bonding situations of the dumbbells. In many single molecule spectroscopy (SMS) studies, emphasis is put on the measurement of the linear dichroism trajectories, $d(t)$. In terms of the single molecule emission intensity along two mutually perpendicular polarization direction I_p and I_s, $d(t)$ is defined as

$$d(t) = (I_p - I_s)/(I_p + I_s) \tag{6}$$

In simulations, an equivalent quantity can be defined as[62]

$$d(t) = (7/8)[(\vec{e}_1\cdot\vec{u})^2 - (\vec{e}_2\cdot\vec{u})^2] \tag{7}$$

where $\vec{e}_1$ and $\vec{e}_2$ are unit vectors along the two in-plane orthogonal polarization directions of the system, and $\vec{u}$ is the unit vector along the dumbbell axis, as before.

As an example we display the second Legendre polynomial autocorrelation function of bonds and dumbbells in Figure 4 for the same two temperatures studied in Figure 1 and Figure 2. For the bond-correlations, obviously the orientation of the less constraint bonds at chain ends decorrelates faster than in the center of the chain. For the dumbbell we observe for both temperatures a stronger decorrelation due to the short time inertial regime than for the bonds. All dumbbell correlation functions are, however, more strongly stretched in the β-relaxation regime than the bond correlation functions so that their asymptotic decay occurs on a longer time scale. Here the free dumbbell shows the fastest decorrelation, followed by the end-attached dumbbell, and the center-attached dumbbell has the largest relaxation time. In the late α-relaxation regime, however, the dumbbell correlation functions and the bond-correlation functions are more or less parallel shifted with respect to each other, indicating that in this time regime it is the relaxation behavior of the matrix which determines also the relaxation of the dumbbells, irrespective of whether they are free or chain-attached.

For all relaxation functions discussed above, we can define a measure for the α-relation time τ_x of the various observables (incoherent scattering function $F_q(t)$: $x = q$, linear dichroism $C_d(t)$: $x = d$ and second order Legendre polynomials $C_2(t)$: $x = 2$ autocorrelation functions by the condition

$$(F/C)_x(t = \tau_x) = 0.3 \tag{8}$$

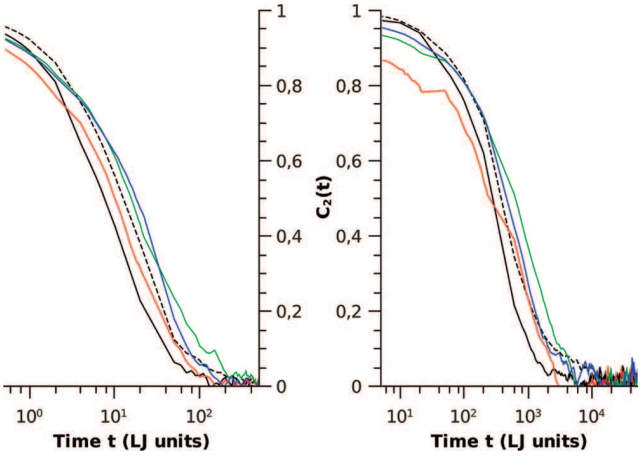

Figure 4. Second order Legendre polynomials autocorrelation functions as a function of time for $T = 0.7$ (left) and $T = 0.5$ (right). The solid (dashed) black curves describe $C_2(t)$ for the bonds at the end (in the center, respectively). The red, green, and blue curves pertain to similar information for the free dumbbell, the dumbbell covalently linked in the center or at the end of one chain.

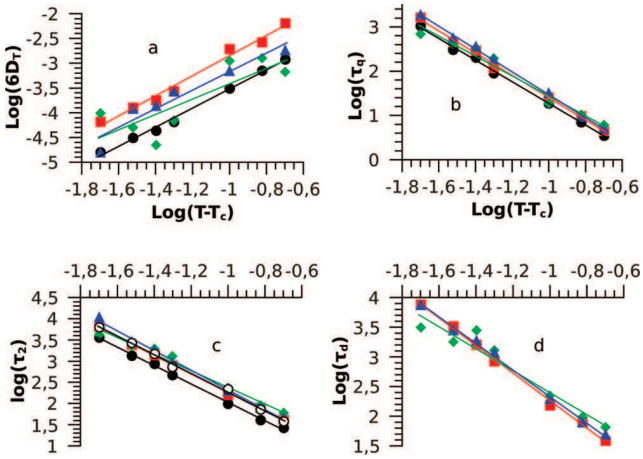

Figure 5. Log−log plots of the translational diffusion coefficients D_t (a) and of the relaxation times τ_q (b), τ_2 (c), and τ_d (d) for the pure polymer system (black circles), the free dumbbell (red squares), the dumbbell covalently linked in the center (green diamonds) or at the end (blue triangles) of one chain. All relaxation times have been determined empirically by the requirement $(F/C)_x(\tau_x) = 0.3$. The parameters γ obtained from the fits to a power law (see text) are given in Table 1. There are no linear dichroism data (d) for the bulk model system because of the lack of characterization technique in this case. In the case of the orientational second order correlation function (c) for the bulk model system, we did differentiate the function where only monomers at the end (filled black circles) of the chains were taken into account from the one where all the monomers except the ones at the end (open black circles) of the chains were taken.

For these α-relaxation times and for the translational diffusion coefficient several predictions for their temperature dependence exist in the literature, the most prominent ones being the mode coupling law[2]

$$D_t \propto (T/T_c - 1)^{\gamma} \tag{9}$$

or

$$\tau_x \propto (T/T_c - 1)^{-\gamma} \tag{10}$$

and the Vogel−Fulcher relation[63]

$$\tau = \tau_0 \exp[B/(T - T_0)] \tag{11}$$

Here τ_0 is a prefactor setting the high-temperature time scale, B is some effective activation energy, and T_0 the Vogel−Fulcher temperature. Comparing Figure 5 and Figure 6 we can see that both the MCT law and the Vogel−Fulcher law provide a reasonable description of our data in the simulated temperature range, when we keep the MCT critical temperature T_c or the Vogel−Fulcher temperature T_0 fixed to their known values for the pure polymer melt system. The essential parameters of these fits are the exponent γ for the MCT power law (see Table 1) and a measure for the fragility B/T_0 for the Vogel−Fulcher law (see Table 2). For the α-relaxation exponent γ we observe a grouping of the fit values with significant scatter between the fits. However, the fit values for the diffusion coefficient are smallest on average, followed by the values for the orientation correlation functions which are similar and, finally, the γ values for the incoherent scattering function are largest. Such a difference in γ value has been observed before comparing relaxation functions involving different length scales,[54] e.g., incoherent scattering functions at different q-values. For our correlation functions this signifies that the orientation correlations are susceptible to larger scale motions than the incoherent scattering function at the wave vector shown. Addressing the scatter between the different fit values for the different dumbbells, we can plot relaxation functions as functions of time in units of the α-relaxation time (Figure 7).

Then we observe that the curves for the incoherent scattering function for all dumbbells and for the temperatures $T = 0.47$, 0.48, 0.49, 0.5 basically scale on top of each other in the late β, early α regime, and the same is true for the orientation correlation functions C_2 and C_d. Performing an analysis of these scaled

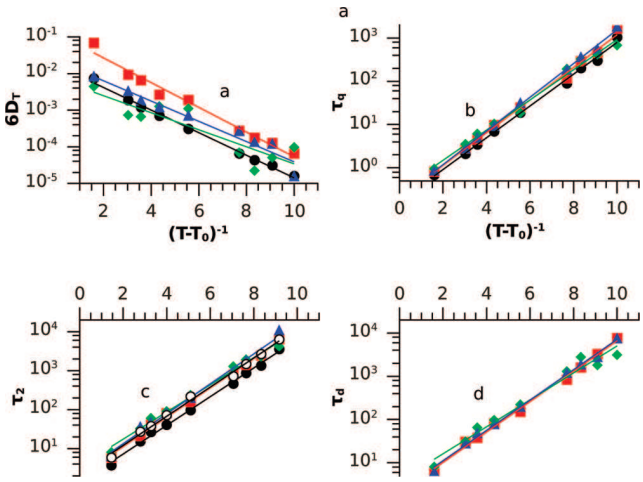

Figure 6. Same as Figure 5 but in a Vogel−Fulcher format.The values of the Vogel temperature T_0 and of the fragility parameter B/T_0 are presented in Table 2.

functions with an extended von Schweidler law

$$H(t) = f - h\left(\frac{t}{\tau_\alpha}\right)^{b} + hB\left(\frac{t}{\tau_\alpha}\right)^{2b} \tag{12}$$

$H(t)$ standing for either $F_q(t)$ or $C_2(t)$ or $C_d(t)$, yields nonergodicity parameters of $f = 0.73$ for the incoherent scattering and $f = 0.87$ for the orientation correlation functions, as well as von Schweidler exponents of $b = 0.57$ and $b = 0.66$. These in turn yield $\gamma = 2.48$ for the scattering and $\gamma = 2.26$ for the orientation correlations employing the exponent relations of MCT. These values are well compatible with the exponents found from free fitting of the temperature dependence of the α-relaxation times in Figure 5. The variation in values reported in Table 1 is therefore attributable to the statistical uncertainty of our data and not

Table 1. γ Parameters Obtained by Fitting the MCT Law to the α Relaxation Times τ_q, τ_2, and τ_d and to the Translational Diffusion Coefficients D_t for the Pure Polymer System, the Free Dumbbell, the Dumbbell Covalently Linked in the Center or at the End of One Chain[a]

	γ			
	D_t	τ_q	τ_2	τ_d
bulk	1.93	2.44	2.21 (c), 2.17 (e)	
free	2.03	2.51	2.18	2.32
center	1.55	2.25	1.96	1.85
end	1.87	2.58	2.32	2.24

[a] The results of the fits were obtained by fixing the critical temperature $T_C = 0.45$.

Table 2. B/T_0 Parameters Obtained by Fitting the Vogel−Fulcher Law to the α Relaxation Times τ_q, τ_2, and τ_d and to the Translational Diffusion Coefficients D_t for the Pure Polymer System, the Free Dumbbell, the Dumbbell Covalently Linked in the Center or at the End of One Chain[a]

	B/T_0			
	D_t	τ_q	τ_2	τ_d
bulk	1.92	2.28	2.13 (c), 2.10 (e)	
free	2.10	2.35	2.14	2.19
center	1.45	2.17	1.99	1.94
end	1.72	2.42	2.19	2.18

[a] The results of the fits were obtained by fixing the Vogel temperature to $T_0 = 0.37$.

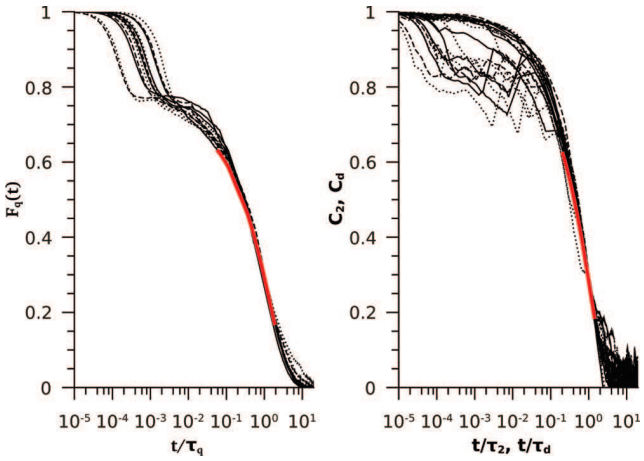

Figure 7. Incoherent scattering function (left side) and orientation correlation functions (right side) plotted vs time scaled by the respective α-relaxation time. The plots contain data for all three types of dumbbell attachment and the temperatures $T = 0.47, 0.48, 0.49, 0.5$. The red line (light gray line) is an extended von Schweidler fit to the scaling regime in these master plots (see text).

indicative of a difference in behavior between the differently attached dumbbells. However, the difference in γ value between the incoherent scattering data and the orientation correlation functions is significant and in agreement with what was discussed before.[54]

For the fragility parameter from the Vogel−Fulcher law no clear trends are discernible. Concerning the flexibility of the Vogel−Fulcher law as a phenomenological fitting function and the limited available temperature range from our simulations, the differences between the quoted B/T_0 values probably just reflect the uncertainty of the fitting procedure.

Figure 5 and Figure 6 confirm again our earlier conclusion that the dynamics of the dumbbells, whether dispersed freely in the polymer matrix or attached covalently to a chain is a faithful

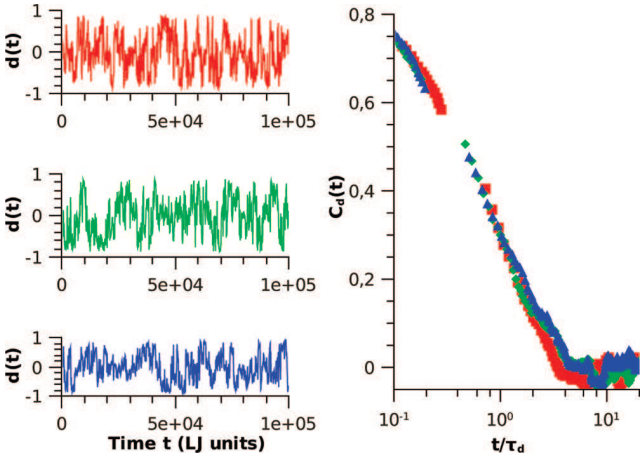

Figure 8. Left: Linear dichroism $d(t)$ trajectories of a free dumbbell (red curve), a dumbbell covalently linked in the center (green curve) or at the end (blue curve) of one chain in a model system at a temperature of $T = 0.5$. Right: Corresponding (red squares, green diamonds, and blue triangles, respectively) orientational time correlation functions $C_d(t)$ versus time scaled by the α-relaxation time τ_d of the linear dichroism.

probe of the glass transition in the matrix. Keeping the critical temperatures fixed in our fits was just necessitated by the statistical scatter, especially for the single dumbbell data. Averaging experimentally over a sufficiently large ensemble of individually measured SMS data will, however, be necessary to determine critical parameters for the MCT law or the Vogel−Fulcher law with sufficient accuracy. Independent of whether we choose to analyze correlation functions in terms of the MCT or the Vogel−Fulcher law, we can plot them versus scaled time, scaling by the respective estimate for the α-relaxation time determined as described above. Figure 8 shows such a plot for the linear dichroism which is the quantity of central interest in SMS experiments. On the left side of the figure we display single time traces of the dichroism signal as obtained for the free, center-attached or end-attached dumbbell (from top to bottom). All three look very similar, with perhaps a subtle difference between the center-attached and end-attached dumbbell on the one hand and the free dumbbell on the other hand. The latter one seems to have a fluctuation pattern somewhat more homogeneous in time than the former two. This subtle difference is also observable in the dichroism time-correlation function shown on the right side of the figure. The curves for the chain-attached dumbbells are more stretched than the one for the free dumbbell, although the observed effect is rather small. One may speculate that this hints at a larger dynamic heterogeneity for the chain-attached dumbbells increasing at lower temperature, especially going below the mode coupling T_c and approaching the calorimetric glass transition temperature T_g. After all, it is this temperature regime where experiments typically show an increase of dynamic heterogeneity.[37]

Dynamic heterogeneity is also at the origin of the breakdown of the Stokes−Einstein and Stokes−Einstein−Debye laws in glass forming materials, leading, e.g., to a power law relation between translational diffusion coefficient and correlation time

$$D_t \propto (\tau_q/T)^{-\xi_t} \tag{13}$$

We have documented this breakdown before[49,50] for our model system and showed that it occurs for the pure polymer and the dumbbell within the matrix as a probe of the matrix glass transition in the same way. In Figure 9 we show a double logarithmic plot of the translational diffusion coefficient as a function of relaxation time over temperature. The exponents for the plotted fit lines are given in Table 3. The exponent values for the pure polymer and the free dumbbell have been reported earlier.[50] They

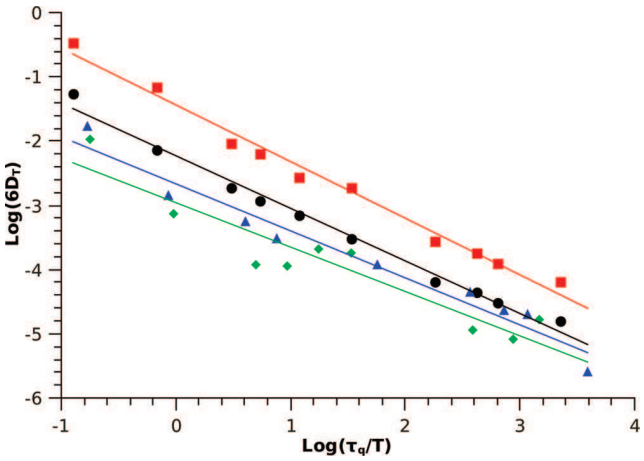

Figure 9. Power law fits of translational diffusivities D_t as a function of τ_q/T ($q = 6.9$): $D_t \approx (\tau_q/T)^{-\xi_t}$ for the bulk (black circles) or the dumbbell either free (red squares) or covalently linked in the center (green diamonds) or at the end (blue triangles) of one chain. Results for the ξ_t exponent are given in Table 3.

Table 3. ξ_t Parameters Obtained by Fitting the Fractional Functional Forms (SE Relation Modified by ξ_t) to the Relaxation Times τ_q for Either the Pure Polymer System, the Free Dumbbell, the Dumbbell Covalently Linked in the Center or at the End of One Chain

$$D_t \propto \left(\frac{\tau_q}{T}\right)^{-\xi_t}$$

	ξ_t
bulk	0.82
free	0.88
center	0.69
end	0.73

are about 10% larger than the values found for the chain-attached dumbbells.

Conclusions

We have performed molecular dynamics simulations of a model system for a glass forming polymer melt into which fluorescent molecules are embedded. Our simulations mimic recent experiments where a fluorophore is either dispersed into the host matrix or where it is covalently bound into the center or at the end of a dilute fraction of chains in the melt. These fluorophores are studied by single molecule spectroscopy techniques and are employed as probes of the glass transition of the melt. Addressing single molecules offers the possibility to study spatial and dynamic heterogeneity in the melt on a single molecule level.

While the measurement of temperature dependence of different translational and rotational autocorrelation functions for the embedded fluorophores in principle allows to determine various characteristic temperatures of the glass forming matrix such as the mode-coupling T_c or the divergence temperature T_0 of the Vogel−Fulcher law, reducing the statistical scatter in such measurements to a sufficient degree to allow for an accurate determination of these temperatures requires a significant experimental effort in averaging over a large sample of independent molecules.

We had shown in earlier studies that a fluorescent molecule dispersed into the polymer melt can be a faithful probe of the glass transition in the host matrix. We show here that this remains true for chain-attached probes as well. Our findings for the dichroism autocorrelation functions agree with the experimental observation in ref 47 that they show no discernible difference for different attachments in the chain. However, we would suggest that experimentally such a comparison should be made to the autocorrelation of dispersed dumbbells which should show a less stretched decay, i.e., smaller dynamic heterogeneity.

While there are no discernible differences in the long-time relaxation behavior of the chain-attached probes (late α-relaxation times), there seem to be subtle differences on the time scale on which the caging between neighboring chains in the melt occurs. These time scales could not be probed in the SMS experiments so far.[46,47] End-attached and center-attached dumbbell are experiencing an equal localization scale in the caging regime, but the end-attached dumbbell breaks out of this caging at a smaller time scale than the center-attached one. We have shown this behavior to occur upon approaching the mode-coupling T_c but experimentally it might be still better observable at temperatures closer to T_g which are not accessible in our simulations. On the one hand, the corresponding time scales then are larger and on the other hand, our results indicate that the difference between the relaxation behavior of the two types of chain-attached dumbbells increases upon cooling.

Acknowledgment. R.A.L.V. thanks the Fonds voor Wetenschappelijk Onderzoek (FWO) Vlaanderen for a postdoctoral fellowship. Partial support from Sonderforschungsbereich 625/A3 of the German National Science Foundation and the EU network of excellence SOFTCOMP is also acknowledged.

References and Notes

(1) Jäckle, J. *Rep. Prog. Phys.* **1986**, *49*, 171.
(2) Götze, W.; Sjögren, L. *Rep. Prog. Phys.* **1992**, *55*, 241.
(3) See: Debenedetti, P. G. *Metastable Liquids*; Princeton Univ. Press: Princeton, NJ, 1997.
(4) See: Donth, E.-W. *The Glass Transition. Relaxation Dynamics in Liquids and Disordered Materials*; Springer: Berlin, 2001.
(5) See: Binder, K.; Kob, W. *Glassy Materials and Disordered solids. An Introduction to their Statistical Mechanics*; World Scientific: Singapore, 2005.
(6) Plazek, D. J. *J. Phys. Chem.* **1965**, *69*, 3480.
(7) Kanaya, T.; Kawaguchi, T.; Kaji, K. *J. Chem. Phys.* **1996**, *104*, 3841.
(8) Pschorn, U.; Rössler, E.; Kaufmann, S.; Sillescu, H.; Spiess, H. W. *MacromolecuIes* **1991**, *24*, 398.
(9) Kuebler, S. C.; Heuer, A.; Spiess, H. W. *Phys. Rev. E* **1997**, *56*, 741.
(10) He, Y.; Lutz, T. R.; Ediger, M. D.; Ayyagari, C.; Bedrov, D.; Smith, G. D. *Macromolecules* **2004**, *37*, 5032.
(11) Lee, H.; Jamieson, A. M.; Simha, R. *Macromolecules* **1979**, *12*, 329.
(12) Patterson, G. D.; Lindsey, C. P. *J. Chem. Phys.* **1979**, *70*, 643.
(13) Saito, S.; Nakajima, T. *J. Appl. Polym. Sci.* **1959**, *4*, 93.
(14) Fukao, K.; Miyamoto, Y. *J. Non-Cryst. Solids* **1994**, *172−174*, 365.
(15) León, C.; Ngai, K. L.; Roland, C. M. *J. Chem. Phys.* **1999**, *110*, 11585.
(16) Inoue, T.; Cicerone, M. T.; Ediger, M. D. *Macromolecules* **1995**, *28*, 3425.
(17) Dhinojwala, A.; Wong, G. K.; Torkelson, J. M. *J. Chem. Phys.* **1994**, *100*, 6046.
(18) Hall, D. B.; Deppe, D. D.; Hamilton, K. E.; Dhinojwala, A.; Torkelson, J. M. *J. Non-Cryst. Solids* **1998**, *235−237*, 48.
(19) Moerner, W. E.; Orrit, M. *Science* **1999**, *283*, 1670.
(20) Xie, X. S.; Trautman, J. K. *Annu. Rev. Phys. Chem.* **1998**, *49*, 441.
(21) Kulzer, F.; Orrit, M. *Annu. Rev. Phys. Chem.* **2004**, *55*, 585.
(22) Vallée, R. A. L.; Cotlet, M.; Hofkens, J.; De Schryver, F. C.; Müllen, K. *Macromolecules* **2003**, *36*, 7752.
(23) Vallée, R. A. L.; Tomczak, N.; Kuipers, L.; Vancso, G. J.; van Hulst, N. F. *Phys. Rev. Lett.* **2003**, *91*, 038301.
(24) Vallée, R. A. L.; Tomczak, N.; Kuipers, L.; Vancso, G. J.; van Hulst, N. F. *Chem. Phys. Lett.* **2004**, *384*, 5.
(25) Tomczak, N.; Vallée, R. A. L.; van Dijk, E. M. H. P.; Kuipers, L.; van Hulst, N. F.; Vancso, G. J. *J. Am. Chem. Soc.* **2004**, *126*, 4748.
(26) Vallée, R. A. L.; Tomczak, N.; Vancso, G. J.; Kuipers, L.; van Hulst, N. F. *J. Chem. Phys.* **2005**, *122*, 114704.
(27) Vallée, R. A. L.; Van der Auweraer, M.; De Schryver, F. C.; Beljonne, D.; Orrit, M. *ChemPhysChem* **2005**, *6*, 81.
(28) Vallée, R. A. L.; Baruah, M.; Hofkens, J.; De Schryver, F. C.; Boens, N.; Van der Auweraer, M.; Beljonne, D. *J. Chem. Phys.* **2007**, *126*, 184902.

(29) Vallée, R. A. L.; Van der Auweraer, M.; Paul, W.; Binder, K. *Phys. Rev. Lett.* **2006**, *97*, 217801.
(30) Vallée, R. A. L.; Marsal, P.; Braeken, E.; Habuchi, S.; De Schryver, F. C.; Van der Auweraer, M.; Beljonne, D.; Hofkens, J. *J. Am. Chem. Soc.* **2005**, *127*, 12011.
(31) Braeken, E.; Marsal, P.; Vandendriessche, A.; Smet, M.; Dehaen, W.; Vallée, R. A. L.; Beljonne, D.; Van der Auweraer, M. *Chem. Phys. Lett.* **2009**, *472*, 48.
(32) Braeken, E.; De Cremer, G.; Marsal, P.; Pépe, G.; Müllen, K.; Vallée, R. A. L. *J. Am. Chem. Soc.* **2009**, *131*, 12201.
(33) Deschenes, L. A.; Vanden Bout, D. A. *J. Phys. Chem. B* **2002**, *106*, 11438.
(34) Tomczak, N.; Vallée, R. A. L.; van Dijk, E. M. H. P.; García-Parajó, M.; Kuipers, L.; van Hulst, N. F.; Vancso, G. J. *Eur. Polym. J.* **2004**, *40*, 1001.
(35) Schob, A.; Cichos, F.; Schuster, J.; von Borczyskowski, C. *Eur. Polym. J.* **2004**, *40*, 1019.
(36) Mei, E.; Tang, J.; Vanderkooi, J. M.; Hochstrasser, R. M. *J. Am. Chem. Soc.* **2003**, *125*, 2730.
(37) Ediger, M. D. *Annu. Rev. Phys. Chem.* **2000**, *51*, 99.
(38) Richert, R. *J. Phys.: Condens. Matter* **2002**, *4*, R703.
(39) Zondervan, R.; Kulzer, F.; Berkhout, G. C. G.; Orrit, M. *Proc. Natl. Acad. Sci. U.S.A.* **2007**, *104*, 12628.
(40) Zondervan, R.; Xia, T.; van der Meer, H.; Storm, C.; Kulzer, F.; van Saarloos, W.; Orrit, M. *Proc. Natl. Acad. Sci. U.S.A.* **2008**, *105*, 4993.
(41) Dickson, R. M.; Norris, D. J.; Moerner, W. E. *Phys. Rev. Lett.* **1998**, *81*, 5322.
(42) Sick, B.; Hecht, B.; Novotny, L. *Phys. Rev. Lett.* **2000**, *85*, 4482.
(43) Lieb, A.; Zavislan, J. M.; Novotny, L. *J. Opt. Soc. Am. B* **2004**, *21*, 1210.
(44) Böhmer, M.; Enderlein, J. *J. Opt. Soc. Am. B* **2000**, *20*, 554.
(45) Bartko, A. P.; Xu, K.; Dickson, R. M. *Phys. Rev. Lett.* **2002**, *89*, 026101.
(46) Bowden, N. B.; Willets, K. A.; Moerner, W. E.; Waymouth, R. M. *Macromolecules* **2002**, *35*, 8122.
(47) Gavranovich, G. T.; Csihony, S.; Bowden, N. B.; Hawker, C. J.; Waymouth, R. M.; Moerner, W. E.; Fuller, G. G. *Macromolecules* **2006**, *39*, 8121.
(48) Vallée, R. A. L.; Paul, W.; Binder, K. *Europhys. Lett.* **2007**, *79*, 46001.
(49) Vallée, R. A. L.; Paul, W.; Binder, K. *J. Chem. Phys.* **2007**, *127*, 154903.
(50) Vallée, R. A. L.; Paul, W.; Binder, K. *J. Chem. Phys.* **2010**, *132*, 034901.
(51) Bennemann, C.; Paul, W.; Binder, K.; Dünweg, B. *Phys. Rev. E* **1998**, *57*, 843.
(52) Bennemann, C.; Baschnagel, J.; Paul, W.; Binder, K. *Comput. Theor. Polym. Sci.* **1999**, *9*, 217.
(53) Bennemann, C.; Baschnagel, J.; Paul, W. *Eur. Phys. J B* **1999**, *10*, 123.
(54) Bennemann, C.; Paul, W.; Baschnagel, J.; Binder, K. *J. Phys.: Cond. Matter* **1999**, *11*, 2179.
(55) Baschnagel, J.; Bennemann, C.; Paul, W.; Binder, K. *J. Phys.: Condens. Matter* **2000**, *12*, 6365.
(56) Aichele, M.; Baschnagel, J. *Eur. Phys. J. E* **2001**, *5*, 229. ibid 245.
(57) Buchholz, J.; Paul, W.; Varnik, F.; Binder, K. *J. Chem. Phys.* **2002**, *117*, 7364.
(58) Baschnagel, J.; Varnik, F. *J. Phys.: Condens. Matter* **2005**, *17*, R851.
(59) Paul, W. In *Reviews in Computational Chemistry*; Wiley: New York, 2007, Vol. *25*, p 1.
(60) The software package OCTA (http://octa.jp) was used.
(61) Binder, K., Ciccotti, G., Eds. *Monte Carlo and Molecular Dynamics of Condensed Matter*; Societa Italiana di Fisica: Bologna, 1996.
(62) Gelin, M. F.; Kosov, D. S. *J. Chem. Phys.* **2006**, *125*, 054708.
(63) Vogel, H. *Phys. Z.* **1921**, *22*, 645. Fulcher, G. S. *J. Am. Ceram. Soc.* **1925**, *8*, 339.

PCCP

Dynamic Article Links

Cite this: *Phys. Chem. Chem. Phys.*, 2011, **13**, 1813–1818

www.rsc.org/pccp

PAPER

Single molecule probing of dynamics in supercooled polymers

G. Hinze,*[a] T. Basché[a] and R. A. L. Vallée*[b]

Received 31st August 2010, Accepted 6th December 2010
DOI: 10.1039/c0cp01654c

Fluorescence experiments with single BODIPY molecules embedded in a poly(methyl acrylate) matrix have been performed at various temperatures in the supercooled regime. By using pulsed excitation, fluorescence lifetime and linear dichroism time trajectories were accessible at the same time. Both observables have been analyzed without data binning. While the linear dichroism solely reflects single particle dynamics, the fluorescence lifetime observable depends on the molecular environment, so that the dynamics from the polymer host surrounding a chromophore contributes to this quantity. We observe that the lifetime correlation decays slightly faster than polarization correlation, indicating the occurrence of large angular reorientations. Additionally, dichroism time trajectories have been adducted to reveal directly the geometry of rotational dynamics. We identify small but also significantly larger rotational jumps being responsible for the overall molecular reorientation.

Introduction

The tremendous slowing down of dynamics in supercooled liquids has triggered a huge variety of different experiments to uncover the basic principles of the glass transition. Dynamics covering many decades in time or frequency has been identified to be relevant in the vitrification process.[1] Concurrently various theories have been put forward in order to explain the observations.[1–3] The concept of the potential energy landscape (PEL)[4] has recently become increasingly popular, particularly for the analysis of computer simulations.[5–8]

Considering the potential energy as a function of the 3N coordinates of the N particles, one can identify local minima (corresponding to the so-called "inherent structures"[5]). At sufficiently low temperatures, *e.g.* below the critical temperature of mode coupling theory (MCT),[2] the system stays for a long time in a "*meta*-basin" (MB) comprising a group of such local minima neighboring in phase space,[6] before a transition from one *meta*-basin to the next one can occur. It is tempting to associate such a "barrier hopping" transition in configuration space with the rearrangement of a "cooperative region" postulated by Adam and Gibbs[9] to account for the Vogel-Fulcher law[10] describing the rapid increase of the structural relaxation time as the temperature is lowered.

While most of the experimental observations stem from ensemble experiments and display distributions of properties like rotational correlation times, some specifically designed experiments have been performed to elude averaging by selecting subensembles of molecules with certain properties,[11] *e.g.* fast rotating molecules.

Ideally, following the dynamics of single molecules would perfectly enable to elucidate the heterogeneity of dynamics. Instead of marking a selected molecule, similar routes used fluorescent probe molecules which could be traced instead of the matrix molecules.[12] While in principle this approach could provide a rich amount of information, its main drawback originates from the limited photo stability of fluorophores which restricts the quality of the data. If the dynamics of the matrix is the main concern, probe and matrix molecules should be as similar as possible. This requirement could be fulfilled by choosing probe molecules similar in size and shape as the matrix molecules. In the case of fluorophores, however, it is already a big challenge to match the size and have a molecule with high photostability and high quantum yield. In a series of optical experiments at the ensemble level, it has been demonstrated that significant size differences are accompanied by different time scales of the dynamics of matrix and probe molecules, respectively.[13] As a further requirement, any additional dynamics introduced by the probe molecules should be avoided, which calls for fluorophores as rigid as possible. Also changes in the dipole moment of the solute molecules due to excitation should not trigger additional dynamics as well.[14]

By avoiding the intrinsic ensemble averaging of bulk techniques, single molecule spectroscopy (SMS) is able to get detailed nanoscale information on the dynamics of heterogeneous materials.[15,16] Recently, we have shown that the fluorescence lifetime trajectories of single probes in an oligo(styrene) matrix in the supercooled regime exhibit rather a jump behavior than a continuous change.[17] Furthermore, by performing molecular dynamics (MD) simulations of a coarse-grained model of short bead-spring chains containing an

[a] *Department of Physical Chemistry, Johannes-Gutenberg University, 55099 Mainz, Germany*
[b] *Centre de Recherche Paul Pascal (CNRS, UPR 8641), 115 avenue du docteur Albert Schweitzer, 33600 Pessac, France*

This journal is © the Owner Societies 2011

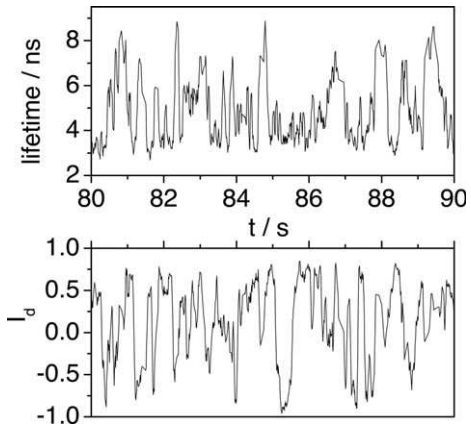

Fig. 1 Fluorescence lifetime $\tau(t)$ and linear dichroism $I_d(t)$ time traces of a SM embedded in a PMA matrix at $T = 292$ K. Both time traces have been obtained by binning the data in 50 ms bins.

additional dumbbell,[17–19] *i.e.* a non-trivial system known to exhibit the essential features of the glass transition phenomenon, we have followed the temporal evolution of the dumb-bell (probe) in the surrounding bead-spring chains medium and have determined the time trajectories of its linear dichroism $I_d(t)$ and fluorescence lifetime $\tau(t)$, *i.e.* two potentially accessible SM observables, at temperatures close to the mode coupling critical temperature T_c.[2] Owing to these simulations, we have been able to (i) identify jumps in the $\tau(t)$ trajectories; (ii) correlate these lifetime jumps to sudden large angular reorientations (SLARs) of the probe molecule and (iii) attribute the origin of these jumps to MB transitions in the PEL of the complex investigated medium by correlating these jumps to maxima of the translational and rotational average square displacements of the probe.[8]

In this paper by following simultaneously the fluorescence lifetime and linear dichroism time traces of BODIPY molecules in a poly(methyl acrylate) (PMA) matrix at various temperatures in the deeply supercooled regime, we provide first experimental evidence of this *meta*-basin signaling process.

Experimental setup

The BODIPY molecule used in our investigations has been designed to meet the requirements of high photostability, high quantum yield (0.99 in toluene) and emission in the red visible part of the spectrum (621 nm in ethyl acetate and 629 nm in toluene).[20] Poly(methyl acrylate) with a glass transition temperature at $T_g = 282$ K has been bought at Sigma-Aldrich ($M_w \sim 40\,000$) and used without further purification.

Single-molecule experiments have been performed with a home-built scanning confocal microscope.[21] To prevent interface effects, we used a bulk sample with an estimated volume of 10 mm^3 placed in a copper cylinder. At the bottom side of the beaker a small bore with a diameter of 3 mm was sealed with a thin glass slide to enable optical experiments. The whole copper cylinder was incorporated in a temperature controlled copper block which could be cooled and heated, respectively. A silicon diode placed close to the sample in conjunction with a temperature controller (Lakeshore) allowed for a temperature stability of about ± 0.05 K. The focus of the objective was placed within the bulk matrix, at a distance of about 10 μm from the glass surface. The chromophore density was low enough to ensure spatially well separated fluorescence spots in the microscope image.

For excitation we used a Ti:Sapphire laser (Mira 900, Coherent) pumped OPO (APE) to generate laser pulses at $\lambda = 590$ nm with a pulse length of about 1.5 ps. A subsequent pulse picker (APE) reduced the repetition rate to 7.6 MHz. By using a dichroic beam splitter (FT600, Zeiss), emitted photons could be separated from the excitation beam. In the detection path a long pass filter (HQ615 LP, Chroma) was blocking remaining excitation light. Fluorescence was collected by two fast avalanche photo diodes (50 ps, MPD-2CTA, PicoQuant) succeeding a polarizing beam splitter. Single photon arrival times were recorded with a stand-alone time-correlated single photon counting (TCSPC) device (PicoHarp300, PicoQuant).

Results and discussion

Fig. 1 exhibits the fluorescence lifetime $\tau(t)$ and linear dichroism trajectories $I_d(t) = (I_p(t) - GI_s(t))/(I_p(t) + GI_s(t))$ of a BODIPY molecule embedded in the PMA matrix at temperatures $T = 292$ K ($T_g + 10$ K). I_p and I_s are the intensities of the fluorescence signal recorded in the two detection channels for orthogonal polarizations. G is the correction factor accounting for the difference in sensitivity of the two APDs in both channels. The collected intensity is smaller in the *s*-channel than in the *p*-channel, leading to a $G = 1.4$ factor. Both $\tau(t)$ and $I_d(t)$ trajectories clearly exhibit jumps at both temperatures.

The linear dichroism $I_d(t)$ is directly related to molecular reorientation, allowing us to analyze the geometry of rotational dynamics. In contrast to most ensemble techniques aimed to probe molecular dynamics, like dielectric spectroscopy or dynamic light scattering, not only rotational correlation times but also details of the reorientation mechanism are accessible. The $I_d(t)$ observable provides similar information as could be obtained with some specific NMR experiments,[22] although on the single molecule level.

The fluorescence lifetime τ of a probe is particularly sensitive to its environment.[16–19] Indeed, by spontaneously emitting a photon, the probe generates an electric field that polarizes the surrounding monomers (inducing dipole moments $\vec{\mu}_k$). The interaction of these induced dipoles with the source transition dipole $\vec{\mu}$ creates an effective transition dipole moment $\vec{\mu}_{tot} = \vec{\mu} + \sum_k \vec{\mu}_k$, so that the measured radiative lifetime $\tau \propto |\vec{\mu}|2/|\vec{\mu}_{tot}|^2$ of the probe crucially depends on the positions and polarizabilities of the monomers surrounding the probe. In order to produce a jump of the lifetime, a significant change of the relative position of the surrounding monomers with respect to the probe must occur: either the environment or the dye itself has to rearrange.

The emergence of jumps in the $I_d(t)$ trajectories involves sudden large angular reorientations (SLARs)[23] of the probe. In MD simulations,[17,18] both manifestations of jumps (in lifetime and in linear dichroism) have been shown to signal MB transitions in the PEL of the investigated system.

 This journal is © the Owner Societies 2011

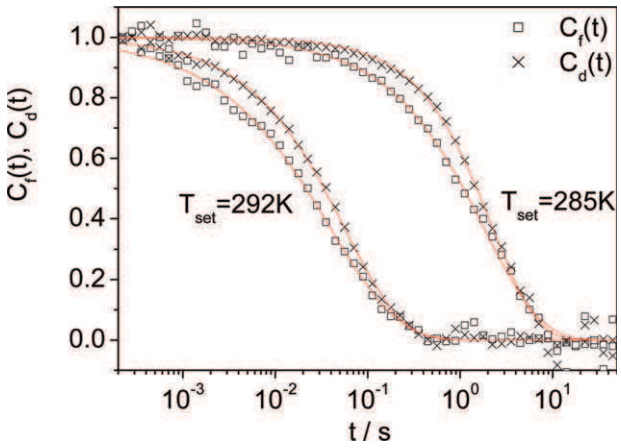

Fig. 2 Auto correlation functions $C_f(t)$, $C_d(t)$ of fluorescence lifetime and linear dichroism fluctuations, respectively. Note that the binning free analysis[25] allows for correlation data even at very short times.

In order to determine the relaxation times of the $\tau(t)$ and $I_d(t)$ observables, we did compute $C_d(t) = (I_d(t + t')\, I_d(t'))$ and $C_f(t) = (\tau(t + t')\tau(t'))$ auto-correlation functions (Fig. 2). However, instead of correlating time binned data,[24] we have employed a statistical analysis without the need of binning the recorded data.[25] Thus the full time resolution of the single photon counts is retained. Note that time binning of the single photon counts either to obtain $I_d(t)$ or $\tau(t)$ would limit the accessible time regime of $C_d(t)$ and $C_f(t)$ to times $t > 10^{-2}$ s...10^{-1} s.[24]

All correlation functions in Fig. 2 have been fitted by stretched exponential functions (solid lines), $\phi(t) \propto \exp(-(t/t_x)^{\beta_x})$, with average time constants $\langle t_x \rangle = (t_x/\beta_x)\, \Gamma\, (1/\beta_x)$. For the example shown in Fig. 2 we have obtained $t_f = 0.040$ s, $\beta_f = 0.59$ and $t_d = 0.056$ s, $\beta_d = 0.71$ at 292 K and $t_f = 1.82$ s, $\beta_f = 0.71$ and $t_d = 2.27$ s, $\beta_d = 0.91$ at 285 K.

In order to get statistically relevant data, we recorded and analyzed more than 200 single molecule trajectories at temperatures $T = 292$ K, $T = 287$ K and $T = 285$ K. At all temperatures we used a high $NA = 1.4$ oil objective to collect light from the sample. Additionally, at 287 and 285 K we used a slightly lower $NA = 0.95$ dry lens in order to modify the thermal isolation between sample and objective. Both types of objectives have been shown to be well suited for performing the experiments, with no appreciable change of the relaxation times when collecting light with a lower light cone collection angle.[24,26,27] Note that the temperatures listed above display the temperatures set at the controller. While the actual temperatures within the sample deviated to some degree, high temperature stability allowed for reproducible experiments. In general, the experiments performed with the oil objective showed a higher signal to noise ratio, therefore in the following we focus on these results.

In Fig. 3 the distributions of mean relaxation times $\langle t_f \rangle$ and $\langle t_d \rangle$ are shown for three temperatures, calculated from all time traces measured. In general, at a given temperature the relaxation times ($\langle t_f \rangle$ or $\langle t_d \rangle$) from all molecules must be identical. However, this would require time traces significantly longer than the slowest relaxation times in the system, since time averaging would then lead to relaxation times similar to ensemble values, owing to the ergodic principle. The broad distributions exhibited in Fig. 3 exemplify the well known issue of the analysis of SM time traces, whose length is limited by irreversible photobleaching of the molecule, leading to an insufficient time averaging within each time trace, possibly accompanied by an insufficient signal to noise ratio related to some low emitting count rate. Nevertheless, the mean values of the shown distributions clearly show the expected reduced relaxation times as the temperature of the system is increased. In the following, we focus on two aspects of the investigated dynamics, which do not suffer from these limitations.

The opportunity to measure linear dichroism and fluorescence lifetime fluctuations at the same time and from the same molecules provides new information on the nanoscale dynamics. The linear dichroism solely depends on the orientation of a single molecule. It represents a single particle interaction, in the sense that fluctuations of the surrounding molecules do not alter the linear dichroism $I_d(t)$ as long as the probe molecule does not rotate itself. Although $C_d(t)$ not exactly represents a rotational correlation function of certain order,[26] it has been shown that the correlation decay is very close to $l = 2$,[28] especially in the case of high NA objectives.[27]

The fluorescence lifetime $\tau(t)$ on the other hand crucially depends on the positions and polarizabilities of the monomers surrounding the probe. That is, either the environment or the dye itself have to rearrange to alter $\tau(t)$. Due to lack of an explicit derivation of $C_f(t)$, the relation to a rotational correlation function of certain order is unclear. However, molecular dynamics simulations of a system of flexible polymers containing fluorescent probe molecules suggested that the relaxation times t_f obtained from the correlation functions $C_f(t)$ are close to an $l = 4$ interaction.[19]

In the case of the Debye model for rotational diffusion, the various orientational time correlation functions decay exponentially while the relaxation times scale as $\tau_l \propto [l(l + 1)]^{-1}$, predicting $\tau_2/\tau_4 = 10/3$. Once molecular reorientation proceeds by discrete rotational jumps, all τ_l converge with increasing jump angles. For random rotational jumps the τ_l are equal for all l. While this behavior could be employed to elucidate the geometry of molecular reorientation, *e.g.* by comparing τ_1 and τ_2, the situation becomes more complex once fluctuations of $\tau_l(t)$ are present. Then τ_n/τ_m depends on both rotational geometry and the timescale of these fluctuations.[22,28] At the same time non-exponentially decaying rotational correlation functions should be observed, which are typical for supercooled liquids and which often are described by a stretched exponential function $C_x \propto \exp(-(t/t_x)^{\beta_x})$.[1] The non-exponentiality $\beta < 1$ has been attributed to different local environments for different molecules while structural relaxation causes exchange between these environments.[28] As a consequence, more slowly decaying correlation functions would allow more exchange or more averaging, that is for $n > m$ we expect $\beta_n < \beta_m$. Under static conditions without exchange, however, the stretching exponents should be equal, $\beta_n = \beta_m$.

In Fig. 4, ratios from the averaged relaxation times $(t_d)/(t_f)$ are plotted for all temperatures measured. Although the scattering of the data points reveals a rather large error, we find that (t_d) is systematically larger than (t_f). Both relaxation

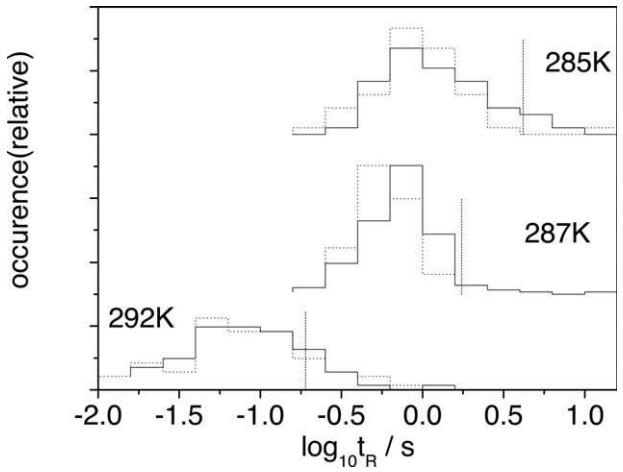

Fig. 3 Distributions of relaxation times t_f, t_d of the fluorescence lifetime $C_f(t)$ (solid lines) and linear dichroism $C_d(t)$ (dotted lines) autocorrelation functions for 44–144 molecules embedded in the matrix at set temperatures T = 285, 287 and 292 K. The vertical dashed lines indicate the average cross-correlation times (t^{cross}), 4.17, 1.74, and 0.19 s, respectively.

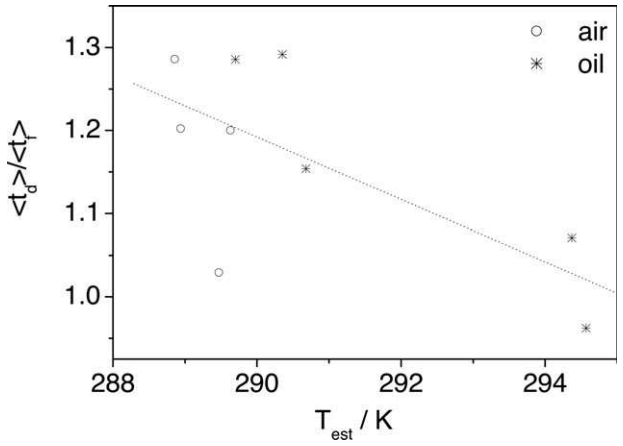

Fig. 4 Ratio of the average relaxation times for each measured temperature. The plotted temperatures have been estimated by relating the relaxation times $\langle t_d \rangle$ to literature data.[33]

times are quite similar, in contrast to the MD simulations recently published, where a factor of $\sim$3 had been found.[19] However, our experiments have been performed at significantly lower temperatures slightly above T_g, while the simulations were restricted to temperatures $T > T_c \approx 1.2\ T_g$ where the dynamics was significantly faster. Hence our findings support the previous assumption[19] that, with decreasing temperatures, the amount of SLARs increases, as is the occurrence of metabasin (MB) transitions in the potential energy landscape of the considered system.[8,17]

The quantities $I_d(t)$ and $\tau(t)$ are related intrinsically in the sense that reorientation of the dye alters mandatorily both. Dynamics only of its environment, however, will be reflected in $\tau(t)$ without modifying $I_d(t)$. The interesting question arises how the dynamics of the dye is correlated to fluctuations in the environment such that a jump in the environment triggers rotational jumps of the monitored dye. A simple cross-correlation between the quantities $I_d(t)$ and $\tau(t)$ fails to reveal the connection between both parameters. This can be rationalized by the fact that the signs of jumps both in lifetime and linear dichroism are uncorrelated, irrespective of whether the jumps are correlated or not. Hence, we have calculated the absolute value of the numerical derivatives $I'_d(t) = |I_d(t + \Delta t) - I_d(t)|/\Delta t$ and $\tau'_d(t) = |\tau_d(t + \Delta t) - \tau_d(t)|/\Delta t$ and determined their cross-correlation function $C^{cross}(t) = \langle I'_d(t + t')\ \tau'_d(t') \rangle$. A quantitative analysis of $C^{cross}(t)$ could be possible presuming sufficient data quality in conjunction with some physical models. However, our data permitted only to extract averaged correlation times $\langle t^{cross} \rangle$ for each temperature, see Fig. 3. We observe similar timescales as for $\langle t_f \rangle$ and $\langle t_d \rangle$, which confirms the intrinsic correlation discussed above. Furthermore, these results imply that the environment cannot fluctuate significantly without affecting the dye under observation.

In a next step we have analyzed the linear dichroism trajectories $I_d(t)$ with respect to the details of the rotational geometry. Although $I_d(t)$ represents the in-plane projection of the SM emission, the full information is recoverable in case of the assumption of an isotropic system. It is noted that techniques have been recently developed allowing to record the 3D orientation of the emission dipole moment.[29] However, we have used $I_d(t)$ as a reliable and easy to measure quantity while it contains at the same time the fully required information.

In Fig. 1, fluctuations with different $I_d(t)$ amplitudes are readily observed. It could be assumed that large jumps in $I_d(t)$ correspond to large rotational jumps of a chromophore. However, as can be seen from the definition of $I_d(t) = (I_p(t) - I_s(t))/I_p(t) + I_s(t))$, a small denominator easily boosts small fluctuations and a visual inspection of $I_d(t)$ may not be very helpful. Therefore, we have performed a statistical analysis of the recorded data.

In a first step we have calculated the rotational correlation times for each molecule by employing the binning free approach,[25] thereby avoiding any bias from too long binning times. In a next step we have binned the data with binning times $t_{bin} = 0.1\ (\tau_d)$ to ensure the same impact of the binning on all data sets. The resulting time trajectories $I_d^{bin}(t)$ have been analyzed with respect to the fluctuations, $\Delta I_d^{bin}(t) = |I_d^{bin}(t) - I_d^{bin}(t + t_{bin})|$. In Fig. 5a the distributions of fluctuation sizes $V(\Delta I_d^{bin})$ have been plotted for all SM trajectories pertaining to the three temperature sets measured with the oil objective. To properly interpret the distributions, we have performed computer simulations assuming a rotational jump model with adjustable jump sizes.[30] The dotted line in Fig. 5a corresponds to a jump angle of 1°, which essentially reflects rotational diffusion. The deviations of this line to the experimental data of the system at the three measured temperatures indicate that significantly larger jump angles are present in the experimental time traces.

Further we have fitted a distribution $V(\Delta I_d^{bin})$ to the experimental data incorporating a superposition of different jump angles (1°, 10°, 20°,..., 80°) with variable amplitudes. Larger angles did not improve the fit. The resulting distributions of jump angles are plotted in Fig. 5b. As a main result, we identify small and larger jump angles in full accordance to former ensemble experiments on supercooled

 This journal is © the Owner Societies 2011

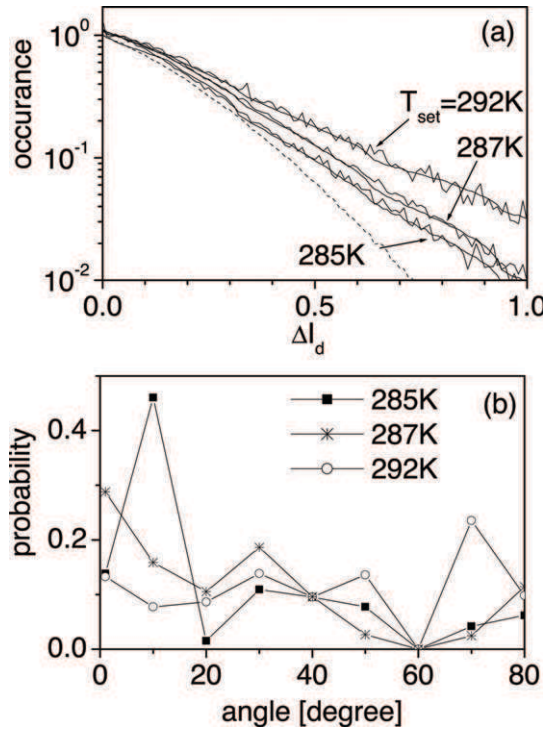

Fig. 5 (a) Distributions of fluctuation sizes $V(\Delta l_d^{bin})$ as defined in the text. The dotted line corresponds to pure rotational diffusion. (b) As can be seen from the fitted distribution of rotational jump angles, small but also larger angles dominate the molecular reorientation.

liquids using NMR techniques.[22,30,31] The resulting data had been interpreted by rotational jump models consisting of large angle jumps mixed with some small angle (diffusion like) dynamics.

It has been stated above, that with decreasing temperatures the amount of SLARs increases. Yet, with respect to the data in Fig. 5a, it seems that with decreasing temperature the deviations to the pure rotational diffusion model become smaller. The fitted distributions of jump angles in Fig. 5b, however, reveal a rather ambiguous scenario. We therefore tend not to over-interpret our results concerning the jump angles. For all measured temperatures we clearly find molecular reorientation consisting of both, large and small angle jumps. For a more accurate judgment of the temperature dependence, however, the investigated temperature regime was too small.

Summary

Compared to NMR experiments, which correspond to q-dependent scattering experiments,[32] polarization resolved single molecule measurements allow for a more direct observation of molecular orientation, either by certain 3D techniques[29] or by following the projection of the molecular 3D orientation (*i.e.* of the molecular transition dipole) on a 2D plane as performed in the present work. Moreover, the simultaneously measured fluorescence lifetime allowed for a comparison of two different observables of the same probe molecule. The linear dichroism on the one hand solely reflects the spatial orientation of the probe molecule itself, representing a kind of 'true' single particle observable (while the environment causes the reorientation of the probe, this interaction is not directly measured). The fluorescence lifetime observable on the other hand is sensitive to changes of the orientation of the probe molecule itself as well as of its surrounding. Accordingly, our experiments allow for a more comprehensive insight into the molecular dynamics than experiments investigating solely rotational dynamics. Indeed, the finding of similar relaxation times for both quantities quite nicely matches theoretical models describing the vitrification process. Within the concept of the potential energy landscape of the polymer, the observed SLARs can be attributed to *meta*-basin transitions in full harmony to recent molecular dynamics simulations of a coarse-grained model mimicking a polymer host lightly doped with fluorescent probe molecules.[17,18] In future experiments, it will be challenging to study the geometry of the rotational dynamics in more detail on a single molecule level. In particular the temperature dependence over a larger range with regard to possible changes in the reorientation mechanism could help to gain additional insight into the interplay of self and collective dynamics and its relevance to the enormous slowing down of the dynamics in supercooled liquids.

Acknowledgements

The authors thank L. Volker, N. Boens and W. Dehaen (KU Leuven, Belgium) for providing us with the BODIPY compound and W. Paul for helpful discussions. R.A.L. V. thanks the Fonds voor Wetenschappelijk Onderzoek (FWO) Vlaanderen (Belgium) for a postdoctoral fellowship and is grateful to the Sonderforschungsbereich 625/A3 of the German National Science Foundation for partial support of his stay in Mainz.

References

1 *Proceedings of the Fourth International Discussion Meeting on Relaxation in Complex Systems*, ed. K. L. Ngai (Special Issues of J. Non-Cryst. Solids 307–310, 2002).
2 W. Götze and L. Sjögren, *Rep. Prog. Phys.*, 1992, **55**, 241.
3 J. Jäckl, *Rep. Prog. Phys.*, 1986, **49**, 171; E.-W. Donth, *The Glass Transition. Relaxation Dynamics in Liquids and Disordered Materials*, Springer, Berlin, 2001; P. G. Debenedetti, *Metastable Liquids*, Princeton Univ. Press, Princeton, 1997; K. Binder and W. Kob, *Glassy Materials and Disordered solids. An Introduction to their Statistical Mechanics*, World Scientific, Singapore, 2005.
4 M. Goldstein, *J. Chem. Phys.*, 1969, **51**, 3728.
5 F. H. Stillinger and T. A. Weber, *Phys. Rev. A: At., Mol., Opt. Phys.*, 1983, **28**, 2408; F. H. Stillinger, *Science*, 1995, **267**, 1935.
6 B. Doliwa and A. Heuer, *Phys. Rev. E: Stat., Nonlinear, Soft Matter Phys.*, 2003, **67**, 031506; B. Doliwa and A. Heuer, *Phys. Rev. Lett.*, 2003, **91**, 235501.
7 L. Angelani, G. Ruocco, M. Sampoli and F. Sciortino, *J. Chem. Phys.*, 2003, **119**, 2120; J. Kim and T. Keyes, *J. Chem. Phys.*, 2004, **121**, 4237; D. Coslovich and G. Pastore, *Europhys. Lett.*, 2006, **75**, 784.
8 G. A. Appignanesi, J. A. Rodrigues Fris, R. A. Montani and W. Kob, *Phys. Rev. Lett.*, 2006, **96**, 057801.
9 G. Adams and J. H. Gibbs, *J. Chem. Phys.*, 1965, **43**, 139.
10 H. Vogel, *Phys. Z.*, 1921, **22**, 645; G. S. Fulcher, *J. Am. Ceram. Soc.*, 1925, **8**, 339.
11 K. Schmidt-Rohr and H. W. Spiess, *Phys. Rev. Lett.*, 1991, **66**, 3020; A. Heuer, M. Wilhelm, H. Zimmermann and H. W. Spiess, *Phys. Rev. Lett.*, 1995, **75**, 2851; R. Bohmer, G. Hinze, G. Diezemann, B. Geil and H. Sillescu, *Europhys. Lett.*, 1996, **36**(1), 55; M. T. Cicerone and M. D. Ediger, *J. Chem. Phys.*, 1995,

103, 5684; B. Schiener, R. Böhmer, A. Loidl and R. V. Chamberlin, *Science*, 1996, **274**, 752.
12 L. A. Deschenes and D. A. Vanden Bout, *J. Phys. Chem. B*, 2002, **106**, 11438; N. Tomczak, R. A. L. Valleé, E. M. H. P. van Dijk, M. F. Garcia-Parajo, L. Kuipers, N. F. van Hulst and G. J. Vancso, *Eur. Polym. J.*, 2004, **40**, 1001; A. Schob, F. Cichos, J. Schuster and C. von Borcyskowski, *Eur. Polym. J.*, 2004, **40**, 1019; E. Mei, J. Tang, J. M. Vanderkooi and R. M. Hochstrasser, *J. Am. Chem. Soc.*, 2003, **125**, 2730; A. N. Adhikaro, N. A. Capurso and D. Bingemann, *J. Chem. Phys.*, 2007, **127**, 114508.
13 M. T. Cicerone, F. R. Blackburn and M. D. Ediger, *J. Chem. Phys.*, 1995, **102**, 471; F. R. Blackburn, C.-Y. Wang and M. D. Ediger, *J. Phys. Chem.*, 1996, **100**, 18249; D. Bainbridge and M. D. Ediger, *Rheol. Acta*, 1997, **36**, 209; T. Inoue, M. T. Cicerone and M. D. Ediger, *Macromolecules*, 1995, **28**, 3425.
14 S. Kinoshita and N. Nishi, *J. Chem. Phys.*, 1988, **89**, 6612; R. Richert, *Chem. Phys. Lett.*, 1990, **171**, 222.
15 W. E. Moerner and M. Orrit, *Science*, 1999, **283**, 1670; X. S. Xie and J. K. Trautman, *Annu. Rev. Phys. Chem.*, 1998, **49**, 441; F. Kulzer and M. Orrit, *Annu. Rev. Phys. Chem.*, 2004, **55**, 585.
16 R. A. L. Vallée, N. Tomczak, L. Kuipers, G. J. Vancso and N. F. van Hulst, *Phys. Rev. Lett.*, 2003, **91**, 038301.
17 R. A. L. Vallée, M. Van der Auweraer, W. Paul and K. Binder, *Phys. Rev. Lett.*, 2006, **97**, 217801.
18 R. A. L. Vallée, M. Van der Auweraer, W. Paul and K. Binder, *Europhys. Lett.*, 2007, **79**, 46001.
19 R. A. L. Vallée, W. Paul and K. Binder, *J. Chem. Phys.*, 2007, **127**, 154903.
20 T. Rohand, W. Qin, N. Boens and W. Dehaen, *J. Org. Chem.*, 2006, **20**, 4658; W. Qin, T. Rohand, W. Dehaen, J. N. Clifford, K. Driesen, D. Beljonne, B. Van Averbeke, M. Van der Auweraer and N. Boens, *J. Phys. Chem. A*, 2007, **111**, 8588.
21 T. Christ, F. Petzke, P. Bordat, A. Herrmann, E. Reuther, K. Müllen and T. Basché, *J. Lumin.*, 2002, **98**, 23.
22 R. Bohmer, G. Diezemann, G. Hinze and E. Rossler, *Prog. Nucl. Magn. Reson. Spectrosc.*, 2001, **39**(3), 191.
23 M. S. Beevers, J. Crossley, D. C. Garrington and G. Williams, *J. Chem. Soc., Faraday Trans. 2*, 1977, **73**(4), 458; D. Kivelson and S. A. Kivelson, *J. Chem. Phys.*, 1989, **90**, 4464.
24 R. A. L. Vallée, T. Rohand, N. Boens, W. Dehaen, G. Hinze and T. Basche, *J. Chem. Phys.*, 2008, **128**, 154515.
25 G. Hinze and T. Basche, *J. Chem. Phys.*, 2010, **132**, 044509.
26 G. Hinze, G. Diezemann and T. Basché, *Phys. Rev. Lett.*, 2004, **93**, 203001.
27 C.-Y. J. Wei, Y. H. Kim, R. K. Darst, P. J. Rossky and D. A. Vanden Bout, *Phys. Rev. Lett.*, 2005, **95**, 173001.
28 G. Diezemann and K. A. Nelson, *J. Phys. Chem. B*, 1999, **103**, 4089.
29 R. M. Dickson, D. J. Norris and W. E. Moerner, *Phys. Rev. Lett.*, 1998, **81**, 5322; B. Sick, B. Hecht and L. Novotny, *Phys. Rev. Lett.*, 2000, **85**, 4482; A. Lieb, J. M. Zavislan and L. Novotny, *J. Opt. Soc. Am. B*, 2004, **21**, 1210; M. Böhmer and J. Enderlein, *J. Opt. Soc. Am. B*, 2003, **20**, 554.
30 G. Hinze, *Phys. Rev. E: Stat. Phys., Plasmas, Fluids, Relat. Interdiscip. Top.*, 1998, **57**(2), 2010.
31 R. Bohmer and G. Hinze, *J. Chem. Phys.*, 1998, **109**(1), 241.
32 F. Fujara, S. Wefing and H. W. Spiess, *J. Chem. Phys.*, 1986, **84**, 4579.
33 Sanchis, M. G. Prolongo, R. M. Masegosa and R. G. Rubio, *Macromolecules*, 1995, **28**, 2693.

 This journal is © the Owner Societies 2011

J|A|C|S
COMMUNICATIONS

Published on Web 02/06/2004

Single-Molecule Conformations Probe Free Volume in Polymers

Renaud A. L. Vallée,[†] Mircea Cotlet,[†] Mark Van Der Auweraer,[†] Johan Hofkens,*[,†] K. Müllen,[‡] and Frans C. De Schryver*[,†]

Department of Chemistry, Katholieke Universiteit Leuven, Celestijnenlaan 200 F, B-3001 Leuven, Belgium, and Max-Planck-Institut für Polymerforschung, Ackermannweg 10, D-55128 Mainz, Germany

Received December 9, 2003; E-mail: frans.deschryver@chem.kuleuven.ac.be; johan.hofkens@chem.kuleuven.ac.be

The free volume is an intuitive theoretical concept[1−12] that has been proposed to explain the molecular properties and physical behavior of liquid and glassy states. Free volume is an open space that is freely moving in a medium.[3−8] It is constituted of sub nanometer-sized holes that appear in the medium due to structural disorder.[9,10] Due to thermal fluctuations, the free volume varies both in time and space.[11,12] At the early stages of its theoretical development, the free volume could only be deduced indirectly from specific volume experiments.[13] Small-angle X-ray and neutron diffractions have subsequently been used to determine density fluctuations and deduce free volume size distributions.[14,15] Finally, measurements of the photoisomerization rates of fluorescent probes[16] and positron annihilation lifetime spectroscopy (PALS) have led to a direct determination of the mean size of sub nanometer holes in polymeric materials.[17,18]

Single molecule spectroscopy (SMS) proved to be a powerful tool to study the local dynamics in polymers, both above and below the glass transition temperature T_g. In contrast to the previously cited ensemble methods, single molecule fluorescence experiments provide information on distributions and time trajectories of observables that would otherwise be hidden.[19,20] Recent studies of rotational and translational diffusion of a dye molecule embedded in a polymer matrix near the glass transition confirmed the spatially heterogeneous dynamics in this region.[21] In the glassy state, triplet lifetimes and intersystem crossing yields[22,23] and fluorescence lifetimes[24] of individual molecules embedded in a polymer host were shown to vary in time. In the latter case, the fluorescence lifetime fluctuations were shown to reveal segmental dynamics in polymers because of a relation with the Simha−Somcynsky[9] free volume theory.

In this communication, we show that the conformational dynamics of a single molecule in a polymer matrix allows a *direct* visualization of the *local* free volume. Specifically, the tetraphenoxy−perylenetetracarboxy diimide (TPDI) dye molecule is known to present a twisted (Figure 1a) or a ≪flat≫ (Figure 1b) conformation of the core, with corresponding fluorescence lifetimes of 6.2 and 3.2 ns, when embedded in a poly(norbornene) (Zeonex) matrix.[25] The calculated van der Waals (VdW) volumes are 1.121 nm^3 for the twisted conformation and 1.322 nm^3 for the ≪flat≫ conformation of the molecule. This results in a 0.201 nm^3 volume difference between the two conformations.

In a polymer film, nonpolar side groups hinder an effective packing of the chains, causing a high mobility of the main chain and a lowering of the glass transition temperature. In two polymers of the same family, namely poly(methyl methacrylate) (PMMA, PI = 1.03, T_g = 378 K, Polymer Standards Service) or poly(*n*-butyl methacrylate) (P*n*BMA, PI = 1.03, T_g = 295 K, Polymer Standards Service), this results in a mean hole volume, which is significantly lower in PMMA (0.105 nm^3),[14] than in P*n*BMA (0.132 nm^3).[18] Notice that the latter value being determined by PALS may underestimate the "real" free volume, as PALS studies report generally smaller mean hole volumes than those reported by photochromic probe studies.[16,28,29] By spin coating a solution of a nanomolar concentration of the TPDI dye in PMMA or P*n*BMA on a glass substrate, we expect and indeed show that the two conformations of the dye may distribute differently in the two matrixes and thus *directly* probe *local* free volume.

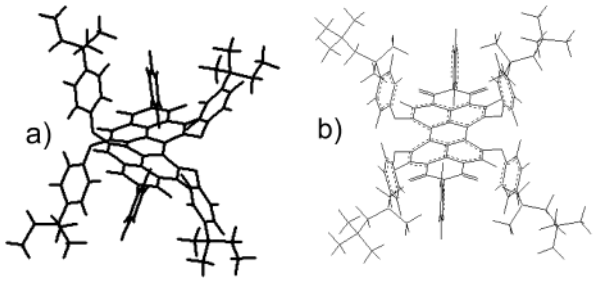

Figure 1. Molecular structures of the two conformations of the dye molecule: (a) twisted core, (b) ≪flat≫ core.

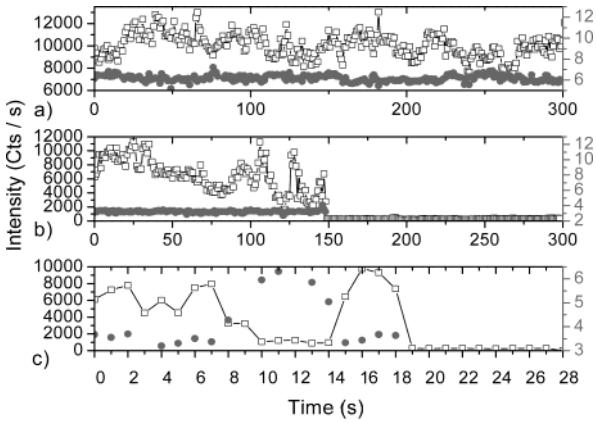

Figure 2. Fluorescence lifetime (●) and intensity (□) time traces of TPDI molecules embedded in a P*n*BMA matrix.

The synthesis and purification of the TPDI dye molecule used in this study is described elsewhere.[26] The dye molecules were excited by 1.2 ps pulses at a wavelength of 543 nm and a repetition rate of 8.18 MHz (Spectra Physics, Tsunami, OPO, pulse picker, frequency doubler) in an inverted confocal microscope (Olympus, 100×). The excitation power P was set to 0.8 μW. The lifetime was measured by use of an avalanche photodiode (SPCM-AQ-14, EG & G Electro Optics) equipped with a time-correlated single photon counting card (Becker & Hickl GmbH, SPC 630) used in FIFO mode.[27]

Figure 2 shows typical fluorescence lifetime time trajectories of TPDI dye molecules embedded in a P*n*BMA matrix. Of the 92

[†] Katholieke Universiteit Leuven.
[‡] Max-Planck-Institut für Polymerforschung.

10.1021/ja031599g CCC: $27.50 © 2004 American Chemical Society

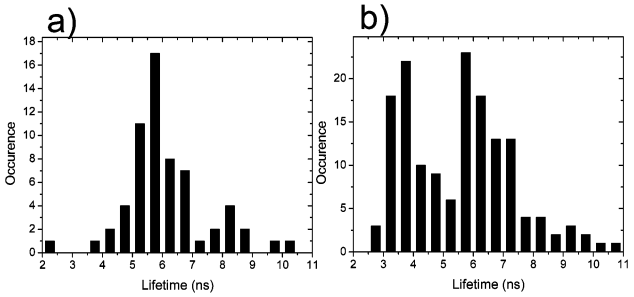

Figure 3. Fluorescence lifetime distributions of TPDI molecules embedded in a PMMA (a) or in a P*n*BMA (b) matrix.

molecules investigated in this matrix, 70% show a continuous trace with a mean lifetime around 6.2 ns (Figure 2a). These molecules possess the most stable conformation with a twisted core and a minimum VdW volume. Similarly, almost all (59) molecules[30] embedded in a PMMA matrix show an analogous trace, with an analogous fluorescence lifetime (Figure 3a). For PMMA, because the mean free volume is 0.105 nm^3, much lower than the volume difference (0.201 nm^3) between the twisted and ≪flat≫ conformations of the dye molecule, the static structural disorder of the matrix does not provide space for the voluminous ≪flat≫ conformation. Since a similar situation arises in P*n*BMA for 70% of the molecules, we can conclude that, for these 66 positions in the matrix, the *local* free volume is much lower than 0.201 nm^3.

On the contrary, 30% of the molecules embedded in P*n*BMA show a trace with a mean lifetime around 3.2 ns (Figure 2b). These 26 molecules correspond to a ≪flat≫ conformation of the core, which requires more volume to settle in the matrix than the twisted molecule. In this case, the static structural disorder of the matrix provides the free volume necessary for these molecules to settle. In 30% of the probed positions of the P*n*BMA matrix, the free volume is thus of the order of 0.201 nm^3.

Finally, five molecules show a trace where the fluorescence lifetime jumps from a low to a high lifetime and reversibly for two of them. For example, Figure 2c shows the trace of a molecule that has first a mean lifetime of 3.5 ns for a period of 10 s, then jumps to a lifetime of 5.9 ns during 5 s, and then jumps back to a lifetime of 3.5 s during 5 s, prior to bleach. At all times, the intensity trace is anticorrelated to the lifetime trace, excluding the occurrence of quenching effects. The observed behavior corresponds merely to a switching of the molecule between the ≪flat≫ and the twisted conformation, followed by the reverse process, due to the dynamic structural disorder of the matrix.

It is worthwhile to notice here that the first switch always occurs from the ≪flat≫ conformation to the twisted conformation, which is the most stable conformation. The reverse switch does not always occur. Figure 3 shows the fluorescence lifetime distribution of 59 TPDI molecules embedded in PMMA (a) and 92 molecules embedded in P*n*BMA (b). The bimodal distribution of lifetimes that appear in P*n*BMA clearly reflects the difference between the free volume distribution present in this matrix and in PMMA. In this respect, it is interesting to note that current experiments are performed at room temperature (292 K) for both polymer matrixes. While this temperature corresponds to a few degrees below the glass transition temperature in P*n*BMA, it is more than 80 K below the glass transition temperature in PMMA. The difference between the distributions observed in PMMA and P*n*BMA thus results from a combination of a different free volume distribution and a difference in cohesion energy in each matrix at the working temperature. The intensity fluctuations observed in the traces of Figure 2 are probably due to the enhanced mobility of the side chains in the P*n*BMA matrix as compared to that in the PMMA matrix.

In conclusion, it is shown in this communication that single-molecule conformational changes can *directly* probe the *local* free volume in amorphous polymers. The spatial (free volume distribution) and temporal (dynamics of free volume) information obtained by monitoring the fluorescence lifetime fluctuations of single molecules situated at different locations of the matrix would have been hidden in ensemble experiments, due to the intrinsic process of averaging involved in these measurements. It is important to notice here that the bimodal form of the fluorescence lifetime distribution shown in Figure 3 does not imply that there are only two sizes of free volume within the P*n*BMA matrix, but is merely a consequence of the fact that the two stable conformations of the probe molecule only allow us to distinguish between free volume sizes larger or smaller than 0.201 nm^3.

Acknowledgment. Renaud A. L. Vallée thanks the FWO for a postdoctoral fellowship. The KULeuven Research Fund, the DWTC through the IAP/V/03, the Flemish Ministry of Education through GOA/1/2001, and the FWO are gratefully acknowledged for supporting this research. The financial support through a Max Planck Research Award is also gratefully acknowledged.

References

(1) Doolittle, A. K. *J. Appl. Polym. Sci.* **1951**, *22*, 1471−1475.
(2) Williams, M. L.; Landel, R. F.; Ferry, J. D. *J. Am. Chem. Soc.* **1955**, *77*, 3701−3707.
(3) Cohen, M. H.; Turnbull, D. J. *Chem. Phys.* **1959**, *31*, 1164−1169.
(4) Turnbull, D.; Cohen, M. H. *J. Chem. Phys.* **1970**, *52*, 3038−3041.
(5) Cohen, M. H.; Grest, G. S. *Phys. Rev. B* **1979**, *20*, 1077−1098.
(6) Grest, G. S.; Cohen, M. H. *Phys. Rev. B* **1980**, *21*, 4113−4117.
(7) Grest, G. S.; Cohen, M. H. *Adv. Chem. Phys.* **1981**, *48*, 455−525.
(8) Cohen, M. H.; Grest, G. S. *J. Non-Cryst. Solids* **1984**, *61*−*62*, 749.
(9) Simha R.; Somcynsky, T. *Macromolecules* **1969**, *2*, 342−350.
(10) Simha, R. *Macromolecules* **1977**, *10*, 1025−1030.
(11) Robertson, R. E.; Simha, R.; Curro, J. G. *Macromolecules* **1985**, *18*, 2239−2246.
(12) Robertson, R. E.; Simha, R.; Curro, J. G. *Macromolecules* **1988**, *21*, 3216−3220.
(13) Plazek, D. J. *J. Chem. Phys.* **1965**, *69*, 3480−3487.
(14) Roe, R. J.; Song, H. H. *Macromolecules* **1985**, *18*, 1603−1609.
(15) Song, H. H.; Roe, R. J. *Macromolecules* **1987**, *20*, 2723−2732.
(16) Victor, J. G.; Torkelson, J. M. *Macromolecules* **1988**, *21*, 3490−3497.
(17) Jean, Y. C. *Microchem. J.* **1990**, *42*, 72−102.
(18) Dlubek, G.; Pionteck, J.; Bondarenko, V.; Pompe, G.; Taesler, C.; Petters, K.; Krause-Rehberg, R. *Macromolecules* **2002**, *35*, 6313−6323.
(19) Xie, X. S.; Trautman, J. K. *Annu. Rev. Phys. Chem.* **1998**, *49*, 441−480.
(20) Moerner, W. E.; Orrit, M. *Science* **1999**, *283*, 1670−1675.
(21) Deschenes, L. A.; Vanden Bout D. A. *Science* **2001**, *292*, 255−258.
(22) Veerman, J. A.; Garcia Parajo, M. F.; Kuipers, L.; van Hulst, N. F. *Phys. Rev. Lett.* **1999**, *83*, 2155−2158.
(23) Köhn, F.; Hofkens, J.; Gronheid, R.; Van Der Auweraer, M.; De Schryver, F. C. *J. Phys. Chem. A* **2002**, *106*, 4808−4814.
(24) Vallée, R. A. L.; Tomczak, N.; Kuipers, L.; Vancso, G. J.; van Hulst, N. F. *Phys. Rev. Lett.* **2003**, *91*, 038301−038304.
(25) Hofkens, J.; Vosch, T.; Maus, M.; Kohn, F.; Cotlet, M.; Herrmann, A.; Müllen, K.; De Schryver, F. C. *Chem. Phys. Lett.* **2001**, *333*, 255−263.
(26) Herrmann, A.; Weil, T.; Sinigersky, V.; Wiesler, U.-M.; Vosch, T.; Hofkens, J.; De Schryver, F. C.; Müllen, K. *Chem.*−*Eur. J.* **2001**, *7*, 4844−4853.
(27) Cotlet, M.; Hofkens, J.; Habuchi, S.; Dirix, G.; Van Guyse, M.; Michiels, J.; Vanderleyden, J.; De Schryver, F. C. *Proc. Natl. Acad. Sci. U.S.A.* **2001**, *98*, 14398−14403.
(28) Liu, J.; Deng, Q.; Jean, Y. C. *Macromolecules* **1993**, *26*, 7149−7155.
(29) Yu, W.-C.; Sung, C. S. P. *Macromolecules* **1988**, *21*, 365−371.
(30) Only four molecules embedded in PMMA showed a switching behavior between the two conformations on a fast millisecond time scale, which was attributed to spatially heterogeneous dynamics in the matrix. Vallée, R. A. L.; Cotlet, M.; Hofkens, J.; De Schryver, F. C.; Müllen, K. *Macromolecules* **2003**, *36*, 7752−7758.

JA031599G

J|A|C|S
ARTICLES
Published on Web 08/06/2005

Single Molecule Spectroscopy as a Probe for Dye−Polymer Interactions

Renaud A. L. Vallée,*,† Philippe Marsal,‡ Els Braeken,† Satoshi Habuchi,† Frans C. De Schryver,† Mark Van der Auweraer,† David Beljonne,‡ and Johan Hofkens*,†

Contribution from the Department of Chemistry, Katholieke Universiteit Leuven, Celestijnenlaan 200 F, B-3001 Leuven, Belgium, and Laboratory for Chemistry of Novel Materials, University of Mons-Hainaut, Place du Parc 20, B-7000 Mons, Belgium

Received February 17, 2005; E-mail: renaud.vallee@chem.kuleuven.be; johan.hofkens@chem.kuleuven.be

Abstract: Experimental (Single Molecule Spectroscopy) and theoretical (quantum-chemical calculations and Monte Carlo and molecular dynamics simulations) techniques are combined to investigate the behavior and dynamics of a polymer−dye molecule system. It is shown that the dye molecule of interest (1,1′-dioctadecyl-3,3,3′,3′-tetramethylindo-dicarbocyanine) adopts two classes of conformations, namely planar and nonplanar ones, when embedded in a poly(styrene) matrix. From an in-depth analysis of the fluorescence lifetime trajectories, the planar conformers can be further classified according to the way their alkyl side chains interact with the surrounding poly(styrene) chains.

I. Introduction

Polymer films with thicknesses of hundreds of nanometers are studied extensively nowadays. The reason for this is twofold. First, they provide ideal sample geometry to investigate the effects of one-dimensional confinement on the structure, morphology, and dynamics of the polymer chains.[1] Second, they are used extensively in technological applications such as optical coatings, protective coatings, adhesives, and packaging materials.

The study of single fluorophores embedded in polymer films has received increasing attention during the past decade. Initially, the polymer matrix was used to immobilize the fluorophores in single molecule studies.[2−5] More recently, an increasing number of investigations have dealt with the reversed situation where the physical properties of polymers are now the focus of these studies using single molecule detection methods.[6−9] At cryogenic temperatures, it has been shown[6] that most of the "spectral trails" of single molecules show a behavior consistent with the double well potential model of glasses, representing motion of a small group of atoms within double well features of the potential energy hypersurface. At higher temperatures, polymer mobility has been probed in the supercooled liquid regime by use of mobility (such as rotational and translational diffusion) observables[7] and in the glassy state by use of spectroscopic observables.[9−13] Very recently, single molecule spectroscopy has allowed us to assess the distribution of local free volume in glassy polymers, using either single dye molecules sensitive to local density fluctuations[9] or dye molecules subjected to conformational changes.[12]

In this paper, we show that an in-depth analysis of single molecule spectroscopy data combined to the input from quantum-chemical calculations and Monte Carlo and molecular dynamics simulations offers a new way to obtain deep insight into the polymer dynamics and polymer−dye molecule interactions at a molecular level.

We present the results of single molecule optical measurements on 1,1′-dioctadecyl-3,3,3′,3′-tetramethylindo-dicarbocyanine (DiD) molecules embedded in a poly(styrene) (PS) matrix. Bimodal spatial distributions of fluorescence lifetimes and spectral widths are observed that are assigned, on the basis of quantum-chemical calculations, to two classes of conformers of the DiD molecule, namely "planar" and "nonplanar" conformers. By comparing the measured temporal lifetime distributions to the lifetime distributions built from Monte Carlo simulations of the system, two "planar" conformers are shown to coexist in the polymer matrix. On the basis of molecular

† Katholieke Universiteit Leuven.
‡ University of Mons-Hainaut.

(1) Roth, C. B.; Dutcher, J. R. Mobility on Different Length Scales in Thin Polymer Films. In *Soft Materials: Stucture and Dynamics*; Dutcher, J. R., Marangoni, A. G., Eds.; Marcel Dekker: 2004.
(2) Macklin, J. J.; Trautman, J. K.; Harris, T. D.; Brus, L. E. *Science* **1996**, *272*, 255.
(3) Xie, X. S.; Trautman, J. K. *Annu. Rev. Phys. Chem.* **1998**, *49*, 441.
(4) Vanden Bout, D. A.; Yip, W.-T.; Hu, D. H.; Swager, T. M.; Barbara, P. F. *Science* **1997**, *277*, 1074.
(5) Veerman, J. A.; Garcia Parajo, M. F.; Kuipers, L.; van Hulst, N. F. *Phys. Rev. Lett.* **1999**, *83*, 2155.
(6) Boiron, A.-M.; Tamarat, Ph.; Lounis, B.; Orrit, M. *Chem. Phys.* **1999**, *247*, 119.
(7) Deschesnes, L. A.; Vanden Bout, D. A. *Science* **2001**, *292*, 255.
(8) Bowden, N. B.; Willets, K. A.; Moerner, W. E.; Waymouth, R. M. *Macromolecules* **2002**, *35*, 8122.
(9) Vallée, R. A. L.; Tomczak, N.; Kuipers, L.; Vancso, G. J.; van Hulst, N. F. *Phys. Rev. Lett.* **2003**, *91*, 038301.
(10) Bartko, A. P.; Dickson, R. M. *J. Phys. Chem. B* **1999**, *103*, 3053.
(11) Vallée, R. A. L.; Cotlet, M.; Hofkens, J.; De Schryver, F. C.; Müllen, K. *Macromolecules* **2003**, *36*, 7752.
(12) Vallée, R. A. L.; Cotlet, M.; Van der Auweraer, M.; Hofkens, J.; Müllen, K.; De Schryver, F. C. *J. Am. Chem. Soc.* **2004**, *126*, 2296.
(13) Tomczak, N.; Vallée, R. A. L.; van Dijk, E. M. H. P.; Kuipers, L.; van Hulst, N. F.; Vancso, G. J. *J. Am. Chem. Soc.* **2004**, *126*, 4748.

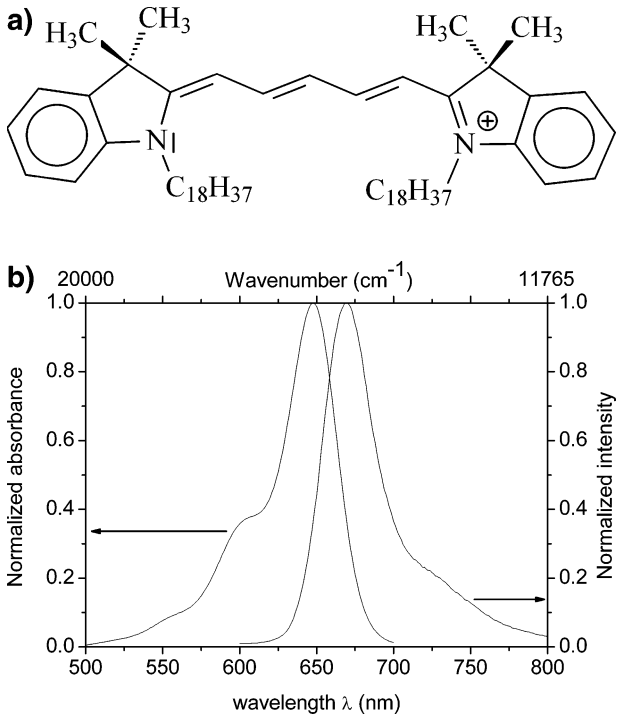

Figure 1. (a) Schematic structure and (b) Absorption and emission spectra of the DiD dye molecule, as measured in a chloroform solution.

dynamics simulations of the dye molecule−polymer system, these two conformers are assigned to molecular structures differing by the relative orientation of their long alkyl chains (positioned either on the same side or on opposite sides with respect to the conjugated backbone of the molecule). This leads to different fractions of holes surrounding the dye molecule and hence different lifetime distributions.

II. Materials and Methods

The polymer films were obtained by spin coating a solution of a nanomolar concentration of the DiD dye in PS (Polymer Standard Service, $M_w = 133\,000$, PI = 1.06, $T_g = 373$ K) on a glass substrate. The dye molecules were excited by pulses of 90 ps at a wavelength λ of 644 nm (Figure 1: the maximum absorbance of the dye molecule is located at $\lambda = 648$ nm, and its maximum emission intensity is located at $\lambda = 670$ nm) and a repetition rate of 10 MHz (PicoQuant) in an inverted confocal microscope (Olympus IX70). The excitation power P was set to 1 μW at the entrance port of the microscope. The emission signal was split equally in two parts. The fluorescence lifetime was measured by use of an avalanche photodiode (SPCM-AQ-15, EG & G Electro Optics) equipped with a time correlated single photon counting card (Becker & Hickl GmbH, SPC 630) used in FIFO mode. Two procedures based on the weighted least-squares (LS) and the maximum likelihood estimation (MLE) method to confidently analyze single-molecule (SM) fluorescence decays with a total number (N) of 500−30 000 counts were used.[14] First, decay profiles were built for each molecule with an integration time of 1s. In this case, the number of counts (5000−30 000) was high enough to fit adequately the profiles with the LS method. The values obtained in this way were used to build the spatial lifetime distribution for all molecules measured in the matrix. Second, to observe the dynamics (lifetime transients) of the single molecules in the polymer matrix, shorter bin sizes have to be taken (100 ms). The decay profiles built on such a time scale count much less photons (500−3000). The MLE method was chosen in this case to fit the decay profiles, as it is known to give stable results over the whole intensity range, even at counts N less than 1000, where the LS analysis delivers unreasonable values. The emission spectra were recorded, with an integration time of 10 s, through a charge coupled device (CCD) camera (Princeton Instruments) fitted with a polychromator (Acton Spectra Pro 150). The experimental spectra are cut by the dichroic mirror (DC-O-660) and the long pass filter (LP660) on the blue edge (25% of the emitted signal transmitted at 655 nm). To determine their width, the spectra were smoothed, by convoluting them with a Gaussian distribution of a 3 nm bandwidth,[15] numerically integrated (in order to determine their area) and divided by the maximum intensity at the peak wavelength. This way of determining the width was chosen as it is the most natural way of defining an effective width of a spectrum, irrespective of its fine structure.

The quantum-chemical calculations were performed using the following methodology. Ground-state optimizations were performed at the semiempirical Hartree−Fock Austin Model 1 (AM1) level[16] and excited-state optimizations by coupling the AM1 Hamiltonian to a full configuration interaction (CI) scheme within a limited active space, as implemented in the AMPAC package.[17] The optical absorption and emission spectra were then computed by means of the semiempirical Hartree−Fock intermediate neglect of differential overlap (INDO) method, as parametrized by Zerner et al.,[18] combined to a single configuration interaction (SCI) technique; the CI active space is built here by promoting one electron from one of the highest sixty occupied to one of the lowest sixty unoccupied levels. To obtain the vibronic progression of the spectra, normal-mode-projected displacements and associated reorganization energies were calculated by the method implemented by Reimers,[19] which is suitable for large molecules. These were then used to simulate the spectra within the framework of a displaced harmonic oscillator model. To take into account the influence of low-frequency external modes, the calculated lines were convoluted with Gaussian lines of 500 cm^{-1} bandwidth, to match the line width of the bulk emission spectrum.

The radiative lifetime has been calculated with the usual formula

$$\tau_0 = \frac{m_e \epsilon_0 c_0^{\,3}}{2e^2 \pi \nu_0 f} \qquad (1)$$

by further taking into account the renormalization of the photon in the medium: $\epsilon_0 \rightarrow \epsilon_r \epsilon_0$ and $c_0 \rightarrow c_0/n$ and the slight change in the transition frequency.

In this formula, e is the charge of the electron, ϵ_0 and c_0 are the permittivity and the speed of light in a vacuum, and ν_0 and f are the transition frequency and the oscillator strength of the probe molecule in a vacuum, respectively. Finally, the polarizabilities were determined by a sum over states (SOS) method encompassing all states involved in the CI space just mentioned.

The Monte Carlo simulations, allowing us to calculate the radiative lifetime of a dye molecule embedded in a disordered medium, were performed using a homemade software.[20] In these simulations, the spectroscopic properties (transition dipole moment, transition energy, polarizability) of DiD determined by quantum-chemical calculations were used. To model the effect of the environment on the probe molecule, the polarizability of a poly(styrene) base unit (hereafter called styrene unit) was also determined.

(14) Maus, M.; Cotlet, M.; Hofkens, J.; Gensch, T.; De Schryver, F. C.; Schaffer, J.; Seidel, C. A. M. *Anal. Chem.* **2001**, *73*, 2078.
(15) Stracke, F.; Blum, C.; Becker, S.; Müllen, K.; Meixner, A. J. *Chem. Phys.* **2004**, *300*, 153.
(16) Dewar, M. J. S.; Zoebisch, E. G.; Healy, E. F.; Stewart, J. J. P. *J. Am. Chem. Soc.* **1985**, *107*, 3902.
(17) AMPAC, Semichem, 7204 Mullen, Shawnee, KS 66216.
(18) Zerner, M. C.; Loew, G. H.; Kichner, R.; Mueller-Westerhoff, U. T. *J. Am. Chem. Soc.* **2000**, *122*, 3015.
(19) Reimers, J. *J. Chem. Phys.* **2001**, *115*, 9103.
(20) Vallée R. A. L.; Van der Auweraer, M.; De Schryver, F. C.; Beljonne, D.; Orrit, M. *ChemPhysChem* **2005**, *6*, 81.

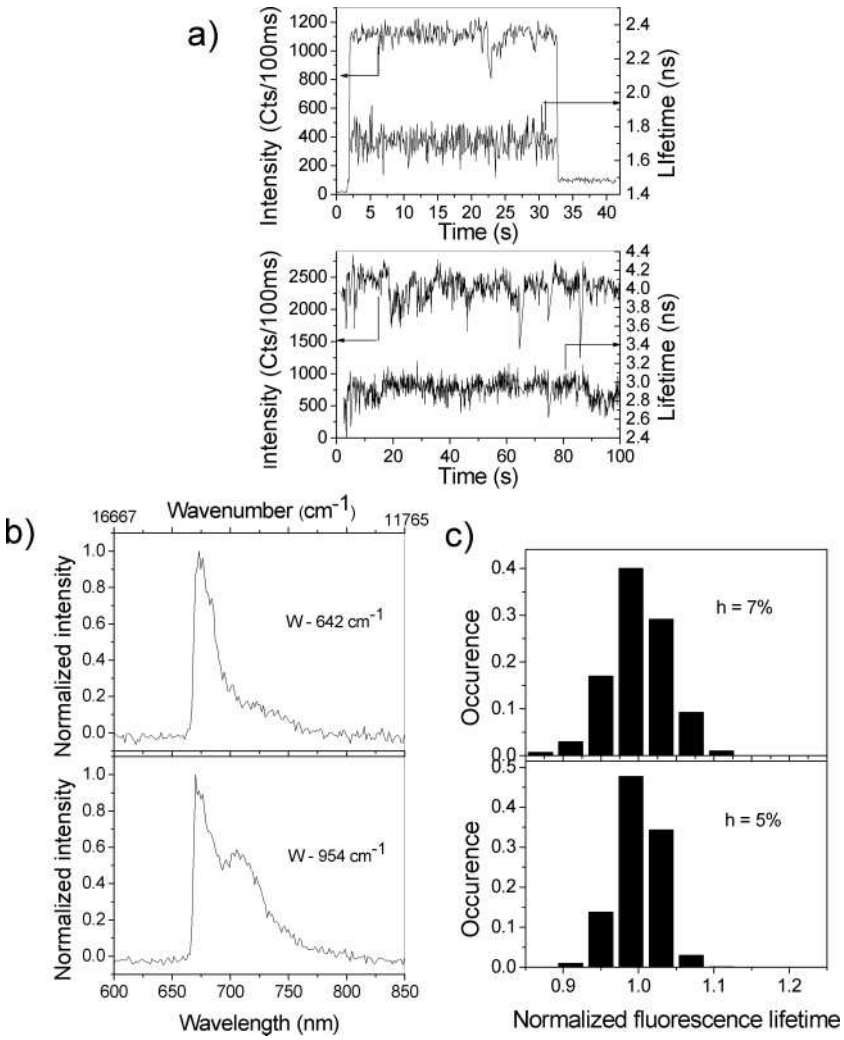

Figure 2. Experimental intensity and fluorescence lifetime time traces (a) and corresponding spectra (b) and distributions (c) of normalized lifetimes, for a planar (top) and a nonplanar (bottom) conformer of the DID molecule embedded in a PS matrix. In (b) the integration time for each spectrum is 10 s. In (c), the lifetime of each conformer is normalized with respect to the mean value of the respective distribution, which is 1.7 ns (2.9 ns) in the case of the planar (nonplanar) conformer.

Molecular dynamics simulations of the DiD molecule−PS system were performed using the Material Studio and Cerius packages by Accelrys. We used the compass[21] force field in order to create an amorphous cell[22] containing a DiD molecule (with its alkyl chains) and two atactic PS chains of 100 monomers each. Ewald summation methods are used to treat Coulombic interactions, and atom based methods are adopted to treat van der Waals interactions with standard cutoffs. All subsequent simulations are performed at a constant number of particles and standard temperature and pressure (NPT ensemble) controlled by a Berendsen thermostat and barostat with a time constant of 145 fs. The Verlet algorithm and a time step of 1 fs are used for all dynamics simulations, which have been run for a total period of 100 ps.

III. Results and Discussion

III.1. Experimental Observations: Existence of Several Species. Cyanine dyes without substituents on the polymethine chain have generally an all-trans geometry in their most stable form.[23] Nevertheless, they exist in several conformers,[24] which can be used to probe particular pockets in microheterogeneous environments. To solubilize the dyes in solvents of low polarity, the nitrogen atoms are substituted by long alkyl chains. Figure 1 shows the structure of DiD (a) and its (room temperature) absorption and emission spectra in a chloroform solution (b). The width of the bulk emission spectrum is $W = 1147$ cm^{-1}.

Figure 2 shows the intensity and fluorescence lifetime time trajectories (a) as well as corresponding spectra (b) of two different representative molecules embedded in a PS matrix. While the first one has a fluorescence lifetime with an average value of 1.7 ns (a, top) and a relatively sharp spectrum (spectral width $W = 642$ cm^{-1}) (b, top) reminiscent of the bulk emission spectrum shown in Figure 1b, the other has a longer average fluorescence lifetime $\tau = 2.9$ ns (a, bottom) and a significantly broader spectrum (spectral width $W = 954$ cm^{-1}) (b, bottom), characterized by an increased amplitude of the 0−1 vibronic peak.

To determine the general character of this behavior and the possible correlation between fluorescence lifetimes and spectra exhibited by the DiD single molecules, an analysis of 164

(21) Sun, H. *J. Phys. Chem. B* **1998**, *102*, 7338.
(22) Theodorou, D. N.; Suter, U. W. *Macromolecules* **1985,** *18*, 1467.
(23) Mishra, A.; Behera, R. K.; Behera, P. K.; Mishra, B. K.; Behera, G. P. *Chem. Rev.* **2000**, *100*, 1973 and references therein.
(24) Vranken, N.; Jordens, S.; De Belder, G.; Lor, M.; Rousseau, E.; Schweitzer, G.; Toppet, S.; Van der Auweraer, M.; De Schryver, F. C. *J. Phys. Chem. A* **2001**, *105*, 10196.

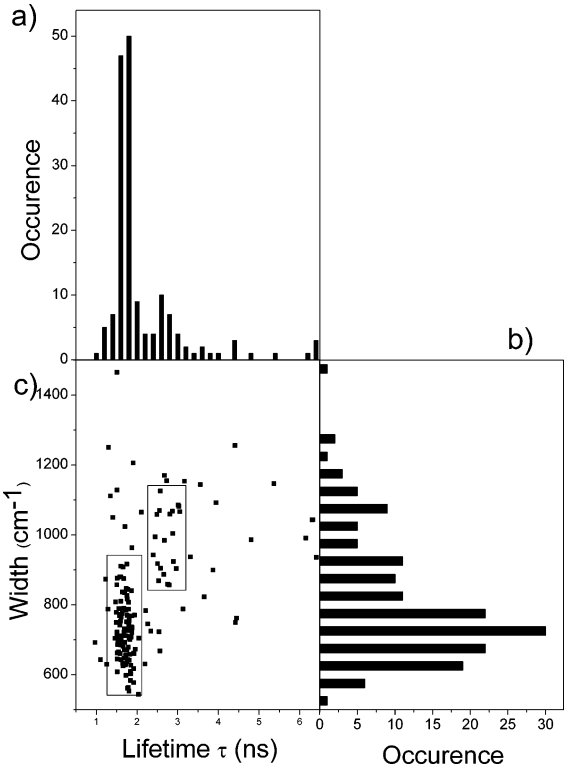

Figure 3. Fluorescence lifetime (a) and spectral width (b) distributions of DiD molecules embedded in a PS matrix. (c) Corresponding correlation plot between fluorescence lifetimes and spectral widths.

molecules embedded in the matrix and surviving irreversible photobleaching for a sufficient period to allow a measurement with good counting statistics (at least 20 000 counts) was performed.

Figure 3 shows histograms of the fluorescence lifetime (a) and spectral width (b) of the single molecules spatially distributed in the polymer matrix. Bimodal distributions of lifetimes and spectral widths are observed. The main and second peaks of the lifetime distribution are located at $\tau \sim 1.8$ ns and $\tau \sim 2.6$ ns, respectively. Similarly, the main and second peaks of the spectral width distribution correspond to a width of $W \sim 700$ cm^{-1} and $W \sim 1100$ cm^{-1}, respectively. The fluorescence lifetimes are shown to be correlated with the spectral widths (Figure 3c), longer fluorescence lifetimes being associated with larger spectral line widths.[25]

III.2. Quantum-Chemical Calculations: Conformational Search. The changes in the spectroscopic observables might be related to the existence of different stereoisomers of the DiD molecule. To check this hypothesis, a search for all possible conformers of DiD was performed at the quantum-chemical level. This was achieved by optimizing the geometries obtained by cis (C)−trans (T) isomerization of each dihedral angle

(25) To draw the boxes shown in Figure 3c, we have proceeded in the following way. We first centred each of them on the lifetime axis exactly at the positions of the first and second peaks in the lifetime distribution (projections from Figure 3a to 3c). The width of the box in lifetime is determined by continuity of the density of points around the center. We proceeded in the same way on the line width axis. For the right upper box, we had to find a compromise between centering the box at the position of the second peak in the line width distribution (projection from Figure 3b to 3c) and the argument of continuity of the density of points within the box. As the two peaks are not so nicely resolved in this case, compared to the lifetime distribution, we decided to favor the continuity argument, which explains why the center of the right upper box is lower than the projection of the second peak in line width.

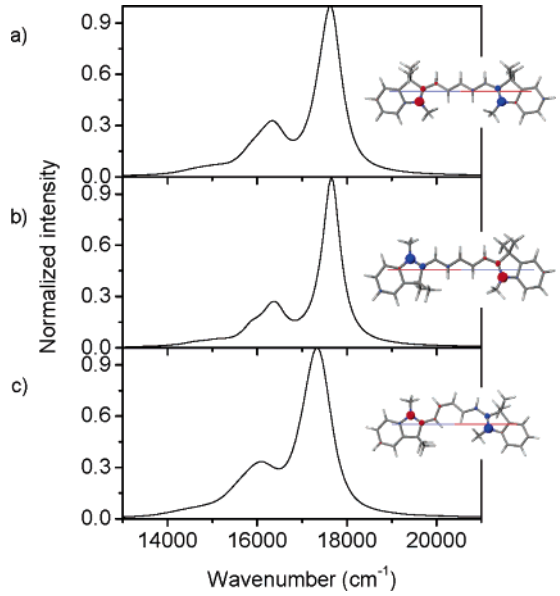

Figure 4. Molecular structure and atomic transition densities associated with the lowest optically allowed electronic excitation of the CTTTTC (a), TTTTTC (b), and CTCTTC (c) conformers. The arrow represents the orientation of the total transition dipole moment. Corresponding calculated emission spectra are also represented.

involved in the polyenic segment joining the nitrogen atoms (Figure 1a). We have used the Hartree−Fock semiempirical Austin Model 1 (AM1) technique to describe both the geometric and electronic structures in the S_0 singlet ground state and S_1 lowest singlet excited state of the studied molecules. Frequency calculations were performed to validate the existence of the local minima uncovered.

Since the DiD molecule has 6 dihedral angles between the N atoms with either cis (C) or trans (T) conformation of the bonds, 2^6 combinations, leading to 64 possible conformers, can be considered. However, some of the 64 conformations can be ruled out right away. This is the case for structures characterized by three consecutive cis conformations along the molecular chain (20 conformers out of the 64), as a result of important sterical constraint. In addition, a number of conformations are identical upon a rotation around the C_2 axis going through carbon 3 of the methine chain (among the 44 conformers left, 19 can be eliminated on the basis of symmetry arguments). 18 of the 25 left conformers lie at an energy much higher (with respect to kT) than that of the global minimum (in the range 2.6−23.5 kcal/mol). This energy difference implies a Boltzmann population below 1% for those molecules, which are therefore very unlikely to be observed. Four of the seven remaining conformers, possessing either zero (1) cis bond or two cis separated by four trans bonds, display almost planar geometries (these are hereafter referred to as TTTTTT, TTTTTC, CTTTTC, TTCTTT). The three others, with several cis bonds close to the center of the polyenic segment, correspond to nonplanar conformers. In all cases, the atomic transition densities are mainly localized on the nitrogen atoms. Figure 4 shows the geometric structures of the three most stable conformers (two "planar" and one "nonplanar") among the seven. Table 1 collects the excited-state properties of the seven conformers, as determined by INDO/SCI calculations on the basis of the AM1 excited-state geometries.

Table 1. Relative Heats of Formation (AM1 ground-state geometries); Transition Energies *E*, Oscillator Strengths *f*, Lengths *l* (distance between the N atoms) of the Transition Dipole Moments and Average Electron−Hole Distances *d* (at the INDO/SCI level on the basis of AM1 excited-state geometries) for the seven most stable stereoisomers of the DiD molecule[a]

conformer	relative heat of formation (kcal/mol)	*E* (eV)	*f*	*l* (10^{-10} m)	*d* (10^{-10} m)
TTTTTT	259.61	2.18	1.80	9.77	6.90
TTTTTC	258.97	2.19	1.74	9.26	7.00
CTTTTC	258.38	2.19	1.68	8.31	7.08
TTTCTC	260.03	2.16	1.50	9.17	6.58
TTCTTT	261.00	2.15	1.48	8.87	6.65
CTCTTC	259.49	2.16	1.36	8.10	6.69
CTTCTT	260.54	2.16	1.34	7.42	6.76

[a] T (C) denotes a trans (cis) linkage along the polyenic segment (see text).

Table 2. Fluorescence Lifetimes τ_f (at the INDO/SCI Level), Polarizabilities χ (INDO/SCI/SOS), Spectral Widths *W*, and Boltzmann Occurrences p_B taking into account degeneracy for the seven most stable stereoisomers of the DiD molecule

conformer	τ_f (ns)	χ (10^{-30} m^3)	W (cm^{-1})	p_B
TTTTTT	1.70	55.7	1048	0.05
TTTTTC	1.75	54.5	1055	0.31
CTTTTC	1.81	53.6	1291	0.43
TTTCTC	2.08	51.2	1156	0.05
TTCTTT	2.13	51.3	1107	0.01
CTCTTC	2.30	49.3	1477	0.13
CTTCTT	2.33	49.1	1430	0.02

A careful analysis of this table reveals that (i) the transition energies of the planar geometries are slightly larger (by about 0.03 eV) than those of the nonplanar geometries. This is a surprising result as the planar conformers should be characterized by a more extended delocalization. Table 1 shows that the transition energies obtained at the INDO/SCI level are correlated with the average electron−hole (e−h) distances, which are larger in the extended planar structures. So, the small variation of the INDO/SCI excitation energy across Table 1 results from partial cancellation between the red-shift induced by increased delocalization and the blue-shift resulting from larger e−h separation upon switching from a nonplanar to a planar conformation. (ii) The oscillator strengths calculated for the seven conformers increase simply as a function of the distance *l* separating the N atoms. As a consequence of (i) and (ii), the radiative lifetime of the dye molecule is a monotonic decreasing function of the distance separating the two N atoms (Table 2).

III.3. Experiment versus Theory. The radiative lifetimes calculated for the seven most stable DiD conformers as a function of their relative occurrence (based on Boltzmann statistics) are displayed in Figure 5a.

By comparing with experimental data (Figure 3), one can readily assign the main measured peak centered on $\tau = 1.8$ ns to the planar conformers, while the presence of other conformers (and especially the CTCTTC stereoisomer, Figure 4) accounts for the second peak in the bimodal lifetime distribution. Note the excellent agreement between the measured and calculated lifetimes. Figure 4 also shows the emission spectrum simulated for each of the three most stable conformers and Table 2 collects relevant data concerning the fluorescence lifetime, spectral line width, and Boltzmann occurrence of the seven conformers.

The calculated emission spectra of the abundant planar TTTTTC (Figure 4b) and nonplanar CTCTTC (Figure 4c) conformers fit reasonably well the measured spectra (Figures 2b top and bottom respectively). The difference in the spectral line widths between both conformers is due to coupling between electronic excitations and low-frequency vibrational modes in the nonplanar structure (resulting from a change in conformation toward a more planar structure when going from the ground state to the excited state). Figure 5c shows the correlation plot between calculated fluorescence lifetimes and spectral widths for the seven conformers. The boxes drawn encompass the most abundant species and clearly correlate with their experimental counterparts (Figure 3c).

III.4. Influence of Local-Field Effects. Up to now, we have paid attention to spatial distributions of fluorescence lifetimes and spectra of DiD molecules in the PS matrix. Single molecule spectroscopy allows one to probe not only spatial but also temporal distributions of spectroscopic observables. Figure 2c,

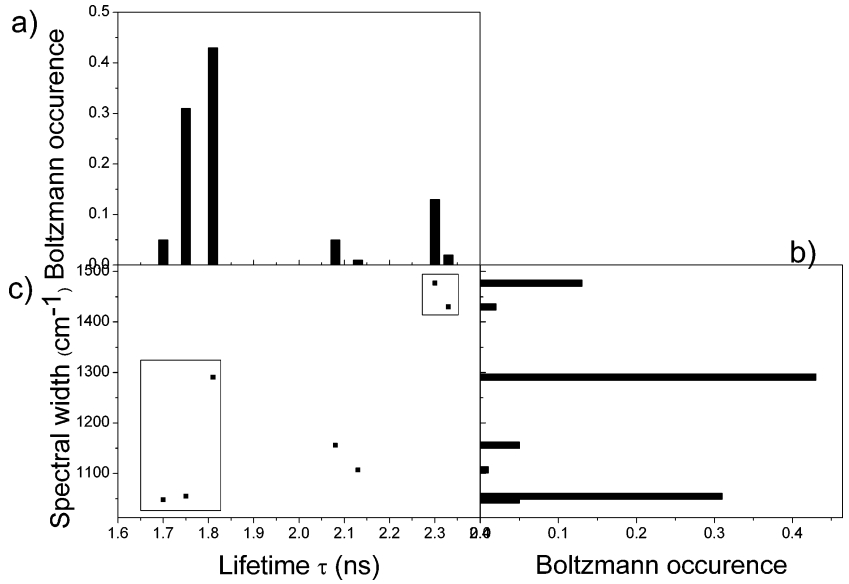

Figure 5. Calculated fluorescence lifetime (a) and spectral width (b) distributions of DiD molecules embedded in a PS matrix. (c) Corresponding correlation plot between fluorescence lifetimes and spectral widths. Note the resemblance with Figure 3.

for example, shows the temporal distributions of normalized fluorescence lifetimes for two different molecular conformations assigned as planar (top) and nonplanar (bottom). Very recently, we have shown, by using either a macroscopic[9,26] or a microscopic[20] approach, that the temporal fluorescence lifetime fluctuations of a DiD molecule are mainly due to local density fluctuations of the surrounding polymer matrix: a given fraction of holes is "moving" around the probe molecule, thereby modifying the local field experienced by the molecule.

On a microscopic scale, a medium consists of discrete atoms or molecules. According to the Lorentz virtual cavity model,[27] a sphere is defined whose radius R is much less than the wavelength of light and greater than the intermolecular distance. The molecules within the sphere are considered as point dipoles, which are embedded in a continuous, isotropic, dielectric medium. To take into account (1) the elongated shape (Figure 4) and specific polarizability of the probe molecule investigated here and (2) the presence of both monomer units and holes around the probe molecule in a polymer matrix (inhomogeneity of the matrix), we have recently extended the Lorentz's model.[20]

The probe molecule is considered as an extended dipole of length l (l being the N−N separation) and polarizability χ (values given in Tables 1 and 2). This view is fully supported by the INDO/SCI calculated atomic transition density distributions that show major contributions on the N atoms (Figure 4). In our simulations, the probe is located at the origin of a 3D cubic lattice and surrounded by z polarizable monomers of polarizability α (calculated to be 1.0×10^{-39} C^2 m^2/J at the INDO/SCI/SOS level). To mimic the motion of the styrene units around the fixed probe molecule, a given fraction of holes (with zero polarizability) is introduced in the lattice. To determine the lattice constant Δ, the van der Waals volume of a styrene unit $V = 119 \times 10^{-30}$ m^3 is simply attributed to the volume $V = \Delta^3$ of a cell in the cubic lattice. After excitation by a laser pulse, the probe molecule, characterized by an emission transition dipole moment μ, spontaneously emits a photon that polarizes the surrounding monomer units. The dipoles μ_k induced on the surrounding monomers, considered as point dipoles, are obtained from the set of coupled equations (k encompasses both probe and solvent molecules):

$$\mu_k = \alpha_k[E(r_k) + \sum_{j=1,j\neq k}^{z} \hat{T}_{kj}u_j] \tag{2}$$

where $E(r_k)$ is the electric field generated by the source dipole at position r_k of the lattice and $\hat{T}_{kj}$ is the dipole−dipole interaction tensor:

$$\hat{T}_{kj} = \frac{1}{r_{kj}^3}\left(\hat{I} - \frac{3r_{kj}r_{kj}}{r_{kj}^2}\right) \tag{3}$$

where $\hat{I}$ is the identity tensor and $r_{kj} = r_k - r_j$.

The second term in eq 2 includes interactions between the monomers once they have been polarized (polarizabilities $\alpha_k = \alpha$) and "back" interactions between the polarized monomers and the polarizable probe molecule (polarizability $\alpha_k = \chi$). The local electric field felt by the probe molecule is thus the sum of all electric fields experienced by the surrounding monomers and of the reaction field induced by all these polarized monomers that act back on the probe molecule.

At this level, all interactions between molecules inside the Lorentz sphere have been taken into account, and one can define an effective transition dipole moment μ_{tot}, which is the sum of the molecular dipole moment (source dipole) μ and of all induced dipoles μ_k within the discretization sphere:

$$\mu_{tot} = \mu + \mu_k \tag{4}$$

with μ_k given by eq 2.

To take into account the influence of the continuous dielectric medium surrounding the Lorentz sphere on the radiative lifetime, we simply introduce the Lorentz local field factor in the description. The spontaneous emission rate $1/\tau_f$ of the probe molecule embedded in the disordered medium thus finally can be written as

$$\frac{1}{\tau_f} = \left(\frac{\epsilon + 2}{3}\right)^2 \left|\frac{\mu_{tot}}{\mu}\right|^2 \frac{1}{\tau_0} \tag{5}$$

with τ_0 given by eq 1. The near-field effect of the disordered heterogeneous medium on the radiative lifetime can thus be evaluated completely once the ratio $|\mu_{tot}/\mu|^2$ between the total dipole in the cavity and the source dipole associated with the probe molecular charge distribution is known. As described above, this is achieved upon classical electrostatic calculations based on eqs 2−4.

To build a statistical distribution of the fluorescence lifetimes τ_f of a DiD molecule embedded in a PS matrix, Monte Carlo realizations of one representative conformer (either the planar TTTTTC or the nonplanar CTCTTC conformation) of the molecule surrounded by styrene units and holes have been achieved. A Monte Carlo run is implemented in the following way: (1) The fraction of holes (threshold value) is first fixed. (2) For each cell on the lattice, a uniformly distributed (between 0 and 1) random number is chosen. (3) If the random number falls below the threshold value, then the given cell is occupied by a hole, or else the cell is occupied by a monomer. The Monte Carlo simulations are repeated typically 1000 times for each given threshold value.

Figures 6 and 7 show the results of these Monte Carlo simulations in the case of the planar TTTTTC and nonplanar CTCTTC conformers, respectively, for a hole fraction ranging from $h = 1\%$ to $h = 10\%$ by a step of 1%. In both cases, the distributions of the normalized fluorescence lifetimes τ_r reduce to single bars centered on $\tau_r = 1$, for $h = 0\%$ (not shown). For $h = 1\%$, the distributions are very narrow and symmetric around $\tau_r = 1$. For h ranging from 2% to 10%, the distributions are getting broader and more asymmetric. The increased asymmetry, which shows up as an increase of the tail of the distributions on the long lifetime side, is slightly more pronounced in the case of the TTTTTC conformer than for the CTCTTC conformer. A detailed study reveals that the asymmetry toward higher fluorescence lifetimes is a simple consequence of the fact that a hole placed longitudinally with respect to the dipole axis of the molecule causes a large upward departure of the fluorescence lifetime with respect to its average, while a hole placed transversally only causes a small downward shift.[22]

(26) Vallée R. A. L.; Tomczak, N.; Kuipers, L.; Vancso, G. J.; van Hulst, N. F. *J. Chem. Phys.* **2005**, *122*, 114704.
(27) Böttcher, C. J. F. *Theory of electric polarization*, 2nd ed.; Elsevier: Amsterdam, 1973; Vol. 1.

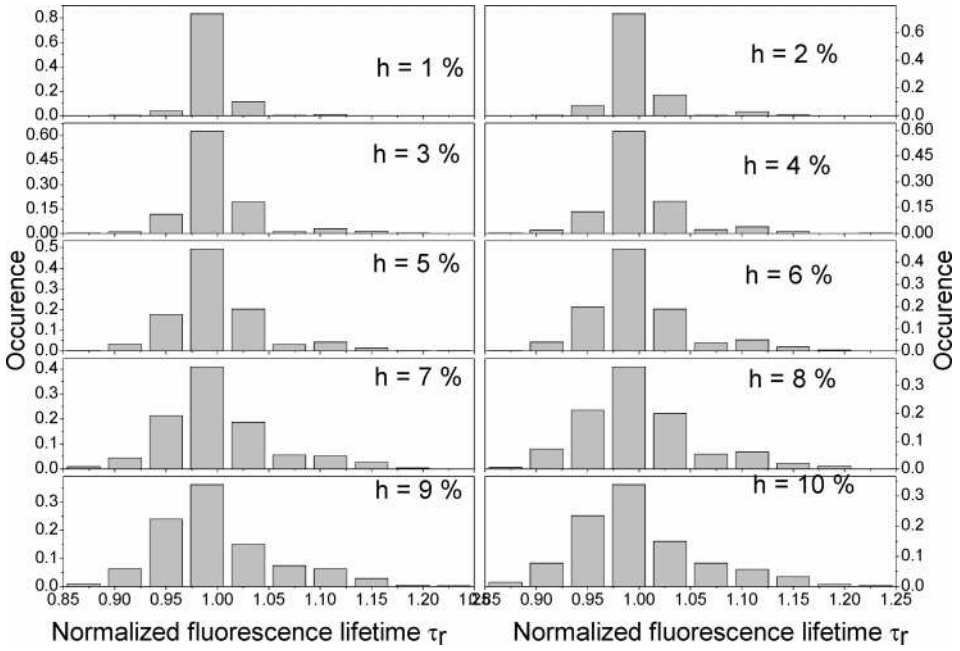

Figure 6. Fluorescence lifetime distributions of the TTTTTC stereoisomer after 1000 Monte Carlo runs. The cubic lattice is filled with six shells of polarizable monomers surrounding the extended dipole of polarizability χ, located at the origin. Holes are placed at random positions on the lattice with a fraction $h =$ 1% to $h = 10\%$ from top left to bottom right.

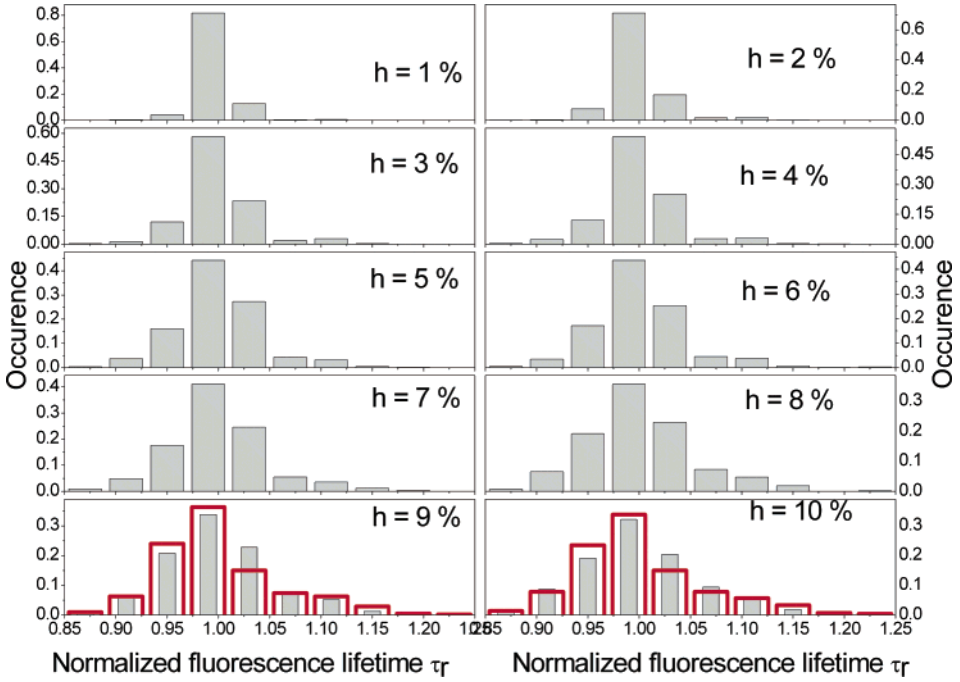

Figure 7. Same as Figure 6 for the CTCTTC conformer. For $h = 9\%$ and 10%, the normalized lifetime distributions (red) of the TTTTTC conformer are superimposed to those of the CTCTTC conformer. These distributions of the TTTTTC conformer are clearly more asymmetric than those of the CTCTTC conformer.

In addition, this effect increases with increasing polarizability of the probe molecule in comparison to that of the medium, which explains the more pronounced asymmetry found for the TTTTTC conformation (as this conformation displays both larger transition dipole moment and polarizability).

III.5. Experimental Validation of Fluctuations in Lifetimes due to Local Field Effects. Figure 2c shows the distributions of normalized fluorescence lifetimes for a planar (top) and a nonplanar (bottom) conformation of the DiD molecule embedded in a PS matrix, as identified from their average lifetimes (obtained from the lifetime trajectories, Figure 2a) and spectral shapes (Figure 2b). The distribution measured for the planar structure (top) is found to be slightly broader than that for the nonplanar structure (bottom). In both cases, the existence of such distribution points to the influence of the nanoenvironment on the probe molecule, which in our picture relates to the fraction of holes h that surrounds the probe molecule. To get a rough estimate of h, the measured lifetime distribution has been superimposed to the distributions predicted from Monte Carlo simulations for a broad range of h values (Figures 6, 7). The

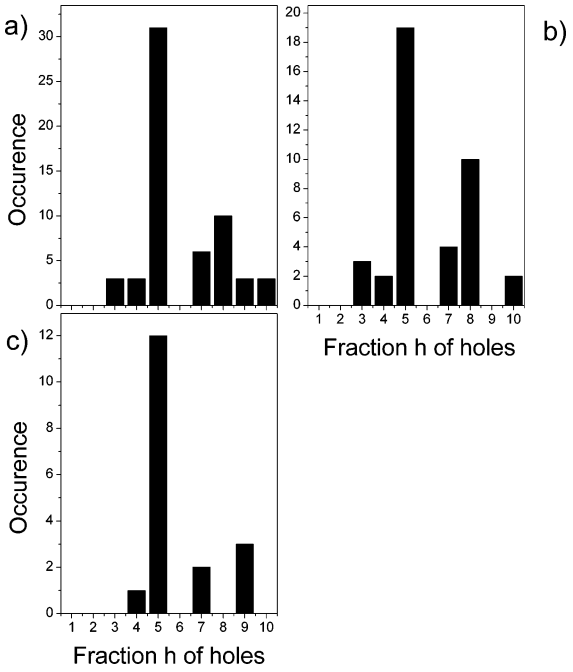

Figure 8. (a) Distribution of the fraction *h* of holes surrounding the DiD molecules embedded in the PS matrix. The distribution of holes surrounding planar and nonplanar conformers is given in (b) and (c), respectively.

best fit between experiment and theory is achieved for $h = 7\%$ in the case of the planar structure and $h = 5\%$ for the nonplanar one (Figure 2c).

The analysis, performed for these two molecules (Figure 2), has been extended to all molecules included in the boxes drawn in Figure 3c that survived a photobleaching event for more than 10 s, allowing us to get at least 100 occurrences of the fluorescence lifetime and to build up reliable histograms. A total number of 57 molecules was analyzed in this way. Among these, 39 molecules can be classified as planar from their emission characteristics. Figure 8 shows the distributions of the fraction of holes *h* surrounding a given molecule by considering (a) both planar and nonplanar conformers, (b) only planar molecules, and (c) only nonplanar molecules. Note that, since we only considered molecules belonging to the boxes drawn in Figure 3 where the fluorescence lifetimes are clearly correlated with the spectral widths, the belonging of a molecule to the planar or nonplanar category is unambiguous.

Very interestingly, the *h* distribution obtained for the planar conformers exhibits a bimodal character[28] (Figure 8b) with peaks at 5% and 8%, while the distribution (Figure 8c) obtained for the nonplanar conformer is monomodal with $h = 5\%$. The bimodal character of the distribution for the planar conformers points to the observation of possibly two conformers of this type, tentatively assigned as the TTTTTC and CTTTTC (Figure 4) conformers, as both are very stable (Tables 1 and 2) according to the quantum-chemical calculations.

III.6. Molecular Dynamics Simulations. The main difference between the two planar conformers lies in the position of the N atoms (to which the long alkyl chains are attached) with respect to the conjugated backbone of the molecule. In the case of the CTTTTC planar conformer, the two N atoms are on the same side, while for the TTTTTC planar conformer, the N atoms are on opposite sides with respect to the conjugated backbone (Figure 4). The nonplanar CTCTTC conformer also has its N atoms on opposite sides with respect to the conjugated backbone. This suggests that the species to be associated with $h = 5\%$ (Figure 8) are the conformers with N atoms on opposite sides and, therefore, the peak at $h = 8\%$ should be assigned to the planar CTTTTC conformer (Figure 4a). Because of the close proximity of the two alkyl chains lying on the same side of the CTTTTC backbone, these chains are expected to interact strongly with each other thereby hindering the segments of the polymer chains to approach the molecule closely and leading to an increased free volume in the close proximity of the dye molecule. On the contrary, for the other two species, the alkyl chains, located on opposite sides with respect to the conjugated skeleton, are free to interact with the polymer chains and should thus be more anchored in the PS matrix.

To check this hypothesis, we have performed molecular dynamics simulations for each conformer of the DiD molecule embedded in a poly(styrene) box comprising two chains of 100 monomers. Figure 9a shows three snapshots of such simulations, corresponding to the CTTTTC (black), TTTTTC (red), and CTCTTC (green) conformers. Figure 9b shows six (two alkyl chains per conformer) time trajectories for the dihedral angle comprising the first four carbon atoms of the alkyl chains attached to the N atom, as provided by these simulations in a 100 ps time scale (the angle is measured by a step of 5 ps). For such a system, the relaxation time related to thermalization, i.e., the time it takes for the non bonded interactions to relax, is about 20 ps (as revealed on a graph plotting the non − bonded interaction versus time, not shown). The vertical bar drawn in Figure 9b marks this limit, over which the fluctuations of the dihedral angles become significant. Figure 9b shows that the dihedral angles are changing considerably in time for the planar CTTTTC conformer (black lines). In contrast, small variations of the dihedral angles are observed in the case of the planar TTTTTC (red lines) and nonplanar CTCTTC (green lines) conformers.

Another very important marker for the amount of local ordering and packing of the system is the pair distribution function $g(r)$, which describes the averaged (over time) density of poly(styrene) at a distance r from the reference molecule. Such pair distribution functions are shown in Figure 9c for the CTTTTC (black line), TTTTTC (red line), and CTCTTC (green line) conformers. At long enough distances (∼12 Å) from the reference molecule, the pair distribution function tends in all cases to the limiting value of the average poly(styrene) density. Interestingly, $g(r)$ displays different evolutions for the different conformers at smaller r values (in the range 4−10 Å), associated to differences in the packing of the poly(styrene) chains: the red curve (planar conformer with the alkyl chains on opposite sides with respect to the conjugated backbone) indeed shows much faster saturation to the limiting value of the polystyrene density than the black curve (planar conformer with the alkyl chains on the same side with respect to the conjugated backbone). The green curve (nonplanar conformer with the alkyl chains on opposite sides with respect to the conjugated backbone) follows closely the red curve.

(28) The depth of the "dip" between both maxima at 5% holes and 8% holes exceeds the standard deviation on the occurrence. The latter equals (assuming a Poisson distribution) the square root of the occurrence. This amounts to 4.4 and 3.2 for 5% and 8% holes, respectively. On the other hand, the probability for the minimum occurrence at 6% holes to be 0 at an expectation value of 3 events or more is less than 0.05. Hence one can safely assume the distribution to be bimodal.

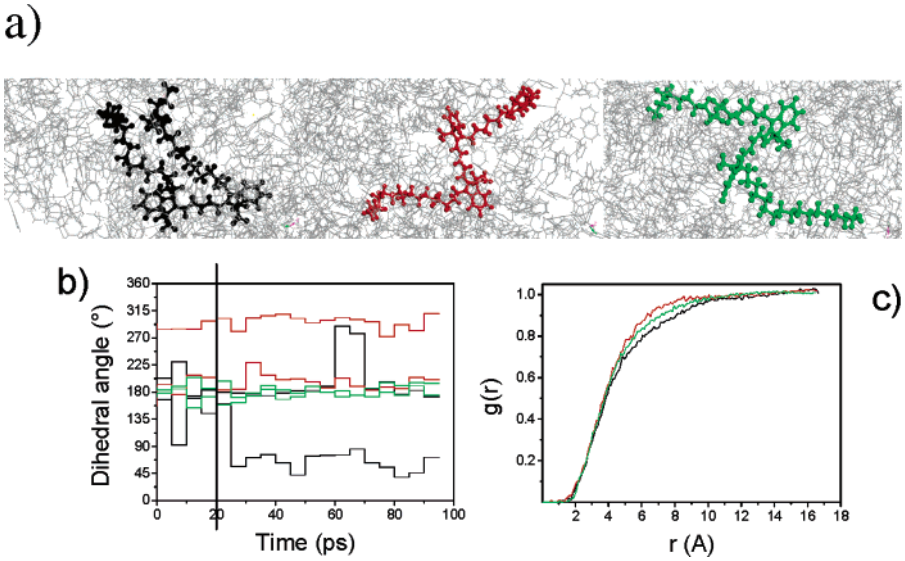

Figure 9. Snapshots (a), time trajectories of the dihedral angles comprising the first four carbon atoms of the long alkyl chains attached on the N atoms (b) and pair distribution functions g(r) (c) obtained from molecular dynamics experiments of the CTTTTC (black), TTTTTC (red) and CTCTTC (green) DiD conformers in a poly(styrene) box consisting of 2 chains with 100 monomers.

These results confirm the following: (i) In the case of the planar molecule with the alkyl chains on the same side of the molecule, the steric interactions between the two chains lead to highly mobile side chains, which hinder the polymer chains from coming close to the molecule and results in an increased local free volume. (ii) In case the alkyl chains are situated on opposite sides of the molecule, their interaction with the polymer chains is favored, which leads to a reduced mobility of the system and thus a lower free volume.

Conclusions

Two subpopulations (bimodal distributions of the fluorescence lifetimes and spectral widths) of the DiD molecule are found (Figure 3) to coexist in a poly(styrene) matrix. The two different species are easily identified from the correlation observed between their fluorescence lifetimes and spectral widths (Figure 3c). As is, the first population is characterized by a fluorescence lifetime around $\tau_f = 1.8$ ns and a spectral width around $W = 700$ cm^{-1}. The second population has a slightly longer lifetime around $\tau_f = 2.6$ ns and a significantly broader spectrum, with a spectral width around $W = 1100$ cm^{-1}. Quantum-chemical calculations have allowed assigning these two subpopulations to two different classes of conformers of the DiD molecule. In brief, within the seven most stable conformers found (Table 1), two of them, the almost all-trans planar molecules (TTTTTC, CTTTTC), are found to have both calculated fluorescence lifetimes (Figure 5a) and spectral widths (Figure 5b, Table 2) compatible with the observed first subpopulation. These are referred to as the planar molecules. The second subpopulation, with a longer lifetime and increased spectral width, is assigned to the other nonplanar molecules (Figure 4), of which the most abundant is the CTCTTC conformer (Table 2, Figure 5).

After having unambiguously established the existence of and assigned the two observed subpopulations of DiD molecules in the PS matrix to planar and nonplanar conformers, the local behavior of the polymer directly surrounding the probe molecule has been investigated. A polymer medium is a highly disordered medium. Chains in the matrix are coiled and entangled so that cooperative motion along the chain is not easy. Only local motions of chain segments are allowed. But these motions require a certain amount of space or holes in the system, which is equivalent to free volume. Free volume is always present due to the poor packing of the chains in the system. As shown recently in the literature, temporal fluctuations of the fluorescence lifetime of a DiD molecule embedded in a poly(styrene) matrix (Figure 2a) can be attributed to the motion of chain segments and thus holes around the probe molecule.[9,20,25] Free volume is modeled hereby putting voids, i.e., sites of zero-polarizability, in the lattice representing the medium (section 3.4). Monte Carlo simulations of the lifetime fluctuations arising from changes in local field factors (as obtained by applying classical electrodynamics theory on the basis of a quantum-chemical input for the characteristics of the probe and the styrene units) have been performed (Figures 6 and 7) for representative conformers and various fractions of holes. Comparing the experimental normalized radiative lifetime distributions (Figure 2a) to the simulated ones then allows an estimate of the fraction of holes surrounding each single DiD molecule. For conformers with the alkyl chains situated on opposite sides (trans-conformers) with respect to the conjugated backbone, a fraction $h = 5\%$ of voids locally surrounding the molecules has been found while this fraction is raised to $h = 8\%$ in the case of the planar conformer with alkyl chains on the same side with respect to the conjugated backbone. Molecular dynamics simulations clearly suggest that the increased fraction of holes surrounding the DiD conformer in the latter case is due to the steric hindrance between the two chains on the nitrogen atoms, which leads to a decreased packing density, an increased local free volume resulting in a higher mobility of the alkyl side chains. On the contrary, for the trans-conformers, the alkyl chains interact more strongly with the surrounding polymer chains, thus lowering mobility and local free volume.

Single molecule spectroscopy proves to be a method of choice to investigate the various conformations of a dye molecule and their interactions with the surrounding polymer matrix.

Acknowledgment. R.A.L.V. thanks the FWO for a postdoctoral fellowship. D.B. is a research associate from FNRS. The

KULeuven Research Fund, the Federal Science Policy through the IAP/V/03, the Flemish Ministry of Education through GOA/1/2001, the European programs LAMINATE and NAIMO, the FNRS (FRFC 9.4532.04), and the FWO are gratefully acknowledged for supporting this research.

JA051016Y

Chemical Physics Letters 472 (2009) 48–54

Contents lists available at ScienceDirect

Chemical Physics Letters

journal homepage: www.elsevier.com/locate/cplett

Investigation of probe molecule–polymer interactions

E. Braeken [a], P. Marsal [b], A. Vandendriessche [a], M. Smet [a], W. Dehaen [a], R.A.L. Vallée [c,*], D. Beljonne [b], M. Van der Auweraer [a]

[a] Department of Chemistry and Institute of Nanoscale Physics and Chemistry, Katholieke Universiteit Leuven, Celestijnenlaan 200F, B-3001 Heverlee, Belgium
[b] Laboratory for Chemistry of Novel Materials, University of Mons-Hainaut, Place du Parc 20, B-7000 Mons, Belgium
[c] Centre de Recherche Paul Pascal (CNRS), 115 Avenue du docteur Albert Schweitzer, F-33600 Pessac, France

ARTICLE INFO

Article history:
Received 8 January 2009
In final form 27 February 2009
Available online 5 March 2009

ABSTRACT

We probe the single molecule–polymer interactions for two types of carbocyanine dyes having the same conjugated core but different side chains. Several conformers of the conjugated core were observed and could be assigned owing to quantum chemistry and molecular dynamics simulations. The relative population of the various conformers is different for the two types of probe molecules in (non) annealed films. The presented results and discussion, of high interest from a fundamental point of view, might also be of primordial importance for the understanding of the plasticizing effect in polymers on a very local scale.

© 2009 Elsevier B.V. All rights reserved.

1. Introduction

Most single molecule fluorescence spectroscopy experiments have been performed with the probe molecules embedded in polymer films in order to immobilize them and investigate opto-electronic properties, like the efficiency of resonance energy transfer or electron transfer between different chromophoric parts of the overall system [1–3]. Nowadays, the fluorophores are more and more used to investigate the polymer properties, especially around the glass transition temperature. In order to measure the rotational dynamics of molecules and the related polymer mobility, polarization measurements [4–6] have been performed. Schob et al. [4] and Deschenes et al. [5] found evidence for static and dynamic heterogeneity in the supercooled regime. Zondervan et al. [6] investigated the rotational motion of perylene diimide in glycerol. The results of their experiments lead them to assume that glycerol consists of heterogeneous liquid pockets separated by a network of solid walls, an assumption that was further confirmed by conducting rheology measurements of glycerol at very weak stresses [7]. These polarization techniques typically allow for the detection of a two-dimensional projection of the real three-dimensional motion. The latter can be measured by using either an annular illumination technique [8], a defocused wide-field imaging technique [9–11] or by directly recording the emission pattern in the objective's back focal plane [12] or in the presence of aberrations [13]. Besides these techniques based on orientational dynamics, the fluorescence lifetime of a single dye molecule has been shown to be able to probe the dynamics of the probe surrounding polymer environment either in the glassy state [14–18] or in the supercooled regime [15,19]. Finally, the fluorescence lifetime observable has been used to probe the interaction of small probe molecules with polymer chains. Indeed, we recently investigated the interaction between the carbocyanine dye 1,1′-dioctadecyl-3,3,3′,3′-tetramethylindodicarbocyanine (DiD) and poly(styrene) (PS) polymer chains [18]. The main results of this investigation were the following: the measured fluorescence lifetimes and spectral widths of the DiD molecules were clearly dispersed in bimodal distributions. Quantum chemical calculations showed that the bimodal character could be attributed to two classes of conformations i.e. planar and non planar conformers. Two different planar conformers and only one type of non planar conformers were experimentally observed and clearly assigned owing to these quantum chemical calculations. The main difference between the two planar conformations was in the position of the alkyl chains with respect to the conjugated core: the alkyl chains lay on either the same side of the conjugated backbone (syn-conformer) or the opposite side (anti-conformer), the latter being true as well in the case of the non planar conformer. We compared the experimentally observed fluorescence lifetimes, widths of their distributions, obtained by recording them successively in time, and emission spectra of the probe molecules to dedicated molecular dynamics simulations. This allowed us to make statements about the local interaction of the probe and its local surrounding. For instance, in the case of the syn-conformer, steric hinder between the two alkyl chains (intramolecular interaction) lead to a decreased packing density and an increased local free volume while the alkyl chains of the anti-conformer could interact more strongly with the surrounding PS chains (inter solute–solvent interaction), thereby lowering the local free volume. This type of investigation is not only of interest for its fundamental nature, but is also useful in order to investigate

* Corresponding author.
E-mail addresses: vallee@crpp-bordeaux.cnrs.fr (R.A.L. Vallée), mark.vanderauweraer@chem.kuleuven.be (M. Van der Auweraer).

0009-2614/$ - see front matter © 2009 Elsevier B.V. All rights reserved.
doi:10.1016/j.cplett.2009.02.083

very locally the effect of the introduction of additives in a polymer matrix (plasticizing effect) on the polymer mobility and the corresponding variation of the glass transition temperature. In this Letter, in order to further investigate this kind of probe molecule – surrounding polymer matrix interaction, we make use of two different probe molecules which, while having the same conjugated core, present different side chains able to interact specifically with the surrounding poly(styrene) chains. Both molecules are carbocyanine dyes with a shorter conjugated backbone than the previously investigated DiD molecule. Due to this shortened backbone, the side chains substituted on the nitrogen atoms (Fig. 1a) are closer, which makes it easier for them to interact. Both molecules differ in the nature of the side chains grafted on the nitrogen atoms. One dye has alkyl chains (1,1′-didodecyl-3,3,3′,3′-tetramethylindo-carbocyanine perchlorate, DiIC12) while the other one has oligostyrene chains (DiIsty) substituted on the nitrogen atoms. These molecules are expected to interact differently with the surrounding PS chains, owing to the differences in rigidity, steric hinder and solvation of the side chains. The schematic structure of the dye molecules is visualized in Fig. 1a. Both types of probe molecules were investigated by fluorescence spectroscopy at the bulk and single molecule level. On the single molecule level, both non annealed and annealed samples were measured. In the non annealed case, the memory of the solvent is retained, which gives rise to results significantly different to those obtained if a chance is given to the chains to relax, i.e. after annealing. For both dyes, i.e. DiIC12 and DiIsty, bimodal distributions of fluorescence lifetimes are obtained both for the non annealed and the annealed samples. In the latter case, the distributions for both dyes are very similar, while they exhibit different characteristics in the non annealed case. Based on quantum chemical calculations, these distributions could be assigned to different conformers of DiIC12 and DiIsty.

2. Materials and methods

2.1. Experimental section

Steady state absorption and emission spectra of DiIsty and DiIC12 in toluene were recorded for concentrations of ca. 10^{-6} M. The absorption measurements were carried out on a Perkin Elmer Lambda 40 UV/Vis spectrophotometer. Corrected emission spectra were recorded on a SPEX fluorolog. For the single molecule measurements, a PS ($M_w = 250000$) solution of 10 mg/ml in toluene was used to make solutions of nanomolar (10^{-9} M) concentrations of DiIC12 and DiIsty in PS. The samples were prepared by spincoating the solutions at a rate of 1000 rpm on glass substrates. The non annealed samples were measured immediately after spincoating. To anneal the samples, they were put in the oven at a temperature of 373 K (T_g of the PS used). After five minutes the oven was switched off and let closed in order to allow for a slow decrease of its temperature to room temperature. The single molecule measurements were performed with a confocal microscope setup. The excitation wavelength was set to 543 nm and the laser power was set to 1 μW at the entrance of the microscope. The excitation at 543 nm (8 MHz, 1.2 ps FWHM) was obtained from the frequency-doubled output of an optical parametric oscillator (GWU)

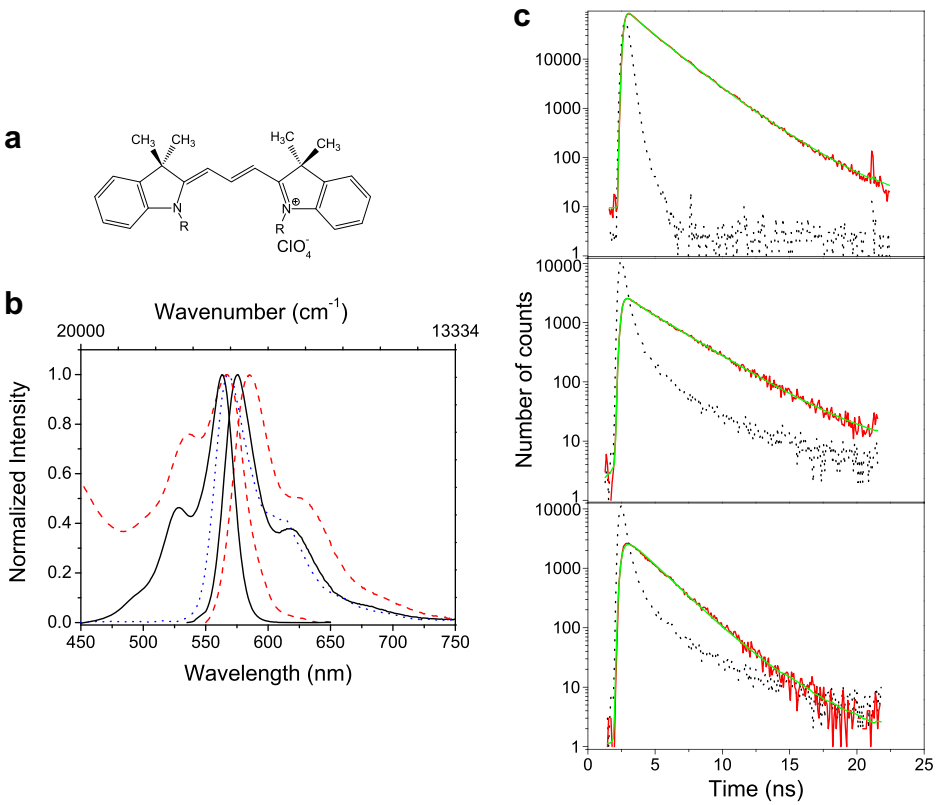

Fig. 1. (a) Schematic structure of the indocarbocyanine dye molecules with R = $C_{12}H_{25}$ for DiIC12 and R = $[CH_2CHC_6H_5]_{23}$ for DiIsty. (b) Normalized absorption and emission spectra of DiIC12 (black solid line) and DiIsty (red dashed line) in toluene. For the sake of comparison, the blue dotted line corresponds to the emission spectrum of a film obtained by spincoating a bulk solution of DiIC12 in PS/toluene onto a glass substrate and further annealed. (c) Fluorescence decay profiles for a diffraction limited volume of a film spincoated from the bulk solution of DiIC12 in PS/toluene (top, this decay profile exhibits two fluorescence decay times: $\tau = 1.8$ ns and $\tau = 2.8$ ns), a single molecule with a long fluorescence lifetime (middle, single exponential decay with $\tau = 2.8$ ns) and a single molecule with a short fluorescence lifetime (bottom, single exponential decay with $\tau = 1.8$ ns). The dotted lines are the instrumental response functions. (For interpretation of the references to color in this figure legend, the reader is referred to the web version of this article.)

pumped by a Ti:sapphire laser (Tsunami, Spectra Physics). The emission light was equally split into two parts. The fluorescence lifetime was measured with an avalanche photodiode (SPCM-AQ-15, EG & G Electro Optics) equipped with a time correlated single photon counting card (TCSPC card, Becker & Hickl GmbH, SPC 630) used in FIFO mode. The bin times that were used to build the decay profiles for the molecules were set to 100 ms in order to have at least 500 counts in the decay. This is the minimum number of counts that is needed to fit the decays using the maximum likelihood estimation method [20]. The emission spectra were recorded with a charge coupled device (CCD) camera with an integration time of 3 s. For DiIC12, the emission spectra and fluorescence decay times of a bulk sample, obtained by spin-coating a solution of DiIC12 (10^{-6} M) in PS/toluene onto a glass substrate were also measured, in a diffraction limited volume, with the same confocal setup used to perform the single molecule experiments, in order to compare these bulk spectra and lifetimes to the single molecule ones. In the latter case, the fluorescence decay profile was built by integrating all photons recorded by the TCSPC card. The integration time was set to 20 s.

2.2. Theoretical section

To calculate spectroscopic properties like the transition dipole moment and the transition energy of the experimentally measured probe molecules (DiIC12 and DiIsty), several quantum chemical approaches have been used. The geometry of the molecule was obtained by using the Hartree–Fock semi empirical Austin Model 1 (AM1) method [21]. Characterization of the lowest electronic singlet excited states has been performed by the semiempirical Hartree–Fock intermediate neglect of differential overlap (INDO) method as parametrized by Zerner et al. [22] This approximation was used in combination with a single configuration interaction (SCI) methodology. For all calculations, the CI active space has been built by promoting one electron from one of the highest sixty occupied to one of the lowest sixty unoccupied levels. Every molecular dynamics simulation has been performed at a constant number of particles, volume and standard temperature (NVT) ensemble. The simulations have been performed at a temperature of 300 K for 500 ps. The configuration of the system has been extracted every 1 ps. The energy was separated in several contributions. The total energy and van der Waals energy have been used in our discussion. These molecular dynamics simulations were performed with the material studio package by Accelrys Software Inc. We have used the universal force field (UFF) [23] in Forcite Studio and a standard cutoff has been kept at 12.5 Å. The radiative lifetime in vacuum has been calculated with the usual formula

$$\tau_0 = \frac{m_e \varepsilon_0 c_0^3}{2e^2 \pi \nu_0 f} \tag{1}$$

by further taking into account the renormalization of the photon in the medium: $\varepsilon_0 \to \varepsilon_r \varepsilon_0$ and $c_0 \to c_0/n$ and the slight change in the transition frequency. In this formula, e is the charge of the electron, ε_0 and c_0 are the permittivity and the speed of light in a vacuum, and ν_0 and f are the transition frequency and the oscillator strength of the probe molecule in a vacuum, respectively. Finally, the polarizabilities were determined by a sum over states (SOS) method encompassing all states involved in the CI space just mentioned.

3. Results and discussion

Fig. 1b shows the normalized absorption and emission spectra of both types of probe molecules in a toluene solution, as measured on the spectrofluorometer. The black curves correspond to the spectra of DiIC12 and the red curves to the spectra of DiIsty. The fluorescence spectrum of DiIsty is significantly broader, is slightly red shifted (10 nm) and has a more intense 0–1 vibronic peak compared to the one of DiIC12. The blue line represents the emission spectrum of DiIC12 in a PS bulk film, i.e. obtained by spin-coating a solution of DiIC12 (10^{-6} M) in PS/toluene (10 mg/ml) onto a glass substrate. It was measured by use of the confocal setup, used in the same conditions as the ones set to perform the single molecule experiments, for the sake of comparison both with the results of these experiments (see hereafter) and with those obtained in solution. The figure clearly exhibits spectra of identical shape but with a slight blue shift (around 5 nm) of the normalized emission spectrum of DiIC12 in a PS bulk film as compared to DiIC12 in a toluene solution. The fluorescence decay profile of the same diffraction limited volume of DiIC12 in the PS bulk film is shown in Fig. 1c (top). It is best fitted (as checked by careful examination of the χ^2 parameter, visual inspection of the residuals and autocorrelation of the latter) by a bi-exponential decay model with decay times $\tau_1 = 1.8$ ns and $\tau_2 = 2.8$ ns with amplitudes of 2.17 and 0.34, respectively. This corresponds to a contribution of 80% of $\tau_1 = 1.8$ ns and 20% of $\tau_2 = 2.8$ ns

Single molecule measurements were performed on thin films, spincoated from a 10^{-9} M solution of DiIsty/DiIC12 in PS/toluene. To localize the single molecules, an area of 10 μm by 10 μm was scanned. Taking into account the number of molecules found in this area and comparing with the expected number to be found for such a low dye concentration (10^{-9} M), we made sure to have the right concentration to measure single molecules. Furthermore, the diffraction limited spots observed on the scanning areas (not shown) confirm the observation of single molecules. Once localized, a fluorescence lifetime trajectory and a fluorescence spectrum were recorded for each individual molecule. Fig. 1c shows the decay profiles, obtained by integrating all photons recorded for two individual DiIC12 molecules (until they get irreversibly photo dissociated) in PS. Both decay curves could be best fitted by a single exponential model with $\tau = 2.8$ ns (middle) and $\tau = 1.8$ ns (bottom). For DiIsty in PS, the fluorescence spectra and lifetime trajectories, obtained by building and fitting with a single exponential model the successive decay profiles in bins of 100 ms, of two different molecules are shown in Fig. 2. One molecule has an average fluorescence lifetime $\tau = 2.6$ ns (Fig. 2a), while the other one has a shorter fluorescence lifetime $\tau = 1.7$ ns (Fig. 2c) as best represented by the mean of the distribution plotted on the right axes in Fig. 2(a, c). In the latter case ($\tau = 1.7$ ns), the corresponding fluorescence spectrum is characterized by an increased amplitude of the 0–1 vibronic peak (Fig. 2d) with respect to the first molecule (Fig. 2b).

For each investigated sample, consisting of either DiIC12 or DiIsty in either non annealed or annealed PS film, more than 150 individual molecules were measured. Every molecule with a low fluorescence lifetime was found to have an emission spectrum with an increased amplitude of the 0–1 vibronic peak, while the intensity of this peak is much lower for a molecule with a longer fluorescence lifetime. This correlation was found for all molecules of DiIsty or DiIC12 embedded in annealed or non annealed PS films and suggested the existence of at least two different species (conformers) for both DiIC12 and DiIsty. Fig. 3 shows a scatter plot of vibronic strength against lifetime together with the distributions of lifetime and vibronic strength for all measured molecules. The vibronic strength is measured here as the maximum intensity of the 0–1 vibronic peak, giving an idea of the coupling with the high frequency modes of the molecule. Clearly, the distribution shows two peaks, one around $\tau = 1.7$ ns with a strong vibronic coupling and one around $\tau = 2.7$ ns with a weak vibronic coupling. Also, the steady state emission spectra in solution (Fig. 1b) showed that the intensity of the 0–1 vibronic peak of DiIsty is larger than the one of DiIC12, already indicating that the common conjugated part of these two types of molecules might adopt a different conforma-

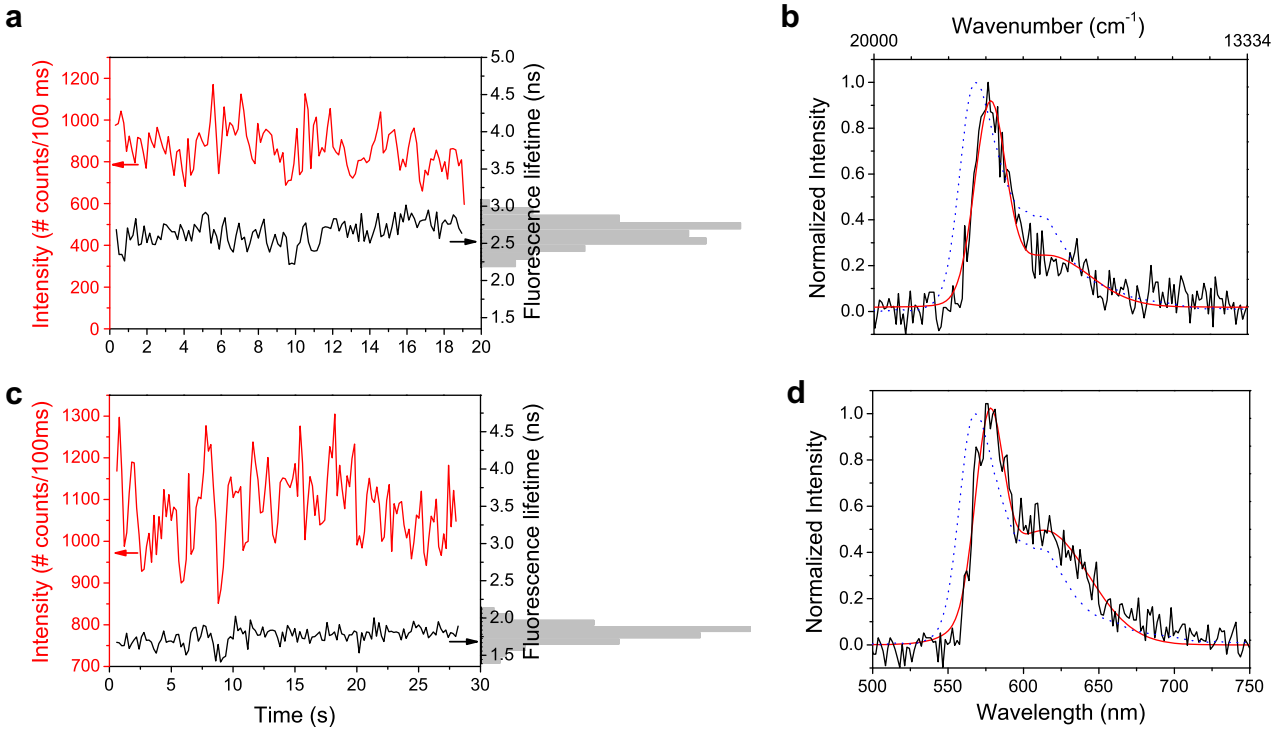

Fig. 2. Intensity and fluorescence lifetime trajectories (a, c) and corresponding fluorescence spectra (b, d) of a molecule with a long fluorescence lifetime (a, b, $\tau \approx 2.8$ ns) and a molecule with a short fluorescence lifetime (c, d, $\tau \approx 1.8$ ns). The blue dotted line in the fluorescence spectra shows the emission spectrum of a diffraction limited volume of the film obtained after spincoating a bulk solution of DiIC12 in PS/toluene on a glass substrate. (For interpretation of the references to color in this figure legend, the reader is referred to the web version of this article.)

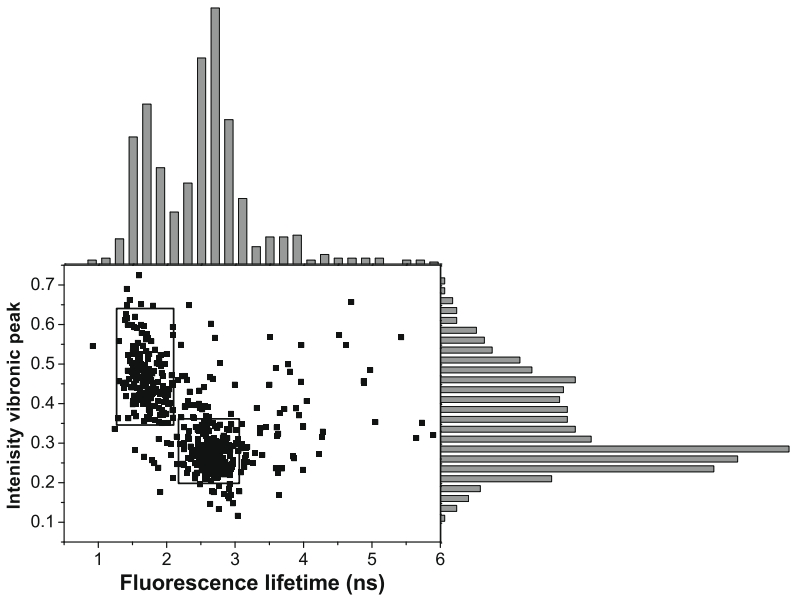

Fig. 3. Scatter plot of the intensity of the 0–1 vibronic peak against the fluorescence lifetime together with their respective distributions for all molecules measured in our investigations. Two clouds can be found, indicated by the surrounding rectangles: one around $\tau = 1.7$ ns with a strong vibronic coupling and one around $\tau = 2.7$ ns with a weak vibronic coupling, thus indicating the clear correlation between these two observables.

tion in solution. Furthermore, a closer look to the emission spectra shown in Fig. 2 (b and d, blue line) and to the decay profile shown in Fig. 1c (top) of DiIC12 in a bulk PS film compared to the emission spectra (Fig. 2b and d) and lifetimes (Fig. 1c middle, bottom) of both types of molecules taken individually clearly indicated that the measured diffraction limited volume of DiIC12 in a bulk PS film is constituted of the two populations just mentioned.

The distributions of the mean fluorescence lifetimes obtained from each individual trajectory are shown in Fig. 4. They all have a bimodal character with peaks centered around $\tau \approx 1.7$ ns and $\tau \approx 2.6$ ns. For DiIC12 non annealed (Fig. 4a) most molecules (80%) show an average lifetime of 2.6 ns, while only a minor fraction (20%) of the molecules exhibits a shorter mean lifetime of about 1.7 ns. For DiIsty in a non annealed sample (Fig. 4b), we

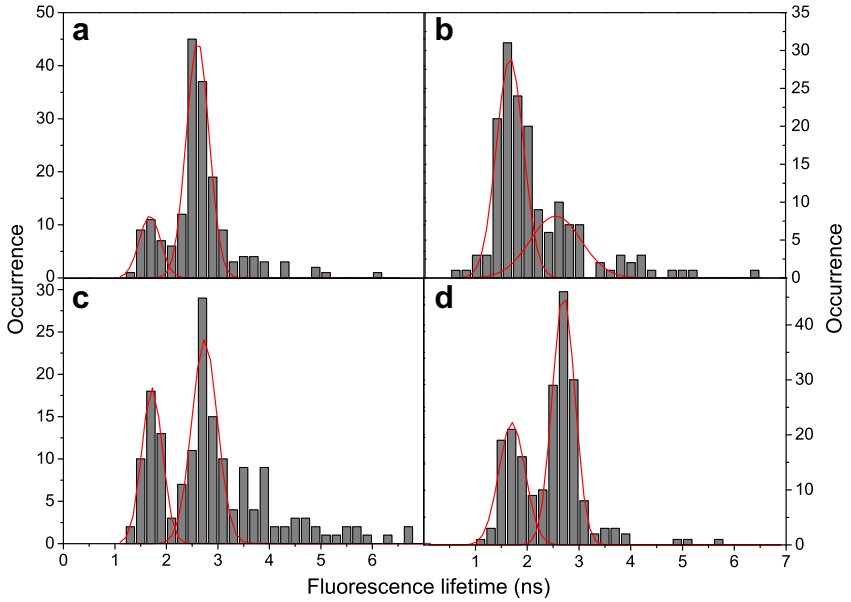

Fig. 4. Bimodal distribution of fluorescence lifetimes for DiIC12 not annealed (a) and annealed (c) and DiIsty not annealed (b) and annealed (d). All distributions are fitted with a double Gaussian which gives for (a): 20% (80%) of the molecules with an average fluorescence lifetime of 1.7 ns (2.6 ns), for (b): 65% (35%) of the molecules with an average fluorescence lifetime of 1.5 ns (2.5 ns), for (c): 38% (62%) of the molecules with an average fluorescence lifetime of 1.7 ns (2.7 ns), for (d) 36% (64%) of the molecules with an average fluorescence lifetime of 1.7 ns (2.7 ns). Only the molecules which show a clear correlation between their fluorescence lifetime and spectrum are taken into account in the Gaussian fits (molecules with a fluorescence lifetime $\tau > 3.5$ ns are not considered).

observe an opposite situation with only 35% of the molecules having a longer fluorescence lifetime. After annealing, allowing for a general relaxation of the matrix and release of the eventual stresses remaining from the spin-coating process, the same type of bimodal distribution is obtained, with a low proportion of molecules having a shorter fluorescence lifetime both for DiIC12 (38%, Fig. 4c) and DiIsty (36%, Fig. 4d).

In order to tentatively assign the origin of each couple of fluorescence lifetime, spectrum to a particular conformer of the common conjugated core, we performed theoretical calculations. DiI possesses four double bonds between the nitrogen atoms (Fig. 1a) of which the configuration can be *cis* (C) or *trans* (T). Due to steric constraint, only 3 of the $2^4 = 16$ possible conformers have been analyzed in our study, the ones that have the highest Boltzmann's occurrence to be observed. The three selected conformers (CTTC, TTTC and TTTT) can be described by the two dihedral angles ϕ_1 and ϕ_2 (see Fig. 5a). The conformers can be expressed by couples as $[\phi_1;\phi_2]$ which gives $[18^\circ;0^\circ]$ for CTTC (steric hinder does not allow a pure planar conjugated DiI core and the minimum angle obtained at AM1 level for all studied molecules is circa 18°), $[180^\circ;0^\circ]$ for TTTC and $[180^\circ;180^\circ]$ for TTTT (Fig. 5a). Instead of using the real systems DiIC12 and DiIsty, model compounds DiIC6 (hexyl alkyl chains instead of dodecyl chains) and DiIPh3 (oligomers of three styrene units instead of 23 units) have been used to keep a reasonable number of degrees of freedom.

Radiative lifetimes computed using the INDO/SCI semi empirical method for variable (18° steps) ϕ_1 and ϕ_2 angles are plotted in Fig. 5b. For both types of substituents (C6 or Ph3) the CTTC conformer exhibits the longest computed radiative lifetime. TTTC has an intermediate value and TTTT is characterized by the shortest radiative lifetime. This can be explained by the strength of the transition dipole moment which is highest for TTTT and weakest for CTTC. For each conformer, the geometry optimization has been performed at the AM1 level of theory. Each exact value of the four torsion angles between the nitrogen atoms has been frozen in order to calculate each energy minimum. On each partially frozen geometry, a molecular dynamics simulation is performed for 500 ps at 300 K in the NVT ensemble. After each ps of the runs, the van der Waals contribution to the total energy is extracted and stored. For both types of substituents the CTTC conformer is the most stable and its van der Waals contribution is the smallest (3 kcal/mol for DiIC6 and around 8 kcal/mol for DiIPh3), as shown in Table 1. Let us note here that, in a molecular modeling approach, the computed van der Waals energy is the sum of all repulsive (sterical hindrance at short distance, important in our case) and attractive components, at longer distance (the classic vdW chemical point of view).

For CTTC, the alkyl and phenyl substituents (the arms) are on the same side of the conjugated core, which means that intramolecular interactions between the arms can occur. The TTTT conformer also has the arms on the same side, but the distance in between them is too large to have a strong intramolecular interaction. For TTTC the arms are on different sides which avoids any interaction. The steric hinder in the conjugated core of CTTC can be seen as a catalyst for the strong intramolecular interaction which will stabilize the overall system.

By comparing the theoretical calculations to the experimental results, it is clear that for DiIsty in a non annealed film, the TTTC or TTTT conformer must be the most abundant since most molecules have a shorter lifetime. In contrast, for the three other samples (both annealed films and DiIC12 in a non annealed film) the most abundant conformer must be CTTC, which is the one with the longest fluorescence lifetime.

For the non annealed samples, the memory of the dye molecule conformation in the solvent is retained since the short (long) lifetime $\tau \approx 1.7$ ns ($\tau \approx 2.6$ ns) exhibited by most molecules of DiIsty (DiIC12) in the non annealed film (Fig. 4b, respectively Fig. 4a) correlates with the enhanced (reduced) 0–1 vibrational peak of their fluorescence spectra and match the results obtained for DiIsty (DiIC12) in a toluene solution (Fig. 1b). A decay profile of both types of dyes in solution will not be enlighting since the internal conversion processes allowed in such a mobile surrounding lead to a drastic reduction of the observed lifetime. For the conformers TTTC and TTTT the interaction between the arms is weak, which favors their respective interaction with the solvent. The interaction between the oligostyrene chains and toluene is stronger than be-

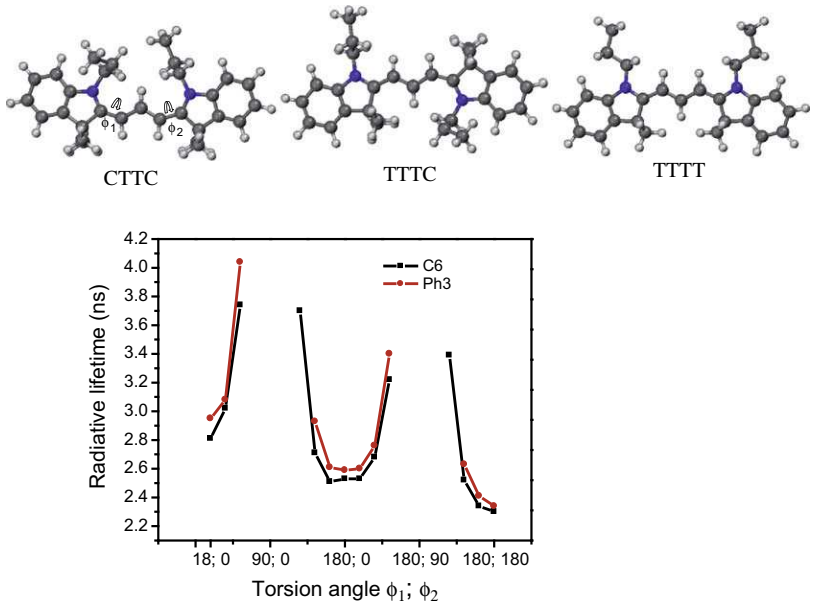

Fig. 5. (a) Schematics of three conformers of DiI having the highest Boltzmann's occurrence to be observed. The dihedral angles ϕ_1 and ϕ_2 taken into account in the discussion are depicted on the CTTC conformer. (b) Radiative lifetimes as a function of peculiar values of the pairs of angles $(\phi_1;\phi_2)$ for both types of molecules (C6 in black for DiIC12, and Ph3 in red for DiIsty). For both types, CTTC shows the longest radiative lifetime, TTTT the shortest one and TTTC has an intermediate value. (For interpretation of the references to color in this figure legend, the reader is referred to the web version of this article.)

Table 1
Calculated radiative lifetime and average van der Waals energy of the different conformers.

		Radiative lifetime (ns) AM1 geometries	Dye substituent contribution Average value (minimum; maximum) (kcal/mol) Molecular dynamic
C6			
	CTTC	2.8	26.6 (23.7; 28.8)
	TTTC	2.5	29.2 (24.1; 31.2)
	TTTT	2.3	30.0 (24.2; 31.8)
Ph3			
	CTTC	3.0	64.6 (58.1; 71.4)
	TTTC	2.6	74.0 (67.0; 81.0)
	TTTT	2.4	72.5 (64.2; 82.0)

tween the alkyl chains and toluene. Hence, for DiIsty molecules in a non annealed film, the TTTC and TTTT conformations will be favored, which explains the higher fraction of molecules having a short fluorescence lifetime $\tau \approx 1.7$ ns. The weaker interaction between the alkyl chains and toluene explains the opposite distribution for DiIC12. This corresponds to the steady state spectrum observed for DiIsty (DiIC12) in solution, where it mainly adopts the TTTC and TTTT (CTTC) conformations. After the samples have been annealed, the polymers have had time to relax and reorganize, the solvent memory is lost and the dye molecules will adopt the most stable CTTC conformation.

4. Conclusions

DiIC12 and DiIsty can adopt different conformations in a poly(styrene) matrix, in non annealed as well as in annealed samples. Experimentally, the evidence for the existence of at least two different conformers was found both in the bi-exponential model necessary to fit the decay profile at the bulk level and in the bimodal character of the fluorescence lifetime distributions found at the single molecule level. These distributions are different for both dyes in the non annealed samples and get similar after annealing. Owing to quantum chemical calculations, different conformations could be assigned to the observed values (mainly two) of the fluorescence lifetime. The two dyes, having a common conjugated core, but with different side chains grafted on the nitrogen atoms, adopt different conformations in the non annealed samples, due to the specific interactions of these side chains with the surrounding medium (competition between intra- and inter- molecular interactions). The strong interactions between oligostyrene and toluene favors the TTTT and TTTC conformers of DiIsty in solution and in the non annealed sample. The interactions between the alkyl chains and toluene are weaker, so that the CTTC conformer of DiIC12 is observed in solution and in the non annealed sample. After annealing, allowing for a complete relaxation of the polymer medium surrounding the dyes, CTTC, the most stable conformer, appears as the most abundant, and the same fluorescence lifetime distributions are obtained for both dye molecules. It is clear that the side chains can play a role in the interaction with the polymer. However, the nature of the side chains only matters for the non annealed samples, i.e. in a non equilibrium system. After annealing, when the matrix has relaxed, i.e. after having reached an equilibrium, the most stable conformer is mostly observed. As the type of conformer found in the matrix and its interaction with the surrounding chains governs the local packing of the matrix and thus its local free volume, the results and perspectives of such investigations might give some new insight to the plasticizing effect as a function of temperature change and ageing.

Acknowledgements

The authors are thankful to the FWO for financial support and a postdoctoral fellowship to R.V., to the research council of K.U. Leuven for funding in the framework of GOA 2006/2, and to Belgian Science policy for funding through IAP V/03 and VI/27/. The 'Instituut voor de aanmoediging van innovatie door Wetenschap en Technologie in Vlaanderen' (IWT) is acknowledged for Grant ZWAP 04/007 and for a fellowship to E.B. D.B. is a research director of the FNRS.

References

[1] X.S. Xie, J.K. Trautman, Annu. Rev. Phys. Chem. 49 (1998) 441.
[2] F. Cichos, C. von Borczyskowski, M. Orrit, Curr. Opin. Colloid Interface Sci. 12 (2007) 272.
[3] J.N. Clifford et al., J. Phys. Chem. B 111 (2007) 6987.
[4] A. Schob, F. Cichos, J. Schuster, C. von Borzyskowski, Eur. Pol. J. 40 (2004) 1019.
[5] L.A. Deschenes, D.A. Vanden Bout, J. Phys. Chem. B 106 (2002) 11438.
[6] R. Zondervan, F. Kulzer, G.C.G. Berkhout, M. Orrit, Proc. Natl. Acad. Sci. USA 104 (2007) 12628.
[7] R. Zondervan, T. Xia, H. van der Meer, C. Storm, F. Kulzer, W. van Saarloos, M. Orrit, Proc. Natl. Acad. Sci. USA 105 (2008) 4993.
[8] B. Sick, B. Hecht, L. Novotny, Phys. Rev. Lett. 85 (2000) 4482.
[9] A.P. Bartko, K. Xu, R.M. Dickson, Phys. Rev. Lett. 89 (2002) 026101.
[10] H. Uji-i et al., Polymer 47 (2006) 2511.
[11] M. Böhmer, J. Enderlein, J. Opt. Soc. Am. B 20 (2003) 554.
[12] M.A. Lieb, J.M. Zavislan, L.J. Novotny, J. Opt. Soc. Am. B 21 (2004) 1210.
[13] R.M. Dickson, D.J. Norris, W.E. Moerner, Phys. Rev. Lett. 81 (1998) 5322.
[14] R.A.L. Vallée, M. Van der Auweraer, F.C. De Schryver, D. Beljonne, M. Orrit, ChemPhysChem 6 (2005) 81.
[15] R.A.L. Vallée, M. Baruah, J. Hofkens, F.C. De Schryver, N. Boens, M. Van der Auweraer, D. Beljonne, J. Chem. Phys 126 (2007) 184902.
[16] R.A.L. Vallée, N. Tomczak, L. Kuipers, G.J. Vancso, N.F. van Hulst, Phys. Rev. Lett. 91 (2003) 038301.
[17] N. Tomczak, R.A.L. Vallée, E.M.H.P. van Dijk, M. García-Parajó, N. van Hulst, G.J. Vancso, Eur. Pol. J. 40 (2004) 1001.
[18] R.A.L. Vallée et al., J. Am. Chem. Soc. 127 (2005) 12011.
[19] R.A.L. Vallée, M. Van der Auweraer, W. Paul, K. Binder, Phys. Rev. Lett. 97 (2006) 217801.
[20] M. Maus, J. Hofkens, T. Gensch, F.C. De Schryver, J. Schaffer, C. Seidel, Anal. Chem. 73 (2001) 2078.
[21] M.J.S. Dewar, E.G. Zoebisch, E.F. Healy, J.J.P. Stewart, J. Am. Chem. Soc. 107 (1985) 3902.
[22] M.C. Zerner, G. Loew, R. Kichner, U.T. Mueller-Westerhoff, J. Am. Chem. Soc. 122 (2000) 3015.
[23] A.K. Rappe, C.J. Casewit, K.S. Colwell, W.A. Goddard III, W.M. Skiff, J. Am. Chem. Soc. 114 (1992) 10024.

J|A|C|S
ARTICLES

Published on Web 08/05/2009

Single Molecule Probing of the Local Segmental Relaxation Dynamics in Polymer above the Glass Transition Temperature

Els Braeken,[†] Gert De Cremer,[†] Philippe Marsal,[‡,§] Gérard Pèpe,[‡] Klaus Müllen,[||] and Renaud A. L. Vallée*[,⊥]

Department of Chemistry and Institute of Nanoscale Physics and Chemistry, Katholieke Universiteit Leuven, Celestijnenlaan 200F, B-3001 Heverlee, Belgium, Centre Interdisciplinaire de Nanoscience de Marseille (UPR 3118, CNRS), Campus de Luminy, Case 913, F-13288 Marseille cedex 09, France, Max-Planck-Institut für Polymerforschnung, Ackermannweg 10, D-55128 Mainz, Germany, and Centre de Recherche Paul Pascal (UPR 8641, CNRS), 115 avenue du docteur Albert Schweitzer, F-33600 Pessac, France

Received March 3, 2009; E-mail: vallee@crpp-bordeaux.cnrs.fr

Downloaded by UNIV DE BORDEAUX 1 on August 31, 2009 | http://pubs.acs.org
Publication Date (Web): August 5, 2009 | doi: 10.1021/ja901636v

Abstract: We investigate the temporal dynamics of terrylene diimide molecule with four phenoxy rings (TDI) in a poly(styrene) (PS) matrix in the supercooled regime by use of single molecule spectroscopy. By recording both fluorescence lifetime and linear dichroism observables simultaneously, we show that the TDI dye molecule is a versatile probe of the local dynamics in the polymer. The molecule is able to undergo conformational changes, as indicated by lifetime fluctuations and/or reorientation jumps, as indicated by both observables on different time scales. Owing to molecular mechanics and quantum calculations, we could assign the conformational changes to folding/unfolding event(s) of one or more arms with respect to the conjugated core. We tentatively attribute the different spatial extents of the locally probed motions to the α and β relaxation processes occurring in the PS matrix.

Introduction

Understanding the mechanisms responsible for the tremendous slowing down of the mobility when approaching the glass transition is one of the most important challenges in modern soft condensed matter physics, both for low molecular weight and polymeric materials.[1−5] Amorphous atactic polystyrene (PS) is one of the most widely used industrial plastics and a classical example of a mechanically brittle polymer. As such, it is perfectly suited for investigating the connection between the local chemical and physical microstructure and the macroscopic mechanical behavior. Rotational motions of both backbone segments and side groups are the principal relaxation mechanisms in amorphous polymers. Such relaxation processes have been studied experimentally in amorphous PS in the vicinity of the glass-transition temperature T_g by viscosity,[6] compliance,[6] quasielastic neutron scattering,[7] NMR,[8−10] photon correlation spectroscopy,[11,12] dielectric relaxation,[13−15] photobleaching,[16] and second harmonic generation techniques.[17,18] It has been established that above the PS glass-transition temperature (T_g = 373 K), the α-relaxation is the primary relaxation process for the collective motion of polymer segments. At lower temperature, the so-called β process appears.[4] Different opinions about the nature of the β-relaxation exist. Usually this process is attributed to the rotational vibration of backbone segments, but some authors have assigned the β process to the rotations of side phenyl groups. Our aim in this paper is to investigate the differences in local segmental dynamics in a polystyrene melt slightly above the glass transition temperature. In order to perform this task, we use a very versatile method based on the single molecule spectroscopy (SMS) of a dedicated probe.

Because it allows bypassing the ensemble averaging intrinsic to bulk studies, SMS constitutes a powerful tool to assess the dynamics of heterogeneous materials at the nanoscale level.[19−22]

[†] Katholieke Universiteit Leuven.
[‡] Centre Interdisciplinaire de Nanoscience de Marseille.
[§] Present address: Laboratory for Chemistry of Novel Materials, University of Mons-Hainaut, Place du Parc 20, B-7000 Mons, Belgium.
[||] Max-Planck-Institut für Polymerforschnung.
[⊥] Centre de Recherche Paul Pascal.

(1) Jäckle, J. *Rep. Prog. Phys.* **1986**, *49*, 171.
(2) Götze, W.; Sjögren, L. *Rep. Prog. Phys.* **1992**, *55*, 241.
(3) See Debenedetti, P. G. In *Metastable Liquids*; Princeton Univ. Press: Princeton, 1997.
(4) See Donth, E.-W. In *The Glass Transition. Relaxation Dynamics in Liquids and Disordered Materials*; Springer: Berlin, 2001.
(5) See Binder, K.; Kob, W. In *Glassy Materials and Disordered Solids. An Introduction to Their Statistical Mechanics*; World Scientific: Singapore, 2005.
(6) Plazek, D. J. *J. Phys. Chem.* **1965**, *69*, 3480.
(7) Kanaya, T.; Kawaguchi, T.; Kaji, K. *J. Chem. Phys.* **1996**, *104*, 3841.
(8) Pschorn, U.; Rossler, E.; Kaufmann, S.; Sillescu, H.; Spiess, H. W. *Macromolecules* **1991**, *24*, 398.
(9) Kuebler, S. C.; Heuer, A.; Spiess, H. W. *Phys. Rev. E* **1997**, *56*, 741.
(10) He, Y.; Lutz, T. R.; Ediger, M. D.; Ayyagari, C.; Bedrov, D.; Smith, G. D. *Macromolecules* **2004**, *37*, 5032.
(11) Lee, H.; Jamieson, A. M.; Simha, R. *Macromolecules* **1979**, *12*, 329.
(12) Patterson, G. D.; Lindsey, C. P. *J. Chem. Phys.* **1979**, *70*, 643.
(13) Saito, S.; Nakajima, T. *J. Appl. Polym. Sci.* **1959**, *4*, 93.
(14) Fukao, K.; Miyamoto, Y. *J. Non-Cryst. Solids* **1994**, *172−174*, 365.
(15) León, C.; Ngai, K. L.; Roland, C. M. *J. Chem. Phys.* **1999**, *110*, 11585.
(16) Inoue, T.; Cicerone, M. T.; Ediger, M. D. *Macromolecules* **1995**, *28*, 3425.
(17) Dhinojwala, A.; Wong, G. K.; Torkelson, J. M. *J. Chem. Phys.* **1994**, *100*, 6046.
(18) Hall, D. B.; Deppe, D. D.; Hamilton, K. E.; Dhinojwala, A.; Torkelson, J. M. *J. Non-Cryst. Solids* **1998**, *235−237*, 48.
(19) Moerner, W. E.; Orrit, M. *Science* **1999**, *283*, 1670.

 © 2009 American Chemical Society

By using two-dimensional (2D) orientation techniques, the in-plane (of the sample) projection of the transition dipole moment of the single molecule (SM) [the so-called linear dichroism $d(t)$] has been followed in time and its time correlation function $C_d(t)$ has been computed and fitted by a stretched exponential function $f(t) = \exp[-(t/\tau)^{\beta}]$.[23−26] These investigations have allowed identifying static and dynamic heterogeneity in the samples;[27,28] i.e., SMs exhibit τ and β values varying according to (i) their actual position in the matrix and (ii) the time scale at which they are probed, as a result of the presence of different nanoscale environments. Zondervan et al.[29] investigated the rotational motion of perylene diimide in glycerol. Observations of environmental exchanges were very scarce. They assumed that glycerol consists of heterogeneous liquid pockets separated by a network of solid walls. This was confirmed by conducting rheology measurements at very weak stresses of glycerol and *o*-terphenyl.[30] With 3D orientation techniques, the emission transition dipole moment of a SM has been recorded as a function of time.[31−34] In particular, the distribution of nanoscale barriers to rotational motion has been assessed by means of SM measurements[35] and related to the spatial heterogeneity and nanoscopic α-relaxation dynamics deep within the glassy state. Owing to the high barriers found in the deep glassy state, only few SMs were able to reorient, while somewhat lower barriers could be overcome when increasing the temperature.

Following the temporal evolution of the fluorescence lifetime of single molecules with quantum yield close to unity, we have shown that this observable is highly sensitive to changes in local density occurring in a polymer matrix.[36−41] Using free volume theories, we have related the lifetime fluctuations to hole (free-volume) distributions and determined the number of polymer segments involved in a rearrangement cell around the probe molecule as a function of temperature,[36,39] solvent content,[37] and film thickness.[38] On the basis of a microscopic model for the fluctuations of the local field,[40] we have established a clear correlation between the fluorescence lifetime distributions measured for single molecules and the local fraction of surrounding holes both in the glassy state and in the supercooled regime for various molecular weight oligo(styrene).[41] Furthermore, fluorescence lifetime trajectories of single probe molecules embedded in a glass-forming PS melt exhibit strong fluctuations of a hopping character. Using MD simulations targeted to explain these fluctuations,[42] we have shown that the lifetime fluctuations correlate strongly with the meta-basin transitions in the potential energy landscape of the matrix particles, thus providing a new tool for the experimental study of long-standing issues in the physics of the glass transition. Finally, the interaction between the probe molecule and the polymer matrix can also be investigated. The interaction between carbocyanine dyes and poly(styrene) (PS) polymer chains has been investigated.[43,44] We have shown that the existence of different conformations of such dyes, stabilized owing to favorable interactions with the surrounding polymer matrix, lead to specific spectroscopic responses, i.e., specific fluorescence lifetimes and emission spectra. We found that the type of conformer found in the matrix and its interaction with the surrounding chains governed the local packing of the matrix and thus allows one to probe the local free volume.

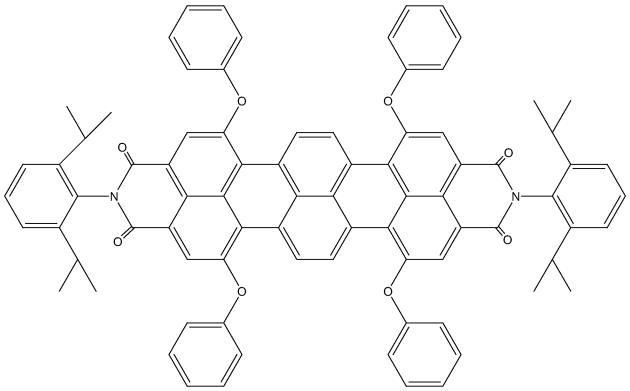

Figure 1. Schematic structure of the terrylene diimide with four phenoxy rings (TDI) dye molecule.

In this paper, we use both 2D orientation techniques and fluorescence lifetime measurements to investigate the mobility of tetraphenoxyterrylene diimide (TDI) molecules (Figure 1) in a low molecular weight ($M_w = 1000$ g mol^{-1}, $T_g \approx 10$ °C) PS matrix. The measurements are performed at room temperature ($T = 19$ °C), thus slightly in the supercooled regime. This allows the dye to reorient substantially during the measurement time. By simultaneously measuring the fluorescence lifetime and linear dichroism trajectories, we can correlate the fluctuations exhibited by both observables. In particular, we can assign jumps occurring simultaneously in both trajectories to reorientational

Downloaded by UNIV DE BORDEAUX 1 on August 31, 2009 | http://pubs.acs.org
Publication Date (Web): August 5, 2009 | doi: 10.1021/ja901636v

(20) Xie, X. S.; Trautman, J. K. *Annu. Rev. Phys. Chem.* **1998**, *49*, 441.
(21) Kulzer, F.; Orrit, M. *Annu. Rev. Phys. Chem.* **2004**, *55*, 585.
(22) Vallée, R. A. L.; Cotlet, M.; Hofkens, J.; De Schryver, F. C.; Müllen, K. *Macromolecules* **2003**, *36*, 7752.
(23) Deschenes, L. A.; Vanden Bout, D. A. *J. Phys. Chem. B* **2002**, *106*, 11438.
(24) Tomczak, N.; Vallée, R. A. L.; van Dijk, E. M. H. P.; García-Parajó, M.; Kuipers, L.; van Hulst, N. F.; Vancso, G. J. *Eur. Polym. J.* **2004**, *40*, 1001.
(25) Schob, A.; Cichos, F.; Schuster, J.; von Borczyskowski, C. *Eur. Polym. J.* **2004**, *40*, 1019.
(26) Mei, E.; Tang, J.; Vanderkooi, J. M.; Hochstrasser, R. M. *J. Am. Chem. Soc.* **2003**, *125*, 2730.
(27) Ediger, M. D. *Annu. Rev. Phys. Chem.* **2000**, *51*, 99.
(28) Richert, R. *J. Phys.: Condens. Matter* **2002**, *4*, R703.
(29) Zondervan, R.; Kulzer, F.; Berkhout, G. C. G.; Orrit, M. *Proc. Natl. Acad. Sci. U.S.A.* **2007**, *104*, 12628.
(30) Zondervan, R.; Xia, T.; van der Meer, H.; Storm, C.; Kulzer, F.; van Saarloos, W.; Orrit, M. *Proc. Natl. Acad. Sci. U.S.A.* **2008**, *105*, 4993.
(31) Dickson, R. M.; Norris, D. J.; Moerner, W. E. *Phys. Rev. Lett.* **1998**, *81*, 5322.
(32) Sick, B.; Hecht, B.; Novotny, L. *Phys. Rev. Lett.* **2000**, *85*, 4482.
(33) Lieb, A.; Zavislan, J. M.; Novotny, L. *J. Opt. Soc. Am. B* **2004**, *21*, 1210.
(34) Böhmer, M.; Enderlein, J. *J. Opt. Soc. Am. B* **2000**, *20*, 554.
(35) Bartko, A. P.; Xu, K.; Dickson, R. M. *Phys. Rev. Lett.* **2002**, *89*, 026101.
(36) Vallée, R. A. L.; Tomczak, N.; Kuipers, L.; Vancso, G. J.; van Hulst, N. F. *Phys. Rev. Lett.* **2003**, *91*, 038301.
(37) Vallée, R. A. L.; Tomczak, N.; Kuipers, L.; Vancso, G. J.; van Hulst, N. F. *Chem. Phys. Lett.* **2004**, *384*, 5.
(38) Tomczak, N.; Vallée, R. A. L.; van Dijk, E. M. H. P.; Kuipers, L.; van Hulst, N. F.; Vancso, G. J. *J. Am. Chem. Soc.* **2004**, *126*, 4748.
(39) Vallée, R. A. L.; Tomczak, N.; Vancso, G. J.; Kuipers, L.; van Hulst, N. F. *J. Chem. Phys.* **2005**, *122*, 114704.
(40) Vallée, R. A. L.; Van der Auweraer, M.; De Schryver, F. C.; Beljonne, D.; Orrit, M. *ChemPhysChem* **2005**, *6*, 81.
(41) Vallée, R. A. L.; Baruah, M.; Hofkens, J.; De Schryver, F. C.; Boens, N.; Van der Auweraer, M.; Beljonne, D. *J. Chem. Phys.* **2007**, *126*, 184902.
(42) Vallée, R. A. L.; Van der Auweraer, M.; Paul, W.; Binder, K. *Phys. Rev. Lett.* **2006**, *97*, 217801.
(43) Vallée, R. A. L.; Marsal, P.; Braeken, E.; Habuchi, S.; De Schryver, F. C.; Van der Auweraer, M.; Beljonne, D.; Hofkens, J. *J. Am. Chem. Soc.* **2005**, *127*, 12011.
(44) Braeken, E.; Marsal, P.; Vandendriessche, A.; Smet, M.; Dehaen, W.; Vallée, R. A. L.; Beljonne, D.; Van der Auweraer, M. *Chem. Phys. Lett.* **2009**, *472*, 48.

Downloaded by UNIV DE BORDEAUX 1 on August 31, 2009 | http://pubs.acs.org
Publication Date (Web): August 5, 2009 | doi: 10.1021/ja901636v

jumps of the dye molecules. On the contrary, jumps only occurring in the fluorescence lifetime trajectories can be assigned to conformational changes of the TDI molecule, related to the folding of one or more phenoxy arms on the conjugated core. These findings are confirmed by molecular mechanics and quantum chemical calculations dedicated to the determination of the possibly allowed conformations of the dye molecule and their expected spectroscopic properties. The use of such a versatile dye, able to either reorient or change conformation in the PS melt, combined with the simultaneous measurement of fluorescence lifetime and linear dichroism observables, shed light in a unique way on the differences in local segmental dynamics possibly related to the α- and β-relaxation mechanisms.

Experimental Methods

Steady state absorption and emission spectra of TDI in toluene were recorded for concentrations of ca. 10^{-6} M. The absorption measurements were carried out on a Perkin-Elmer Lambda 40 UV/vis spectrophotometer. Corrected emission spectra were recorded on a SPEX fluorolog.

A PS (M_w = 1000 g mol^{-1}, T_g = 10 °C, Polymer Source Inc.) solution of 10 mg/mL in toluene (Sigma Aldrich, spectrophotometric grade) was used to make solutions of nanomolar (10^{-9} M) concentrations of TDI (Figure 1) in PS. Besides this hydrophobic solution, a hydrophilic 10 mg/mL solution of poly(vinyl alcohol) (PVA, M_w = 130 000, Clariant) in water was also prepared. The samples were prepared by spin-coating, at a rate of 1000 rpm, a layer of TDI in PS in between two layers of PVA, situated on the bottom and on top of the PS layer, respectively. This procedure ensured that the TDI dye molecules embedded in the PS layer will not be exposed to either the polymer−glass or the air−glass interfaces, thus avoiding possible electromagnetic boundary effects to interfere on the subsequent measurement of fluorescence lifetimes. Indeed, it has been shown that the fluorescence lifetime of a dye molecule can increase significantly when it is situated close to the polymer−air interface, especially if the transition dipole of the molecule is perpendicular to the interface.[45−47]

The measurements were performed with an inverted confocal fluorescence microscope (Olympus IX 70), with a 100× oil immersion objective (Olympus, NA = 1.3). As an excitation source, a Picoquant pulsed diode laser producing 90 ps pulses of 644 nm, with a repetition rate of 10 MHz was used. This wavelength was well-suited to excite the dye molecule close to its absorption maximum (Figure 2) and the excitation power was set to 1 μW at the entrance of the microscope. The emission signal was separated from the excitation light, circularly polarized by a dichroic filter (DC-Q-600-LP, Chroma) and a long pass filter (HQ600LP, Chroma) in order to get the maximum integrated signal of the emission spectrum (Figure 2), and split into parallel ($I_{\parallel}$) and orthogonal ($I_{\perp}$) components owing to a 50/50% beam splitter. The emission signal was collected by two avalanche photodiodes (SPCM-AQ-15, EG & G Electro Optics) equipped with a time-correlated single photon counting card (TCSPC card, Becker & Hickl GmbH, SPC 630) used in FIFO mode in order to subsequently determine fluorescence lifetimes. The sample was scanned with a piezo-controlled scanning stage (Physics Instruments), and the instrumental response function of the system is ≈500 ps. The bin times used to build the decay profiles for the molecules were set to 100 ms in order to have at least 500 counts in the decay. This is the minimum number of counts that is needed to fit the decays using the maximum likelihood

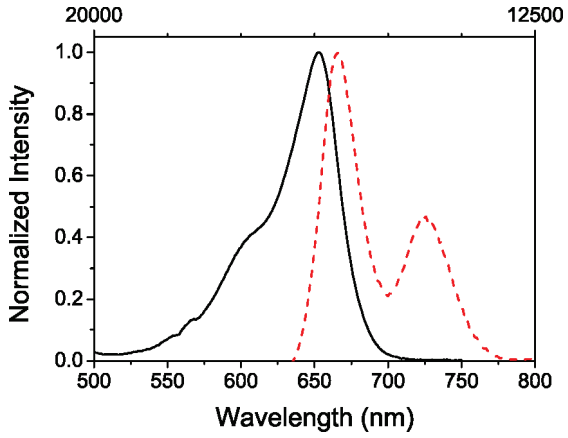

Figure 2. Steady-state absorption and emission spectra of TDI in a toluene solution.

estimation method.[48] The linear dichroism was measured according to the usual formula:

$$d(t) = \frac{I_{\parallel} - GI_{\perp}}{I_{\parallel} + GI_{\perp}} \quad (1)$$

in which G is a correction factor accounting for the difference in sensitivity between the two detectors. The correction factor is determined by using a homogeneous fluorescent sample (a sample with high concentration of dye molecules) and dividing $I_{\parallel}$ by $I_{\perp}$.

The measurements were performed at room temperature, which is above the glass transition temperature of the PS used.

Theoretical Methods

Geometries and conformations of TDI are issued from GenMol calculations. GenMol is a software based upon molecular mechanics[49] except for the atomic charge calculations that are issued from semiempirical approximations.[51,52] A genetic algorithm is used to find the preferred conformations of the molecule. A molecule conformation is described by N torsion angles, with values α_i. A preferred conformation (corresponding to a minimum of the strain energy) of a molecule is thus characterized by a unique set of α_i values. For bonds not belonging to rings, complete rotations are allowed around σ bonds. Only partial rotations around σ bonds with a π character conformation are permitted, in order to stay close to the planarity. Each torsion angle value is considered as one gene. The algorithm used to find the preferred conformations of a molecule is described elsewhere.[52]

The characterization of the lowest electronic singlet excited states has been performed by the semiempirical Hartree−Fock intermediate neglect of differential overlap (INDO) method as parametrized by Zerner et al.[53] This approximation was used in combination with a single configuration interaction (SCI) methodology. For all calculations, the CI active space has been

(45) Vallée, R.; Tomczak, N.; Gersen, H.; van Dijk, E. M. H. P.; García-Parajó, M. F.; Vancso, G. J.; van Hulst, N. F. *Chem. Phys. Lett.* **2001**, *348*, 161.
(46) Schroeyers, W.; Vallée, R.; Patra, D.; Hofkens, J.; Habuchi, S.; Vosch, T.; Cotlet, M.; Müllen, K.; Enderlein, J.; De Schryver, F. C. *J. Am. Chem. Soc.* **2004**, *126*, 14310.
(47) Enderlein, J. *Chem. Phys.* **1999**, *247*, 1.
(48) Maus, M.; Hofkens, J.; Gensch, T.; De Schryver, F. C.; Schaffer, J.; Seidel, C. *Anal. Chem.* **2001**, *73*, 2078.
(49) See Pèpe, G.; Siri, D. In *Modeling of Molecular Structures and Properties Studies in Physical and Theoretical Chemistry*; Rivail, J. L., Eds.; Elsevier B. V.: Amsterdam, 1990.
(50) Pèpe, G.; Perbost, R.; Courcanbeck, J.; Jouanna, P. *J. Cryst. Growth* **2009**, *311*, 3498.
(51) Del Re, G. *J. Chem. Soc.* **1958**, *40*, 4031.
(52) Pèpe, G.; Serres, B.; Laporte, D.; Del Re, G.; Minichino, C. *J. Theor. Biol.* **1985**, *115*, 571.
(53) Zerner, M. C.; Loew, G.; Kichner, R.; Mueller-Westerhoff, U. T. *J. Am. Chem. Soc.* **2000**, *122*, 3015.

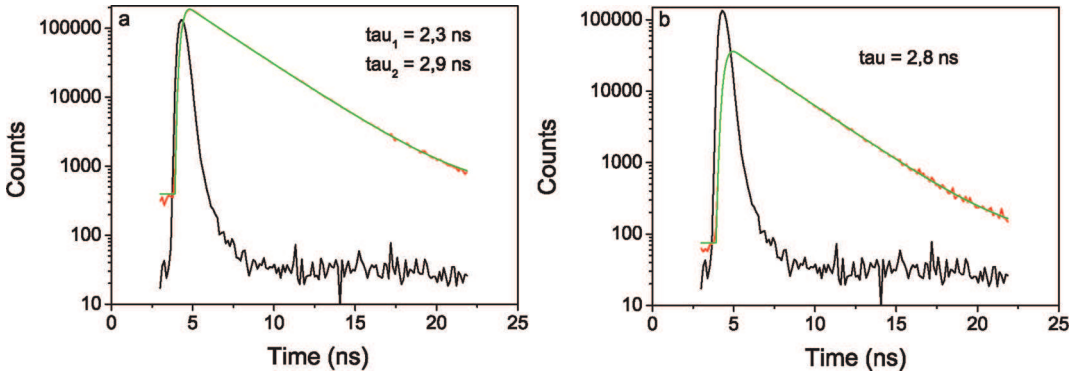

Figure 3. Decay profiles obtained by integrating all photons recorded during the measurement time of a molecule. The profile shown in a was best fit with a biexponential decay model with decay times of $\tau_1 = 2.3$ ns with a contribution of 20% and $\tau_2 = 2.9$ ns with a contribution of 80%. The decay profile shown in b was best fit with a monoexponential decay model with decay time $\tau = 2.8$ ns. The black curve is the instrumental response function of the setup, which has a fwhm of about 0.5 ns.

built by promoting one electron from one of the highest 60 occupied to one of the lowest 60 unoccupied levels.

Results and Discussion

The normalized (relative to the maximum value) absorption and emission spectra of TDI (Figure 1) are shown in Figure 2. The absorption and emission spectra have a maximum around 653 and 666 nm, corresponding to the $S_0 \rightarrow S_1$ and $S_1 \rightarrow S_0$ electronic transitions, respectively.

Single molecule measurements were performed on thin films, spin-coated from a 10^{-9} M solution of TDI in PS/toluene in between two layers of PVA/H_2O. To localize the individual molecules, an area of 10 μm by 10 μm was scanned. Taking into account the number of molecules found in this area and comparing with the expected number to be found for such a low dye concentration (10^{-9} M), we made sure to have the right concentration to measure individual molecules. Furthermore, the diffraction limited spots observed on the scanning areas and the one-step bleaching (not shown) confirm the observation of single molecules. Once localized, fluorescence lifetime and linear dichroism trajectories were recorded for each individual molecule.

In a first step, the decay time(s) of each individual molecule is (are) obtained by integrating all photons recorded during the measurement time of the molecule (until photobleaching irreversibly occurs) in a decay profile. Figure 3 exhibits such profiles for two different molecules. One of the two decay profiles shown was best fit by a biexponential decay model (a) with decay times of 2.3 and 2.9 ns while the other could be best fit by a monoexponential decay model (b) with decay time of 2.8 ns. In all cases, the best fits have been determined on the basis of a careful examination of the χ^2 parameter, visual inspection of the residuals, and autocorrelation of the latter. Figure 4 collects the distribution of decay times obtained by fitting the decay profiles of all measured molecules. Clearly, this distribution is bimodal with peaks centered at $\tau = 2.0$ and 2.9 ns with a respective contribution of 23% and 77%. The recurrent occurrence of these two specific decay times in the decay profiles gives us a strong indication of the probable emission detection of various conformers of the TDI dye molecule.

In a simplistic picture, one may imagine TDI as a conjugated core surrounded by fours arms (phenoxy rings). According to the position of the arms with respect to the conjugated core, one can see five different conformations emerging: the one

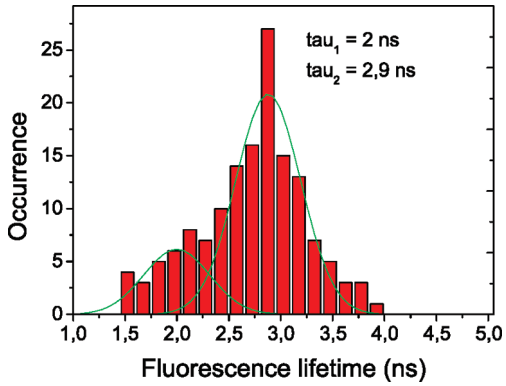

Figure 4. Distribution of the decay times obtained by fitting the decay profiles of all individual molecules either by biexponential or monoexponential decay models, as appropriate.

where all arms are collapsed on the core (hereafter called 0E for zero extended arm) and the ones where one, two, three or the four arms are brought away from the core and thus extended (hereafter called 1E, 2E, 3E, and 4E, depending on the number of arms extending away from the core). Following this simplistic view, changes in transition dipole moment and in transition energy are expected for the different conformations, due to the various extension of the arms, giving rise to various decay times of the dye molecule.

In order to give a theoretical support to this statement, we performed an in-depth theoretical investigation of this molecular system. As pointed out elsewhere,[54] perylene diimide (PDI) molecules substituted in the bay area by four phenoxy groups exhibit several radiative lifetimes depending of the number of phenoxy subtituents strongly interacting with the conjugated core, in an autosolvation scheme. We have demonstrated that this strong interaction led to a coupling of the transition densities, essentially between the two nitrogen atoms of the PDI conjugated core. Depending on the number of folded arms (from zero to four), this coupling of the transition densities can be more or less delocalized on the phenoxy arms, thus strongly modifying the transition dipole of the studied conformer and, in turn, its radiative lifetime.[54] The molecule investigated here is characterized by a longer conjugated core. Performing GenMol[49] molecular mechanic studies of the conformational space, we

(54) Fron, E.; Schweitzer, G.; Osswald, P.; Würthner, F.; Marsal, P.; Beljonne, D.; Müllen, K.; De Schryver, F. C.; Van der Auweraer, M. *Photochem. Photobiol. Sci.* **2008**, *7*, 1509.

Downloaded by UNIV DE BORDEAUX 1 on August 31, 2009 | http://pubs.acs.org
Publication Date (Web): August 5, 2009 | doi: 10.1021/ja901636v

Table 1. Calculated Radiative Lifetime and Total Energy of the Different Conformers

n	$S_0 \rightarrow S_1$ transition energy (eV)	total transition dipole	transition dipole *X* (D)	transition dipole *Y* (D)	transition dipole *Z* (D)	radiative lifetime (ns)	energy (kJ/mol)
0	1.941	14.6531	14.6528	0.0564	0.0653	3.9	145.2
1	1.999	14.8115	14.8115	0.2217	−0.172	3.5	153.2
2	1.995	14.8939	14.8852	0.4873	−0.1488	3.5	151.9
3	1.995	14.969	14.9657	0.3058	−0.0767	3.4	151.2
4	1.988	15.1075	15.1073	−0.0085	−0.0602	3.4	150.2

determined the preferred conformations of the molecule. We then used these optimized geometries as starting points for single point INDO/SCI excited states calculations and compute, in this way, the radiative lifetime of each conformer. This approach has already been validated in various studies,[43,44,54] which allowed us to stress, with a high accuracy, the consequences of a change of molecule conformation on the measured radiative lifetime obtained at the single molecule spectroscopy level. In Table 1, we report the computed vertical transition energies, transition dipole moments, energies, and radiative lifetimes of the five selected conformers (Figure 5), depending on the numbers of folded phenoxy units in strong van der Waals interactions with the conjugated core. We can highlight two different groups of conformers. The first group is the molecule with zero extended phenoxy substituents (0E), the most stable conformer, having a long lifetime $\tau = 3.9$ ns and a small energy gap due to a strong energetic stabilization of the π systems owing to favorable interactions with the arms. Such a conformation leads to the smallest computed transition dipole moment, as due to the opposite contributions of the transition dipole moment of the conjugated core and of those of all the phenoxy susbtituents to the total transition dipole moment. The second group is the molecules with nonzero extended (1E, 2E, 3E, or 4E) phenoxy substituents, having a short lifetime $\tau \approx 3.4-3.5$ ns, high energy gap, and a large transition dipole moment due to phenoxy decoupling. Let us strongly stress here that the unfolding of a single arm is enough to provide the full decrease of the computed radiative lifetime, going from 3.9 to 3.4−3.5 ns. In this respect, let us note that several 2E conformers may occur, with the other two phenoxy groups being either below or above the ring system in diagonal or neighboring positions. All these 2E conformers have similar spectroscopic properties. These results are very interesting when contrasted with those obtained for the previously investigated PDI molecule,[54] where the unfolding led to a linear modification of the radiative lifetime with the number of arms extending far away from the conjugated core: in this longer conjugated core, the phenoxy substituents are less polarized by the strongly delocalized transition densities on the conjugated core. This lack of polarization leads to a stronger decoupling of the arms with respect to the conjugated core and, consequently, to a smaller contribution of the arms to the total transition dipole moment and transition energy. Both contributions, in turn, have an opposite effect and lead to similar radiative lifetimes, as soon as the fully symmetric autosolvated conformation (0E) is destroyed.

These calculations have been performed in vacuum. The radiative lifetime in vacuum has been calculated with the usual formula

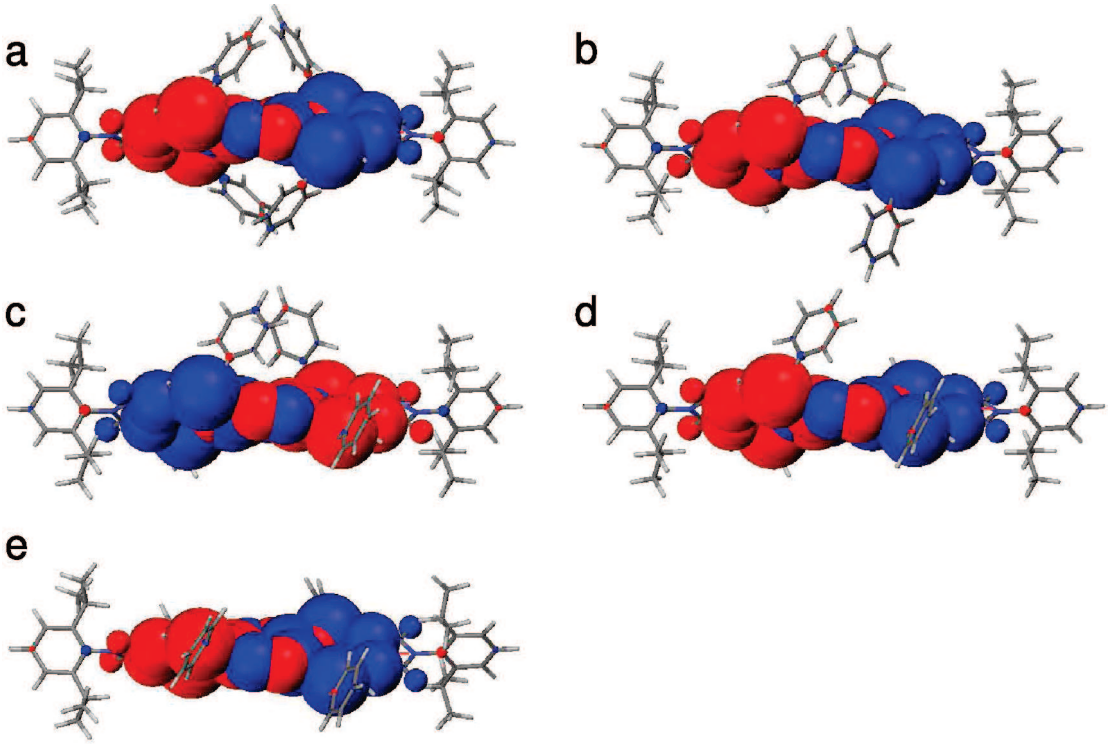

Figure 5. Molecular structures and atomic transition densities associated with the lowest optically allowed electronic excitation for the five most stable conformers of TDI. From a to e, the conformers range from the folded structures (a, 0E) progressively to the completely extended structure (e, 4E). The size of the spheres is proportional to the amplitude of the atomic transition densities.

Downloaded by UNIV DE BORDEAUX 1 on August 31, 2009 | http://pubs.acs.org
Publication Date (Web): August 5, 2009 | doi: 10.1021/ja901636v

$$\tau_0 = \frac{m_e \varepsilon_0 {c_0}^3}{2e^2 \pi \nu_0 f} \quad (2)$$

where e is the charge of the electron, ε_0 and c_0 are the permittivity and the speed of light in a vacuum, and ν_0 and f are the transition frequency and the oscillator strength of the probe molecule in a vacuum, respectively.

By further taking into account the renormalization of the photon in the medium, $\varepsilon_0 \rightarrow \varepsilon_r \varepsilon_0$ and $c_0 \rightarrow c_0/n$, the lifetimes are $\tau = 2.5$ ns for the 0E conformation and $\tau = 2.2$ ns for the others, close enough to the experimentally obtained values.

In a second step, the fluorescence lifetime and linear dichroism trajectories have been built for each single molecule, with a binning time of 100 ms. Thus, we did collect the photons in time intervals of 100 ms, calculate both observables for this time interval, and build the time trace as well as the time distribution of both observables for each individual molecule. Furthermore, for each molecule exhibiting significant fluctuations of one or both observables during its measurement time, we did calculate the corresponding autocorrelation function: $C_d(t')$ for the autocorrelation function of the linear dichroism $d(t)$

$$C_d(t') = \frac{\sum_{t=0}^{t=T-t'} d(t+t')\, d(t) - d(\bar{t})\, d(\bar{t})}{\sum_{t=0}^{t=T} d(t)\, d(t) - d(\bar{t})\, d(\bar{t})} \quad (3)$$

where $d(\bar{t})$ is the average value of the linear dichroism on the length T of its time trace. Correspondingly, $C_f(t')$ has been calculated for the autocorrelation function of the fluorescence lifetime $\tau(t)$.

The relaxation times were obtained by either fitting the autocorrelation curves with a monoexponential decay model or by simply reporting the value for which the curve has decayed to one-third of its initial value. The relaxation times obtained indicate the time scale of the fluctuations of the corresponding observable for each individual molecule.

Among the 86 molecules investigated in this study, 11 exhibit nonfluctuating fluorescence lifetime and linear dichroism time traces. Figure 6 shows such a molecule with an average lifetime $\tau = 3$ ns and linear dichroism $d = -0.25$. The distributions of both observables are monomodal and very narrow, indicating a molecule frozen in the matrix during its measurement time (i.e., until irreversible photodissociation of the molecular structure occurs). So, while in the supercooled regime, some 10 °C above its glass transition temperature, the PS matrix can trap TDI molecules for such a long time scale. A molecule of this class exhibited the integrated decay profile shown in Figure 3b.

Contrasting with the previous behavior, Figure 7 shows an example of a molecule with fluctuating lifetime time trace while the linear dichroism time trace remains at a constant value. The lifetime time trace and bimodal distribution clearly indicate transitions between lifetime values peaked at $\tau_1 = 2$ ns and $\tau_2 = 2.8$ ns. On the contrary, the linear dichroism does not change substantially during the experiment (roughly the same time scale as the measurement time for the molecule observed in Figure 6), as best indicated by its monomodal and narrow distribution. The relaxation time obtained from the autocorrelation curve performed for the lifetime observable (Figure 7b) is $\zeta = 2$ s. Nine molecules only showed jumps in the fluorescence lifetime and not in linear dichroism. We attribute this behavior to molecules that are able to perform a conformational change in the matrix, while not able to reorient significantly, and tentatively assign the occurrence of a folding/unfolding event of one or more arms of the TDI dye molecule to uncorrelated motions of lateral phenyl groups of the surrounding PS chains. Such motions, due to the β relaxation mechanism, are expected to occur on shorter time scales than the α relaxation process, involving a collective rearrangement of the PS chain skeletal, only able to bring on a reorientation of the whole TDI probe molecule. An example of integrated decay profile of a molecule belonging to this class is shown in Figure 3a.

In order to test our attempt of attribution, we use the results of the INDO/SCI quantum calculations performed on the optimized calculated geometries to investigate the expected change in linear dichroism related to a change of conformation from the zero extended structure (0E) to one of the unfolded structures (1E, 2E, 3E, or 4E). The X, Y, and Z components for the different conformations are reported in Table 1. Only small changes of the transition dipole moment components are found upon a conformational change. By setting the transition dipole moment vector of the 0E conformer at the origin of a traditional spherical coordinate system,[55] we did measure the changes in linear dichroism occurring due to a change of conformation from the 0E structure to any of the unfolded ones for all colatitude θ angles ranging from 0° to 90° and azimuthal ϕ angles ranging from 0° to 180°, by steps of 15°, in order to also account for the different orientations of the molecule transition dipole moment possibly encountered in the measurements. Figure 8 shows the values of linear dichroism and fluorescence lifetime for a given orientation $\theta = 90°$ and $\phi = 52°$ of the five different conformers. Figure 8 clearly shows that a change of conformation of the TDI molecule may indeed give rise to a bimodal distribution of lifetimes and monomodal distribution of linear dichroism, in accordance with the observations reported in Figure 7.

In a third class, we find 58 molecules for which lifetime fluctuations occur partly simultaneously (correlated) to jumps in linear dichroism and partly independently to any linear dichroism change. Figure 9 exhibits the fluorescence lifetime and linear dichroism trajectories for such a molecule. Some jumps occurring simultaneously in lifetime and linear dichroism are indicated by the vertical dashed lines. The main values of lifetime and dichroism between which the transitions occur are signaled by horizontal lines. We find essentially a bimodal distribution of lifetimes with peaks centered at $\tau = 2.2$ and 2.8 ns and a trimodal distribution of linear dichroism with $d = -0.2$, 0.25, and 0.75. Figure 9a shows that many more fluctuations occur in the lifetime time trace than in the linear dichroism time trace, i.e., in between each simultaneous jump of lifetime and linear dichroism, we can still observe many fluctuations of the lifetime only. This observation is better quantified by analysis of the autocorrelation functions of both observables. While the linear dichroism autocorrelation curve exhibits essentially a one-step decay on a time scale $\zeta = 23$ s, the fluorescence lifetime autocorrelation function presents a two-steps relaxation process, with a first decay to a plateau at $C_f(t) = 0.55$ (see horizontal dotted line in Figure 9b), corresponding to a relaxation time $\zeta \approx 2$ s (see vertical arrow in Figure 9b) followed by a second and final decay with a relaxation time $\zeta = 11$ s. These

(55) Wei, C. J.; Kim, Y. H.; Darst, R. K.; Rossky, P. J.; Vanden Bout, D. A. *Phys. Rev. Lett.* **2005**, *95*, 173001.

Downloaded by UNIV DE BORDEAUX 1 on August 31, 2009 | http://pubs.acs.org
Publication Date (Web): August 5, 2009 | doi: 10.1021/ja901636v

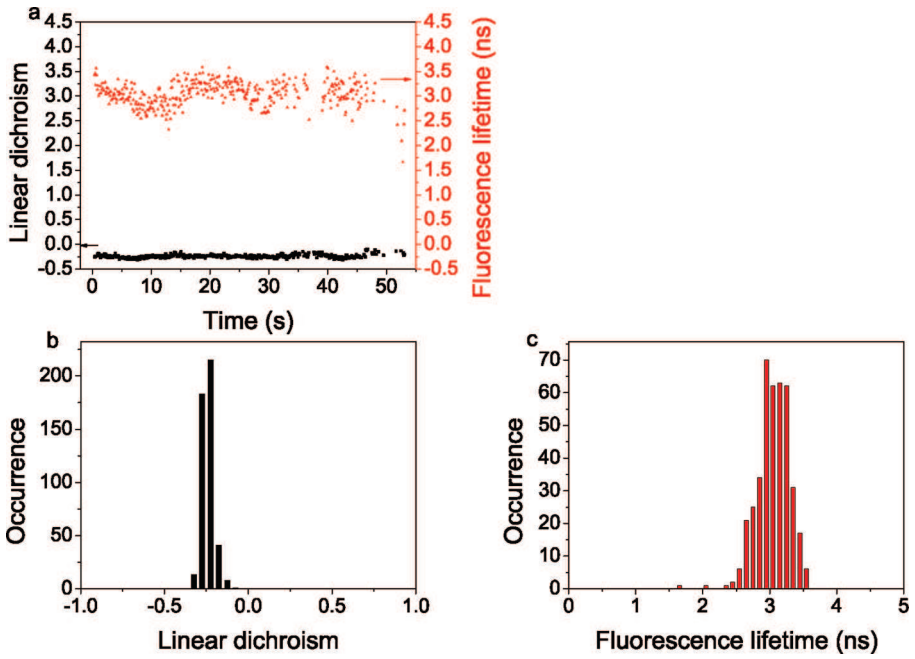

Figure 6. (a) Linear dichroism (black) and fluorescence lifetime (red) trajectories of a molecule that neither reorients nor undergoes conformational changes. (b) Narrow distribution of the linear dichroism trajectory shown in part a with a single peak at $d = -0.25$ (c) Narrow fluorescence lifetime distribution of the trajectory shown in part a with a single peak at $\tau = 3$ ns.

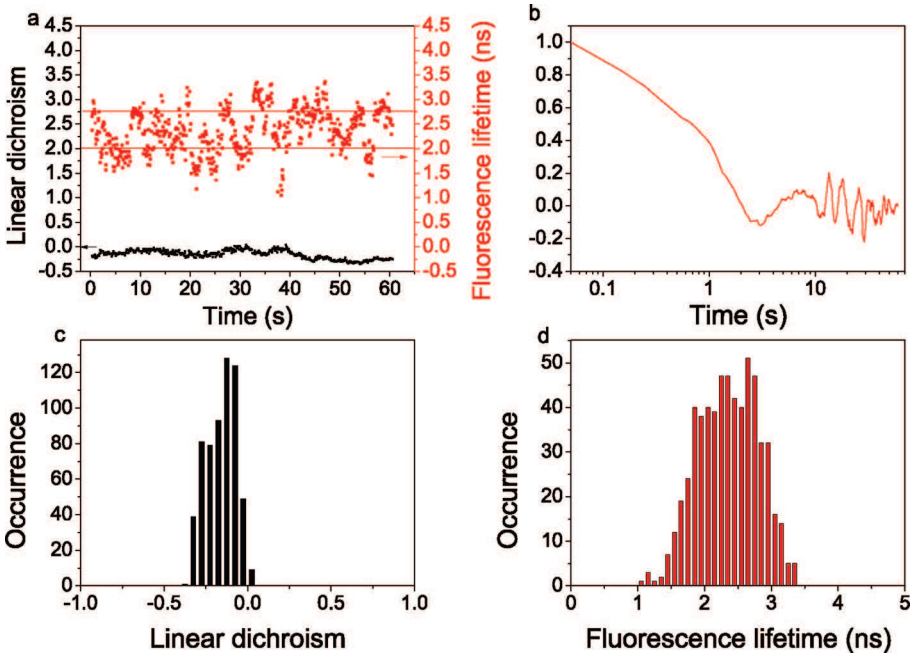

Figure 7. (a) Linear dichroism (black) and fluorescence lifetime (red) trajectories of a molecule that undergoes conformational changes but does not perform a rotational move. The horizontal lines are guidelines for the different levels in fluorescence lifetime. (b) Corresponding correlation curve of the fluorescence lifetime with a relaxation time of 2 s. (c) Distribution of the linear dichroism trajectory shown in part a, which is very narrow and peaks at $d = -0.2$. (d) Fluorescence lifetime bimodal distribution of the trajectory shown in part a with peaks corresponding to the red horizontal lines at values of $\tau = 2$ and 2.75 ns.

observations may be rationalized as follows: the relaxation time corresponding to roughly 2 s and corresponding to the numerous fluctuations of the fluorescence lifetime alone must be attributed to "pure" conformational changes of the TDI probe molecule in a mechanism assisted by the uncorrelated motions of lateral phenyl groups of PS chains, i.e., due to the β-relaxation process in the PS matrix. On this time scale, the molecule does not rotationally move as a whole; hence, the linear dichroism is not modified. Besides these uncorrelated motions and on a longer time scale, roughly 1 order of magnitude slower, the α-relaxation process occurs, where collective segmental rearrangements of the PS backbone give rise to a reorientation of the probe molecule as a whole, mainly accompanied by a conformational change of the probe molecule and signaled by simultaneous jumps of the lifetime and linear dichroism. The slight variations theoretically found in the transition dipole orientation for the different molecular states are so small compared to the reorientation of the molecule as a whole that

Downloaded by UNIV DE BORDEAUX 1 on August 31, 2009 | http://pubs.acs.org
Publication Date (Web): August 5, 2009 | doi: 10.1021/ja901636v

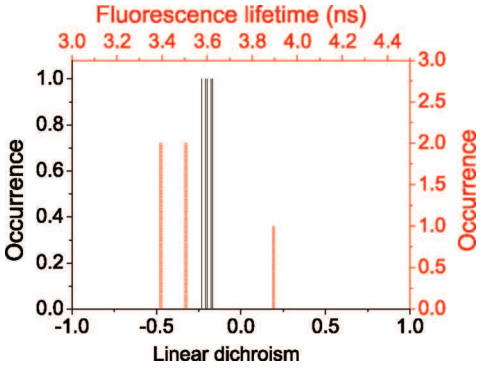

Figure 8. Calculated values of fluorescence lifetime (red) and linear dichroism (black) for the different conformers of TDI for an initial orientation of the 0E conformer at $\theta = 90°$ and $\phi = 52°$.

they are not noticeable experimentally. On average, for the 58 molecules belonging to this class, the correlation times for linear dichroism and fluorescence lifetime corresponding to the long relaxation time attributed to the α-relaxation process are 27 and 8 s, respectively, indicating that the fluorescence lifetime and linear dichroism observables do not probe the α-relaxation mechanism on the same spatial scale. As reported already elsewhere,[16,56−58] the time scale for reorientation indeed greatly depends on the size of the probe and on the particular observable chosen to determine the reorientation dynamics. As such, the linear dichroism relaxation time of a single molecule, as measured on a confocal microscope with a high NA objective, has been shown to correspond to the relaxation time of a second rank [based on $P_2(t)$] reorientational correlation function while the fluorescence lifetime is essentially sensitive to the very first shells of the polymer chains surrounding the probe molecule and thus has a relaxation time corresponding to that of a higher rank [based on $P_l(t)$, $l \geq 4$] reorientational correlation function.[58]

Finally, the fourth class comprises the rare molecules (eight) that exhibit fluorescence lifetime fluctuations only simultaneously to linear dichroism jumps as a result of both reorientations and conformational changes of the dye molecule; i.e., these molecules probe the α-relaxation mechanism without probing the β-relaxation process. Figure 10 shows the lifetime and linear dichroism time traces of such a molecule. Clearly, the jumps observed in both observables always correlate in time. Their distributions are broad and multimodal with peaks centered at $d = -0.2$, 0.1, and 0.35 for the linear dichroism and $\tau = 2.6$ and 3.4 ns for the fluorescence lifetime. The correlation curves of both observables for this molecule are similar with a one-step decay and provide relaxation times $\zeta = 38$ and 57 s for the linear dichroism and fluorescence lifetime, respectively. The average correlation times of linear dichroism and fluorescence lifetime for the eight molecules classified here are 14 and 18 s, respectively.

Figure 11 collects the relaxations times attributed to the α-relaxation process for all molecules reorientating as a whole in the PS matrix and for both observables. Both methods of determination of these relaxation times (fitting the autocorrelation curves with a monoexponential decay model or simply reporting the value for which the curve has decayed to one-third of its initial value) have been used and are shown to match very well: the distributions obtained in both cases are very similar. The correlation times obtained for the fluorescence lifetime are on average shorter than those obtained for the linear dichroism.

At this point, it is interesting to compare our results to those, essentially originating from ensemble measurements, previously reported in the literature. In the past, dynamics associated with the α-relaxation in PS have been probed at and above T_g by a variety of techniques such as viscosity,[6] compliance,[6] quasielastic neutron scattering,[7] NMR,[8–10] photon correlation spectroscopy,[11,12] dielectric relaxation,[13–15] photobleaching,[16] second harmonic generation techniques,[17,18] and molecular dynamic simulations.[10] The relaxation times obtained by these techniques are very similar and are about 1−5 min at T_g while 1 or 2 orders of magnitude faster a few degrees slightly above T_g. The relaxation times obtained here, $\zeta \geq 10-20$ s, are slightly longer than the expected α-relaxation time scale at the working temperature $T_g/T = 0.97$. This slight discrepancy can be explained by the relative size of our probe as compared to the surrounding monomers. Indeed, the TDI molecule investigated in this study is rather huge as compared to the styrene surrounding monomers, and it is a well-known fact[56] that, as the probe molecule exceeds the surrounding constituents in size, the rotational correlation slows down and leads to a significant increase of the rotational time scale.

Concerning the presence of a secondary relaxation process, the so-called β-relaxation process, experimental[11,15] and theoretical[59] studies agree to associate a β-relaxation time scale roughly 3 orders of magnitude faster than the α-relaxation time scale at around T_g. Some previous work by Leon et al.[15] concerning dielectric relaxation measurements of propylene glycol and oligomers having different number (N) of repeat units clearly shows that the separation between the α- and β-relaxations decreases with decreasing N, so it is difficult to resolve the β-relaxation from the more intense α-relaxation in propylene glycol. In this study, we deal with oligomers of a few styrene monomers. The same effect as discussed by Leon et al.[15] could thus explain the "small" 5−10 times ratio between the α- and β-relaxation time scales observed in our case.

One could also ask if we really probe two time scales, given the fact that our trajectories are only 10−50 times longer that the longest decay times actually determined. It is a well-known fact that finite trajectory lengths have a significant influence on the determination of the associated relaxation times.[60] Trajectories only 20 times longer than the determined decay constant lead to errors on this decay constant of about 50%. However, in the case of our study, fluorescence lifetime autocorrelation curves, like the one shown in Figure 9b, clearly exhibit a two-steps behavior with a first decay to a plateau, shown by the dotted line and the arrow in the figure on a time scale of about 2 s, followed by a second decay with a time scale of about 11 s. It is worthwhile to mention here that this behavior has been exhibited for all 58 molecules pertaining to this class. This behavior is also very reminiscent of a theoretical study performed by Lyulin et al.,[59] where the finding of two peaks in the distribution function of relaxation times for the P_2 autocor-

Downloaded by UNIV DE BORDEAUX 1 on August 31, 2009 | http://pubs.acs.org
Publication Date (Web): August 5, 2009 | doi: 10.1021/ja901636v

(56) Wang, L.-M.; Richert, R. *J. Chem. Phys.* **2004**, *120*, 11082.
(57) Huang, W.; Richert, R. *Philos. Mag.* **2007**, *87*, 371.
(58) Vallée, R. A. L.; Paul, W.; Binder, K. *J. Chem. Phys.* **2007**, *127*, 154903.
(59) Lyulin, A. V.; Balabaev, N. K.; Michels, M. A. *Macromolecules* **2002**, *35*, 9595.
(60) Lu, C.-Y.; Vanden Bout, D. A. *J. Chem. Phys.* **2006**, *125*, 124701.

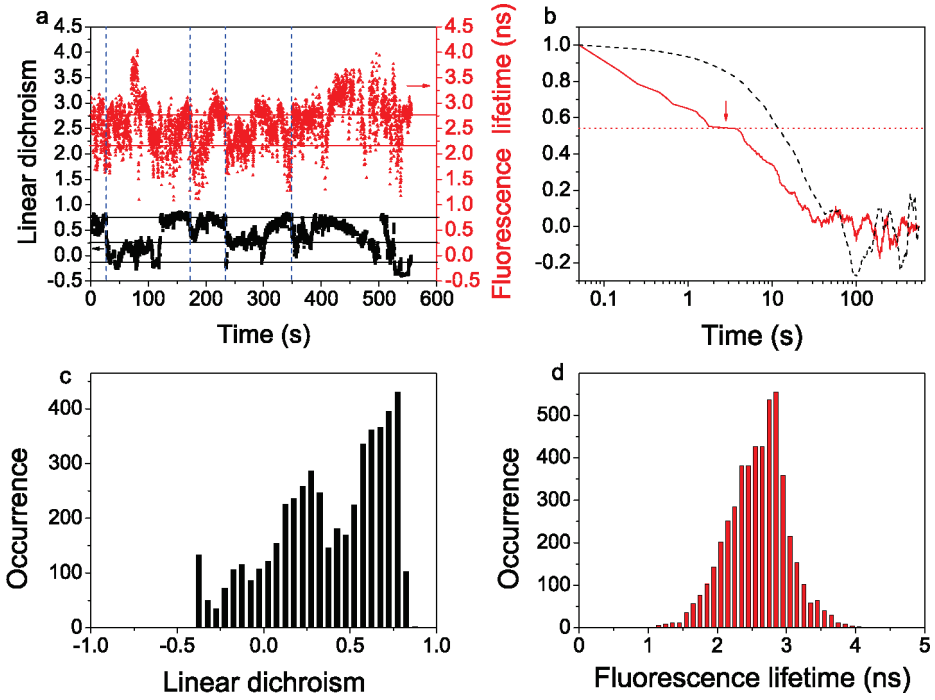

Figure 9. (a) Linear dichroism (black) and fluorescence lifetime (red) trajectories of a molecule that reorients and undergoes conformational changes. The horizontal lines are guidelines for the different levels in linear dichroism (black) and fluorescence lifetime (red). The vertical lines indicate a few correlated jumps occurring simultaneously in linear dichroism and fluorescence lifetime (blue dashed vertical line). (b) Corresponding correlation curves of linear dichroism (black dashed) and fluorescence lifetime (red solid) with relaxation times of 23 and 11 s, respectively. (c) Distribution of the linear dichroism trajectory shown in part a with peaks corresponding to the black horizontal lines at values of $d = -0.2$, 0.25, and 0.75. (d) Fluorescence lifetime distribution of the trajectory shown in part a with peaks corresponding to the red horizontal lines at values of $\tau = 2.2$ and 2.75 ns.

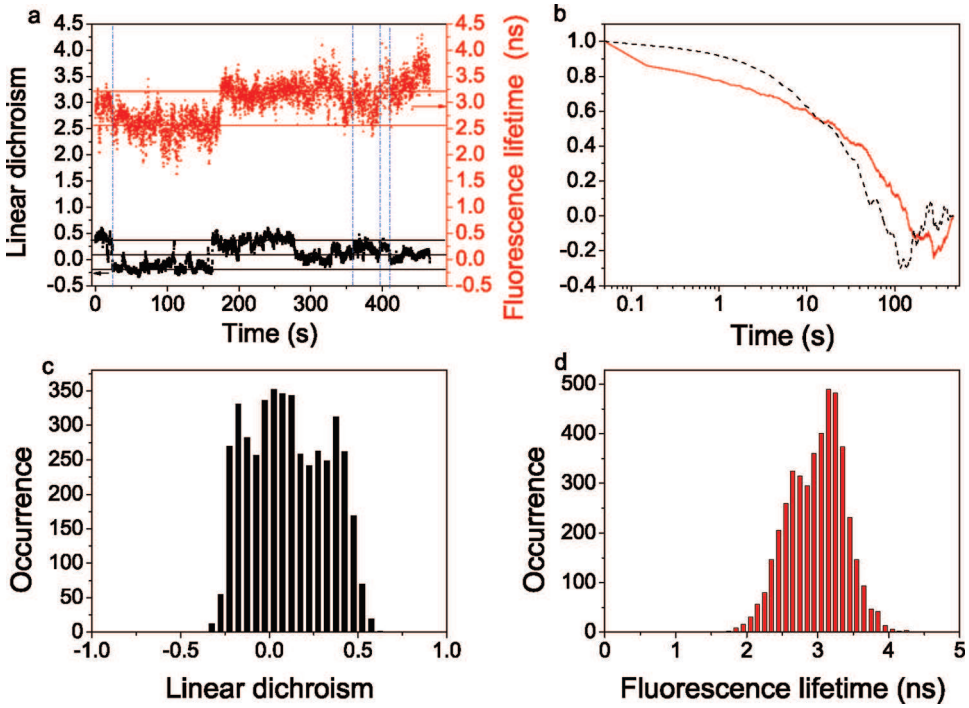

Figure 10. (a) Linear dichroism (black) and fluorescence lifetime (red) trajectories of a molecule that reorients but does not undergo any conformational change not associated with a reorientation of the dye molecule. The horizontal lines are guidelines for the different levels in linear dichroism (black) and fluorescence lifetime (red). The vertical lines indicate a few correlated jumps occurring simultaneously in linear dichroism and fluorescence lifetime (blue dashed vertical line). (b) Corresponding correlation curve of linear dichroism (black dashed) and fluorescence lifetime (red solid) with relaxation times of 38 and 57 s, respectively. (c) Distribution of the linear dichroism trajectory shown in part a with peaks corresponding to the black vertical lines at values of $d = -0.2$, 0.1, and 0.35. (d) Fluorescence lifetime distribution of the trajectory shown in part a with peaks corresponding to the red horizontal lines at values of $\tau = 2.6$ and 3.4 ns.

relation functions in low molecular weight PS slightly above the glass transition has been assigned to the α-relaxation dynamics and to a β-activated process for the slow and fast relaxation times, respectively. Of course, a very interesting

Downloaded by UNIV DE BORDEAUX 1 on August 31, 2009 | http://pubs.acs.org
Publication Date (Web): August 5, 2009 | doi: 10.1021/ja901636v

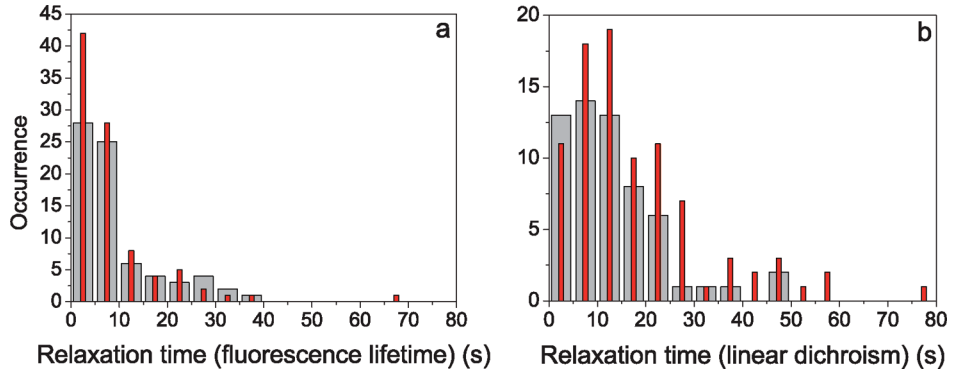

Figure 11. Distribution of correlation times for (a) fluorescence lifetime and (b) linear dichroism. The narrow red bars give the correlation time obtained from taking the relaxation time as the time at which the correlation function has decayed to one-third of its initial value, and the broader gray bars give the correlation times obtained by fitting the autocorrelation curves with an exponential decay model.

perspective of the work performed in this paper would be to perform a temperature-dependent investigation, allowing one to probe the expected non-Arrhenius, Arrhenius types of behavior for the α and β types of relaxation dynamics.

Conclusions

In conclusion, we have shown in this paper that both fluorescence lifetime and linear dichroism of single molecules are observables able to probe the α-relaxation dynamics of the surrounding polymer matrix. The α-relaxation times associated with both observables agree well together and with data reported in the literature concerning ensemble measurements. Furthermore and contrarily to the linear dichroism, the fluorescence lifetime observable of the versatile TDI dye is able to trace small changes occurring in the surrounding polymer matrix, owing to the ability of the TDI phenoxy rings to fold/unfold onto the conjugated core, giving rise to a new conformer, i.e., to a small change of the transition dipole moment orientation, but substantial enough in magnitude to be noticeable by the fluorescence lifetime observable. As such, the β-relaxation process, associated with uncorrelated motions of lateral phenyl groups of PS chains and assigned to be responsible of the folding/unfolding event of one or more arms of the TDI dye molecule, can be probed as well at the single molecule level. It has an average relaxation time of about 2 s, i.e., is 1 order of magnitude slower than the relaxation time associated with the α-relaxation mechanism, under the conditions of this study. Performing single molecule fluorescence spectroscopy experiments with simultaneous determination of the fluorescence lifetime and linear dichroism observables for a dye molecule so versatile as TDI, able to reorient and change conformation, proves thus here to be a unique tool to probe subtle differences in local segmental dynamics related to the α- and β-relaxation mechanisms.

Acknowledgment. The authors are thankful to the FWO for financial support and a postdoctoral fellowship to R.V., to the research council of K. U. Leuven for funding in the framework of GOA 2006/2, and to Belgian Science policy for funding through IAP V/03 and VI/27/. The "Instituut voor de aanmoediging van innovatie door Wetenschap en Technologie in Vlaanderen" (IWT) is acknowledged for grant ZWAP 04/007 and for a fellowship to E.B. P.M. thanks Dr. D. Beljonne for useful support and discussions.

JA901636V

Downloaded by UNIV DE BORDEAUX 1 on August 31, 2009 | http://pubs.acs.org
Publication Date (Web): August 5, 2009 | doi: 10.1021/ja901636v

Spectral narrowing of emission in self-assembled colloidal photonic superlattices

Kasper Baert, Kai Song, Renaud A. L. Vallée, Mark Van der Auweraer, and Koen Clays[a)]
Department of Chemistry, University of Leuven, Celestijnenlaan 200D, BE-3001 Leuven, Belgium

(Received 5 April 2006; accepted 9 October 2006; published online 29 December 2006)

We report on the influence of a well-designed passband in the stop band of a suitably engineered self-assembled colloidal photonic crystal superlattice on the steady-state emission properties of infiltrated fluorophores. The photonic superlattice was built by convective self-assembly of slabs of silica spheres of two different sizes. Transmission experiments on the engineered photonic crystal structure show two stop bands with an effective passband in between. The presence of this passband results in a narrow spectral range of increased density of states for photon modes. This shows up as a decrease in the emission suppression (enhancement of the emission) in the narrow effective passband spectral region. These experiments indicate that the threshold for lasing can possibly be lowered by spectrally narrowing the emission of fluorophores infiltrated in suitably engineered self-assembled photonic crystal superlattices, and are therefore important towards the realization of efficient all-optical integrated circuits from functionalized photonic superlattices and heterostructures. © *2006 American Institute of Physics*. [DOI: 10.1063/1.2402029]

I. INTRODUCTION

Photonic crystals, often also called photonic band gap (PBG) materials, are the optical analogues of electronic crystals, i.e., semiconductor crystals, which form the basis of all electronics' applications.[1,2] While the periodicity in the materials' properties is on the angstrom scale in electronic (ionic) crystals, it is on the optical wavelength scale in photonic crystals. In electronic crystals, the periodic potential results in a band gap, i.e., a forbidden range of energies for the electrons. In photonic crystals, the periodicity in refractive index results in an optical band gap, i.e., a forbidden spectral range for the photons.

The periodicity of the refractive index can be realized along one dimension (1D) in so-called 1D PBG materials. Dielectric mirrors, made by vapor deposition, are a good example of such 1D PBG structures. Physical top-down techniques, such as lithography, are suitable to realize two-dimensional (2D) PBG materials. To engineer a PBG in all dimensions, the periodicity of the refractive index should be realized in all three dimensions (3D). Physical top-down approaches are less amenable to 3D PBG structures. Chemical self-assembly of colloidal particles, on the other hand, is particularly well suited towards close-packed 3D photonic crystals. The self-assembly results in the thermodynamically most stable face-centered cubic (fcc) crystal structure or in the (random) hexagonal closed packing [(R)hcp] crystal structure, both with a packing of 74%. The size of the colloidal particles, together with the refractive index, determines the spectral position of the band gap. The combination of these dense crystal structures [fcc or (R)hcp] with the low refractive index of most colloidal particles (latex, silica) results in an incomplete band gap.[3] For a complete band gap, i.e., a forbidden spectral region for all incidence angles, either a more effective crystal structure (diamond structure),[4,5] less dense packing (inverted opals), or higher refractive index contrast (e.g., titania or zirconia particles) is necessary.[6,7]

A further accomplishment in the design of PBG materials is the realization of a passband inside the band gap,[8] to allow an emission narrowing of the inserted fluorophores and possibly lasing of the photonic crystal. By engineering lower-dimensional intentional defects in a photonic crystal, the band gap can be designed to have allowed passband defect modes. While it is difficult to introduce such defects by physical top-down lithographic techniques, interfacial self-assembly techniques are naturally effective in introducing 2D defect layers in 3D colloidal crystals. By introducing a monolayer of particles of different sizes or different refractive indices in a photonic crystal, it is possible to impart a passband in the stop band.[9–11]

The spectrometric study of the resulting optical filter (combined stop band and passband) is possible by transmission spectroscopy with white light incident on the bare photonic crystal or by emission spectroscopy of fluorophores with appropriate emission spectrum infiltrated in the crystal.[12] The suppression effect by the band gap has been observed for both semiconductor[13,14] and organic chromophore emission,[15–18] and also in inverted opals,[19] and has been interpreted in terms of partial suppression of radiation modes,[17] resulting in a low photon density of states.[14] The importance of the perpendicular incidence on the photonic crystal in transmission, versus the omnidirectional emission in incomplete photonic band gap materials, has been discussed.[20] The important result is that the light intensity contrast ratio, obtained in transmission, between a passband and a stop band PBG material is experimentally larger for transmission than for emission experiments. Transmission experiments are therefore the most appropriate to study the spectral features of passband and stop band. However, the

[a)]Author to whom correspondence should be addressed; FAX: +3216327982; electronic mail: koen.clays@fys.kuleuven.be

 © 2006 American Institute of Physics

Downloaded 08 Jan 2007 to 134.58.253.113. Redistribution subject to AIP license or copyright, see http://jap.aip.org/jap/copyright.jsp

effect on the emission is naturally weakened in incomplete band gaps due to the omnidirectional nature of the emission.[18]

While we have succeeded in inserting a passband in a stop band by introducing a monolayer defect of silica particles of different sizes by using the Langmuir-Blodgett interfacial technique,[9–11] the partial nature of the passband that is realized in this way does not allow its observation in fluorescence emission. The engineered passband shows up as a narrow dip in a single, narrow stop band. The spectral position of this dip and stop band is dependent on the angle of incidence of the light. Therefore, for detection with omnidirectional emission, the narrow band is washed out. Therefore, we reverted to a different strategy that would impart a stronger (deeper and wider) allowed passband in a broad forbidden range of wavelengths, resulting from an engineered effective stop band. The stop band results from the linear addition of the individual stop bands from slabs of photonic crystals made from colloidal particles with different sizes. By proper choice of the relative particle sizes in such a photonic superlattice, the effective width of total stop band and passband within the stop band can be tuned.

II. EXPERIMENTS

The monodisperse spherical silica particles of different sizes used in this study (*A*, 250 nm, and *B*, 260 nm) were produced by a strict control of the conditions for the well-known Stöber-Fink-Bohn approach.[21] After completion of the hydrolysis of the tetraethylorthosilicate, followed by the condensation to silica, the colloidal suspension is centrifuged and resuspended in ethanol by sonication four times. The convective self-assembly process makes use of the suspending power of ethanol for these silica particles, in combination with an appropriate vapor pressure for this solvent at 32 °C.[22] The glass substrate and the vial containing the suspension are cleaned with piranha acid (1/3 sulfuric acid, 2/3 hydrogen peroxide as oxidant) prior to use. The substrate is placed vertically in the vial. Photonic *AB* or *ABAB* superlattices were made by successive deposition of photonic crystal slabs composed of colloidal particles of the two different sizes. The slabs were deposited out of an ethanolic suspension of approximately 0.3 vol % (sample 1, reference sample with photonic band gap at 371 nm; sample 2, single thin-slab photonic crystal of *A*; sample 3, *AB* thin-slab photonic superlattice; and sample 5 *ABAB* thin-slab photonic superlattice) or 0.6 vol % (sample 4, *ABAB* thick-slab photonic superlattice). The slab superlattice structure of the samples is schematically represented in Figs. 8(a), 9(a), and 10(a), for samples 3, 4, and 5, respectively. The multiple-slab *ABAB* superlattices were prepared to investigate the effect of the emission being preferentially collected through one side of the crystal. It also allowed controlling the linear additivity of the individual band gaps.

After each deposition of a single slab, the resulting structure was dried at approximately 130 °C to remove any residual solvent. The photonic superlattices exhibit dual photonic band gaps resulting from the linear combination of the band gaps of the individual stacks (*A* at 532 and *B* at 577 nm, respectively).[23]

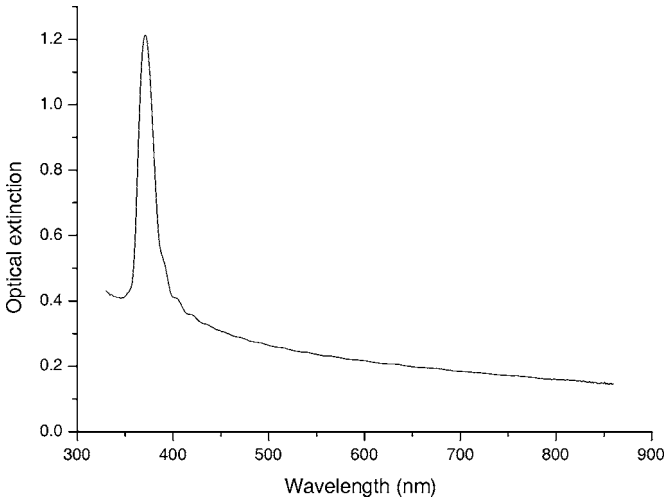

FIG. 1. Extinction spectrum of the photonic crystal sample 1: reference crystal with photonic band gap out of the emission spectral region.

It has been reported that the insertion of a defect layer of larger particle diameter in between two slabs made up of particles with smaller diameter results in increased disorder for a diameter ratio of 1.5.[11] The difference in particle size here is only 4%, allowing for a (quasi)epitaxial growth of particles of both diameters upon each other. While the interface between each two slabs could be considered as a defect, the effectively observed passband is not a true defect mode. The passband simply results from the superposition of two spectrally shifted stop bands. In between the two stop bands, a net resulting allowed passband emerges.

Transmission spectra were taken to ascertain quality and spectral features of the samples using a Perkin-Elmer Lambda 900 UV-VIS-NIR spectrophotometer. The extinction spectra for samples 1–5 are shown in Figs. 1–5, respectively.

The spectral properties of the passband/stop band combination obtained by this approach are compared with those

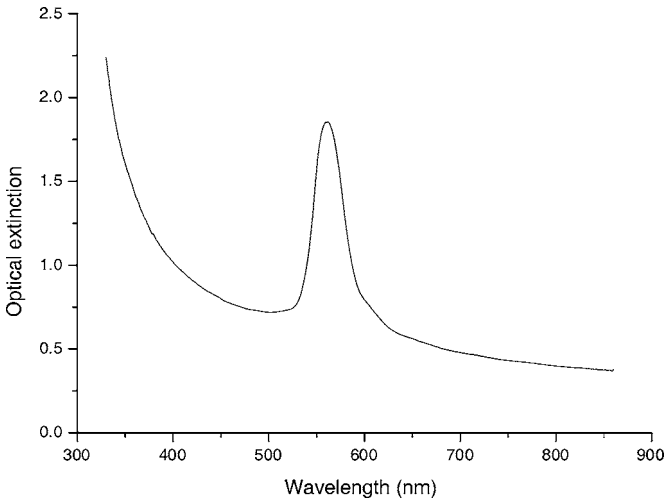

FIG. 2. Extinction spectrum of the photonic crystal sample 2: single thin-slab photonic crystal of *A* with single photonic band gap in the emission spectral region.

Downloaded 08 Jan 2007 to 134.58.253.113. Redistribution subject to AIP license or copyright, see http://jap.aip.org/jap/copyright.jsp

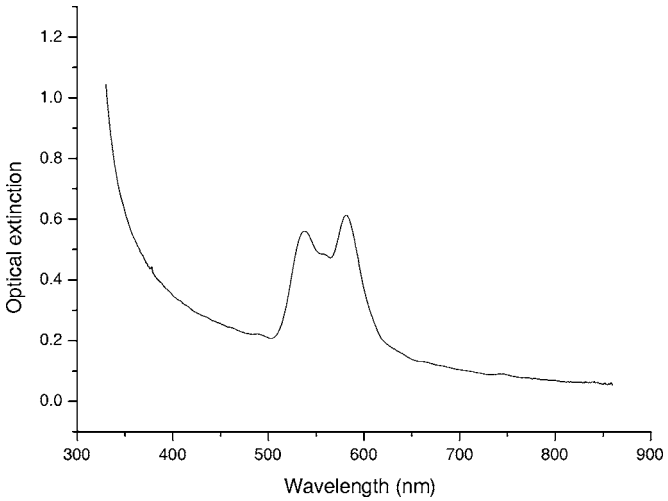

FIG. 3. Extinction spectrum of the photonic crystal sample 3: *AB* thin-slab superlattice photonic crystal with engineered forbidden stop band and allowed passband in stop band in the emission spectral region.

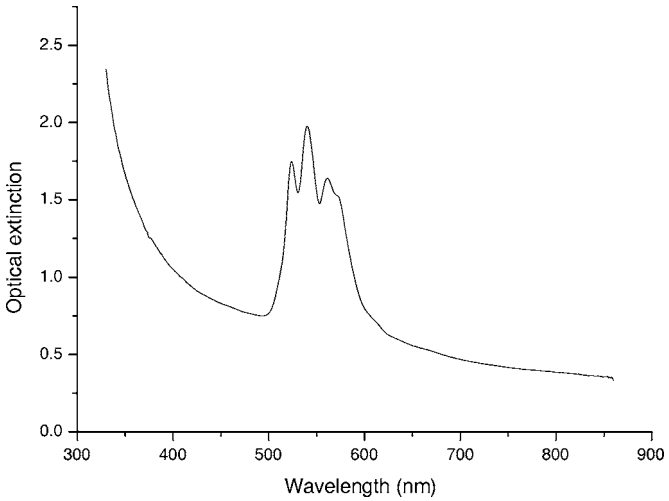

FIG. 5. Extinction spectrum of the photonic crystal sample 5: *ABAB* thin-slab superlattice photonic crystal with engineered forbidden stop band and allowed passband in stop band in the emission spectral region.

obtained from a true monolayer defect mode between two identical crystal stacks[10] in Table I. With our multiple-slab approach, we have been able to engineer a wider stop band (twice as wide), with a more pronounced (twice as wide and 50% more amplitude) passband.

In order to investigate the effect of the stop band/passband on the emission properties (spectral narrowing) of fluorophores, disodium fluorescein molecules [fluorescence quantum yield of 0.97 in basic ethanol, emission spectrum in the spectral range of the stop band of our photonic crystals (500–700 nm)] have been inserted in the photonic crystals. The crystals were placed in a $1.1\times10^{-3}M$ solution of the fluorophore in methanol for 30 min. All five different crystals were infiltrated: (1) sample 1 with a forbidden band gap at 371 nm, clearly out of the emission spectral region, as reference; (2) one with a single and narrow (yet incomplete) band gap at 562 nm; and the crystals with their engineered dual stop band with effective passband in between (3) sample 3, *AB* thin-slab superlattice, (4) sample 4, *ABAB* thick-slab superlattice, and (5) sample 5, *ABAB* thin-slab superlattice.

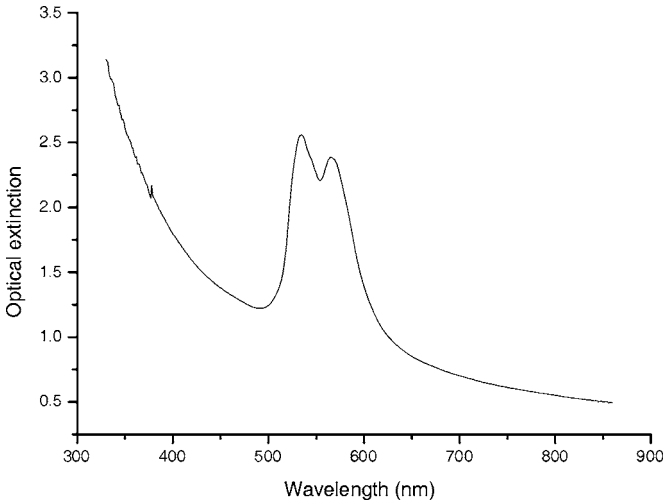

FIG. 4. Extinction spectrum of the photonic crystal sample 4: *ABAB* thick-slab superlattice photonic crystal with engineered forbidden stop band and allowed passband in stop band in the emission spectral region.

In the fluorescence experiments, the fluorophores were excited by pulses of 1 ps at a wavelength of 488 nm and a repetition rate of 8 MHz (Spectra Physics Tsunami+Pulse Picker+Doubler) in an inverted confocal microscope (Olympus IX70). The excitation power was set, according to each specific crystal's thickness, to a few nanowatts at the entrance port of the microscope. The emission spectra were recorded, with integration time of 10 s, by a liquid-nitrogen-cooled, back-illuminated charge-coupled device (CCD) camera (LN/CCD-512SB, Princeton Instruments) coupled to a 150 mm polychromator (SpectraPro 150, Acton Research Cooperation). The excitation signal was eliminated in the detection path owing to the use of appropriate dichroic mirror (DC-O-495) and long pass filter (LP520). The setup is described elsewhere in more detail.[24] For the measurements described here, the photonic crystal superlattices were oriented with the crystal side towards the objective lens of the microscope. Neither the excitation nor the emitted light passed through the glass substrate with this backward detection scheme. To ensure that the emission would be affected by the combined passband structure from all slabs, the excitation was focused in the slab closest to the substrate, ensuring the backward detection of the emission through the multislab superlattice. Please note that the experimental setup (confocal microscope) does not allow simply flipping over the sample with the photonic superlattice on the glass substrate to check for any effect due to the asymmetry of the sample. The resulting emission spectra, corrected for the background, the response of the CCD camera, and the optics used, are shown in Fig. 6 and were divided by the reference spectrum from reference sample 1 and normalized at long wavelengths, where the effect of the photonic band gap is no longer present.

III. RESULTS

The corrected emission spectra (before dividing by the reference spectrum from sample 1) for samples 1 (reference),

Downloaded 08 Jan 2007 to 134.58.253.113. Redistribution subject to AIP license or copyright, see http://jap.aip.org/jap/copyright.jsp

TABLE I. Comparison of spectral properties for designed passband in stop band obtained by two different engineering approaches. The data in the second column are derived from sample 3, while the data in the third column are derived from Ref. 10.

Crystal type	Two stacks of different particle size, no monolayer	Monolayer defect of different particle size in between two stacks of identical particle size
Passband nature	Gap between two stop bands	Passband defect mode
Central position stop band (nm)	556	635
FWHM total stop band (FWHM, nm) (FWHM, cm^{-1})	80 2600	50 1228
Position passband (nm)	532	632
FWHM passband (FWHM, nm) (FWHM, cm^{-1})	19 612	10 260
Relative amplitude passband/stop band	0.25 25%	0.17 17%

2 (single thin slab), and 3 (thin-slab *AB* superlattice) are shown in Figs. 6(a)–6(c) with cut-off dichroic at 500 nm. The first observation is the strongest emission for the engineered superlattice sample 3 and the weakest for the reference. This is explained by the different thicknesses of the crystals: while all slabs have the same number of layers, the reference crystal 1 is formed from a single slab with the smallest particles. This results in the thinnest thickness containing the lowest number of infiltrated fluorophores. By the same token, the strongest emission from the engineered superlattice is explained by its largest thickness, since it is built up from two slabs of the same number of layers. The emission spectra for samples 4 and 5 are very similar to the spectrum for sample 3.

To analyze the relative influence of the presence of the stop band and the passband on the steady-state emission properties, we have normalized the emission spectra of the samples 2–5 with respect to the emission spectrum for the high-quality reference photonic crystal sample 1. A comparison of this relative emission spectrum with the corresponding extinction spectrum is shown in Fig. 7 for sample 2 (single thin-slab photonic crystal of *A* with single stop band at 562 nm). The effect of the stop band on the emission spectrum is clearly observed as a suppression of the relative emission intensity in the spectral region of the band gap. The amplitude of the emission band is lower than the amplitude of the extinction, as expected and explained earlier in terms of the perpendicular incidence of the light in transmission experiments versus the omnidirectional emission in incomplete band gaps.[18]

To study the effect of an allowed passband in an engineered broad stop band, three different photonic crystal samples with *AB* superlattice were studied (with long pass filter at 520 nm). For sample 3, an *AB* thin-slab superlattice with passband located at 550 nm in a broad stop band covering the range from 500 to 600 nm and showing a very weak miniband[25,26] (see extinction spectrum in Fig. 3), we very clearly observe a suppression of the emission in the right stop band region of 570 to 600 nm, with a maximum suppression (to the right) at approximately the extinction

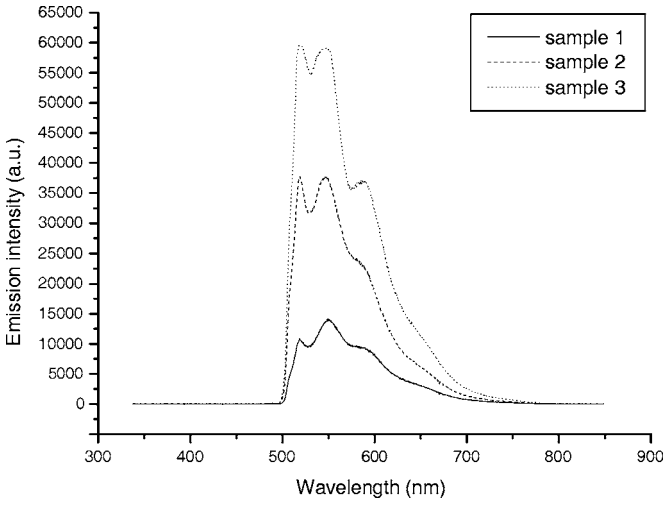

FIG. 6. Emission spectra taken from photonic crystal samples 1, 2, and 3 (see figure caption of Figs. 1–3) after infiltration with fluorophore.

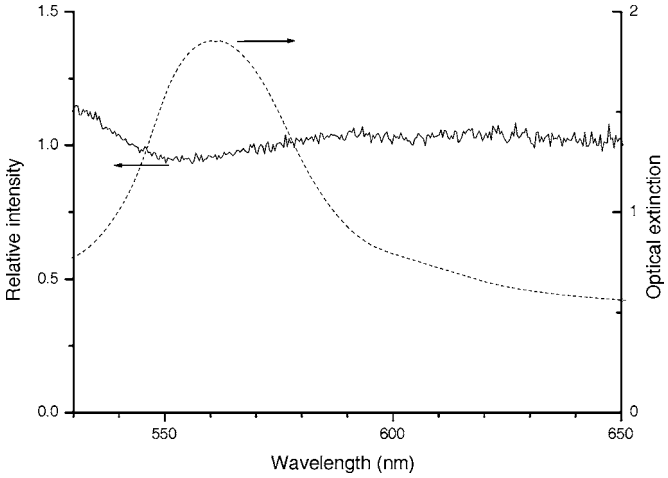

FIG. 7. Relative emission spectrum for photonic crystal sample 2, single thin-slab photonic crystal of *A* (solid line, left axis), compared with extinction spectrum (dotted line, right axis).

Downloaded 08 Jan 2007 to 134.58.253.113. Redistribution subject to AIP license or copyright, see http://jap.aip.org/jap/copyright.jsp

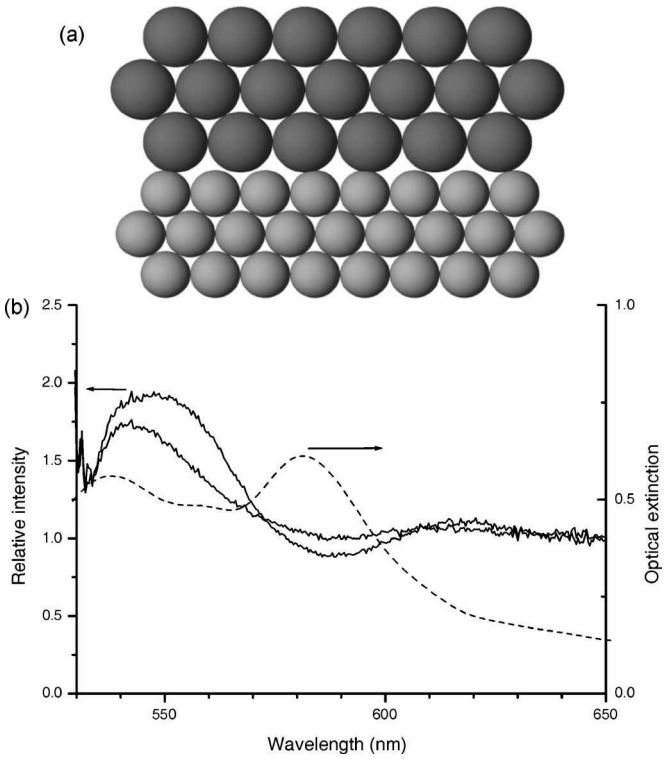

FIG. 8. (a) Schematic representation of thin-slab *AB* photonic superlattice sample 3. (b) Relative emission spectrum for thin-slab *AB* photonic superlattice sample 3 (solid lines, different positions in sample, left axis) compared with extinction spectrum (at 0° incidence angle, dotted line, right axis).

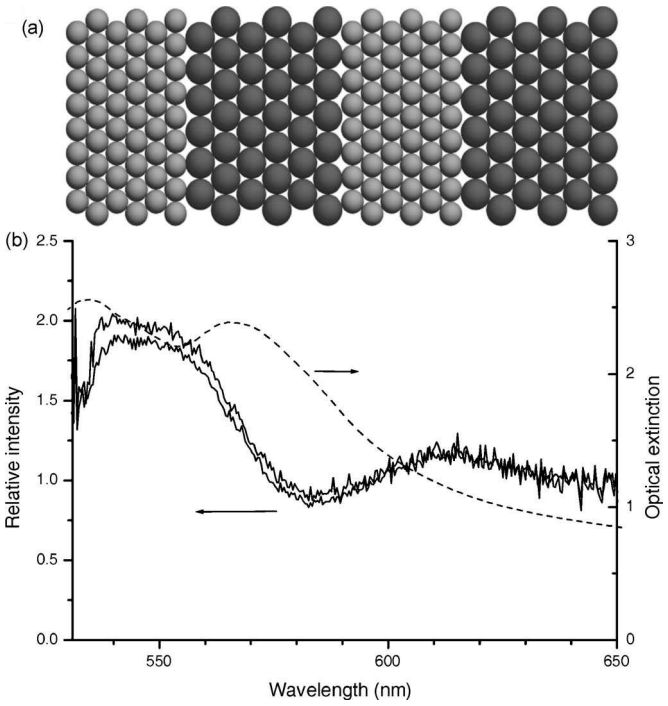

FIG. 9. (a) Schematic representation of thick-slab *ABAB* photonic superlattice sample 4. (b) Relative emission spectrum for thick-slab photonic superlattice sample 4 (solid lines, different positions in sample, left axis) compared with extinction spectrum (at 0° incidence angle, dotted line, right axis).

maximum (to the right). At the same time, an enhancement of the emission intensity in the allowed passband region around 550 nm is also observed. The dotted line in Fig. 8 represents the extinction spectrum. The two solid lines represent relative emission spectra at two different confocal positions in the sample, both close to the glass substrate. Both emission spectra clearly show the suppression and the enhancement of the emission at the appropriate spectral regions (stop band and passband, respectively). Please note that the emission spectra were taken with a long pass filter at 520 nm, precluding the observation of the full emission spectrum (to the left of the passband) of the fluorophore for samples 3–5. However, the onset of the emission suppression to the left of the passband at below 540 nm is clearly discernible for all three samples, with the very sharp cut-off dichroic having a 90% transmission already at 525 nm and a 95% transmission from 530 nm onwards.

Since sample 3 did exhibit miniband features in the passband, which could weaken the effect or complicate the analysis, we also made sample 4, a thick-slab *ABAB* superlattice. This four-layer sample also minimizes the spectral effect of the emission being collected preferentially through one side of the crystal. As expected, the main spectral features (both the combined photonic band gap features and the Rayleigh scattering background) are enhanced in amplitude, while the miniband has disappeared indeed in the extinction spectrum (Fig. 4). Correspondingly, the effect of this more pronounced extinction spectrum on the emission is also enhanced with respect to sample 3. Figure 9 very clearly shows the fluorescence suppression in the region of 570 to 600 nm and the fluorescence enhancement around 550 nm.

To ascertain our interpretation of the miniband effect, we have additionally prepared sample 5, a thin-slab *ABAB* superlattice, to specifically excite miniband features in the extinction spectrum and to study their effect on the emission. Figure 5 clearly shows well-resolved miniband structure that precludes the observation of the linear additivity of the two individual stop bands of photonic crystals *A* and *B* in the photonic superlattice *ABAB*. However, since these miniband features are very sharp, it was expected that they would be washed out in the emission spectra. The same concepts of omnidirectional emission in an incomplete (angle-sensitive) band gap would fully explain this. The angular sensitivity of the miniband features is experimentally evidenced in Fig. 10(b), where the dotted lines show extinction spectra at two different incidence angles. Already for a difference of only 10° in incidence angle, we can observe that local minima and maxima in the miniband features are almost inverted. The effect on the emission of infiltrated fluorophores is evinced by the solid lines. The narrow miniband spectral features in the extinction spectra have the same effect as a single passband: they allow for enhanced emission in the central region of the complete stop band where these miniband features emerge (around 550 nm), while still resulting in suppression to the right of this region (575 to 600 nm). This is a very interesting result with technological implications, since it relaxes the fabrication conditions of the *AB* photonic superlattices for narrowing the fluorescence by this approach. It is not necessary to fabricate a clean passband without any mini-

Downloaded 08 Jan 2007 to 134.58.253.113. Redistribution subject to AIP license or copyright, see http://jap.aip.org/jap/copyright.jsp

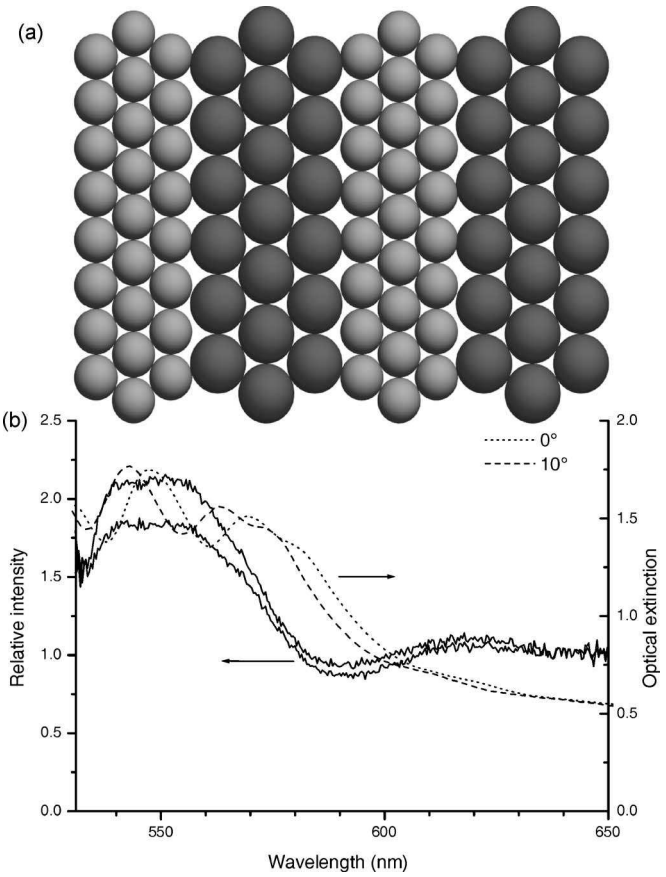

FIG. 10. (a) Schematic representation of thin-slab *ABAB* photonic superlattice sample 5. (b) Relative emission spectrum for thin-slab *ABAB* photonic superlattice sample 5 (solid lines, different positions in sample, left axis) compared with extinction spectrum (dotted lines, at 0 and at 10° incidence angle, right axis).

band features. This can be explained, again, by invoking the omnidirectional nature of the emission in combination with the angular dependence of these sharp spectral features.

The extinction spectra of the samples clearly show the additivity of the band gaps that are caused by the different slabs in the complete photonic crystal. In the samples with thin slabs, we observe the appearance of minibands in our engineered passband.[25,26] To investigate this, and to rationalize our attempt to minimize this effect, we have fabricated both thin-slab and thick-slab *ABAB* superlattices. As expected, the minibands are much more clearly pronounced in the thin-slab *ABAB* superlattices (Fig. 5). On the other hand, a clear passband, free of minibands, is exhibited by the thick-slab *ABAB* superlattice (Fig. 4). Also, comparison of the emission spectra from both the thin-slab samples *AB* and *ABAB* shows that there is no significant effect of the asymmetry of the sample.

IV. CONCLUSION AND PERSPECTIVES

We have successfully implemented a strategy to produce, by convective self-assembly, a predesigned broad effective stop band with a well-pronounced allowed passband in this forbidden photonic stop band. We have experimentally shown spectral narrowing by such a well-designed passband in the stop band of a self-assembled colloidal photonic superlattice. The importance of this result can be appreciated by considering the wide spectral range of the suppression (the width of the effective stop band, from 500 to 600 nm) covering the spectral breath of fluorophore emission, in combination with the narrow range of the enhanced emission [full width at half maximum (FWHM) of relative emission spectra of Figs. 8, 9, 10(a), and 10(b) approximately 30 nm] that can be sufficient to suppress all but one lasing mode in small optically integrated devices. Spectral narrowing and spectral collapse into a single mode is often considered as the first indication of lasing. Therefore, we have shown that properly engineered self-assembled colloidal photonic superlattices could become good candidates for low-threshold and/or single mode photonic crystal lasers.

Towards the development of self-assembled colloidal photonic crystal lasers, the realization of feedback structures at the design wavelength asks for Bragg reflectors (narrow stop bands) at both ends of the engineered photonic crystals at the lasing wavelength, in combination with the allowed passband at the same design wavelength, in a broad stop band extending over the emission spectrum of the fluorophore, realized in a double stack that constitutes the central part of the lasing crystal. To limit the designed functionality to the envisioned photonic crystal part (feedback only in two extreme crystal stacks, narrowed emission in central double stack), the fluorophores need to be nanostructured in the latter part, instead of postinfiltrated in the total crystal structure (including extreme feedback stacks). This can be realized by functionalization by covalent chemical bonds of silica particles with fluorophores with the appropriate chemical functional group (e.g., isocyanate).[18]

ACKNOWLEDGMENTS

This work has been supported by the University of Leuven, Concerted Research Actions (Geconcerteerde OnderzoeksActie, GOA/2006), by the regional Flemish Fund for Scientific Research (FWO-V, Fonds voor Wetenschappelijk Onderzoek—Vlaanderen) under the form of a postdoctoral fellowship for one of the authors (R.A.L.V.) and a research grant (G.0458.06), and by the federal Belgian IUAP programme V/3.

[1] E. Yablonovitch, Phys. Rev. Lett. **58**, 2059 (1987).
[2] S. John, Phys. Rev. Lett. **58**, 2486 (1987).
[3] K. Wostyn, Y. Zhao, B. Yee, G. de Schaetzen, L. Hellemans, K. Clays, and A. Persoons, J. Chem. Phys. **118**, 10752 (2003).
[4] K. M. Ho, C. T. Chan, and C. M. Soukoulis, Phys. Rev. Lett. **65**, 3152 (1990).
[5] K. Busch and S. John, Phys. Rev. E **58**, 3896 (1998).
[6] M. M. Sigalas, C. M. Soukoulis, R. Biswas, and K. M. Ho, Phys. Rev. B **56**, 959 (1997).
[7] K. Busch and S. John, Phys. Rev. Lett. **83**, 967 (1999).
[8] E. Yablonovitch, T. J. Gmitter, R. D. Meade, A. M. Rappe, K. D. Brommer, and J. D. Joannopoulos, Phys. Rev. Lett. **67**, 3380 (1991).
[9] Y. Zhao, K. Wostyn, G. de Schaetzen, K. Clays, Lo. Hellemans, A. Persoons, M. Szekeres, and R. A. Schoonheydt, Appl. Phys. Lett. **82**, 3764 (2003).
[10] K. Wostyn, Y. Zhao, G. de Schaetzen, L. Hellemans, N. Matsuda, K. Clays, and A. Persoons, Langmuir **19**, 4465 (2003).
[11] P. Massé, S. Reculusa, K. Clays, and S. Ravaine, Chem. Phys. Lett. **422**, 251 (2006).
[12] M. Megens, J. E. G. J. Wijnhoven, A. Lagendijk, and W. L. Vos, J. Opt. Soc. Am. B **16**, 1403 (1999).

Downloaded 08 Jan 2007 to 134.58.253.113. Redistribution subject to AIP license or copyright, see http://jap.aip.org/jap/copyright.jsp

[13]A. Blanco, C. Lopez, R. Mayoral, H. Miguez, F. Meseguer, A. Mifsud, and J. Herrero, Appl. Phys. Lett. **73**, 1781 (1998).
[14]J. Zhou, Y. Zhou, S. Buddhudu, S. L. Ng, Y. L. Lam, and C. H. Kam, Appl. Phys. Lett. **76**, 3513 (2000).
[15]K. Yoshino, S. B. Lee, S. Tatsuhara, Y. Kawagishi, M. Ozaki, and A. A. Zakhidov, Appl. Phys. Lett. **73**, 3506 (1998).
[16]S. G. Romanov, T. Maka, C. M. S. Torres, M. Muller, and R. Zentel, J. Appl. Phys. **91**, 9426 (2002).
[17]T. Yamasaki and T. Tsutsui, Appl. Phys. Lett. **72**, 1957 (1998).
[18]K. Song, R. Vallée, M. Van der Auweraer, and K. Clays, Chem. Phys. Lett. **421**, 1 (2006).
[19]R. C. Schroden, M. Al-Daous, and A. Stein, Chem. Mater. **13**, 2945 (2001).
[20]T. Maka, D. N. Chigrin, S. G. Romanov, and C. M. T. Torres, Prog. Electromagn. Res. (PIER) **41**, 307 (2003).
[21]W. Stöber, A. Fink, and E. Bohn, J. Colloid Interface Sci. **26**, 62 (1968).
[22]P. Jiang, J. F. Bertone, K. S. Hwang, and V. L. Colvin, Chem. Mater. **11**, 2132 (1999).
[23]S. Reculusa, P. Massé, and S. Ravaine, J. Colloid Interface Sci. **279**, 471 (2004).
[24]J. Hofkens *et al.*, J. Am. Chem. Soc. **122**, 9278 (2000).
[25]R. Rengarajan, P. Jiang, D. C. Larrabee, C. L. Colvin, and D. M. Mittleman, Phys. Rev. B **64**, 205103 (2001).
[26]P. Jiang, G. N. Ostojic, R. Narat, D. M. Mittleman, and V. L. Colvin, Adv. Mater. (Weinheim, Ger.) **13**, 389 (2001).

Downloaded 08 Jan 2007 to 134.58.253.113. Redistribution subject to AIP license or copyright, see http://jap.aip.org/jap/copyright.jsp

Nonexponential decay of spontaneous emission from an ensemble of molecules in photonic crystals

R. A. L. Vallée,* K. Baert, B. Kolaric, M. Van der Auweraer, and K. Clays
Department of Chemistry and Institute of Nanoscale Physics and Chemistry (INPAC), Katholieke Universiteit Leuven, Leuven 3001, Belgium

(Received 7 April 2007; revised manuscript received 7 June 2007; published 19 July 2007)

Photonic crystals (PCs) with relatively low dielectric contrast (i.e., with pseudogaps) have significant influence on the fluorescence decay of internal emitters. Fluorescence decays of ensembles of dye molecules measured at different positions in the PCs exhibit a nonexponential behavior, which is best fitted by a continuous distribution of decay rates. The most frequent decay rates of these distributions are smaller and their widths are narrower in a PC with a pseudogap acting in the emission range of the emitters than in a PC having the pseudogap out of this range. These experimental results have been well accounted for by calculations of the local density of states and rate constant for spontaneous emission.

DOI: 10.1103/PhysRevB.76.045113 PACS number(s): 42.70.Qs

I. INTRODUCTION

The control of the spontaneous rate delivered by an ensemble of emitters is fundamental for the engineering of such applications as miniature lasers, light-emitting diodes,[1,2] and solar cells.[3] The rate of spontaneous emission is determined by both the internal structure of the emitters and their environment.[4,5] Periodic dielectric structures, known as photonic crystals (PCs), have been predicted to radically change the photonic local density of states (LDOS), which governs the interaction between the emitter and the electric field in the structure.[1] The achievement of a photonic band gap (PBG), i.e., a range of frequencies for which the LDOS vanishes, is an active field of research. To engineer a three dimensional (3D) PBG material, the periodicity of the refractive index should be realized in 3D. Physical top-down approaches are less amenable to such PBG structures. Chemical self-assembly of colloidal particles, on the other hand, is particularly well suited toward close-packed 3D photonic crystals. The self-assembly results in the thermodynamically most stable face-centered cubic (fcc) crystal structure or in the (random) hexagonal closed packing (Rhcp) crystal structure, both with a packing of 74%. The size of the colloidal particles, together with the refractive index, determines the spectral position of the band gap. The combination of these dense crystal structures (fcc or Rhcp) with the low refractive index of most colloidal particles (latex and silica) results in an incomplete band gap (pseudogap or stop band).[6] For a complete band gap, i.e., a forbidden spectral region for all incidence angles, either a more effective crystal structure (diamond structure),[7,8] less dense packing (inverted opals), or higher refractive index contrast (e.g., titania or zirconia particles) is necessary.[9,10]

Because of the difficulty in the fabrication of samples, most of the experimental studies concerning the emission properties of atoms, molecules, and/or quantum dots in PCs have been achieved only in 3D PC's with pseudogaps (pseudo-PBG's). The first report of the inhibition of the spontaneous emission rate in a PC (Ref. 11) turned out to be due to non-PC effects.[12] Recently, wide lifetime distributions containing both enhanced and inhibited decay components were reported for dyes 1,8-naphthoylene-1′,2′-benzimidazole(7H-benzimidazo [2,1-a] benz [de] isoquinolin-7-one) (NBIA) embedded in a polymer network filling the voids of an opal structure.[13] In this experiment, the dye molecules were spread homogeneously over the sample. However, if the dye molecules are homogeneously embedded in a spherical layer inside the silica spheres for a similar system,[14] only a single decay lifetime was found, slightly changed with respect to the reference sample. These contradictory results concerning the influence of the stop band on the radiative lifetime of the emitters have been extensively discussed.[15–19] More recently, depending on the emission frequency, lifetime fluctuations up to 30% have been reported[20] for CdSe quantum dots in inverse PCs. Furthermore, nonexponential decay profiles of quantum dots embedded in 3D fcc inverse opals have been experimentally observed. The profiles have been analyzed in terms of a continuous distribution of decay rates. Very interestingly, the widths of these distributions have been related to the variation of the LDOS at the various positions and orientations of the emitter in the unit cell.[21,22]

In this context, it is still unclear whether PCs with relatively low dielectric contrast (as it is the case for most opal structures) can have significant influence on the emission rate of internal emitters. Additionally, defects in the crystal structure can lead to changes in the observed fluorescence spectra, due to diffuse scattered light,[23] making a real quantitative analysis difficult. It is the purpose of this paper to provide such a detailed analysis, combining both macroscopic and microscopic experimental investigations of dyes embedded in silica opals to theoretical predictions of the LDOS. We show that the normalized emission spectra of the molecules have a shape varying with the lateral position of the investigated ensemble of emitters in the sample. Furthermore, the decay profiles of these ensembles of emitters show indeed a nonexponential behavior, with an extent that depends on the lattice constant of the grown PC, and are best described by a continuous distribution of decay rates.[21,22] These distributions of decay time vary slightly from position to position in the sample, indicating slight heterogeneities in the structures. Finally, we provide a theoretical investigation that evidences the role played by the pure LDOS on these observations.

 ©2007 The American Physical Society

The paper is organized as follows. In Sec. II, we provide the details concerning the sample preparation and the experimental setup. Section III presents the experimental results, both on the macroscopic [optical extinction spectra of the PC structure, (Sec. III A)] and microscopic scales [emission spectra (Sec. III B) and emission rates (Sec. III C) of the embedded fluorophores]. Section IV continues with the theoretical investigations of the LDOS in structures parametrized as closely as possible to the experimentally grown structures. Finally, we conclude in Sec. V.

II. SAMPLE PREPARATION AND EXPERIMENTAL SETUP

Monodisperse spherical silica particles ($\epsilon=2.1$) with diameter sizes of 171 nm for the reference samples and 260 nm for the photonic stop band (PSB) samples were produced by a strict control of the conditions for the well known Stöber-Fink-Bohn approach.[24] After completion of the hydrolysis of the tetraethylorthosilicate, followed by the condensation to silica, the colloidal suspension was centrifuged and resuspended four times by sonication in ethanol.

The growth of the colloidal crystal, by convective self-assembly, makes use of the suspending power of ethanol on the silica particles and requires an appropriate vapor pressure for this solvent at 305 K.[25] The glass substrate and the vial containing the suspension are cleaned with piranha acid (2/3 sulfuric acid and 1/3 hydrogen peroxide as oxidant) prior to use. The substrate is placed vertically in the vial. Reference and PSB lattices were made by deposition of colloidal particles with diameters of 171 nm and 260 nm, respectively. The slabs were deposited from an ethanolic suspension of approximately 0.3 vol %. The resulting structure was dried at approximately 403 K to remove any residual solvent. Figure 1 shows transversal (top) and top (bottom) views of a PSB colloidal crystal obtained by using a scanning electron microscope (Philips XL30 ESEM FEG). The figure allows one to judge the good quality of the 10 μm thick crystal constituted by 42 layers of colloidal particles.

Optical extinction spectra were performed on large areas (millimeter sized) to ascertain the quality and spectral features of the samples using a Perkin-Elmer Lambda 900 UV-vis-NIR spectrophotometer. In order to investigate the effect of the stop band on the emission properties of fluorophores, disodium fluorescein molecules were postinfiltrated in the colloidal crystals. Reference samples were grown from smaller silica spheres in order to present a stop band out of the visible range spanning the emission of the fluorophores. This allowed us to compare their emission properties with those in the effectively active (PSB) sample with a photonic stop band in the visible range. The disodium fluorescein molecules have a fluorescence quantum yield $\Phi=0.97$ in basic ethanol, an emission spectrum spanning a spectral range from 500 to 700 nm, i.e., covering the spectral range of the stop band of the PSB samples (expected maximum at 565 nm) and a fluorescence lifetime of 4 ns. The infiltration was performed by placing the crystals in a $1.1\times10^{-3}M$ solution of the fluorescein in methanol for 30 min.

The fluorescence experiments were performed with an inverted confocal scanning optical microscope (Olympus IX70). The excitation light, i.e., pulses of 1.2 ps at a repetition rate of 8 MHz (Spectra Physics, Tsunami, Pulse Picker, and Doubler) and a wavelength $\lambda=488$ nm, was circularly polarized and the power set to 10 nW at the entrance port of the microscope. The emission light was collected through the same objective [Olympus 0.5 NA (numerical aperture), 25×] used to focus the excitation light on the sample, in a epifluorescence configuration. The spatial resolution of the confocal microscope is then about 300 nm transversally (x and y directions) and about 1 μm longitudinally (z direction). In order to eliminate any residual excitation signal in the fluorescence emission, a suitable combination of filters was used, consisting of a bandpass (BP488, Chroma) placed in the excitation path, a dichroic (Olympus 495), a notch (Kaiser Optics, 488) that matches the bandpass, and a long pass (LP505, Chroma) in the emission path. The emission spectra were recorded, with an integration time of 10 s, by a liquid-nitrogen-cooled backilluminated charge-coupled device (CCD) camera (LN/CCD-512SB, Princeton Instruments) coupled to a 150 mm polychromator (SpectraPro 150, Acton Research Cooperation). Furthermore, an additional dichroic mirror (Olympus 570) was placed in the emission path

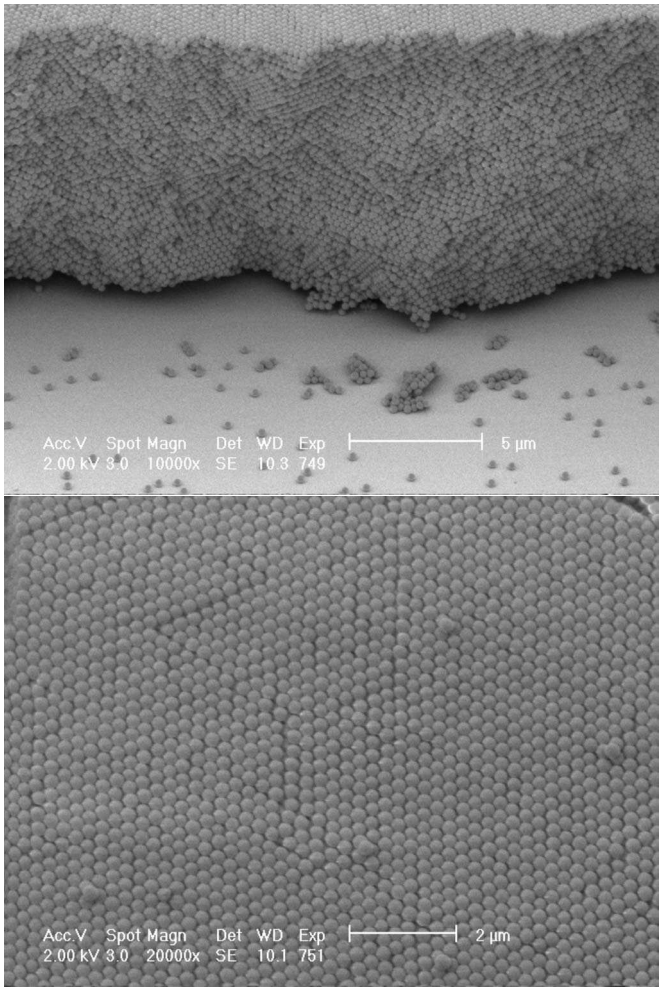

FIG. 1. Scanning electron microscope views of a PSB colloidal crystal obtained by convective self-assembly from a colloidal dispersion (size of the particles: 260 nm). Top: Transversal view. Bottom: Top view.

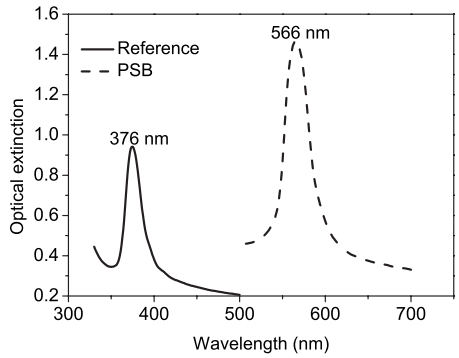

FIG. 2. Optical extinction spectra of the reference (solid) and photonic stop band (PSB, dash) samples. The reference sample, grown from spheres of diameter $D=171$ nm, has its stop band in the UV range, while the PSB sample, grown from spheres of diameter $D=260$ nm, has its stop band in the visible range.

in order to separate the emission originating from photons with a transition frequency in ($\lambda<570$ nm) and out [$\lambda>580$ nm, with an additional long pass filter (LP580, Chroma)] of the stop band of the PSB sample. The split signals were sent to two avalanche photodiodes (SPCM-AQ-14, EG & G Electro Optics) equipped with a time-correlated single photon counting card (Becker & Hickl GmbH, SPC 630) used in the first in first out (FIFO) mode to measure the time lags between excitation and emission. A suitable window of 16.1 ns (time width of 63 ps per channel for the 256 channels available in the FIFO mode) was chosen to adequately build the decay profiles.

The samples were oriented so that the PC lattices have their [111] axis along the z direction of the microscope, i.e., with the crystal top side oriented toward the objective lens of the microscope. Neither the excitation nor the emitted light passed through the glass substrate with this backward detection scheme. As mentioned in the literature already,[26] the main advantage of such a microscopic approach, as compared to macroscopic investigations, is its ability to probe the crystal structure locally. As the main intensity of the excitation laser beam is focused to a diffraction limited spot, only molecules within a small sample volume contribute to the detected fluorescence signal. Varying the focus position laterally provides direct information on the local quality of the crystal domains and/or distribution of molecules in the sample volume.

III. EXPERIMENTAL RESULTS

A. Macroscopic scale: Optical extinction spectra

The prepared PC samples exhibit a strong opalescence in the visible region of the spectrum, which indicates the presence of a photonic stop band due to the regular ordering of the silica spheres. UV-vis-NIR spectroscopies are fundamental techniques to ascertain the quality and characterize the optical properties of colloidal crystals.[27,28] Figure 2 shows the optical extinction spectra of the reference and PSB samples. In both cases, one main peak is observed according to the Bragg diffraction law:

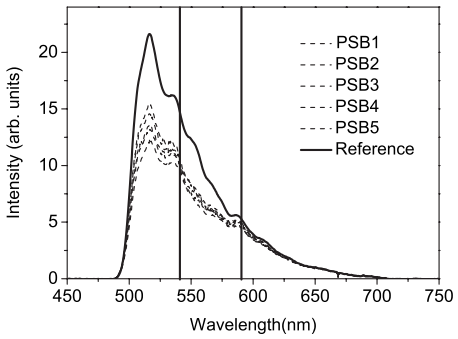

FIG. 3. Emission spectra of ensembles of molecules located at five different positions of a PSB sample (dash), among the 18 investigated. The solid line stands for the emission spectra averaged over ensembles of molecules located at 18 different positions of the reference sample.

$$\lambda = 2n_e d_{hkl} \sin \alpha, \tag{1}$$

where λ is the Bragg diffracted wavelength, n_e is the effective refractive index of the crystal at the wavelength of interest, d_{hkl} is the interdistance between consecutive lattice planes with Miller indices (h,k,l), and α is the Bragg angle. In the used experimental conditions, the diffracted intensity is taken at normal incidence. Consequently, with $\alpha=\pi/2$, we obtain

$$\lambda = 2n_e d_{111}, \tag{2}$$

with $d_{111}=\sqrt{2/3}D$ in the case of a fcc lattice of colloidal spheres with diameter D. The effective refractive index is determined as $n_e=\sqrt{x\epsilon_s+(1-x)\epsilon_a}$, where the dielectric constants of silica and air are $\epsilon_s=2.1$ and $\epsilon_a=1$. The packing fraction $x=0.74$ for closely packed spheres in a fcc lattice.

According to these considerations, $n_e=1.35$ in the case of a close-packed fcc lattice of silica spheres and the expected Bragg peaks for spheres of diameter $D=171$ nm ($D=260$ nm) are $\lambda=376$ nm ($\lambda=572$ nm) in the case of the reference (PSB) samples. These values are in excellent agreement with the maxima of the optical extinction spectra shown in Fig. 2 and can be ascribed to the L gap of a fcc structure. The extinction peak is slightly shifted to shorter wavelengths in the case of the PSB sample, which may be due to shrinking of the silica spheres during the drying process. The nearly perfect symmetry in the shape of the spectra ascertains the very good quality of both samples, free of significant defaults that would otherwise lead to broadening and flattening of the peaks.[17]

B. Microscopic scale: Fluorescence emission spectra

We used microscopic techniques to study the emission of fluorescein molecules in our photonic structures (reference and PSB samples). The recorded emission spectra are highly sensitive to the depth and lateral position of the focus (focal volume investigated) in the sample. As noticed in the literature already,[26] the dip in the emission intensity, usually related to the PSB, increased as the focus penetrated into the sample, according to the growing number of lattice planes between focus and detector. Furthermore, by moving the fo-

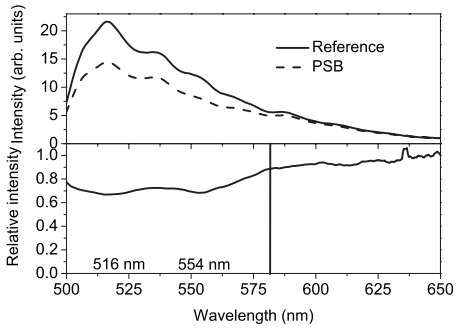

FIG. 4. Averaged emission spectra of 18 ensembles of molecules located at 18 different positions in the reference (solid) or PSB (dash) samples (top) and corresponding relative emission spectrum (bottom). The dip in the relative emission spectrum is blueshifted (12 nm) with respect to the position of the stop band of the PSB sample (Fig. 2). The second dip at 516 nm is located at the peak position of the fluorescein emission spectrum (Ref. 29).

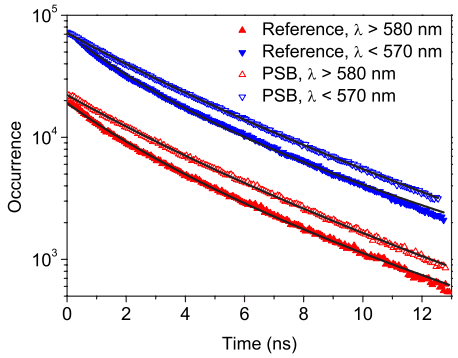

FIG. 5. (Color online) Decay profiles of ensembles of emitters located either in a reference (close triangles) or in a PSB (open triangles) sample. The time lags between excitation and emission have been recorded in two different channels: the photons emitted with $\lambda < 570$ nm (in the stop band of the PSB sample, down triangles) and $\lambda > 580$ nm (outside the stop band of the PSB channel, up triangles) have been collected separately. Note the strong nonexponential decays displayed in this semilogarithm plot.

cus laterally while keeping it at a constant depth, the dip in the emission intensity was also affected, varying significantly from position to position in the sample. Figure 3 shows the PSB emission spectra (dash) taken at 5 (among the 18 investigated) different positions within two distinct PSB samples. Also shown is the reference emission spectrum (solid) obtained by averaging 18 spectra corresponding to 18 positions taken randomly within two reference samples. All spectra are normalized to 1 at the wavelength $\lambda = 650$ nm, i.e., outside (long wavelength range) the stop band exhibited by these structures (Fig. 3), in order to fairly compare them. The emission spectra of fluorescein in PSB clearly exhibit a qualitative change (of convexity) of the shape in the range 540–590 nm (in between the vertical lines represented in the figure, where the stop band is active) with respect to the reference emission spectrum. This change manifests as a dip, with a depth depending on the lateral position in the PSB sample where the recording of the emission spectrum took place. Interestingly, a significant dip is also observable at lower wavelength, namely, at the peak position of the emission spectrum ($\lambda = 516$ nm), where the effect of the stop band is normally vanished.[29]

In order to get a quantitative estimation of these dips, we calculated the averaged PSB emission spectrum (average of 18 spectra corresponding to 18 positions taken randomly within the two PSB samples investigated), normalized it to 1 at $\lambda = 650$ nm, and divided it by the averaged and normalized reference emission spectrum. Figure 4 shows the results of these manipulations with the reference (solid) and PSB (dash) emission spectra on the top and the divided spectrum on the bottom of the figure. The two above mentioned dips are located at $\lambda = 516$ nm, i.e., precisely at the peak maximum of the fluorescein emission spectrum and $\lambda = 554$ nm. The latter dip is slightly blueshifted with respect to the peak maximum of the stop band of the PSB sample ($\lambda = 566$ nm, Fig. 3), as already noticed previously.[30]

C. Microscopic scale: Spontaneous emission rates

Besides getting the emission spectra at different positions in the samples, our setup allows us to also determine fluorescence decays (single photon timing) by recording the histograms of the time lags between excitation photons and fluorescence photons. In order to distinguish between photons emitted at a transition frequency in (mainly $\lambda < 570$ nm) and out ($\lambda > 580$ nm) of the range of the dip of the PSB emission spectrum (Fig. 4), we determined the fluorescence decays collected for both wavelength ranges. Figure 5 shows the fluorescence decays of all photons emitted at a particular position of a reference (close triangles) and PSB (open triangles) samples. Clearly, the decays exhibit a nonexponential behavior. The origin of such nonexponential behavior has been discussed recently in the literature in the case of quantum dots embedded in fcc inverse opals consisting of air spheres in a titania backbone.[21,22] These authors attribute this complex behavior to one or more of the following four reasons. (i) As the emitters are distributed at different positions and orientations in the unit cell of a PC, they experience different LDOSs. (ii) Single emitters may reveal a nonexponential decay due to van Hove singularities in the LDOS.[31] (iii) Nonexponential decays may appear if the emitters have more internal levels than the usually considered two level systems. (iv) Temporal fluctuations of the emitter environment on time scales larger than the fluorescence lifetime can lead to apparent nonexponential decays.

At first glance, we may exclude reasons (ii)–(iv) to affect our results. Indeed, van Hove singularities in the LDOS can only be observed with single molecule experiments, which is not the case here. Furthermore, the fluorescein molecules used in this study have a quantum yield of $\Phi = 0.97$, which rules out practically the contribution of any nonradiative decay channel, and have a single exponential decay with a lifetime of 4 ns in ethanol. This suggests that even relative large intermolecular fluctuations in the rate of the nonradiative decay will only marginally influence the fluorescence decays. We are thus left with reason (i) as the possible cause of the nonexponential decays observed in Fig. 5, i.e., the curves result from a distribution of radiative decay rates caused by a spatial and orientational variation of the LDOS.

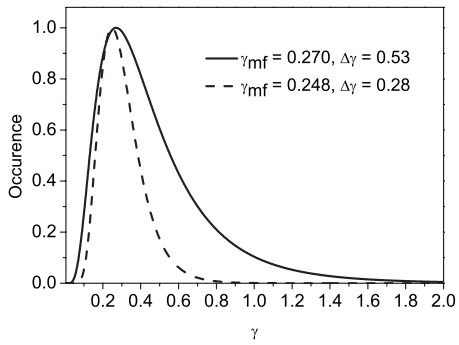

FIG. 6. Continuous distributions of decay rates obtained in the fitting of the nonexponential decay profiles shown in Fig. 5. The two curves correspond to the decay profiles of an ensemble of molecules in the reference (solid) and PSB (dash) samples in the blue zone of the spectra ($\lambda < 570$ nm).

Accordingly, we applied the framework developed in Refs. 21 and 22 to analyze our results. The procedure consists in modeling the curves with a continuous distribution of decay rates:

$$I(t) = I(0)\int_{\gamma=0}^{\infty} \phi(\gamma)\exp(-\gamma t)d\gamma, \tag{3}$$

where $\phi(\gamma)$ is the log-normal distribution of decay rates with dimension of time:

$$\phi(\gamma) = A\exp\left(-\frac{\ln^2(\gamma/\gamma_{mf})}{w^2}\right), \tag{4}$$

where γ_{mf} is the most frequent decay rate corresponding to the maximum of $\phi(\gamma)$, w is a dimensionless width parameter that determines the distribution width at $1/e$,

$$\Delta\gamma = 2\gamma_{mf}\sinh(w), \tag{5}$$

and A is a normalization constant such that $\int_{\gamma=0}^{\infty}\phi(\gamma)d\gamma = 1$. The important feature of the log-normal distribution is its positiveness, which excludes the occurrence of unphysical negative decay rates and a full description in terms of only two parameters γ_{mf} and $\Delta\gamma$.

Figure 5 shows the excellent fits performed on the experimental decay curves by using this model. It is important to note here that neither a double exponential nor a stretched Kohlrausch-Williams-Watts (KWW) exponential form was able to fit appropriately these curves. Figure 6 shows the resulting decay-rate distributions in the case of the two curves measured in the wavelength range $\lambda < 570$ nm (Fig. 5), i.e., in the spectral range where the PSB is active. Clearly, for the examples chosen, the distribution of decay rates measured at one position in the reference sample (solid) is much broader than the one in the PSB sample (dash). Also, the most frequent rates γ_{mf} slightly differ between the two samples. In order to investigate if such differences reflect the fact that we have a stop band (PSB sample) or not (reference sample) in the spectral zone of interest or merely result from the heterogeneity of the samples, as already observed in the emission spectra (Fig. 3), we determined the decay-rate distributions at 18 positions both in the reference and PSB samples and for both spectral regions ($\lambda < 570$ nm, $\lambda > 580$ nm). Figure 7 (left) shows the most frequent decay rates γ_{mf} (top) and widths $\Delta\gamma$ (bottom) of these decay-rate distributions of an ensemble of molecules as a function of position in the reference (close triangles) and PSB (open triangles) and in the blue $\lambda < 570$ nm (down triangles) and red $\lambda > 580$ nm (up triangles) spectral ranges.

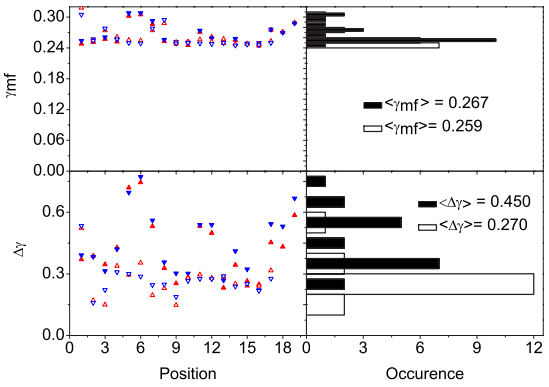

FIG. 7. (Color online) Left: Most frequent decay rates γ_{mf} and widths $\Delta\gamma$ of the continuous distributions of decay rates $\phi(\gamma)$ for 18 ensembles of molecules measured at 18 different positions in the reference (close triangles) or PSB (open triangles) samples. The down triangles correspond to the emission at $\lambda < 570$ nm (in the stop band of the PSB sample) and the up triangles correspond to the emission at $\lambda > 580$ nm (outside the stop band of the PSB channel) of these ensembles of emitters. Right: Corresponding distributions of these two parameters in the blue zone of the spectra ($\lambda < 570$ nm). The errors on the determination of the γ_{mf} and $\Delta\gamma$ were estimated to be 0.004 and 0.01, respectively.

Figure 7 exhibits several interesting features. (i) For both types of samples (reference and PSB) and both spectral ranges (blue and red), the distribution of the widths $\Delta\gamma$ among various positions of the sample is much broader than that of the most frequent rates γ_{mf}. (ii) For PSB (reference) samples, the widths of the decay-rate distributions are (twice) as large as the most frequent rates. (iii) In most cases (all minus 1), the γ_{mf} corresponding to ensembles of molecules located in the reference sample in the red spectral zone (close up triangles) are smaller than or equal to the corresponding ones in the blue spectral zone (close down triangles). (iv) Conversely, most (all minus 3) γ_{mf} corresponding to ensembles of molecules located in the PSB sample in the red spectral zone (open up triangles) are larger than the corresponding ones in the blue spectral zone (open down triangles). These observations are further exemplified on the right side of Fig. 7, which shows the distributions of the γ_{mf} and $\Delta\gamma$ of ensembles of molecules located in the reference (solid) and PSB (dash) samples in the blue spectral range, i.e., for $\lambda < 570$ nm where the PSB is active.

These observations exemplify the power of the approach, in giving detailed physical information on decay rates. They point (i) to the heterogeneity of the samples on the local scale and (ii) to the fact that the reference samples seem more heterogeneous than the PSB samples. Furthermore, the dependence of the rate $\gamma \propto \omega^3$ on the third power of the transition frequency ω for emitters embedded in an effective homogeneous medium (EHM, the reference sample has its

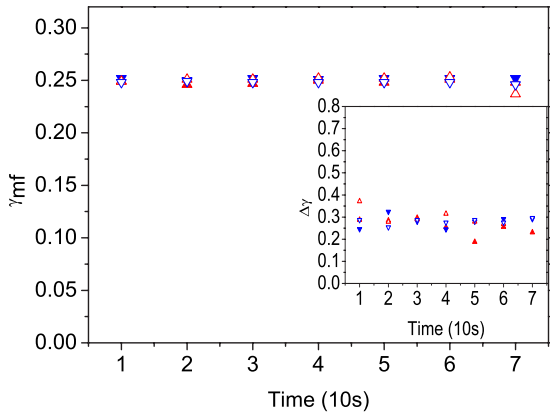

FIG. 8. (Color online) Most frequent decay rates γ_{mf} and widths $\Delta\gamma$ of the continuous distributions of decay rates $\phi(\gamma)$ for one ensemble of molecules measured as a function of time at one position in the reference (close triangles) or PSB (open triangles) samples. The symbols have the same meaning as in Fig. 7. The errors on the determination of the γ_{mf} and $\Delta\gamma$ were estimated to be 0.004 and 0.01, respectively.

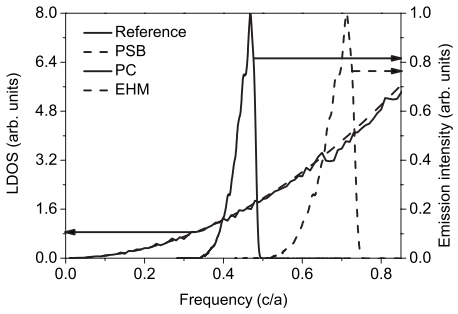

FIG. 9. Computed (averaged over 992 positions of the Wigner-Seitz cell of the PC) local photonic density of states (LDOS) as a function of frequency for an ensemble of emitters located in a photonic crystal (solid line). The dash line corresponds to the extrapolation toward higher frequencies of the LDOS of an effective homogeneous medium, which manifested at the low frequencies of the averaged LDOS of the PC. The reference emission spectra of the fluorescein are also plotted as a function of frequency rescaled by a $(=\sqrt{2}D)$, the lattice constant of the reference (solid) or PSB (dash) samples.

stop band out of the emission range of the emitter and so acts as an EHM in the considered range) explains the observation (iii) that the largest γ_{mf} are observed for the largest transition frequencies collected. Finally, we conjecture that the converse observation (iv) of the smallest γ_{mf} observed for the largest transition frequencies collected in the case of emitters in the PSB sample results from the stop band active in the zone $\lambda < 570$ nm (Fig. 3), which inhibits the emission of the molecules having their transition frequency in this range (LDOS effect).

Figure 8 exhibits the most frequent rates γ_{mf} and the widths $\Delta\gamma$ of the decay-rate distributions of an ensemble of molecules located in the reference sample (close triangles) and in the PSB sample (open triangles) at a given position as a function of time. The aim here is to investigate if the nonexponential character of the decay profiles (Fig. 5) is not affected in time by some environmental change occurring on the time scale of the experiment. Clearly, it is not the case, as exemplified by the (almost) constant values of the various γ_{mf} and $\Delta\gamma$ [emitters in the reference (PSB) samples, with transition frequencies in the red (blue) spectral range]. Let us note once more the validity of observations (i)–(iv) here above concerning the large width $\Delta\gamma$ of the decay-rate distributions and the dependence of the γ_{mf} on the transition frequencies of the emitters embedded either in the reference or in the PSB samples. In order to further validate the influence of the LDOS present in these structures on the observation of such features, we performed some theoretical investigations of the LDOS.

IV. THEORETICAL RESULTS

The local photonic density of states counts the number of electric field modes per unit volume at a given frequency ω to which the molecular transition dipole moment oriented along $\vec{\mu}$ and positioned at $\vec{r}$ can couple. In a PC, knowing the eigenfrequencies $\omega_{n\vec{k}}$ of the eigenmodes of the electric field $\vec{E}_{n\vec{k}}(\vec{r})$ with wave vector $\vec{k}$ and band index n, the projected LDOS is defined as[31,32]

$$\rho(\omega,\vec{r},\vec{\mu}) = \frac{1}{2\pi^3}\sum_n \int_{1.BZ} d\vec{k}\,\delta(\omega-\omega_{n\vec{k}})|\vec{\mu}\cdot\vec{E}_{n\vec{k}}(\vec{r})|^2. \quad (6)$$

The integral runs over all wave vectors within the first Brillouin zone (1.BZ). In this paper, we study the spontaneous emission from an ensemble of molecules with randomly orientated transition dipole moments. Accordingly, the dipole orientation is averaged over all solid angles, which gives

$$\rho(\omega,\vec{r}) = \frac{1}{6\pi^2}\sum_n \int_{1.BZ} d\vec{k}\,\delta(\omega-\omega_{n\vec{k}})|\vec{E}_{n\vec{k}}(\vec{r})|^2. \quad (7)$$

The scheme of our LDOS calculations proceeds as follows. Firstly, fully vectorial eigenmodes of Maxwell's equations with periodic boundary conditions were computed by preconditioned conjugate-gradient minimization of the block Rayleigh quotient in a plane wave basis, using a freely available software package.[33] The eigenfrequencies and electric field energy densities up to the eighth band were computed for 87 126 equally spaced k points in the 1.BZ. The irreducible Wigner-Seitz cell (WSC) was divided into 4096 segments, respectively, defining the spatial resolution of the calculated field energy densities. Secondly, the calculation of the LDOS was performed for each possible location $\vec{r}$ of the emitter in the PC, i.e., at each segment (992 in total) of the WSC containing an air-silica sphere interface, owing to the condition that the local (segment) dielectric constant $1.1 < \epsilon(\vec{r}) < 2.0$. Due to the spatial distribution of the fluorescein molecules in our samples, we always measure an average fluorescence signal from various lattice sites and therefore have contributions from the LDOS at different positions $\vec{r}$. Accordingly, we have also calculated the LDOS averaged over the 992 predefined segments. The resulting LDOS is shown in Fig. 9 (solid) together with the reference emission spectra of the fluorescein molecules rescaled on the fre-

quency scale with respect to the unit cell parameter of the lattices built from the assembly of small (large) spheres in the case of the reference (PSB) samples. The calculations reveal a simple parabolic behavior in the lower frequency part of the LDOS. This behavior has been extrapolated to higher frequencies (dash) and represents the expected behavior of an EHM $\rho(\omega,\vec{r}) \propto \omega^2$. The validity of this law proves that the PCs (reference or PSB samples) do not affect the propagation of light at these low frequencies and justifies the normalization of the emission spectra on the long wavelength part. Figure 9 shows that the averaged LDOS, and therefore the total radiative rate of the molecules, is not disturbed very much by the photonic band structure. Only a slight decrease in the mode density is observable between $0.66c/a$ and $0.80c/a$.

In order to compare these results with the experimental ones, the spontaneous emission rate of the molecules has to be calculated. According to Fermi's golden rule (within the Wigner-Weisskopf approximation[34] expressed in SI),

$$\Gamma(\omega_{if},\vec{r}) = \frac{4\pi}{3\hbar^2}\rho(\omega_{if},\vec{r}), \tag{8}$$

where $\hbar$ is the reduced Planck constant $\hbar = \frac{h}{2\pi}$. This expression is valid only when the transition is sharp and its spectrum can be associated with a Dirac delta function $\delta(\omega - \omega_{if})$, with ω_{if} the frequency of the transition. Nevertheless, real transitions have a finite width described by the line shape function $\int g(\omega)d\omega$, with $g(\omega)$ the homogeneous line shape of the transition. Accordingly, the spontaneous emission rates are expressed as

$$\Gamma(\vec{r}) = \frac{4\pi}{3\hbar^2}\int_0^\infty d\omega\rho(\omega,\vec{r})g(\omega). \tag{9}$$

It should be noted here that the local field effects[35] are important in determining the spontaneous emission rate. However, our experiments deal with comparisons between inhibited and enhanced effects of the PC's on the spontaneous emission rates in the reference and PSB samples. The reference sample was prepared expressively as a point of comparison for the spontaneous rate. As the host mediums of the reference and PSB samples are of the same nature (74% of silica particles), it is unnecessary to consider the modification of the local field effects in the calculations of the rates.

In determining the spontaneous emission rate of molecules located either in a reference or in a PSB sample (solid and dash spectra in Fig. 9, respectively), we choose to compute the relative spontaneous emission rate, i.e., the spontaneous emission rate determined by Eq. (9) in the case of the sample (solid line) normalized by the one of the corresponding EHM (dash line). The relative spontaneous emission rates observed are 0.99 in the case of the reference sample and 0.95 in the case of the PSB sample. This calculated 4% decrease in the rates of emitters embedded in the PSB samples compared to emitters in the reference samples agrees very well with our experimental results (Fig. 7), where the averaged values of the most frequent rates γ_{mf} over all 18 positions in the reference and PSB samples are $\langle\gamma_{mf}\rangle = 0.267$ and $\langle\gamma_{mf}\rangle = 0.259$, respectively, i.e., a 3% decrease. Such a small difference was expected, in agreement with previous calculations of the LDOS for systems with a low refractive index contrast.[17,26]

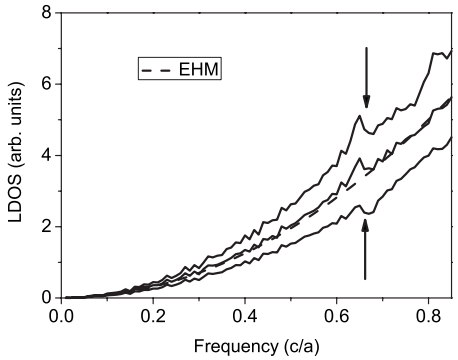

FIG. 10. Computed LDOS for three different positions (among the 992) $\vec{r}_1 = (0.375, 1, 0.125)$, $\vec{r}_2 = (0.625, 0.5, 0.0625)$, and $\vec{r}_3 = (0.0625, 0.75, 1)$ (from bottom to top) of the emitters in the crystal lattice. The dash line corresponds to the LDOS of the effective homogeneous medium obtained by extrapolation from the averaged (on the 992 positions) LDOS of the PC.

The last result concerns the spontaneous emission rates computed on the basis of Eq. (9) with a LDOS averaged over 992 spatial positions (Fig. 9) in the reference or PSB samples. Our experimental results exhibit strongly nonexponential fluorescence decay profiles (Fig. 5) that have been attributed to the spatial and orientational variations of the LDOS. In order to investigate the effect of the spatial variation of the LDOS on the spontaneous emission rate $\Gamma(\vec{r})$, we have calculated the latter at the 992 predefined positions of the WSC. Figure 10 shows the LDOS curves (solid) as a function of frequency for three different positions in the WSC of the PC. The three curves differ significantly. Also shown in the figure is the LDOS of the EHM as extrapolated from the averaged (on the 992 positions, see *supra*) LDOS. The ratios exhibited between the curves imply that the spontaneous rates of the molecules possess a wide distribution. To clearly show this, we plot in Fig. 11 the (relative) $\Gamma(\vec{r})$ distributions of ensembles of molecules dispersed homogeneously in the reference (solid) or PSB (dash) samples. Indeed, the distributions are broad with a full width at half maximum of ≈ 0.4 in the case of the reference sample (solid) and ≈ 0.2 in the case of the PSB sample. Furthermore, the $\Gamma(\vec{r})$ distribution of the PSB sample is clearly shifted to lower values with respect to the one of the reference sample. These results agree nicely with our experimental results as best seen by comparison of Fig. 11 with Figs. 6 and 7 (right). They are also in agreement with previous results described in the literature,[13] concerning dyes (NBIA) embedded in a polymer network filling the voids in an opal structure, and theoretically discussed.[18] It turns out indeed that both the large width $\Delta\gamma$ of the decay-rate distributions and the shift of these distributions in the case of emitters embedded either in the reference and or in the PSB samples are pure LDOS effects.

V. CONCLUSIONS

We have shown in this paper that PCs with relatively low dielectric contrast have significant influence on the emission

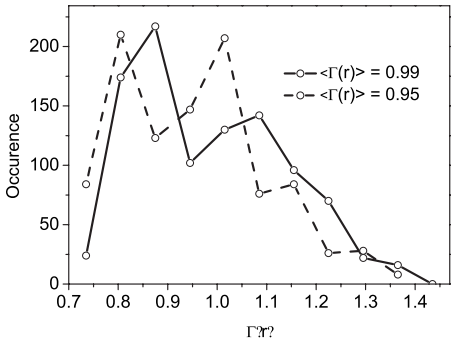

FIG. 11. Spontaneous emission rate distributions computed for emitters spread in all directions at 992 positions of the Wigner-Seitz cell for the reference (solid) or PSB (dash) photonic crystal.

rate of internal emitters. Decay profiles of ensembles of emitters measured at different positions in the PCs have exhibited a nonexponential behavior (Fig. 5). These nonexponential profiles have been best fitted by continuous distributions of decay rates (Fig. 6) and have been attributed, as previously done for ensembles of quantum dots in inverse opals,[21,22] to spatial and orientational variations of the LDOS in the unit cells. The two parameters of the continuous distributions of decay rates, the most frequent decay rate γ_{mf} and the width $\Delta\gamma$ of the distribution, have been shown to slightly vary from position to position in each sample, and also, to a larger extent, when measured either in the reference or PSB samples (Fig. 7). While the variations of these two parameters as a function of the investigated samples (the most frequent rates of the continuous distributions are smaller and their widths are narrower in a PC with a pseudogap acting in the emission range of the emitters than in a PC having the pseudogap out of this range) have been well accounted for by the LDOS and spontaneous emission rate calculations (Figs. 9–11), their slight variation as a function of position in the same sample can only be attributed to some local imperfections in the structure or difference in the concentration of fluorophores at these positions. The latter effects are supposed to also give rise to the various spectra observed as a function of position in a given sample (Fig. 3).

ACKNOWLEDGMENTS

P. Dedecker and M. Sliwa are acknowledged for help in aligning the setup. The authors thank the Research Fund of the KULeuven for financial support through GOA2006/2 and GOA2006/3, ZWAP 4/07 and the Belgium Science Policy through IAP 5/03. The Fonds voor Wetenschappelijk Onderzoek Vlaanderen is thanked for Grants No. G.0421.03 and No. G.0458.06. INPAC is thanked for a postdoctoral grant for B.K.

*renaud.vallee@chem.kuleuven.be

[1] E. Yablonovitch, Phys. Rev. Lett. **58**, 2059 (1987).
[2] H.-G. Park, S.-H. Kim, S.-H. Kwon, Y.-G. Ju, J.-K. Yang, J.-H. Baek, S.-B. Kim, and Y.-H. Lee, Science **305**, 1444 (2004).
[3] M. Grätzel, Nature (London) **414**, 338 (2001).
[4] K. H. Drexhage, J. Lumin. **12**, 693 (1970).
[5] D. Kleppner, Phys. Rev. Lett. **47**, 233 (1981).
[6] K. Wostyn, Y. Zhao, B. Yee, G. de Schaetzen, L. Hellemans, K. Clays, and A. Persoons, J. Chem. Phys. **118**, 10752 (2003).
[7] K. M. Ho, C. T. Chan, and C. M. Soukoulis, Phys. Rev. Lett. **65**, 3152 (1990).
[8] K. Busch and S. John, Phys. Rev. E **58**, 3896 (1998).
[9] M. M. Sigalas, C. M. Soukoulis, R. Biswas, and K. M. Ho, Phys. Rev. B **56**, 959 (1997).
[10] K. Busch and S. John, Phys. Rev. Lett. **83**, 967 (1999).
[11] J. Martorell and N. M. Lawandy, Phys. Rev. Lett. **65**, 1877 (1990).
[12] B. Y. Tong, P. K. John, Y. Zhu, Y. S. Liu, S. K. Wong, and W. R. Ware, J. Opt. Soc. Am. B **10**, 356 (1993).
[13] E. P. Petrov, V. N. Bogomolov, I. I. Kalosha, and S. V. Gaponenko, Phys. Rev. Lett. **81**, 77 (1998).
[14] M. Megens, J. E. G. J. Wijnhoven, A. Lagendijk, and W. L. Vos, Phys. Rev. A **59**, 4727 (1999).
[15] M. Megens, H. P. Schriemer, A. Lagendijk, and W. L. Vos, Phys. Rev. Lett. **83**, 5401 (1999).
[16] E. P. Petrov, V. N. Bogomolov, I. I. Kalosha, and S. V. Gaponenko, Phys. Rev. Lett. **83**, 5402 (1999).
[17] Z. Y. Li and Z. Q. Zhang, Phys. Rev. B **63**, 125106 (2001).
[18] X. H. Wang, R. Wang, B. Y. Gu, and G. Z. Yang, Phys. Rev. Lett. **88**, 093902 (2002).
[19] S. Y. Zhu, G. X. Li, Y. P. Yang, and F. L. Li, Europhys. Lett. **62**, 210 (2003).
[20] P. Lodahl, A. F. van Driel, I. S. Nikolaev, A. Irman, K. Overaa, D. Vanmaekelbergh, and W. L. Vos, Nature (London) **430**, 654 (2004).
[21] A. F. van Driel, I. S. Nikolaev, P. Vergeer, P. Lodahl, D. Vanmaekelbergh, and W. L. Vos, Phys. Rev. B **75**, 035329 (2007).
[22] I. S. Nikolaev, P. Lodahl, A. F. van Driel, A. F. Koenderink, and W. L. Vos, Phys. Rev. B **75**, 115302 (2007).
[23] A. F. Koenderink and W. L. Vos, Phys. Rev. Lett. **91**, 213902 (2003).
[24] W. Stöber, A. Fink, and E. Bohn, J. Colloid Interface Sci. **26**, 62 (1968).
[25] P. Jiang, J. F. Bertone, K. S. Hwang, and V. L. Colvin, Chem. Mater. **11**, 2132 (1999).
[26] M. Barth, A. Gruber, and F. Cichos, Phys. Rev. B **72**, 085129 (2005).
[27] L. M. Goldenberg, J. Wagner, J. Stumpe, B.-R. Paulke, and E. Görnitz, Langmuir **18**, 3319 (2002).
[28] H. Miguez, C. Lopez, F. Meseguer, A. Blanco, L. Vazquez, R. Mayoral, M. Ocana, V. Fornes, and A. Mifsud, Appl. Phys. Lett. **71**, 1148 (1997).
[29] The origin of the second dip in the emission spectrum at $\lambda = 516$ nm (Fig. 3) is not clear, since the stop band is not active in this region anymore (Fig. 2). However, the extinction spectra obtained in Fig. 2 were performed under normal incidence. On the contrary, the fluorescence emission of the dyes is omnidirectional in nature, which might be responsible for this observation.

It is indeed remarkable that the lowering of the LDOS in the PSB sample with respect to an effective homogeneous medium, as obtained by calculations [Eq. (7)], extends to this frequency range (Fig. 9).

[30] K. Baert, K. Song, R. A. L. Vallée, M. Van der Auweraer, and K. Clays, J. Appl. Phys. **100**, 123112 (2006).

[31] N. Vats, S. John, and K. Busch, Phys. Rev. A **65**, 043808 (2002).

[32] R. Sprik, B. A. van Tiggelen, and A. Lagendijk, Europhys. Lett. **35**, 265 (1996).

[33] S. G. Johnson and J. D. Joannopoulos, Opt. Express **8**, 173 (2001).

[34] V. Weisskopf and E. Wigner, Z. Phys. **63**, 54 (1930).

[35] R. J. Glauber and M. Lewenstein, Phys. Rev. A **43**, 467 (1991).

Controlling the Fluorescence Resonant Energy Transfer by Photonic Crystal Band Gap Engineering

Branko Kolaric,* Kasper Baert, Mark Van der Auweraer, Renaud A. L. Vallée, and Koen Clays*

Department of Chemistry, K.U. Leuven and the Institute of Nanoscale Physics and Chemistry (INPAC), Celestijnenlaan 200F and 200D, B-3001, Heverlee, Belgium

Received May 23, 2007. Revised Manuscript Received August 9, 2007

The fluorescence of dye molecules embedded in a photonic crystal is known to be inhibited by the presence of a pseudo-gap acting in their emission range. Here we present the first account of the influence that an incomplete photonic band gap or pseudo-gap has on the fluorescence emission and fluorescence resonant energy transfer. By inserting synthetic, donor (D)−acceptor (A)-labeled oligonucleotide structures in self-organized colloidal photonic crystals, we were able to measure simultaneously the emission spectra and lifetimes of both donor and acceptor. Our results clearly show an inhibition of the donor emission together with an enhancement of the acceptor emission spectra, indicating improved energy transfer from donor to acceptor. These results are mainly attributed to a decrease of the number of available photonic modes for radiative decay of the donor in a photonic crystal in comparison to that of the effective homogeneous medium. The fluorescence decay parameters are also dominated by the pseudo-gap acting on the energy-transfer efficiency.

Introduction

Recently, there has been an intensive effort to develop photonic devices based on organic materials, especially DNA.[1] A DNA structure (oligonucleotide) is based on two intertwined spirals of sugar and phosphate molecules mostly linked by hydrogen bonding and electrostatic interactions between base pairs. Synthesizing and manipulating different DNA molecules by physical and chemical techniques can lead to a variety of structures at the nanoscale level.[1] Since the labeling of oligonucleotides is a well-established technology, we use such labeled structures as a tool to investigate the fluorescence resonance energy transfer between D (Cy3)−A (Cy5) pairs (Figure 1) in a photonic crystal. The oligonucleotides allow for the precise control of the distance between the donor and the acceptor. The rigidity of the double strand (ds) linker provides for a very efficient energy transfer between donor and acceptor, relatively insensitive to local fluctuations that might appear in the alternative case of dyes attached to a neutral or charged polymer backbone.[2]

Photonic crystals (PCs) are materials that do not allow propagation of light in all directions, for a given frequency range, due to the periodical change of their refractive index.[3−5] An omnidirectional, propagation-free frequency range is known as a photonic band gap (PBG).[6] It has been shown that an active material (e.g., dye) with a free space radiative transition will be unable to emit a photon, if located deep inside a full PBG, due to the formation of a photon-atom bound state.[7] Therefore, the total inhibition of fluorescence emission at frequencies inside the band gap is a strong indicator for the existence of a full PBG. However, the engineering of such a full band gap photonic crystal in

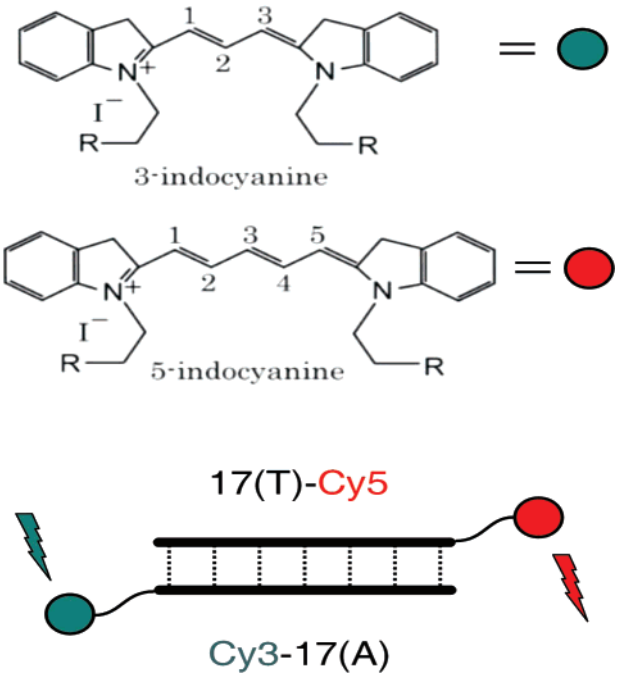

Figure 1. Schematic view of FRET between the two complementary dyes Cy3 and Cy5 attached to a double-strand backbone.

* Authors to whom correspondence should be addressed. E-mail: Branko.Kolaric@chem.kuleuven.be; Koen.Clays@fys.kuleuven.be.

(1) Steckl, J. A. *Nat. Photonics* **2007**, *1*, 3.
(2) Lakowicz, J. R. *Principles of Fluorescence Spectroscopy*; Plenum Press: New York, 1999.
(3) Yablonovitch, E. *Phys. Rev. Lett.* **1987**, *58*, 2059.
(4) Joannopoulos, J.; Meade, R. D.; Winn, J. W. *Photonic crystals: Molding the Flow of Light*; Princton Univ. Press: Princeton, NJ, 1995.
(5) Singh, M. R.; Haque, I. *Phys. Status Solidi C* **2005**, *2*, 2998.
(6) Biswas, R.; Sigalas, M. M.; Subramania, G.; Ho, K.-M. *Phys. Rev. B* **1998**, *57*, 3701.
(7) Vats, N.; John, S.; Busch, K. *Phys. Rev. A* **2002**, *65*, 043808.

10.1021/cm0713935 CCC: $37.00 © 2007 American Chemical Society
Published on Web 10/19/2007

the visible region is very challenging and has not yet been realized experimentally.[8−12]

To date, only a few reports have been published considering the fluorescence resonant energy transfer (FRET), a distance-dependent dipole−dipole interaction between a donor and an acceptor, with an efficiency E_{ET} inversely proportional to the sixth power of the intermolecular separation, in nanostructured environments. In one report, the donor and acceptor dyes were statistically distributed, without control of the D−A distance in a concentrated colloidal suspension.[13] Another report of FRET in an optical microcavity suggests its importance in photonic crystals.[14] FRET plays a key role in photosynthesis[15] and its importance in the improvement of both the functionality and the efficiency of light-emitting diodes and organic lasers is increasing.[16,17] Our aim is to investigate the influence of a photonic pseudogap on the emission properties of D−A pairs embedded in a photonic crystal. Furthermore, with this approach, we extend the investigations of the radiative emission properties of single dyes embedded in a photonic crystal structure,[18−23,34] to FRET in a PC, which will allow us to develop more qualitative and quantitative descriptions of the interaction between emitters and the electromagnetic modes the emitters can couple to in a PC. This last point is crucial for the description of quantum optical phenomena in these materials.[6,9,23]

Experimental Section

To investigate and control the FRET process, two different single-strand (ss) homo-oligonucleotides (either 17 T or 17 A), one labeled with Cy3 and the other with the complementary Cy5 dye, were purchased from Jena Bioscience. These two complementary homo-oligomers were chosen to avoid the possible quenching of fluorescence emission by electron transfer that appears if a guanine base is located in the vicinity of the dye.[24] The double-strand (ds) oligonucleotide backbone was obtained by annealing.[25] For annealing and infiltration the oligonucleotides were dissolved in TRIS buffer pH = 8.5 in the presence of Mg ions.

To anneal the double-strand oligonucleotides, equal volumes of both complementary oligonucleotides (at a concentration of 100 nM dissolved in TRIS which contains 50 mM $MgCl_2$ and 50 mM NaCl, the concentration of magnesium ions was varied to optimize the annealing protocol) was mixed in a 1.5 mL microfuge tube. The tube was heated to 85−90 °C, a temperature approximately 40−50 °C higher than the melting point of the oligonucleotide. After heating, the tube was allowed to cool to room temperature (below 30 °C) on the workbench. After that the tube was stored at 4 °C until use.

Monodisperse spherical silica particles of 208 and 272 nm were synthesized by the Stöber method.[26]

The particles of 208 nm were used for the preparation of PC1 while the particles of 272 nm were used for the preparation of PC2. Photonic crystals were fabricated using the convective self-assembly approach, using the suspending power of ethanol on the silica particles, in combination with an appropriate vapor pressure for this solvent at 32 °C.[27] Both the glass substrates and the vials used for evaporation were cleaned with piranha acid ($^2/_3$ sulfuric acid, $^1/_3$ hydrogen peroxide as oxidant) prior to use. After evaporation, the resulting structures were dried at approximately 130 °C to remove any residual solvent. This resulted in photonic crystals with a face-centered cubic (fcc) or (random) hexagonal closed packing (Rhcp) crystal structures, both with a packing of 74%.

The single-strand and double-strand labeled oligonucleotides were dissolved in TRIS buffer at a 100 nM concentration. The PCs were transferred into the oligonucleotide solution with a total volume of around 500 μL. After 45 min of incubation, the slabs were dried by an argon stream, then dried at room temperature for a few hours, stored overnight at 4 °C, and measured the following day.

The extinction spectra of photonic crystals were measured using a Perkin-Elmer Lambda 900 UV−Vis NIR spectrophotometer. The ranges were presented in Figure 3a (435−480 nm for PC1; 555−640 nm for PC2). All extinction spectra were taken at normal incidence. Fluorescence emission spectra of ss-Cy3 and ds-Cy3-Cy5 dissolved in buffer were measured using a FluoroMax-3 (SPEX Instruments, Edison, NJ).

Fluorescence experiments were performed with an inverted confocal scanning optical microscope (Olympus IX70) and an excitation at 543 nm (8 MHz, 1.2 ps fwhm) from the frequency doubled output of an optical parametric oscillator (GWU) pumped by a Ti:Sapphire laser (Tsunami, Spectra Physics). The excitation light was rendered circularly polarized by a Berek compensator, to avoid the excitation polarization that was perpendicular to the transition dipole moments of the dyes which are randomly oriented in the sample. The excitation light was then directed into the inverted microscope and focused onto the sample through an oil immersion objective (1.3 NA, 100×, Olympus). The photonic crystals were oriented with the (111) direction parallel to the *z*-axis

(8) Hynninen, A.-P.; Thijssen, J. H. J.; Vermolen, E. C. M.; Esther, C. M.; Dijkstra, M.; van Blaaderen, A. *Nat. Mater.* **2007**, *6*, 202.
(9) Maldovan, M.; Ullal, C. K.; Carter, W. C.; Thomas, E. L. *Nat. Mater.* **2003**, *2*, 664.
(10) Park, H.-G.; Kim, S.; Kwon, H. S.; Ju, H. Y.; Yang, G. J.; Baek, K. J.; Kim, H. S. B.; Lee, Y. H. *Science* **2004**, *305*, 1444.
(11) John, S. *Phys. Rev. Lett* **1987**, *58*, 2486.
(12) Yablonovitch, E.; Gmitter, T. J.; Leung, K. M. *Phys. Rev. Lett.* **1991**, *67*, 2295.
(13) Shibata, K.; Kimura, H.; Tsuchida, A.; Okubo, T. *Colloid Polym. Sci.* **2006**, *285*, 127.
(14) Andrew, P.; Barnes, W. L. *Science* **2000**, *290*, 785.
(15) Oppenheimer, J. R. *Phys. Rev.* **1941**, *60*, 158.
(16) Drexhage, K. H. In *Progress in Optics*; Wolf, E., Ed.; North-Holland: Amsterdam, 1974; Vol. XII, pp 163−232.
(17) Gérard, J. M.; Sermage, B.; Gayral, B.; Legrand, B.; Costard, E.; Thierry-Mieg, V. *Phys. Rev. Lett.* **1998**, *81*, 1110.
(18) Yoshino, K.; Lee, S. B.; Tatsuhara, S.; Kawagishi, Y.; Ozaki, M.; Zakhidov, A. A. *Appl. Phys. Lett.* **1998**, *73*, 3506.
(19) Song, K.; Vallée, R. A. L.; Van der Auweraer, M.; Clays, K. *Chem. Phys. Lett.* **2006**, *421*, 1.
(20) Hennessy, K.; Badolato, A.; Winger, M.; Gerace, D.; Atatüre, M.; Gulde, S.; Fäl, S.; Hu, E. L.; Imamoglu, A. *Nature* **2007**, *445*, 896.
(21) Ródenas, A.; Jaque, D.; Sole, J. Garcia; Speghini, A.; Bettinelli, M.; Cavalli, E. *Opt. Mat.* **2006**, *28*, 1280.
(22) Megens, M.; Wijnhoven, J. E. G. J.; Lagendijk, A.; Vos, W. L. *J. Opt. Soc. Am. B* **1999**, *16*, 1403.
(23) Megens, M.; Wijnhoven, J. E. G. J.; Lagendijk, A.; Vos, W. L. *Phys. Rev. A* **1999**, *59*, 4727.
(24) Saito, I.; Takayama, M.; Sugiyama, H.; Nakatani, K. *J. Am. Chem. Soc.* **1995**, *117*, 6406.
(25) Sambrook, J.; Russell, D. W. *Molecular Cloning: A Laboratory Manual*; CSHL Press: Cold Spring Harbor, NY, 2002.
(26) Stöber, W.; Fink, A.; Bohn, E. *J. Colloid Interface Sci.* **1968**, *26*, 62.
(27) Jiang, P.; Bertone, J. F.; Hwang, K. S.; Colvin, V. L. *Chem. Mater.* **1999**, *11*, 2132.
(28) Schlick, T.; Li, B.; Olson, W. K. *Biophys. J.* **1994**, *67*, 2146.
(29) Kunze, K.-K.; Netz, R. R. *Phys. Rev. Lett.* **2000**, *85*, 4389.
(30) Sabanayagam, C. R.; Eid, J. S.; Meller, A. *J. Chem. Phys.* **2005**, *123*, 224708.
(31) Pallavidino, L.; Santamaria Razo, D.; Geobaldo, F.; Balestreri, A.; Bajoni, D.; Galli, M.; Andreani, L. C.; Ricciardi, C.; Celasco, E.; Quaglio, M.; Giorgis, F. *J. Non-Cryst. Solids* **2006**, *352*, 1425.
(32) http://www.iss.com/resources/fluorophores.html. Malicka, J.; Gryczynski, I.; Fang, J.; Kusba, J.; Lakowicz, J. R. *J. Fluoresc.* **2002**, *12*, 439.

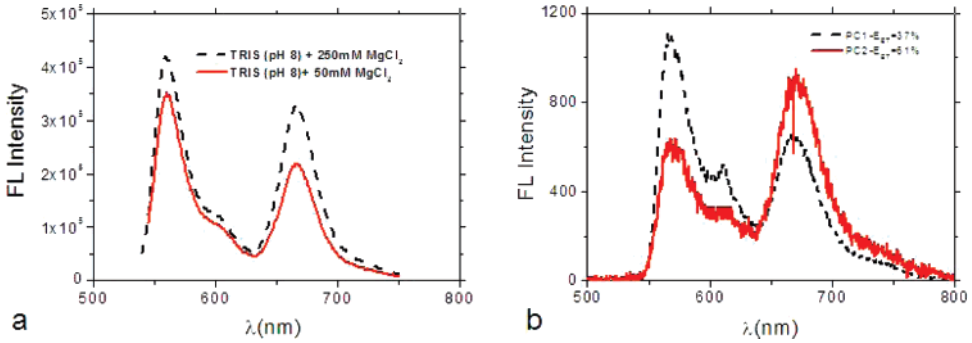

Figure 2. (a) Fluorescence of double-strand Cy3-Cy5 oligonucleotides. The strand concentration was 0.1 μM. The oligonucleotide was excited at 535 nm and the corresponding emission was recorded. (b) Fluorescence spectra of energy transfer between dyes Cy3 and Cy5 attached to a ds oligonucleotide backbone embedded within photonic crystals PC1 and PC2, respectively, measured using a confocal microscope.

of the microscope. Even though the oligonucleotides could be situated on the top of the crystal, it is reasonable to assume that the dye-labeled oligonucleotides present on the top of the crystal did not affect our results as in our detection scheme neither the excitation light nor the emission light collected passed through the top of the crystal. The fluorescence was collected through the same objective, split with a nonpolarizing beam splitter (50:50), and one path was focused into a polychromator (Spectra Pro 150 Acton Research Corporation) coupled to a back-illuminated liquid nitrogen cooled charge-coupled device (CCD) camera (LN/CCD-1340SB, Princeton Instruments) to record fluorescence spectra with a resolution down to 1 nm. In the other path, the fluorescence was again split with a dichroic mirror (Chroma 630dcxr), filtered with one bandpass filter in each path (Chroma HQ580/70 and HQ670/50) to separate the emission originating from Cy3 and Cy5, respectively, and then focused onto two avalanche photodiodes (SPCMAQ- 14, EG & G Electro Optics). The time-resolved data were collected with a TCSPC card (SPC 630, Becker & Hickl) used in the FIFO (First In First Out) mode (256 channels). To summarize, first the emission light was split in a component that went to the CCD camera to measure the fluorescence spectra; the second part was again split to record the fluorescence decay from the donor (Cy3) in one channel and from the acceptor (Cy5) in the second channel. The nonexponential decay curves were fitted with a continuous distribution of decay rates as described in detail elsewhere.[33,34]

Results

Our experimental results show the influence of a PC, with a pseudo-gap acting in the range of the spectral emission of the donor (Cy3), on the fluorescence emission of this donor covalently bound to either a single-strand oligonucleotide (ss-Cy3) or a double-strand oligonucleotide (ds-Cy3-Cy5) and on the FRET between the donor (Cy3) and acceptor (Cy5) of the labeled double-strand (ds-Cy3-Cy5). The labeled strands were infiltrated in photonic crystals with a pseudo-gap (i) outside the spectral range of the donor emission (PC1: reference) and (ii) in the spectral range of the donor emission (PC2: sample), to investigate their influence on both the fluorescence and the fluorescence energy transfer.

Figure 2a shows the fluorescence emission spectra of the annealed ds-Cy3-Cy5 labeled oligonucleotides. To optimize the annealing protocol, different salt concentrations were used.[28,29] Only conditions which were used for infiltration were shown. The highest emission peak corresponds to the donor emission (Cy3) at 562 nm and the second peak to the acceptor emission (Cy5) at 667 nm. With use of eq 1, the energy-transfer efficiency E_{ET} was determined. $E_{ET} = 38\%$ and $E_{ET} = 45\%$ respectively for a concentration of 50 and 250 mM $MgCl_2$ in a TRIS (2-amino-2-hydroxymethyl-1,3-propanediol) buffer

$$E_{ET} = 1 - \frac{I_d}{I_d + I_a} \quad (1)$$

where I_d is the intensity of the donor emission and I_a is the intensity of the acceptor emission.[2,30]

After determination of the best conditions for the annealing, ss-Cy3 and ds-Cy3-Cy5 oligonucleotides were infiltrated in a photonic crystal. Figure 3 (top) shows the extinction spectra of both the PC1 (reference) and the PC2 (sample) photonic crystals. As expected, the pseudo-gap of PC1 is outside the range of emission of the donor (562 nm, Figure 2) and the pseudo-gap of PC2 is inside this range. Furthermore, Figure 3b clearly shows that the presence of ss-Cy3 at micromolar concentrations does not significantly affect the extinction spectra and thus the photonic properties of the crystals. The observed, small blue shift is a consequence of the drying of the crystal and is not connected to the infiltration procedure. The fluorescence emission spectra were recorded to determine the influence of the pseudo-gap on the fluorescence emission of the dyes. The fluorescence emission of Cy3 embedded in PC2 divided by the Cy3 emission from PC1 (after normalization at long wavelength) is shown in Figure 3c. The presence of the photonic pseudo-gap in the spectral range of the emission of Cy3 causes a decrease in the fluorescence emission compared with the emission from the dye embedded in the reference photonic crystal (PC1). A band diagram for photonic crystals similar to the ones used in our experiments can be found in Pallavidino et al.[31]

Figure 2b shows the fluorescence energy transfer between the donor (Cy3) and the acceptor (Cy5) attached to the double-strand oligonucleotide backbone and embedded within photonic crystals PC1 (reference, black curve) and PC2 (sample, red curve). The presence of the pseudo-gap in the spectral region of the donor emission (PC2) causes a decrease

(33) van Driel, A. F.; Nikolaev, I. S.; Vergeer, P.; Lodahl, P.; Vanmaekelbergh, D.; Vos, W. L. *Phys. Rev. B* **2007**, *75*, 035329.
(34) Vallée, R. A. L.; Baert, K.; Kolaric, B.; Van der Auweraer, M.; Clays, K. *Phys. Rev. B* **2007**, *76*, 045113.
(35) Chakraborty, A.; Seth, D.; Setua, P.; Sarkar, N. *J. Phys. Chem. B* **2006**, *110*, 5359.

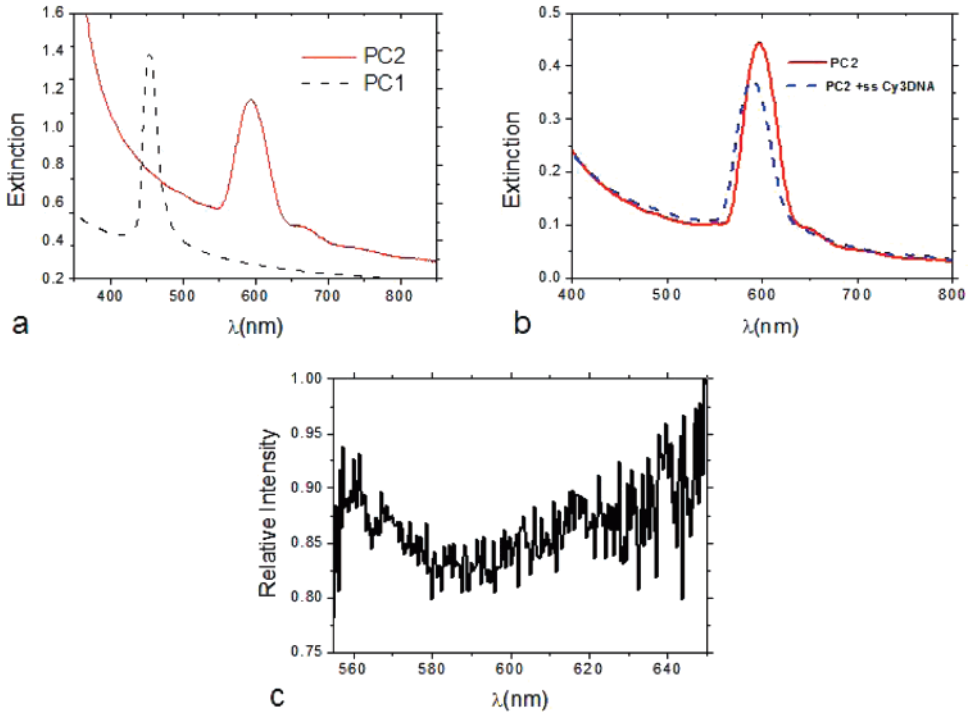

Figure 3. Extinction spectra of the photonic crystal with a pseudo-gap outside the emission region of the dye (PC1) and of the photonic crystal with a pseudo-gap in the range of Cy3 emission (black), (a) without ss-Cy3, (b) after infiltration with ss-Cy3 (0.1 μM) in PC2, and (c) the fluorescence emission of ss-Cy3 embedded in PC2 divided by the Cy3 emission from PC1 (after normalization at longer wavelength).

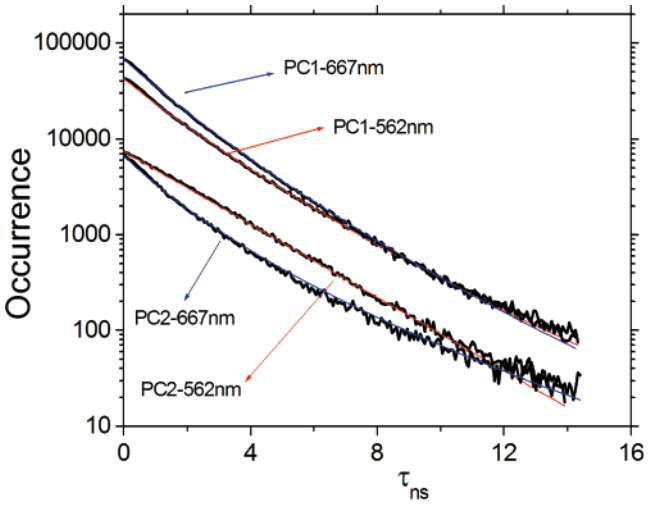

Figure 4. Measured and fitted fluorescence decay of the dyes attached to a ds oligonucleotide and embedded within PC1 and PC2 respectively measured at 562 and 667 nm.

of the spontaneous emission of the donor and an increase of the spontaneous emission of the acceptor. The FRET efficiency (eq 1) is $E_{ET} = 37\%$ for D−A pairs embedded in PC1 (reference) and $E_{ET} = 61\%$ for PC2 (sample).

To get more detailed investigations of the influence exerted by the pseudo-gap on the fluorescence emission of Cy3 and the energy transfer between Cy3 and Cy5, fluorescence decay profiles of ss-Cy3 and ds-Cy3-Cy5 oligonucleotides embedded in photonic crystals PC1 and PC2 were measured and analyzed. A typical example of the fitted decay profiles can be found in Figure 4. Please note that in phosphate buffer (PBS) the pure dyes exhibit single exponential fluorescence decays (decay time of Cy3, 0.3 ns; Cy5, 1.5 ns).[32] The presence of a DNA backbone causes an increase of the decay times of the dyes due to a partial stabilization of the excited

Table 1. Decay of ss-Cy3 Embedded in a Photonic Crystal Was Recorded at 562 nm, Taken from Different Spots in the Crystal[a]

PC1 (τ,Γ_{mf})	PC2 (τ,Γ_{mf})	$\Delta\gamma$ PC1 562	$\Delta\gamma$ PC2 562
2.4 (0.42)	2.8 (0.36)	0.72	0.32
2.4 (0.42)	2.8 (0.36)	0.72	0.37
2.3 (0.43)	2.6 (0.38)	0.68	0.39

[a] τ, average decay time; Γ_{mf}, most frequent rate; $\Delta\gamma$, distribution width.

states of the dyes by the hydrophobic part of the oligonucleotide backbone.[2,30,32] Only bases very close to the dyes can have a significant influence on their excited states. Accordingly, the decay times of Cy3 and Cy5 vary for different oligonucleotides and oligonucleotide structures due to the different direct environment of the dyes.[2,36] In the case of Cy3 and Cy5, the presence of the backbone causes the appearance of multiexponential decay profiles.[29,35,32]

By infiltration of the labeled oligonucleotides in a PC, the decay profiles of the dyes are drastically changed, so that it was no longer possible to fit these decays with a single, double or stretched (KWW) exponential function. According to an approach developed by van Driel and others for emitters in a photonic crystal,[33,34] we used a nonexponential fitting procedure with a continuous distribution of decay rates. The idea behind this model is that the (emission transition dipole moment of the) emitters are spatially and orientationally distributed in the photonic crystal. As such, each emitter probes a different local environment with a different density of optical modes to which it can couple to, leading to a distribution of decay rates. The results from the fitting, i.e., the most frequent decay rates (Γ_{mf}) and the widths ($\Delta\gamma$) of the continuous distributions of decay rates, are shown in Tables 1 and 2. These two parameters are fully described

(36) Hopkins, B. B.; Reich, N. O. *J. Biol. Chem.* **2004**, *279*, 37049.

Table 2. Decays of ds-Cy3-Cy5 Embedded in a Photonic Crystal Were Recorded at 562 and 667 nm, Respectively, Taken from Different Samples[a]

Cy3				Cy5			
PC1 (τ,Γ_{mf}) 562	PC2 (τ,Γ_{mf}) 562	$\Delta\gamma$ PC1 562	$\Delta\gamma$ PC2 562	PC1 (τ,Γ_{mf}) 667	PC2 (τ,Γ_{mf}) 667	$\Delta\gamma$ PC1 667	$\Delta\gamma$ PC2 667
2.4 (0.42)	2.4 (0.42)	0.017	0.017	2.5 (0.40)	1.9 (0.52)	0.28	0.78
2.5 (0.40)	2.4 (0.42)	0.21	0.03	2.5 (0.40)	2.2 (0.46)	0.24	0.43
2.4 (0.42)	2.2 (0.46)	0.17	0.017	2.4 (0.42)	2.0 (0.50)	0.26	0.32
2.3 (0.44)	2.5 (0.40)	0.018	0.018	2.1 (0.48)	1.9 (0.52)	0.4	0.49
2.4 (0.42)	2.5 (0.40)	0.017	0.016	2.0 (0.50)	2.2 (0.46)	0.30	0.46
2.2 (0.46)	2.6 (0.38)	0.018	0.016	2.0 (0.50)	2.2 (0.46)	0.45	0.46
2.3 (0.44)	2.2 (0.46)	0.016	0.015	1.8 (0.54)	1.8 (0.56)	0.54	0.66
2.4 (0.42)	2.4 (0.42)	0.018	0.018	1.9 (0.52)	1.8 (0.54)	0.45	0.53

[a] τ, average decay time; Γ_{mf}, most frequent rate; $\Delta\gamma$, distribution width.

elsewhere.[33,34] The reciprocal value of the most frequent rate $\tau = \Gamma^{-1}$ represents the average decay time of the dye.

Table 1 shows that the infiltration of the ss-Cy3 oligonucleotides in photonic crystals (at void−silica spheres interfaces) causes an increase of the decay time in comparison with the solution measurements.[2,32] This increase can be explained by a geometrical confinement effect which suppresses internal conversion[35] and by the adsorption of the dye on the silica sphere surface which results in a different environment around the dye in comparison with a buffer solution. Furthermore, the presence of the pseudo-gap (PC2) in the emission range of Cy3 causes an increase of the decay time of approximately 0.3 ns in comparison to ss-Cy3 embedded in PC1. Also, $\Delta\gamma$, the width of the distribution of decay rates,[33] decreases by 45% when the dye is embedded in PC2 rather than in PC1.

Table 2 shows that the Γ_{mf} and $\Delta\gamma$ of the continuous distributions of decay rates for Cy3 attached to a ds oligonucleotide are very similar in the PC1 and PC2 photonic crystals. In this case, the energy transfer occurs between the donor (Cy3) and the acceptor (Cy5). The observed width $\Delta\gamma$ of the distributions of Cy3 becomes very narrow, indicating an almost single exponential behavior. For all samples the widths $\Delta\gamma$ of the continuous decay rate distributions for Cy5 in PC2 are higher than for those embedded in PC1.

Discussion

In the previous section, we mentioned that different buffers and concentrations of salts were used to optimize the annealing procedure, i.e., to get a more rigid and compact ds oligonucleotide, which would then optimize the efficiency of the fluorescence energy transfer.[2,36] The presence of salts is crucial for stabilizing the electrostatic interactions between the oligonucleotide strands.[29] The stabilization must be strong enough to overcome interactions between the oligonucleotides and the surface of the colloidal spheres that compose the photonic crystal. These interactions occur during the infiltration of the labeled oligonucleotides in the photonic crystal. If the stabilization is not strong enough, the ds oligonucleotides start to unfold, leading to an increased distance between D−A pairs and the FRET process is suppressed. Figure 2a clearly exhibits that this goal has been reached with an optimized concentration of 250 mM $MgCl_2$ in a TRIS buffer, causing a E_{ET} of 45%.

Recently, it was shown that inside an opal the distribution of dye molecules is not uniform and that near the edges of the crystal it fills voids and channels connecting those voids, whereas in the center dye molecules are primarily found in the voids.[37] The dye aggregation within the voids is concentration-dependent (and is observed at higher concentrations) and depends strongly on solvent, ionic strength, and temperature. Taking into account that we used a labeled oligonucleotide at a concentration of 100 nM, the aggregation within voids should be excluded since aggregation was not observed in the emission spectra. The observed spectra correspond nicely to the spectra of dyes in solution. Considering that both PCs are made from silica spheres, electrostatic and van der Waals interactions, which control the interactions between oligonucleotides and silica, are the same for both PC1 and PC2 due to the identical chemical structure of the silica spheres used to make both PC1 and PC2. The observed differences in energy transfer between PC1 and PC2 can only be attributed to the photonic confinement and the presence of a band gap in PC2 where the photonic band gap position corresponds to the range of the dye emission.

Figure 3 clearly shows that we succeeded in engineering a photonic crystal PC2 with a pseudo-gap in the spectral range of 561−615 nm that covers a substantial part of the fluorescence emission of Cy3. Because of the low dielectric contrast between the silica particles and air, the band is not a full gap and hence the fluorescence emission was not inhibited completely in all directions in this range of frequencies: only a fluorescence emission decrease of the Cy3 dye in PC2 as compared to PC1 was observed. This suppression of emission was expected due to the decrease[38,19,34] of the number of available optical modes in the pseudo-gap for PC2.

In the case of energy transfer between the D−A pairs attached to the ds oligonucleotide backbone, the presence of a pseudo-gap (PC2) in the spectral range of the donor (Cy3) causes a decrease of donor emission and an increase in acceptor emission, with respect to the reference sample (PC1) (Figure 2b). Inside the PC2, the Cy3 spontaneous emission is inhibited. A redistribution of energy thus has to take place so that the nonradiated energy is partially or totally transferred to the acceptor Cy5, leading to an enhancement of the energy transfer with respect to the reference sample (PC1). As such, an increased suppression of the donor emission will lead to the increased enhancement of the

(37) Kurbanov, S. S.; Shaymardanov, Z. Sh.; Kasymdzhanov, M. A.; Khabibullaev, P. K.; Kang, T. W. *Opt. Mater.* **2007**, *29*, 1177.
(38) Hagen, J. A.; Li, W.; Grote, J.; Steckl, A. J. *Appl. Phys. Lett.* **2006**, *88*, 171109.

acceptor emission.[7] At this point, it is not possible to determine quantitatively which part of the energy is transferred to the acceptor and which part is dissipated to the environment. To obtain more detailed information about energy transfer in the photonic crystals, the fluorescence decays were measured using single-photon timing spectroscopy.

The decrease of the spontaneous emission rate for ss-Cy3 within PC2 in comparison to PC1 is around 15% (Table 1). This decrease is bigger than the one observed for fluorescein molecules (4%) embedded in similar colloidal crystals.[34] The decrease with respect to PC1 of both spontaneous emission rates and distribution widths correlates well with the observed suppression of fluorescence in the emission spectra when the labeled oligonucleotide (ss-Cy3) is embedded in, and thus controlled by, the pseudo-gap of PC2.[33,34,39]

In the case of the ds-Cy3-Cy5 structure (Table 2), the vanishing of the difference between the Cy3 decay times in PC1 compared to PC2, which was seen for the ss-Cy3 case (Table 1), is governed by the aperture of a nonradiative channel where energy is transferred to the acceptor. The fact that these decay times are very similar in both samples indicates that the energy-transfer process is taking place at a slightly faster rate than the radiative rate irrespective of the control by the pseudo-gap. The same argument explains the (re) appearance of a single exponential decay ($\Delta\gamma \sim 0.02$): as the energy-transfer rate is the dominant rate, it tends to homogenize the observed rates as well.

In the case of the acceptor Cy5, the average decay rates are similar for all samples whether the ds oligonucleotides are embedded in PC1 or in PC2. It is important to stress that the width of the continuous rate distributions of Cy5 in PC2 are higher than the ones for Cy5 embedded in PC1. As the energy transfer is enhanced in PC2, more emitters, situated at different locations with different orientations, are excited, which leads to a higher $\Delta\gamma$. This increase of $\Delta\gamma$ correlates nicely with the enhancement of energy transfer in PC2 observed in the steady-state measurements.

(39) Baert, K.; Song, K.; Vallée, R. A. L.; Van der Auweraer, M.; Clays, K. *J. Appl. Phys.* **2006**, *100*, 123112.

Conclusion

We have shown that photonic crystal band gap engineering of a pseudo-gap can be used to modify the FRET between a D−A pair. Steady-state spectra of the donor and acceptor dyes embedded in photonic crystals clearly show that a correctly engineered pseudo-gap causes a decrease in donor emission and an increase in acceptor emission. The suppression of the donor emission and enhancement of the energy transfer is explained by a lack of available modes for radiative decay of the donor in the photonic crystal compared with the effective homogeneous medium. The influence of the photonic crystal on energy transfer is confirmed by the decay time of the dyes. The photonic crystal modifies the absolute value of the decay time of the dye and causes nonexponential fluorescence decays. The most frequent decay rate Γ_{mf} and the distribution width $\Delta\gamma$ for a Cy3 labeled ss oligonucleotide decrease when it is embedded in a PC that suppresses Cy3 emission as compared to a PC that does not. In the case of FRET in a photonic crystal, differences in the decay rates between Cy3 embedded in PC1 and PC2 disappear due to the opening of a nonradiative channel which transfers energy from the donor to the acceptor.

Acknowledgment. M. Sliwa is acknowledged for help in aligning the setup. The authors thank the Research Fund of the KULeuven for financial support through GOA2006/2 and GOA2006/3, ZWAP 4/07, and the Belgium Science Policy through IAP 5/03. The Fonds voor Wetenschappelijk Onderzoek Vlaanderen is thanked for a postdoctoral fellowship for R. A. L. V. and for Grants G.0421.03 and G.0458.06. INPAC is thanked for a postdoctoral grant for B. K.

CM0713935

Colloids and Surfaces A: Physicochem. Eng. Aspects 339 (2009) 13–19

Contents lists available at ScienceDirect

Colloids and Surfaces A: Physicochemical and Engineering Aspects

journal homepage: www.elsevier.com/locate/colsurfa

Engineering colloidal photonic crystals with magnetic functionalities

Wim Libaers[a], Branko Kolaric[a,b], Renaud A.L. Vallée[a,c], John E. Wong[d], Jelle Wouters[a], Ventsislav K. Valev[a], Thierry Verbiest[a], Koen Clays[a,*]

[a] Department of Chemistry, K.U. Leuven and Institute of Nanoscale Physics and Chemistry (INPAC), Celestijnenlaan 200D, 3001 Heverlee, Belgium
[b] Laboratoire Interfaces & Fluides Complexes, Centre d'Innovation et de Recherche en Matériaux Polymères, Université de Mons Hainaut, 20 Place du Parc, B-7000 Mons, Belgium
[c] Centre de Recherche Paul Pascal (CNRS), 115 avenue du docteur Schweitzer, 33600 Pessac, France
[d] RWTH Aachen University, Institute of Physical Chemistry, Landoltweg 2, 52056 Aachen, Germany

ARTICLE INFO

Article history:
Received 16 May 2008
Received in revised form 9 January 2009
Accepted 15 January 2009
Available online 23 January 2009

Keywords:
Photonic crystals
Magnetic colloids
Faraday rotation
Maghemite
Superparamagnetic

ABSTRACT

An engineering approach towards combined photonic band gap properties and magnetic functionalities, based on independent nanoscale engineering of two different materials at different length scales, is conceptually presented, backed by simulations, and experimentally confirmed. Large (>200 nm) monodisperse nanospheres of transparent silica self-assemble into a photonic crystal with a visible band gap, which is retained upon infiltration of small (<20 nm) nanoparticles of magnetic iron oxide. Enhancing and tuning Faraday rotation in photonic crystals is demonstrated.

© 2009 Elsevier B.V. All rights reserved.

1. Introduction

Magnetic nanoparticles are of great importance for various fields of chemistry and physics such as magnetic fluids and drug delivery, and magneto-optic data storage [1–8]. Considering their wide range of applications, various methods have been developed for their synthesis [1–4,9–11]. The size of these magnetic nanoparticles affects their properties. When the size of such a particle lies in the range of 5–25 nm, superparamagnetic behaviour is observed, i.e. every single nanoparticle becomes a single domain [1], behaves like a giant paramagnetic atom in a magnetic field and shows a fast response to magnetic fields with negligible remanence, which is essential for various applications [1]. In our research, we intend to use the superparamagnetic properties of iron oxide particles in order to design photonic crystals (PCs) with magnetic functionality.

PCs make up a new class of dielectric material in which the basic electromagnetic interaction is controllably altered over certain frequencies and length scales [12]. This control is achieved by creating spatially periodic dielectric structures in one (1D), two (2D) or three dimensions (3D). Due to the periodicity of the 3D dielectric medium, the propagation of light is inhibited in a given direction and for a given frequency range a photonic band gap is created. A convenient way to produce (3D) photonic crystals consists of ordering, through convective self-assembly [13,14], Langmuir–Blodgett deposition [15,16], sedimentation [17] or spin-coating [18,19] of monodisperse, colloidal spheres in colloidal crystals. In these colloidal crystals, the spectral position, width and amplitude of the band gap is a function of the size of the colloidal spheres and of the refractive index contrast between these spheres and the surrounding voids in the fcc, hcp or rhcp crystal structures obtained by close packing of the spheres. It should also be noted that the band gap in this type of photonic crystal is not a complete, omnidirectional band gap, but has some angular dependence, a property we exploit in this study.

The engineering of a photonic band gap material with magnetic functionality is one of biggest goals in the field of optical materials since magnetic materials can be used for additional control of the properties of light, e.g. nonreciprocal effects in the magnetic PCs [20,21]. Nonreciprocity, which is a known feature of magnetic photonic crystals [22], includes the possibility of unidirectional propagation of light. The use of magnetic particles with a high refractive index, like iron oxide particles, must also lead to an enhancement of the photonic band gap effect, in addition to the magnetic effects expected under application of an external magnetic field [23,24].

Considering our interest in using superparamagnetic particles for photonic applications, a size range of ~10 nm for the iron oxide particles is far too small to be used for fabrication of PCs with applications in the visible range. Additionally, at the bulk level, the magnetic particles are opaque, which is also not useful for photonic applications. In order to engineer crystals useful for photonic applications, we have considered several strategies that aim at increasing

* Corresponding author.
E-mail address: Koen.Clays@fys.kuleuven.be (K. Clays).

0927-7757/$ – see front matter © 2009 Elsevier B.V. All rights reserved.
doi:10.1016/j.colsurfa.2009.01.012

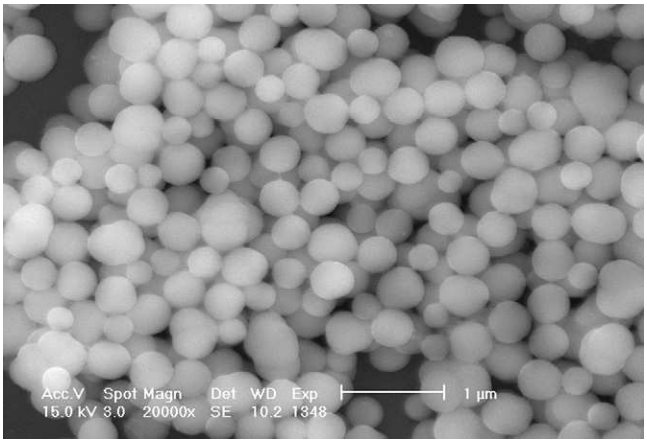

Fig. 1. SEM image of a layer of hybrid particles with an iron oxide core and a silica shell. Clearly, the polydispersity in size of the particles causes a lack of long-range ordering [22].

the size of the magnetic particles and making them transparent. A first attempt was made to create a magnetic photonic crystal in which superparamagnetic particles were used as a core for the synthesis of core–shell particles [25]. In this approach the superparamagnetic core was coated with silica using the classical Stöber method [26]. Note that the shell thickness then determines the total size of the particle. In that approach, the biggest problem was to control the size and monodispersity of the particles, and to suppress their intrinsic instability, which led to further polydispersity due to aggregation over long periods of time. The polydispersity of the core causes polydispersity of the hybrid particle making these hybrids inadequate for photonic applications [25]. The polydispersity of the core–shell particles was observed using SEM imaging (Fig. 1).

In this manuscript, two other approaches are explored to form PCs with magnetic properties. The motivation for our research was to establish a better protocol for designing core/shell photonic crystal as well as to see the effect of a high refractive index material on the photonic band gap. The first approach is to start by synthesizing monodisperse silica nanoparticles covalently functionalized with a coating of superparamagnetic particles on their surface, followed by the assembly of these colloidal particles, hopefully into a photonic crystal. The second approach, conversely, is to start by creating the photonic crystal from monodisperse silica nanospheres, which is only afterwards infiltrated with the superparamagnetic particles. Since iron oxide is incorporated into the silica photonic crystal (also known as an artificial opal), it is possible to at the same time investigate the effect of added high refractive index material on the band gap properties as well as the magnetic effect since the form of iron oxide used here has superparamagnetic properties. Comparative magnetic investigations were performed by measuring the Faraday rotation in a magnetic versus a non-magnetic photonic crystal, and in and out of the band gap.

2. Experimental part

2.1. Synthesis

Acid-stabilized maghemite colloids were prepared based on an existing procedure [9,10]. A solution of 16 mmol $FeCl_3$ and 8 mmol $FeSO_4$ in 200 ml of pure water was stirred at 500 rpm, and a 13.5 ml of 25% NH_3 aqueous solution was added rapidly to form black particles (magnetite), which were quickly precipitated using a permanent magnet. The supernatant was decanted, and the colloids were resuspended using 20 ml of 2 M nitric acid. Subsequently a solution of 10 mmol $Fe(NO_3)_3$ in 30 ml of water was added, and the suspension was stirred at 80 °C for 1 h to oxidize the particles to maghemite. The particles were then washed twice with 50 ml of 2 M nitric acid, and finally resuspended in 40 ml of water.

Silica colloids of approximately 200, 260 and 385 nm diameter were prepared using the Stöber method [26]. These were coated by functionalization with 3-mercaptopropyltrimethoxysilane (MPTMS) [9,10], by mixing 30 ml of a 1 mass% silica particle suspension in ethanol, with 0.5 ml MPTMS (85%) and 0.8 ml NH_3 25% in water. This mixture was stirred vigorously for 45 min, and then the temperature was raised to 76 °C to distill off about one-third of the ethanol. The remainder was then cooled and washed by centrifugation, the supernatant decanted, and the particles resuspended. This procedure was repeated twice with ethanol, then twice with water.

Coating the functionalized silica particles with the iron oxide particles was done by mixing equal volumes of the silica and maghemite suspensions obtained above and shaking strongly for 1 day. Excess iron particles were then removed by repeatedly allowing the silica to settle under gravitational forces and decanting the supernatant, which was then replaced with clean water. For the fabrication of PCs, the water was replaced by ethanol.

Convective self-assembly was used for the preparation of colloidal crystals from these suspensions [25,27]. This procedure is already well-established for unfunctionalized silica particles [13,28]. It is performed by putting a clean glass substrate vertically in a vial containing the ethanolic colloid suspension, and letting the solvent evaporate at a fixed temperature, typically at 33 °C in our experiments. The glass substrate and the vial containing the suspension were cleaned with piranha acid (2/3 sulfuric acid, 1/3 hydrogen peroxide as oxidant) prior to use.

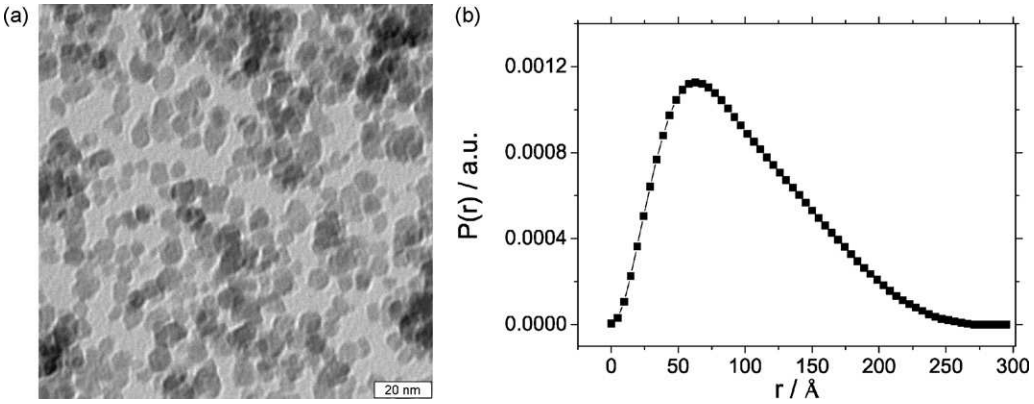

Fig. 2. (a) TEM image of iron oxide particles and (b) pair distance distribution function of the same iron oxide particles obtained by SAXS.

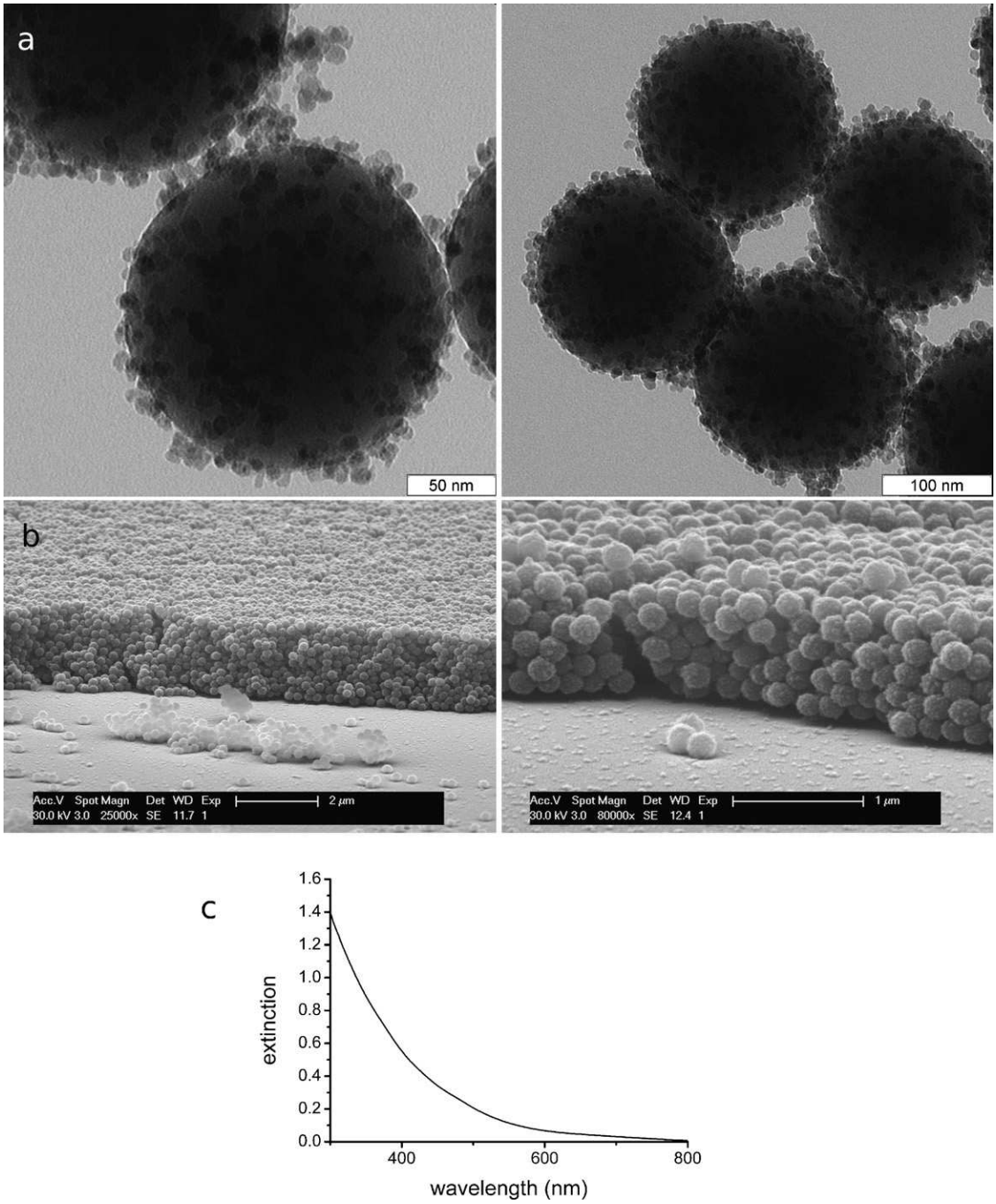

Fig. 3. (a) TEM images at several scales (indicated) of monodisperse spherical MPTMS functionalized silica particles coated by a layer of iron oxide particles. (b) SEM images from a multilayer film of the iron oxide-coated silica particles show a relatively dense packing. Nevertheless, the structures are less ordered than in typical PCs made of noncoated silica. (c) Transmission spectrum of such a multilayer film shows no evidence of a band gap.

3. Methods

Imaging of the particles was done using SEM (Philips Scanning Electron Microscope XL30 FEG). In order to make the surface conductive, a thin layer of gold was sputtered onto the sample.

Optical extinction spectra were performed on large areas (millimeter sized) to ascertain the quality and spectral features of the samples using a PerkinElmer Lambda 900 UV–VIS–NIR spectrophotometer. The vertical axis for these spectra uses a logarithmic scale, defined as follows: extinction = $-\log_{10}$(fraction of light transmitted).

Small angle X-ray scattering (SAXS) measurements were carried out on a S-Max3000 system with a MicroMaxTM-002 + X-ray microfocus generator (Rigaku). The Bayesian weighted distance distribution function p(r) was calculated from the angle dependent scattering using a fit routine included in the manufacturer supplied software [29].

TEM images were provided to us through a cooperation with the Max Planck Institute of Colloids and Interfaces (MPI KGF Golm, Germany).

Faraday rotation was measured at a wavelength of 830 nm on a homemade experimental setup [30,31].

Simulations were performed with the finite-difference time-domain (FDTD) method [32], using a freely available software package with subpixel smoothing for increased accuracy [33].

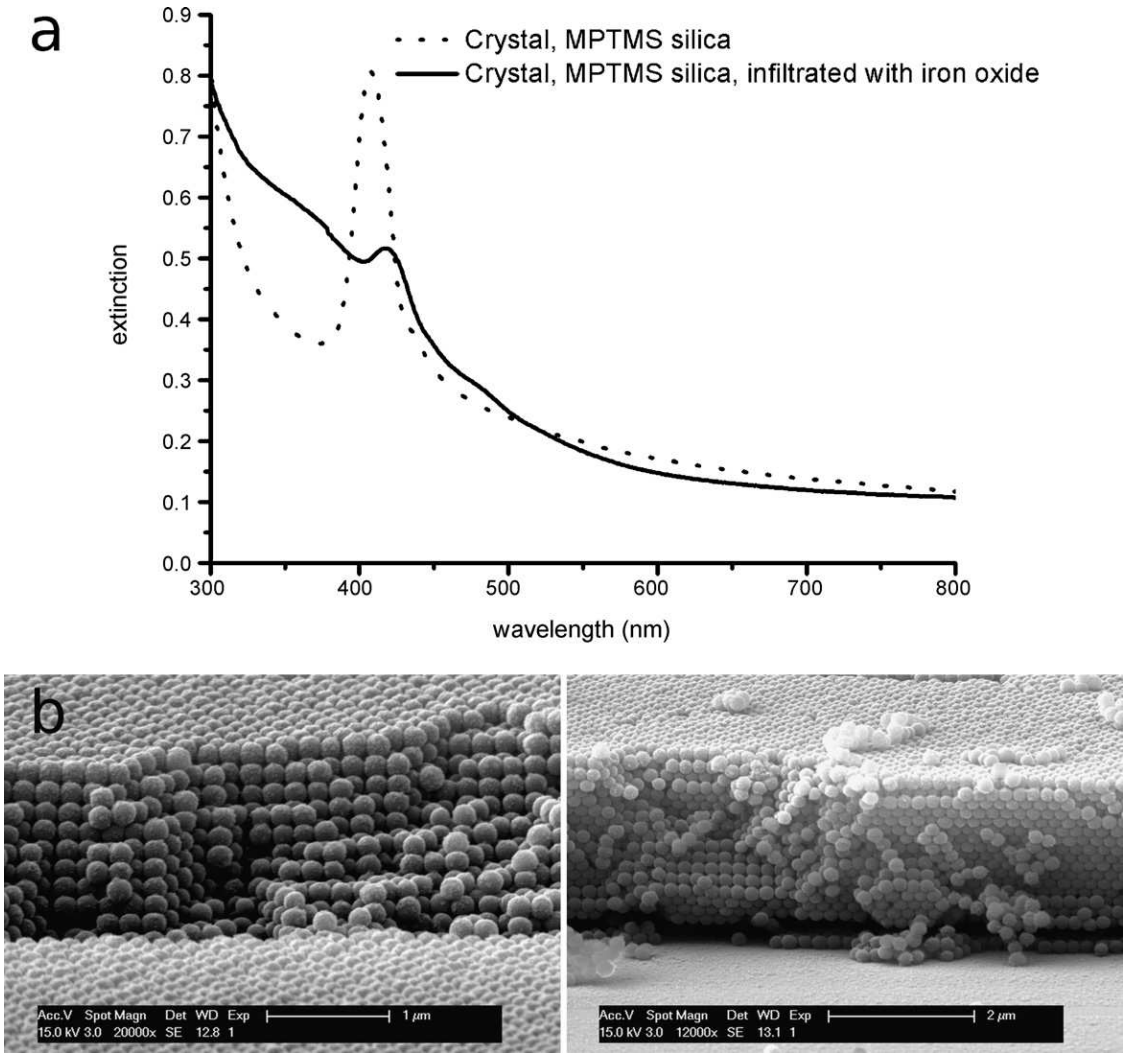

Fig. 4. (a) Extinction spectra recorded in absorbance mode (i.e. the vertical axis is logarithmic). The dotted line shows the spectrum of a crystal made from MPTMS-coated silica colloids, without iron oxide. The solid line shows the spectrum of such a crystal after infiltration with iron oxide particles. (b) SEM images of the crystal that was infiltrated with iron oxide particles after fabrication: long-range ordering is visible.

In all simulations, the colloidal crystals have been represented by monodisperse silica spheres of given size (refractive index of 1.45) arranged along a cubic face centered lattice, i.e. with a packing fraction of 74%. Theoretical calculations were done assuming that the deposition of maghemite was layered, meaning that silica spheres are surrounded by maghemite shells. The filling of the pores (which could be up to 26%) with maghemite (refractive index of 2.42) has been implemented by underfilling the opal with spheres of larger size than the silica ones, but centered at the same positions, thus featuring an underlying interpenetrated maghemite network.

The computational cell, in which the incoming wave propagates along the *z*-direction, has been implemented with periodic boundary conditions in the *x*- and *y*-directions and perfectly matched layers (PMLs) in the *z*-direction. The resolution of the grid has been refined such that the convergence of the results was insured.

4. Results and discussion

Fig. 2a shows a TEM image of the iron oxide particles. The polydispersity of these particles is clearly visible, with an average size of the iron particles determined to be approximately 10 nm. Fig. 2b shows the pair distance distribution function (PDDF) of the iron oxide particles obtained by SAXS. The unsymmetrical shape of the curve suggests that the iron oxide particles are not spherical but more likely to be close to a prolate ellipsoid [34]. D_{max}, defined as the maximum distance within the particle, is about 26.5 nm. From the curve fitting, using a Bayesian weighted inverse Fourier transform [29], a radius of gyration R_G of ~8 nm was calculated for the iron oxide particles. The scattering profile also shows that the particles are highly polydisperse with a mean value around 8 nm. The size of our iron oxide suggests that the particles are superparamagnetic [25]. TEM images (Fig. 2a) allow us to visualize the structure and polydispersity of the iron oxide sample. Note that the TEM images are in excellent agreement with data obtained by SAXS (between 8 and 10 nm).

Because these magnetic particles themselves are too small for photonic applications and due to the lack of transparency, they have to be combined with another material to impart the required structural (monodisperse nanospheres at the optical wavelength scale) and optical properties (transparent). The high polydispersity of the magnetic particles did not allow us to use iron oxide as a core for a shell of silica in order to produce monodisperse core–shell particles, as was described in previous publications [25].

Therefore, we developed an alternative strategy to obtain monodisperse colloids for magnetic photonic crystals, by covalently functionalizing iron oxide particles on top of monodisperse silica spheres. Fig. 3a shows TEM images of iron oxide particles bound to

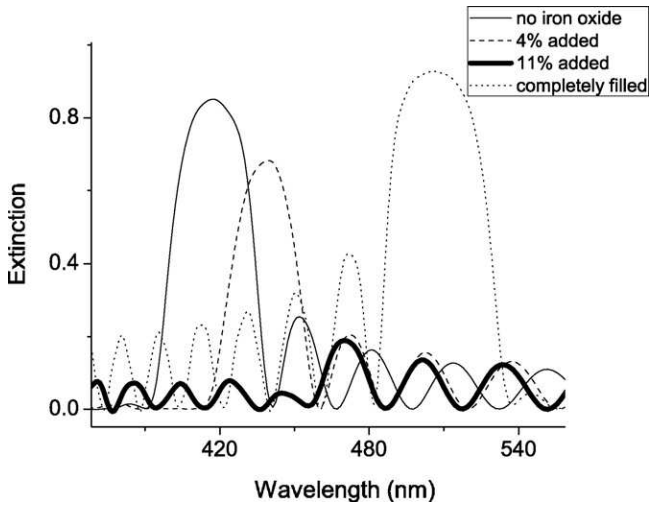

Fig. 5. Simulated transmission spectra showing the effect of increasing amounts of iron oxide in the pores, starting with the silica photonic crystal without iron oxide. A small addition of iron oxide causes a band gap shift without much reduction of the peak. At 11% iron oxide (thick solid line) the band gap almost disappears, to reappear at even longer wavelengths when more iron oxide is introduced until the crystal is completely filled.

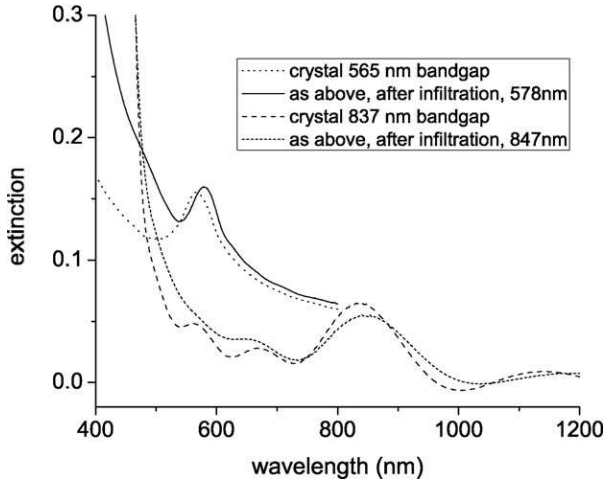

Fig. 6. Photonic crystals with band gaps at 565 and 837 nm, shifting to 578 and 847 nm after infiltration with iron oxide. Only minor amplitude changes are observed, as expected for relatively small amounts of iron oxide compared to the spectra shown in Fig. 4.

the surface of silica particles. These silica/iron oxide coated particles were used in an attempt to fabricate PCs.

Surprisingly these monodisperse hybrid particles cannot produce a highly ordered colloidal crystal as we can see in the SEM images (Fig. 3b). Two factors are probably responsible for this lack of long-range ordering. The most plausible factor is surface roughness which causes steric hindrance between colloids. A second non-negligible factor to be taken into consideration is the presence of magnetic interactions between the magnetic shells. Both of these factors may be responsible for the reduced ordering quality of the crystals made from these hybrid particles, as compared to crystals obtained from bare silica particles.

The lack of ordering is additionally confirmed by optical measurements: transmission spectroscopy does not show a photonic band gap. In fact, the observed spectrum (Fig. 3c) can be explained by a combination of the absorption of the iron oxide and random scattering.

Finally, in order to improve the ordering, colloidal crystals were made by using MPTMS functionalized silica, without iron oxide coating. These crystals show a band gap (Fig. 4a, dotted line) with a peak at 408 nm, in good agreement with the known particle size (200 nm diameter). When these crystals were infiltrated with the iron oxide suspension for 1 h, then rinsed, iron particles remained bound due to the presence of the MPTMS linker. The resulting crystal shows good ordering in SEM imaging (Fig. 4b) and exhibits a band gap in the blue region of the visible spectrum (Fig. 4a, solid line), albeit less pronounced than prior to infiltration, in addition to a strong absorption of light in the UV region due to iron oxide. The shift of the band gap to a slightly longer wavelength can be explained by the introduction of a high refractive index material filling some of the pores in the crystal, thereby increasing the average index of the structure, while the lattice constant remains the same. By using the latter protocol, it is thus possible to fabricate photonic crystals with magnetic functionalities.

The changes in the transmission spectrum observed on infiltration, a shift to longer wavelength and decreased height of the peak, are also confirmed by simulations of a photonic crystal where the voids between the spheres ($n = 1.45$) are gradually filled with a material having a higher index of refraction ($n = 2.42$). These simulation results (Fig. 5) show an increase of the wavelength where the band gap occurs and a decreased peak height as the amount of iron oxide is increased. This explains why we experimentally observe a smaller band gap even though SEM images show good ordering was retained. The simulation also shows the peak becoming bigger again when very large amounts of iron oxide are included, but our infiltration experiments did not reach this point.

Further confirmation of these results was obtained by making photonic crystals from larger silica colloids and infiltrating them with the same iron oxide particles. Such crystals have their band gap at longer wavelengths (see Fig. 6). The iron oxide nanoparticles adsorb on the surface of the silica particles inside the voids of the photonic crystals. It follows that the amount of iron oxide adsorbed is proportional to the surface area, and thus the colloid diameter squared, while the amount of silica is proportional to the volume, or the colloid diameter cubed. Thus, as larger silica colloids are used to prepare the crystal, the relative amount of iron oxide included becomes smaller, and we expect a smaller wavelength shift and

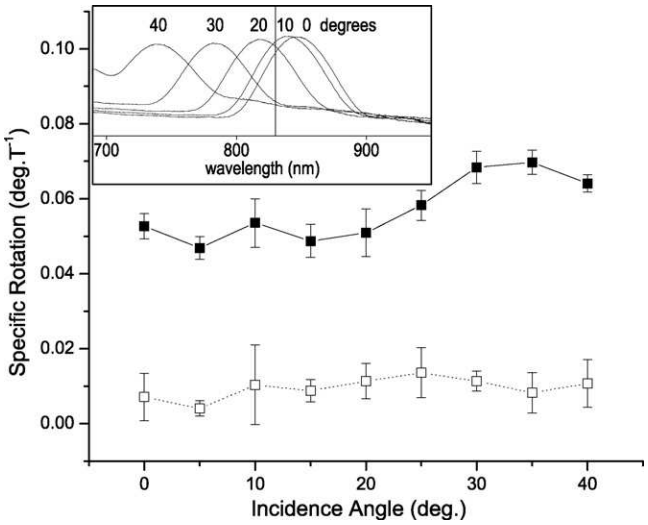

Fig. 7. Experimental setup for Faraday rotation. After passing the polarizer P, the 830 nm laser beam is focused on the sample, mounted on a rotation stage, by a lens L. It is then collimated with a second lens and then traverses an interference bandpass filter IF. Finally, it is directed through the Wollaston prism WP, set at an appropriate angle, at the photodiodes (PDs). The lock-in drives the magnetic coil through the amplifier and detects the signal from the PD in phase and at the same frequency.

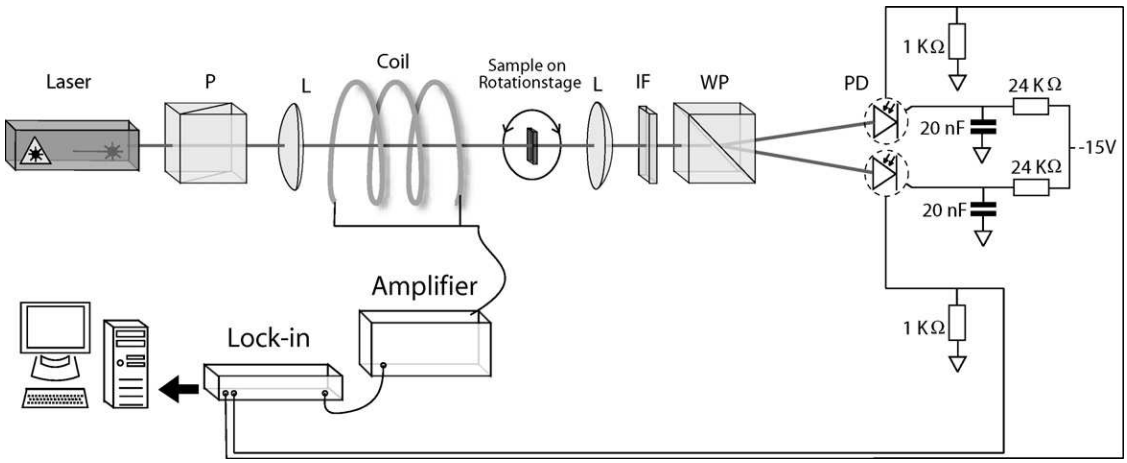

Fig. 8. Results from Faraday rotation measurements at 800 nm on the photonic crystal with band gap at 837 nm (before infiltration with iron oxide particles, open squares) and 847 nm (the same crystal after infiltration, solid squares), with the sample rotated from 0 (perpendicular to the laser beam) to 40°. The inset shows the shift of the band gap to shorter wavelength from 0 to 40° in 10° steps with the laser line at 830 nm indicated by a vertical line.

only a minor effect on the peak height. Transmission spectra confirming this for crystals made using two different colloid sizes are shown in Fig. 6. We also note a pronounced increase in absorption for the infiltrated crystal with band gap at 578 nm, caused by the high optical extinction of the iron oxide at short wavelengths. The much sharper increase of absorption below 500 nm for the crystals with band gap at 837 and 847 nm is however attributed to higher order peaks of the crystal.

In order to demonstrate the effect of magnetic fields on the optical properties of these crystals, Faraday rotation measurements were performed. Faraday rotation data of the photonic crystal before and after infiltration, measured at 830 nm are shown in Fig. 8. The experimental setup is shown in Fig. 7. AC magnetic fields up to 4 G were applied to the sample, ensuring that we stay well below saturation for the magnetic particles. The data show the results of averaging over 4 experiments. The constant background due to the glass substrate was subtracted. After insertion of the magnetic nanoparticles, the specific Faraday rotation of the photonic crystal shows a substantial increase compared to the non-infiltrated crystal. Each sample was measured for incidence angles ranging from 0 to 40° to study the effect of the band gap position for these incomplete band gaps. For these colloidal crystals, which do not exhibit an omnidirectional band gap, the band gap shifts to shorter wavelengths as the sample is rotated away from the perpendicular direction [14]. This means that we can use sample rotation as a way to measure both in and out of the band gap on the same sample. At larger angles, where the band gap is below 830 nm, the Faraday rotation appears to increase even more. Further experimental investigation (wavelength dependence) and theoretical analysis are needed in order to better understand this observation, but a clear positive effect of the presence of the magnetic particles for Faraday rotation in colloidal photonic crystals has been observed.

5. Conclusion

We have developed a successful strategy towards colloidal photonic crystals with combined optical and magnetic properties derived from nanoscale engineering of these two properties at different length scale. Superparamagnetic properties were imparted by the synthesis of small (<20 nm) magnetic maghemite nanoparticles. Optical band gap properties were induced by the convective self-assembly of large (>200 nm) transparent monodisperse silica nanospheres. Insertion of the small magnetic particles after the fabrication of the photonic crystal ensures retention of the photonic band gap upon imparting magnetic functionality. Comparative Faraday rotation measurements confirm the effect of the magnetic particles in a photonic crystal towards enhancing and tuning magnetic interactions in photonic crystals.

Acknowledgments

The authors thank the Research Fund of the KU Leuven for financial support through GOA2006/2 and GOA2006/3, ZWAP 4/07. The Fonds voor Wetenschappelijk Onderzoek Vlaanderen is thanked for a postdoctoral fellowship for R.A.L.V. and for grant G.0458.06. INPAC is thanked for a postdoctoral grant for B.K. All authors warmly acknowledge J. Chen and R. Pitschke (MPI KGF, Golm, Germany) for TEM images, and Thomas Eckert (RWTH Aachen University, Aachen, Germany) for SAXS measurements and useful discussions.

References

[1] A.-H. Lu, E.L. Salabas, F. Schüth, Magnetic nanoparticles: synthesis, protection, functionalization, and application, Angew. Chem. Int. Ed. 46 (2007) 1222.
[2] A.K. Gupta, M. Gupta, Synthesis and surface engineering of iron oxide nanoparticles for biomedical applications, Biomaterials 26 (2005) 3995.
[3] Z. Li, L. Wei, M.Y. Gao, H. Lei, One-pot reaction to synthesize biocompatible magnetite nanoparticles, Adv. Mater. 17 (2005) 1001.
[4] T. Hyeon, Chemical synthesis of magnetic nanoparticles, Chem. Commun. 8 (2003) 927.
[5] A.-H. Lu, W. Schmidt, N. Matoussevitch, H. Bönnermann, B. Spliethoff, B. Tesche, E. Bill, W. Kiefer, F. Schüth, Nanoengineering of a magnetically separable hydrogenation catalyst, Angew. Chem. Int. Ed. 43 (2004) 4303.
[6] S.C. Tsang, V. Caps, I. Paraskevas, D. Chadwick, D. Thompsett, Magnetically separable, carbon-supported nanocatalysts for the manufacture of fine chemicals, Angew. Chem. Int. Ed. 43 (2004) 5645.
[7] S. Mornet, S. Vasseur, F. Grasset, P. Verveka, G. Goglio, A. Demourgues, J. Portier, E. Pollert, E. Duguet, Magnetic nanoparticle design for medical applications, Prog. Solid State Chem. 34 (2006) 237.
[8] H. Schomig, S. Halm, G. Bacher, A. Forchel, A.A. Maksimov, P.S. Dorozhkin, V.D. Kulakovskii, M. Dobrowolska, J.K. Furdyna, Nanooptics on single magnetic semiconductor quantum dots, OSA Trends in Optics and Photonics (TOPS) vol. 89, Quantum Electronics and Laser Science (QELS), Technical Digest, Postconference Edition (Optical Society of America, Washington, DC, 2003) pp. QThe5.
[9] E.M. Claesson, Magnetic core–shell silica particles, Doctoral Thesis, Utrecht University, 2007, ISBN 978-90-393-4559-7.
[10] E.M. Claesson, A.P. Philipse, Monodisperse magnetizable composite silica spheres with tunable dipolar interactions, Langmuir 21 (2005) 9412.
[11] V. Salgueiriño-Maceira, M.A. Correa-Duarte, M. Spasova, L.M. Liz-Marzán, M. Farle, Composite silica spheres with magnetic and luminescent functionalities, Adv. Funct. Mater. 16 (2006) 1266.
[12] E. Yablonovitch, Inhibited spontaneous emission in solid-state physics and electronics, Phys. Rev. Lett. 58 (1987) 2059.
[13] P. Jiang, J.F. Bertone, K.S. Hwang, V.L. Colvin, Single-crystal colloidal multilayers of controlled thickness, Chem. Mater. 11 (1999) 2132.
[14] K. Wostyn, Y.X. Zhao, B. Yee, K. Clays, A. Persoons, G. de Schaetzen, L. Hellemans, Optical properties and orientation of arrays of polystyrene spheres deposited using convective self-assembly, J. Chem. Phys. 118 (2003) 10752.

[15] M. Szekeres, O. Kamalin, R.A. Schoonheydt, K. Wostyn, K. Clays, A. Persoons, I. Dekany, Ordering and optical properties of monolayers and multilayers of silica spheres deposited by the Langmuir–Blodgett method, J. Mater. Chem. 12 (2002) 3268.
[16] S. Reculusa, S. Ravaine, Colloidal photonic crystals obtained by the Langmuir–Blodgett technique, Appl. Surf. Sci. 246 (2005) 409.
[17] H. Míguez, F. Meseguer, C. López, Á. Blanco, J.S. Moya, J. Requena, A. Mifsud, V. Fornés, Control of the photonic crystal properties of fcc-packed submicrometer SiO_2 spheres by sintering, Adv. Mater. 10 (1998) 480.
[18] P. Jiang, M.J. McFarland, Large-scale fabrication of wafer-size colloidal crystals, macroporous polymers and nanocomposites by spin-coating, J. Am. Chem. Soc. 126 (2004) 13778.
[19] A. Mihi, M. Ocana, H. Miguez, Oriented colloidal-crystal thin films by spin-coating microspheres dispersed in volatile media, Adv. Mater. 18 (2006) 2244.
[20] I.L. Lyubchanskii, N.N. Dadoenkova, M.I. Lyubchanskii, E.A. Shapovalov, T. Rasing, Magnetic photonic crystals, J. Phys. D: Appl. Phys. 36 (2003) R227.
[21] M. Inoue, R. Fujikawa, A. Baryshev, A. Khanikaev, P.B. Lim, H. Uchida, O. Aktsipetrov, A. Fedyanin, T. Murzina, A. Granovsky, Magnetophotonic crystals, J. Phys. D: Appl. Phys. 39 (2006) R151.
[22] A. Figotin, I. Vitebsky, Nonreciprocal magnetic photonic crystals, Phys. Rev. E 63 (2001) 066609.
[23] R. Biswas, M.M. Sigalas, G. Subramania, K.-M. Ho, Photonic band gaps in colloidal systems, Phys. Rev. B 57 (1998) 3701.
[24] H.S. Sözüer, J.W. Haus, R. Inguva, Photonic bands—convergence problems with the plane-wave method, Phys. Rev. B 45 (1992) 13962.
[25] K. Baert, W. Libaers, B. Kolaric, R.A.L. Vallee, M. Van der Auweraer, K. Clays, D. Grandjean, M. Di Vece, P. Lievens, Development of magnetic materials for photonic applications, J. Nonlinear Opt. Phys. Mater. 16 (2007) 281.
[26] W. Stöber, A. Fink, E. Bohn, Controlled growth of monodisperse silica spheres in the micron size range, J. Colloid Interface Sci. 26 (1968) 62.
[27] R.A.L. Vallée, K. Baert, B. Kolaric, M. Van der Auweraer, K. Clays, Nonexponential decay of spontaneous emission from an ensemble of molecules in photonic crystals, Phys. Rev. B 76 (2007) 045113.
[28] K. Wostyn, Y.X. Zhao, G. de Schaetzen, L. Hellemans, N. Matsuda, K. Clays, A. Persoons, Insertion of a two-dimensional cavity into a self-assembled colloidal crystal, Langmuir 19 (2003) 4465.
[29] B. Vestergaard, S. Hansen, Application of Bayesian analysis to indirect Fourier transformation in small-angle scattering, J. Appl. Cryst. 39 (2006) 797.
[30] V.K. Valev, J. Wouters, T. Verbiest, Precise measurements of Faraday rotation using ac magnetic fields, Am. J. Phys. 76 (2008) 626.
[31] V.K. Valev, J. Wouters, T. Verbiest, Differential detection for measurements of Faraday rotation by means of ac magnetic fields, Eur. J. Phys. 29 (2008) 1099.
[32] A. Taflove, S.C. Hagness, Computational Electrodynamics: The Finite-Difference Time-Domain Method, third ed., Artech, Norwood, MA, 2005.
[33] A. Farjadpour, D. Roundy, A. Rodriguez, M. Ibanescu, P. Bermel, J.D. Joannopoulos, S.G. Johnson, G. Burr, Improving accuracy by subpixel smoothing in FDTD, Opt. Lett. 31 (2006) 2972.
[34] O. Glatter, in: P. Linder, Th. Zemb (Eds.), Neutrons, X-rays and Light: Scattering Methods Applied to Soft Condensed Matter, North-Holland Delta Series, 2002.

Fine tuning of emission through the engineering of colloidal crystals

Jean-François Dechézelles,[a] Tangi Aubert,[b] Fabien Grasset,[b] Stéphane Cordier,[b] Carlos Barthou,[c] Catherine Schwob,[c] Agnès Maître,[c] Renaud A. L. Vallée,[a] Henri Cramail[d] and Serge Ravaine*[a]

Received 5th April 2010, Accepted 2nd September 2010
DOI: 10.1039/c0cp00129e

We describe the preparation and characterization of photonic colloidal crystals from silica spheres with incorporated luminescent $[Mo_6Br_{14}]^{2-}$ cluster units. These structures exhibit strong angle-dependent luminescent properties. The incorporation of one or several planar defects in the periodic structures gives rise to the creation of a passband in the stopband. In the energy range of this passband, an increase of the emission intensity has been found.

Introduction

Photonic crystals (PCs) are a class of artificial structures with a periodic dielectric function in one, two, or three dimensions, in which the propagation of electromagnetic waves within a certain frequency band is forbidden. This forbidden frequency band has been dubbed the photonic band gap (PBG). The position, width, depth, and shape of the PBG strongly depend on the periodicity, symmetry properties, dielectric constant contrast, and internal lattice structure of the unit cell. There is a common belief that PCs will perform many functions with light that ordinary crystals do with electrons.

Various important scientific and engineering applications, such as control of spontaneous emission,[1–11] zero-threshold lasing,[12] very sharp bending of light,[13,14] light-emitting diodes,[15,16] and so on, have been demonstrated by utilizing the photonic bandgap and/or light-emitters. Especially, a stopband, *i.e.* an incomplete photonic bandgap, can inhibit light propagation in a certain direction for a given frequency. Many groups have reported that PCs can modify significantly the emission characteristics of emitters (organic dyes,[5,17] semiconductors,[7,18] rare earth doped particles,[19,20] *etc.*) as the emission wavelength of the optically-active material overlaps the stopband. In most of these studies, the emitters have been incorporated within pre-fabricated PCs owing to a simple infiltration process. As the efficiency of controlled emission is highly dependent on the organization of the PCs, which may be disturbed by the solvent used, and the homogeneous infiltration of the dyes, we chose to incorporate the emitters in the silica particles themselves, which were thus used to fabricate luminescent colloidal crystals following the strategy reported by only a few groups.[10,21,22]

Moreover, more emphasis in the PCs research field is placed on the incorporation of point, channel, and planar defects within the PCs structures for the creation of localized points and pathways for photons. With regard to the planar defects, which can be introduced within PCs by chemical vapor deposition,[23,24] spin-coating,[25,26] or the Langmuir–Blodgett (LB) technique,[27–31] the emergence of a localized state for photons within the stopband, known as a defect mode, has been revealed. The obtained heterostructures present a dip, also called passband, inside the stopband in the extinction spectrum. As far as we know, there is only one report on the spectral narrowing of emission in self-assembled colloidal photonic superlattices, though no clear effect of the passband was observed in the fluorescence emission spectrum.[32] This situation motivated us to investigate the influence of the introduction of one or several defect layers inside a 3D colloidal crystal on the emission spectrum of the incorporated emitters.

In this paper, we present a study of stopband/passband effects on the spontaneous emission of $[Mo_6Br_{14}]^{2-}$ clusters-doped silica particles organized in 3D colloidal crystals. Let us recall that $[(Mo_6L^i_8)L^a_6]$ cluster units (Fig. 1a, L = halogen and or chalcogen), constitute the basic building blocks in molybdenum octahedral cluster chemistry. The Mo_6 cluster is face-capped by eight inner ligands (L^i) and is additionally bonded to six apical ligands (L^a).[33,34] The physical properties of Mo_6 solid-state compounds are related to the number of electrons available for metal–metal bonding within the cluster (valence electron count, VEC). Mo-centered electrons are located on twelve metal–metal bonding molecular orbitals of the molecular orbital diagram. Their full occupation leads to a closed-shell configuration with a VEC of 24.[35] Using high temperature synthesis, it turns out that halogen ligands favor the formation of solid-state molecular compounds based on $[Mo_6X^i_8X^a_6]^{2-}$ (X = Cl, Br, I) units with VEC values of 24 that can be discrete or poorly interconnected within the solid. The dissolution of inorganic solid-state halide precursors affords nanometric $[Mo_6X_{14}]^{2-}$ anionic units that exhibit interesting structural, photophysical, and redox properties that can be used for the formation and organization of

[a] *Université Bordeaux 1, Centre de Recherche Paul Pascal, 115 avenue Dr Schweitzer, 33600 Pessac, France. E-mail: ravaine@crpp-bordeaux.cnrs.fr; Fax: +33-556-84-56-00; Tel: +33-556-84-56-67*
[b] *Université de Rennes 1, Unité Science Chimiques de Rennes, UMR 6226 CNRS-UR1, Campus de Beaulieu, CS74205, F-35042 Rennes cedex, France*
[c] *Institut des NanoSciences de Paris, UMR – CNRS 7588, Université Pierre et Marie Curie, Campus Boucicaut, 140 rue de Lourmel, 75015, France*
[d] *Université Bordeaux 1, Laboratoire de Chimie des Polymères Organiques, UMR 5629 CNRS – ENSCPB, 16 avenue Pey-Berland, 33607 Pessac, France*

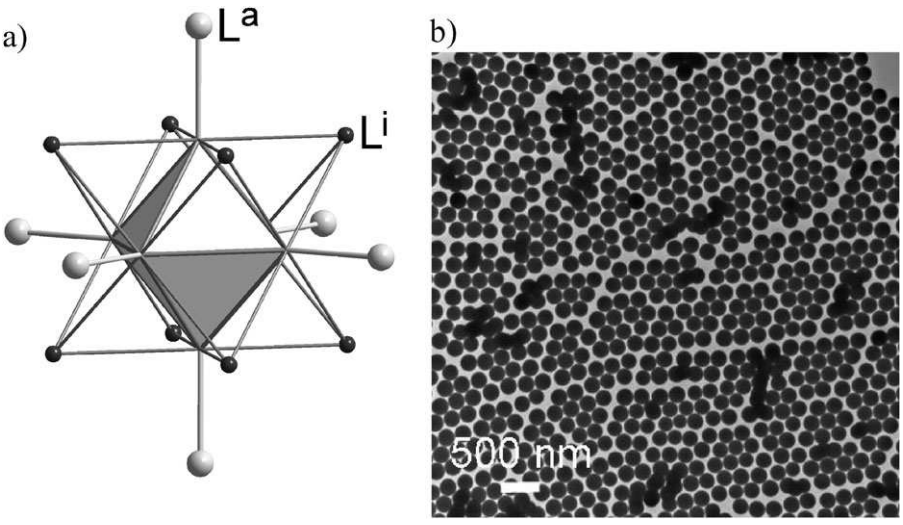

Fig. 1 (a) Representation of a $Mo_6L^i_8L^a_6$ cluster unit. The Mo_6 cluster is represented as a grey octahedron. Apical ligands (L^a) are in terminal positions and inner ligands (L^i) are in face-capping position; (b) TEM image of the 270 nm $Cs_2Mo_6Br_{14}@SiO_2$ particles.

supramolecular assemblies as well as hybrid materials.[36–39] For instance, the large emission region of the $[Mo_6X_{14}]^{2-}$ anion in the red and near infrared (580–900 nm)[40–42] is particularly interesting for biotechnology applications. In this frame, some of us recently prepared by water in oil microemulsion synthesis luminescent $Cs_2Mo_6X_{14}@SiO_2$ and bifunctional luminescent magnetic Fe_2O_3–$Cs_2Mo_6X_{14}@SiO_2$ nanoparticles containing a $[Mo_6X_{14}]^{2-}$ unit as red inorganic dye.[43,44] $Cs_2Mo_6Br_{14}$ precursors were encapsulated in silica by a classical sol–gel synthetic procedure and the obtained colloidal spheres were organized by the LB technique to elaborate 3D colloidal crystals. Heterostructures containing one or three planar defects made of silica spheres with a different size were also fabricated. We clearly observed that the emission of the incorporated light sources was inhibited by the presence of a stopband and was enhanced in the spectral region of a passband.

Experimental

$Cs_2Mo_6Br_{14}$ clusters synthesis

The $Cs_2Mo_6Br_{14}$ ternaries were synthesized from a stoichiometric amount of CsBr and $MoBr_2$ binary halides according to the procedure described in the literature.[45,46]

Fabrication of the $Cs_2Mo_6Br_{14}@SiO_2$ colloidal particles

$Cs_2Mo_6Br_{14}@SiO_2$ spheres with a mean diameter of 270 ± 15 nm and 330 ± 15 nm were synthesized following the well-known Stöber-Fink-Bohn method.[47] As an example, for the synthesis of the 330 nm spheres, 100 mg of $Cs_2Mo_6Br_{14}$ clusters, 195 ml of absolute ethanol (Prolabo), 11 ml of ammonia (29% in water, J. T. Baker), 29 ml of water were introduced in a 500 mL three-neck round flask equipped with a refrigerating system and stirred at 40 °C at 400 rpm to homogenize. 16.5 ml of tetraethoxysilane (TEOS, 99%) (Fluka) were then introduced and the solution was left under stirring for 24 h. A transmission electron microscopy (TEM) picture of the 270 nm $Cs_2Mo_6Br_{14}@SiO_2$ spheres is shown in Fig. 1b. The good monodispersity in the size of the particles can be seen. Nevertheless, the $[Mo_6Br_{14}]^{2-}$ units cannot be distinguished inside the SiO_2 particles due to the strong absorption of the mineral particles.

The above suspension of 330 nm particles was used as a seed for the growth of silica in order to get particles with a final diameter of 460 ± 25 nm. Typically, 250 mL of the suspension of seeds were introduced in a 500 mL three-neck round flask. A solution of 6.5 mL of TEOS diluted in 25 mL of absolute ethanol was added dropwise at an addition rate of 2 mL h^{-1} under stirring at 400 rpm and at room temperature. Synthesis was carried out for 24 h.

In order to use the $Cs_2Mo_6Br_{14}@SiO_2$ colloidal beads as building units to elaborate colloidal crystals by the LB technique, their surface was functionalized with aminopropyltriethoxysilane (99%, Aldrich) as previously described.[48]

Fabrication of the colloidal crystals

Multilayer colloidal crystals were deposited by the Langmuir–Blodgett technique onto glass substrates (24 mm × 60 mm). Details of the fabrication have already been published.[48] 3D colloidal crystals including one or three defect layers of particles of larger size were elaborated by alternately depositing 5 layers of 330 nm $Cs_2Mo_6Br_{14}@SiO_2$ particles (host particles), and one layer of 460 nm $Cs_2Mo_6Br_{14}@SiO_2$ spheres (guest spheres).

The 3D heterostructures are stable over years and can be manipulated without any damage if one takes care not to rub them up.

Characterizations

The size of the colloidal particles was determined statistically by analyzing TEM pictures taken with a Hitachi H-600 microscope.

Scanning electron microscopy (SEM) observations of the photonic crystals were performed with a JEOL JSM-6700F scanning electron microscope operating at 10 kV. The specimens

 This journal is © the Owner Societies 2010

were carbon-coated and simply cut into pieces using a glass cutter prior to examination.

Ultra-violet visible (UV-vis) extinction spectra were obtained by recording the transmitted intensity at normal incidence on a UV4 Spectrometer from Unicam. The extinction spectrum is defined as 1 − T where T is the transmitted intensity spectrum normalized to the incident intensity spectrum on the sample. For specular reflection, samples were illuminated with a fibered and collimated halogen source covering the whole 350–800 nm spectral range. The reflected light was collected by a second optical fiber symmetric to the first one. The fibers were mounted on rotating stages allowing for a precise selection of the incident and collection angles. The light spot on the opal had a size of 4 mm^2 (at 20° incidence) and the distance between the sample and the optical fiber was 10 cm. As for the extinction spectra, specular reflection spectra are normalized to the incident light spectrum.

The photoluminescence (PL) emission spectra were obtained by exciting the samples with the 337 nm nitrogen laser line (Laser Photonics LN 1000, 1.4 mJ pulse energy, 0.6 ns pulse duration). The emitted light from the sample, collected at 8 cm by an optical fiber on the same side as the excitation, was analyzed with a Jobin-Yvon Spectrometer HR460 and a multichannel CCD detector (2000 pixels). The spectra were corrected in intensity to take into account the experimental setup response. This setup has a resolution of 0.3 nm/point for a 30 μm slit.

Simulations

Finite-difference time-domain (FDTD) simulations[49] of the extinction, reflection spectra of the various photonic architectures experimentally investigated were performed, integrated in a freely available software package with sub-pixel smoothing for increased accuracy.[50] The computational cell, in which the incoming wave propagates along the z direction at normal incidence, has been implemented with periodic boundary conditions in x and y directions and perfectly matched layers (PMLs) in the z direction. The resolution of the grid has been refined such that the convergence of the results was ensured. To be in close agreement with the experimental conditions, the opals have been represented by monodisperse spheres of a given size (330 nm) and dielectric constant, $\varepsilon = 2.1$, arranged along a face-centered cubic (fcc) lattice. The lattice has been truncated to 25 (for Fig. 2c) or 10 (for Fig. 3b) planes normal to the direction [111], and the resulting crystal was set on a substrate with a dielectric constant of 2.3, which corresponds to the glass slides that were used, extending to the PMLs in the z direction. In the case of a defect layer of larger spheres (with a diameter of 1.5 larger than the host particles) being introduced between two stacks of 5 layers of host particles on the experimental side, we represented this layer on the simulation side by a bloc of the appropriate thickness with an effective refractive index $n_e = 1.35$.

Results and discussion

The luminescence properties of the $Cs_2Mo_6Br_{14}@SiO_2$ particles were first analyzed. Fig. 2a shows the room-temperature PL spectra measured under 337 nm excitation of aqueous solutions of the particles at various concentrations. The spectra show a broad band centered around 705 nm and exhibit a similar shape to those of the starting compounds,[43] evidencing that the emission properties of clusters are preserved when incorporated inside the silica particles.

The photonic crystals fabricated with the $Cs_2Mo_6Br_{14}@SiO_2$ particles display a strong iridescence in the visible region of the spectrum, which indicates the presence of a photonic stopband due to the regular ordering of the building spherical units. In fact, the good crystalline quality of a crystal made of 25 layers of 330 nm particles can be seen on the SEM side view shown in Fig. 2b. Fig. 2c shows the optical extinction/reflection spectra of the crystal (solid lines), taken at various incidence angles (from 0° to 40°). One main peak, which shifts to shorter wavelength when the angle of incidence is increased, is observed according to Bragg-Snell diffraction law:

$$\lambda_{\max} = 2\sqrt{\frac{2}{3}}D\sqrt{n_e^2 - \sin^2\alpha}$$

where $\lambda_{\max}$ is the Bragg diffracted wavelength, α is the angle between the [111] direction and the incident beam, D is the diameter of the colloidal particles and n_e is the effective refractive index of the crystal at the wavelength of interest. Spectra were simulated using the FDTD method. Calculated spectra (dashed lines) are plotted along the experimental ones in Fig. 2c. Note that the vertical axis is arbitrarily scaled and the spectra are arbitrarily shifted in order to clearly distinguish them, as a function of angle. A good agreement between theoretical and experimental data can be observed.

The successful engineering of the crystal is clearly shown in Fig. 2c, as the pseudo-gap maximum overlaps completely (α = 0, 20, 25, 30°) or partially (α = 35°) with the emission band of the $Cs_2Mo_6Br_{14}@SiO_2$ particles, represented in the figure as a grey vertical rectangle. Therefore, one should expect the emission spectrum to change when the detection angle is modified. In order to verify this point, we conducted an angle-resolved emission study during which the excitation wavelength was chosen to be 337 nm, which is outside the stopband of the crystal, in order to penetrate well into the sample and interact with the emitters. Fig. 2d shows the emission spectra recorded at six different detection angles (solid lines), while the experimental extinction/reflection spectra of the sample are also shown (dashed lines). A profound dip in the emission band is observed. Its position shifts to shorter wavelengths when α increases, coinciding with the spectral position of the stopband. This indicates that an inhibition of the light emission from the $Cs_2Mo_6Br_{14}@SiO_2$ particles occurs due to a low density of photonic states in the wavelength range of the stopband. A maximum inhibition of the luminescent emission of ~35% was estimated at α = 0°, whereas the emission band of the $Cs_2Mo_6Br_{14}@SiO_2$ particles is unaffected at α = 40° as the stopband is brought completely out of the emission range.

In order to investigate the influence of a passband on the emission spectrum of the $Cs_2Mo_6Br_{14}@SiO_2$ particles, we exploited our capability to build multilayer colloidal crystals in a controlled manner with the Langmuir–Blodgett technique.

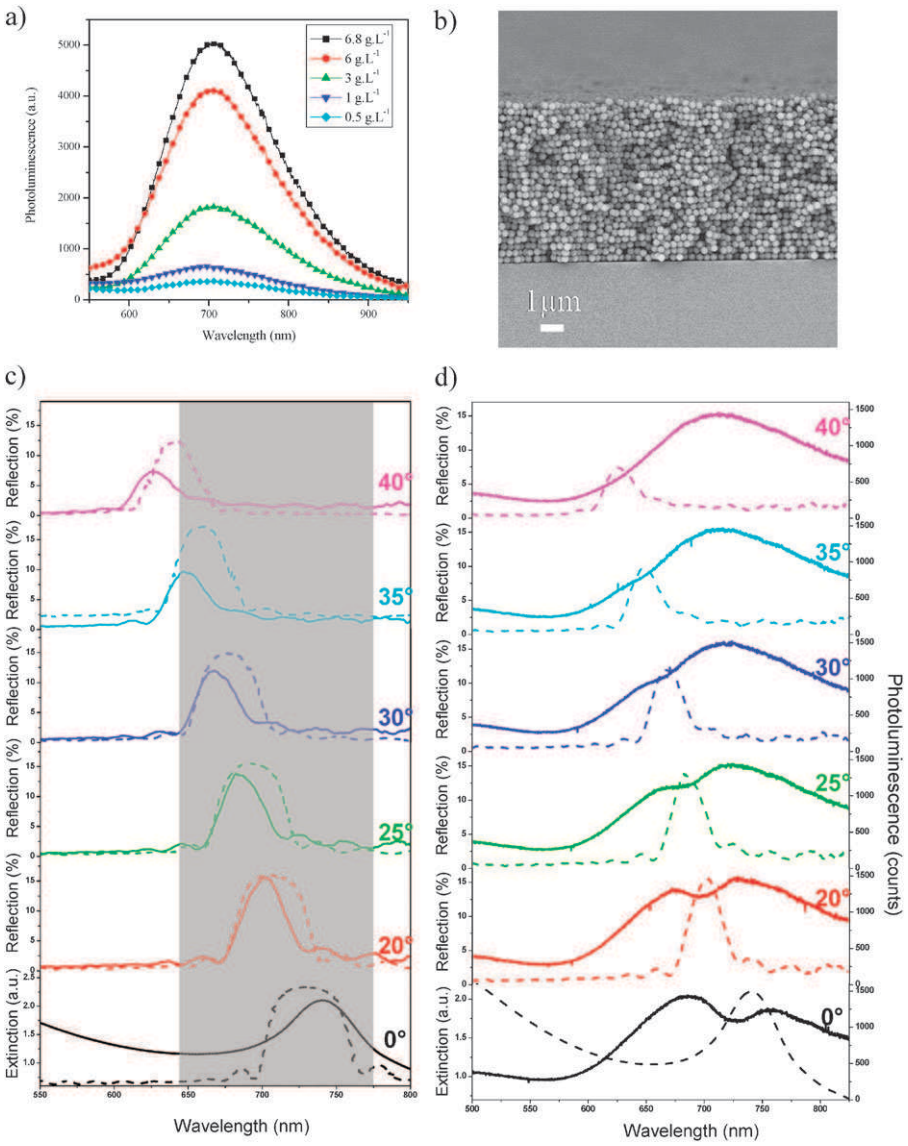

Fig. 2 (a) Concentration dependence of the photoluminescence spectra of the 330 nm $Cs_2Mo_6Br_{14}$@SiO_2 particles in water; (b) SEM side view of a colloidal crystal composed of 25 layers of 330 nm $Cs_2Mo_6Br_{14}$@SiO_2 particles; (c) Angle dependence of the extinction (at $\alpha = 0°$)/reflection (for larger angles) experimental and simulated spectra of the engineered colloidal structure; (d) Angle dependence of the extinction (at $\alpha = 0°$)/reflection (for larger angles) and corresponding photoluminescence spectra of the engineered colloidal structure. In (c), the grey rectangle represents the spectral range of the emission peak of the $Cs_2Mo_6Br_{14}$@SiO_2 particles.

We engineered a colloidal crystal composed by one layer of 460 nm $Cs_2Mo_6Br_{14}$@SiO_2 spheres embedded between two stacks of five layers of 330 nm $Cs_2Mo_6Br_{14}$@SiO_2 particles. The crystal's structure can be described as $(330)_5/(460)_1/(330)_5$ by listing the sphere size from bottom to top. Both the defect layer and the good crystalline quality of the sample can be seen on the SEM side view shown in Fig. 3a. The insertion of such a defect layer induces the appearance of localized states for photons within the L pseudo-gap of the host particles structure. Accordingly, a passband is created within the stopband. On the basis of the particle diameters of the guest and host particles used for the preparation of the sample, the passband position is expected to overlap the emission profile of the colloidal building units. This has been verified experimentally by recording the extinction/reflection spectra of the sandwich-like crystal as a function of angle. Indeed, Fig. 3b shows that these spectra (solid lines) exhibit a dip within the pseudogap, which shifts to the blue and passes through the emission range of the $Cs_2Mo_6Br_{14}$@SiO_2 particles as α increases. Calculated spectra (dashed lines) are also plotted along the experimental ones in Fig. 3b. Here again, the simulations fit the experimental ones accurately in all cases. Fig. 3c shows the emission (solid lines) and extinction/reflection (dashed lines) spectra of the sandwich-like crystal recorded at six different detection angles. For $0° \leq \alpha \leq 35°$, both an inhibition of the emission in the dielectric and air band regions and an exaltation within the passband are clearly observed, as the result of the redistribution of the photonic local density of states. Only a weak shoulder in the PL spectrum around 650 nm is visible for $\alpha = 40°$, as a result of

 This journal is © the Owner Societies 2010

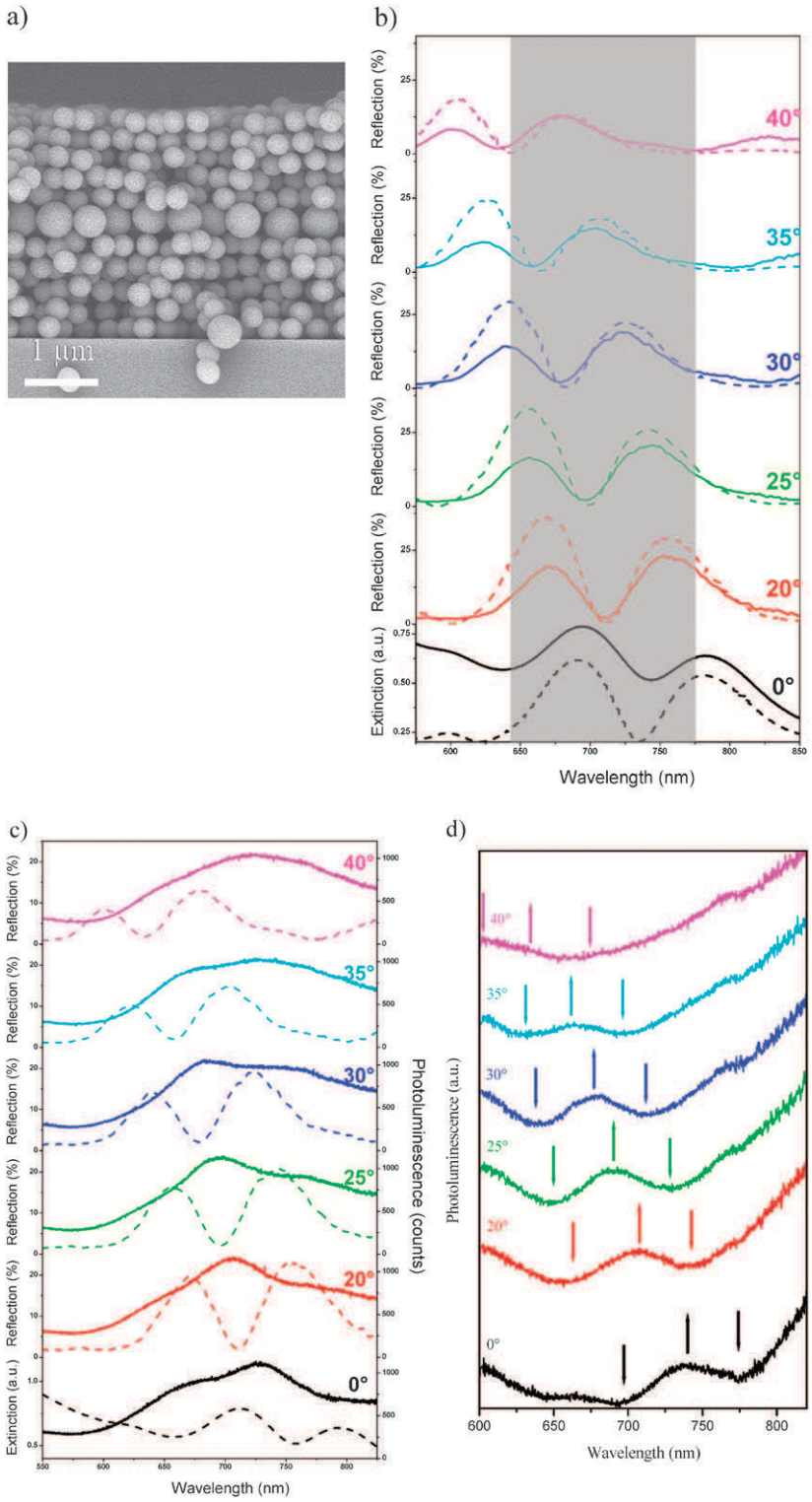

Fig. 3 (a) SEM side view of a colloidal crystal composed of one layer of 460 nm $Cs_2Mo_6Br_{14}@SiO_2$ spheres embedded between two stacks of five layers of 330 nm $Cs_2Mo_6Br_{14}@SiO_2$ particles. (b) Angle dependence of the extinction (at $\alpha = 0°$)/reflection (for larger angles) experimental and simulated spectra of the engineered colloidal structure. (c) Angle dependence of the extinction (at $\alpha = 0°$)/reflection (for larger angles) and corresponding photoluminescence spectra of the engineered colloidal structure. (d) Emission spectra of the $(330)_5/(460)_1/(330)_5$ crystal divided by the emission from a $(270)_{10}$ reference crystal. The downward arrows indicate the positions of the dielectric and air bands while the upward arrows indicate the positions of the passband. In (b), the grey rectangle represents the spectral range of the emission peak of the $Cs_2Mo_6Br_{14}@SiO_2$ particles.

the blue shifting of the passband towards the low wavelength edge of the emission band. To quantify the effects of the $(330)_5/(460)_1/(330)_5$ crystal on the emission spectra, we took the ratio of the emission spectra to the spectrum recorded from

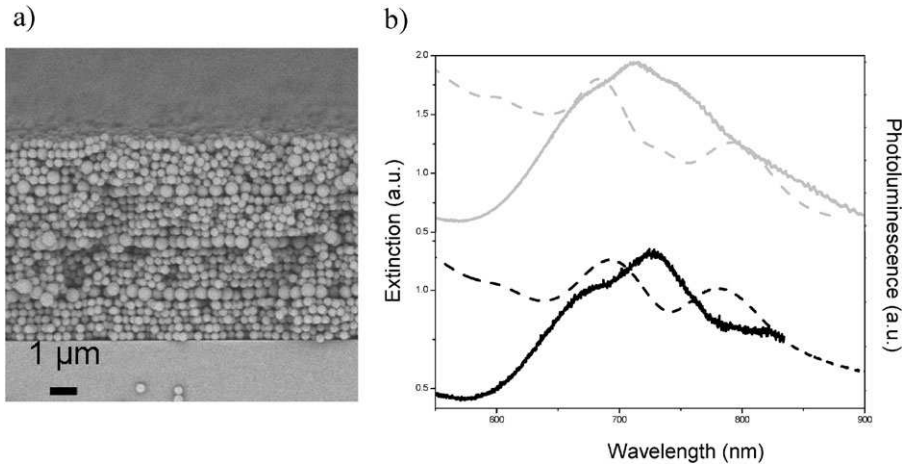

Fig. 4 (a) SEM side view of an $A(BA)_3$ heterostructure. (b) Experimental extinction (at $\alpha = 0°$) (dashed lines) and photoluminescence spectra (solid lines) of the $A(BA)_1$ (black curves) and $A(BA)_3$ (grey curves) heterostructures. Spectra are vertically shifted for better clarity.

a reference sample made of 10 layers of 270 nm $Cs_2Mo_6Br_{14}@SiO_2$ spheres, which exhibits a photonic band gap at 595 nm (not shown). We thus obtained the relative intensity spectra displayed in Fig. 3d. For $\alpha = 0°$, the data clearly show a 15% attenuation of the emission in the dielectric and air band regions as well as an 8% enhanced emission in the passband region. The simultaneous observation of attenuation and enhancement means that the effect of the PC is not a simple filter action.

We further took advantage of the versatility of the Langmuir–Blodgett technique by engineering a photonic heterostructure made by alternated deposition of stacks (A) made of five layers of 330 nm $Cs_2Mo_6Br_{14}@SiO_2$ particles with one monolayer (B) of 460 nm $Cs_2Mo_6Br_{14}@SiO_2$ particles. Fig. 4a shows a SEM side view of an $A(BA)_3$ heterostructure. The thickness of each stack is controlled at the layer level as the number of deposited layers matches perfectly with the predefined value of transfer cycles. The overall thickness of the sample is uniform despite the presence of defect layers B of larger silica particles which periodically separate the A substructures. The periodic alternation between A and B substructures gives rise to a superlattice, whose periodic parameter corresponds to the sum of the thicknesses of stacks A and B. We have recently shown that the passband becomes wider as the layering is repeated.[30] The comparison of the extinction spectra of $A(BA)_1$ and $A(BA)_3$ heterostructures taken at normal incidence ($\alpha = 0°$) and shown in Fig. 4b confirms this assertion, as the width of the defect state of the latter is larger than for the $A(BA)_1$ crystal. In agreement with our previous observations,[30] weak oscillations are also visible inside the passband of the $A(BA)_3$ sample. They can be assimilated to minibands, which result from the coupling of the individual defect modes in the heterostructure. Fig. 4b further illustrates the influence of the structure of the colloidal crystals on the emission characteristics of their building units. An enhancement of the emission is observed between 700 nm and 770 nm in the PL spectrum of the $A(BA)_3$ heterostructure, *i.e.* in the whole spectral zone of the passband. One should also note a decrease of the detected intensity at 730 nm and 765 nm, which correspond to the spectral positions of the minibands, which thus act as stopbands.

Conclusions

In summary, we have engineered colloidal crystals from silica spheres with incorporated luminescent $[Mo_6Br_{14}]^{2-}$ cluster units. An inhibition of the emission intensity from the light sources was observed in the spectral region of the stopband, which was found to nicely correspond to and follow the Bragg-Snell law as the angle between the [111] direction and the incident beam was varied. Heterostructures containing one or three planar defects displayed increased emission in the spectral region of the passband. The 3D photonic colloidal structures investigated here are very promising for both basic and applied research related to the confinement and exaltation of spontaneous emission in given frequency ranges and thus are good candidates for low-threshold and/or single mode photonic crystal lasers.

Acknowledgements

The authors thank B. Agricole (CRPP) and E. Sellier (CREMEM, Talence) for Langmuir–Blodgett experiments and SEM observations, respectively.

References

1 S. Fan, P. R. Villeneuve, J. D. Joannopoulos and E. F. Schubert, *Phys. Rev. Lett.*, 1997, **78**, 3294.
2 E. P. Petrov, V. N. Bogomolov, I. I. Kalosha and S. V. Gaponenko, *Phys. Rev. Lett.*, 1998, **81**, 77.
3 S. V. Gaponenko, V. N. Bogomolov, E. P. Petrov, A. M. Kapitonov, D. A. Yarotsky, I. I. Kalosha, A. A. Eychmueller, A. L. Rogach, J. McGilp, U. Woggon and F. Gindele, *J. Lightwave Technol.*, 1999, **17**, 2128.
4 S. V. Gaponenko, V. N. Bogomolov, E. P. Petrov, A. M. Kapitonov, A. A. Eychmueller, A. L. Rogach, I. I. Kalosha, F. Gindele and U. Woggon, *J. Lumin.*, 2000, **87–89**, 152.
5 L. Bechger, P. Lodahl and W. L. Vos, *J. Phys. Chem. B*, 2005, **109**, 9980.
6 M. Megens, J. E. G. J. Wijnhoven, A. Lagendijk and W. L. Vos, *J. Opt. Soc. Am. B*, 1999, **16**, 1403.

 This journal is © the Owner Societies 2010

7 P. Lodahl, A. F. van Driel, I. S. Nikolaev, A. Irman, X. Overgaag, D. Vanmaekelbergh and W. L. Vos, *Nature*, 2004, **430**, 654.
8 A. F. Koenderink and W. L. Vos, *Phys. Rev. Lett.*, 2003, **91**, 213902.
9 R. C. Schroden, M. Al-Daous and A. Stein, *Chem. Mater.*, 2001, **13**, 2945.
10 F. Fleischhaker and R. Zentel, *Chem. Mater.*, 2005, **17**, 1346.
11 M. Müller, R. Zentel, T. Maka, S. G. Romanov and C. M. Sotomayor Torres, *Chem. Mater.*, 2000, **12**, 2508.
12 L. K. Teh, C. C. Wong, H. Y. Yang, S. P. Lau and S. F. Yu, *Appl. Phys. Lett.*, 2007, **91**, 161116.
13 A. Chutinan and S. Noda, *Appl. Phys. Lett.*, 1999, **75**, 3739.
14 S. Y. Lin, E. Chow, V. Hietala, P. R. Villeneuve and J. D. Joannopoulos, *Science*, 1998, **282**, 274.
15 M. Boroditsky, T. F. Krauss, R. Coccioli, R. Vrijen, R. Bhat and E. Yablonovitch, *Appl. Phys. Lett.*, 1999, **75**, 1036.
16 Y. R. Do, Y. C. Kim, Y. W. Song, C. Cho, H. Jeon, Y. J. Lee, S. H. Kim and Y. H. Lee, *Adv. Mater.*, 2003, **15**, 1214.
17 B. Kolaric, K. Baert, M. Van der Auweraer, R. A. L. Vallée and K. Clays, *Chem. Mater.*, 2007, **19**, 5547.
18 Y. A. Vlasov, K. Luterova, I. Pelant, B. Honerlage and V. N. Astratov, *Appl. Phys. Lett.*, 1997, **71**, 1616.
19 A. Chiappini, C. Armellini, A. Chiasera, M. Ferrari, Y. Jestin, M. Mattarelli, M. Montagna, E. Moser, G. Nunzi Conti, S. Pelli, G. C. Righini, M. Clara Goncalves and R. M. Almeida, *J. Non-Cryst. Solids*, 2007, **353**, 674.
20 Y.-S. Lin, Y. Hung, H.-Y. Lin, Y.-H. Tseng, Y.-F. Chen and C.-Y. Mou, *Adv. Mater.*, 2007, **19**, 577.
21 R. V. Nair, R. Vijaya, K. Kuroda and K. Sakoda, *J. Appl. Phys.*, 2007, **102**, 123106.
22 Y. Li, T. Kunitake, S. Fujikawa and K. Ozasa, *Langmuir*, 2007, **23**, 9109.
23 E. Palacios-Lidón, J. F. Galisteo-López, B. H. Juárez and C. López, *Adv. Mater.*, 2004, **16**, 341.
24 N. Tétreault, A. Mihi, H. Miguez, I. Rodriguez, G. A. Ozin, F. Meseguer and V. Kitaev, *Adv. Mater.*, 2004, **16**, 346.
25 L. Wang, Q. Yan and X. S. Zhao, *Langmuir*, 2006, **22**, 3481.
26 R. Pozas, A. Mihi, M. Ocaña and H. Míguez, *Adv. Mater.*, 2006, **18**, 1183.
27 K. Wostyn, Y. Zhao, G. de Schaetzen, L. Hellemans, N. Matsuda, K. Clays and A. Persoons, *Langmuir*, 2003, **19**, 4465.
28 Y. Zhao, K. Wostyn, G. de Schaetzen, K. Clays, L. Hellemans, A. Persoons, M. Szekeres and R. A. Schoonheydt, *Appl. Phys. Lett.*, 2003, **82**, 3764.
29 P. Massé, S. Reculusa, K. Clays and S. Ravaine, *Chem. Phys. Lett.*, 2006, **422**, 251.
30 P. Massé, G. Pouclet and S. Ravaine, *Adv. Mater.*, 2008, **20**, 584.
31 P. Massé, R. A. L. Vallée, J.-F. Dechézelles, J. Rosselgong, E. Cloutet, H. Cramail, X. S. Zhao and S. Ravaine, *J. Phys. Chem. C*, 2009, **113**, 14487.
32 K. Baert, K. Song, R. A. L. Vallée, M. Van der Auweraer and K. Clays, *J. Appl. Phys.*, 2006, **100**, 123112.
33 H. Schäfer and H. G. Schnering, *Angew. Chem.*, 1964, **76**, 833.
34 S. Cordier, K. Kirakci, D. Méry, C. Perrin and D. Astruc, *Inorg. Chim. Acta*, 2006, **359**, 1705.
35 T. Hughbanks and R. Hoffmann, *J. Am. Chem. Soc.*, 1983, **105**, 1150.
36 D. Méry, L. Plault, C. Ornelas, J. Ruiz, S. Nlate, D. Astruc, J. C. Blais, J. Rodrigues, S. Cordier, K. Kirakci and C. Perrin, *Inorg. Chem.*, 2006, **45**, 1156.
37 G. Prabusankar, Y. Molard, S. Cordier, S. Golhen, Y. Le Gal, C. Perrin, S. Kalal, J. F. Halet and L. Ouahab, *Eur. J. Inorg. Chem.*, 2009, (14), 2153.
38 Y. Molard, F. Dorson, V. Cîrcu, T. Roisnel, F. Artzner and S. Cordier, *Angew. Chem., Int. Ed.*, 2010, **49**, 3351.
39 B. Fabre, S. Cordier, Y. Molard, C. Perrin, S. Ababou-Girard and C. Godet, *J. Phys. Chem. C*, 2009, **113**, 17437.
40 A. W. Maverick and H. B. Gray, *J. Am. Chem. Soc.*, 1981, **103**, 1298.
41 A. W. Maverick, J. S. Najdzionek, D. MacKenzie, D. G. Nocera and H. B. Gray, *J. Am. Chem. Soc.*, 1983, **105**, 1878.
42 D. G. Nocera and H. B. Gray, *J. Am. Chem. Soc.*, 1984, **106**, 824.
43 F. Grasset, F. Dorson, S. Cordier, Y. Molard, C. Perrin, A.-M. Marie, T. Sasaki, H. Haneda, Y. Bando and M. Mortier, *Adv. Mater.*, 2008, **20**, 143.
44 F. Grasset, Y. Molard, F. Dorson, S. Cordier, M. Mortier, V. Demange, C. Perrin, V. Marchi-Artzner and H. Haneda, *Chem. Commun.*, 2008, (39), 4729.
45 K. Kirakci, S. Cordier and C. Perrin, *Z. Anorg. Allg. Chem.*, 2005, **631**, 411.
46 H. Schäfer, H. G. Schnering, J. Tillack, F. Kuhnen, H. Wöhrle and H. Baumann, *Z. Anorg. Allg. Chem.*, 1967, **353**, 281.
47 W. Stöber, A. Fink and E. Bohn, *J. Colloid Interface Sci.*, 1968, **26**, 62.
48 S. Reculusa and S. Ravaine, *Chem. Mater.*, 2003, **15**, 598.
49 A. Taflove and S. C. Hagness, *Computational Electrodynamics: The Finite-Difference Time-Domain Method*, Artech House, Inc., Norwood, MA, 3rd edn, 2005.
50 A. Farjadpour, D. Roundy, A. Rodriguez, M. Ibanescu, P. Bermel, J. D. Joannopoulos, S. G. Johnson and G. Burr, *Opt. Lett.*, 2006, **31**, 2972.

Colloids and Surfaces A: Physicochem. Eng. Aspects 373 (2011) 1–5

Contents lists available at ScienceDirect

Colloids and Surfaces A: Physicochemical and Engineering Aspects

journal homepage: www.elsevier.com/locate/colsurfa

Inhibition and exaltation of emission in layer-controlled colloidal photonic architectures

J.-F. Dechézelles[a], G. Mialon[b], T. Gacoin[b], C. Barthou[c], C. Schwob[c], A. Maître[c], R.A.L. Vallée[a,*], H. Cramail[d], S. Ravaine[a]

[a] Centre de Recherche Paul Pascal (CNRS, UPR 8641), 115 avenue du docteur Albert Schweitzer, 33600 Pessac, France
[b] Groupe de Chimie du Solide, Laboratoire de Physique de la Matière Condensée (CNRS, UMR 7643), Ecole Polytechnique, 91128 Palaiseau Cedex, France
[c] Institut des NanoSciences de Paris (CNRS, UMR 7588), Université Pierre et Marie Curie, Campus Boucicaut, 140 rue de Lourmel, 75015 Paris, France
[d] Laboratoire de Chimie des Polymères Organiques (CNRS, UMR 5629), ENSCPB, 16 avenue Pey-Berland, 33607 Pessac, France

ARTICLE INFO

Article history:
Received 1 June 2010
Received in revised form 28 July 2010
Accepted 28 July 2010
Available online 6 August 2010

Keywords:
Colloids
Crystals
Photonics

ABSTRACT

We described the engineering and characterization of photonic colloidal crystals based on silica spheres with incorporated YVO_4:Eu luminescent nanoparticles. These structures exhibit strong angle-dependent luminescent properties. The controlled incorporation of a planar defect in the periodic structures gives rise to the creation of a pass band in the pseudo-gap. In the energy range of this pass band, we observed a strong increase in combination with a sharp width of the emission spectrum, which opens new possibilities for the design of low-threshold and/or single mode photonic crystal lasers.

© 2010 Elsevier B.V. All rights reserved.

1. Introduction

The control of the spontaneous emission delivered by an ensemble of light sources is fundamental for the engineering of devices such as miniature lasers [1,2], light-emitting diodes [3], and solar cells [4]. The rate of spontaneous emission is determined by both the intrinsic nature of the emitters and their environment [5–7]. Periodic dielectric structures, known as photonic crystals (PCs), have been predicted to radically change the photonic local density of states (LDOS), which governs the interaction between the emitter and the electric field in the structure [3]. The achievement of a photonic band gap (PBG), i.e., a range of frequencies for which the LDOS vanishes, is an active field of research. To engineer a three dimensional (3D) PBG material, the periodicity of the refractive index should be realized in 3D. Physical top-down approaches are not so prone to engineer such PBG structures. Chemical self-assembly of colloidal particles and layer by layer self-assembly of nanostructured hybrid layers [8,9] are more suited to the formation of 3D photonic crystals (PCs). In the case of colloidal particles, the self-assembly results in the thermodynamically most stable face-centered cubic (fcc) crystal structure or in the (random) hexagonal closed packing (rhcp) crystal structure, both with a packing of 74%. The size of the colloidal particles, together with the refractive index, determines the spectral of the band gap. The combination of these dense crystal structures (fcc or rhcp) with the low refractive index of most colloidal particles (latex, silica) results in an incomplete band gap (pseudo-gap or stop band) [10]. For a complete band gap, i.e., a forbidden spectral region for all incidence angles, either a more effective crystal structure (diamond structure) [11,12] or a less dense packing combined with a higher refractive index contrast (e.g., titania or zirconia inverted opals) is necessary [13,14].

The controlled insertion of a defect causes a rupture in the periodicity of the photonic crystal and induces the appearance of localized states for photons within the gap. Recently, different techniques were developed to introduce a planar defect into 3D PCs [15–18]. The obtained heterostructures present a dip, also called pass band, inside the stop band in the transmission spectrum.

With the aim of manipulating the spontaneous emission of light sources, many studies [19–22] have been performed on 3D photonic crystals by incorporating different types of sources. Organic dyes [23–25], semiconductor quantum dots (QDs) [26–28] or rare earth doped particles [29,30] showed an inhibition of the emission due to the presence of a stop band. Spectral narrowing of emission in self-assembled colloidal photonic superlattices was reported, due to the confinement of the fluorescence emission in the engineered pass band [31]. However, most of these studies were performed with light sources post-infiltrated in the colloidal structures and/or exhibiting a broad band emission spectrum. Post-infiltrating the sources into the voids left in the engineered photonic structure presents two drawbacks. Firstly, the infiltration

* Corresponding author. Tel.: +33 556845612; fax: +33 556845600.
E-mail address: vallee@crpp-bordeaux.cnrs.fr (R.A.L. Vallée).

0927-7757/$ – see front matter © 2010 Elsevier B.V. All rights reserved.
doi:10.1016/j.colsurfa.2010.07.033

step can provoke a disruption of the crystalline structure. Secondly, the emitters are non-homogeneously distributed in the medium. They are located in the vicinity of the surface of the beads with a random distribution of positions and orientations of their transition dipole moments. On the ensemble level, the LDOS felt by any single emitter differs from the others, due to specific local electromagnetic boundary conditions [6,32], causing a broadening of the emission spectrum and the appearance of a non-exponential fluorescence decay profile [24], which obscures the purely expected band gap effect. Finally, a broad band emission spectrum of the light source makes it difficult to fully cover it with the stop band of the engineered colloidal crystal, which would favor the strong inhibition of the spontaneous emission.

To overcome these difficulties, we have encapsulated YVO_4:Eu nanoparticles exhibiting very sharp and intense emission peaks in silica spheres by a classical sol–gel approach. The obtained colloidal spheres were organized into 3D colloidal crystals using the Langmuir–Blodgett technique. Heterostructures containing a planar defect made of spheres with a different size were also fabricated. We clearly observed that the emission of the incorporated light sources is strongly inhibited by the presence of a stop band covering its emission peak and is strongly enhanced as the emission peak perfectly matches the pass band.

2. Materials and methods

2.1. Experimental section

YVO_4:Eu nanoparticles with an average diameter of about 10 nm were prepared following a chemical process already published [33]. Upon UV excitation, the most intense emission of the nanoparticles is related to the europium $^5D_0$–$^7F_2$ transition at 617 nm, and the emission mechanism is an energy transfer between the vanadate group, which absorbs the UV light, and the europium ions.

YVO_4:Eu@SiO_2 spheres of various diameters were synthesized following the well-known Stöber–Fink–Bohn method [34], while the YVO_4:Eu nanoparticles were directly incorporated in the precursor solution. Typically, 2.8 mg of YVO_4:Eu nanoparticles were mixed with 195 ml of ethanol (Prolabo), 11 ml of ammonia (29% in water, J.T. Baker), 29 ml of water and 16.5 ml of tetraethoxysilane (Fluka). After mixing during 12 h at $40 \pm 1^\circ$, 285 nm diameter YVO_4:Eu@SiO_2 particles were obtained. As usual, such silica particles synthesized owing to the Stöber–Fink–Bohn method [34] present a microporosity with pore sizes of about 0.9 nm. The surface functionalization of the colloidal beads with aminopropyltriethoxysilane (Aldrich) was carried out as previously described [35].

Multilayer colloidal crystals were fabricated by the Langmuir–Blodgett technique. Details of the fabrication have been already published [35]. 3D colloidal crystals including a defect layer of particles of larger size (sandwich-like structure) were elaborated by successively depositing a multilayer colloidal crystal of YVO_4:Eu@SiO_2 particles (host particles), then depositing one layer of YVO_4:Eu@SiO_2 spheres with another diameter (guest spheres) and finally depositing again a multilayer colloidal crystal of host particles. The 3D heterostructures are stable over years and can be manipulated without any damage if one takes care not to rub them up.

The size of the colloidal particles was statistically determined by analyzing transmission electron microscopy (TEM) pictures taken with a Hitachi H-600 microscope. SEM observations were performed with a JEOL JSM-840A scanning electron microscope operating at 10 kV. The specimens were carbon-coated and simply cut into pieces using a glass cutter prior to examination.

Ultra-violet–visible (UV–vis) extinction spectra were obtained by recording the transmitted intensity at normal incidence on a UV4 Spectrometer from Unicam. The extinction spectrum is defined as $1 - T$ where T is the transmitted intensity spectrum normalized to the incident intensity spectrum on the sample. For specular reflection, samples were illuminated with a fibered and collimated halogen source covering the whole 350–800 nm spectral range. The reflected light was collected by a second optical fiber symmetric to the first one. The fibers were mounted on rotating stages allowing for a precise selection of the incident and collection angles. The light spot on the opal had a size of 4 mm^2 (at 20° incidence) and the distance between the sample and the optical fiber was 10 cm. As for the extinction spectra, specular reflexion spectra are normalized to the incident light spectrum.

The photoluminescence emission (PLE) spectra were obtained by exciting the samples with a 450 W Xenon lamp. The 280 nm excitation wavelength was selected by a double Jobin-Yvon Fluorolog 3 monochromator with a bandwidth of 3 nm. For the emission spectra, the visible emitted light from the sample, collected at 8 cm by an optical fiber on the same side as the excitation, was analyzed with a Jobin-Yvon Spectrometer HR460 and a multichannel CCD detector (2000 pixels). This setup has a resolution of 0.3 nm/point for a 30 μm slit. The detector for the excitation spectra is a Photomultiplier Hamamatsu R928.

2.2. Theoretical section

Finite-difference time-domain (FDTD) simulations [36] of the extinction, reflection spectra of the various photonic architectures experimentally investigated were performed, integrated in a freely available software package with sub pixel smoothing for increased accuracy [37]. The computational cell, in which the incoming wave propagates along the z direction at normal incidence, has been implemented with periodic boundary conditions in x and y directions and perfectly matched layers (PMLs) in the z direction. The resolution of the grid has been refined such that the convergence of the results was ensured. To be in close agreement with the experimental conditions, the opals have been represented by monodiperse spheres of given size (285 nm) and dielectric constant $\epsilon = 2.1$ arranged along a face-centered cubic (fcc) lattice. The lattice has been truncated to 10 planes normal to the direction [1 1 1], and the resulting crystal was set on a substrate with a dielectric constant of 2.3 extending to the PMLs in the z direction. In case a defect layer of larger spheres (with a diameter of 1.5 larger than the host particles) has been introduced between two stacks of 5 layers of host particles on the experimental side, we represented this layer on the simulation side by a bloc of the appropriate thickness with an effective refractive index $n_e = 1.35$.

3. Results and discussion

The prepared PC samples exhibit a strong iridescence in the visible region of the spectrum, which indicates the presence of a photonic stop band (PSB) due to the regular ordering of the silica spheres. Fig. 1a and b shows a TEM view of colloidal particles with a diameter $D = 285$ nm and a transversal view of a PSB colloidal crystal, respectively, allowing one to judge the small degree of polydispersity of the particles on the one side and the good quality of the 10 layers thick crystal based on these building blocks on the other side. UV–vis–NIR spectroscopies are fundamental techniques to ascertain the quality on a larger scale and characterize the optical properties of colloidal crystals [38,39]. Fig. 1c shows the optical extinction spectrum of the PSB sample, taken at normal incidence ($\alpha = 0^\circ$). One main peak is observed according to the Bragg–Snell diffraction law:

$$\lambda_{max} = 2d_{1\,1\,1}\sqrt{n_e^2 - \sin^2\alpha}, \quad (1)$$

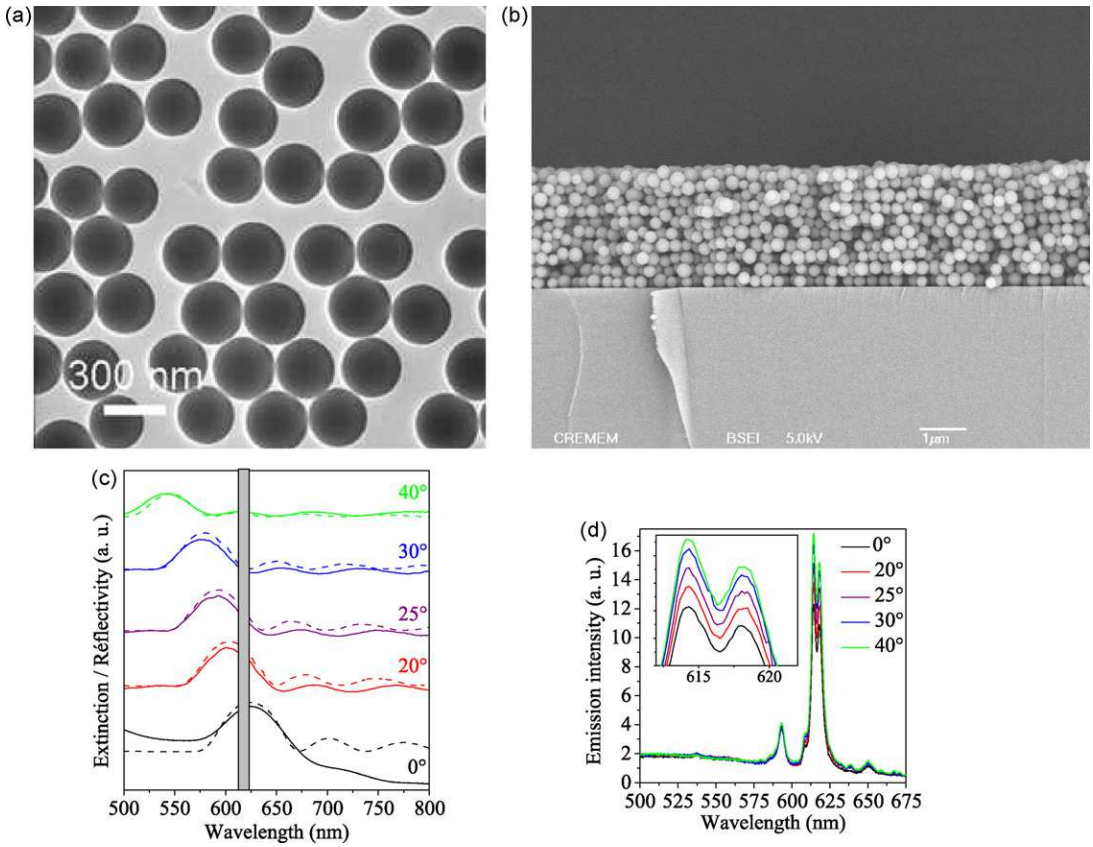

Fig. 1. (a) TEM view of 285 nm YVO_4:Eu@SiO_2 particles and (b) SEM side view of a colloidal crystal composed of 10 layers of 285 nm YVO_4:Eu@SiO_2 particles. Angle dependence of the extinction (at $\alpha = 0^\circ$)/reflection (for larger angles) spectra of the engineered colloidal structure (c) and of the corresponding photoluminescence spectra of the incorporated YVO_4:Eu light sources (d). In (c), the vertical line represents the main emission peak of the YVO_4:Eu emitters; the good matching between the experimentally measured (solid lines) and FDTD simulated (dashed lines) spectra is also shown.

where λ_{max} is the Bragg diffracted wavelength, n_e is the effective refractive index of the crystal at the wavelength of interest. It is determined as $n_e = \sqrt{x\epsilon_s + (1-x)\epsilon_a}$, where the dielectric constants of silica and air are $\epsilon_s = 2.1$ and $\epsilon_a = 1$. The packing fraction $x = 0.74$ for closely packed spheres in a fcc lattice. $d_{1\,1\,1}$ is the interdistance between consecutive lattice planes with Miller indices (1,1,1). $d_{1\,1\,1} = \sqrt{2/3}D$ in the case of a fcc lattice of colloidal spheres with diameter D. α is the angle between the [1 1 1] direction and the incident beam.

According to these considerations, $n_e = 1.35$ in the case of a closed packed fcc lattice of silica spheres and the expected Bragg peak for spheres of diameter $D = 285$ nm is $\lambda = 627$ nm, in excellent agreement with the maximum of the optical extinction spectrum shown at normal incidence (L pseudo-gap) in Fig. 1c. The angular dependence of the measured reflection spectra (solid lines) and the simulated FDTD spectra (dashed lines) are also shown in the figure. Note that the vertical axis is arbitrarily scaled and the spectra are arbitrarily shifted in order to clearly distinguish them, as a function of angle. The figure exhibits a good agreement between theoretical and experimental data and the positions of the main diffraction peak as a function of angle coincide with the predictions of the Bragg–Snell law. Fig. 1c also shows very characteristics features that further assert for the good quality of the grown crystals: secondary periodic oscillations appear in the reflection spectra of the structure. These oscillations, the so-called "Fabry–Pérot" fringes are due to interferences of light propagating among various optical paths back and forth in the structure and appear in a spectral region where the dispersion relation is linear [40]. In this region, the crystal can be assimilated to a homogeneous transparent medium with an effective refractive index. As such, only good quality crystals, with a homogeneous optical thickness, can exhibit "Fabry–Pérot" fringes. It is important to note here the excellent matching between the spectral positions of the fringes observed on both theoretical and experimental extinction ($\alpha = 0^\circ$)/reflection ($\alpha < 0^\circ$) spectra. Based on the experimental spectral positions of the fringes, the crystal's thickness was calculated to be about 2.7 μm, in very good agreement with the value measured from a SEM side observation of the colloidal structure (Fig. 1b).

The colloidal particles constituting the PSB structure shown in Fig. 1 are not made of pure SiO_2 but are silica particles doped with YVO_4 : Eu nanoparticles exhibiting a very sharp and intense emission peak at $\lambda = 617$ nm. Fig. 1c clearly shows the successful engineering of the PSB with the pseudo-gap maximum extinction covering completely ($\alpha = 0^\circ$) or partially ($\alpha = 20^\circ, 25^\circ, 30^\circ$) the narrow emission spectrum of the YVO_4:Eu nanoparticles, represented in the figure as a grey vertical rectangle. Fig. 1d further illustrates the influence of the PSB on the emission characteristics of the embedded YVO_4:Eu nanoparticles as a function of angle. With a maximum reduction of the emission intensity at $\alpha = 0^\circ$, where the pseudo-gap best matches the spectral position of the YVO_4:Eu@SiO_2 emission peak, the intensity gradually increases as the pseudo-gap is shifted to the blue while tilting the sample over the ΓL direction, to reach a complete recovery of the emission intensity as the pseudo-gap is brought completely out of the emission range of the YVO_4:Eu nanoparticles, at $\alpha = 40^\circ$. The effect is spectacular and can be better seen in the inset of Fig. 1d, leading to a 40% maximum inhibition of the luminescent emission at $\alpha = 0^\circ$.

Owing to the versatility of the Langmuir–Blodgett technique, allowing us to control the deposition layer by layer, we could also engineer a photonic heterostructure built with two stacks of 5

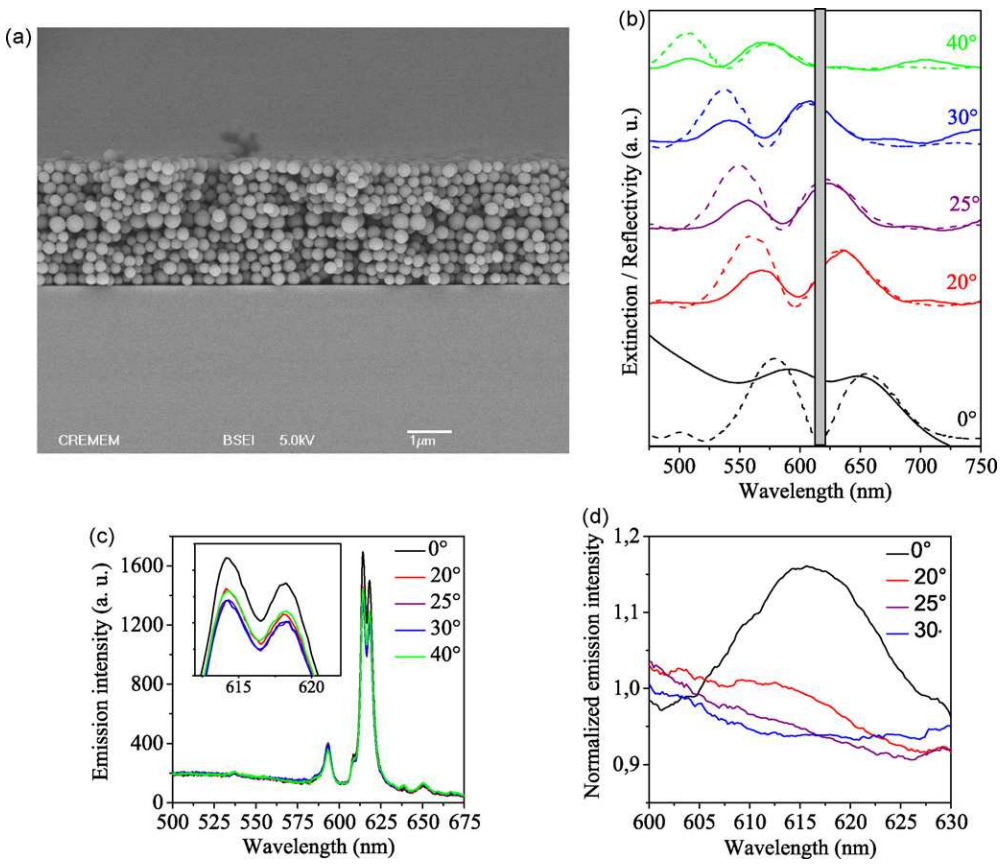

Fig. 2. (a) SEM side view of a colloidal crystal composed by one layer of 430 nm YVO_4:Eu@SiO_2 spheres embedded between two stacks of five layers of 285 nm YVO_4:Eu@SiO_2 particles. Angle dependence of the extinction (at $\alpha = 0^\circ$)/reflection (for larger angles) spectra of the engineered colloidal structure (b) and of the corresponding photo luminescence spectra of the incorporated YVO_4:Eu light sources (c). (d) Normalized (with respect to the spectrum measured at $\alpha = 40^\circ$) emission spectra of the YVO_4:Eu light sources as a function of angle. In (b), the vertical line represents the main emission peak of the YVO_4:Eu emitters; the good matching between the experimentally measured (solid lines) and FDTD simulated (dashed lines) spectra is also shown.

layers of 285 nm diameter YVO_4:Eu@SiO_2 colloidal host particles surrounding a defect layer constituted by a monolayer of 430 nm diameter YVO_4:Eu@SiO_2 colloidal guest particles. Fig. 2a shows a transversal view of the structure, obtained by scanning electron microscopy. The good ordering of the structure is clearly visible, with slight positional disorder generated in the layer situated on top of the guest particles layer, as already reported elsewhere [41]. The insertion of such a defect layer induces the appearance of localized states for photons within the L pseudo-gap of the host particles fcc structure. Accordingly, a pass band (dip) is created within the stop band, as observed on the extinction spectrum ($\alpha = 0^\circ$) shown in Fig. 2b. Note once more the good engineering of the structure performed such that the spectral position of the pass band coincides with the narrow emission peak of the YVO_4:Eu nanoparticles, represented in the figure by a grey vertical rectangle. Also shown in Fig. 2b are the reflection spectra experimentally obtained (solid lines) as a function of angle while tilting the sample over the ΓL direction together with the extinction ($\alpha = 0^\circ$)/reflection ($\alpha > 0^\circ$) spectra obtained by FDTD simulations. The agreement between experimental specular reflection spectra and simulations is striking, with a nearly perfect concordance of the pass band position as a function of angle. As in Fig. 1c, the vertical axis is arbitrarily scaled and the spectra are arbitrarily shifted in order to clearly distinguish them. However, the extinction spectrum ($\alpha = 0^\circ$) obtained by FDTD simulation does not account for the increase experimentally observed at low wavelength as a result of diffusion in the structure, either due to positional disorder, stacking faults, etc.

In order to test the influence of the pass band within the stop band on the emission properties of the embedded nanoparticles, we measured the emission spectra of the latter, as a function of angle. The goal here is to observe the result of the redistribution of the photonic local density of states, leading to a confinement (inhibition) of the emission within the stop band and exaltation within the pass band. Fig. 2c nicely confirms our expectation, with a sharp increase of the emission at ($\alpha = 0^\circ$), i.e., as the pass band perfectly matches the emission peak of the YVO_4:Eu nanoparticles. As readily seen in the inset of the figure, this strong enhancement is lost as soon as the pass band is shifted out of the emission peak, as a result of the blue shifting of the pseudo-gap induced by the tilting of the sample. As the high wavelength edge of the pseudo-gap still covers (for angles $\alpha = 20^\circ$, 25°, 30°) the emitter's spectral range, the emission spectrum is clearly inhibited and a (small) recovery of the intensity is found for $\alpha = 40^\circ$, once the whole effect of the pass band within the stop band manifests outside of the emission range of the YVO_4:Eu nanoparticles. Normalizing all spectra obtained for angles smaller than $\alpha < 40^\circ$ by the one at 40° allows us to better show the overall effect, as seen in Fig. 2d. An enhancement of about 20%, with respect to the reference situation where the pseudo-gap is clearly out of the YVO_4:Eu emission range, is observed for $\alpha = 0^\circ$ as a result of the presence of the pass band perfectly superposing to the emission peak of YVO_4:Eu nanoparticles. The enhancement is suppressed and a small inhibition is instead observed as the high wavelength edge of the pseudo-gap covers the spectrum of the emitters. The latter effect is best seen for $\alpha = 30^\circ$, where the high wavelength edge of the

pseudo-gap best superposes to the spectral position of the emitter.

4. Conclusions

In this paper, we have engineered colloidal crystals from silica spheres with incorporated luminescent YVO_4:Eu nanoparticles. As a function of angle, the maxima of the experimental and FDTD simulated extinction/reflection spectra have been seen to nicely correspond and follow the Bragg–Snell law. An inhibition of the emission intensity from the light sources was observed in the spectral region of the stop band. Heterostructures containing a planar defect displayed an enhanced emission in the spectral region of the pass band. Let us note here that, to the best of our knowledge, this is the first experimental demonstration, for a direct silica opal structure, of such an enhancement factor (20%) in combination with the narrow range of the enhanced emission having a full width at half maximum of the normalized emission spectrum (Fig. 2d) of approximately 15 nm. We believe that this result originates from our original approach consisting in encapsulating YVO_4:Eu nanoparticles in silica spheres by a classical sol–gel approach, allowing us to fully control the nanoenvironment of the emitters and thus to avoid a heterogeneous broadening of the spectra. Furthermore, this emitter has been chosen for its very sharp and intense emission peak, allowing us to fully superpose the pass band or the stop band to its emission range, leading to a strong enhancement or inhibition of the emission, respectively. We have thus also shown that properly engineered colloidal photonic heterostructures could become good candidates for low-threshold and/or single mode photonic crystal lasers.

Acknowledgments

The authors thank B. Agricole (CRPP) and E. Sellier (CREMEM, Talence) for Langmuir–Blodgett experiments and SEM observations, respectively.

References

[1] H.-G. Park, S.-H. Kim, S.-H. Kwon, Y.-G. Ju, J.-K. Yang, J.-H. Baek, S.-B. Kim, Y.-H. Lee, Electrically driven single-cell photonic crystal laser, Science 305 (2004) 1444.
[2] S. Noda, Seeking the ultimate nanolaser, Science 314 (2006) 260.
[3] E. Yablonovitch, Inhibited spontaneous emission in solid-state physics and electronics, Phys. Rev. Lett. 58 (1987) 2059.
[4] M. Grätzel, Photoelectrochemical cells, Nature 414 (2001) 338.
[5] E.M. Purcell, H.C. Torrey, R.V. Pound, Resonance absorption by nuclear magnetic moments in a solid, Phys. Rev. 69 (1946) 37.
[6] K.H. Drexhage, Influence of a dielectric interface on fluorescence decay time, J. Lumin. 12 (1970) 693.
[7] D. Kleppner, Inhibited spontaneous emission, Phys. Rev. Lett. 47 (1981) 233.
[8] D. Sebök, K. Szendrei, T. Szabó, I. Dékány, Optical properties of zinc oxide ultrathin hybrid films on silicon wafer prepared by layer-by-layer method, Thin Solid Films 516 (2008) 3009.
[9] E. Pál, D. Sebök, V. Hornok, I. Dékány, Structural, optical and adsorption properties of ZnO_2/poly(acrylic acid) hybrid thin porous films prepared by ionic strength controlled layer-by-layer method, J. Colloid Interface Sci. 332 (2009) 173.
[10] K Wostyn, Y. Zhao, B. Yee, K. Clays, A. Persoons, G. de Schaetzen, L Hellemans, Optical properties and orientation of arrays of polystyrene spheres deposited using convective self-assembly, J. Chem. Phys. 118 (2003) 10752.
[11] K.M. Ho, C.T. Chan, C.M. Soukoulis, Existence of a photonic gap in periodic dielectric structures, Phys. Rev. Lett. 65 (1990) 3152.
[12] K. Busch, S. John, Photonic band gap formation in certain self-organizing systems, Phys. Rev. E 58 (1998) 3896.
[13] M.M. Sigalas, C.M. Soukoulis, R. Biswas, K.M. Ho, Effect of the magnetic permeability on photonic band gaps, Phys. Rev. B 56 (1997) 959.
[14] K. Busch, S. John, Liquid-crystal photonic-band-gap materials: the tunable electromagnetic vacuum, Phys. Rev. Lett. 83 (1999) 967.
[15] F. Fleischhaker, A.C. Arsenault, Z. Wang, V. Kitaev, F.C. Peiris, G. Von Freymann, I. Manners, R. Zentel, G.A. Ozin, Redox-tunable defects in colloidal photonic crystals, Adv. Mater. 17 (2005) 2455.
[16] R. Pozas, A. Mihi, M. Ocaña, H. Míguez, Building nanocrystalline planar defects within self-assembled photonic crystals by spin-coating, Adv. Mater. 18 (2006) 1183.
[17] P. Massé, S. Reculusa, K. Clays, S. Ravaine, Tailoring planar defects in three-dimensional colloidal crystals, Chem. Phys. Lett. 422 (2006) 251.
[18] P. Massé, G. Pouclet, S. Ravaine, Periodic distribution of planar defects in colloidal photonic crystals, Adv. Mater. 20 (2008) 584.
[19] V.N. Bogomolov, S.V. Gaponenko, I.N. Germanenko, A.M. Kapitonov, E.P. Petrov, N.V. Gaponenko, A.V. Prokofiev, A.N. Ponyavina, N.I. Silvanovich, S.M. Samoilovich, Photonic band gap phenomenon and optical properties of artificial opals, Phys. Rev. E 55 (1996) 7619.
[20] E. Bovero, F.C.J.M. Van Veggel, Wavelength redistribution color purification action of a photonic crystal, J. Am. Chem. Soc. 130 (2008) 15374.
[21] L. Bechger, P. Lodahl, W.L. Vos, Directional fluorescence spectra of laser dye in opal and inverse opal photonic crystals, J. Phys. Chem. B 109 (2005) 9980.
[22] C. Blum, A.P. Mosk, I.S. Nikolaev, V. Subramaniam, W.L. Vos, Color control of natural fluorescent proteins by photonic crystals, Small 4 (2008) 492.
[23] K. Song, R.A.L. Vallée, M. Van der Auweraer, K. Clays, Fluorophores-modified silica sphere as emission probe in photonic crystals, Chem. Phys. Lett. 421 (2006) 1.
[24] R.A.L. Vallée, K. Baert, B. Kolaric, M. Van der Auweraer, K. Clays, Nonexponential decay of spontaneous emission from an ensemble of molecules in photonic crystals, Phys. Rev. B 76 (2007) 045113.
[25] B. Kolaric, K. Baert, M. Van der Auweraer, R.A.L. Vallée, K. Clays, Controlling the fluorescence resonant energy transfer by photonic crystal band gap engineering, Chem. Mater. 19 (2007) 5547.
[26] C. Vion, C. Barthou, P. Bénalloul, C. Schwob, L. Coolen, A. Grusintsev, G. Emel'chenko, V. Masalov, J.-M. Frigerio, A. Maître, Manipulating emission of CdTeSe nanocrystals embedded in three-dimensional photonic crystals, J. Appl. Phys. 105 (2009) 113120.
[27] P. Lodahl, A.F. Van Driel, I.S. Nikolaev, A. Irman, K. Overgaag, D. Vanmaekelbergh, W.L. Vos, Controlling the dynamics of spontaneous emission from quantum dots by photonic crystals, Nature 430 (2004) 654.
[28] Y.A. Vlasov, K. Luterova, I. Pelant, B. Honerlage, V.N. Astratov, Enhancement of optical gain of semiconductors embedded in three-dimensional photonic crystals, Appl. Phys. Lett. 71 (1997) 1616.
[29] A. Chiappini, C. Armellini, A. Chiasera, M. Ferrari, Y. Jestin, M. Mattarelli, M. Montagna, E. Moser, G. Nunzi Conti, S. Pelli, G.C. Righini, M. Clara Goncalves, R.M. Almeida, Design of photonic structures by solgel-derived silica nanospheres, J. Non-Cryst. Solids 353 (2007) 674.
[30] Y.-S. Lin, Y. Hung, H.-Y. Lin, Y.-H. Tseng, Y.-F. Chen, C.-Y. Mou, Photonic crystals from monodisperse lanthanide-hydroxide-at-silica core/shell colloidal spheres, Adv. Mater. 19 (2007) 577.
[31] K. Baert, K. Song, R.A.L. Vallée, M. Van der Auweraer, K. Clays, Spectral narrowing of emission in self-assembled colloidal photonic superlattices, J. Appl. Phys. 100 (2006) 123112.
[32] R. Vallée, N. Tomczak, H. Gersen, E.M.H.P. van Dijk, M.F. García-Parajó, G.J. Vancso, N.F. van Hulst, On the role of electromagnetic boundary conditions in single molecule fluorescence lifetime studies of dyes embedded in thin films, Chem. Phys. Lett. 348 (2001) 161.
[33] A. Huignard, V. Buissette, G. Laurent, T. Gacoin, J.-P. Boilot, Colloidal synthesis of luminescent rhabdophane $LaPO_4$:$Ln_{3+x}H_2O$ (Ln = Ce, Tb, Eu; $x \approx 0.7$) nanocrystals, Chem. Mater. 14 (2002) 2264.
[34] W. Stöber, A. Fink, E. Bohn, Controlled growth of monodisperse silica spheres in the micron size range, J. Colloid Interface Sci. 26 (1968) 62.
[35] S. Reculusa, S. Ravaine, Synthesis of colloidal crystals of controllable thickness through the Langmuir–Blodgett technique, Chem. Mater. 15 (2003) 598.
[36] A. Taflove, S.C. Hagness, Computational Electrodynamics: The Finite-Difference Time-Domain Method, 3rd ed., Artech House, Inc., Norwood, MA, 2005.
[37] A. Farjadpour, D. Roundy, A. Rodriguez, M. Ibanescu, P. Bermel, J.D. Joannopoulos, S.G. Johnson, G. Burr, Improving accuracy by subpixel smoothing in the finite-difference time domain, Opt. Lett. 31 (2006) 2972.
[38] L.M. Goldenberg, J. Wagner, J. Stumpe, B.-R. Paulke, E. Görnitz, Ordered arrays of large latex particles organized by vertical deposition, Langmuir 18 (2002) 3319.
[39] H. Míguez, C. Lopez, F. Meseguer, A. Blanco, L. Vazquez, R. Mayoral, M. Ocaña, V. Fornes, A. Mifsud, Photonic crystal properties of packed submicrometric SiO_2 spheres, Appl. Phys. Lett. 71 (1997) 1148.
[40] J.F. Galisteo-López, E. Palacios-Lidón, E. Castillo-Martínez, C. López, Optical study of the pseudogap in thickness and orientation controlled artificial opals, Phys. Rev. B 68 (2003) 115109.
[41] P. Massé, R.A.L. Vallée, J.-F. Dechézelles, J. Rosselgong, E. Cloutet, H. Cramail, X.S. Zhao, S. Ravaine, Effects of the position of a chemically or size-induced planar defect on the optical properties of colloidal crystals, J. Phys. Chem. C 113 (2009) 14487.

Optical cavity modes in semicurved Fabry–Pérot resonators

Stéphane Mornet,[1] Lionel Teule-Gay,[1] David Talaga,[2] Serge Ravaine,[3] and Renaud A. L. Vallée[3,a)]

[1]*Institut de Chimie de la Matière Condensée de Bordeaux, CNRS, Université Bordeaux I, 87 av. Dr A. Schweitzer, 33608 Pessac Cedex, France*

[2]*Institut des Sciences Moléculaires, Université Bordeaux I, 351 cours de la libération, 33405 Talence Cedex, France*

[3]*Centre de Recherche Paul Pascal (CNRS-UPR8641), 115 av. Dr A. Schweitzer, 33600 Pessac Cedex, France*

(Received 23 August 2010; accepted 24 August 2010; published online 25 October 2010)

We present a nanofabrication method which combines bottom-up and top-down techniques to realize nanosized curved Fabry–Pérot cavities. These cavities are made of a hexagonal closed packed monolayer of silica particles enclosed between flat and curved metallic mirrors. They exhibit geometric cavity modes such as those found in gold shell colloids. These modes manifest as dips in the reflection spectra which shift as a function of the diameter of the used nanoparticles. An excellent agreement is found between experiment and theory which allows us to properly interpret our data. The work presented here constitutes a further step to the development of curved photonics. © *2010 American Institute of Physics*. [doi:10.1063/1.3493691]

Noble metal structures with dimensions smaller than or comparable to the wavelength of light exhibit interesting optical properties due to the collective oscillation of conduction electrons (surface plasmons). In the case of small particles, this localized surface plasmon mode causes confinement of the electromagnetic field near the surface and leads to strong extinction in the visible and near infrared, depending on the geometry, size, and shape of the metal particle.[1,2] The enhanced local fields can be used to enhance the fluorescence emission,[3,4] the Raman signals,[5,6] or the photostability of luminescent dyes close to the metal surface by shortening the excited-state lifetime.[7–11] Beyond these noble metal nanoparticles, core-shell colloids, composed of a dielectric core surrounded by a metallic shell are particularly interesting to investigate. The plasmon frequency of these particles can be tuned throughout the visible and near-infrared part of the spectrum by varying either the core diameter or the shell thickness.[12–14] Besides these well-known collective extinction resonances the geometric cavity modes,[15,16] which result from the confinement of light inside the dielectric core while the cavity boundaries are determined by the metal shell, have not yet received much attention up to now.

In this letter, we aim to investigate such geometric cavity modes and demonstrate the possibility of designing efficient nano-optical devices, such as curved nanosized Fabry–Pérot resonators by a unique combination of sol-gel chemistry and top-down deposition techniques. The enhanced local field together with the focusing effect due to the curvature itself allows us to strengthen the cavity properties. The main features of such a cavity are analyzed numerically, using the finite-difference time-domain (FDTD) algorithm.

The optical cavities described here are obtained by deposition of a monolayer of monodisperse silica (SiO_2) particles arranged in a hexagonal closed packed (hcp) structure (dielectric layer) in between two reflecting slabs. The front mirror is a curved thin gold (Au) slab while the back mirror is either a silicon substrate (Si) or a thin gold-coated silicon substrate (Si+Au). Figure 1(a) shows the scheme of these two types of cavities. The gold layers, of 20 nm thickness, were deposited by reactive magnetron sputtering using pure Au (99.99%) target. The silica nanoparticles were synthesized following the Stöber–Fink–Bohn method[17] from tetraethoxysilane (Fluka) and ammonia (29% in water, J.T. Baker). The two-dimensional (2D) particle arrays were generated following the procedure previously described by Wang *et al.*[18] This procedure was applied for various sizes of silica nanoparticles ranging from 180 to 470 nm. The sputtering deposition parameters were set to get a reproducible deposition rate (around 12.5 nm min^{-1}), ensuring a good uniformity of the film thickness for all substrates. The optical properties of the cavities were investigated by reflection spectroscopy using a home-made system equipped with a deuterium tungsten–halogen fiber optic light source mikropack dh-2000 as sample excitation source. For collection, the reflected light was sent to a Horiba Jobin-Yvon HR800 spectrometer equipped with a 150 grooves mm^{-1} grating and a Symphony CCD detector providing a 2 nm resolution. In the spectra, the reflection signal was always normalized with respect to the corresponding one of either a pure silicon substrate or a 20 nm gold-coated silicon substrate. The FDTD simulations[19] were performed with a freely available software package.[20] The computational cell, in which the incoming wave propagates along the z direction with a linear polarization in the x direction, has been implemented with periodic boundary conditions in x and y directions and perfectly matched layers in the z direction. The dielectric permittivity of gold was specified by using the Drude–Lorentz model with parameters determined by Vial *et al.*,[21] based on the best fits, following a FDTD approach, to the relative permittivity of gold as tabulated by Johnson and Christy.[22]

a)Electronic mail: vallee@crpp-bordeaux.cnrs.fr.

 © 2010 American Institute of Physics

Downloaded 26 Oct 2010 to 147.210.82.88. Redistribution subject to AIP license or copyright; see http://jap.aip.org/about/rights_and_permissions

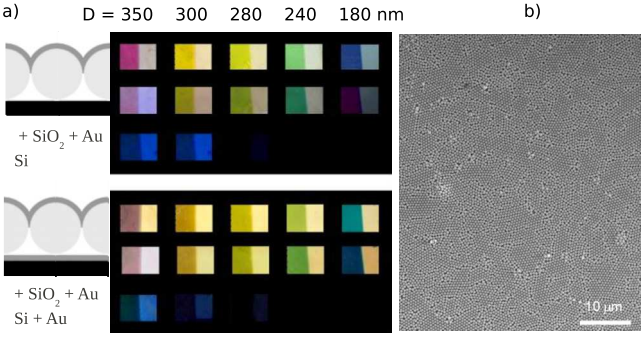

FIG. 1. (Color online) (a) Scheme of the designed cavities and photographs illustrating their change in color as a function of the increasing (from right to left) diameter D of the hcc-arranged particles and inclination of the samples with respect to the direction of acquisition (90°, 45°, 0° from top to bottom). The top (bottom) scheme pertains to silica (SiO_2) particles deposited on a pure silicon substrate (Si) [20 nm gold-coated silicon substrate (Si+Au)]. In both series, the right part of each sample has been masked before final gold sputtering. (b) SEM top view of a gold-coated monolayer of 470 nm silica particles.

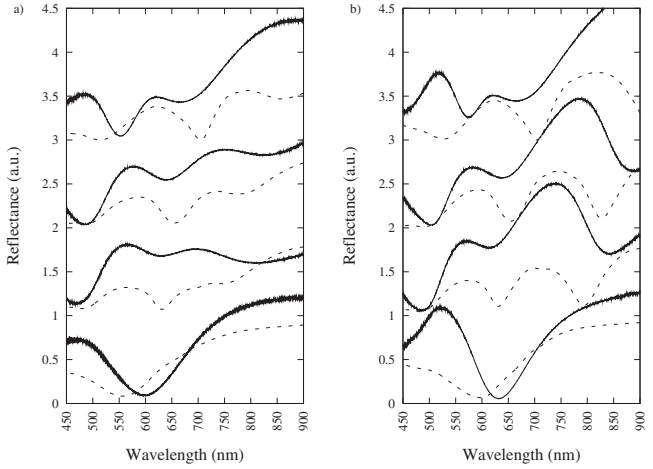

FIG. 2. Experimental (solid lines) and simulated (dashed lines) reflection spectra of the semicurved cavities for particles diameters D ranging from 180 nm to 240, 280, 300, and 350 nm, from bottom to top deposited either directly on the silicon wafer (a) or on the gold-coated silicon wafer (b). The spectra are offset by 1.0 from one another for visibility.

Figure 1(a) shows photographs of the various samples obtained with silica particles of diameter D decreasing from left $D=350$ nm to right $D=180$ nm. Two series are exhibited depending on whether the particles have been deposited directly on the silicon wafer (Si, top) or on the 20 nm thick gold-coated silicon wafer (Si+Au, bottom). In both cases, the considered structures have been closed (left part of each sample) with a thin gold film (Au, 20 nm thick), which adopted the curvature of the silica particles underneath, thus forming a semicurved cavity. A rich panel of colors is exhibited, depending on the diameter D of the silica particles. Furthermore, a progressive extinction is observed as the angle α is decreased from $\alpha=90°$ to $\alpha=0°$ (from top to bottom). The uniformity of the color areas extending on centimeter square can only be reached for perfectly designed micro/nanocavities, the quality of which is further exemplified in the scanning electron microscope (SEM) picture presented in Fig. 1(b).

In most cases, resonance in a nanostructure can be probed with far-field signals.[23] In this study, the entrance surfaces of the cavities were illuminated with a nearly collimated white light, and the backscattering spectrum was only measured from a selected area (50 μm) of each semicurved cavity. The measured quantity, hereafter simply called reflectance, is depicted in Fig. 2 (solid lines) as a function of wavelength and diameter of the silica particles deposited either directly on the silicon wafer (a) or on the gold-coated silicon wafer (b). Dips are observed in the reflection spectra and they systematically shift to the long wave range as a function of D. The same dips are observed while slightly shifted and with distinct amplitudes in case the used back mirror is either the pure silicon wafer or the gold-coated silicon wafer. The simulated reflection spectra (dashed lines) are superimposed on each figure. The good agreement between these spectra and the ones obtained experimentally is clearly observed and points to the usefulness of subsequent simulations to explain some behavioral characteristics.

Let us perform a close inspection to the case of silica particles with $D=300$ nm enclosed by the gold-coated silicon wafer and the front gold curved mirror. The usual interband transition exhibited by gold at around 500 nm manifests clearly as a dip in the reflectance [Fig. 2(b)]. It barely changes its position as a function of the cavity thickness. Besides this "pure" plasmonic resonance, the two extradips (at 654 nm and 828 nm, Fig. 2(b) exhibit a shift in their positions as a function of the cavity thickness, which is a clear sign of coupling of a cavity mode to some plasmonic collective oscillation. Furthermore, the simulated reflection and transmission spectra [Fig. 3(a)] of this structure exhibit some peculiar behavior: while the reflectance dip (detected at the entrance surface of the structure, Fig. 3, inset) shown at

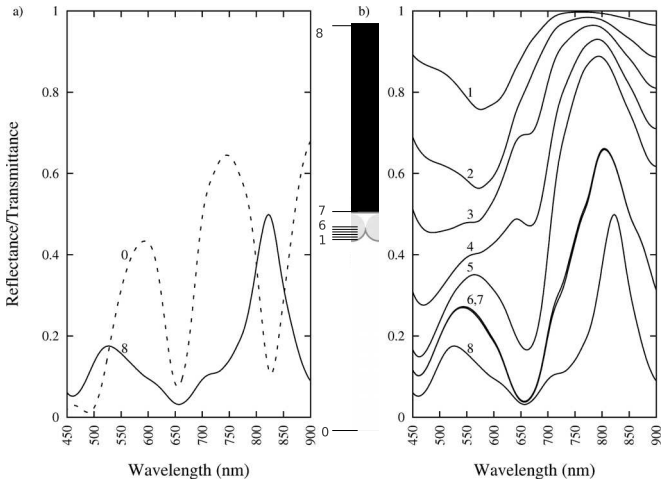

FIG. 3. (a) Simulated reflection (0, dashed) and transmission (8, solid) spectra of an array of hcp arranged monodisperse silica particles of diameter $D=300$ nm enclosed in between a front gold curved mirror and a gold-coated silicon wafer. (b) Simulated transmission spectra through flux planes situated at distances 5 (1), 30 (2), 50 (3), 70 (4), 90 nm (5) from the curved front mirror, in the center (6), at the back of the cavity (7) and at the outlet of the structure (8). Inset: geometry of the simulated structure with indication of the positions of the planes used for flux detection. The source originates from plane O and goes upwards. It is partially reflected/transmitted by the cavity. The reflected flux is detected back through plane O. The transmitted flux goes through the cavity, entering at the front mirror, is detected successively through planes 1 (5 nm after the front mirror) to 7 (back mirror) prior to continue through the substrate to be finally detected through plane 8 (outlet of the structure).

Downloaded 26 Oct 2010 to 147.210.82.88. Redistribution subject to AIP license or copyright; see http://jap.aip.org/about/rights_and_permissions

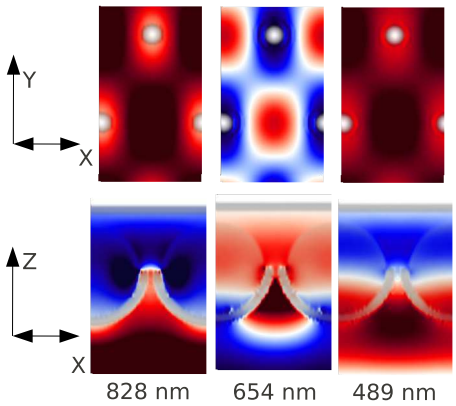

FIG. 4. (Color online) FDTD snapshots of the x-component of the electric field of a very narrow Gaussian pulse propagating in the z-direction of the curved cavity shown in Fig. 3. for wavelengths corresponding to the three reflectance dips observed.

828 nm coincides with a transmittance peak (detected at the outlet of the structure, Fig. 3, inset), the reflectance dip at 654 nm also exhibits a transmittance dip. Following the usual formula $T+R+A+Dif=1$, where T, R, A, and Dif stand for the transmittance, reflectance, absorbance, and diffusion, respectively, a minimum in both transmittance and reflectance clearly indicates a strongly absorbant and/or diffusive mode at 654 nm.

The fluxes transmitted through planes situated at various depths from the front gold curved mirror are presented in Fig. 3(b). Close to the front mirror (plane 1), a broad peak extending from about 600 nm to more than 900 nm emerges as a manifestation of a highly diffusing collective plasmon oscillation. As the distance from the front mirror increases, the extension of this peak reduces and it splits into two parts: a dip and a peak which reinforce and localize at $\lambda=654$ nm and $\lambda=828$ nm, respectively. The transmission spectra are almost indistinguishable as detected in the middle (plane 6) or at the back (plane 7) of the cavity. The behavior exhibited by the mode at $\lambda=654$ nm is reminiscent of a quadripolar plasmon resonance mode, mainly localized to the near field of the front mirror. The incoming light at that wavelength is completely absorbed/scattered by the front gold curved mirror and accordingly shows a dip in reflectance as in transmittance far from it. On the contrary, the mode at $\lambda=828$ nm. looks like a dipolar plasmon resonance mode, able to propagate on longer distances. The fact that these modes are coupled to the cavity is best illustrated by the shift they exhibit as a function of the cavity length (Fig. 2).

Finally, we simulated FDTD snapshots of the x-component of the electric field of a very narrow Gaussian pulse propagating in the z-direction of the structure shown in Fig. 3 for the three wavelengths of interest. The resonance at $\lambda=828$ nm clearly exhibits (Fig. 4) a dipolar character, very similar (while stronger) to the one of the interband transition at $\lambda=489$ nm. This indicates that this resonance is due to a cavity mode coupled to the dipolar collective mode. On the contrary, the FDTD snapshot (Fig. 4) corresponding to the dip at $\lambda=654$ nm is more quadripolar in nature and points to a resonance due to a cavity mode coupled to a collective quadripolar mode.

In conclusion, we have presented a simple nanofabrication method which combines bottom-up and top-down techniques to realize nanosized curved Fabry–Pérot cavities. These cavities exhibit geometrical cavity resonances that depend on the size of the dielectric core. Contrarily to our investigations, Yu *et al.*[24] reported the effect of the Al_2O_3 coating thickness on the reflectance properties of a similar structure. Owing to FDTD simulations, we could discriminate between dipolar and quadripolar resonances which result from the coupling of cavity modes and plasmonic collective modes. The strong exaltations observed (Fig. 4) in the vicinity of the front gold curved mirror are of particular interest: potential emitters could be inserted by functionalization at these positions and benefit of the maximum field. This feature could prove very important for applications as nanoscale light sources, sensors, or lasers. In this respect, the variation in the thickness of the metal shell will be a parameter of choice to increase the cavity quality factor.

Jean-Pierre Manaud (ICMCB) and Isabelle Ly (CRPP) are acknowledged for gold sputtering and SEM observations, respectively.

[1] U. Kreibig and M. Vollmer, *Optical Properties of Metal Clusters* (Springer, Berlin, 1995).
[2] C. F. Bohren and D. R. Huffman, *Absorption and Scattering of Light by Small Particles* (Wiley, New York, 1983).
[3] J. Gersten and A. Nitzan, J. Chem. Phys. **73**, 3023 (1980).
[4] J. S. Biteen, N. S. Lewis, H. A. Atwater, H. Mertens, and A. Polman, Appl. Phys. Lett. **88**, 131109 (2006).
[5] M. Moskovits, Rev. Mod. Phys. **57**, 783 (1985).
[6] J. B. Jackson and N. J. Halas, Proc. Natl. Acad. Sci. U.S.A. **101**, 17930 (2004).
[7] A. Parfenov, I. Gryczynski, J. Malicka, C. D. Geddes, and J. R. Lakowicz, J. Phys. Chem. B **107**, 8829 (2003).
[8] A. Moroz, Chem. Phys. **317**, 1 (2005).
[9] O. G. Tovmachenko, C. Graf, D. J. van den Heuvel, A. van Blaaderen, and H. C. Gerritsen, Adv. Mater. **18**, 91 (2006).
[10] J. Enderlein, Appl. Phys. Lett. **80**, 315 (2002).
[11] J. Enderlein, Phys. Chem. Chem. Phys. **4**, 2780 (2002).
[12] A. L. Aden and M. Kerker, J. Appl. Phys. **22**, 1242 (1951).
[13] A. E. Neeves and M. H. Birnboim, J. Opt. Soc. Am. B **6**, 787 (1989).
[14] S. J. Oldenburg, R. D. Averitt, S. L. Westcott, and N. J. Halas, Chem. Phys. Lett. **288**, 243 (1998).
[15] T. V. Teperik, V. V. Popov, and F. J. García de Abajo, Phys. Rev. B **69**, 155402 (2004).
[16] J. J. Penninkhof, L. A. Sweatlock, A. Moroz, H. A. Atwater, A. van Blaaderen, and A. Polman, J. Appl. Phys. **103**, 123105 (2008).
[17] W. Stöber, A. Fink, and E. Bohn, J. Colloid Interface Sci. **26**, 62 (1968).
[18] W. Wang, B. Gu, L. Liang, and W. Hamilton, J. Phys. Chem. B **107**, 3400 (2003).
[19] A. Taflove and S. C. Hagness, *Computational Electrodynamics: The Finite-Difference Time-Domain Method*, 3rd ed. (Artech House, Norwood, MA, 2005).
[20] A. F. Oskooi, D. Roundy, M. Ibanescu, P. Bermel, J. D. Joannopoulos, and S. G. Johnson, Comput. Phys. Commun. **181**, 687 (2010).
[21] A. Vial, A.-S. Grimault, D. Macías, D. Barchiesi, and M. Lamy de la Chapelle, Phys. Rev. B **71**, 085416 (2005).
[22] P. Johnson and R. Christy, Phys. Rev. B **6**, 4370 (1972).
[23] D. P. Fromm, A. Sundaramurthy, P. J. Schuck, G. Kino, and W. E. Moerner, Nano Lett. **4**, 957 (2004).
[24] X. Yu, L. Shi, D. Han, J. Zi, and P. V. Braun, Adv. Funct. Mater. **20**, 1 (2010).

Downloaded 26 Oct 2010 to 147.210.82.88. Redistribution subject to AIP license or copyright; see http://jap.aip.org/about/rights_and_permissions

Journal of Materials Chemistry

Cite this: DOI: 10.1039/c0jm03829f

www.rsc.org/materials

View Online
Dynamic Article Links

COMMUNICATION

Tuning nanopatterns on fused silica substrates: a theoretical and experimental approach†

Rodica Morarescu,*[a] Lars Englert,[b] Branko Kolaric,[a] Pascal Damman,[a] Renaud A. L. Vallée,[c] Thomas Baumert,[b] Frank Hubenthal[b] and Frank Träger[b]

Received 8th November 2010, Accepted 7th February 2011
DOI: 10.1039/c0jm03829f

Published on 21 February 2011 on http://pubs.rsc.org | doi:10.1039/C0JM03829F
Downloaded by Universitaetsbibliothek Kassel on 21 February 2011

In this study we develop a novel approach to tune nanopatterns on fused silica substrates exploiting the polarization dependence of the strongly localized near field of highly ordered triangular nanoparticle arrays. For this purpose such arrays were prepared by nanosphere lithography on fused silica substrates and subsequently irradiated with single 35 fs long laser pulses. The irradiation leads to the excitation of localized surface plasmon polariton resonances, followed by ablation of the nanoparticles and partially of the substrate. By this means, nanostructures were generated on the substrate surface, reflecting the local fields in the vicinity of the triangular nanoparticles. Depending on the applied fluence, small holes as well as extended nanostructures with dimensions well below the diffraction limit have been created. Furthermore, by rotating the linear polarization of the laser light by 90° with respect to the orientation of triangular nanoparticles, different plasmon modes have been excited, which in turn, alter the local field distribution. As a result, either nanochannels or bone like shaped nanogrooves in a chequered structure were generated on the fused silica substrates. Finite-difference time-domain simulations demonstrate, that the results can, in fact, be explained by the enhanced near field distribution, which is dominated by the excitation of localized surface plasmon polariton resonances in the triangular nanoparticles. It is shown, that the fluence and the polarization of the laser light are the key parameters in nanogroove and nanochannel formation.

I. Introduction

In nanotechnology, the generation of nanopatterns with complex morphologies having dimensions well below the optical diffraction limit remains an ambitious challenge. Behind the fundamental interest in understanding the physical process of morphogenesis at a surface, the motivation to study nanopatterning is also driven by the great potential of such nanostructures for advanced applications in *e.g.* nanofluidics, nanophotonics and biomedical devices.[1–3]

Nowadays numerous methods are able to generate nanopatterns *e.g.* combining different physical stresses (electric, magnetic, thermal, elastic) conventional top-down lithography techniques or laser induced surface structuring. The latter method is a method of choice that allows the precise generation of nanopatterns with dimensions below the optical diffraction limit.[4] One approach to achieve such nanostructures is to exploit the near field of a microscope tip illuminated with laser light,[5] although this technique is not suitable for many applications due to its limited throughput. A more promising approach, which has attracted increasingly more attention in recent years, exploits the near field of latex or SiO_2 micro- and nanosphere arrays on substrates, irradiated with ns- or fs-pulsed laser light.[6,7] Due to the lens effect of the spheres, high electromagnetic fields in the vicinity of the substrate are generated, which overcome the ablation threshold.[8,9] Depending on the arrangement of the spheres, highly ordered arrays of nanoholes are created in the substrate.[10] Recently similar experiments were undertaken using spherical noble metal particles, exploiting their unique optical properties, which are dominated by the excitation of localized surface plasmon polariton resonances (LSPPRs). These collective oscillations of the conduction band electrons are accompanied by an enhancement of the local field in the vicinity of the nanoparticle (NP) surface. This enhanced local field in combination with the focusing effect due to the sphere itself, allows generation of distinct types of nanopatterns.[11,13–15] It was shown that when gold nanospheres with a diameter of approximately 200 nm are illuminated with linearly polarized fs-pulsed laser light, the local field distribution underneath the NP creates elongated holes[13] oriented along the polarization direction. Motivated by these results, great attention has been paid to nonspherical NPs, which generate much stronger and more sophisticated local electromagnetic fields.[16] In particular, NPs with sharp tips, such as triangular nanoprisms show a great potential to generate well defined nanoscale structures over large areas of the substrate.[17]

In this paper we demonstrate an innovative and inexpensive method for tuning nanopatterns with dimensions well below the diffraction limit on fused silica substrates. The method is based on local ablation of the substrate surface due to the electromagnetic field

[a]*Laboratoire Interfaces & Fluides Complexes, Centre d'Innovation et de Recherche en Matériaux Polymères, Université de Mons, 20 Place du Parc, B-7000 Mons, Belgium. E-mail: rodica.morarescu@umons.ac.be*
[b]*Institut für Physik and Center for Interdisciplinary Nanostructure Science and Technology (CINSaT), Universität Kassel, Heinrich-Plett-Str. 40, 34132 Kassel, Germany*
[c]*Centre de Recherche Paul Pascal (CNRS-UPR8641), 115 avenue du docteur Schweitzer, 33600 Pessac, France*

† Electronic supplementary information (ESI) available: Experimental information and additional characterisation. See DOI: 10.1039/c0jm03829f

View Online

Downloaded by Universitaetsbibliothek Kassel on 21 February 2011
Published on 21 February 2011 on http://pubs.rsc.org | doi:10.1039/C0JM03829F

enhancements in the vicinity of highly ordered triangular gold NPs. Large surface areas can be patterned with well-defined nanostructures, by applying single 35 fs laser pulses to the sample. The advantage of this approach lies in its versatility: for a given geometry of the highly ordered NP arrays, several nanopatterns can be generated by ablation controlling the applied fluence and, more importantly the polarization direction of the laser light with respect to the NP orientation. To explain the morphology of the generated nanostructures, finite-difference time-domain simulations (FDTD) have been performed. The simulations show, that the generated nanostructures can indeed be explained by the local field enhancements. These structures are expected to play a major role in technological applications, such as biochemical chips and waveguides.[18,19]

Experiments presented here use arrays of triangular gold NPs prepared by nanosphere lithography,[20] utilizing the drop coating method of Micheletto *et al.*[21] Subsequently the samples were irradiated under ambient conditions with a single femtosecond light pulse, generated by an amplified Ti : sapphire laser system, coupled to a modified microscope set-up. The pulse duration was 35 fs full width at half maximum and the diameter of the laser spot on the sample was set to 22 μm. The NP arrays were irradiated using linear or circular polarized light under normal incidence with a central wavelength of $\lambda \approx 790$ nm. In order to increase the energy range, the pulse energy has been varied from $E = 0.1$ μJ to $E = 7.0$ μJ. The NPs have an aspect ratio (AR) of 2.47 (edge length divided by the NP height). The extinction spectrum of the NPs (see ESI†) exhibits a strong plasmon resonance at $\lambda = 730$ nm due to the excitation of the dipolar mode.[22–24] Hence, the chosen wavelength of the laser light, at $\lambda \approx 790$ nm, strongly excites this mode of the triangular gold NPs. The NPs as well as the imprinted nanopatterns have been characterized by atomic force microscopy (AFM), scanning electron microscopy (SEM), and extinction spectroscopy. A detailed description of the experimental procedure, samples characterization, experimental set-up and FDTD simulations respectively is presented in the Electronic Supplementary Information†.

II. Results and discussion

A broad range of laser fluences have been studied in single shot experiments, exploiting the Gaussian intensity distribution of the incident laser light. Along these lines, four different regions have been identified. We emphasize, that the triangular gold NPs have been completely removed from the substrate after a single pulse. According to our definition, the applied fluence is low, medium, high, and beyond the ablation threshold in regions 1, 2, 3, and 4, respectively. While in regions 1 to 3, well-defined nanopatterns appear, the fluence in region 4 is so high, that an unstructured ablation occurs. The definition of theses 4 regions is justified, because similar local fluences on the surface irradiating spot result in similar structures, independent of the applied energy. The only difference is, that the regions 1 to 3 appear further away from the spot center for increasing energy and region 4 increases in diameter for higher energies. In the following, we present different generated nanostructures and show that these structures are the result of the localization of the electromagnetic field due to excitation of plasmon resonances in the triangular NPs. For an appropriately chosen energy, the ablation threshold of the substrate is surmounted exclusively in tiny areas in close vicinity of the triangular NPs.

A. Influence of the Gaussian intensity distribution on nanopattern formation

In first experiments the influence of the applied energy on the morphology of the generated nanopattern was investigated. For this purpose, the Gaussian energy distribution of the intensity profile within the laser spot was exploited. The energy was set to $E = 0.16$ μJ and the incident polarization direction was almost parallel to the bisectors of the triangles. Fig. 1a–c show AFM images of fused silica surfaces after irradiation, obtained in regions 1, 2, and 3. Although the illuminated area had a diameter of 22 μm, only in an area with a diameter of 16 μm are nanostructures created. The reason is, that outside this region even the enhanced local field in the vicinity of the NPs does not overcome the ablation threshold of fused silica (~2 J cm^{-2}).[25,26] In region 1, where the approximate local fluence was 0.056 J cm^{-2} small elliptical holes are generated (Fig. 1a). In region 2 (local fluence ≈ 0.072 J cm^{-2}) nanostructures composed of three clearly distinct holes are created, one of them being large and two others being small (Fig. 1b). Finally, for high fluence (region 3, the local fluence ≈ 0.082 J cm^{-2}) the holes are completely merged and form nanogrooves with a bone-like shape in a chequered structure (Fig. 1c). The morphological details of the different nanostructures are summarized in Table 1. The results clearly demonstrate, that even the largest generated nanostructures have dimensions well below the diffraction limit. We emphasize, that minor shape variations of the nanostructures are mainly due to the strong Gaussian intensity

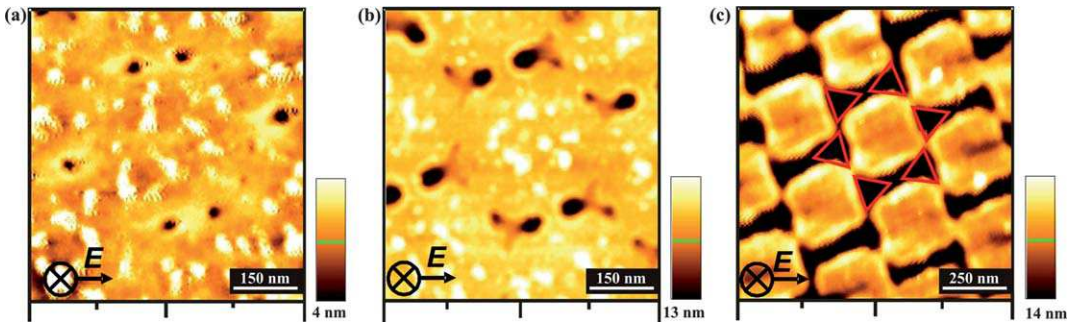

Fig. 1 AFM images of the generated nanopatterns in region 1 (a), region 2 (b), and region 3 (c). The applied pulse energy was $E = 0.16$ μJ. The red triangles indicate the original position of the triangular NPs on the substrate prior to irradiation. For clarity reasons, the red triangles have been drawn larger than the original NPs, which, in fact, have a tip to tip distance of approximately 100 nm. The black arrows indicate the polarization direction of the incoming laser light.

 This journal is © The Royal Society of Chemistry 2011

View Online

Table 1 Characteristic features of the generated nanostructures for different fluences. The polarization of the applied laser light was parallel to the common bisector of two neighboring NPs, (*cf.* Fig. 1)

Region	Average local fluence/J cm^{-2}	Structure	Average depth/nm	Average length/nm	Average width/nm
1	0.056	Holes	4.5 ± 0.5	23 ± 3	23 ± 3
2	0.072	Large subholes	13 ± 2	45 ± 5	34 ± 4
		Small subholes	4.5 ± 1.5	23 ± 2	23 ± 2
3	0.082	Nanogrooves	14 ± 2	287 ± 10	44 ± 8

Downloaded by Universitaetsbibliothek Kassel on 21 February 2011
Published on 21 February 2011 on http://pubs.rsc.org | doi:10.1039/C0JM03829F

distribution of the laser spot. As shown in our previous publication,[17] a homogeneous intensity distribution, *i.e.*, a larger spot diameter, results in nanopatterns of high uniformity. For an easy interpretation of the morphology of the generated nanostructures, the initial position of the triangular NPs (red triangles) and the polarization direction (black *E*-field vector) of the laser light are indicated in Fig. 1. Although the average fluence of the laser light is below the ablation threshold in regions 1 to 3, ablation occurs. This can be explained by the strong localization and enhancement of the fields in the vicinity of the NPs. The general trend, that larger structures appear closer to the center of the laser spot, can be easily explained by the Gaussian energy distribution of the laser beam. At the edge of the laser spot, the fluence is relatively low and no or only minor ablation occurs. In contrast, close to the center (region 3), the fluence increases, more material is ablated and larger nanostructures appear. We emphasize, that all created nanostructures are located at the original positions of the removed triangular NPs and the distance between the structures corresponds to the diameter of the nanospheres used for the lithographic mask.

To confirm the origin of the generated nanostructures, FDTD simulations have been performed. Fig. 2 illustrates the electric field energy density distribution for a polarization direction parallel to the bisector of the triangular NPs. In this case, the largest fields are generated only on the tip that points in the polarization direction. The two tips oriented perpendicular to this direction exhibit only small field enhancements. These calculations explain the origin of the observed experimental results presented in Fig. 1. For a low applied fluence, only at the tips exhibiting the largest field enhancements, the ablation threshold has been overcome (Fig. 1a). Increasing the fluence, the confinement of the light energy on the two other tips exhibiting the lowest field enhancements in Fig. 2 produce energy densities able to overcome the ablation threshold, such that besides the major hole, two minor holes are created (Fig. 1b). Finally, the generation of the most important structure, the nanogrooves, is an interplay of two effects. Firstly, due to the high applied fluence, the electric field energy densities significantly increase so that their distribution shows overlapping areas. Secondly, the energy densities of the two mainly excited tips of neighboring triangles merge together creating the ablation areas shown in Fig. 1c. Both effects lead to a nearly homogeneous ablation of material and the bone-like structures are generated. We thus have perfect agreement between the experiments and the simulations.

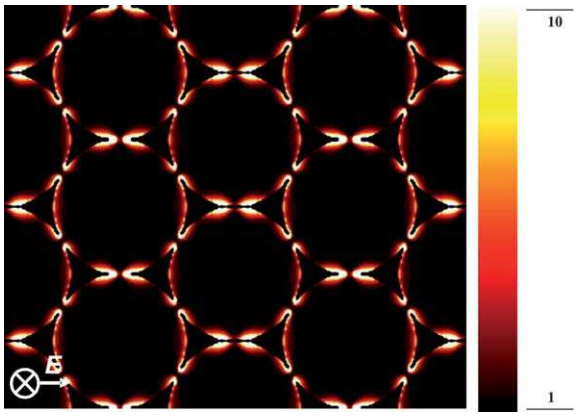

Fig. 2 Normalized electric field energy density distribution for an array of triangular NPs arranged on a fused silica substrate. The normalization is performed with respect to the electric field energy density distribution of a fused silica substrate. The incident electric field is linearly polarized along the common bisector of the triangles. The energy density has been time-averaged on the duration of the incident pulse.

B. Influence of the applied energy

As mentioned before, the pulse energy has been varied from $E = 0.1$ μJ to $E = 7.0$ μJ. However, for the same direction of the polarization of the laser light with respect to the orientation of the triangles, similar nanopatterns have been formed in regions 1 to 3, independent of the applied energy. Fig. 3a depicts a 3D-AFM image of the nanogrooves, which exhibit the same bone-like shape and almost similar dimensions as before. The nanogrooves have been generated in region 3, after irradiation with a single laser pulse with an energy of $E = 2$ μJ.

The polarization of the laser light was again almost parallel to the bisectors of the triangles. The only difference is, that the generated nanogrooves appear at larger distances from the central spot due to the higher fluence of the laser light (≈ 0.8 J cm^{-2}). The grooves have an average depth of $\langle D \rangle = (11 \pm 2)$ nm, an average length of $\langle L \rangle = (267 \pm 10)$ nm, and an average width of $\langle W \rangle = (39 \pm 5)$ nm. Fig. 3b depicts a height profile of the generated nanogrooves, as indicated in Fig. 3a. It demonstrates that the generated nanogrooves have the same depth. Therefore, homogeneous ablation in the areas with high local fields occurs. In addition, the height profile reveals, that the nanogrooves are surrounded by a rim. Very likely, it is caused by surface melting, which resolidifies on the substrate at the borders of the nanostructures, as previously explained by other authors.[11,12]

C. Influence of the polarization direction

To demonstrate the influence of the polarization direction, an additional set of experiments has been performed. For these experiments, the polarization direction has been rotated by 90° with respect to the triangular NPs. Hence, the polarization is almost parallel to a base of the triangles. The energy of the laser light was set to $E = 3.8$ μJ. Due to the high energy, the area where nanostructures are generated, coincides with the laser spot diameter of 22 μm. Fig. 4 depicts AFM images, which show the evolution of the nanostructures as a function

View Online

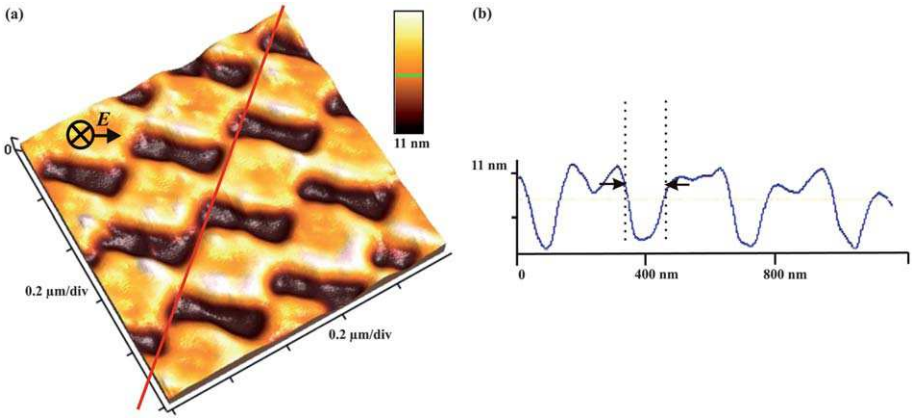

Fig. 3 (a) 3-D AFM image of the generated nanogrooves in region 3. The applied pulse energy was set to $E = 2$ μJ. The black arrow indicates the polarization direction of the incoming laser light. (b) Height profile of the generated nanogrooves, demonstrating that all the nanogrooves have the same depth.

Published on 21 February 2011 on http://pubs.rsc.org | doi:10.1039/C0JM03829F
Downloaded by Universitaetsbibliothek Kassel on 21 February 2011

of energy, *i.e.*, in regions 1 to 3. Again, the nanopatterns are located at the original position of the removed triangles. Minor shape variations of the nanostructures are mainly due to the pronounced Gaussian intensity distribution of the laser spot. Although the formation of the nanopattern is the same as before—higher fluences generate larger structures—the images show remarkable differences in the morphology, as compared to the nanostructures presented in section II A. Even in region 1 (see Fig. 4a) double holes are created at a single NP. These double holes merge together with increasing fluence in region 2 (Fig. 4b). For high fluences in region 3 (Fig. 4c), micrometer long nanochannels are formed. Nevertheless, the average width and depth of the nanochannels amount to only $\langle W \rangle = (94 \pm 3)$ nm and $\langle D \rangle = (31 \pm 4)$ nm, respectively, *i.e.*, well below the diffraction limit. The dimensions of all nanostructures depicted in Fig. 4 are listed in Table 2.

As already mentioned above, the morphology of the nanostructures depends on the polarization direction of the laser light with respect to the NPs. It is obvious, that the double holes are created at the two tips of the baseline, which is parallel to the polarization direction of the laser light. In contrast to the experiments described in section II A, the third tip causes nearly no ablation, even for the highest fluence. To explain the generated structures, again FDTD simulations have been performed. Fig. 5 shows the FDTD simulation where the polarization direction of light is parallel to the base line of the triangles. The simulations easily explain the observed double holes structures in regions 1 and 2, *i.e.*, for low and medium fluences. For high fluences, again two effects occur. First, the ablation areas underneath the two strongly excited tips of a single NP overlap and the double holes merge together. Second, the ablation areas created underneath the tips of two neighboring NPs also overlap. If the overlap is sufficiently high, an almost homogeneous ablation of the substrate occurs, leading to the formation of micrometer long nanochannels. These channels exhibit homogeneous depths and their widths are well below the diffraction limit. Again, we thus have perfect agreement between experiments and simulations.

We emphasize, that the length of the nanochannels is limited only by the area in which highly ordered triangular NPs are located and by the area which is homogeneously illuminated by the laser light. It has been demonstrated, that 6 μm long channels with an extremely homogeneous depth are easily prepared.[17]

D. Circular polarization

In order to investigate the effect of an enlarged polarization space on nanopatterning, experiments with circularly polarized light were performed. As compared to the nanostructures obtained with linearly polarized laser light, the ones obtained by circularly polarized light are more symmetric (see Fig. 6a and 6b). This can be explained as

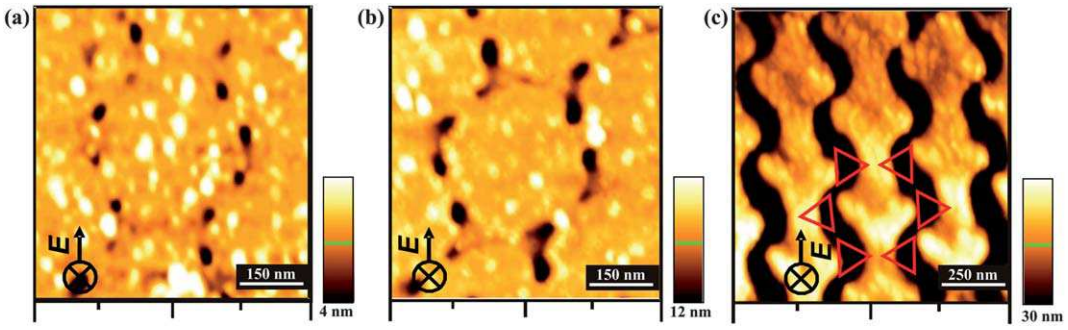

Fig. 4 AFM image of the generated nanopatterns in region 1 (a), region 2 (b), and region 3 (c). The applied pulse energy was $E = 3.8$ μJ. The red triangles indicate the original position of the triangular NPs on the substrate prior to irradiation. Again, for clarity reasons, the red triangles have been drawn larger than the original NPs, which, in fact, have a tip to tip distance of approximately 100 nm. The black arrow indicates the polarization direction of the laser light.

 This journal is © The Royal Society of Chemistry 2011

View Online

Downloaded by Universitaetsbibliothek Kassel on 21 February 2011
Published on 21 February 2011 on http://pubs.rsc.org | doi:10.1039/C0JM03829F

Table 2 Characteristic features of the generated nanostructures for different fluences. The polarization of the applied laser light was parallel to a baseline of the triangular NPs (*cf.* Fig. 4)

Region	Average local fluence/J cm^{-2}	Structure	Average depth/nm	Average length/nm	Average width/nm
1	0.38	Elliptical holes	4 ± 1	34 ± 4	28 ± 3
2	0.70	Elliptical double holes	9 ± 3	47 ± 5	40 ± 4
3	1.73	Nanochannels	31 ± 4	several μm	93 ± 3

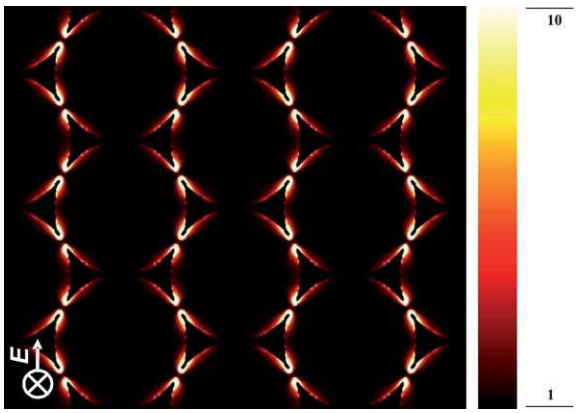

Fig. 5 Normalized electric field energy density distribution for an array of triangular NPs arranged on a fused silica substrate. The normalization is performed with respect to the electric field energy density distribution of a fused silica substrate. The incident electric field, is linearly polarized along a base of the triangles. The energy density has been time-averaged on the duration of the incident pulse.

follows: circularly polarized light is nothing more than a linearly polarized light rotating at the optical frequency of interest. The light pulse launched on the sample has a finite temporal width (35 fs). As compared to the optical frequency of interest (a wavelength of 790 nm corresponds to a frequency of 0.38 PetaHertz), the polarization direction of the light crossing the interface between the fused silica substrate and the gold triangles has time to rotate more than 12 cycles during the pulse duration. The ablation process thus results from the averaging of the linear polarization over many rotations, leading to the observation of a more symmetric pattern in Fig. 6a and 6b. The same high symmetry pattern has been obtained in our simulations (Fig. 6c), by averaging the electric field energy density on the time scale of the pulse duration. The differences exhibited between the simulated (perfect) pattern and experimentally obtained pattern can be easily explained with the fact that the triangular NPs observed experimentally may present different kinds of imperfections such as a slight disorder intrinsically due to the deposition procedure. Such imperfections are random in nature and so are not taken into account in the simulations. They are more clearly revealed in circular polarization with respect to the linear polarizations previously investigated as a result of the broader configuration space explored.

III. Conclusions

In this paper we have demonstrated a simple method for designing and tuning nanopatterns on fused silica substrates exploiting the polarization dependence of the strongly localized near field of highly ordered triangular NP arrays. To generate strong enough near fields, the samples were irradiated with single 35 fs laser pulses. Although the average fluence was significantly below the ablation threshold of the fused silica substrates, ablation occurs in the vicinity of the triangular NPs due to enhanced near fields. Since these near fields are strongly localized, the ablation threshold can be overcome in tiny areas, leading to nanostructures well below the diffraction limit. Different nanostructures have been created, depending on applied fluence and the polarization direction of the laser light with respect to the NP orientation on the substrate. Besides hole structures, nanogrooves and micrometer long nanochannels, all with lateral dimensions well below the diffraction limit, have been generated. FDTD simulations perfectly explain the different obtained nanostructures due to strong local fields, which are driven by the excitation of plasmon resonances in the triangular NPs. Bone-like nanogrooves in a chequered structure are obtained for a polarization direction of the incoming laser light parallel to the bisector of two neighboring triangles. Nanochannels are generated, if the polarization is parallel to a base of the triangular NPs. In particular, the generated nanogrooves and nanochannels open up a new dimension for applications in modern nanotechnology.

R.M and P.D acknowledge financial support from the EU-FEDER and Interreg IV, project "PlasmoBio". B.K acknowledges financial support from Smart film grant 830039 (ECV12020020892F) in the framework of Convergence Project. R.M, P.D, B.K and R.A.L.V acknowledge financial support of F.N.

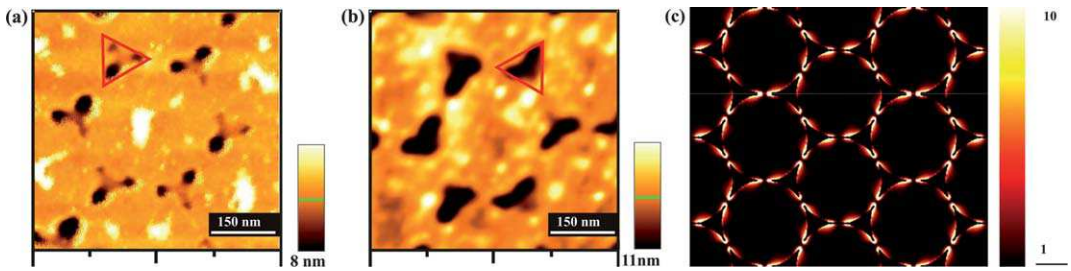

Fig. 6 AFM images of the generated nanopatterns after applying a single fs light pulse with an average fluence of $F \approx 0.072$ J cm^{-2} (a) and $F \approx 0.7$ J cm^{-2} (b) using circular polarized light. (c) Normalized electric-field energy density distribution for an array of triangular NPs arranged on a fused silica substrate where the incident electric field is circularly polarized.

View Online

R.S. F.H and F.T acknowledge project European Commission under Contract No. MRTN-CT-2003-504233. L.E and T.B acknowledge financial support by DFG.

References

1 J. M. Perry, K. M. Zhou, Z. D. Harms and S. C. Jacobson, *ACS Nano*, 2010, **4**, 3897.
2 S. M. Xiao, V. P. Drachev, A. V. Kildishev, X. Ni, U. K. Chettiar, H. K. Yuan and V. M. Shalaev, *Nature*, 2010, **466**, 735.
3 G. R. Hendrickson, M. H. Smith, A. B. South and L. A. Lyon, *Adv. Funct. Mater.*, 2010, **20**, 1697.
4 N. Tate, H. Tokoro, K. Takeda, W. Nomura, T. Yatsui, T. Kawazoe, M. Naruse, S.-I. Ohkoshi and M. Ohtsu, *Appl. Phys. B: Lasers Opt.*, 2010, **98**, 685.
5 Y. F. Lu, Z. H. Mai, G. Qiu and W. K. Chim, *Appl. Phys. Lett.*, 1999, **75**, 2359.
6 Y. Lu and S. C. Chen, *Nanotechnology*, 2003, **14**, 505.
7 W. Cai and R. Piestun, *Appl. Phys. Lett.*, 2006, **88**, 111112.
8 H. J. Münzer, M. Mosbacher, M. Bertsch, J. Zimmermann, P. Leiderer and J. Boneberg, *J. Microsc.*, 2001, **202**, 129.
9 M. Mosbacher, H. J. Münzer, J. Zimmermann, J. Solis, J. Boneberg and P. Leiderer, *Appl. Phys. A: Mater. Sci. Process.*, 2001, **72**, 41.
10 D. Brodoceanu, L. Landström and D. Bäuerle, *Appl. Phys. A: Mater. Sci. Process.*, 2007, **86**, 313.
11 D. Eversole, B. Luk'yanchuk and A. Ben-Yakar, *Appl. Phys. A: Mater. Sci. Process.*, 2007, **89**, 283.
12 P. Leiderer, C. Bartels, J. König-Birk, M. Mosbacher and J. Boneberg, *Appl. Phys. Lett.*, 2004, **85**, 5370.
13 N. N. Nedyalkov, T. Miyanishi and M. Obara, *Appl. Surf. Sci.*, 2007, **253**, 6558.
14 N. N. Nedyalkov, T. Sakai, T. Miyanishi and M. Obara, *Appl. Phys. Lett.*, 2007, **90**, 123106.
15 A. Heltzel, S. Theppakuttai, S. C. Chen and J. Howell, *Nanotechnology*, 2008, **19**, 025305.
16 R. K. Harrison and A. Ben-Yakar, *Opt. Express*, 2010, **18**, 22556.
17 F. Hubenthal, R. Morarescu, L. Englert, L. Haag, T. Baumert and F. Träger, *Appl. Phys. Lett.*, 2009, **95**, 063101.
18 N. Gupta, B. F. Lin, L. Campos, M. D. Dimitriou, S. T. Hikita, N. D. Treat, M. V. Tirrell, D. O. Clegg, E. J. Kramer and C. J. Hawker, *Nat. Chem.*, 2010, **2**, 138.
19 A. V. Krasavin and A. V. Zayats, *Appl. Phys. Lett.*, 2010, **97**, 041107.
20 J. C. Hulteen, D. A. Treichel, M. T. Smith, M. L. Duval, T. R. Jensen and R. P. V. Duyne, *J. Phys. Chem. B*, 1999, **103**, 3854.
21 R. Micheletto, H. Fukuda and M. Ohtsu, *Langmuir*, 1995, **11**, 3333.
22 L. J. Sherry, R. Jin, C. A. Mirkin, G. C. Schatz and R. P. V. Duyne, *Nano Lett.*, 2006, **6**, 2060.
23 K. L. Shuford, M. A. Ratner and G. C. Schatz, *J. Chem. Phys.*, 2005, **123**, 114713.
24 J. E. Millstone, S. Park, K. L. Shuford, L. Qin, G. C. Schatz and C. A. Mirkin, *J. Am. Chem. Soc.*, 2005, **127**, 5312.
25 L. Englert, B. Rethfeld, L. Haag, M. Wollenhaupt, C. Sarpe-Tudoran and T. Baumert, *Opt. Express*, 2007, **15**, 17855.
26 M. Lenzner, J. Krüger, S. Sartania, Z. Cheng, C. Spielmann, G. Mourou, W. Kautek and F. Krausz, *Phys. Rev. Lett.*, 1998, **80**, 4076.

Downloaded by Universitaetsbibliothek Kassel on 21 February 2011
Published on 21 February 2011 on http://pubs.rsc.org | doi:10.1039/C0JM03829F

 This journal is © The Royal Society of Chemistry 2011

Wavelength-dependent emission enhancement through the design of active plasmonic nanoantennas

Mélanie Ferrié,[1] **Nicola Pinna,**[2,3] **Serge Ravaine,**[1] **and Renaud A. L. Vallée**[1,*]

[1]*Centre de Recherche Paul Pascal (CNRS-UPR8641), 115 av. Dr A. Schweitzer, 33600 Pessac, France*

[2]*Department of Chemistry, CICECO, University of Aveiro, 3810-193 Aveiro, Portugal*

[3]*World Class University (WCU) Program of Chemical Convergence for Energy and Environment (C2E2), School of Chemical and Biological Engineering, College of Engineering, Seoul National University (SNU), Seoul 151-744, Korea*

**vallee@crpp-bordeaux.cnrs.fr*

Abstract: Owing to the competition between the radiative and non-radiative decay channels occurring in plasmonic assemblies, we show here how to conceive a long pass emission filter and actually design it. We report the synthesis of gold@silica nanoparticles grafted with dye molecules. The control of the thickness of the silica shell allows us to tune the distance between the metal core and the dye molecules. Assemblies of small number (1 to 7) of these core-shell (CS) particles, considered as multimers, have also been produced for the first time. We show that the shaping of the emission spectra of the multimers is drastically enhanced by comparison with the corresponding monomers. We also show a strong enhancement of the decay rates at the LSP resonance, dominated by the non-radiative energy tranfer from the active medium to the metal. The decay rates decrease as the detuning between the long wavelength emission and the LSP resonance increases.

© 2011 Optical Society of America

OCIS codes: (160.2540) Fluorescent and luminescent materials; (160.4236) Nanomaterials; (250.5403) Plasmonics.

References and links

1. U. Kreibig and M. Vollmer, *Optical Properties of Metal Clusters* (Springer, 1995).
2. C. F. Bohren and D. R. Huffman, *Absorption and Scattering of Light by Small Particles* (Wiley, 1983).
3. J. Gersten and A. Nitzan, "Electromagnetic theory of enhanced Raman scattering by molecules adsorbed on rough surfaces," J. Chem. Phys. **73**, 3023 (1980).
4. J. S. Biteen, N. S. Lewis, H. A. Atwater, H. Mertens, and A. Polman, "Spectral tuning of plasmon-enhanced silicon quantum dot luminescence," Appl. Phys. Lett. **88**, 131109 (2006).
5. T. H. Taminiau, R. J. Moerland, F. B. Segerink, L. Kuipers, and N. F. van Hulst, "Lambda/4 resonance of an optical monopole antenna probed by single molecule fluorescence," Nano Lett. **7**, 28–33 (2007).
6. F. Tam, G. P. Goodrich, B. R. Johnson, and N. J. Halas, "Plasmonic enhancement of molecular fluorescence," Nano Lett. **7**, 496–501 (2007).
7. A. Parfenov, I. Gryczynski, J. Malicka, C. D. Geddes, and J. R. Lakowicz, "Enhanced fluorescence from fluorophores on fractal silver surfaces," J. Phys. Chem. B **107**, 8829–8833 (2003).
8. O. G. Tovmachenko, C. Graf, D. J. van den Heuvel, A. van Blaaderen, and H. C. Gerritsen, "Fluorescence enhancement by metal-core/silica-shell nanoparticles," Adv. Mater. **18**, 91-95 (2006).
9. J. Enderlein, "Theoretical study of single molecule fluorescence in a metallic nanocavity," Appl. Phys. Lett. **80**, 315–317 (2002).

#149911 - $15.00 USD Received 27 Jun 2011; revised 26 Jul 2011; accepted 27 Jul 2011; published 24 Aug 2011
(C) 2011 OSA

10. M. Thomas, J.-J. Greffet, R. Carminati, and J. R. Aria-Gonzales, "Single-molecule spontaneous emission close to absorbing nanostructures," Appl. Phys. Lett. **85**, 3863–3865 (2004).
11. M. Purcell, H. C. Torrey, and R. V. Pound, "Resonance absorption by nuclear magnetic moments in a solid," Phys. Rev. **69**, 37 (1946).
12. R. Carminati, J.-J. Greffet, C. Henkel, and J. Vigoureux, "Radiative and non-radiative decay of a single molecule close to a metallic nanoparticle," Opt. Commun. **261**, 368 (2006).
13. E. Dulkeith, A. C. Morteani, T. Niedereichholz, T. A. Klar, J. Feldmann, S. A. Levi, F. C. J. M. van Veggel, D. N. Reinhoudt, M. Möller, and D. I. Gittins, "Fluorescence quenching of dye molecules near gold nanoparticles: radiative and nonradiative effects," Phys. Rev. Lett. **89**, 203002 (2002).
14. B. Dubertret, M. Calame, and A. J. Libchaber, "Single-mismatch detection using gold-quenched fluorescent oligonucleotides," Nat. Biotechnol. **19**, 365–370 (2001).
15. D. J. Maxwell, J. R. Taylor, and S. Nie, "Self-assembled nanoparticle probes for recognition and detection of biomolecules," J. Am. Chem. Soc. **124**, 9606–9612 (2002).
16. C. S. Yun, A. Javier, T. Jennings, M. Fisher, S. Hira, S. Peterson, B. Hopkins, N. O. Reich, and G. F. Strouse, "Nanometal surface energy transfer in optical rulers, breaking the FRET barrier," J. Am. Chem. Soc. **127**, 3115–3119 (2005).
17. E. Dulkeith, M. Ringler, T. A. Klar, J. Feldmann, A. M. Javier, and W. J. Parak, "Gold nanoparticles quench fluorescence by phase induced radiative rate suppression," Nano Lett. **5**, 585–589 (2005).
18. N. Liu, B. S. Prall, and V. I. Klimov, "Hybrid gold/silica/nanocrystal-quantum-dot superstructures: synthesis and analysis of semiconductor-metal interactions," J. Am. Chem. Soc. **128**, 15362 (2006).
19. G. Schneider, G. Decher, N. Nerambourg, R. Praho, M. H. V. Werts, and M. Blanchard-Desce, "Distance-dependent fluorescence quenching on gold nanoparticles ensheathed with layer-by-layer assembled polyelectrolytes," Nano Lett. **6**, 530–536 (2006).
20. S. Kuehn, U. Hakanson, L. Rogobete, and V. Sandoghdar, "Enhancement of single-molecule fluorescence using a gold nanoparticle as an optical nanoantenna," Phys. Rev. Lett. **97**, 017402 (2006).
21. O. Kulakovich, N. Strekal, A. Yaroshevich, S. Maskevich, S. Gaponenko, I. Nabiev, U. Woggon, and M. Artemyev, "Enhanced luminescence of CdSe quantum dots on gold colloids," Nano Lett. **2**, 1449–1452 (2002).
22. J. Song, T. Atay, S. Shi, H. Urabe, and A. Nurmikko, "Large enhancement of fluorescence efficiency from CdSe/ZnS quantum dots induced by resonant coupling to spatially controlled surface plasmons," Nano Lett. **5**, 1557–1561 (2005).
23. Y. Chen, K. Munechika, and D. Ginger, "Dependence of fluorescence intensity on the spectral overlap between fluorophores and plasmon resonant single silver nanoparticles," Nano Lett. **7**, 690–696 (2007).
24. J. B. Khurgin, G. Sun, and R. A. Soref, "Electroluminescence efficiency enhancement using metal nanoparticles," Appl. Phys. Lett. **93**, 021120 (2008).
25. G. Sun, J. B. Khurgin, and R. A. Soref, "Plasmonic light-emission enhancement with isolated metal nanoparticles and their coupled arrays," J. Opt. Soc. Am. B **25**, 1748–1755 (2008).
26. J.B. Khurgin, G. Sun, and R. A. Soref, "Practical limits of absorption enhancement near metal nanoparticles," Appl. Phys. Lett. **94**, 071103 (2009).
27. G. Sun, J. B. Khurgin, and R. A. Soref, "Practical enhancement of photoluminescence by metal nanoparticles," Appl. Phys. Lett. **94**, 101103 (2009).
28. T. Förster, "Transfer mechanisms of electronic excitation," Discuss. Faraday Soc. **27**, 7–17 (1959).
29. V. N. Pustovit and T. V. Shahbazyan, "Cooperative emission of light by an ensemble of dipoles near a metal nanoparticle: the plasmonic Dicke effect," Phys. Rev. Lett. **102**, 077401 (2009).
30. V. N. Pustovit and T. V. Shahbazyan, "Plasmon-mediated superradiance near metal nanostructures," Phys. Rev. B **82**, 075429 (2010).
31. J. N. Farahani, D. W. Pohl, H.-J. Eisler, and B. Hecht, "Single quantum dot coupled to a scanning optical antenna: a tunable superemitter," Phys. Rev. Lett. **95**, 017402 (2005).
32. J. Zhang, Y. Fu, M. H. Chowdhury, and J. R. Lakowicz, "Metal-enhanced single-molecule fluorescence on silver particle monomer and dimer: coupling effect between metal particles," Nano Lett. **7**, 2101–2107 (2007).
33. O. L. Muskens, V. Giannini, J. A. Sánchez-Gil, and J. Gómez Rivas, "Strong enhancement of the radiative decay rate of emitters by single plasmonic nanoantennas," Nano Lett. **7**, 2871–2875 (2007).
34. A. Bek, R. Jansen, M. Ringler, S. Mayilo, T. A. Klar, and J. Feldmann, "Fluorescence enhancement in hot spots of AFM-designed gold nanoparticle sandwiches," Nano Lett. **8**, 485–490 (2008).
35. M. Ringler, A. Schwemer, M. Wunderlich, A. Nichtl, K. Kürzinger, T. A. Klar, and J. Feldmann, "Shaping emission spectra of fluorescent molecules with single plasmonic nanoresonators," Phys. Rev. Lett. **100**, 203002 (2008).
36. J. Rodríguez-Fernández, I. Pastoriza-Santos, J. Pérez-Juste, F. J. García de Abajo, and L. M. Liz-Marzán, "The effect of silica coating on the optical response of sub-micrometer gold spheres," J. Phys. Chem. C **111**, 13361–13366 (2007).
37. Y. Lu, Y. Yin, Z.-Y. Li, and Y. Xia, "Synthesis and self-assembly of Au@SiO2 core-shell colloids," Nano Lett. **2**, 785–788 (2002).
38. L. Novotny and N. F. van Hulst, "Antennas for light," Nat. Photonics **5**, 83–90 (2011).

#149911 - $15.00 USD Received 27 Jun 2011; revised 26 Jul 2011; accepted 27 Jul 2011; published 24 Aug 2011
(C) 2011 OSA

39. P. Anger, P. Bharadwaj, and L. Novotny, "Enhancement and quenching of single-molecule fluorescence," Phys. Rev. Lett. **96**, 113002 (2006).
40. P. Viste, J. Plain, R. Jaffiol, A. Vial, P. M. Adam, and P. Royer, "Enhancement and quenching regimes in metal-semiconductor hybrid optical nanosources," ACS Nano **4**, 759–764 (2010).
41. Manuscript in preparation.
42. R. Zorn, "Logarithmic moments of relaxation time distributions," J. Chem. Phys. **116**, 3204–3209 (2002).
43. R. A. L. Vallée, K. Baert, B. Kolaric, M. Van der Auweraer, and K. Clays, "Nonexponential decay of spontaneous emission from an ensemble of molecules in photonic crystals," Phys. Rev. B **76**, 045113 (2007).
44. K. R. Brown, D. G. Walter, and M. J. Natan, "Seeding of colloidal Au nanoparticle solutions. 2. improved control of particle size and shape," Chem. Mater. **12**, 306–313 (2000).
45. C. Graf and A. van Blaaderen, "Metallodielectric colloidal core-shell particles for photonic applications," Langmuir **18**, 524–534 (2002).
46. X. Gao, J. He, L. Deng, and H. Cao, "Synthesis and characterization of functionalized rhodamine B-doped silica nanoparticles," Opt. Mater. **31**, 1715–1719 (2009).
47. S. Kang, S. I. Hong, C. R. Choe, M. Park, S. Rim, and J. Kim, "Preparation and characterization of epoxy composites filled with functionalized nanosilica particles obtained via sol-gel process," Polymer **42**, 879–887 (2001).
48. M. Ibisate, Z. Zou, and Y. Xia, "Arresting, fixing, and separating dimers composed of uniform silica colloidal spheres," Adv. Funct. Mater. **16**, 1627–1632 (2006).
49. A. Taflove and S. C. Hagness, *Computational Electrodynamics: The Finite-Difference Time-Domain Method*, 3rd ed. (Artech House Inc., 2005).
50. A. F. Oskooi, D. Roundy, M. Ibanescu, P. Bermel, J. D. Joannopoulos, and S. G. Johnson, "MEEP: a flexible free-software package for electromagnetic simulations by the FDTD method," Comput. Phys. Commun. **181**, 687–702 (2010).
51. A. Vial, A.-S. Grimault, D. Macas, D. Barchiesi, and M. Lamy de la Chapelle, "Improved analytical fit of gold dispersion : application to the modelling of extinction spectra with the FDTD method," Phys. Rev. B **71**, 085416 (2005).
52. P. Johnson and R. Christy, "Optical constants of the noble metals," Phys. Rev. B **6**, 4370–4379 (1972).

1. Introduction

The interaction between light and metal nanoparticles (NPs) is dominated by localized surface plasmon (LSP) resonances, or charge-density oscillations on the closed surfaces of the particles. These LSP resonances cause confinement of the electromagnetic field near the surface and lead to strong extinction in the visible and near infrared, depending on the geometry, size, and shape of the NP [1, 2]. The large local enhancements of the electromagnetic fields can be used to exalt the fluorescence emission [3–6] or the photostability of dye molecules (atoms, molecules, quantum dots) close to the metal surface by shortening the excited-state lifetime [7–9], possibly leading to new intense and stable light sources confined to the nanometer scale.

Understanding the interaction between light, NPs and dye molecules is a real challenge since at least three competing phenomena occur simultaneously. In the absence of metal NPs, the optical excitation is absorbed directly by the molecules. With a metal NP located in the vicinity of the molecules, the excitation beam can firstly be coupled into the tighly confined LSP mode, which then enhances the optical energy density near the molecule field and so the absorption rate. The same LSP mode (generally at slightly longer wavelength [10]) also enhances the energy-emission efficiency of the excited molecules and so the radiative emission rate through the Purcell [11] effect. Finally, an extra non-radiative decay channel is opened which allows the energy transfer from the molecule to the metal [12]. While the first two effects combine to enhance the overall emission rate, the third quenches it. As a matter of fact, all three effects depend strongly and differently on the separation between the metal NP and the molecule [8, 13–19], as well as the detuning between the LSP resonance and the absorption and luminescence wavelengths of the molecule [6, 8, 20–23], the shape of the NP, and the orientation of the molecules dipole moment [10, 24–27]. In addition, the molecules eventually might interact between themselves if appropriately located and oriented [28], and a new mechanism for cooperative emission of light by an ensemble of N dipoles near a metal NP, dubbed as plasmonic Dicke effect, has

#149911 - $15.00 USD Received 27 Jun 2011; revised 26 Jul 2011; accepted 27 Jul 2011; published 24 Aug 2011
(C) 2011 OSA

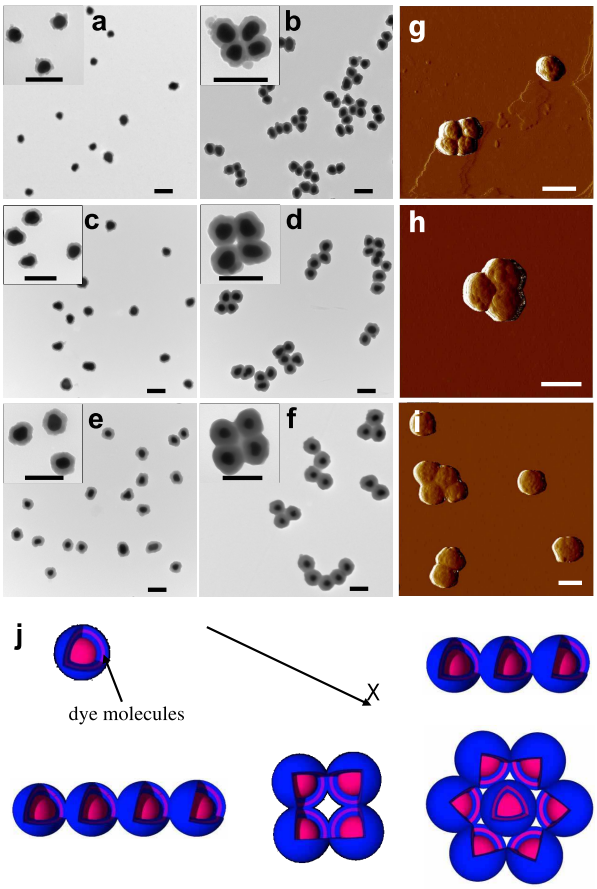

Fig. 1. TEM pictures of the various CS+ (a,c,e) monomers and CS+M (b,d,f) multimers with shell thicknesses ranging from 10 (a,b) to 20 (c,d) and 30 *nm* (e,f). AFM phase images of CS1 CS2+ CS3+ (g, h, i) multimers. Scale bar: 200 *nm* (both for TEM and AFM). (j) Schemes of the active monomer, dimer, trimer, quadrimer in line, tetramer and heptamer NPs.

been reported recently [29, 30]. Finally, inside nanoparticle dimer resonators, strong enhancement of the fluorescence intensity and of the overall decay rates haven been reported [31–34] as well as shaping of the fluorescence emission spectra due to the selective, resonant enhancement, of radiative transitions [35].

In this paper, owing to the competition between the radiative and non-radiative parts of the overall relaxation process, we show how to and actually design a long pass emission filter. We designed several types of size controlled, spherical monomer and multimer nanoantennas. We show shaping of the emission spectra and modification of the radiative decay rates as a function of wavelength and spacing between the metal cores and the dye molecules. The decay rates are shown to decrease as the distance from the molecules to the NP increases and as the detuning between the long wavelength emission and the LSP resonance increases.

The experimental situations concern two types of nanostructures: passive and active ones. For the first series, the particles consist of a gold NP core of 60 *nm* diameter, with a silica shell thickness varying from 10 to 20 and 30*nm*, here after labeled as Core-Shell (CS) particles CS1, CS2 and CS3, respectively. The second series is built from the first one, by firstly grafting a

#149911 - $15.00 USD Received 27 Jun 2011; revised 26 Jul 2011; accepted 27 Jul 2011; published 24 Aug 2011
(C) 2011 OSA

rhodamine B derivative with ethoxy-silano group on the silica shell and then covering this layer by a second protective silica shell of 10 *nm* (see scheme in Fig. 1(j)). The NPs of the second series are called active since they comprise an active gain material (dye molecules). Depending on the NPs used from the first series, the samples of the second category are labeled as CS1+, CS2+ and CS3+, respectively. The good uniformity in shape and size of the CS+ particles can be observed in the TEM pictures shown in Figs. 1(a), 1(c) and 1(e). Finally, multimers were formed (mixtures of dimers, trimers, quadrimers, heptamers, ...) from both seriess CS and CS+ and are labeled as CS1M, CS2M, CS3M, CS1+M, CS2+M and CS3+M, respectively (TEM and AFM pictures for the last three species are displayed in Figs. 1(b), 1(d), 1(f) and 1(g)–1(i), respectively; see Materials for details). The various nanostructures are investigated on the ensemble level in ethanol solution in order to determine their UV-visible absorption spectra, fluorescence emission spectra and decay rates (see Methods for details).

2. Results and Discussion

We predicted the optical properties of various experimental situations owing to finite-difference time-domain (FDTD) simulations (see Methods for details). In all simulations, the polarization direction of the excitation has been chosen along the x axis, i.e. along the line joining the particles in the multimers in line (Fig. 1(j)). Figure 2(a) shows the simulated reflexion spectra of the monomers, trimers and heptamers corresponding to silica shells of 10 to 20 and 30 *nm*, respectively. Clearly, for each type of monomers and multimers, a shift of the LSP resonance to long wavelengths is observed as the shell thickness is increased. This effect is well-known for CS monomers and simply results from an increase of the local refractive index around the gold particles, since amorphous silica has a higher refractive index ($n = 1.45$) than that of the solvent (ethanol, $n = 1.36$) [36]. For shell ticknesses above the core radius, light scattering from the shell dominates and the shift of the LSP resonances saturates, since the metal cores are no longer sensitive to the solvent outside [36, 37]. A red-shift of the the LSP resonances is also observed as the number of coupled monomers in a multimer increases. This is nicely illustrated in Fig. 2(b) showing the dependance of the near field coupling between resonance modes of adjacent particles as a function of shell thickness: the LSP resonance strongly shifts to longer wavelengths when considering monomer, dimer, trimer, quadrimer as the distance between neighbouring cores is reduced from 30 to 10 *nm*. This effect is also noticeable for the tetramers and heptamers but to a lesser extent, due to the fact that, in the latter cases, the plasmonic dipole interactions can interfere constructively and destructively while, for multimers in line, only constructive interferences give rise to the enhanced near field coupling.

The classical picture of plasmonic exaltation is an enhancement of the optical energy density near the molecule field, followed by the enhancement of the energy-emission efficiency of the excited molecules and the concomittant energy transfer from the molecule to the metal. In such a process, the total enhancement factor is the product of the excitation enhancement factor at the chosen excitation wavelength by the wavelength-dependent emission enhancement factor

$$g = g_{exc}(\lambda = \lambda_{exc}) g_{em}(\lambda). \quad (1)$$

However, since quantitative interpretations based on fluorescence intensities are prone to major errors related to the difficulty of properly taking into account notably (i) the number of molecules grafted to the surface; (ii) the excitation and collection efficiences and (iii) the spatial pattern of emission due to the coupling with the NP antenna (especially in the case of multimers) [38], we focused on the measurement of spontaneous decay rates and normalized emission spectra, so that the only factor to take into account is $g_{em}(\lambda)$ or, equivalently, the radiative $g_r(\lambda)$, non-radiative $g_{nr}(\lambda)$ decay rates and apparent quantum yield η [39]. In order to estimate these factors numerically, we placed a broadband point current source in the gap region

#149911 - $15.00 USD Received 27 Jun 2011; revised 26 Jul 2011; accepted 27 Jul 2011; published 24 Aug 2011
(C) 2011 OSA

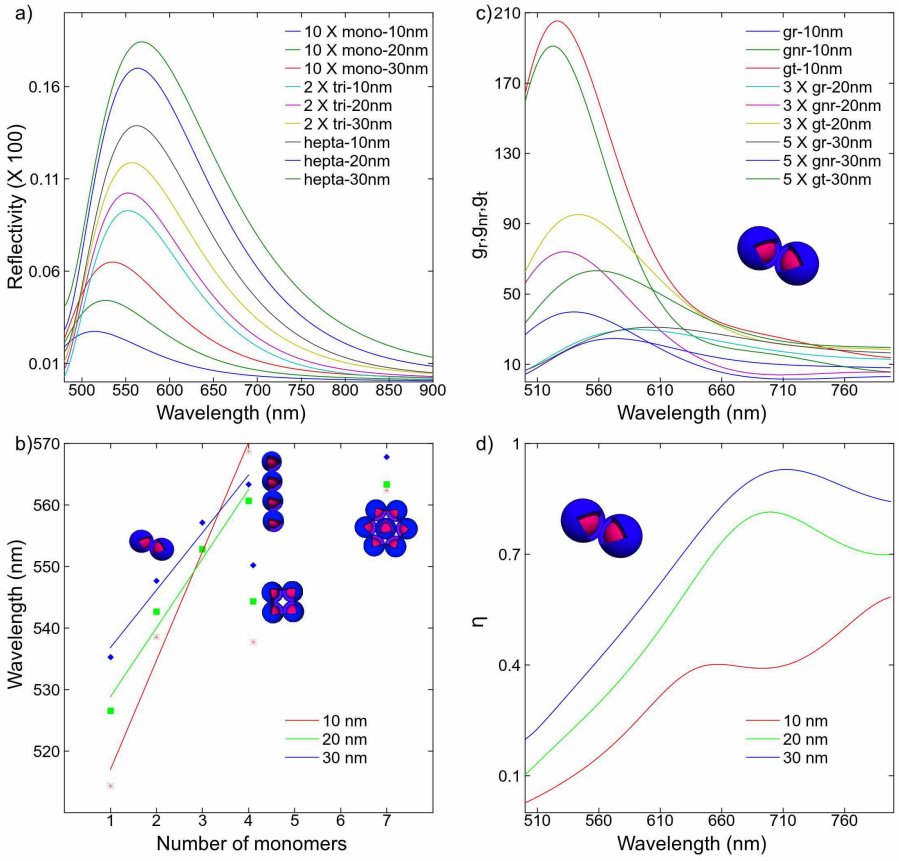

Fig. 2. (a) Simulated reflectivity spectra of monomers, trimers in line and heptamers with gold core diameter of 60 *nm* and silica shell thickness of 10, 20 and 30 *nm*, respectively. (b) LSP resonance as a function of the number of monomers coupled in a multimer for a silica shell thickness ranging from 10, 20 to 30 *nm*, respectively. Solid lines are linear fits of the LSP resonances as a function of the number of monomers coupled in a multimer. Non-radiative, radiative and total enhancement rates (c) as well as the apparent quantum yield (d) as a function of wavelength for dimers with a shell varying from 10 to 20 and 30 *nm*, respectively.

#149911 - $15.00 USD Received 27 Jun 2011; revised 26 Jul 2011; accepted 27 Jul 2011; published 24 Aug 2011
(C) 2011 OSA

of a CS+ dimer. The radiated power $P_r(\lambda)$ into the far field and the power dissipated in the metal $P_{nr}(\lambda)$ were calculated. The enhancement factors were then obtained by normalization with respect to the radiated power $P_0(\lambda)$ of the same point current source in the absence of the antenna. As a result, for a point current source polarized in the x-direction, i.e. normal to the CS surface (Fig. 1(j)), the radiative $g_r(\lambda) = Pr(\lambda)/P_0(\lambda)$ and non-radiative $g_{nr}(\lambda) = P_{nr}(\lambda)/P_0(\lambda)$ factors are both enhanced, as shown in Fig. 2(c). Clearly the non radiative factor is dominant at the LSP resonance, while the radiative factor gets dominant at longer wavelengths, as a driving force for the shaping of fluorescence emission spectra [35]. Figure 2(c) further illustrates a drastic reduction of the non-radiative rate $g_{nr}(\lambda)$ as the distance between the active layer and the gold surface increases. The total decay rate $g_t(\lambda) = g_r(\lambda) + g_{nr}(\lambda)$ is shown to be maximum on the long wavelength side of the LSP resonance (reaching a value of roughly 200, 30 and 12 for 10, 20 and 30 *nm* shell thicknesses, respectively) and strongly decreases as the long wavelength detuning of the emission increases with respect to the LSP resonance. The wavelength-dependent apparent quantum yield $\eta(\lambda)$, given by

$$\eta(\lambda) = \frac{g_r(\lambda)}{g_r(\lambda) + g_{nr}(\lambda)} \tag{2}$$

is shown in Fig. 2(d) for the three shell thicknesses of interest. In all cases, $\eta(\lambda)$ is small at the LSP resonance and shows a sharp increase at longer wavelengths. This result, obtained in the case of a dimer nanoantenna is further enhanced in the case of larger multimers (not shown). Clearly, from the shape of the apparent quantum yield $\eta(\lambda)$, one expects the multimer nanostructures to act as a long pass filter in emission.

On the experimental side, the CS monomers and multimers of the first series in ethanol have very similar UV-visible absorption spectra (Fig. 3(a)), with the multimer solutions showing LSP resonance slighly red shifted with respect to the monomer solutions. The absorption and emission spectra of Rhodamine B isothiocyanate (RITC) molecules in ethanol are also shown in Fig. 3(a) and illustrate the carefull design of the CS NPs with extinction spectrum always red-shifted with respect to the emission spectrum of the dye molecules [40]. The UV-visible absorption spectra recorded for the second series of samples, i.e. the CS+ particles show a completely different trend. Fig. 3(b) indeed clearly exhibits LSP resonances shifted to longer wavelengths as the shell thickness is reduced. In all cases, the CS+ and CS+M spectra are close to each other, by respective pairs. Furthermore, in the case of the CS1+, CS1+M and CS2+, CS2+M, the long wavelength sides of the spectra exhibit a significantly enhanced absorption with respect to the corresponding samples of the first series, related to a loss compensation mechanism [41].

Figures 4(a)–4(c) exhibit the spectro-temporal intensity plots of RITC, CS3+ and CS3+M particles in ethanol. Projecting the intensity on the x axis provides us with the emission spectra, showing a shift of the maximum emission to longer wavelengths as the sample investigated switches from pure RITC (a) to CS3+ monomers (b) and CS3+M multimers (c). By projecting the intensity on the y axis, one alternatively obtains decay rates profiles with shortened decay times as the sample investigated switches from pure RITC to CS3+ and CS3+M samples (note that, on the graph (a), the y-axis extends over 20 *ns* while, on the graphs (b) and (c), it extends over 2 *ns*). Figure 5 further exemplifies these results for all samples investigated in this study. The emission spectra of RITC in ethanol and RITC grafted on 100 *nm* diameter silica beads in ethanol are almost indistinguishable and show an emission maximum at $\lambda = 577\,nm$, indicating that the energy levels of the RITC molecules are not affected by grafting and that there is no self-quenching by non-radiative energy transfer between molecules. A similar behaviour is expected for RITC molecules incorporated in the CS+ and CS+M NPs. The emission maximum is shifted to a longer wavelength $\lambda = 586\,nm$ and a broadening of the spectra is observed for

#149911 - $15.00 USD Received 27 Jun 2011; revised 26 Jul 2011; accepted 27 Jul 2011; published 24 Aug 2011
(C) 2011 OSA

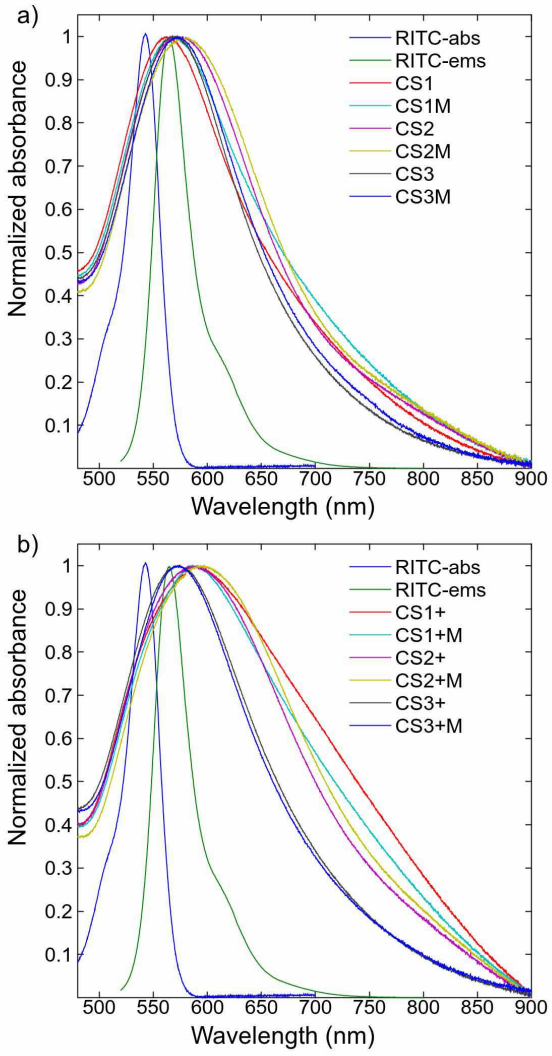

Fig. 3. (a) Absorption and emission spectra of RITC molecules, absorption spectra of CS monomers and CSM multimers in ethanol. (b) Absorption and emission spectra of RITC molecules, absorption spectra of CS+ and CS+M NPs in ethanol.

#149911 - $15.00 USD Received 27 Jun 2011; revised 26 Jul 2011; accepted 27 Jul 2011; published 24 Aug 2011
(C) 2011 OSA

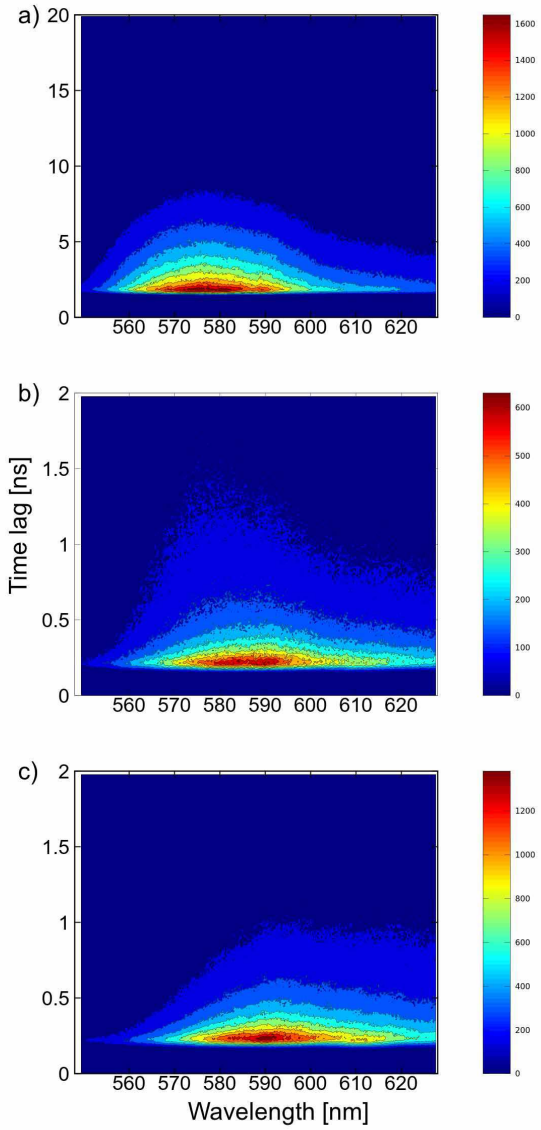

Fig. 4. Time and spectrally resolved spontaneous emission intensities of RITC molecules (a), CS+3 (b) and CS+3M in ethanol (c).

#149911 - $15.00 USD Received 27 Jun 2011; revised 26 Jul 2011; accepted 27 Jul 2011; published 24 Aug 2011
(C) 2011 OSA

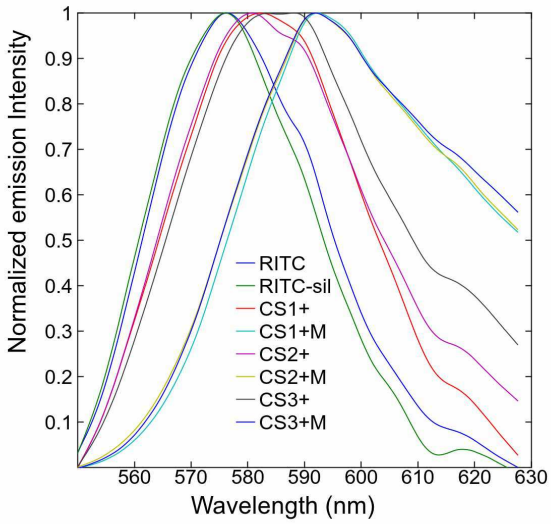

Fig. 5. Emission spectra of RITC molecules, RITC molecules grafted to 100 *nm* diameter silica beads, CS+ active monomer and CS+M active multimer NPs in ethanol solutions.

RITC molecules in the active monomer CS+ NPs. Further red-shift of the emission maximum to $\lambda = 594\,nm$ and broadening / complete reshaping to the long wavelength range of the spectra are observed for RITC molecules in the active multimer CS+M NPs. The reshaping of the emission spectra in the case of CS+M multimers is in complete agreement with the predictions made already at the level of the dimer (Fig. 2(d)).

To investigate further the emission properties as a function of wavelength, we built the decay profiles for all active samples by dividing the wavelength range in 10 regions of 8 *nm* width and proceeded to fitting of these decay profiles. Figures 6(a)–6(c) show the 6 more intense decay profiles (at least 10^4 counts at maximum) for three different samples, namely RITC molecules, CS3+ and CS3+M NPs in ethanol. On the one side, the decay profiles of RITC in ethanol (a) show a clear single exponential decay profile with a decay rate independent of wavelength. According to the spectrum shown in Fig. 5, the absolute intensity increases from the region at 565 *nm* to the one at 580 *nm*, prior to decrease to the one at 604 *nm*. On the other side, the decay profiles of the CS3+ (b) and CS3+M (c) in solutions strongly deviates from a single exponential decay profile. In order to fit such decay profiles adequately, we used a stretched exponential function

$$I(t) = I_0 exp(-(t/\tau_K)^{\beta}), \tag{3}$$

i.e., introducing a stretching parameter $0 < \beta <= 1$ in the logarithmic time [42], convoluted to the instrumental response function (IRF), instead of directly fitting with the convolution product of a linear superposition of simple exponential decays [42, 43] and the IRF. The decay time (mean relaxation time) is then obtained from the relation

$$\langle \tau \rangle = \frac{\tau_K}{\beta} \Gamma(\frac{1}{\beta}), \tag{4}$$

where Γ is the gamma function.

#149911 - $15.00 USD Received 27 Jun 2011; revised 26 Jul 2011; accepted 27 Jul 2011; published 24 Aug 2011
(C) 2011 OSA

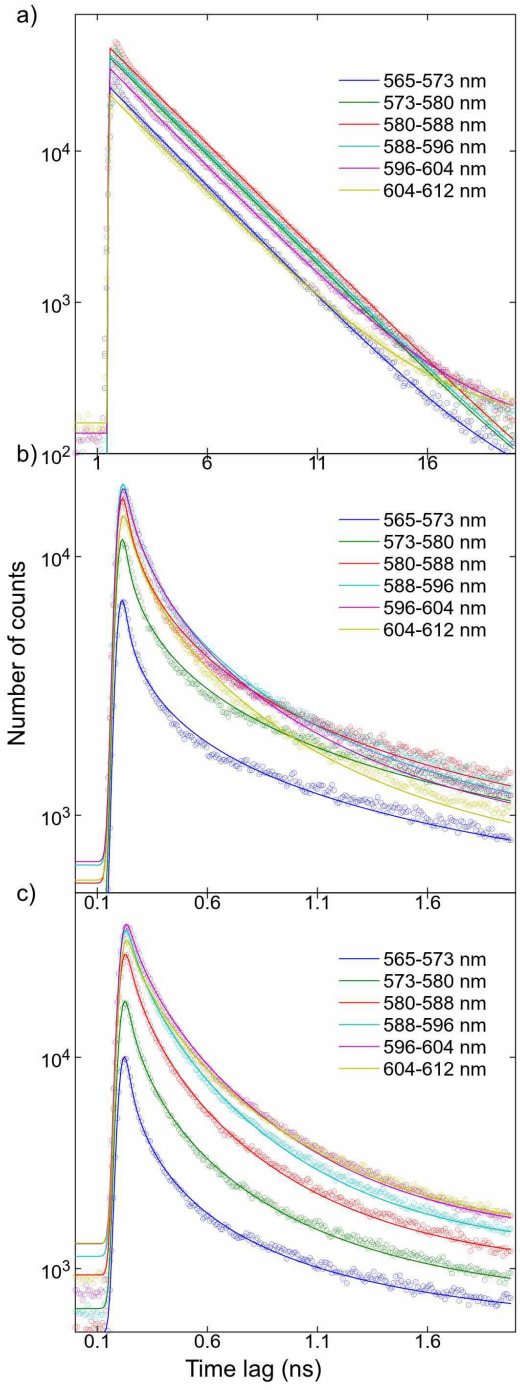

Fig. 6. Decay profiles as a function of wavelength for RITC molecules (a), CS+3 monomers (b) and CS+3M multimers in ethanol (c). The solid lines are convoluted stretched exponentials fits with the instrumental response function of the setup of the various decay profiles.

#149911 - $15.00 USD Received 27 Jun 2011; revised 26 Jul 2011; accepted 27 Jul 2011; published 24 Aug 2011
(C) 2011 OSA

For $\beta = 1$, the exponential decay $\langle\tau\rangle = \tau_K$ is recovered and the larger departure of β from 1, the more exponential relaxations are involved in the superposition. Figures 6(b) and 6(c) clearly reveal that the τ_K and β (degree of nonexponentiality) values are increasing as the wavelength is increased. To quantitatively trace these features, the τ_K, β and τ values are reported in Table 1 for the 18 curves fitted in Fig. 6.

Table 1. τ_K, β and τ Values as a Function of Wavelength and Sample (RITC, CS3+ and CS3+M) for the 18 Fits of the Experimental Data Curves shown in Fig. 6

Sample	Wavelength (nm)	τ_K (ns)	β	$\tau(ns)$
RITC	565	2.94	1.0	2.94
	573	3.0	1.0	3.0
	580	3.03	1.0	3.03
	588	3.01	1.0	3.01
	596	2.95	1.0	2.95
	604	2.96	1.0	2.96
CS3+	565	0.010	0.25	0.041
	573	0.015	0.28	0.055
	580	0.026	0.33	0.080
	588	0.046	0.40	0.115
	596	0.065	0.44	0.146
	604	0.084	0.47	0.178
CS3+M	565	0.012	0.33	0.038
	573	0.033	0.41	0.080
	580	0.056	0.48	0.116
	588	0.079	0.54	0.148
	596	0.098	0.56	0.175
	604	0.115	0.57	0.201

We reported in Fig. 7 the decay times $\langle\tau(\lambda)\rangle$ as a function of wavelength for all samples CS+ and CS+M taken pair by pair. For comparison, the wavelength-independent fluorescent lifetime $\tau_0 = 3\,ns$ of RITC molecules in ethanol is also shown. As such, the decay times of monomers and multimers in which the fluorescent molecules are separated from the core metal NPs by the same silica shell thickness show the same linear increase as a function of wavelength. The slope of this linear relationship is further enhanced as the spacer size increases, as further indicated in Table 2.

In terms of the decay rate enhancement defined as $g_t = \frac{\tau_0}{\tau(\lambda)}$, Fig. 8 equivalently shows the $g_t \propto \frac{1}{\lambda}$ proportionaly law. Remarquably, the decay rate enhancement reaches values up to 120 and 60 for spacings of 10 and $30\,nm$ between the RITC molecules and the gold NPs and go down to 40 and 20 as the detuning between the long wavelength emission and the LSP resonance increases.

The trends shown by the decay rate enhancement to decrease as the distance from the molecules to the NP increases and as the detuning between the long wavelength emission and the LSP resonance increases is in agreement with the simulated results presented here above (Fig. 2(c)). Also the orders of magnitude of the rate enhancements are compatible between the simulated (Fig. 2(c)) and experimental results (Fig. 8). The observed differences may be assigned to numerous factors, the dominant one being that the experimental results deal with multimers which are mixtures of monomers, dimers, trimers, quadrimers, tetramers, heptamers,

#149911 - $15.00 USD Received 27 Jun 2011; revised 26 Jul 2011; accepted 27 Jul 2011; published 24 Aug 2011
(C) 2011 OSA

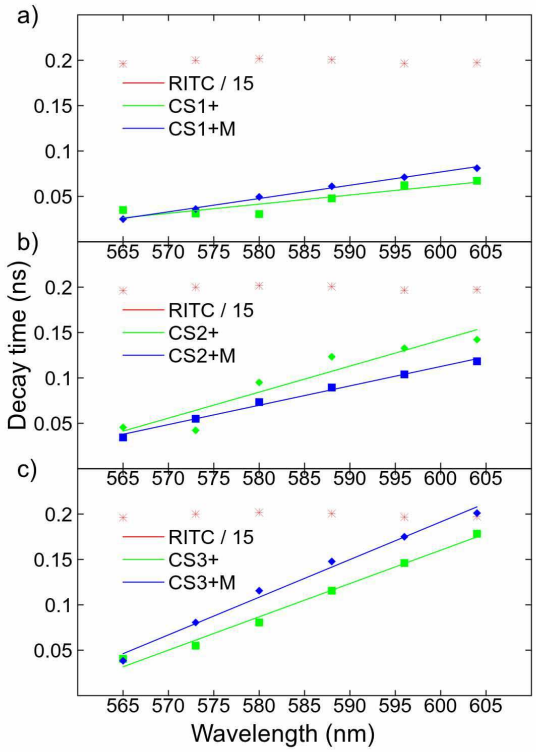

Fig. 7. Decay times as a function of silica shell thickness, 10 (a), 20 (b) and 30 *nm* (c) and as a function of the emission wavelength for the monomers CS+ and multimers CS+M. Also shown for comparison are the wavelength-independent decay times of pure RITC molecules in ethanol.The solid lines are linear fits of the decay times as a function of wavelength.

etc. while the simulated configuration concerns a single ideal dimer. Furthermore, although the CS particles synthesized in this study are very well controlled in size, shape and spacing distance between the RITC molecules and the gold core, they cannot be compared to an ideal case: the NPs are never perfectly spherical (Fig. 1), the silica shell acting as a spacer is not uniformly thick (Fig. 1), the control of the orientation of the RITC molecules with respect to the gold core surface is missing, etc. These factors make the LSP resonance shifting from one NP to another and the strength of the dipole-dipole interaction between the RITC molecules and the gold cores changing from one NP to another, explaining the origin of the non-exponential decay profiles shown in Fig. 6. As a whole, these factors also explain the slight (strong) reshaping on the long wavelength side of the spectra in Fig.5 for the CS+, CS+M NPs with respect to the emission spectra of RITC molecules: according to Fig. 2(b), the longer is the multimer in line probed, the longer is the wavelength of its LSP resonance and the more red-shifted will be the radiative signal from the nanoantennas. The NP thus also acts as a resonator that selectively enhances the probability of resonant transitions from the RITC excited state to a particular vibrational sublevel of the electronic ground state.

#149911 - $15.00 USD Received 27 Jun 2011; revised 26 Jul 2011; accepted 27 Jul 2011; published 24 Aug 2011
(C) 2011 OSA

Table 2. Slopes of the Linear Relationships Fitting the Experimental Curves Shown in Fig. 7

Sample	Slope (ns / 100 nm)
CS1+	0.10
CS1+M	0.15
CS2+	0.27
CS2+M	0.21
CS3+	0.37
CS3+M	0.41

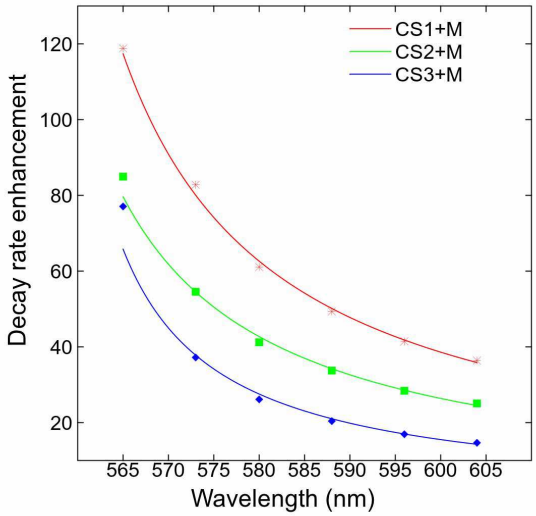

Fig. 8. Decay rate enhancement $g_t(\lambda)$ as a function of silica shell thickness (10, 20 and 30nm) and as a function of the emission wavelength for the multimers CS+1M, CS+2M and CS+3M. The solid lines are fits $g_t(\lambda) \propto \frac{1}{\lambda}$ of the decay times as a function of wavelength.

3. Conclusion

In conclusion, we have synthesized several types of size controlled, spherical monomer and multimer plasmonic nanoantennas with well defined silica shell thicknesses used as spacers between the active dye molecules and the gold core. We show shaping of the absorbance and emission spectra and modification of the decay rates as a function of wavelength and spacing between the metal NPs and the dye molecules. The decay rate enhancement is shown to decrease as the distance from the molecules to the NP increases and as the detuning between the long wavelength emission and the LSP resonance increases. The experimental and simulated results are in agreement. The shaping of the emission spectra and the origin of the nonexponential decay profiles of the various samples are explained as a result of both imperfections in the morphology of the NPs in both monomer and multimer samples and near field couplings bewteen neighbouring particles in the case of multimer samples. The strong reshaping of the spectra in the latter case make these nanostructures good candidates for long pass emission

#149911 - $15.00 USD Received 27 Jun 2011; revised 26 Jul 2011; accepted 27 Jul 2011; published 24 Aug 2011
(C) 2011 OSA

filters.

4. Materials and Methods

$60 \pm 5\,nm$ gold nanoparticles were synthesized through the reduction of hydrogen tetrachloroaurate (III) ($HAuCl_4$) in the presence of sodium citrate ($Na_3C_6H_5O_7.2H_2O$) and sodium borohydride ($NaBH_4$) according to the procedure published by Brown et al. [44] The gold particles were coated with a silica shell (CS NPs) according to the procedure published by Graf et al. [45] The thickness of the shell was controlled by changing the amount of silica precursor (tetraethyl orthosilicate, TEOS). The active particles (CS+) were obtained from the CS ones by firstly grafting a rhodamine B derivative with ethoxy-silano group, which was previously prepared by reacting rhodamine B isothiocyanate (RITC) with aminopropyltriethoxysilane in absolute ethanol [46], on the silica shell. To do so, an amount corresponding to 15 RITC molecules / nm^2 of silica surface was added in an ammonia (6 % v/v) / ethanol suspension of CS particles. The reactive medium was heated at $80^0\,C$ during 1h. The CS+ particles were collecvted by centrifugation and washed three times with absolute ethanol. A second protective silica shell of 10 nm diameter was then grown by dropwise addition of an ethanolic solution of TEOS [47]. The increase of the concentration of the CS or CS+ particles during the addition of the TEOS solution lead to the formation of multimers (mixture of dimers, trimers, quadrimers, heptamers, ...). These mulitmers are formed as a result of collisions between CS or CS+ particles and are permanently fixed via the hydrolysis and condensation of TEOS molecules on their surface [48].

Various experimental situations have been simulated by solving Maxwell equations using the three-dimensional finite-difference time-domain (FDTD method) [49], as implemented in the freely available MEEP software package [50]. The dielectric permittivity of gold was specified by using the Drude-Lorentz model with parameters determined by Vial et al. [51], based on the best fits, following a FDTD approach, to the relative permittivity of gold as tabulated by Johnson and Christy [52]. By Fourier-transforming the response to a short, broadband, spatially extended gaussian pulse in the far field of the passive structures and normalizing with the response in vacuum for the same excitation conditions, a single simulation yielded the reflexion spectra over a wide spectrum of frequencies. Similarly, in order to compute the emission properties $g_r(\lambda)$, $g_{nr}(\lambda)$ and $\eta(\lambda)$ for the active nanostructures, we performed Fourier-transforms of the response to a short, broadband, point dipole (electric current) gaussian pulse polarized along the axis joining the monomers in the dimer and located in the gap of the dimer. We then normalized this response with the one obtained in vacuum for the same excitation conditions.

Atomic Force Microscopy images were recorded by a commercial ICON AFM (from Brucker, Santa Barbara, CA) equipped with a $90\,\mu m$ scanner (EV-scanner). The samples were imaged using tapping-mode phase imaging and a standard silicon cantilever ($50\,N/m$, $300\,kHz$) to provide topographic and corresponding phase images. The particles were cast on a glass substrate by leaving a drop of a dilute suspension evaporating. TEM observations were performed with a Hitachi H-600 microscope operating at 75 kV. The UV-visible spectra have been recorded with a UNICAM UV/Vis spectrometer (UV4). The spontaneous emission properties of RITC molecules and the various active samples CS+ and CS+M in ethanol solutions were recorded with a spectral- and time- resolved setup consisting of a streak camera (HAMAMATSU Streak Scope C10627) pre-fitted with a spectrograph (Princeton Instruments) with a $100\,gr/mm$ choice of the grating. The excitation light was the frequency doubled output of the $\lambda = 1030\,nm$ wavelength, $10\,MHz$ repetition rate, $300\,fs$ line width pulses delivered by a diode-pumped Ytterbium femtosecond oscillator from Amplitude systems (t-Pulse 200). The beam was collimated to a $3\,mW$, $5\,mm$ diameter spot to excite the particles in a quartz cuvette prior to focus the $530\,nm$ long-pass filtered emission intensity on the entrance slit of the spectrograph.

#149911 - $15.00 USD Received 27 Jun 2011; revised 26 Jul 2011; accepted 27 Jul 2011; published 24 Aug 2011
(C) 2011 OSA

Acknowledgments

The authors acknowledge le Conseil Régional d'Aquitaine and the European Research Network FAME for the Ph.D scholarship of Mélanie Ferrié. Hassan Saadaoui is thanked for AFM measurements.

#149911 - $15.00 USD Received 27 Jun 2011; revised 26 Jul 2011; accepted 27 Jul 2011; published 24 Aug 2011
(C) 2011 OSA